

# **Testing and Analysis of Hybrid Composite/Metal Connections and Hull Section for the MACH Project**

## **Final Report for the Modular Advanced Composite Hull form (MACH) Technology Project**

by

Jean-Paul Kabche, Graduate Research Assistant,

Vincent Caccese, PhD. P.E , Associate Professor and Principal Investigator, and

Keith A. Berube, Research Engineer

Prepared for:



Office of Naval Research  
800 N Quincy St.  
Arlington VA. 22217-5660

Grant No. N00014-01-1-0916  
Dr. Roshdy G.S. Barsoum,  
Program Manager



University of Maine  
Department of Mechanical Engineering  
Orono, ME 04469-5711

**DISTRIBUTION STATEMENT A**  
Approved for Public Release  
Distribution Unlimited

March 2006

Report No. UM-MACH-RPT-01-01



## ABSTRACT

This report summarizes the development, testing and analysis of hybrid composite/metal connections and hybrid structural systems under the Modular Advanced Composite Hullform (MACH) project. The MACH project, funded by the Office of Naval Research, is part of a joint effort between the University of Maine, Navatek of Honolulu, HI, and Applied Thermal Sciences (ATS) of Sanford, Maine, and is performed in conjunction with the Naval Surface Warfare Center at Carderock, MD (NSWCCD). The primary motivation for the work summarized herein is to provide alternatives to conventional hull construction techniques and conventional hull forms by using modular hybrid construction methods. Included is a description of tests performed on sub-scale hybrid bolted connections, where the objective was to develop watertight connections for removable panels. An experimental study was conducted to quantify the performance of numerous hybrid joints with various geometries, loaded in flexure. The test results showed that for resisting bending loads, joints with doubler plates can be made stronger and rotationally stiffer than standard bolted joints, while also mitigating opening of the joint, thereby improving the ability to seal the connection for watertight integrity.

The results of this study were used to select a connection geometry, which was incorporated into the hydrostatic testing of a full-scale four-panel assembly. Testing of the assembly is described in this report and shows that a linear response of the system was observed up to its design pressure load of 82.74 kPa. Damage initiated as stiffener delamination at 1.4 times the design load. After failure of several stiffeners, the hybrid assembly withstood up to 3 times its design load without leakage. Hence, the response of the hybrid joint employed was deemed successful.

Numerical analysis of the connections and assembly are also presented. Simplified shell finite element models were developed at both local and global levels. These models were for estimation of the joint stiffness and good correlation with the test results was observed. Strength of the system was predicted using detailed plane strain contact models to capture the three-dimensional effects of the connection.

## **ACKNOWLEDGMENTS**

The authors gratefully acknowledge funding for this project through the Office of Naval Research under grant number N00014-01-1-0916. Dr. Roshdy G..S. Barsoum of ONR is the cognizant program officer. His support and encouragement is greatly appreciated. The authors would also like to thank Milt Crichfield, Loc Nguyen and Gene Camponeschi of NSWC Carderock (NSWCCD) for their assistance and advice throughout this effort. Furthermore, the support of the other partners involved, particularly Steven Loui, Todd Pelzer and Eric Schiff of Pacific Marine, Navatek Division and the guidance and support of personnel at Applied Thermal Sciences including Steve Webber, Kendrick Light, Larry Thompson and Josh Walls. The assistance of the project team at the University of Maine including research engineer Randy Bragg and undergraduate students Ryan Beaumont, Marilyn Nichols, Mike Robinson, Ethan Brush and Will Hotchkiss III.

# TABLE OF CONTENTS

	Page
ABSTRACT .....	ii
ACKNOWLEDGEMENTS.....	iii
1. INTRODUCTION .....	1
1.1. Overview .....	1
1.2. Project Background and Objectives.....	3
1.2.1 Previous Work Performed Under the MACH Project .....	6
1.2.2 Lifting Body Case Study .....	7
1.3. Objectives .....	8
1.4. Scope .....	8
2. LITERATURE REVIEW.....	10
2.1. Naval Structures and Composites.....	10
2.2. Material Systems and Manufacturing Methods.....	11
2.3. Hybrid Structures for Marine Applications.....	12
2.3.1. Connections in Hybrid Structures.....	14
2.4. Bolted Joints.....	14
2.4.1. Hybrid Composite/Metal Bolted Joints.....	16
2.4.2. Failure Modes in Composite Bolted Joints.....	17
2.4.3. Composite Bolted Joints Subjected to Axial and Flexure Loading .....	20
2.4.4. Composite Bolted Joints Subjected to Fatigue Loading .....	23
2.5. Summary of the Literature and Research Significance.....	25
3. STRUCTURAL TESTING OF HYBRID JOINTS UNDER FLEXURAL LOADING.....	26
3.1. Joint Testing Rationale.....	26
3.2. Joint Testing Objectives.....	26
3.3. Hybrid Joint Configuration and Geometry.....	27
3.3.1. Bolted Joints.....	27
3.3.2. Bolted Joints with Doubler Plates.....	30
3.4. Materials and Test Article Fabrication.....	37
3.5. Joint Testing Procedures.....	40
3.5.1. Test Setup.....	40
3.5.2. Testing Method.....	40
3.5.3. Instrumentation.....	44
3.5.4. Data-Acquisition Configuration.....	49
3.6. Joint Testing Results.....	50
3.6.1. Cyclic Response: Load versus Displacement Curves.....	50



	Page
3.6.2. Cyclic Response: Load versus Strain Curves.....	57
3.6.3. Load versus Displacement Envelopes.....	60
3.6.3.1. Load versus Displacement Envelopes for Bolted Joints.....	60
3.6.3.2. Load versus Displacement Envelopes for Bolted Joints with Doubler Plates.....	63
3.6.4. Failure Modes.....	65
3.6.5. Damage Load and Ultimate Load.....	70
3.6.6. Initial Joint Rotational Stiffness, $J$ .....	73
3.7. Hybrid Joint Selection for Large-Scale Panel Testing .....	75
4. STRUCTURAL TESTING OF A LARGE-SCALE, HYBRID PANEL ASSEMBLY UNDER HYDROSTATIC LOADING.....	77
4.1. Panel Testing Rationale.....	77
4.2. Panel Testing Objectives.....	77
4.3. Geometry of the Hybrid Panel Assembly.....	78
4.3.1. Component Panel Design and Geometry.....	80
4.3.2. Description of the Hybrid Joint Region.....	84
4.4. Materials and Test Article Fabrication.....	86
4.5. Panel Testing Procedures.....	90
4.5.1. Test Setup.....	90
4.5.2. Testing Method.....	95
4.5.3. Instrumentation.....	97
4.5.4. Data-Acquisition Configuration.....	108
4.6. Panel Testing Results.....	110
4.6.1. Load versus Displacement Curves.....	110
4.6.2. Displaced Panel Shapes.....	115
4.6.3. Correlation of Displaced Panel Shapes to Photogrammetry.....	116
4.6.4. Load versus Strain Curves.....	119
4.6.5. Failure Modes.....	125
5. FINITE ELEMENT ANALYSIS OF HYBRID BOLTED ASSEMBLY.....	129
5.1. Rationale.....	129
5.2. Finite Element Analysis Objectives .....	130
5.3. Local Finite Element Model Using Shell Elements .....	132
5.3.1. Finite Element Model Description.....	132
5.3.2. Computing the Effective Properties of the Hybrid Region.....	135
5.3.3. Local Shell Model Verification.....	139
5.4. Global Finite Element Model of Isolated Stiffened Panels.....	144
5.4.1. Verification of Isolated Panel Models.....	145
5.5. Global Finite Element Model of Hybrid Assembly.....	151
5.5.1. Global Finite Element Model Description.....	152

	Page
5.5.2. Modeling of the Hybrid Joint Region.....	154
5.5.3. Global Shell Model Verification.....	156
5.5.4. Parametric Study of Global Structural Response.....	165
5.5.4.1. Effect of the Doubler Plate Thickness.....	165
5.5.4.2. Effect of the Composite Thickness .....	168
5.5.4.3. Effect of the Flange Thickness (W8x31 and W14x53 I-Beams).....	171
5.6. Plane Strain Finite Element Model of the Hybrid Joint .....	177
5.6.1. Plane Strain Model Description.....	178
5.6.2. Contact Modeling.....	182
5.6.3. Modeling the Bolt.....	184
5.6.4. Model Verification.....	188
5.6.5. Plane Strain Modeling Results Using Contact and Spring Elements .....	189
5.6.6. Strength Prediction .....	201
6. CONCLUSIONS AND RECOMMENDATIONS.....	205
6.1. Sub-component Joint Testing .....	205
6.2. Panel Testing .....	206
6.3. Finite Element Analysis of Hybrid Connections .....	207
REFERENCES.....	208
APPENDICES.....	212
Appendix A. Material Specifications.....	212
Appendix B. Instrumentation Specifications.....	218
Appendix C. Load versus Outer Displacement Plots of Hybrid Joints.....	220
Appendix D. Load versus Middle Displacement Plots of Hybrid Joints.....	248
Appendix E. Load versus Inner Displacement Plots of Hybrid Joints.....	276
Appendix F. Load versus Strain Plots of Hybrid Joints.....	304
Appendix G. Assembly of Stiffened Panels and Doubler Plates onto the Hydrostatic Test Tank.....	332
Appendix H. Load versus Displacement Plots of Stiffened Panels.....	343

## **1. INTRODUCTION**

### **1.1. Overview**

The work presented herein was performed under the Modular Advanced Composite Hull-form (MACH) project, which focused on the development and testing of hybrid composite/metal structural systems for naval ship applications. The MACH project, funded by the Office of Naval Research, is part of a joint effort between the University of Maine, Navatek of Honolulu, HI, and Applied Thermal Sciences (ATS) of Sanford, Maine and is performed in conjunction with the Naval Surface Warfare Center at Carderock, MD (NSWCCD). The mission of the MACH program is to develop technology for fast efficient surface vessels that use the addition of underwater bodies attached to a more traditional hull-form. The primary motivation for the work, summarized herein, is to provide alternatives to conventional hull construction techniques and conventional hull-forms by using modular hybrid construction methods. One goal of the MACH project is to develop a methodology for design and construction of lightweight hybrid composite/metallic hull forms to be used on high-speed ships. The goal is to deploy ships where more payload and/or higher speeds can be achieved at little or no additional power consumption and with excellent sea keeping ability.

The implementation of composite materials in conjunction with metals into hybrid structural systems is currently being developed in several key applications such as ships, aircraft and other transportation vehicles. One example found in ship structures is where E-Glass/vinyl ester (EG/VE) composites are connected to a metallic framework, in order to enhance their functionality and environmental resistance. Hybrid systems such as this, where metals are used as the backbone of the structure and composites are used for the bulk of the system, are of particular interest. A hybrid structure can potentially be more advantageous than a single material system when cost, maintenance, weight, and structural performance are considered simultaneously.

Traditional hull-forms, however, have been constructed using steel and aluminum. Using metals for hull-form construction typically has made it difficult and costly to achieve complex hydrodynamic shapes, which in turn has led to higher structural weight.



Concerns over cost, weight, stealthiness and corrosion have led designers to look at advanced materials for hull form construction. Although very good in fatigue, carbon steel, for instance, is magnetic, dense and highly susceptible to corrosion when at sea, which translates into higher maintenance costs. Stainless steels solve the magnetic signature and corrosion issues, however they are typically costly. Aluminum, although lightweight, corrosion resistant and non-magnetic is prone to fatigue failures. In light of these disadvantages, advanced composite materials have emerged as a viable alternative to the conventional hull construction methods. Accordingly, EG/VE systems are of particular interest for large ship structures, provided that they can lead to superior hydrodynamic shapes, weight reduction and higher speeds. Additionally, using composites for the bulk of the structure could help achieve a more stealthy and corrosion-resistant structure. That being said, recent research such as Barsoum [2003] and Boyd [2004] have pointed to the difficulties associated with construction of an all composite naval vessel. Hence, the hybrid composite/metal concept has emerged as a viable alternative.

During the last few decades, the shipbuilding industry has been investigating innovative designs and manufacturing methods as a way to achieve greater performance and to reduce maintenance costs. For example, Navatek, Ltd., of Honolulu, HI, has successfully built experimental ships that incorporate lifting bodies, in order to provide enhanced sea-keeping through reduction in motions, higher lift-to-drag ratios, and greater compatibility with multiple hull types. The MIDFOIL, shown in Figure 1.1, is one example of these ships.

As a way to solve the issues that have slowed the development of the next generation of hull forms, the University of Maine (UMaine) teamed up with industry and Navy partners, in order to develop innovative, modular hull construction techniques for naval and civilian applications. This effort involving Navatek, ATS and NSWC-CD centered upon the case of applying hybrid construction to an underwater lifting body. The multi-year effort was named the Modular Advanced Composite Hull-form project (MACH). The collective project goal was to develop modular hull construction techniques for fast surface ship and hybrid hull applications.

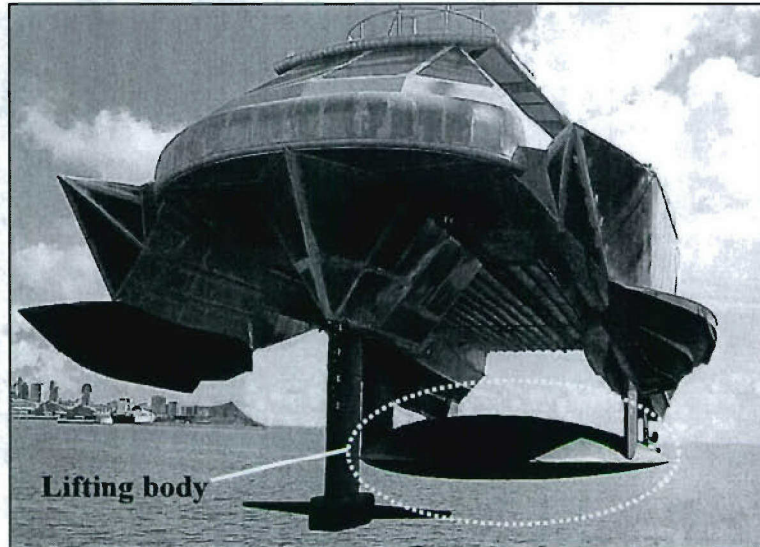


**Figure 1.1. Hybrid High-Speed Vessel, *MIDFOIL***

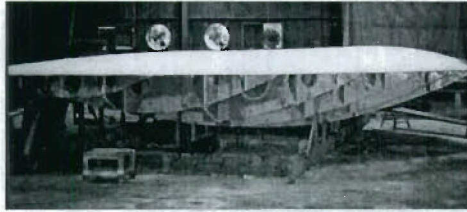
## **1.2. Project Background and Objectives**

The MACH concept was developed as a blending of marine and space technologies, as illustrated in Figure 1.2. Conventional composite ship construction was being used at the inception of this project in 1999, as demonstrated in Figure 1.2a. The composite MIDFOIL displacement pod was constructed in a monolithic fashion, as shown in Figure 1.3. This method has led to smooth hydrodynamic shapes, but has made internal access to the lifting body and ship hull a difficult task. Also, these vessels were designed for proof-of-concept testing and improvements are required if they are to be scaled up in size and deployed for long-term military or commercial use.

The panelized construction concept with removable panels was inspired by work conducted by the University of Maine in support of NASA's X-38 crew return vehicle project (Figure 1.2b). The highly complex outer shape of this spacecraft was attained by a system of composite panels over a metallic structural frame. The concept behind the X-38 structure led the University of Maine and Navatek to propose a panelized construction concept for advanced high-speed vessels. This transformed into the MACH concept, shown in Figure 1.2c, where complex shaped composite panels are joined to a metallic structural framework by bolting, adhesion, or welding of sub-components.



a) *MIDFOIL* Displacement Pod



- Conventional composites
- Internal access is difficult

b) NASA X-38 Panelized Composite Outer Structure



+

- Modular construction with removable panels
- Successful implementation

c) MACH Concept

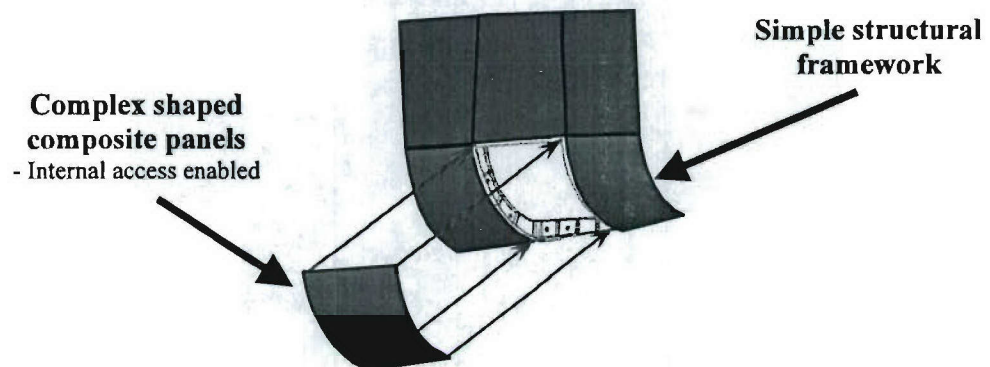


Figure 1.2. The MACH Concept: Blending of Marine and Space Technologies

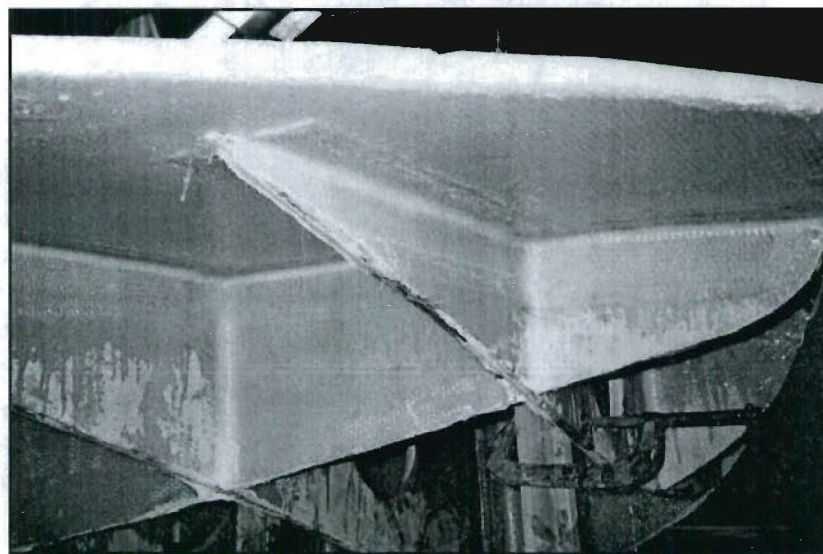
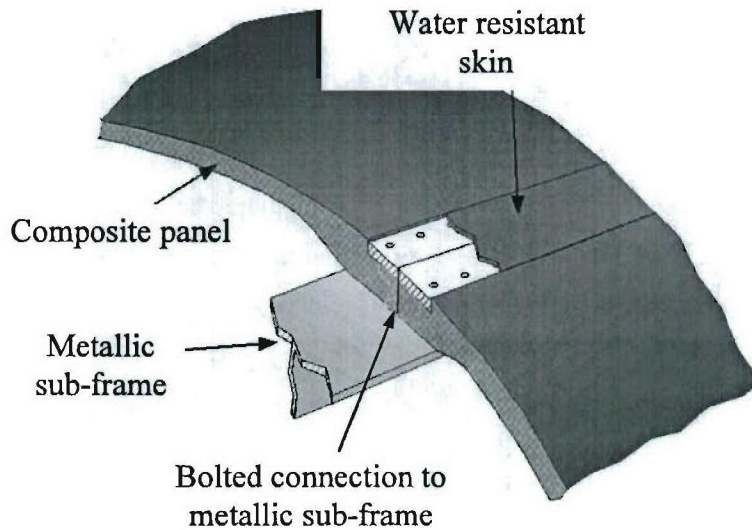


Figure 1.3. Monolithic Composite Construction

The overall objective of the MACH effort was to develop and demonstrate hybrid composite/metal systems and joining concepts for naval ship hull applications. The core of the project aimed at developing hybrid systems consisting of composite structural sections attached to a metallic supporting structure. By combining composite and metallic components, it is possible to take advantage of the beneficial properties of each material. In general, the complex shapes required for advanced ship designs will benefit from the use of composite materials in construction. This technology was demonstrated at both the joint sub-component level and at the hybrid system level as summarized in this report.

A schematic of the proposed MACH method for construction of a hybrid composite/metal version of an underwater lifting body with removable panels is shown in Figure 1.4. The concept consists of modular panels, made of composite materials, attached to a metallic sub-frame, by means of a bolted connection. The composite panel designs can be monocoque (unstiffened), rib-stiffened or sandwich construction, depending upon the geometry and loading requirements. The panels must be able to withstand the applied loads, while maintaining watertight integrity. The primary advantages of the MACH concept are summarized as follows:

- 1) Advanced hull shapes can be achieved due to the extensive use of composite materials for the bulk of the structure,
- 2) Use of composite panels instead of metallic skins is expected to decrease the overall weight of the system, which would make high-speed surface ships faster and more efficient for a given payload,
- 3) Modularity of the system (use of removable panels) would improve access to the hull and lifting body, which in turn would allow for ease of maintenance of equipment housed inside the lifting body, and
- 4) Use of a stiff metallic skeleton will facilitate the attachment of propulsion equipment, while providing structural integrity.



**Figure 1.4. Composite Panels over Metal Framework for Ships.**

#### **1.2.1. Previous Work Performed Under the MACH Project**

Several tasks were undertaken under the MACH effort which include: 1) Design and implementation of an underwater lifting body; 2) assessment of stress relaxation in composite bolted connections; 3) assessment of adhesives in connections; 4) study of cavitation erosion resistant systems; and 5) study of a hybrid system for the Sea Flyer lifting body. Along with construction of an underwater body by Navatek these efforts were compiled into prior reports, which are summarized as follows:

- 1) Detection of Bolt Stress Relaxation in Hybrid Bolted Connections by Mewer, Vel and Caccese [2003].
- 2) Mechanical Testing of Epoxy Adhesives for Naval Applications by Boone and Caccese [2003].
- 3) Influence of Stress Relaxation in Hybrid Composite/Metal Bolted Connections by Pelletier, Caccese and Berube [2005].
- 4) Development of a Cavitation Erosion Resistant Advanced Material System by Light and Caccese [2005].
- 5) Design and Analysis of a Hybrid Composite/Metal Structural System For Underwater Lifting Bodies by Thompson, Walls and Caccese [2005].



### 1.2.2. Lifting Body Case Study

Navatek Ltd. has built and deployed numerous experimental and commercial ships that incorporate lifting bodies, in order to provide enhanced sea-keeping through reduction in ship motion, higher lift-to-drag ratios, and greater compatibility with multiple hull types. The lifting body used on the Sea Flyer, shown in Figures 1.5 and 1.6, was a baseline for study in this MACH program. The Sea Flyer is a modified Surface Effect Ship, the (SES-200), which was reconditioned and retrofit with an underwater lifting body as shown in Figure 1.6. The MACH research team studied a hybrid version of the lifting body used on this vessel.



**Figure 1.5. SEA FLYER (photo courtesy of ONR via [www.military.com](http://www.military.com))**

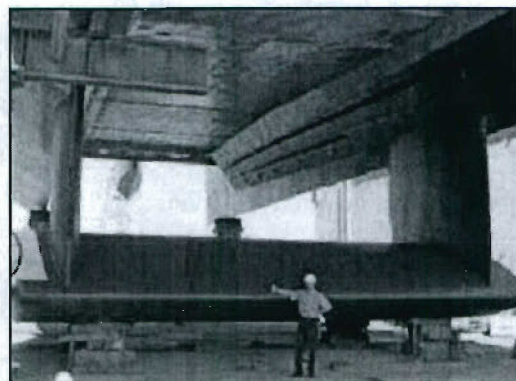


**Figure 1.6. Underwater Lifting Body (photo courtesy of Navatek via [www.military.com](http://www.military.com))**



### **1.3. Objectives**

The objective of this effort is to quantify the structural response of a hybrid composite/metal structural system with removable panels. The development of hybrid structures requires extensive research prior to their application. A robust and reliable hybrid structure depends upon an adequate connection between composites and metals. It is imperative to understand the inherently non-linear behavior of these joints, the interactions between the constituents, and the structural response in severe environments.

Both analytical and experimental studies were performed, including testing at the sub-component and component level. The intent was to perform a case study of the design and development of hybrid connections and a hybrid structural system implemented on an existing lifting body design. The main research goals of the work presented herein are as follows:

- 1) Structural testing of hybrid composite/metal joints. The current effort includes testing of various joint configurations at the sub-component level.
- 2) Hydrostatic testing of a large-scale, hybrid panel assembly to demonstrate the applicability and watertight integrity of hybrid joints at the component level.
- 3) Develop a simplified approach to model hybrid joints in large-scale structures, by using finite element analysis.

### **1.4. Scope**

Section 2 of this report provides a summary of the pertinent literature on hybrid systems, hybrid connections and bolted composite connections. Presented in Section 3 is a comprehensive experimental study performed to quantify the response of hybrid joints with different connection geometry. Connection details were chosen for their potential to be watertight and cost effective. A relative assessment of the structural response of these joints, loaded in flexure, is provided. This laboratory study served as a precursor to more complex and costly component panel studies, and as a verification tool for local finite element models of hybrid joints. Section 4 deals with the hydrostatic testing of a full-

scale, four-panel assembly. The modular panel assembly incorporated a hybrid joint, which was selected based on the sub-component joint test results. The assembly was loaded to failure, using uniform water pressure. This test served as verification of the design of the hybrid panel assembly, as well as proof of the joint concept and demonstration of the fabrication details and techniques using a VARTM process. Additionally, these results are used to verify the global finite element models.

Finite element analysis as presented in Section 5 was conducted in order to devise a simplified approach for modeling hybrid joints in large-scale structures. Models were validated using the experimental data available for both local and global systems. Parametric studies were conducted to observe the sensitivity of the structural response to changes in the joint geometry.

## **2. Literature Review**

### **2.1. Naval Structures and Composites**

The use of advanced composite materials in structural applications has been on the increase during the past several decades. In marine structures, composites have been used in small vessels and are potentially feasible for superstructures, decks, bulkheads, propellers, and other equipment on large ships. For large vessels, however, the implementation of composites for ship hull structural components is currently at the developmental stage. Increased use of composites has arisen with the intention to improve the structural performance of ships, while reducing manufacturing and maintenance costs. The numerous potential applications of composite materials for naval structures were outlined by Mouritz et al. [2001], and are illustrated in Figure 2.1 for a naval surface vessel.

According to Black [2003] and Kimpara [1991], modern naval ship designs have been primarily concerned with achieving lighter, faster, lower maintenance and more stealthy structures. Speed can be increased by the use of advanced propulsion systems, reducing structural weight and by implementing innovative complex shaping of the hull-form. Advanced materials and structural systems are required to achieve these goals. In turn, a departure from traditional hull construction methods, which primarily use aluminum and steel, is necessary. Mouritz [2001] stated that replacing metallic naval vessels and components with composites is a difficult and slow process, given that metals perform very well in most applications. Currently, complete composite hull sections can be found in relatively small naval ships, such as patrol boats and corvettes, or non-structural, non-critical components in large ships.

A paper by Gullberg and Olsson [1990] describes carbon fiber construction methods to manufacture various types of ships in Sweden. Chalmers [1994] has stated that, although the technology of composite materials in the marine industry is considered to have matured sufficiently, extensive research, empirical data and complete design guidelines are still required in order to safely and efficiently incorporate composite materials into larger-scale applications. This is particularly true when considering the



implementation of hybrid composite/metal components for long-term, commercial or military applications.

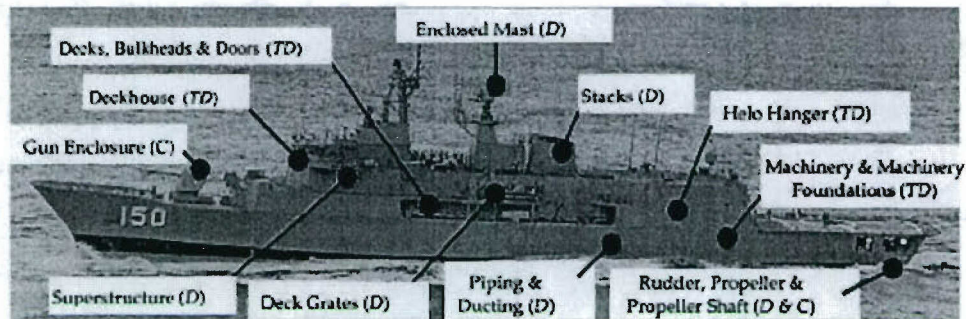


**Figure 2.1. Applications of Composite Materials for Naval Structures [Mouritz, 2001]**

## **2.2. Material Systems and Manufacturing Methods**

Ship structures are generally large and, in turn, require a vast amount of material for their construction. An efficient hull-form structure must be lightweight and stiff, in order to maintain its shape while resisting the applied loads. In addition, the structure must be fatigue, impact and shock resistant. To achieve these goals, it is essential to choose a low cost-per-pound material system and a manufacturing process that performs to requirements. One of the primary cost drivers in developing advanced hull-forms with conventional techniques is the metal forming of complex shapes. Using metals for the bulk of the structure has made it difficult to achieve complex hydrodynamic shapes. Hybrid composite/metal systems have emerged as a viable alternative to conventional construction and manufacturing methods, due to the ease of manufacturing complex shapes at relatively little incremental cost, when compared to fabrication with metals.

E-Glass/vinyl ester (EG/VE) systems are of particular interest for large ship structures, since they can lead to weight reduction and complex curvatures. Some of the major advantages of EG/VE systems, as outlined by Chu et al. [2004], are: 1) corrosion resistance; 2) relatively high ultimate failure strains; and 3) damage tolerance. Recently, much emphasis has been placed on the use of (EG/VE) systems, manufactured using a vacuum-assisted resin transfer molding process (VARTM). This process offers good strength characteristics which can be achieved at a much lower cost than, for example,

aerospace grade carbon fiber composites. As discussed by Critchfield and Judy [1994], the U.S. Navy has demonstrated the applicability of VARTM as a low-cost process for fabricating high-performance composite ship structures, including monocoque, single-skin stiffened, and sandwich configurations. Using composites for the bulk of the vessel could help achieve a more stealthy and corrosion-resistant structure, especially when used in combination with corrosion-resistant metals, such as stainless steel and aluminum.

In spite of their apparent advantages, Barsoum [2003] stated that composites alone lack the stiffness and strength to adequately withstand the loads of a large ship structure. Furthermore, in a quasi-isotropic lay-up, the elastic modulus of an EG/VE system is nearly one order of magnitude less than steel. The stiffness mismatch between composites and metals poses a great challenge when joining of these dissimilar materials. These observations will potentially cause designs that are typically performed on a strength basis, to become stiffness-driven, particularly when equipment requirements set a lower bound on the natural frequencies of the structure. For instance, a study by Alm [1983] estimated that a 50-m composite naval ship was 2.4 times less stiff than its steel counterpart. Similarly, an article by Boyd [2004a] states that an all composite ship structure greater than 150 meters is currently unfeasible, and that the application of hybrid composite/metal construction needs to be explored further.

### **2.3. Hybrid Structures for Marine Applications**

To alleviate the lack of stiffness of composite materials alone, the hybrid structure concept has arisen as a potential solution, where composites are used for stealth, weight savings and reduced maintenance purposes, and metals are used to achieve structural integrity. Barsoum [2003] discusses one example of this concept, where non-magnetic stainless steel is used in combination with composites in order to create hybrid hull-forms with low electromagnetic signatures.

Berube and Caccese [1999] identified a major type of hybrid structural system, which incorporates composite panels as skins attached to a metallic sub-frame, as shown in Figure 2.2. The composite panels can be monocoque (unstiffened), rib-stiffened or sandwich construction, depending on the geometry and loading requirements. Recently, Grenestedt and Sause [2005] tested a vierendeel truss version of this system using



composite sandwich panels over an AL6XN stainless steel frame. Another type of hybrid system consists of complete composite sections attached to metallic sections as described by Barsoum [2003]. An example of this system is the composite bow and stern shown in Figure 2.3, where composite sections are attached to an advanced stainless steel double-hull structure. In this case, the use of composites is advantageous due their ability to be shaped into the complex curves typically required for the bow and stern sections in advanced hull designs. Also, the potential weight reduction in the composite sections can mitigate shock loads.

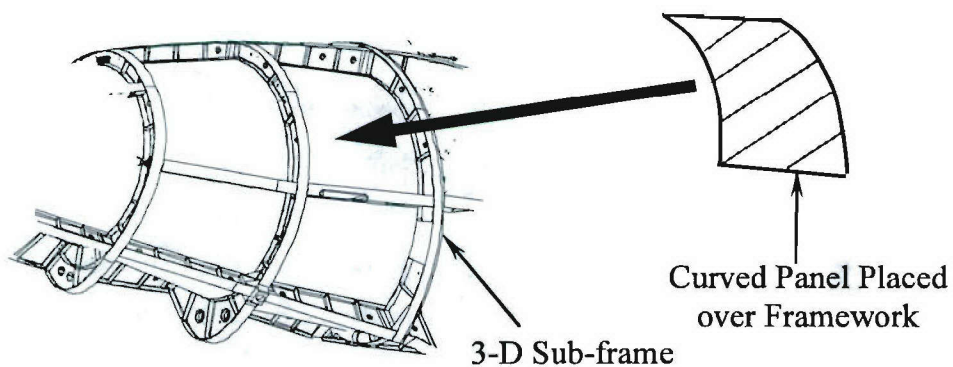


**Figure 2.2. Composite Panels Attached to a Metallic Sub-Frame [Berube and Caccese, 1999]**

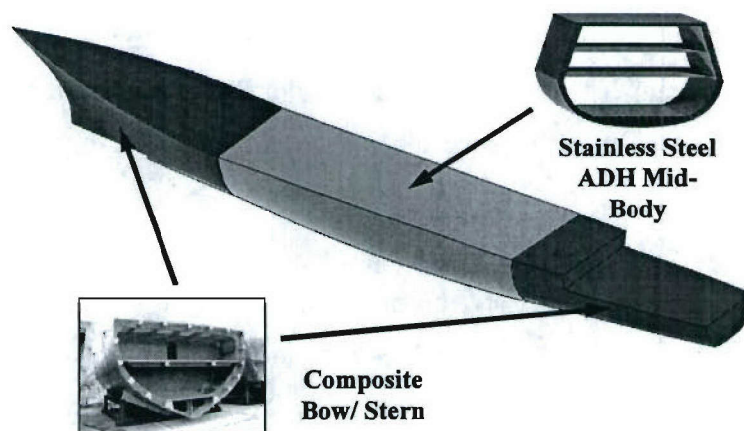


**Figure 2.3. Composite Sections Attached to Metallic Sections**



Due to the lack of availability of specific design guidelines for structures involving composite materials, the development of hybrid structures requires extensive research prior to their application. A robust and reliable hybrid structure relies upon the adequate connection between its composite and metallic components. Hence, a critical issue in the design of these structures is the joining of composite sections to metallic sub-structures [Dodkins et al. (1994), Pei and Shenoi (1996), Clifford et al. (2002), and Cao and Grenestedt (2003)]. In order to provide a safe design, it is imperative to understand the inherently non-linear behavior of hybrid joints, the interactions between their constituents, and the structural response in severe environments.

### **2.3.1. Connections in Hybrid Structures**

The application of hybrid composite to metal structures has been gaining momentum over the past several years. Accordingly, hybrid composite/metal connections are required that can withstand the applied loads and other environmental effects. Connection details are application specific, especially for cases where composites need be connected to metal structures. Several studies have emerged recently with regard to ship applications of composite/metal joints. Cao and Grenestedt [2003] describe the testing of a sandwich panel to metal interface, where they looked at the change in structural response with embedment depth of the interface. They concluded that placement of the steel has a significant effect on the strength and should be moved away from the point of stress concentrations. Boyd et al. [2004a, 2004b] describe an embedded metal joint connecting a composite sandwich panel to a steel deck for a helicopter hangar. In this application, a steel plate was embedded at the end of a tapered composite sandwich section panel made from FRP skins and a balsa core. The fatigue life and residual strength were evaluated for this joint.

### **2.4. Bolted Joints**

Mechanical joints are the preferred method to assemble structural members in cases where removable sections are required. Their main advantage over other techniques is that it is easy to disassemble the structure, which facilitates maintenance and allows for replacement of damaged parts. Researchers have conducted numerous

studies on composite bolted joints to identify the key parameters affecting joint efficiency. In particular, it is necessary to understand the mechanisms that induce damage and the loads at which failure occurs. The single-bolt configuration, regardless of the type of lap joint, is the most commonly used configuration for experimental and analytical studies found in the literature. However, in the majority of practical engineering applications, multi-row bolted joints are used to transfer loads between components.

Bolted joints are critical structural regions and must be properly designed so that the desired performance from the overall structure is obtained. Because of large stress concentrations, joints can become a source of weakness if proper design practice is not followed. Accordingly, failures typically occur at connections and interfaces, rather than within the bulk of the system. To provide a safe and cost-effective joint design, it is typical to configure the joint with respect to the geometry and the constituent materials, which affect both strength and failure modes.

The simplest type of mechanical joint is the single-lap joint, shown in Figure 2.4, in which two members are joined together by using a bolt or rivet. The key geometric variables used in design are: hole size ( $h$ ), bolt diameter ( $d$ ), end distance ( $e$ ), width of the member ( $w$ ) and member thickness ( $t$ ). While this joint scheme may be the most weight efficient due the few parts involved when loaded in-plane, the eccentric load path induces undesirable bending moments, commonly known as secondary bending. According to Vangrimde and Boukhili [2003], secondary bending typically leads to lower strength values. In order to mitigate the moment caused by the load eccentricity, the double-lap joint configuration, shown in Figure 2.5, was introduced. The double-lap connection requires at least two fasteners and two doubler plates. Bending moments will not be introduced when this connection is subject to in-plane loads.

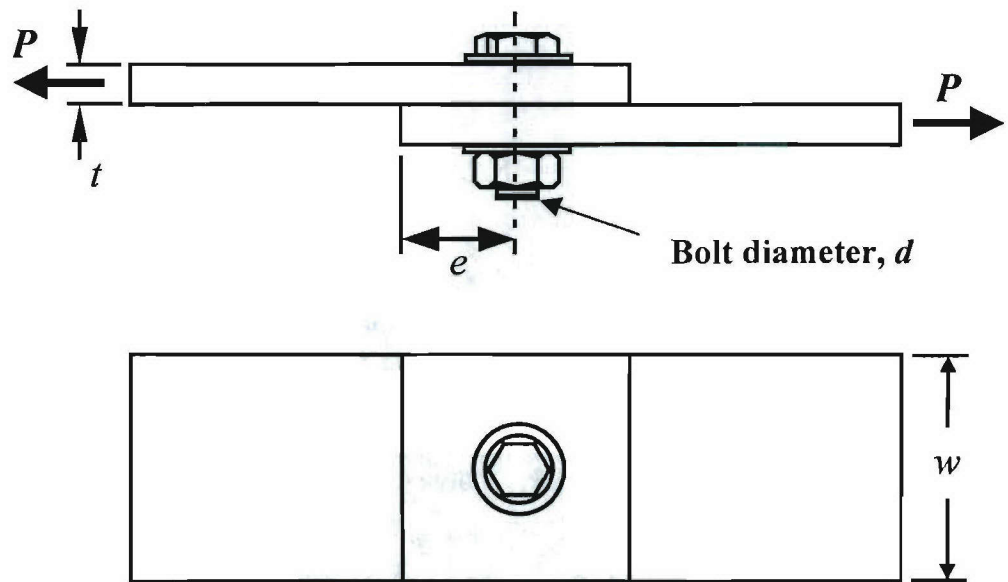


Figure 2.4. Bolted Joint: Single-Lap Configuration

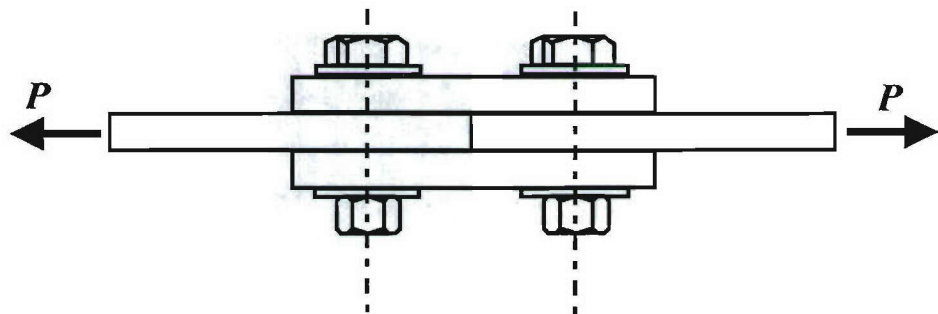


Figure 2.5. Bolted Joint: Double-Lap Configuration

#### 2.4.1. Hybrid Composite/Metal Bolted Joints

Joining composite materials and metals is more complex than joining isotropic materials, due to the interfaces, material property mismatch, large number of possible lamination configurations and the difficulty to accurately predict failure loads. Since most isotropic metals exhibit plastic behavior, yielding may occur in regions of high stress and shift some of the load resistance to lower stress regions. On the other hand,



composites are generally elastic until failure occurs, and stress concentrations may give rise to catastrophic and unexpected failures.

The apparent difficulties in composite joint designs and the potential consequences of in-service joint failures result in the use of large factors of safety. There is a constant need for more detailed information about the behavior of these joints in order to improve the design methods. A comprehensive report on joint design for naval vessels was compiled by Bonanni et al. [2001], in which joint design guidelines for naval ship construction and multiple examples of hybrid connections are presented.

#### **2.4.2. Failure Modes in Composite Bolted Joints**

Failure modes in composite bolted joints have been well documented in the literature. Vangrimde and Boukhili [2003], Persson and Eriksson [1999], Camanho and Matthews [2000] and Ireman et al. [2000] are some examples. Failure is typically divided into macroscopic and microscopic categories. Macroscopic failure refers to a damage state at which a structure is no longer able to withstand an increase in the applied loads. This type of failure is readily observable and indicates a significant loss of stiffness. In other words, macroscopic failure is considered to be the final stage in the damage development process. In bolted composite laminates, the prominent macroscopic failure modes are: net-section, bearing, shear-out and bolt failure.

The net-section mode, depicted in Figure 2.6, refers to failure transverse to the direction of the bolt load and is mainly initiated by tangential and compressive stresses acting at the edge of the hole. For a joint subjected to uniaxial loading, net-section failure typically occurs when the ratio of by-pass load (load applied to the plate) to bearing load (load going through the bolt) is high, or when the ratio  $d/w$  (bolt size to plate width) is high.

Bearing failure, shown in Figure 2.7, consists of damage to the area near the contact region between the laminate and the bolt, and is a direct result of the compressive stresses acting on the surface of the hole. The bolt pre-load (lateral constraint) strongly affects this mode, since lateral constraint prevents delamination and buckling of the fibers. Bearing occurs when either the ratio of the bearing load to the by-pass load is high or when the  $w/d$  ratio is high.

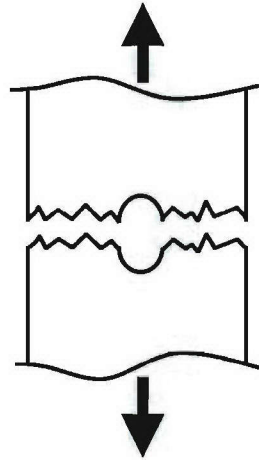


**Figure 2.6. Net Section Failure Mode**

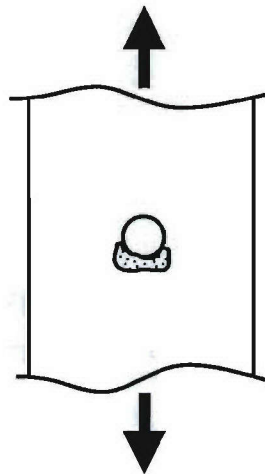


**Figure 2.7. Bearing Failure Mode**

Shear-out failure occurs along shear-out planes on the boundary of the hole in the principal direction of the bolt load, as shown in Figure 2.8. This mode is most common for joints with short end distances ( $e$ ). However, it may also occur for highly orthotropic laminates, regardless of the value of  $e$ . Shear-out failure can be avoided by an appropriate selection of lamination scheme and end distance.

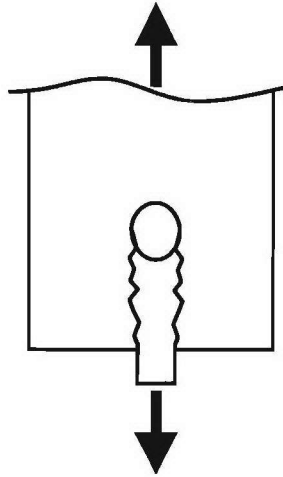


**Figure 2.8. Shear-Out Failure Mode**

The bolt failure mode, shown in Figure 2.9, occurs as a consequence of high shear stresses in combination with bending stresses in the bolt. This mode typically occurs as a secondary failure, following the onset of bearing failure.

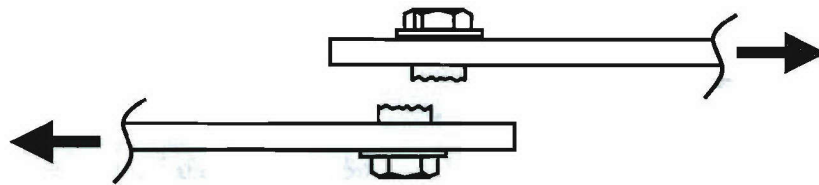


**Figure 2.9. Bolt Failure Mode**

In joint design, all failure modes should be considered. Bearing failure is the preferred mode in composite bolted joints, as the joint can continue to withstand loads beyond the onset of failure. The other failure modes are usually catastrophic and do not provide the opportunity to resolve the onset of damage before ultimate failure occurs. A study by Vangrimde and Boukhili [2003] found that the development of bearing failure assures the highest strength for a single-bolt joint. Hart-Smith [1991] stated that high-strength joints with multiple bolt rows are often critical in tension due to high by-pass loads in the innermost bolt row.

Design charts for composite bolted joints loaded in tension, for both single-bolt and multi-bolt configurations, are often found in the literature [Hart-Smith (1978),



Cooper and Turvey (1995) and Collings (1977)]. These charts relate the geometric ratios,  $e/d$  and  $w/d$ , to specific failure modes and are geared towards helping the design engineer avoid the aforementioned macroscopic failure modes. An example of these charts, as presented by Cooper and Turvey [1995], is shown in Figure 2.10.

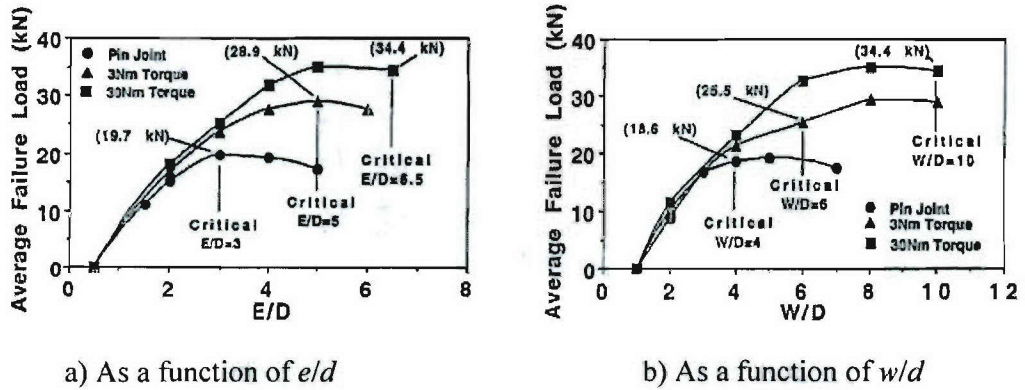


**Figure 2.10. Average Joint Load Capacities for Different Bolt Pre-Loads [Cooper and Turvey, 1995]**

Microscopic failure refers to damage that occurs near the edge of the holes in bolted laminated composite materials. Damage of the structure initiates at the microscopic level, becomes macroscopic damage and consequently leads to final rupture of the structure. Microscopic failure modes include: tensile, compressive and shear fiber and matrix failure, debonding and delamination between plies. For example, hole machining is a clear source of microscopic damage. Improper drilling techniques may lead to delamination and fiber fracture, which will ultimately have an influence on the strength and fatigue resistance of the structure.

#### 2.4.3. Composite Bolted Joints Subjected to Axial and Flexure Loading

An experimental study by Collings [1982] investigated the factors affecting the strength of bolted joints in multi-directional carbon fiber reinforced polymer (CFRP) laminates. For single-hole joints loaded in tension, the ultimate strength was found to be strongly dependent on ply orientation, bolt size ( $d$ ) and specimen width ( $w$ ). It was also observed that the best overall performance was exhibited by  $\pm 45^\circ$  laminates. In multi-hole joints, no adverse interaction was observed between holes. In other words,

increasing the number of holes did not cause a discernable loss in joint efficiency, for the set of parameters investigated.

Ireman et al. [2000] conducted an experimental investigation to characterize the damage development around holes in bolted graphite/epoxy single-lap joints, subjected to quasi-static tension. The laminates were fabricated from the unidirectional pre-preg system HTA/6376, and quasi-isotropic and zero-dominated lamination schemes were investigated. It was found that, in general, specimens with tapered-head bolts have a lower strength than those specimens with protruding-head bolts. The difference in joint strength between tapered-head and protruding-head joints decreases as the diameter of the tapered-head bolt increases. Secondary bending was observed to occur as a consequence of significant joint damage. The failure sequence was determined to initiate as matrix cracking at 25 percent of the failure load, fiber fracture at 35 percent of ultimate failure, and delamination at 70 percent of final rupture. Joints with quasi-isotropic lay-ups exhibited higher strength and slower failure sequences than those joints with zero-dominated lay-ups.

Cooper and Turvey [1995] conducted an experimental investigation for double-lap, single-bolt joints, loaded in tension. The laminates were manufactured from a pultruded fiberglass reinforced polyester (FRP) flat sheet material. Eighty-one specimens were tested to determine the effects of the geometric ratios,  $e/d$  and  $w/d$ , and bolt clamping torque on the strength of the joint. Their results showed that fully clamped joints increased in strength by as much as 80 percent. It was also found that the initial joint stiffness was mainly affected by the  $w/d$  ratio, while the effect of the  $e/d$  ratio and the bolt clamping torque was small.

Smith et al. [1986] conducted a similar investigation on the strength of CFRP single-lap bolted joints loaded in flexure, as a function of plate width ( $w$ ) and edge distance ( $e$ ). The results of the study revealed that the effects of overall joint bending were a likely factor in the reduced strength observed in single-lap joints, when compared to double-lap joints. Also, larger values of  $w/e$  (plate width to edge distance ratio) led to higher strength values.

A study by Oh et al. [1997] investigated the influence of ply angle, lamination sequence, ratio of constituent materials, and clamping pressure, on the strength of double-



lap, bolted joints loaded in tension. Glass/epoxy and carbon/epoxy laminates were tested. It was found that the bearing strength increased as the  $\pm 45$  plies were distributed evenly in the thickness direction, regardless of the ratio of the constituent materials. It was also observed that higher bearing strength values could be attained as the bolt clamping pressure was increased.

A study by Cohen et al. [1995] provided a strength comparison of multi-row bolted composite joints under axial loading, as a function of the number of holes (3, 5, 7 and 9 holes) and the lamination sequence. The laminates were fabricated using Hercules IM7G/3501-6 graphite/epoxy pre-impregnated tape and cured in an autoclave. The lamination sequence used represents a typical lay-up for joint regions of a composite rocket booster. With a total of 168 plies and a laminate thickness of 26.04 mm, the sequence was as follows:  $[\{(\pm 15)_3/90_2/0/\pm\theta/0/\pm\theta/0/\pm\theta/0/\pm\theta/0/\pm\theta/0/90_2\}]_6/[(\pm 15)_3]$ , where  $\theta = 30, 45$ , and  $60$  degrees. The test results showed higher strength values for the joint specimens with 9 holes. For a given number of holes, joint configurations with  $\pm 45$  reinforcing plies attained the highest strength values, when compared to joints with reinforcing fibers oriented at  $30$  and  $60$  degrees. When compared to 3-hole specimens, 9-hole joints only resulted in a 4 percent strength increase. Hence, for experimental purposes, the three-hole joint configuration was recommended as the most affordable and not overly conservative joint, when considering joint strength.

Starikov and Schön [2001] conducted an experimental investigation on the quasi-static behavior of single-lap and double-lap, protruding-head, bolted joints loaded in tension and compression. The composite plates were made of carbon fiber/epoxy (HTA7/6376) using two lamination sequences: 1) quasi-isotropic  $[(\pm 45/0/90)_3]_s$ , and 2)  $(\pm 45/0/90/0_4/90/0_3)_s$ . The plates were joined by two (single-bolt row), four (double-bolt row), and six (triple-bolt row) titanium, protruding-head bolts. The results of these tests showed that the specimens joined with three bolt rows (either single-lap or double-lap joints) exhibited the highest quasi-static tensile and compressive strengths. It was also observed that, for the same specimen type, the ultimate strength and strain values were higher for the compressive loading case. The lowest resistance to quasi-static loading was observed for specimens with a single row of bolts. However, multi-row joints failed catastrophically in net-section, while single-row joints failed in bearing mode. Load-



transfer measurements between different bolt rows showed that, in general, the first bolt row transfers the largest amount of load.

#### **2.4.4. Composite Bolted Joints Subjected to Fatigue Loading**

The relationships between material properties, geometric variables, lamination sequence, failure loads and failure modes in composite bolted joints have been the subject of much of the research found in the literature. Persson and Eriksson [1999] conducted an experimental investigation with the objective of ranking the factors that most significantly affect strength and fatigue life in multi-row, carbon-epoxy bolted joints, using a linear regression analysis. For static loading, it was found that the most influential factors were the bolt diameter to laminate thickness ratio ( $d/t$ ), the bolt pre-load, and the bolt-head type. Use of protruding-head bolts increased the gross section strength, when compared to tapered-head bolts. Variation in pre-preg type for a given fiber type and environmental conditions were found to have a lesser effect on the strength.

In the same study, Persson and Eriksson [1995] also investigated the joint response when subjected to fatigue loading of constant amplitude, with initial deflections varying no more than 0.05 mm. In the latter part (from 90 percent) of the fatigue life, deflections increased catastrophically due to the addition of the local stiffness loss. It was concluded that damage may have been growing without affecting the overall structural response of the specimen, until a critical point was reached. At this point, the significant stiffness loss caused large deflections which resulted in sudden and catastrophic failure of the laminate.

Herrington and Sabbaghian [1993] studied the effects of the load magnitude, orientation of reinforcing fibers, and bolt pre-load on the fatigue life of composite bolted joints. Their results showed that the outer ply angle had a small effect on the joint strength. The most influential factor was found to be the bolt pre-load, which increased the joint strength. It was also suggested that the pre-load could increase the fatigue life of the joint.

Starikov and Schön [2002a] performed experimental studies on the fatigue resistance of single-row and multi-row, composite bolted joints with protruding-head

bolts. Quasi-isotropic and highly orthotropic lay-ups were investigated. The results of the protruding-head bolted joint tests indicated that a multi-row configuration with a quasi-isotropic lay-up displayed the highest fatigue resistance. Bolt failure was the dominant mode. For all lay-ups, the fatigue behavior of the composite joints was observed to vary linearly with the number of bolts.

Starikov and Schön [2002b] performed a similar fatigue study for joints with tapered-head bolts. Three types of bolts were used: all-composite fasteners (ACF), titanium torque-set bolts, and titanium Huck-comp bolts. The results showed that joints using titanium bolts attained a higher fatigue life than those using composite bolts. At high load levels, the fatigue resistance of specimens with Huck-comp bolts was comparable to that of joints with protruding-head bolts. It was concluded that failure of the joints with composite bolts was due to the low ability of the bolts to carry cyclic shear loading. The dominant failure mode observed was bolt fracture.

Benchekchou and White [1995a] conducted both theoretical and experimental studies to determine the stresses around bolts in composite joints subjected to fatigue loading. The cantilever-type specimens, made of CFRP and XAS/914 CUD material, were subjected to cyclic loading. Three different quasi-isotropic lamination sequences were investigated. Three-dimensional finite element analysis was used to determine the highest normal and shear stress regions. The experimental results showed that the greater the flexural amplitude, the more quickly damage initiated in the plates. Damage developed earlier for plates with smaller holes, when compared to those with larger diameter holes. For a given applied load, the reduced area between the bolt and the laminate led to higher stresses, which resulted in delamination. It was also observed that, for all bolt diameters and flexural amplitudes,  $[(\pm 45/0/90)_2]_s$  was the most fatigue-resistant lamination sequence. Finite element results showed that the maximum stresses occurred near the holes, where the bolt-head is positioned, when the structure was loaded away from the fixed support. When loaded towards the support, some of the maximum and minimum normal and shear stresses occurred near the holes, while other stresses occurred at the edge of the plate. For a given end displacement, stress values around the holes were lower for bending towards the clamp than away from the clamp. Analytical data was compared with the experimental results, with an 8 percent difference.



Benchekchou and White [1995b] conducted the same type of fatigue study for joints with tapered-head bolts. Higher shear stresses were observed for joints with tapered-head bolts than those with protruding-head bolts, as fewer fatigue cycles were needed to initiate damage. A direct correlation between high normal and shear stresses from the models and initiation of delamination and shear cracks in the experiments was observed. High normal and shear stresses occurred in the regions around the holes, with maximum stresses occurring in the first and last  $\pm 45$  plies. Changing the bolt pre-load did not affect the maximum normal and shear stresses. Both the finite element models and the test results showed that the  $[(\pm 45/0/90)_2]_s$  lay-up was the most resistant to fatigue loading.

## **2.5. Summary of the Literature Findings and Research Significance**

The summary of the literature shows that considerable research has been conducted on composite bolted joints subjected to in-plane and fatigue loads. For the most part, researchers have outlined the major factors affecting the joint capacity and the types of failures that may occur under various loading conditions. The geometric ratios, the bolt pre-load, and the lamination sequence have been ranked as the most influential factors affecting the structural integrity of the joint. Because of the inherent difficulty of predicting failure in composite bolted joints, these investigations have typically involved comprehensive experimental programs.

A few papers have stated that hybrid joints are considered to have great potential for future engineering applications, but are currently at the developmental stage. A limited number of major investigations on hybrid systems were found in the literature and this is an area that requires further research. In order to characterize the structural behavior of hybrid joints, these systems need to be investigated experimentally and their applicability for large-scale structures needs to be demonstrated at the sub-component and component levels. An extensive experimental investigation, including in-plane, flexural, and fatigue loading, is required to achieve these goals. Accordingly, the study presented herein aims at providing a comparative study of the performance of various hybrid bolted joint configurations loaded in flexure. Also, this study provides a basis for assessing the applicability of hybrid joints to underwater marine structures.



### **3. Structural Testing of Hybrid Joints Under Flexural Loading**

#### **3.1. Joint Testing Rationale**

In marine applications, any vessel using composite materials for the bulk of the system will require hybrid connections of some sort, where composite components are attached to metallic sub-structures. The structural integrity and performance of a ship will be strongly influenced by the performance of attachments and internal connections. Therefore, assessing the structural integrity of a hybrid system must include detailed studies of the connection behavior. An accurate appraisal of structural integrity depends primarily on proper assessment of the structural response of the connections and interfaces and a sound estimate of the loads that induce failure. Accordingly, a thorough investigation of the hybrid connection mechanics is an essential part of this research.

#### **3.2. Joint Testing Objectives**

One of the primary objectives of the MACH project is to develop a watertight, hybrid composite/metal joint for lifting body structures. In doing so, it is desired to attach removable, modular composite panels to the metallic lifting body sub-structures. Because dissimilar materials are being joined, the connection of composite sections to metallic components is a critical issue in the design of hybrid systems. Hybrid joint design is more complex than conventional metallic joints, because of the dissimilar interfaces and the numerous failure modes that can be induced by the use of composite materials. Hybrid joints are inherently non-linear and characterization of their behavior requires complex analytical models that need experimental verification. In order to provide a reliable design, it is imperative to investigate the non-linear connection mechanics, the interactions between the constituents, and the response of the system under severe environmental conditions.

Marine structures are subjected to in-plane and out-of-plane loads, and are therefore susceptible to both through-the-thickness and bending failure modes. The experimental study presented in this section is aimed at assessing the structural response of hybrid joint specimens subjected to primarily flexural loading. For this investigation, hybrid joint test

articles were isolated as sub-components of the large-scale panel assembly. Test articles were configured with representative panel cross-sections and representative interface attachment conditions. The primary goal was to develop a watertight joint that would maintain a hydrodynamic profile when implemented into a modular, four-panel assembly of the lifting body structure. The relative performance of various joint designs was assessed on the basis of initial joint rotational stiffness, strength, and the types of failure modes observed.

Sub-component testing was conducted to evaluate critical panel configuration parameters, such as panel attachments, tapering, and use of stiffening doubler plates and foam inserts. This testing phase is a precursor to the more costly and geometrically complex testing of a large-scale, modular panel assembly, presented in Section 4. Additionally, the experimental data obtained from these tests can be used to verify analytical models and to develop design guidelines for hybrid joints.

### **3.3. Hybrid Joint Configuration and Geometry**

Potential hybrid joint configurations were judged and selected based upon their ability to be made watertight, smooth shaped, and cost effective. A total of fifteen joint specimens were tested. Specimens were grouped into two main categories: bolted joints and bolted joints with doubler plates. The major geometric parameters investigated were: bolt type, bolt diameter, and doubler plate geometry.

#### **3.3.1. Bolted Joints**

The bolted joint sub-component, presented in Figure 3.1, was selected as the baseline for the experimental investigation, as this configuration is common in practice and is relatively inexpensive to manufacture and assemble. The joint consists of two composite beams attached to a steel I-beam member by using two rows of bolts, with three bolts per row. Both protruding-head and tapered-head, grade 8, steel bolts, were used for this study. Tapered-head bolts entail more work during installation, but provide a smooth top surface, when compared to protruding-head bolts. To better distribute the clamping force through the thickness of the joint, steel washers were used at the top and bottom surfaces of the specimens with protruding-head bolts, and at the underside of the steel I-beam member for

specimens with tapered-head bolts. The baseline geometry of the bolted joint sub-component is presented in Figure 3.2. Table 3.1 provides a description of the geometric parameters used.

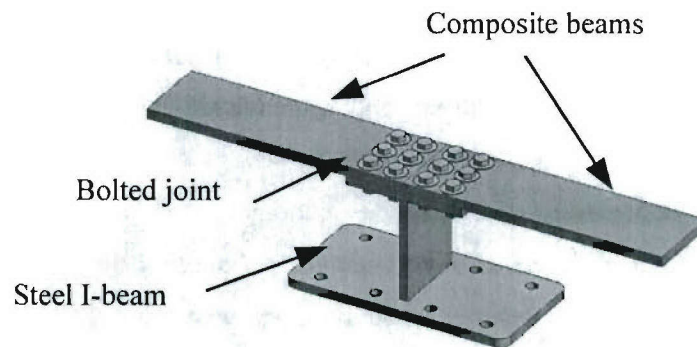


**Figure 3.1. Schematic of the Bolted Joint Sub-Component**

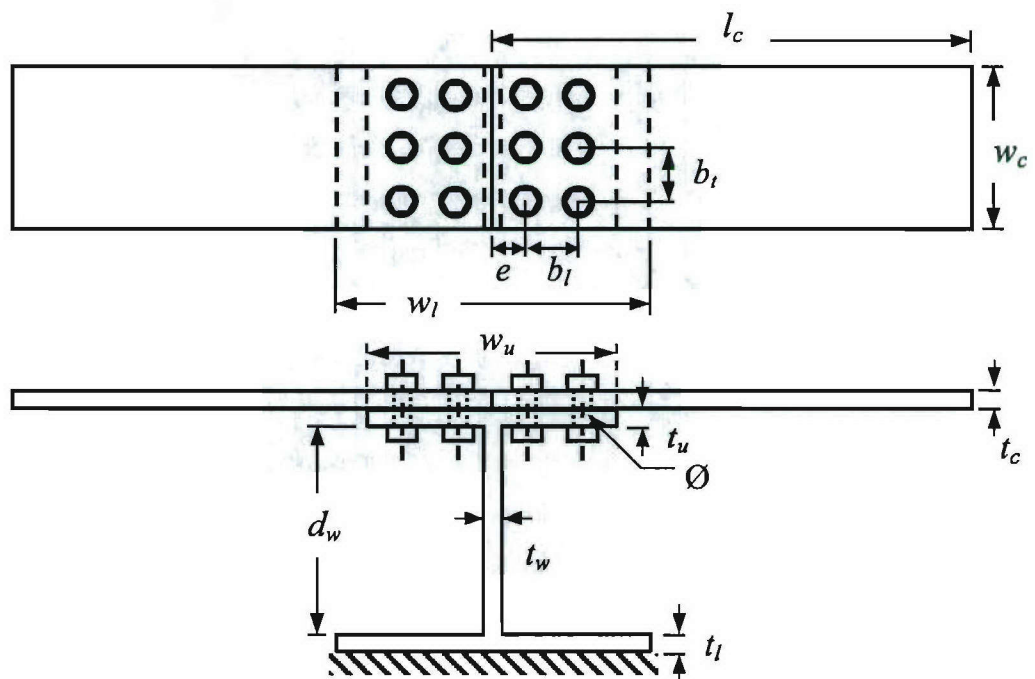


**Figure 3.2. Baseline Geometry of Bolted Joints**



**Table 3.1. Geometric Parameters of Bolted Joints**

Symbol	Description	Dimension (mm)
$l_c$	Length of the composite beam	381
$w_c$	Width of the composite beam	174
$\emptyset$	Bolt diameter	12.7; 19
$b_l$	Bolt-hole spacing in the longitudinal direction	57
$b_t$	Bolt-hole spacing in the transverse direction	57
$e$	Edge distance	38
$t_c$	Thickness of the composite beam	19
$t_u$	Thickness of the upper steel flange	19
$t_l$	Thickness of the lower steel flange	19
$w_u$	Width of the upper steel flange	267
$w_l$	Width of the lower steel flange	508
$t_w$	Thickness of the steel web	19
$d_w$	Depth of the steel web	229

The composite and steel I-beam assembly is a representative section of the hybrid joint of a modular panel region, at the sub-component level. Steel I-beams represent the metallic sub-structure or skeleton of the vessel, and the composite panels represent the acreage of the structural skins. In order to appropriately simulate an interface condition between two bolted panels at the hybrid joint region, the composite beams were assembled as double cantilever beams. In other words, the composite sections were not continuous through the joint region. Figure 3.3 shows a variation of the bolted joint concept, in which gussets were welded to the steel flanges of the I-beam members to increase the stiffness of the flange and ultimately the joint rigidity.

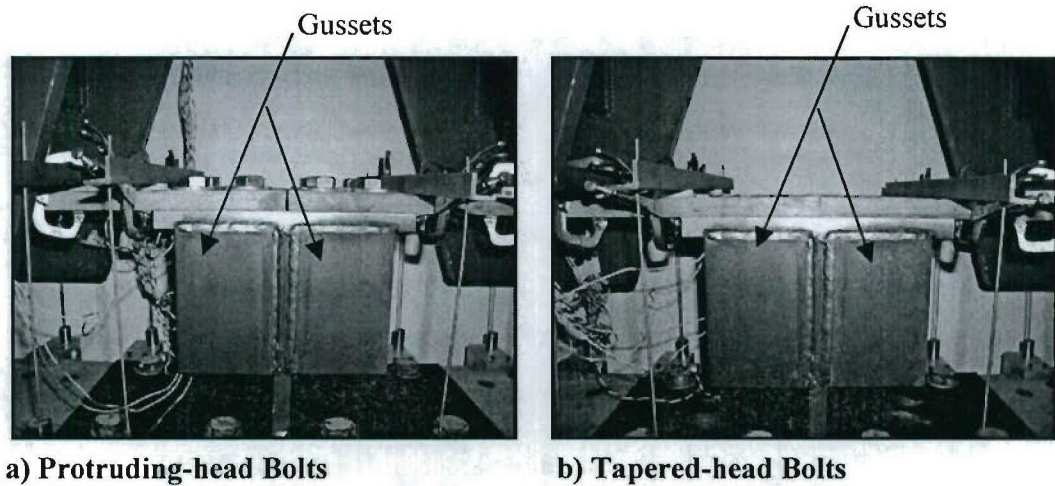


**Figure 3.3. Bolted Joint Specimens with Steel Gussets**

### **3.3.2. Bolted Joints with Doubler Plates**

A schematic of the bolted joint with doubler plate concept is shown in Figure 3.4. This joint consists of two composite beams sandwiched between the flange of a steel I-beam member and a steel doubler plate. These members are joined by using one or two rows of grade 8, tapered-head, steel bolts. Steel washers were used at the underside of the steel flanges. Figure 3.5 shows the baseline geometry of the bolted joint with doubler plate configuration and its geometric parameters are described in Table 3.2.

At the top region of the joint, the doubler plate acts as a large washer and provides better clamping force distribution through the thickness of the joint, when compared to standard bolted joints. A study by Pelletier et al. [2005] showed that hybrid bolted joints with protruding-head bolts resulted in an initial bolt pre-load loss of about 45 percent, while bolted joints with evenly distributed bolt forces showed a bolt pre-load loss of only 15 percent. The use of doubler plates will help mitigate bolt load loss due to the creep in the composite. Also, doubler plates can help achieve a more watertight connection, by sealing the joint and preventing it from opening when loaded. For some underwater

applications, these observations may justify the additional cost and geometric complexity of using doubler plates.

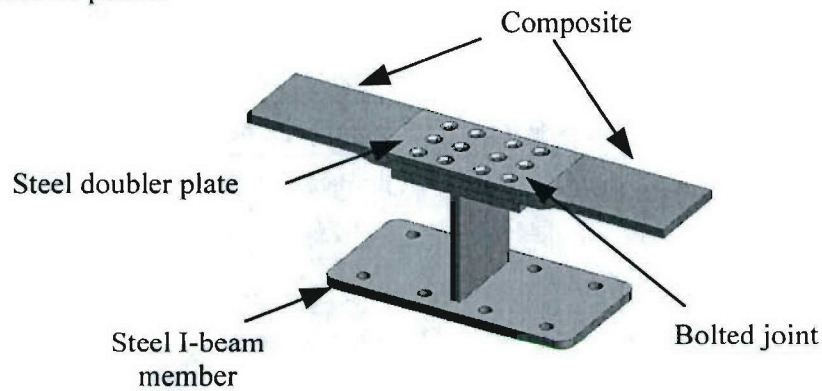


Figure 3.4. Schematic of the Bolted Joint with Doubler Plate Concept

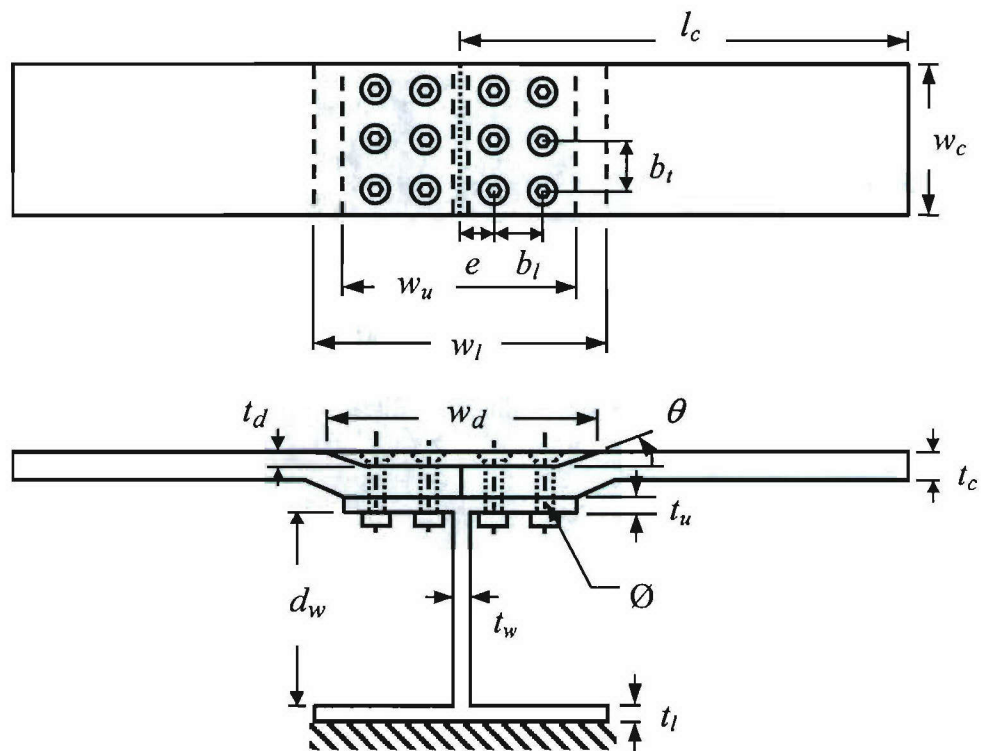


Figure 3.5. Baseline Geometry of Bolted Joints with Doubler Plates



**Table 3.2. Geometric Parameters of Bolted Joints with Doubler Plates**

Symbol	Description	Dimension
$l_c$	Length of the composite beam, mm	381
$w_c$	Width of the composite beam, mm	174
$\emptyset$	Bolt diameter, mm	12.7; 19
$b_l$	Bolt-hole spacing in the longitudinal direction, mm	57
$b_t$	Bolt-hole spacing in the transverse direction, mm	57
$e$	Edge distance, mm	38
$t_c$	Thickness of the composite beam, mm	19
$t_u$	Thickness of the upper steel flange, mm	19
$t_l$	Thickness of the lower steel flange, mm	19
$w_u$	Width of the upper steel flange, mm	267
$w_l$	Width of the lower steel flange, mm	508
$t_w$	Thickness of the steel web, mm	19
$d_w$	Depth of the steel web, mm	229
$w_d$	Width of the doubler plate, mm	146; 267; 324
$t_d$	Thickness of doubler plate, mm	6.35; 12.7
$\theta$	Taper angle,deg	24

Figure 3.6 shows photographs of bolted joints with doubler plates, for specimens with and without a foam insert. Foam inserts were used at the tapered region of the composite beam to increase the strength and stiffness of the joint, and to align the start of the taper with the edge of the steel flange. Using foam inserts required modifications to the thickness of the composite beam at the joint region. In order to accommodate the insert and align the start of the taper with the edge of the steel flange, the thickness of the composite beam was tapered from 25.4 mm at the joint region, to 19 mm at the free end of the beam.

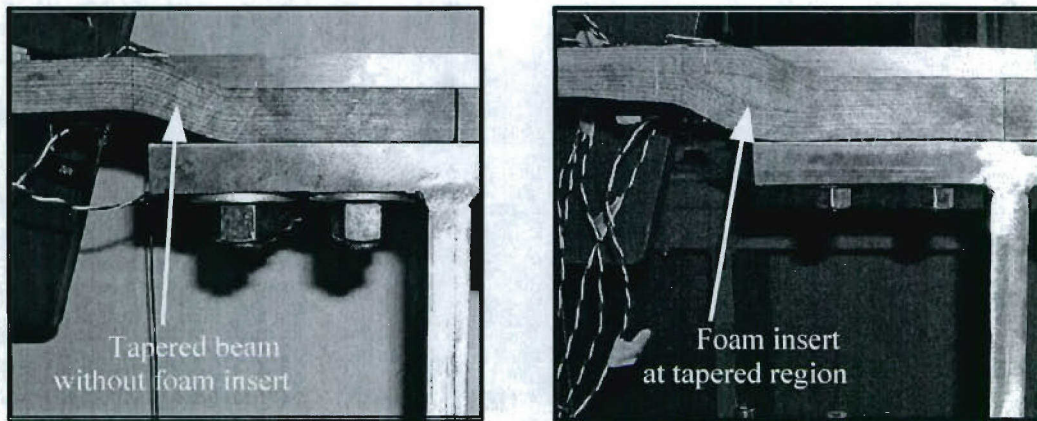


**Figure 3.6. Bolted Joints with Doubler Plates**

Table 3.3 summarizes the geometric configurations of the hybrid joint specimens that were tested. The geometric variables considered for this study are: bolt type, bolt diameter, doubler plate dimensions, and dimensions of the foam inserts. A total of fifteen joints were tested: seven bolted joints, seven bolted joints with doubler plates, and a bonded joint. Figures 3.7 and 3.8 present photographs of standard bolted joints and bolted joints specimens with doubler plates, respectively. From this point forward, joint specimens will be referred to according to the naming convention shown in Table 3.3, as follows:

For standard bolted joints:

- BP: Bolted joint, Protruding-head bolts;
- BT: Bolted joint, Tapered-head bolts.

For bolted joints with doubler plates:

- DS: Doubler, Short length, with one row of bolts;
- DM: Doubler, Medium length, with two rows of bolts;
- DL: Doubler, Long length, with two rows of bolts.

The bonded joint specimen was designated as BD-1.

**Table 3.3. Geometric Configuration of Hybrid Joint Specimens**

Specimen	Bolt type	Bolt diameter, $\varnothing$ (mm)	Doubler width, $w_d$ (mm)	Doubler thickness, $t_d$ (mm)	Remarks
BP-1	Protruding	12.7	---	---	---
BT-2	Tapered	12.7	---	---	---
BP-3	Protruding	19	---	---	---
BT-4	Tapered	19	---	---	---
BP-5	Protruding	19	---	---	Gussets
BT-6	Tapered	19	---	---	Gussets
BT-7	Tapered	19	---	---	SIA2119 Adhesive
DM-1	Tapered	12.7	267	12.7	Foam insert
DL-2	Tapered	12.7	324	6.35	---
DL-3	Tapered	12.7	324	6.35	SIA2119 Adhesive
DS-4	Tapered	12.7	146	6.35	Foam insert
DL-5	Tapered	19	324	12.7	---
DM-6	Tapered	19	267	12.7	---
DL-7	Tapered	19	324	12.7	Foam insert
BD-1	---	---	---	---	SIA2119 Adhesive



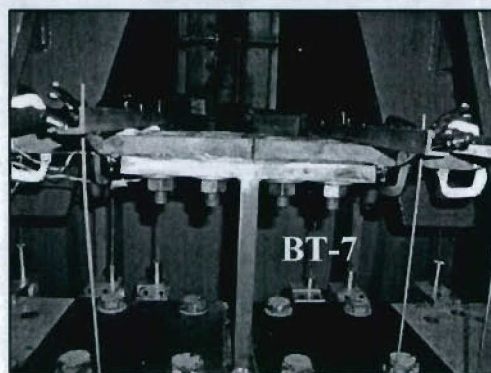
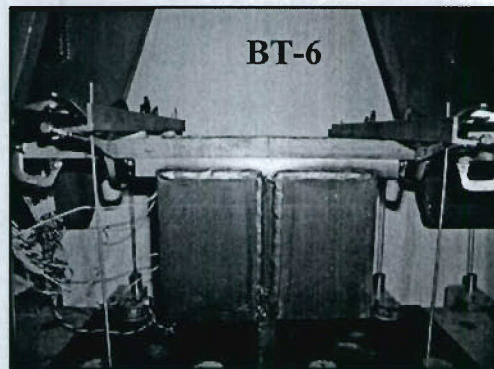
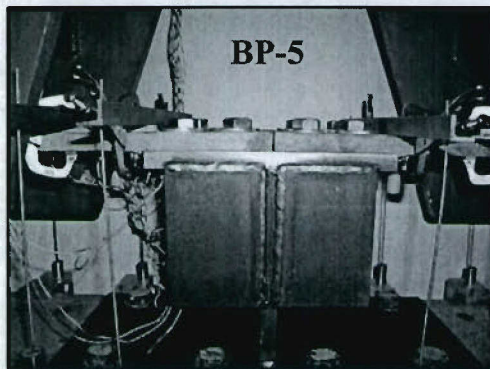
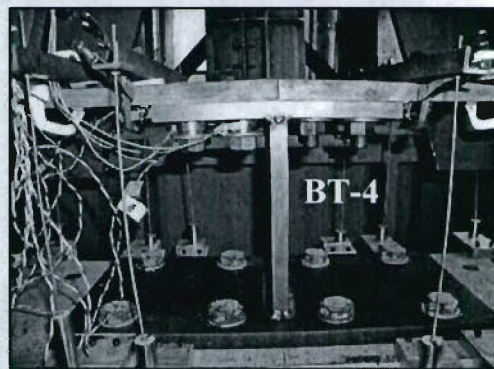
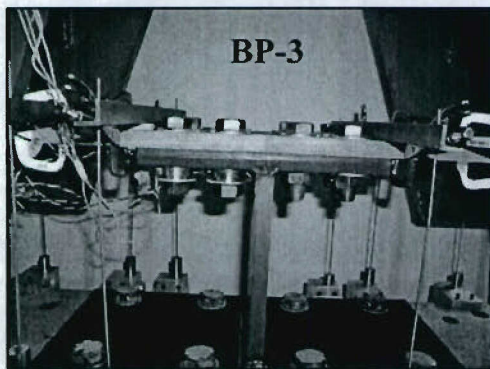
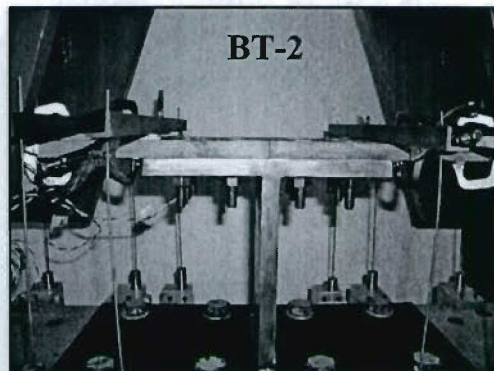
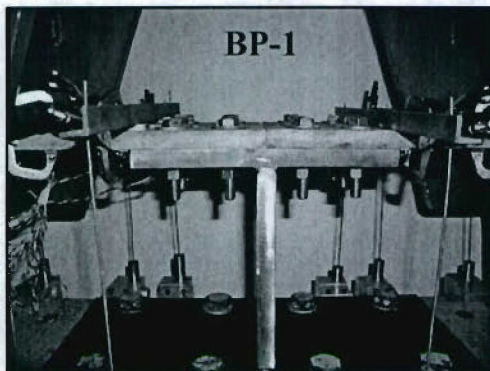


**Figure 3.7. Photographs of Bolted Joint Specimens**

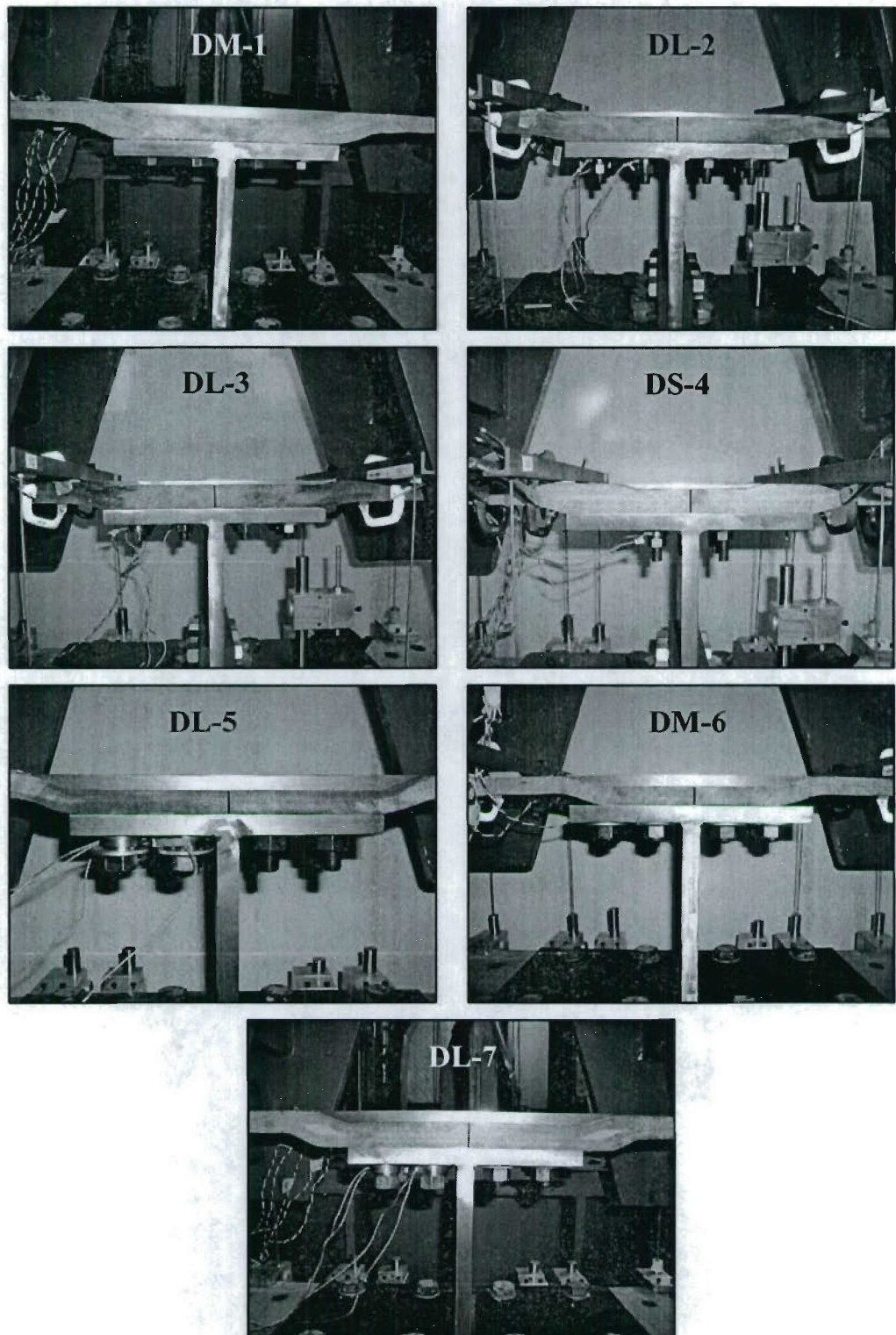


**Figure 3.8. Photographs of Bolted Joint Specimens with Doubler Plates**



### 3.4. Materials and Test Article Fabrication

Another objective of the MACH project was to use innovative material systems and processes, in order to reduce structural weight, achieve complex shapes of the hull-form, and improve the corrosion resistance of the structure. Using composite materials for the bulk of the system can help achieve these goals in a cost-effective manner. E-Glass/vinyl ester (EG/VE) systems, manufactured using a vacuum-assisted resin transfer molding process (VARTM), offer an attractive approach, as this process can be carried out in the laboratory at a lower cost than, for instance, fabrication with metals. Additionally, the U.S. Navy is currently investigating EG/VE systems and VARTM processes as preferred choices for fabrication of marine structures. Accordingly, these were selected for manufacturing the composite beam specimens.

DOW Derakane 8084 vinyl ester resin and E-Glass fibers were used as the composite specimen constituents. The reinforcing fibers were 680-gm 0-90° and 680-gm ± 45° knit fabric, manufactured by Brunswick Technologies, Inc. (BTI). It is noted that the 0° and 90° fibers are stitched together, as well as the + 45° and - 45° fibers. The foam inserts were fabricated using DIAB Divinycell® H80 foam. The steel components were fabricated by Alexander's Welding & Machine, Inc., of Greenfield, Maine. Steel I-beam members were made from a 19-mm thick, A36 grade, plate. The steel doublers were made from 12.7-mm and 6.35-mm thick, A36 grade, plates. Material specifications are presented in Appendix A.

Fabrication of the composite specimens was carried out in the Hybrid Structures Laboratory, at the University of Maine, using a VARTM process. A forty-eight layer, quasi-isotropic,  $[(\pm 45, 0/90)_6]_s$  configuration was used as the baseline laminate architecture. The nominal thickness of each layer was 0.397 mm, and the total laminate thickness was 19 mm. Material coupon tests were conducted periodically during the fabrication cycles of the project. ASTM standard tension, compression, flexure, and constituent volume tests were conducted with the intent of determining the elastic modulus and ultimate strength values for the three loading conditions, as well as the fiber volume fraction of the test articles. Panels of 7.0 mm nominal thickness,  $[(0/90)_4]_s$ , were fabricated for these tests. Four sets of tests were conducted for tension and compression, and three test sets were conducted for the flexure. 5 to 8 specimens were used in each test set. Table 3.4 presents a summary of



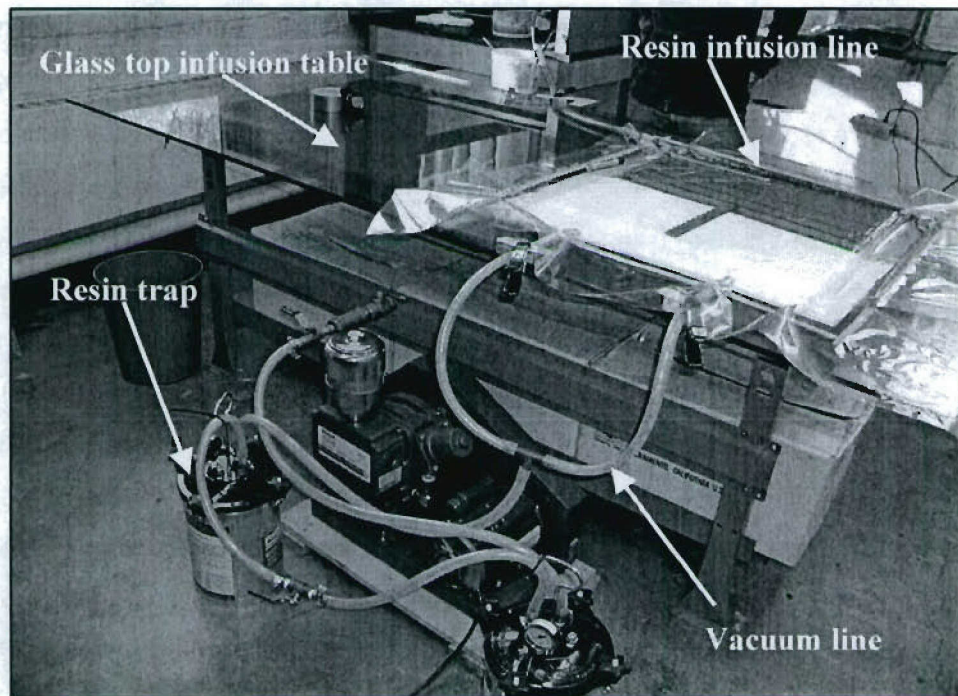
these material test results. The modulus and failure strength for each specimen are given in columns 4 and 5, respectively, along with the averages for each set. The average fiber volume fraction was  $50.5\% \pm 1\%$

**Table 3.4. Summary of Material Tests Results**

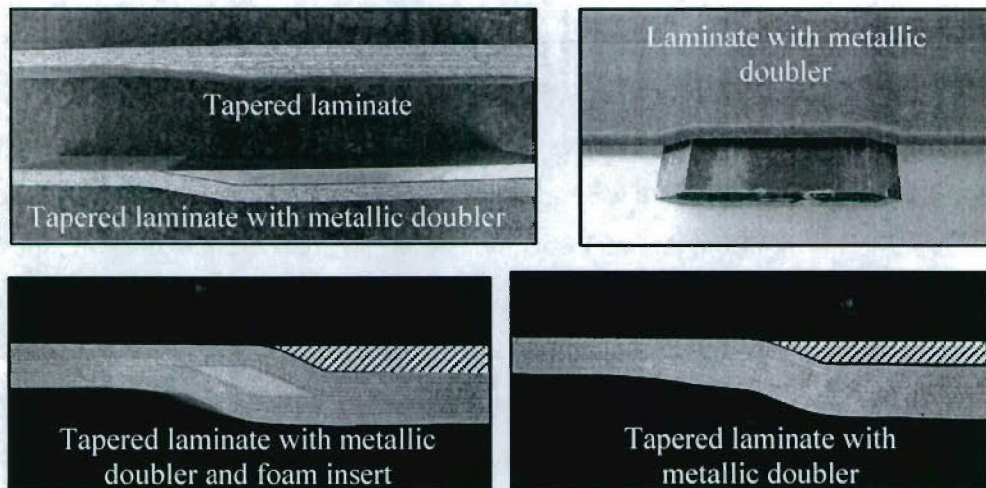
Test Set Designation	Specimen Width (mm)	Specimen Thickness (mm)	$E$ (GPa)	Failure Strength (MPa)
<b>Tension Tests</b>				
Test Set 1	24.13	7.53	15.26	262.74
Test Set 2	26.29	6.96	14.97	259.96
Test Set 3	25.45	7.35	16.80	281.21
Test Set 4	22.86	7.28	15.21	235.77
<b>Average</b>	<b>24.68</b>	<b>7.28</b>	<b>15.56</b>	<b>259.92</b>
<b>Compression Tests</b>				
Test Set 1	25.45	6.99	18.62	259.75
Test Set 2	26.92	7.26	19.39	261.76
Test Set 3	23.47	7.09	16.47	271.87
Test Set 4	26.09	7.06	16.40	270.41
<b>Average</b>	<b>25.48</b>	<b>7.10</b>	<b>17.72</b>	<b>265.95</b>
<b>Flexure Tests</b>				
Test Set 1	32.39	9.62	16.41	406.75
Test Set 2	32.44	9.48	17.10	401.48
Test Set 3	32.32	9.80	18.96	427.23
<b>Average</b>	<b>32.58</b>	<b>9.67</b>	<b>17.49</b>	<b>411.82</b>

Figure 3.9 shows a photograph of the VARTM fabrication setup. E-Glass layers were laid-up on a 1.54-m by 2.44-m glass-top bench and a nylon vacuum bag was placed on top of the arrangement and sealed along the edges. A resin line was placed along one edge of the panel, while a vacuum line was placed at the opposite edge. The resin was mixed according to the manufacturer's specifications and drawn into the mold by a vacuum. Once the panel was infused, the resin and vacuum ports were closed and the VARTM process completed. After curing, the beam specimens were cut using a diamond

coated wet saw and the required holes were drilled using diamond coated drill bits. In the case of the tapered holes, the holes were tapered using a high-speed tool-steel countersink bit. Figure 3.10 presents photographs of various tapered EG/VE composite specimens.



**Figure 3.9. VARTM Fabrication Setup**



**Figure 3.10. Tapered EG/VE Composite Specimens**



### 3.5. Joint Testing Procedures

#### 3.5.1. Test Setup

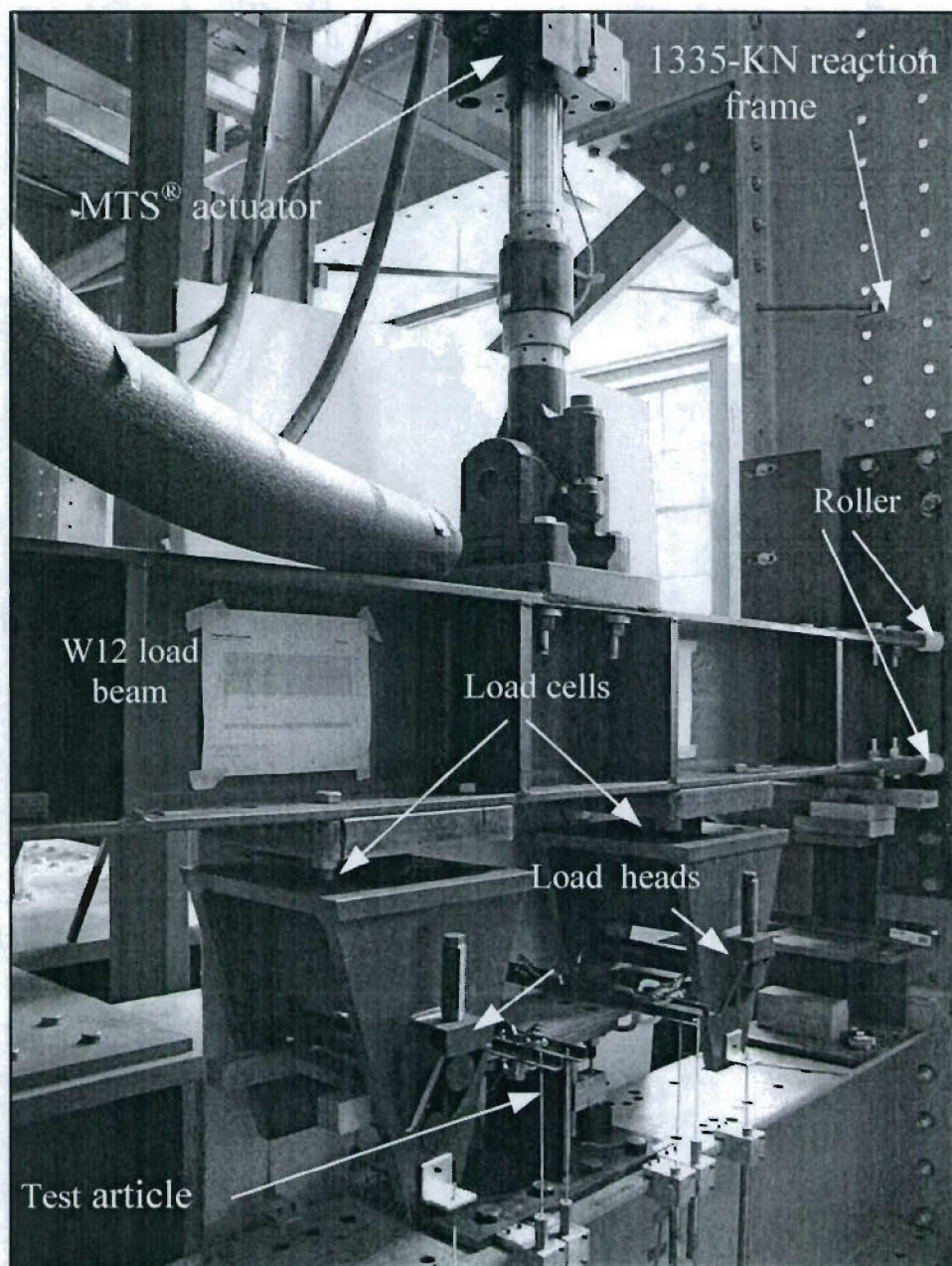
Testing of the hybrid joint specimens was conducted at the Hybrid Structures Laboratory, at the University of Maine. A photograph of the experimental test setup is shown in Figure 3.11. It consists of a 245-KN,  $\pm 254$ -mm, MTS<sup>®</sup> actuator, mounted on a 1335-KN+ modular, reaction frame. The end of the actuator was attached to the upper surface of a 2.82-m long, guided, W12 load beam, using four grade 8, 25.4-mm, steel bolts. Load heads were attached to the lower surface of the load beam, in order to transfer the applied MTS<sup>®</sup> load to the test article. Rollers were attached to the ends of the load beam to achieve a tight fit with the side plates, in order to avoid rotation of the W12 beam. Figure 3.12 shows the dimensions of the W12 load beam and the load heads.

Figure 3.13 depicts the connection of the test article to the reaction frame and the load heads. The bottom flange of the steel I-beam member was attached to the reaction frame by using eight, grade 5, 22.22-mm, steel bolts. The free ends of the composite beams were secured between the two roller pins of the load heads using the 25.4-mm diameter setscrews.

#### 3.5.2. Testing Method

A schematic of the testing method is shown in Figure 3.14. All tests were operated in displacement control mode. The test articles were loaded in flexure, in a reversed cyclic fashion. The applied load was transferred to the test article by means of the load heads. Reversed cyclic loading was carried out by pushing (towards the steel I-beam member) and pulling (away from the steel I-beam member) at the free ends of the composite beams, with a load application point at  $\pm 381$  mm from the joint centerline. The rationale for performing cyclic testing is to study the stiffness degradation upon repetition of a displacement cycle. Stiffness degradation is typically an indicator of permanent structural damage of the system. Therefore, by conducting cyclic loading tests, it is possible to ascertain the load level at which damage will begin to accumulate.





**Figure 3.11. Experimental Test Setup**

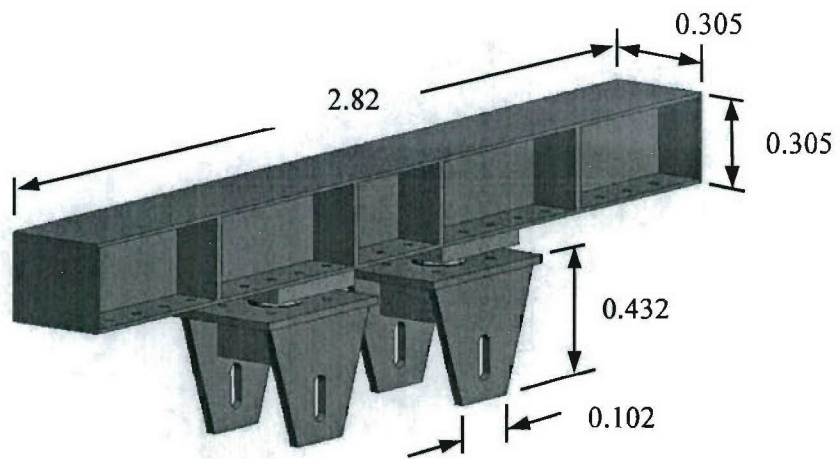


**Figure 3.12. Dimensions of the W12 Load Beam and Load Heads (in meters)**

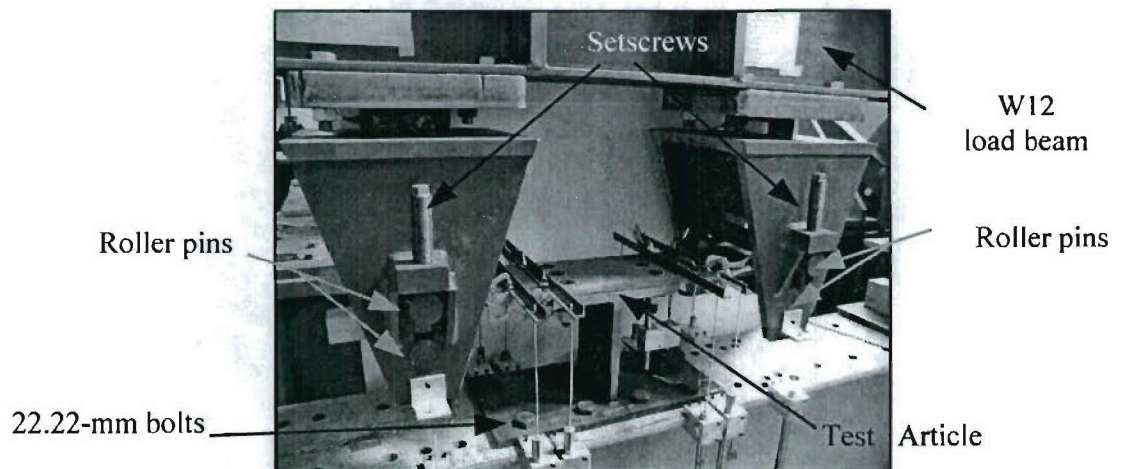


**Figure 3.13. Connection of the Test Article to the Reaction Frame and Load Heads**

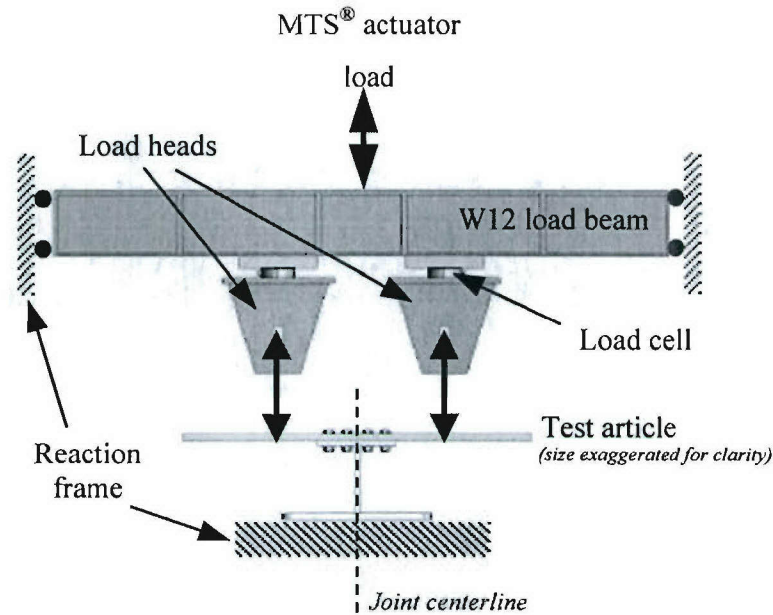


**Figure 3.14. Schematic of the Testing Method**

Figure 3.15 presents a typical loading history plot for reversed cyclic testing. Loading was typically carried out over twelve cycle sets. Each cycle set was comprised of three equal load cycles. The load head displacement range for a complete test was 5.08 mm to 61 mm, with each cycle set increasing in amplitude by approximately 5.08 mm (5 increments per inch). In Figure 3.15, “load up” corresponds to pulling of the composite beams away from the steel I-beam member, and “load down” corresponds to pushing the beams against the I-beam member. The first loading cycle was pushing downward and corresponds to positive load values and negative displacement values (actuator extension). Loading of the composite beams away from the I-beam corresponds to negative load values and positive displacement values (actuator retraction). A typical full-level test takes approximately four hours to complete.



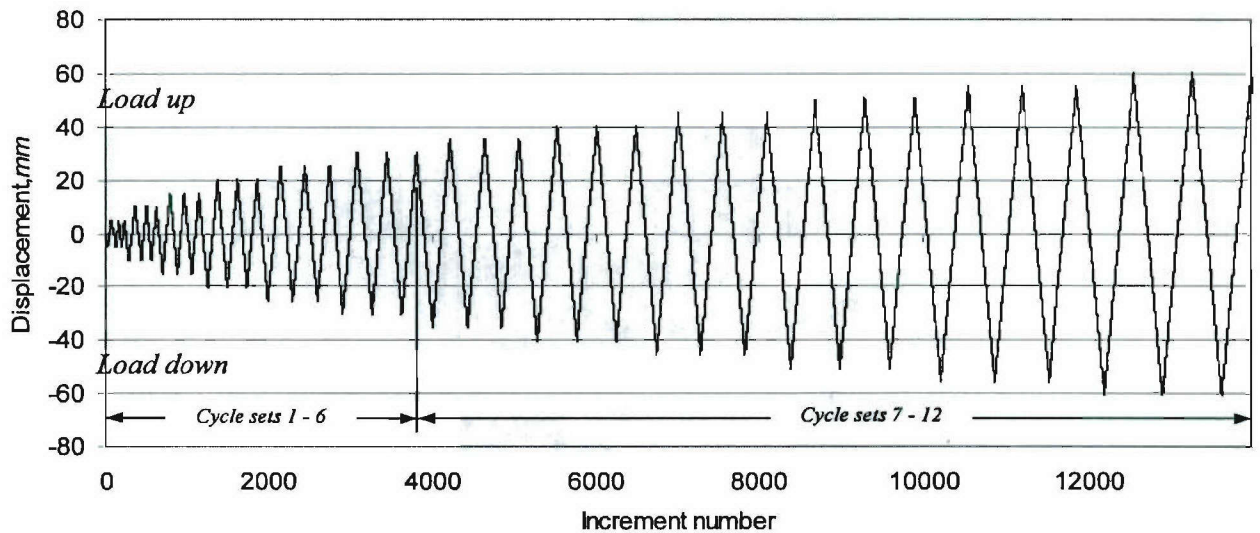


**Figure 3.15. Typical Reversed Cyclic Loading History**

Prior to testing until failure, low-level tests were conducted for all joint specimens to ensure that all instrumentation and data-acquisition channels were functioning properly. For these tests, only the first loading cycle set was carried out, to a peak displacement 5 mm. A typical low-level test takes approximately 20 minutes to complete.

### 3.5.3. Instrumentation

Test articles were instrumented with both metal foil strain gages and linear variable displacement transducers (LVDTs), to measure strains and vertical displacements, respectively. The applied load was measured using the internal 245-KN load cell of the MTS® test system and two Lebow™ 3174 load cells with an 89-KN capacity. As shown in Figure 3.16, the Lebow™ load cells were mounted between each load head and the load beam to monitor the load being transferred to each end of the test article. Each load cell was attached to the top surface of the load heads using twelve grade 5, 9.53-mm, steel bolts. A 32-mm, fine-thread, steel bolt was used to attach each load cell to a 356-mm x 305-mm x 51-mm steel plate. The top of the steel plate was then attached to the lower surface of the W12 load beam by using six grade 5, 25.4-mm, steel bolts.

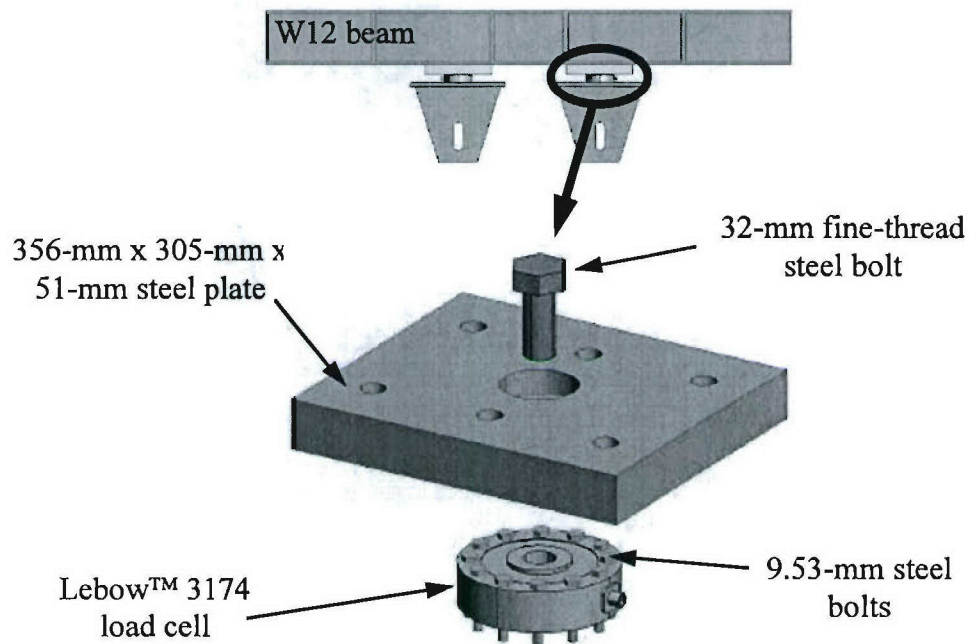


**Figure 3.16. Load Cell Setup Schematic (Exploded View)**

In addition to the MTS® test system displacement load cell, a total of twelve MacroSensors™ LVDT position sensors were used to record the vertical displacement of the top surface of the composite beams at the discrete locations shown in Figure 3.17. Two sensors were placed across the top surface of the beam at each location. Displacements were recorded at three distinct locations on each composite beam. The LVDT locations, presented in Table 3.5, are measured with respect to the centerline of the test article. LVDTs were mounted on the reaction frame by using spring-loaded supports, as shown in Figure 3.18. For each pair of sensors, the LVDT connecting threaded rods were screwed into L-braces, clamped on top of the composite beam. All LVDTs were calibrated using a Fowler® Ultra-digit digital caliper prior to each test.

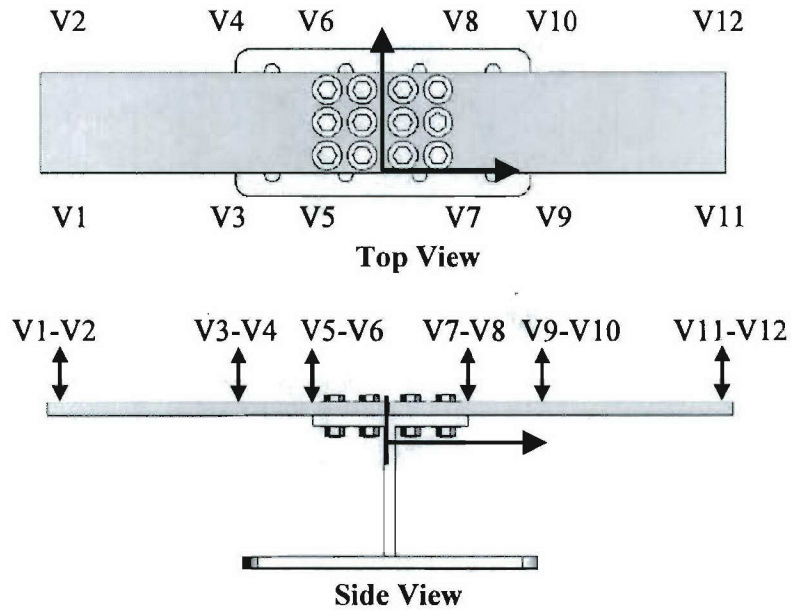


**Figure 3.17. LVDT Configuration**

**Table 3.5. LVDT Location by Coordinates**

Sensor I.D	Range (mm)	x (mm)	y (mm)
V1 (outer)	+/- 50.8	- 381	0
V2 (outer)	+/- 50.8	- 381	172
V3 (middle)	+/- 25.4	- 203	0
V4 (middle)	+/- 25.4	- 203	172
V5 (inner)	+/- 12.7	- 133	0
V6 (inner)	+/- 12.7	- 133	172
V7 (inner)	+/- 12.7	133	0
V8 (inner)	+/- 12.7	133	172
V9 (middle)	+/- 25.4	203	0
V10 (middle)	+/- 25.4	203	172
V11 (outer)	+/- 50.8	381	0
V12 (outer)	+/- 50.8	381	172



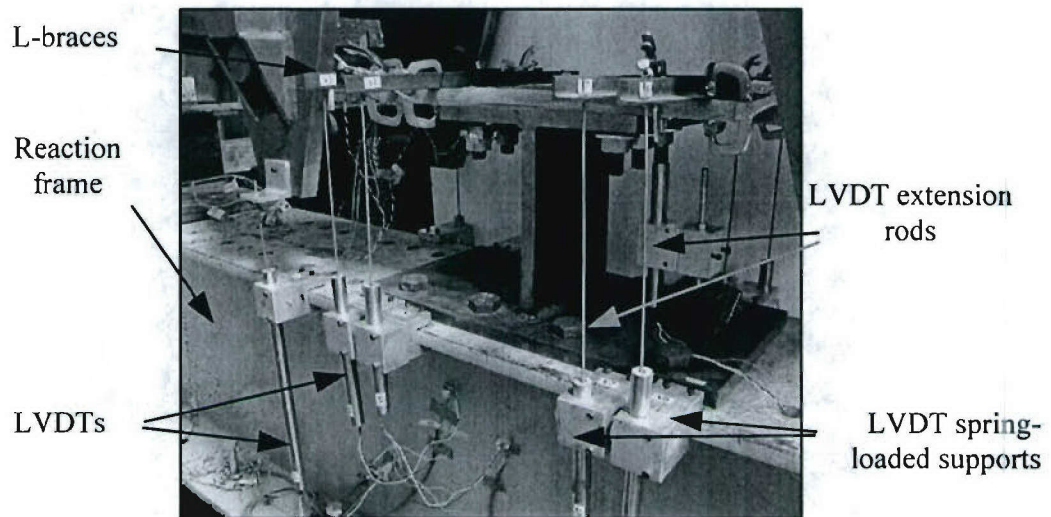


**Figure 3.18. LVDT Setup on Reaction Frame**

Figure 3.19 shows a schematic of the strain gage configuration. Strain gages and adhesives were procured from Micro-Measurements Group, Inc. Four uniaxial strain gages, type CEA-00-125UW-350, were mounted on one of the composite beams, using AE-10 adhesive. A CEA-13-250UW-350 strain gage was bonded to the underside of the steel flange. Gages SG1 and SG2 were used to monitor strains in the composite beam, SG3 and SG4 were used to monitor strains on the composite at the joint region, and SG5 was used to monitor yielding of the steel I-beam member. SG-1 was bonded to the bottom surface of the composite beam, while SG2, SG3 and SG4 were bonded to the top surface. Prior to each test, strain channels were calibrated using a 350- $\Omega$  strain calibrator. Table 3.6 presents the strain gage locations, measured from the bottom left corner of the composite beam. Vishay™ 2120 multi-channel signal conditioners were used for load and strain data-acquisition. Instrumentation specifications are presented in Appendix B.

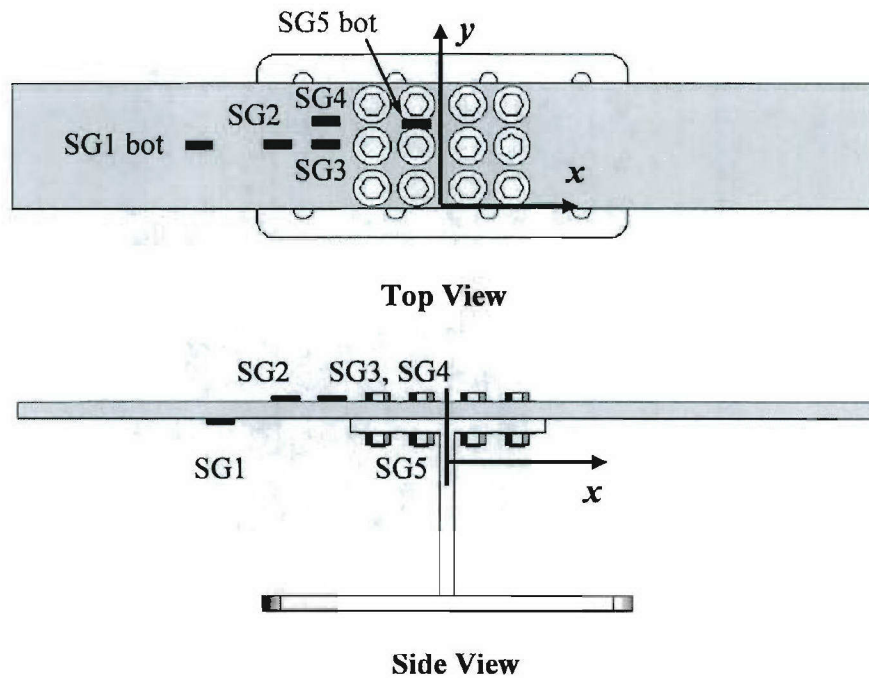


**Figure 3.19. Strain Gage Configuration**

**Table 3.6. Strain Gage Location by Coordinates**

Sensor I.D	$x$ (mm)	$y$ (mm)
SG1 (bottom)	- 203	86
SG2 (top)	- 140	86
SG3 (top)	- 133	86
SG4 (top)	- 133	129
SG5 (bottom)	- 6.35	129

### 3.5.4. Data-Acquisition Configuration

The data-acquisition process was PC-controlled, using a Pentium™ 4, 2.4 GHz, 512-MB RAM system. A schematic of the data-acquisition system is shown in Figure 3.20. The *DAQFI\_D5* software, written at the University of Maine, and an IOTECH™ Daqboard 2000 card, were used for data-acquisition. This system has 16 bit analog-to-digital conversion resolution and is capable of reading thirty-two channels at a throughput rate of 1 kHz, which is more than adequate for the rate of testing used in this study. A minimum of sixty data points were taken for each half cycle. Multiple data samples were averaged during acquisition to reduce the error due to instrumentation noise.

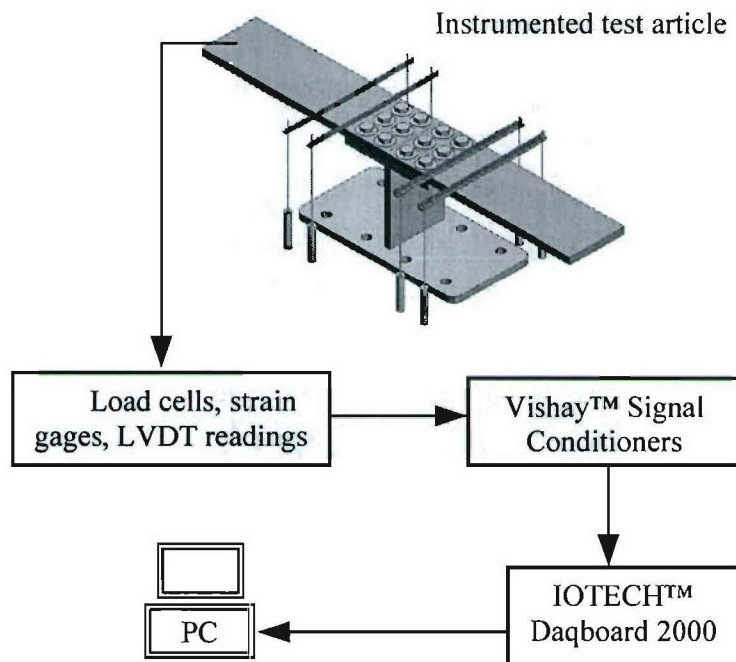


Figure 3.20. Data-Acquisition System Schematic

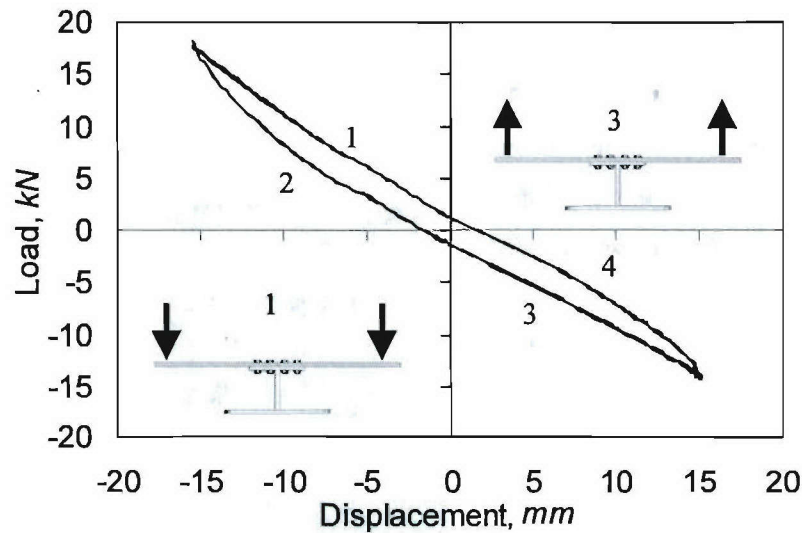


### **3.6. Joint Testing Results**

The relative response of the various joint configurations tested was assessed by quantifying: 1) the cyclic response of load versus displacement curves, in order to observe the stiffness degradation of the connection with increasing displacement levels ; 2) the cyclic response of load versus strain curves; 3) the load versus displacement envelopes, to compare the relative strength of the various joints; 4) the failure modes, to visualize how damage initiated and how quickly it propagated within the joint until ultimate failure occurred; 5) the damage and ultimate loads; and 6) the initial rotational stiffness of the joint, which provides an estimate of the flexibility of the joint. Each one of these is discussed in the remainder of this section.

#### **3.6.1. Cyclic Response: Load versus Displacement Curves**

Load versus displacement curves were created by plotting the load values recorded by the load cells versus the average displacement recorded by the pair of LVDTs at each discrete location. These curves provide a depiction of stiffness loss for each subsequent cycle set. Figure 3.21 presents a typical load versus displacement curve for a complete loading cycle set. Numbers within the figure indicate the displacement direction. The segment of the curve denoted by “1” corresponds to pushing of the composite beams against the steel I-beam member; segment “2” corresponds to unloading of the beams and its return to the neutral position. Segment “3” corresponds to loading by pulling the composite beams away from the steel I-beam member; and segment “4” denotes unloading of the beams by moving toward the support, back to its neutral position.



- |   |                   |
|---|-------------------|
| 1. Loading path, pushing against the I-beam   | 2. Unloading path |
| 3. Loading path, pulling away from the I-beam | 4. Unloading path |

**Figure 3.21. Typical Load versus Displacement Curve**

Load versus displacement curves for specimens BT-6 and DS-4 are presented in Figures 3.22 through 3.27, as examples of the cyclic behavior of the joints. Each figure presents three different sets of load versus displacement cycles, as well as the complete hysteresis loop. As described in Section 3.3, specimen BT-6 is a tapered-head bolted joint, with gussets welded to the steel I-beam member. This configuration represents a case of a very stiff sub-structure. Specimen DS-4 uses a short doubler plate with tapered-head bolts and a foam insert at the tapered region of the composite. Curves are presented for displacements recorded at the LVDT locations shown in Figure 3.17. Appendix C presents the complete load versus outer displacement curves for all specimens.

Figures 3.22 and 3.23 present the load versus displacement curves for specimens BT-6 and DS-4, respectively, using the displacement values recorded at the free ends of the composite beams (outer LVDTs). The first of twelve displacement cycle sets, with a peak displacement of 5.08 mm, is shown in Figures 3.22a and 3.23a, where it is observed that the response of the joint is stiffer when displaced against the steel I-beam, due to the additional bending resistance of the steel flange. The three cycles plotted in these figures loop upon themselves, indicating a stable hysteresis response. The slight opening of the

hysteresis loops is a typical non-linearity observed in bolted joints. This behavior is attributed to opening and closing of the gap between the joint components as the displacement direction changes. For instance, when moved against the I-beam member, the gap between the composite and the flange is already closed at the neutral position. On the other hand, when moving upwardly, a gap opens up between these two components before the steel member begins to take load. Friction between the joint components also contributes to the opening of the load versus displacement loops.

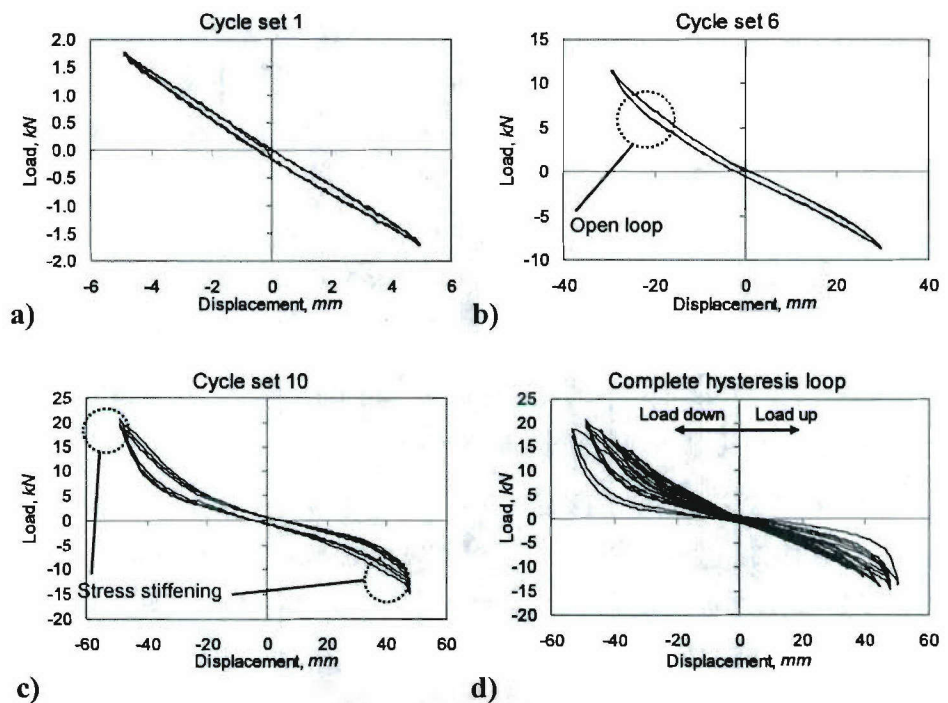
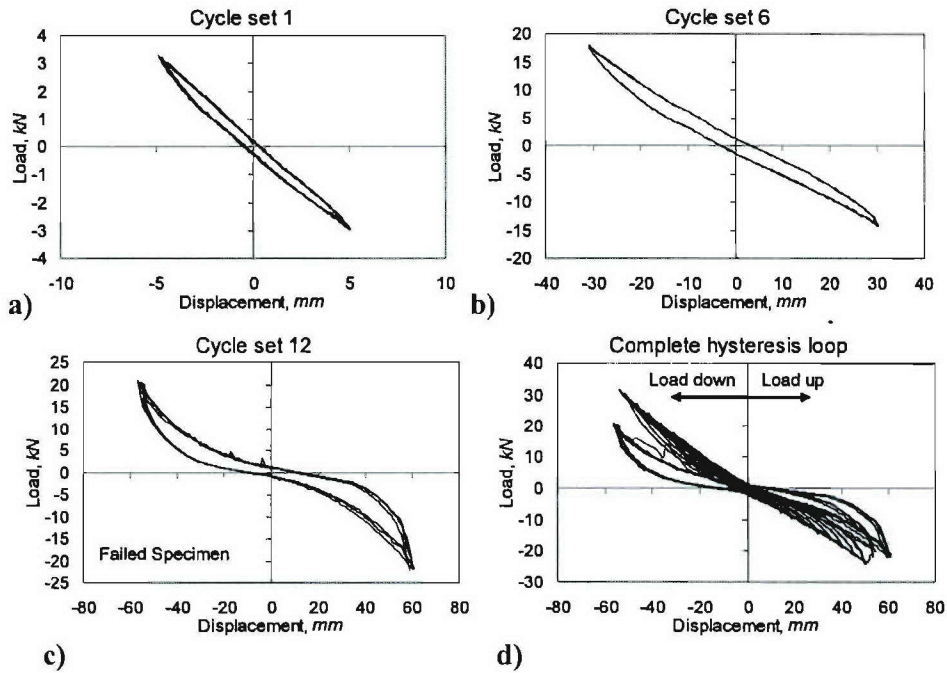


Figure 3.22. Load versus Displacement Curves for BT-6 (Outer LVDTs)





**Figure 3.23. Load versus Displacement Curves for DS-4 (Outer LVDTs)**

Figures 3.22b and 3.23b show the load versus displacement curves for the sixth set of cycles, with a peak displacement of 30.48 mm. Opening of the loops became more pronounced with increasing cycle sets. Non-linear behavior in the form of stress-stiffening was observed toward the end of this set of cycles, and is depicted in these figures. For DS-4, the initiation of this behavior was observed toward the end of the fifth set of cycles. Stress-stiffening was attributed to large deformation of the structure, given that the end displacement-to-thickness ratio was approximately 1.6 at this loading stage.

Figures 3.22c and 3.23c present the load versus displacement curves for the tenth set of cycles (BT-6) and the twelfth set of cycles (DS-4), respectively, after the specimens had undergone severe damage. For BT-6, the loading and unloading paths began to differ significantly at the beginning of the tenth set of cycles. At the end of this cycle set, the specimen had reached ultimate failure and further data were not available. For DS-4, significant loading/unloading path discrepancies were observed at the beginning of the twelfth cycle set and permanent damage resulted in a significant drop in load during subsequent cycles. The complete hysteresis loops are presented in Figures 3.22d and 3.23d,

where stiffness degradation is indicated by the drastic drop in load, which also accounted for ultimate failure of the specimens.

Figures 3.24 and 3.25 present the load versus displacement curves for BT-6 and DS-4, using the displacements recorded by the middle LVDTs. Catastrophic load drops were observed after the ninth cycle set for BT-6 and at the twelfth cycle set for DS-4. When displaced downward, the rigidity of the steel flange accounts for the slightly steeper slope of the curves, when compared to displacing upward. Appendix D presents the complete load versus middle displacement curves for all specimens.

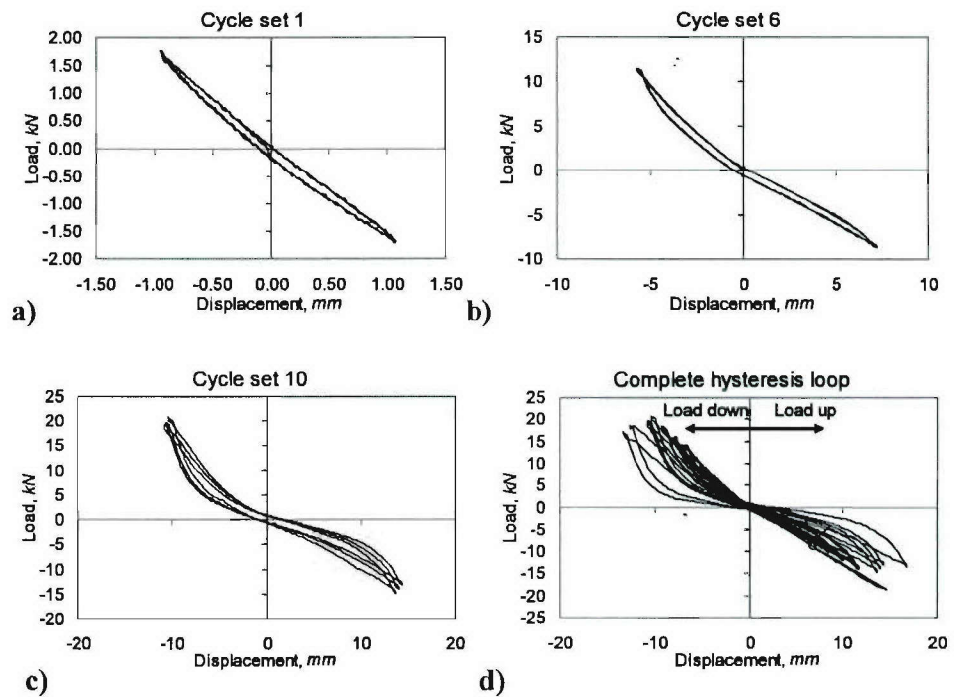


**Figure 3.24. Load versus Displacement Curves for BT-6 (Middle LVDTs)**

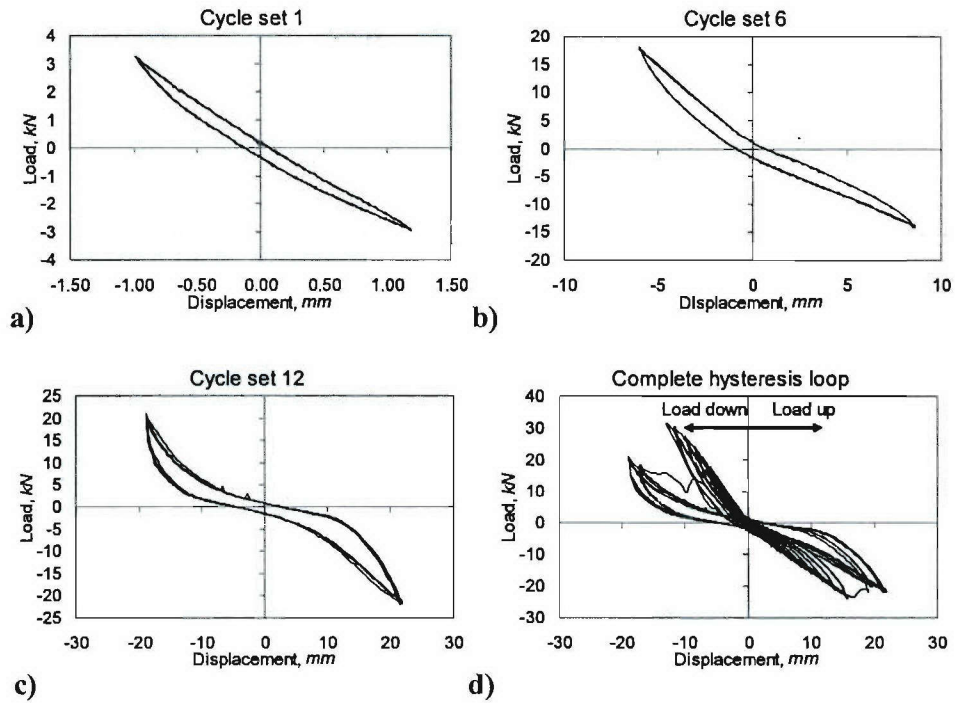


**Figure 3.25. Load versus Displacement Curves for DS-4 (Middle LVDTs)**

Figures 3.26 and 3.27 present the load versus displacement curves for displacements recorded at the joint region (inner LVDTs). Because these LVDTs are aligned with the edge of the steel flange, the data in these figures indicate the actual joint response. In Figures 3.26a and 3.27a, opening of the loops is more clearly captured by this set of LVDTs than by the middle or outer LVDTs. For the sixth set of cycles presented in Figures 3.26b and 3.27b, the added rigidity of the steel gussets (BT-6) is observed when the specimen is displaced against the I-beam, as the curves have a steeper slope, when compared to displacing upward. In Figure 3.26c, failure of specimen BT-6 is depicted by the different loading and unloading paths, particularly for displacing away from the steel I-beam. Imminent failure is depicted in Figures 3.26d and 3.27d, where DS-4 shows a more dramatic load drop during the final loading cycle sets. Appendix E presents the complete load versus inner displacement curves for all specimens.



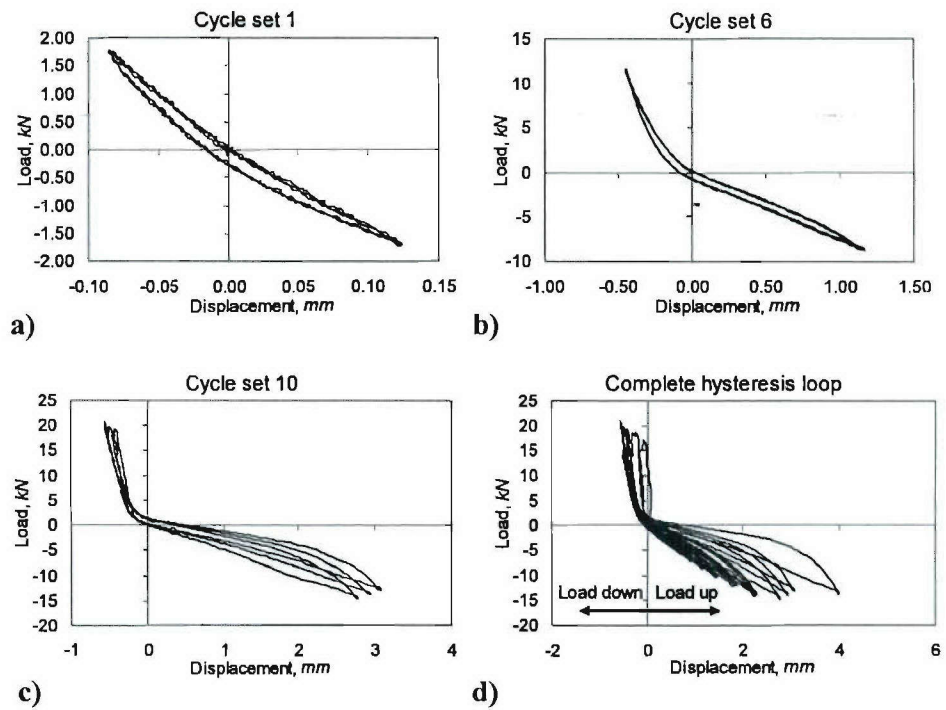


Figure 3.26. Load versus Displacement Curves for BT-6 (Inner LVDTs)

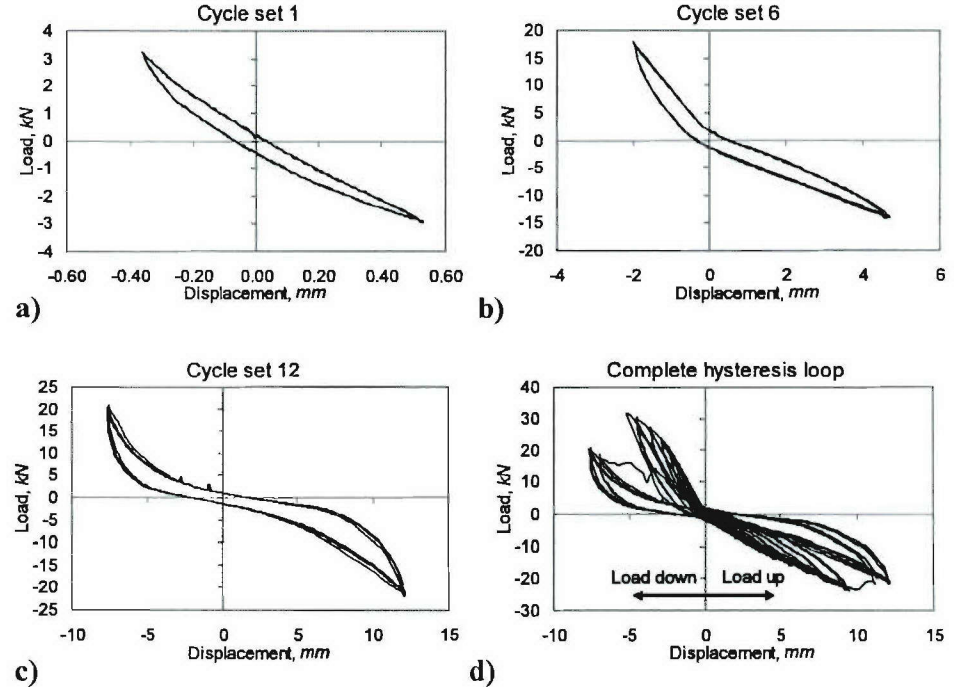


Figure 3.27. Load versus Displacement Curves for DS-4 (Inner LVDTs)

### 3.6.2. Cyclic Response: Load versus Strain Curves

Selected load versus strain curves for specimens BT-6 and DS-4 are presented in Figures 3.28 and 3.29, respectively. Each figure contains four different sets of cycles for each specimen. When the specimen is displaced against the steel I-beam, the gages on the top surface of the composite beam are in tension (SG2, SG3, and SG4) and the gages at the underside of the composite beam (SG1) and at the bottom of the steel I-beam (SG5) are in compression. When the specimen is displaced away from the steel I-beam, SG2, SG3 and SG4 are in compression and SG1 and SG5 are in tension. The complete load versus strain plots, for all cycle sets, are presented in Appendix F.

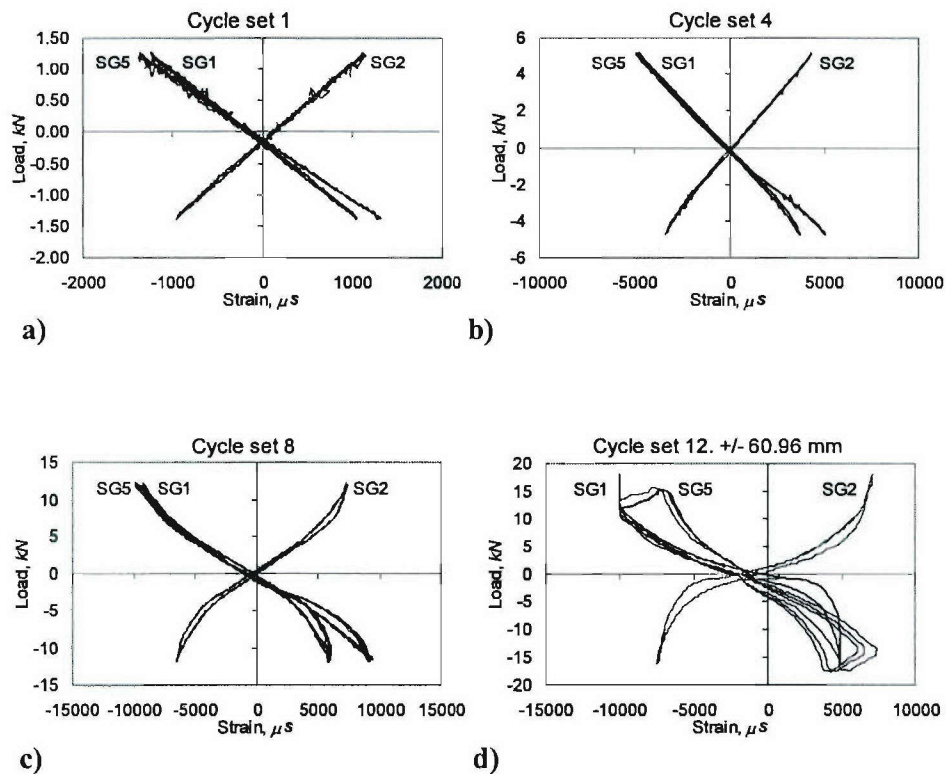
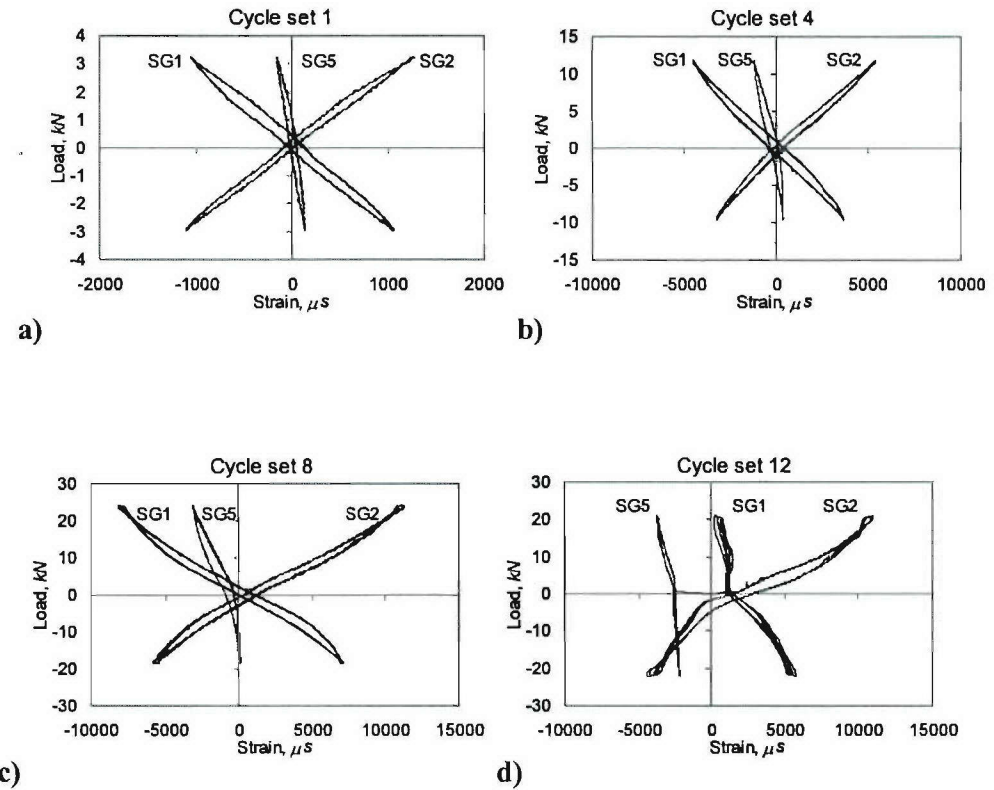


Figure 3.28. Load versus Strain Curves for BT-6



**Figure 3.29. Load versus Strain Curves for DS-4**

Figures 3.28a and 3.29a present the load versus strain curves for the first displacement cycle set. For specimen BT-6, the strain response was observed to be fairly linear, with closed loops during initial cycle sets. On the other hand, the curves for specimen DS-4 are slightly open during this displacement cycle. This was attributed to the effect of the doubler plate when the specimen was displaced upward.

Figures 3.28b and 3.29b correspond to the load versus strain curves during the fourth set of cycles, where the peak strain recorded at the composite surface was about 5700 microstrain. Yielding of the steel flange (SG5) is observed in Figure 3.28c, where the unloading and loading paths begin to differ. The hysteresis loops in Figures 3.28d and 3.29d indicate imminent failure in the composite beams.

Tables 3.8 and 3.9 present a summary of the peak strains recorded for displacing down and displacing up, respectively. The strains recorded at the composite region (SG1) when displacing downward are, in general, at least 20 percent higher than those recorded



when displacing upward. In the case of BC-5 and BT-6, this difference is roughly 50 percent. In general, the strains recorded at the joint region (SG3) are lower for downward displacement, when compared to upward displacement. This indicates that the applied load is being transferred to the steel I-beam by the bearing action of the composite beam. When displaced up, however, the applied force is being transferred to the steel mainly by the bolts, which accounts for the higher strain values in the composite. The strains recorded at the underside of the steel flange (SG5) for downward displacement are, in general, higher than those for upward loading. As in the case of SG3, this indicates that more of the applied load is being transferred to the steel member when the composite beam is displaced against the I-beam.

**Table 3.7. Peak Strain Measurements - Load Down (in microstrain)**

<b>Specimen</b>	<b>SG1</b>	<b>SG2</b>	<b>SG3</b>	<b>SG4</b>	<b>SG5</b>
BP-1	9670	8850	8970	12450	13245
BT-2	9510	8590	6350	9900	12367
BP-3	8310	11100	10789	7430	9690
BT-4	8266	8590	6579	9967	11682
BC-5	12790	9610	12766	12854	10877
BT-6	12050	8310	8990	12309	11745
BT-7	8580	7320	8260	9750	12354
DM-1	12304	7899	8456	9300	12008
DL-2	6380	8400	8990	8710	11099
DL-3	6070	7920	8330	9140	12544
DS-4	8810	12380	7909	8955	9788
DL-5	6230	10678	9500	8577	9144
DM-6	4580	8050	8657	6530	9590
DL-7	4890	7600	8400	4100	8270
BD-1	3220	1470	2460	5170	5520

**Table 3.8. Peak Strain Measurements - Load Up (in microstrain)**

<b>Specimen</b>	<b>SG1</b>	<b>SG2</b>	<b>SG3</b>	<b>SG4</b>	<b>SG5</b>
BP-1	5890	7710	11290	11567	9982
BT-2	6060	8290	11005	12356	9220
BP-3	7550	9780	12098	12589	11066
BT-4	6357	7510	9788	11678	10456
BC-5	6030	9850	11890	11223	8690
BT-6	6600	7550	12349	11890	9630
BT-7	6260	7000	12390	12390	9010
DM-1	11456	5677	8699	10798	9870
DL-2	6830	11245	11772	12578	12890
DL-3	5940	12357	12880	12790	12130
DS-4	3890	11156	12130	10899	11557
DL-5	5670	9589	12007	9078	9740
DM-6	6910	4630	8203	11280	10678
DL-7	5200	10700	10677	9877	11409
BD-1	1560	3210	5100	2430	2820

### **3.6.3. Load versus Displacement Envelopes**

Load versus displacement envelopes were created by plotting the peak load and displacement values for each set of cycles, for both displacing against and away from the steel I-beam member. These curves provide a depiction of the relative response, strength and stiffness of the various joint configurations tested.

#### **3.6.3.1. Load versus Displacement Envelopes for Bolted Joints**

Load versus displacement envelopes for bolted joints with protruding-head bolts and tapered-head bolts are presented in Figure 3.30 and Figure 3.31, respectively. For comparison purposes, these curves were plotted using the same scale. When displaced in the downward direction (against the I-beam member), the specimens with gussets welded to the steel I-beams, BP-5 and BT-6, were the stiffest and strongest, with capacities of 24 KN and 21 KN, respectively. When displaced away from the I-beam member (load up)

specimens BP-1 and BT-4 attained the highest capacities of 18 kN and 19 kN, respectively. In a general sense, the response of the bolted joints was tightly grouped for the set of parameters investigated. For these specimens, opening of the joint was observed to occur at higher loading cycle sets (after cycle set 6), when loaded against the support. This is depicted in Figure 3.32, which shows a photograph of the joint opening (specimen BP-1) during the tenth set of cycles.

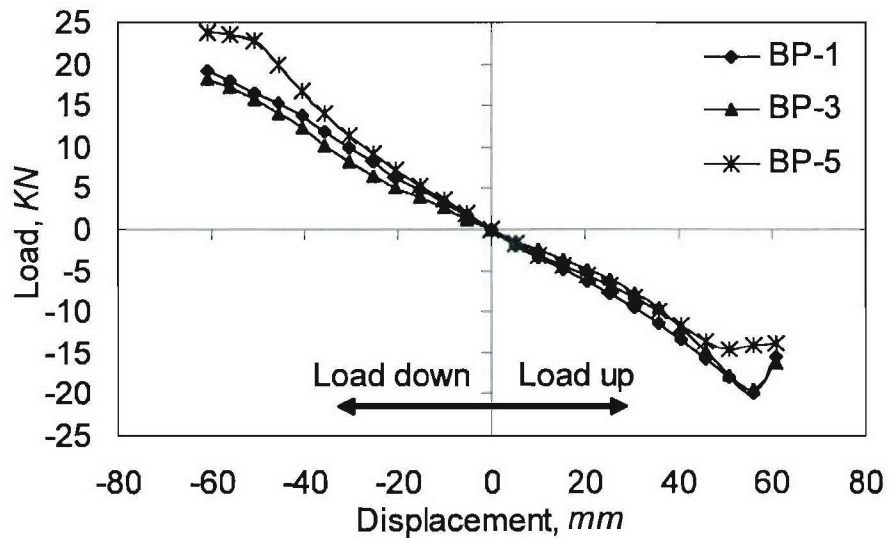


Figure 3.30. Load versus Displacement Envelopes for Protruding-head Bolted Joints



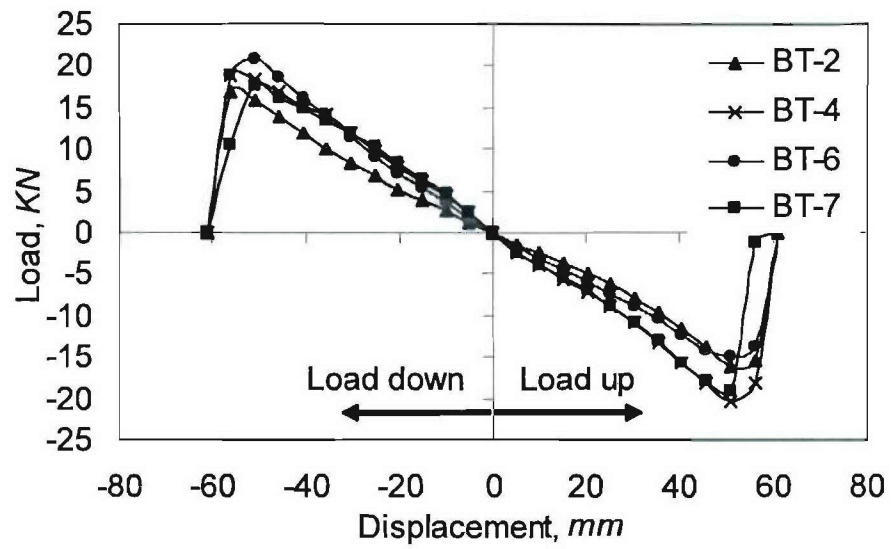


Figure 3.31. Load versus Displacement Envelopes for Tapered-head Bolted Joints

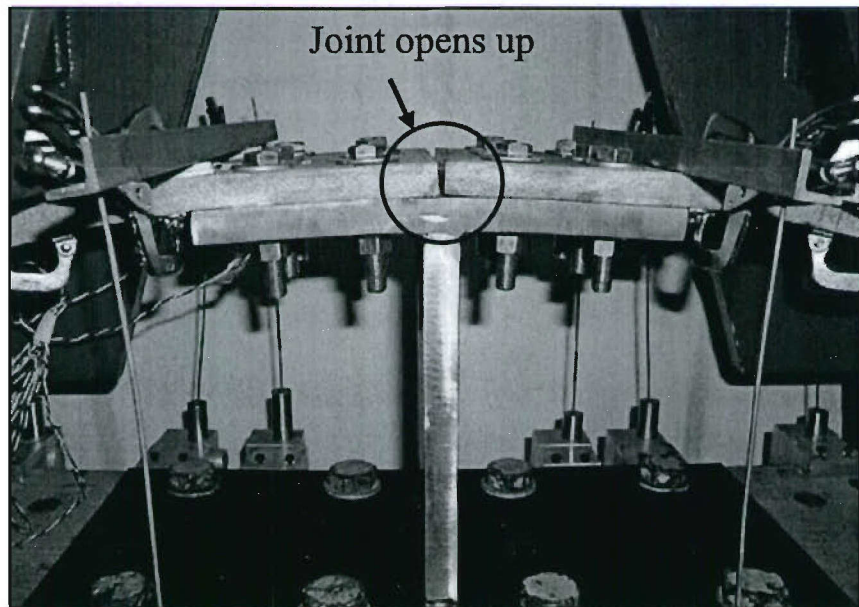
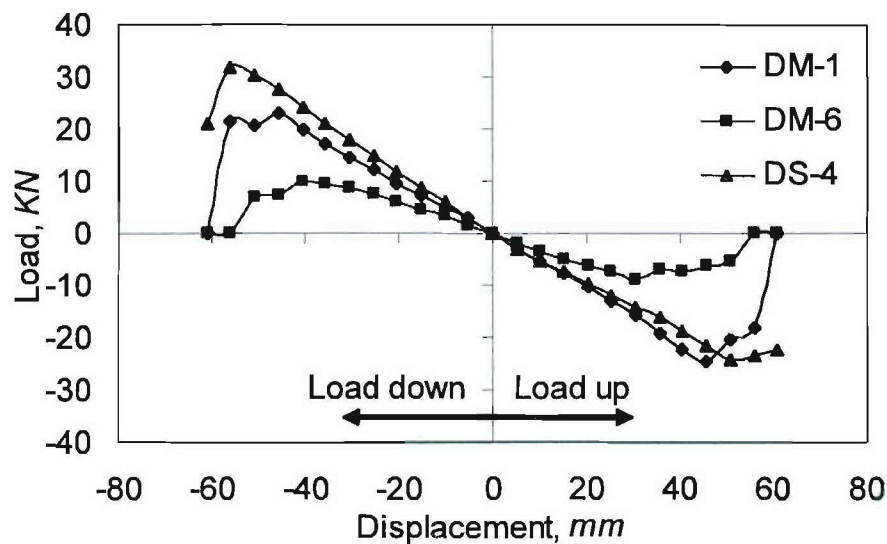


Figure 3.32. Specimen BP-1 Displaced Downward at Cycle Set 10

### 3.6.3.2. Load versus Displacement Envelopes for Bolted Joints with Doubler Plates

Load versus displacement envelopes for bolted joints with doubler plates are presented in Figures 3.33 and 3.34. Figure 3.33 shows the response of specimens with short and medium doubler plates. When displaced against the steel I-beam member (load down), DS-4, a specimen with a short doubler plate and foam insert, showed the highest capacity of 32 KN, followed by DM-1, at 23 KN. DM-1 and DM-6 are both specimens with medium doubler plates. When compared to DM-6, with the lowest capacity of 10 KN, the better performance of DM-1 was attributed to the use of foam inserts at the tapered region. When displaced away from the support (load up), DM-1 performed slightly better than DS-4, with a capacity of 25 KN.



**Figure 3.33. Load versus Displacement Envelopes for Bolted Joints with Short and Medium Doubler Plates**

Figure 3.34 presents the load versus displacement envelopes for joints with long doubler plates. When displaced against the steel I-beam (load down), specimens DL-2 and DL-3 attained the highest capacities of 34 KN and 31 KN, respectively. Both of these specimens use 6.35-mm thick, long doubler plates. The same was true for the case of displacing away from the support. DL-7, a specimen with a 12.70-mm thick, long doubler

plate and foam insert, attained peak loads comparable to DL-2 and DL-3, up until the sixth cycle set (displaced down, 30 mm) and the eighth cycle set (displaced up, 40 mm). After these cycle sets, the drop in peak loads for DL-7 is suspected to be a consequence of the doubler geometry, which led to premature failure by bearing of the steel at the top surface of the composite. DL-5 attained the lowest capacity of about 9.91 kN.

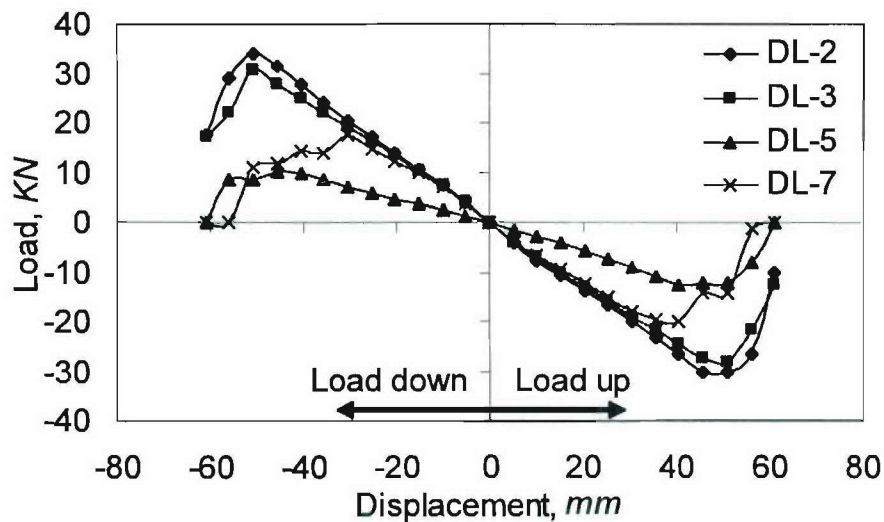


**Figure 3.34. Load versus Displacement Envelopes for Bolted Joints with Long Doubler Plates**

Overall, the response of joints with doubler plates was more widespread than that of standard bolted joints, due to the variations used for the doubler plate geometry. Specimen DS-4 (short doubler and foam insert) attained comparable capacities to long doubler plate joints, DL-2 and DL-3, with half the number of bolts and roughly half of the material used to fabricate the doubler plates.

The load versus displacement results show that incorporating doubler plates and foam inserts can increase the joint capacity, particularly when the joint is displaced away from the I-beam support. Additionally, Figure 3.35 shows that the use of doubler plates is effective in keeping the joint closed (specimen DM-1, shown), which will improve the



ability to seal the joint and to maintain watertight integrity, when implementing such a configuration into a large-scale structure.

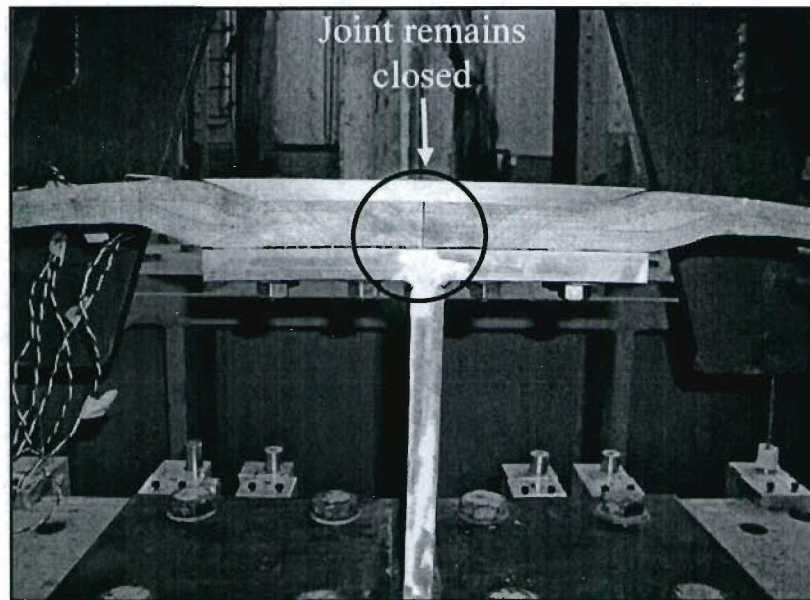


**Figure 3.35. Specimen DM-1 Displaced Downward at Cycle Set 10**

#### **3.6.4. Failure Modes**

Initiation of damage in composite bolted joints typically occurs as a combination of delamination, fiber fracture, and bearing, which can take place either at the net section or the gross section of the connection, depending upon the geometry and loading conditions. For the tests presented in this chapter, the non-linear behavior observed in the steel members was primarily due to yielding, which is typical for a structural steel, such as A36.

Macroscopic damage in the composite was monitored by visual inspection and by the behavior of the load versus displacement curves and the load versus strain curves. Photographs of the joint specimens were taken at the beginning and the end of each

displacement cycle set, in order to document the onset of damage and correlate its occurrence with the recorded load, displacement and strain data.

For each specimen, the onset of damage occurred in different forms, at different loading stages, and at different locations along the specimen. One dominant failure mode was typically observed for each specimen, though a combination of two or more modes was identified. A naming convention for the failure modes was devised, based on the type of damage and its location on the specimen, as follows:

1. **BLSC**: Bearing at the Lower Surface of the Composite beam, shown in Figure 3.36. Damage is caused by the bearing action of the steel support at the lower surface of the composite beam. Fiber fracture along the transverse direction of the composite beam is observed in the gross section. This mode occurred for joints displaced in the downward direction.

2. **BUDE**: Bearing at the Upper surface of the composite beam under the Doubler Edge, shown in Figure 3.36. Damage is caused by the bearing action of the edge of the doubler plate at the top surface of the composite beam, when the beam is displaced away from the support.

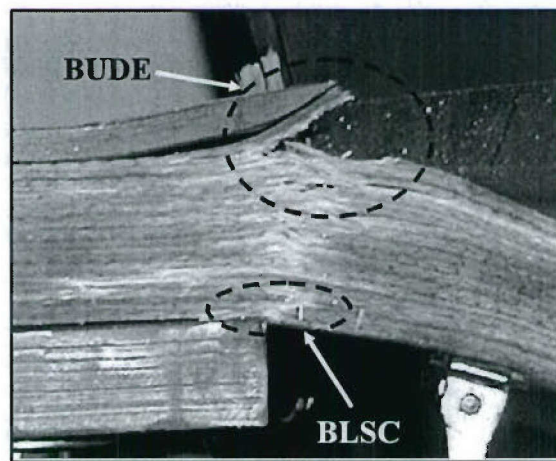


**Figure 3.36. Failure Modes BLSC and BUDE**

3. **NSBL**: Net Section along the Bolt-Line, shown in Figure 3.37. Failure of the composite beam occurs in the transverse direction, along the bolt-line of the outer row. This mode is a consequence of cyclic loading and the bearing action of the steel I-beam

member. Damage typically initiates as fracture of the outer fibers at the top surface of the composite beam, when displaced against the steel I-beam.

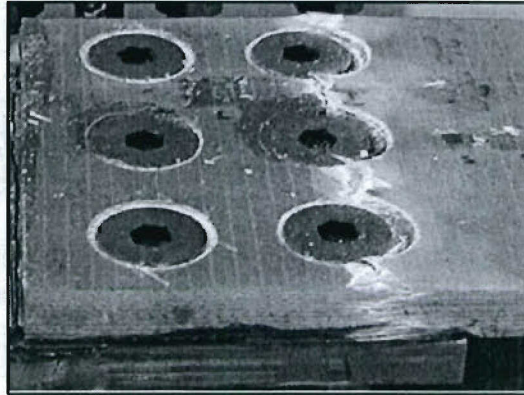


**Figure 3.37. Failure Mode NSBL**

4. **GSDE:** Gross Section along the Doubler Edge. This mode is defined as the complete separation of the composite beam from the hybrid region of the joint, as shown in Figure 3.38. This mode is typical of specimens with long doubler plates.



**Figure 3.38. Failure Mode GSDE**

5. **FFIB:** Fracture along the Foam Insert Boundary. As shown in Figure 3.39, damage initiates at the lower surface of the composite beam and then propagates to the interface between the foam insert and the composite layers, until fracture of the insert occurs. This mode is typical of joints with doubler plates and foam inserts (DM-1, DS-4 and DL-7).



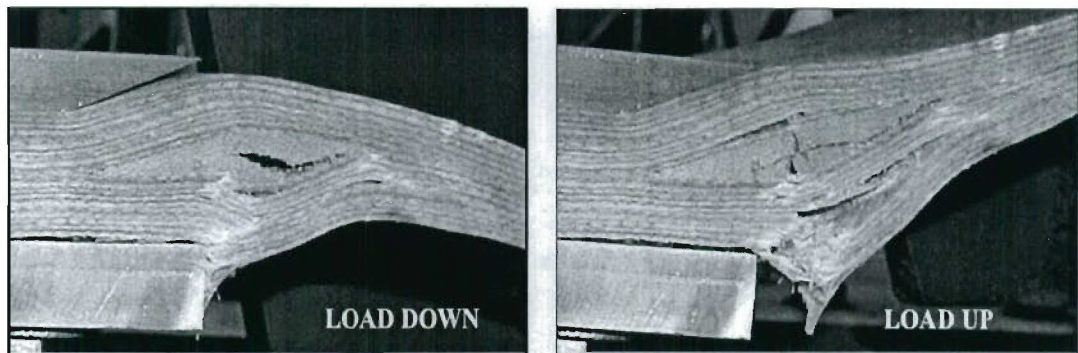


**Figure 3.39. Failure Mode FFIB**

6. **DUEC**: Delamination at the Upper Edge of the Composite beam, as shown in Figure 3.40. Failure occurs at the top layers of the composite beam, initiated at the outer edges of the beam.

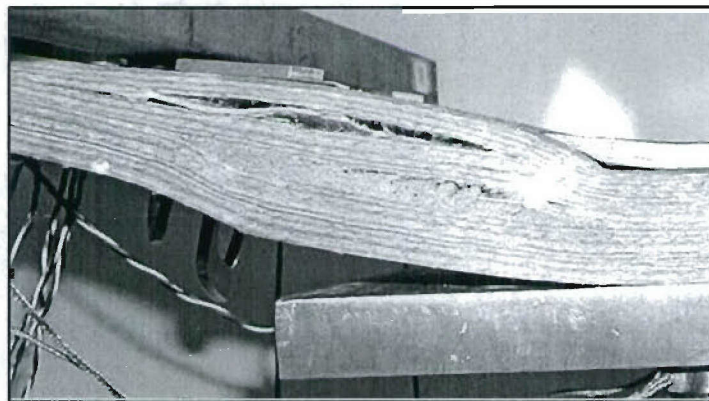


**Figure 3.40. Failure Mode DUEC**

7. **DLEC**: Delamination at the Lower Edge of the Composite beam. As shown in Figure 3.41, failure occurs as separation of the bottom layers of the composite beam, and initiates at the outer edges of the beam.

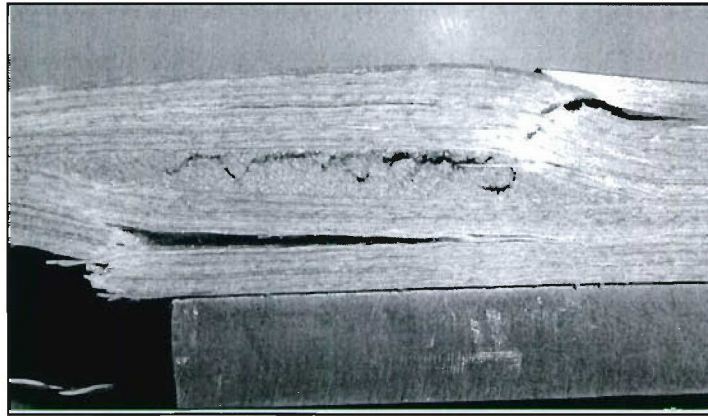


**Figure 3.41. Failure Mode DLEC**

8. **DACB:** Debonding at the Adhesive and Composite Beam interface. This mode occurred for specimen BD-1, as shown in Figure 3.42. In this case, complete separation of the composite beams from the steel flanges occurred as a consequence of the stresses acting at the interface between the adhesive and the lower surface of the composite beam.

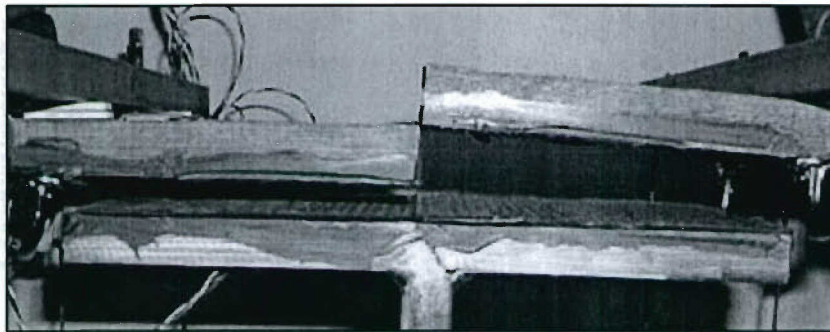


**Figure 3.42. Failure Mode DACB**

### **3.6.5. Damage Load and Ultimate Load**

The damage load,  $P_{dmg}$ , was defined as the load magnitude at which discrepancies in the loading/unloading curves and/or macroscopic damage were first observed. This load value represents the onset of macroscopic damage, though microscopic damage may have

been developing prior to this load. The ultimate load,  $P_{ult}$ , was taken to be the maximum force that the joint was able to withstand (joint capacity).

Figure 3.43 presents a bar plot of the damage and ultimate loads for all joint specimens. These values are summarized in Table 3.9. Arrows within the table are used to indicate the displacement direction when the onset of a particular mode was recorded. The failure modes are listed in the sequence in which they were observed to occur. The performance of standard bolted joints was tightly grouped, while a more widespread performance was observed for bolted joints with doubler plates.

For downward displacement of joints without doubler plates, the peak ultimate loads were observed for the gusseted specimens, BP-5 and BT-6, at 23.74 KN and 20.94 KN, respectively. Specimen BT-2 showed the lowest peak capacity, at 16.99 KN. The peak capacity of specimens with protruding-head bolts showed a 5 percent increase, when compared with specimens with tapered-head bolts. The use of gusseted steel I-beam members produced a 24 percent strength increase for the protruding-head bolt configurations (BP-3 versus BP-5), and a 10 percent increase for the tapered-head bolt configurations (BT-4 versus BT-6).

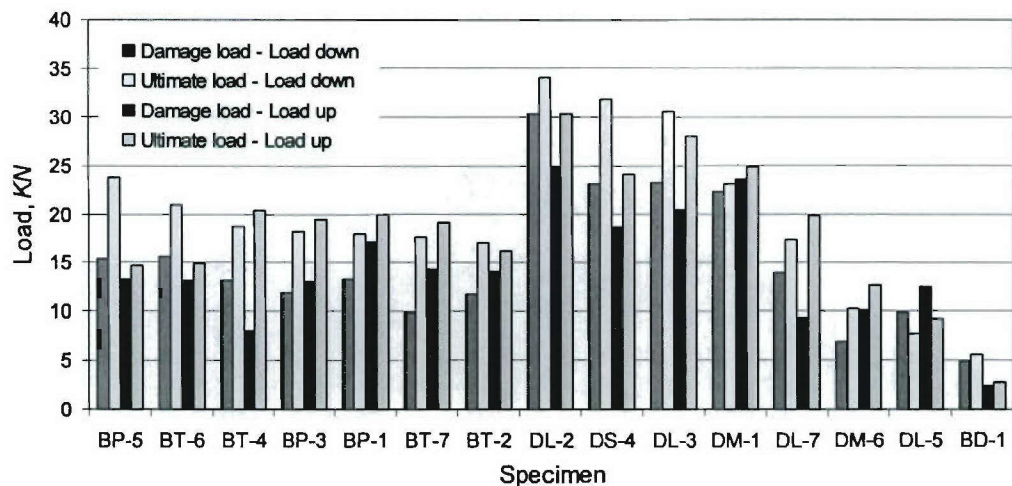


Figure 3.43. Damage Load and Ultimate Load



**Table 3.9. Damage Load, Ultimate Load and Failure Modes**

Specimen	$P_{dmg}$ (KN)		$P_{ult}$ (KN)		Failure Modes
	Load Down	Load Up	Load Down	Load Up	
BP-1	13.26	17.13	17.93	19.92	BLSC ↓, NSBL ↑
BT-2	11.73	14.10	16.99	16.18	NSBL ↑
BP-3	11.92	13.08	18.15	19.48	BLSC ↓, NSBL ↑
BT-4	13.15	8.10	18.82	20.38	NSBL ↑
BP-5	15.45	13.34	23.74	14.67	BLSC ↓, NSBL ↑
BT-6	15.67	13.20	20.94	14.87	BLSC ↓, NSBL ↑
BT-7	9.95	14.33	17.65	19.10	NSBL ↑
DM-1	22.23	23.61	23.05	24.79	BLSC ↓, DLEC ↑, FFIB ↑
DL-2	30.36	25.00	34.00	30.27	BUDE ↓, BLSC ↓, DLEC ↑, DUEC ↓, GSDE ↓
DL-3	23.18	20.38	30.50	27.97	DLEC ↑, BLSC ↓, GSDE ↓
DS-4	23.06	18.62	31.81	24.17	DUEC ↑, FFIB ↓, BLSC ↓, DLEC ↑
DL-5	7.71	9.27	9.91	12.52	BLSC ↓, BUDE ↑, DLEC ↑
DM-6	6.88	10.20	10.30	12.78	BLSC ↓, DLEC ↓, GSDE ↓
DL-7	13.99	9.38	17.43	19.84	BLSC ↓, DLEC ↓, FFIB ↓, BUDE ↑, DUEC ↓, GSDE ↑
BD-1	5.60	2.77	4.89	2.46	DACB ↑↓

When subjected to upward displacement, the peak ultimate loads were recorded for specimens BT-4 and BP-1, with magnitudes of 20.38 KN and 19.92 KN, respectively. The lowest capacity was observed for specimen BP-5, at 14.67 KN. The use of protruding-head bolts and steel washers resulted in larger bending rigidity and joint capacity, when compared to tapered-head bolted joints. For specimens BP-5 and BT-6, the use of gussets led to failure by BLSC, which resulted in higher capacities when displaced downward, but did not lead to ultimate failure.

In specimens with gusseted I-beam supports, for both protruding-head and tapered-head bolts, damage first occurred in the form of BLSC and ultimate failure occurred by

NSBL, when displaced downward. NSBL developed at the upper surface of the composite beam, particularly in specimens with tapered-head bolts, due to the lower bending resistance of the section when displaced upward. NSBL was the dominant failure mode for specimens with tapered-head bolts and typically occurred during upward loading. BLSC and NSBL were the dominant failure modes for specimens with protruding-head bolts and ultimate failure occurred when loaded upward. It was apparent that the gussets substantially increased the stiffness of the steel I-beam member, and to some degree, they also increased the strength of the joint. Also, by using gussets, damage initiated as BLSC, which is a less catastrophic mode than, for instance, net-section failure (NSBL). Specimens without gussets were prone to failure initiation in the upward direction.

In joints with doubler plates subjected to downward displacement, the peak ultimate load was observed for specimen DL-2, at 34 KN, followed by specimen DS-4, at 31.81 KN. Specimen DL-5 attained the lowest capacity of 9.91 KN. When displaced in the upward direction, the peak ultimate load was attained by specimen DL-2, at 30.27 KN, followed by specimen DL-3, at 27.97 KN. Due to the complex geometry of the joint, combinations of failure modes were observed for these specimens. BLSC was identified as the only common mode for all specimens and it occurred when displacing the beams in the downward direction.

For specimens with foam inserts, delamination at the upper and lower surfaces of the composite (DUEC, DLEC) was typically observed, followed by FFIB, in which fracture along the foam insert occurred as a consequence of delamination and later expanded to the center of the foam insert. Specimen DL-7, using a long doubler, showed a combination of virtually all of the failure modes, including BUDE and GSDE, the latter being the more catastrophic type of failure. This observation suggested that reducing the width of the doubler plates (and thereby altering the geometry of the foam inserts) resulted in a more gradual and less catastrophic sequence of failure modes, which was the case for DM-1 and DS-4, where GSDE was not present and larger joint capacities were achieved (23 KN and 32 KN, respectively). For the specimens without foam inserts, ultimate failure by GSDE was observed, as well as delamination and bearing modes. Of all the joints tested, DL-2 achieved the peak capacity, but ultimate failure occurred by GSDE.

### 3.6.6. Initial Joint Rotational Stiffness, $J$

The initial joint rotational stiffness,  $J$ , is defined as the initial slope of the moment versus rotation curve, during the first loading cycle, where the displacement ranges from 0 to 5.08 mm. A typical moment versus rotation curve for the first loading cycle set is presented in Figure 3.44, where  $J_d$  is the slope of the curve for downward loading and  $J_u$  is the slope of the curve for upward loading. These curves were created by plotting the bending moment at the centerline of the joint versus the rotation computed from the centerline to the edge of the steel flange.

Figure 3.45 presents a schematic of the force and joint rotation during loading of the test specimen in the downward direction. In the figure,  $P_R$  (or  $P_L$ ) is the applied load at the end of the composite beam;  $d$  is the moment arm, defined as the distance measured from the load application point to the joint centerline (381 mm);  $M$  is the bending moment at the joint, computed as the product of  $P_R$  (or  $P_L$ ) times  $d$ ; and  $\theta$  is the joint rotation. Assuming small displacements during the first loading set of cycles ( $\pm 5.08$  mm),  $\theta$  was computed as the average displacement reading at the inner LVDTs (V5, V6, V7 and V8), divided by the distance from these transducers to the symmetry plane of the specimen,  $l$  (133 mm).

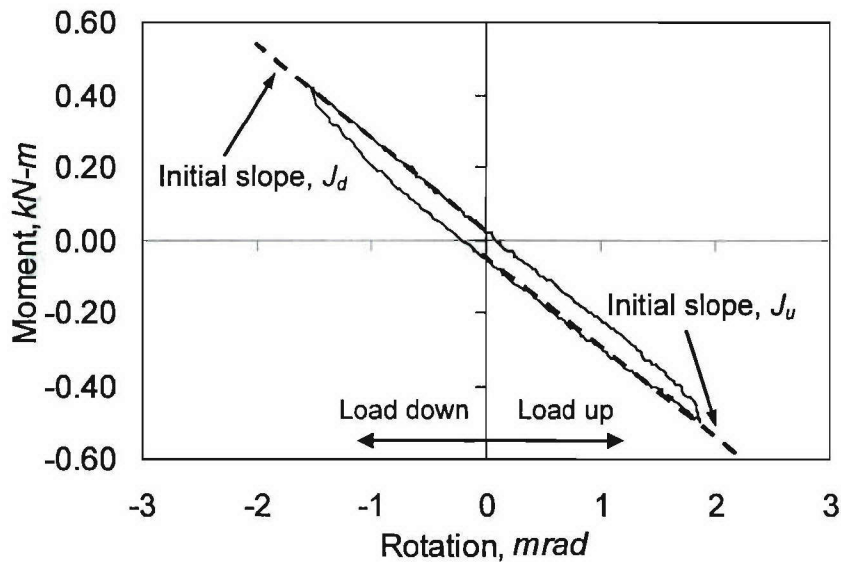
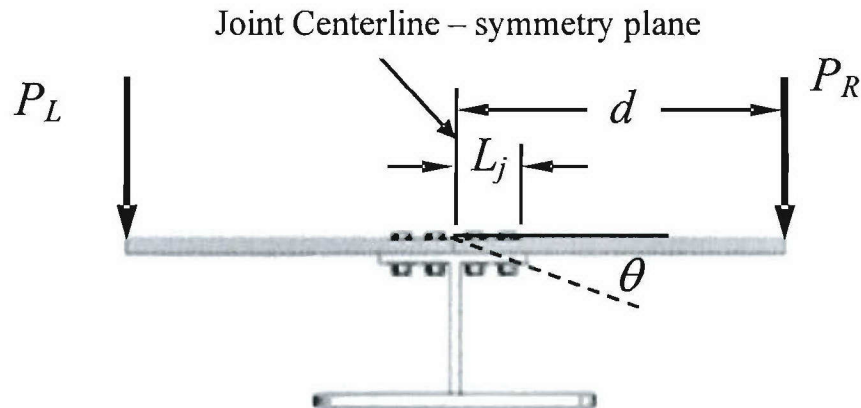


Figure 3.44. Typical Moment versus Rotation Curve for Cycle Set 1





**Figure 3.45. Loading of Test Article in Flexure**

Table 3.10 presents a summary of the computed values for  $J_d$  and  $J_u$ . For standard bolted joints, specimens BP-5 and BT-6 are the stiffest due to the additional resistance of the steel gussets. When compared to specimen BT-2 (bolted joint with two rows of bolts), specimen DS-4, with a single row of the same diameter bolts, is 30 percent stiffer when displaced downward, and 34 percent stiffer when displaced upward. In general, these results show that bolted joints with doubler plates and foam inserts can be made rotationally stiffer than standard bolted joints, when loaded in bending.

**Table 3.10. Initial Joint Rotational Stiffness,  $J$** 

Specimen	$J$ (KN-m/rad)	
	$J_d$	$J_u$
BP-1	269.40	230.11
BT-2	271.60	226.79
BP-3	252.19	218.71
BT-4	242.26	227.37
BP-5	315.83	291.67
BT-6	318.77	282.51
BT-7	249.74	231.88
DM-1	205.91	173.20
DL-2	350.30	330.92
DL-3	356.42	317.48
DS-4	389.12	346.21
DL-5	348.27	328.54
DM-6	212.32	182.11
DL-7	371.55	322.68
BD-1	221.33	187.34

### 3.7. Hybrid Joint Selection for Large-Scale Panel Testing

The primary goal of the sub-component joint testing study presented in this chapter was to develop a watertight, hybrid connection, which could be implemented into the hydrostatic testing of a large-scale, four-panel assembly. Selection of an acceptable joint configuration was based upon the relative performance of potential concepts with regards to joint capacity, rotational stiffness, failure mode sequence, and the ability to seal the joint for watertight integrity.

The results of this study have shown that, for resisting bending loads, joints with doubler plates can be made stronger and rotationally stiffer than standard bolted joints. For example, when compared to its standard bolted joint counterpart (BT-2, two rows of the same diameter bolts), a joint using a short doubler plate, a foam insert, and a single row of bolts (DS-4), was found to be at least 46 percent stronger and 29 percent stiffer when displaced downward, and 33 percent stronger and 34 percent stiffer when displaced upward. Doubler plates proved effective in mitigating opening of the joint, which will improve the ability to seal the joint and maintain watertight integrity. Hence, the additional expense and geometric complexity of bolted joints with doubler plates and foam inserts may be justified for some underwater applications.

When comparing the performance of all joint configurations with doubler plates, it was observed that a joint with a short doubler plate, such as DS-4, can attain capacities comparable to those of joints with long doubler plates (DL-2, DL-3). When compared to DS-4, the use of long doublers induced more catastrophic failure sequences, which ultimately led to complete separation of the composite beam from the joint region (GSDE). Moreover, DS-4 requires roughly half of the material for fabrication of the doubler plates and half the number of bolts than those joints with medium and long doubler plates. This may be a significant factor when considering installation and/or maintenance of large-scale structures that require multi-panel assemblies using bolted connections. In light of these observations, the short doubler and foam insert joint configuration (DS-4) was selected for implementation into the hybrid, four-panel assembly presented in Chapter 4.



## **4. Structural Testing of the Panel Assembly under Hydrostatic Load**

### **4.1. Panel Testing Rationale**

This section presents the structural testing of a large-scale, modular panel assembly, which incorporates the DS-4 joint configuration described in Chapter 3. Four modular panels were assembled using this joint scheme, and loaded with uniform hydrostatic pressure, until failure was attained. A novel hydrostatic test system was developed and implemented for this study. The results obtained from this test serve as verification of the design of the hybrid panel assembly, proof of the hybrid joint concept, and demonstration of the fabrication details and techniques using a VARTM process. Additionally, the test results are used to validate global finite element models of the panel assembly response.

### **4.2. Panel Testing Objectives**

The main goal of testing a large-scale region of the hybrid lifting body was to assess the structural performance of the MACH concept, when applied to a modular, multi-panel assembly. The region selected for testing consists of four panels, located at the lower, aft section of an existing hybrid lifting body design, as shown in Figure 4.1. This region represents a highly stressed area on the lifting body, where the actual panels had a slight curvature. Flat panels were used to simplify the test system and the manufacturing process, as well as to reduce test cost. In an effort to accurately represent the panel assembly and hybrid joint regions, a testing scheme using four stiffened panels was chosen for this study. This configuration encompassed the testing of multiple panels, as well as an assessment of the watertight integrity of the hybrid joint region.

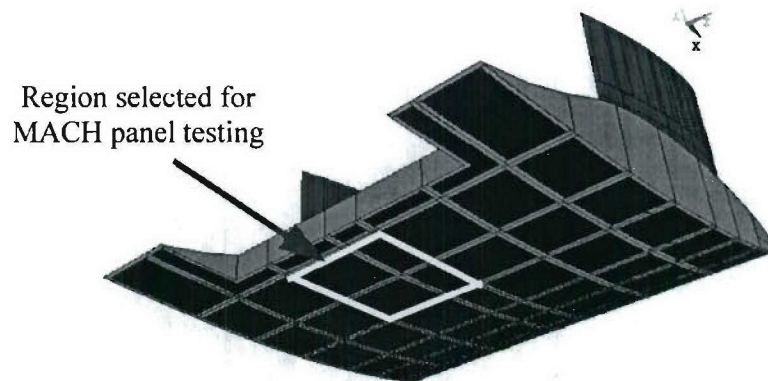


**Figure 4.1. Hybrid Lifting Body Schematic**

#### **4.3. Geometry of the Hybrid Panel Assembly**

The hybrid panel assembly consists of four EG/VE composite panels, attached to steel I-beam members by means of the DS-4 joint configuration, and bolted down to the boundaries of a test tank. As shown in Figure 4.2, the hybrid panel assembly was attached as the top element in a hydrostatic pressure tank test system, by using bolts at the tank boundaries. An O-ring gasket was used to create a watertight seal between the test tank and the outer edges of the assembly. Figure 4.3 presents the geometry of the hybrid panel assembly, where the small panels were labeled as P01 and P02, while the large panels were labeled as P03 and P04. The I-beam arrangement, representing the bulkheads of the lifting body structure, was composed of one 3.14-meter W14x53 beam, and two, 1.74-meter W8x31, beams. As described by Thompson et al. [2005], these I-beams were chosen to attain panel displacements that are as close as practical to the displacements computed for the actual lifting body, using a global finite element analysis.

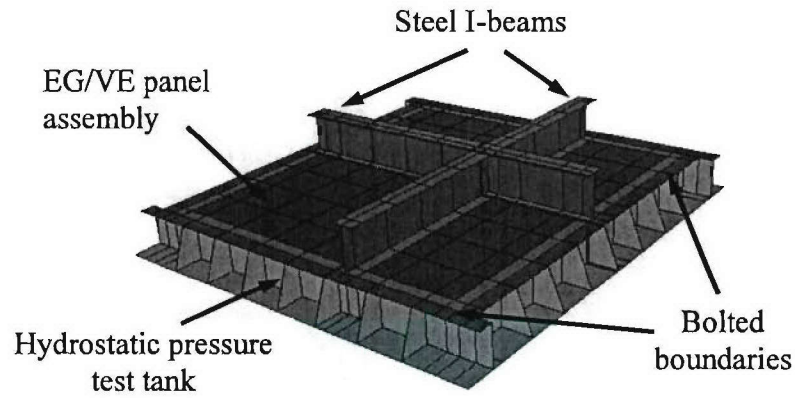


Figure 4.2. Hybrid Panel Assembly and Hydrostatic Test Tank Configuration

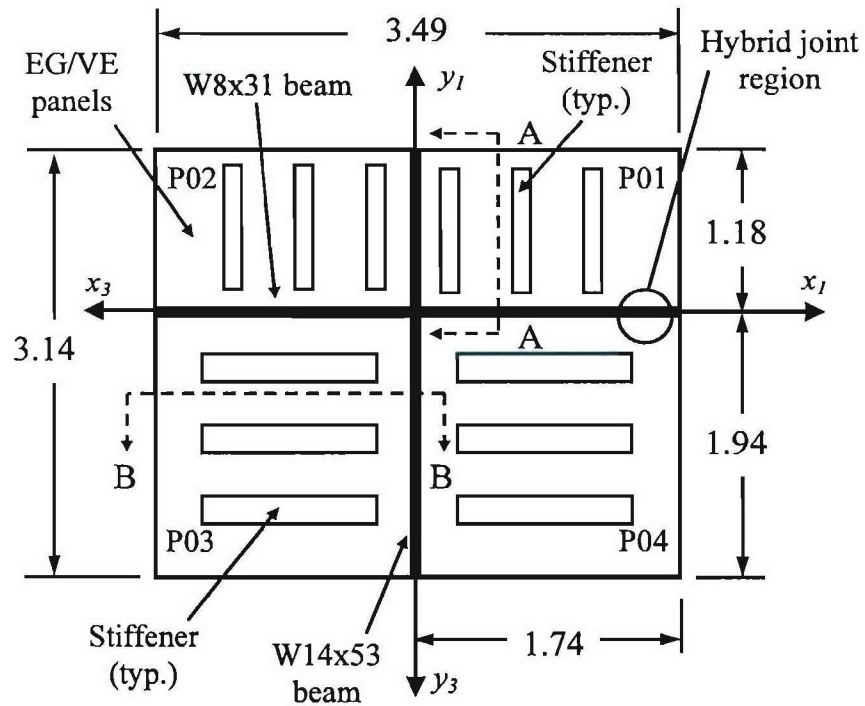


Figure 4.3. Geometry of the Hybrid Panel Assembly (in meters)



#### 4.3.1. Component Panel Design and Geometry

The bulk of the composite panel design was based upon parametric, global finite element analyses conducted by Thompson et al. [2005]. This study determined that, for a quasi-isotropic EG/VE panel, for panel sizes ranging from 1.22 meters to 1.83 meters, the optimal number of stiffeners is three, with a trapezoidal tapered hat shape.

Figure 4.4 and Figure 4.5 present the top and cross-sectional views of the small panel geometry, respectively. Figure 4.5 corresponds to section A-A in Figure 4.3. This view depicts the connection of a small panel to a W8x31 steel I-beam member at the hybrid joint region, as well as the connection of the panel to the tank side wall. The small panels use three 51-mm deep, trapezoidal shape hat-stiffeners, aligned with the short dimension of the panel. Figure 4.6 shows the geometry of the hat stiffeners on the small panels.

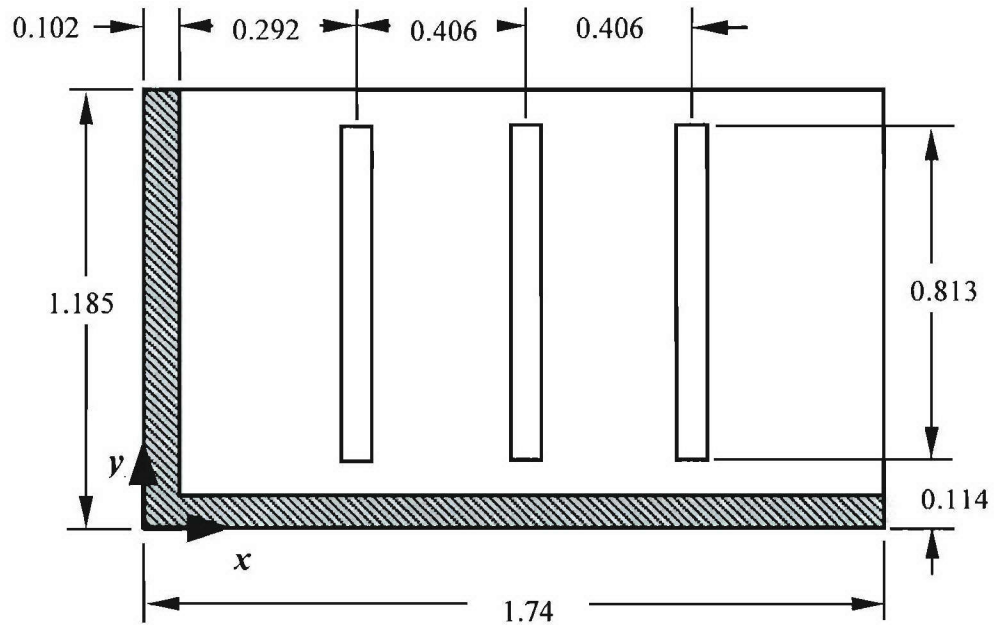


Figure 4.4. Geometry of the Small Panels - P01, Top View (in meters)

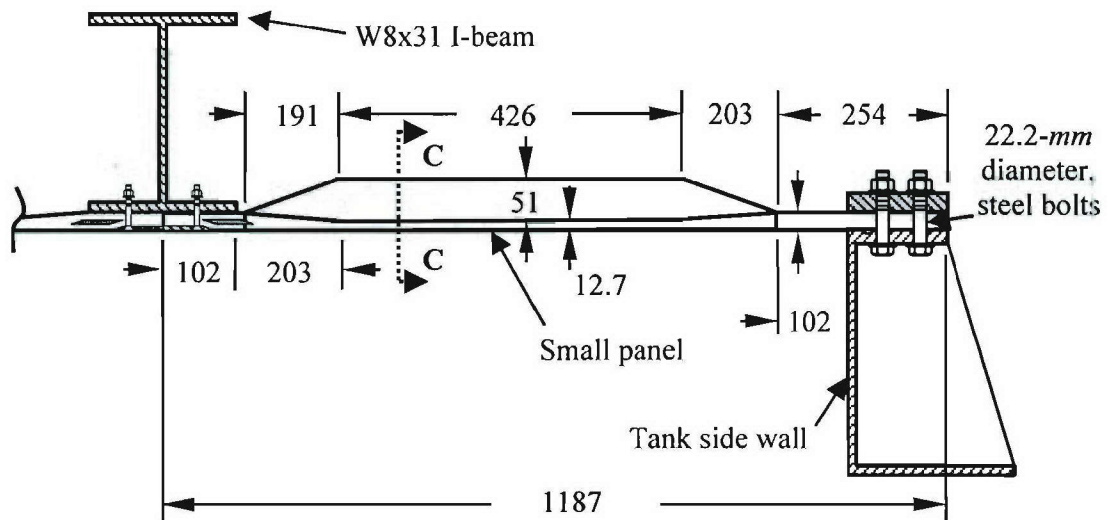


Figure 4.5. Geometry of the Small Panels - P01, Cross-Sectional View (in mm)

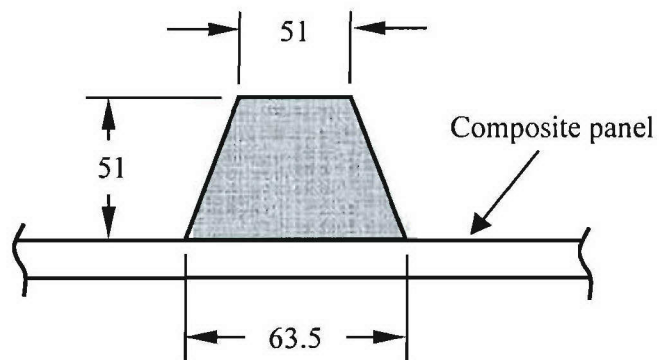
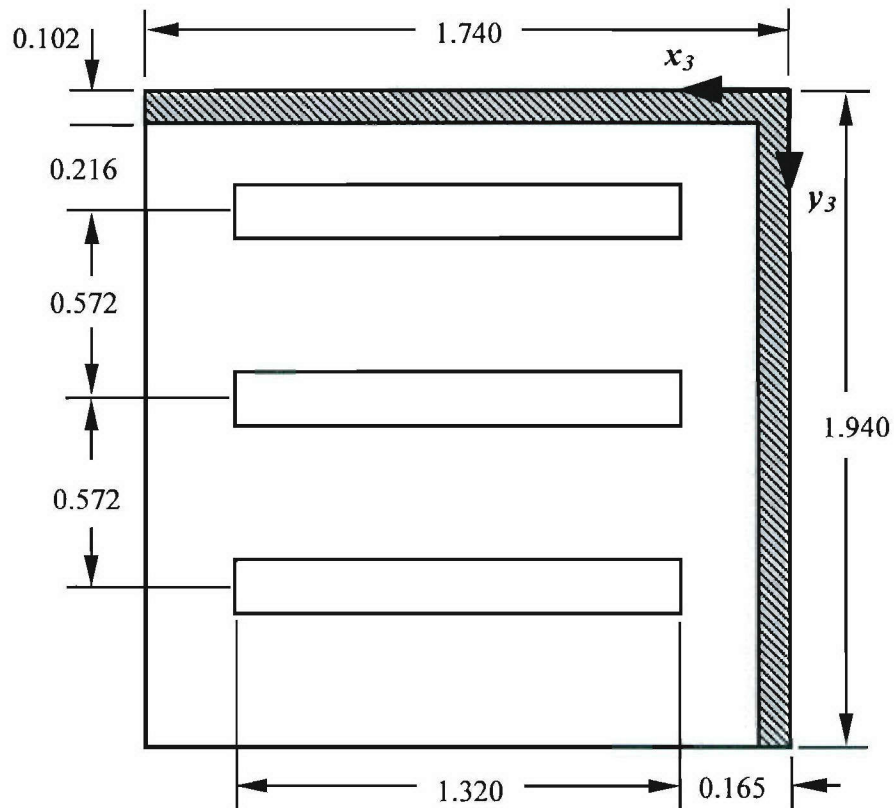


Figure 4.6. Section C-C Hat-Stiffener Geometry for Small Panels (in mm)

Figure 4.7 and Figure 4.8 present the top and cross-sectional views of the large panel geometry, respectively. Figure 4.8 corresponds to section B-B (Figure 4.3), which depicts the connection of a large panel to a W14x53 steel I-beam member and the connection of the panel to the tank side wall. These panels use three 152-mm deep, trapezoidal shape hat-stiffeners, aligned with the short dimension of the panel. A sectioned view of the hat-stiffener geometry of the large panels is shown in Figure 4.9. For both small and large panels, the laminate thickness was tapered from 25.4 mm at the edges, to 12.7 mm at the center of the panels.



**Figure 4.7. Geometry of the Large Panels - P03, Top View (in meters)**



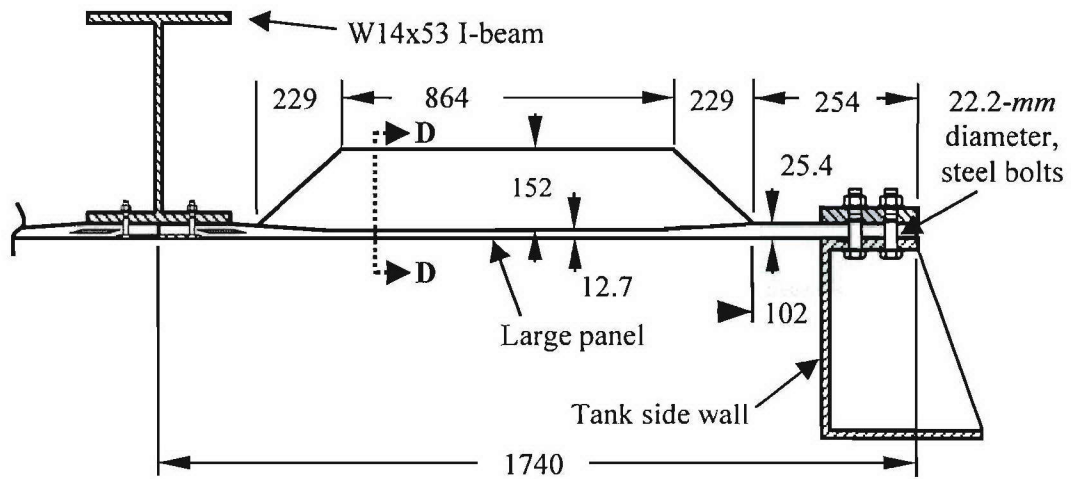


Figure 4.8. Geometry of the Large Panels - P03, Cross-Sectional View (in mm)

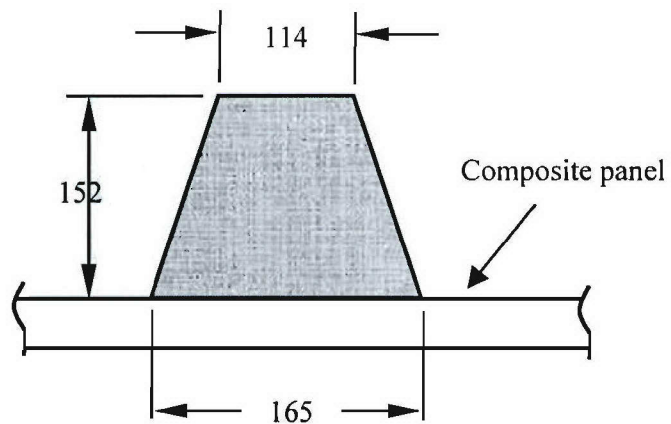
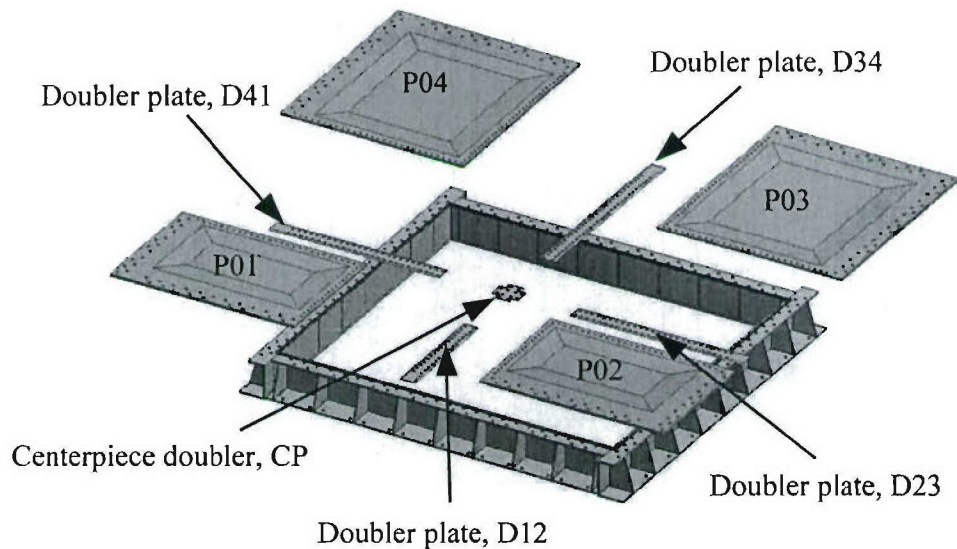


Figure 4.9. Section D-D Hat-Stiffener Geometry of Large Panels (in mm)

#### 4.3.2. Description of the Hybrid Joint Region

Based on the sub-component test results presented in Chapter 3, a hybrid joint with a short doubler plate and a foam insert (DS-4) was selected to connect the composite panels to the steel I-beam members. An exploded view of the hybrid assembly schematic is shown in Figure 4.10. The panel assembly consists of four hat-stiffened panels, bolted onto the boundaries of the hydrostatic test tank. The hybrid joint region is composed of four doubler plate sections (with two rows of bolts), a centerpiece doubler plate, the edges of the composite panels, and two steel I-beams. For clarity, the steel I-beams are not shown in this figure. It is noted that the surfaces with doubler plates represent the wet side of the actual hybrid lifting body. Doubler plates are designated as “D##,” where “D” stands for “doubler,” and the digits represent the panels that the doubler plate connects. For instance, D34 is the doubler plate connecting the large panels, P03 and P04.



**Figure 4.10. Hybrid Assembly Schematic (Exploded View)**

A photograph of the short doubler with foam insert joint (DS-4) is shown in Figure 4.11 and Figure 4.12 shows a schematic of the joint details and dimensions. As described in Chapter 3, the joint consists of a composite panel sandwiched between a

steel I-beam member and a 146-mm wide by 6.35-mm thick, steel doubler plate. Foam inserts were used to increase the strength and rigidity of the joint and to fix the start of the tapered region with the edge of the steel flange. These members were joined together by two rows of 12.7-mm, grade 5 tapered-head bolts, spaced at 38.1 mm on each side of the steel web. A total of 206 bolts were used at the hybrid joint region. For watertight integrity, a layer of RTV, clear silicone was applied at the interfaces between the steel members and the composite panels. The hybrid joint and panel assembly procedures are summarized in Appendix G.

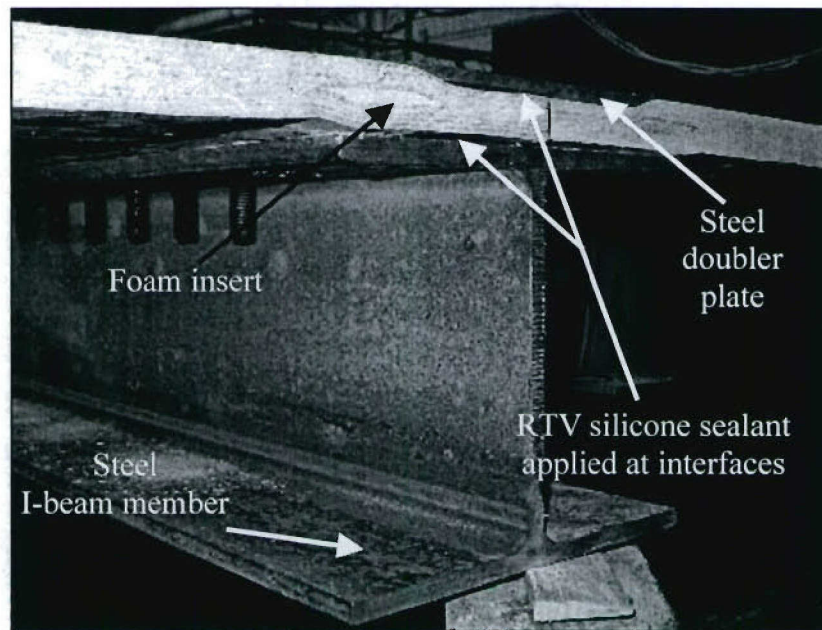


**Figure 4.11. Photograph of Short Doubler and Foam Insert Joint (DS-4)**



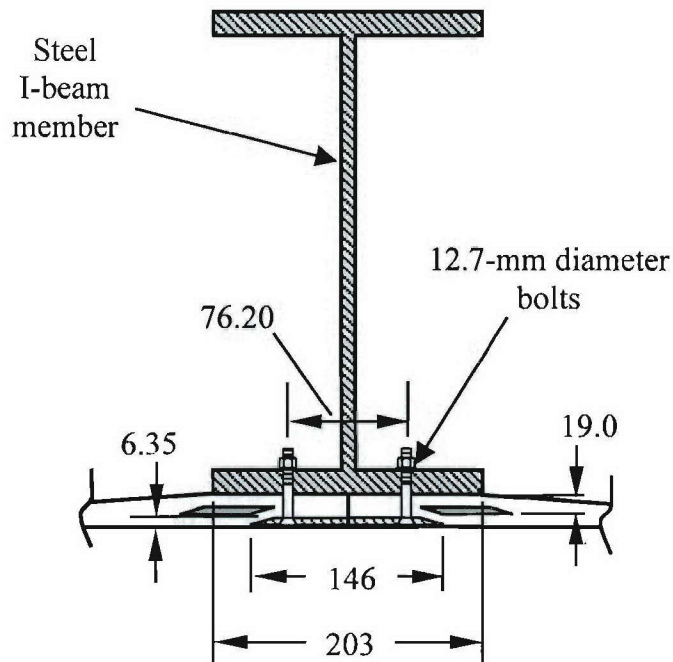


**Figure 4.12. Schematic of Hybrid Joint Details and Geometry (in mm)**

Use of the DS-4 joint configuration provided a relatively simple and cost-effective connection scheme to manufacture and assemble, while achieving good watertight integrity, when compared to a standard bolted joint configuration. The steel doubler plate prevented the joint from opening and allowed a better clamping force distribution through the thickness. The use of tapered-head bolts allowed a more hydrodynamic profile by providing a flushed surface on the wet side of the assembly.

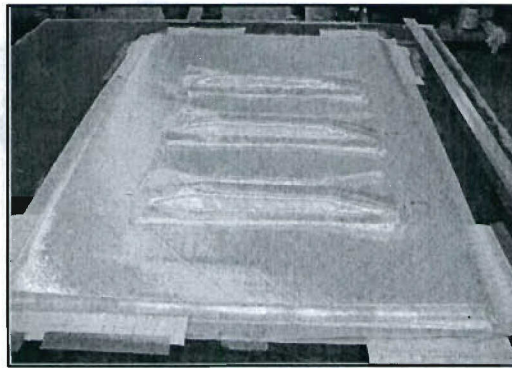
#### **4.4. Materials and Test Article Fabrication**

Fabrication of the composite panels was carried out at the Hybrid Structures Laboratory, at the University of Maine, using a vacuum assisted resin transfer molding process (VARTM). DOW Derakane 8084 Vinyl Ester resin and E-Glass fibers were used as the panel constituents. The reinforcing fibers were 680-gm, 0/90, and 680-gm,  $\pm 45$ , knit fabric, and were provided by Brunswick Technologies, Inc. (BTI). DIAB Divinycell H-80 foam was used to fabricate the foam inserts and the hat-stiffener sections.

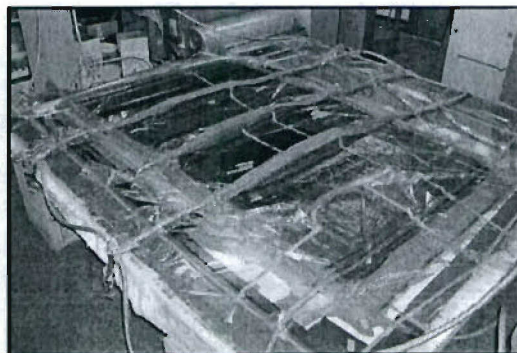
A 12.7-mm thick,  $[(\pm 45)_r (0/90)_r]_{4s}$  quasi-isotropic lay-up was used as the laminate architecture. The tapered region of the composite panels was created by

interleaving  $\pm 45$  and 0/90 full-panel sheets with 0/90 drop ply strips at the boundaries. This arrangement provided a total laminate thickness of 25.4 mm at the edges, tapering down to 12.7 mm at the center of the panels. In order to account for the doubler plate region, fabrication of the panels was performed on a 3-m by 3-m table, with a pre-fabricated steel mold.

The small panels and the hat-stiffeners were co-infused and photographs of their fabrication stages are shown in Figure 4.13. Resin infusion lines were placed on top of the stiffeners and vacuum lines were located at the edges of the fabrication table. To manufacture the stiffeners, the foam sections were positioned at the desired stiffener locations and a total of eight E-Glass layers were placed on top of each foam arrangement. A schematic of the lamination sequence for the hat-stiffener fabrication is shown in Figure 4.14.



**a) Panel and Hat-Stiffener Lay-Up**



**b) Panel Infusion**

**Figure 4.13. Fabrication of Small Panels**

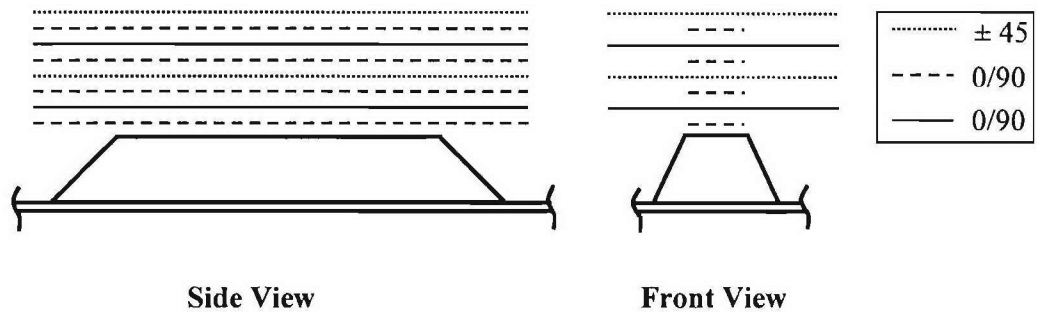
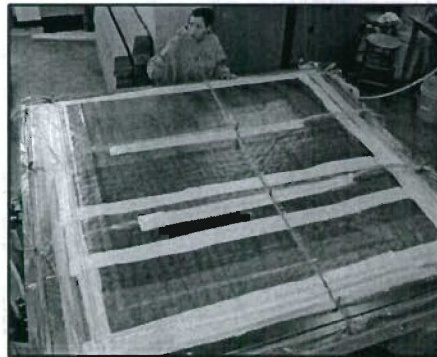
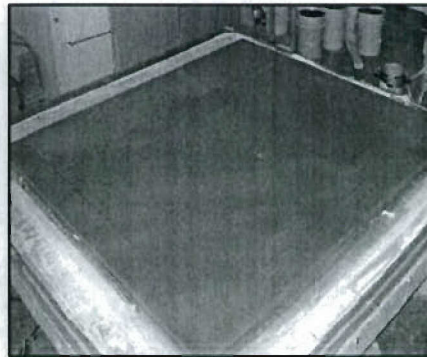


**Figure 4.14. Lamination Sequence for Hat-Stiffener Fabrication**

Fabrication of the large panels was carried out in two stages: 1) fabrication of the flat panels, and 2) fabrication of the hat-stiffeners. The first stage is shown in Figure 4.15, where the flat panels were infused and allowed to cure. Infusion lines were placed at 1/3 and 2/3 of the width of the fiber arrangement, and vacuum lines were located at the boundaries of the fabrication table. This insured a relatively even resin flow. After curing, the surfaces where the stiffeners were to be applied were rough sanded and wiped with acetone to remove debris.



**a) Panel Lay-Up**

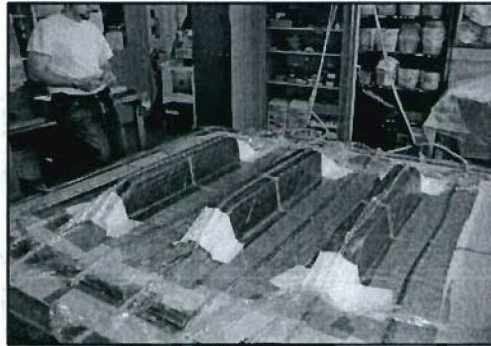


**b) Cured Flat Panel**

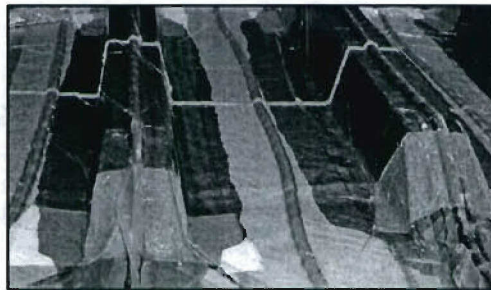
**Figure 4.15. Large Panel Fabrication, Stage 1: Flat Panels**



During the secondary stage, shown in Figure 4.16, foam sections were placed at the desired locations on the panels and the E-Glass fabric arrangement in Figure 4.14 was laid up on top of the foam forms. Resin infusion lines were placed on top of the stiffeners, while vacuum lines were located between stiffeners and at the boundaries of the fabrication table. After curing, the edges of the panels were trimmed and drilled for installation onto the hydrostatic test tank.



**a) Hat-Stiffener Lay-Up**



**b) Resin Infusion**



**c) Cured Stiffened Panel**

**Figure 4.16. Large Panel Fabrication, Stage 2: Hat-Stiffeners**

## 4.5. Panel Testing Procedures

### 4.5.1. Test Setup

A schematic of the hydrostatic test setup is presented in Figure 4.17. The testing apparatus for the panel assembly consisted of two main components: a hydrostatic test tank, used as the fixed base for the hybrid assembly; and a pressure vessel, used to apply the desired load to the panels. Figure 4.18 shows the geometry of the hydrostatic test tank. Design of the test tank was based upon the geometry of the hybrid assembly, the required pressure load, and the space constraints of a 1335-KN grillage and reaction frame in the laboratory. With a panel design load of 82.74 kPa, and using a maximum safety factor of three, a minimum test pressure capability of 248 kPa was required to insure failure of the panels. A final pressure of 690 kPa was established as the target design pressure for the test tank.

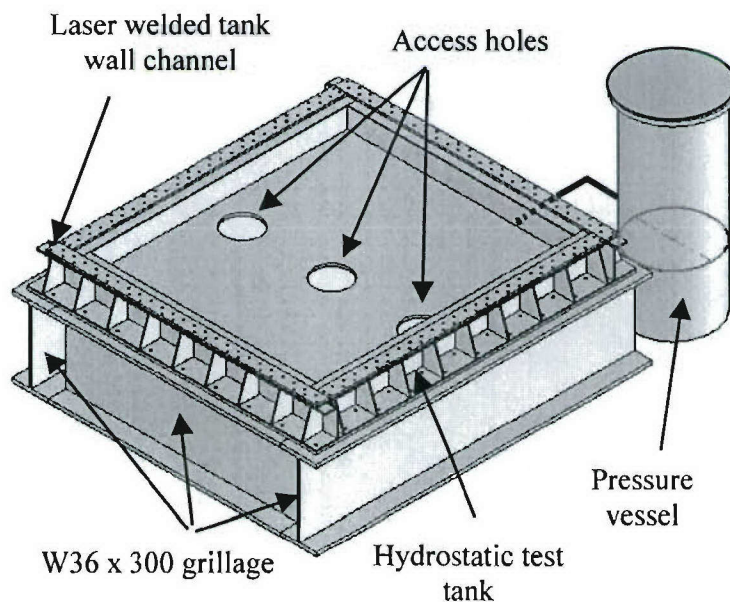


**Figure 4.17. Schematic of Hydrostatic Test Setup**

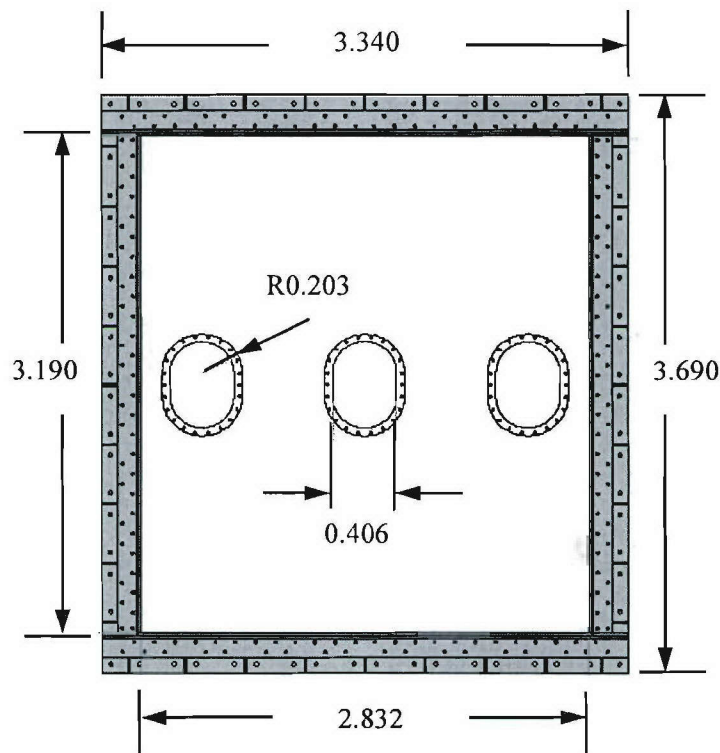


**Figure 4.18. Geometry of the Hydrostatic Test Tank (in meters)**

The hydrostatic test tank was comprised of four, custom laser welded, 337-mm deep, steel channel sections to form the walls, and a 38-mm thick steel plate to form the bottom of the tank. Figure 4.19 shows a typical laser welded channel. To provide adequate stiffness to the top and bottom flanges, 12.7-mm thick web stiffeners were welded to the channels, on 381-mm centers. A photograph of a welded channel, prior to welding of the stiffeners, is shown in Figure 4.20, and its cross-sectional dimensions are shown in Figure 4.21. The steel channel sections were fabricated at the Applied Thermal Sciences, Inc. Laser Processing Facility, in Sanford, Maine. Use of laser welding made it possible to create custom channel sections, while minimizing welding distortion and insuring watertight integrity at the tank and composite panel interfaces.



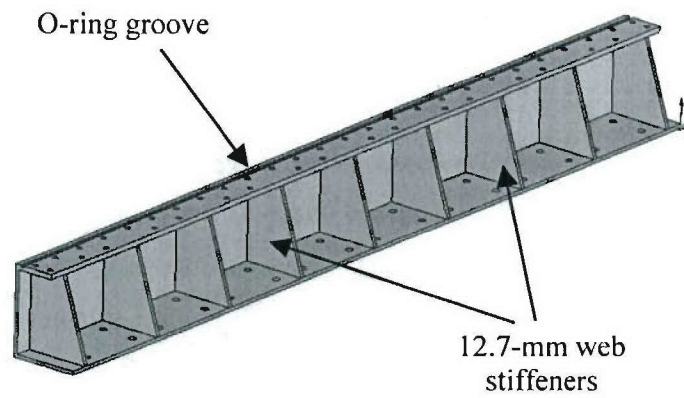


**Figure 4.19. Typical Laser Welded Channel with Stiffeners**



**Figure 4.20. Laser Welded Channel at ATS Processing Facility**

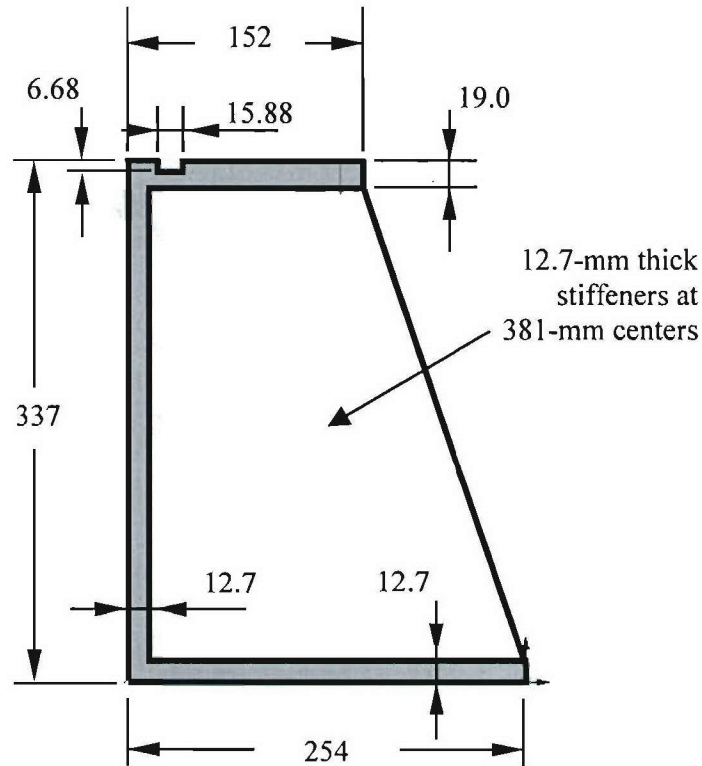


**Figure 4.21. Cross-Sectional Dimensions of a Laser Welded Channel (in mm)**

Figure 4.22 depicts the connection of a laser welded channel to the test tank base plate and the W36x300 grillage. As illustrated in Figure 4.23, the composite test panels were connected to the hydrostatic test tank by sandwiching the panels between the top flange of the tank channels and a 25.4-mm thick, steel backing plate. The panels were bolted to the tank using 22.2-mm, grade 8 steel bolts, arranged in a pattern shown in Figure 4.18. A watertight seal was created by using a 9.53-mm, square rubber O-ring, located in a 15.88-mm x 6.68-mm deep gland, on the top flange of the tank, inside the first bolt row. The bottom flanges of the laser welded channels were bolted to the 38-mm thick, steel bottom plate. The bottom plate was then attached to the top flange of the W36x300 grillage, by using 25.4-mm, grade 8, steel bolts.

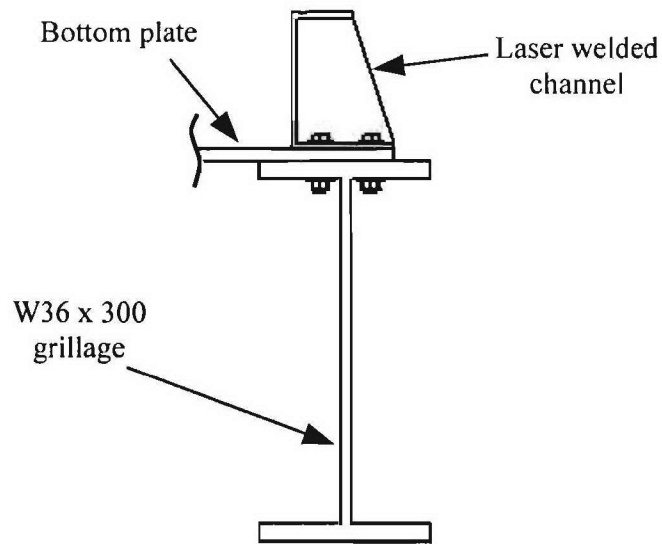


**Figure 4.22. Connection of a Laser Welded Channel to the W36x300 Grillage**

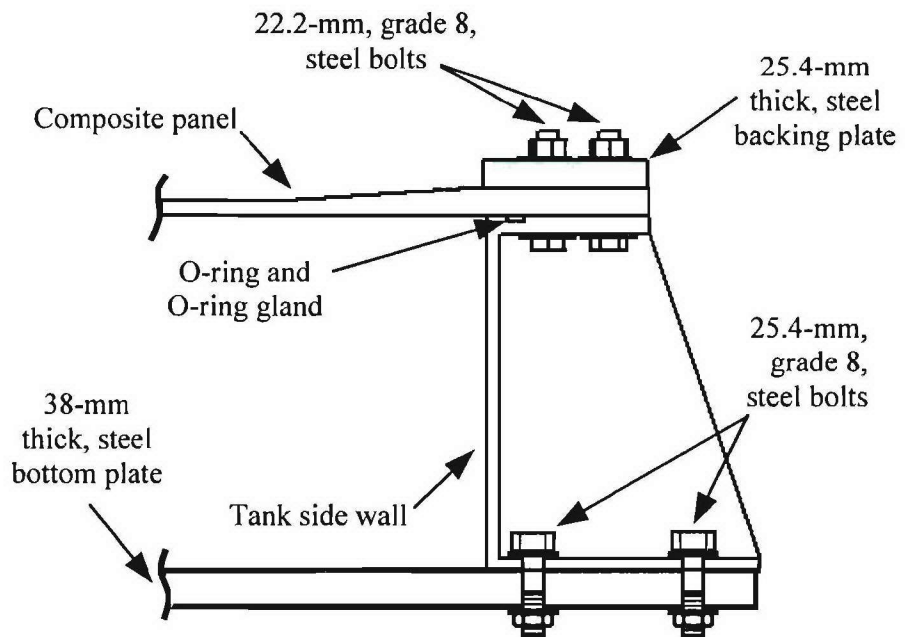


**Figure 4.23. Connection of a Composite Panel to a Laser Welded Channel Using a Steel Backing Plate**



#### 4.5.2. Testing Method

Testing of the panel assembly was conducted at the Hybrid Structures Laboratory, at the University of Maine. A critical aspect of the hydrostatic testing procedure was to devise a method to accurately regulate the tank pressure. Researchers have utilized various methods for simulating hydrostatic and aerodynamic loads for testing of panels. Some of these approaches were reviewed for their potential application to the MACH concept panel testing.

Among the methods considered for loading of the hybrid assembly was a pressure bladder approach, in which a distributed flexural load is applied in conjunction with a traditional load frame [ASTM D6416-99, 2004]. Though this method could be adapted for large-scale panel testing, the watertight integrity of the joint could not be adequately evaluated. Another approach considered was the D-Box test fixture, developed by Lockheed Aeronautical Systems and later applied by NASA Langley Research center [Arbur et al., 1995], which utilizes a sealed box pressurized with air or other inert gas to generate flexural loading on full-scale curved panels. Due to the complexity and cost associated with the test fixture, this technique was not well suited for panel testing. Another technique used is multiple point loading, where pads are bonded to a plate or outer skin. The nature of this technique makes it difficult to evaluate watertight integrity and to achieve a realistic distributed panel load.

In light of the apparent inadequacies of the aforementioned techniques for panel testing and their application to the MACH concept, devising a hydrostatic/hydrodynamic test system was essential. By utilizing water as the testing medium, it is possible to evaluate both the structural response of the panel assembly and the watertight integrity of the hybrid joint, thereby avoiding potentially dangerous situations associated with high volumes of compressed air. An air-over-water method was selected to apply pressure to the hybrid panel assembly, based on its safety, simplicity, and relatively low cost. This method also allowed the use of the laboratory's existing 827-kPa air supply.

Figure 4.24 shows a schematic of the hydrostatic pressure test setup. A 984-L pressure vessel, filled with water, was the interface between the compressed air and the test tank. To insure that no initial hydrostatic pressure was developed, the vessel was filled to a height equal to the top of the test tank. A Control Air, Inc. 700 precision,

manual regulating valve was used to achieve the desired pressure level, by manually dialing in each pressure step.

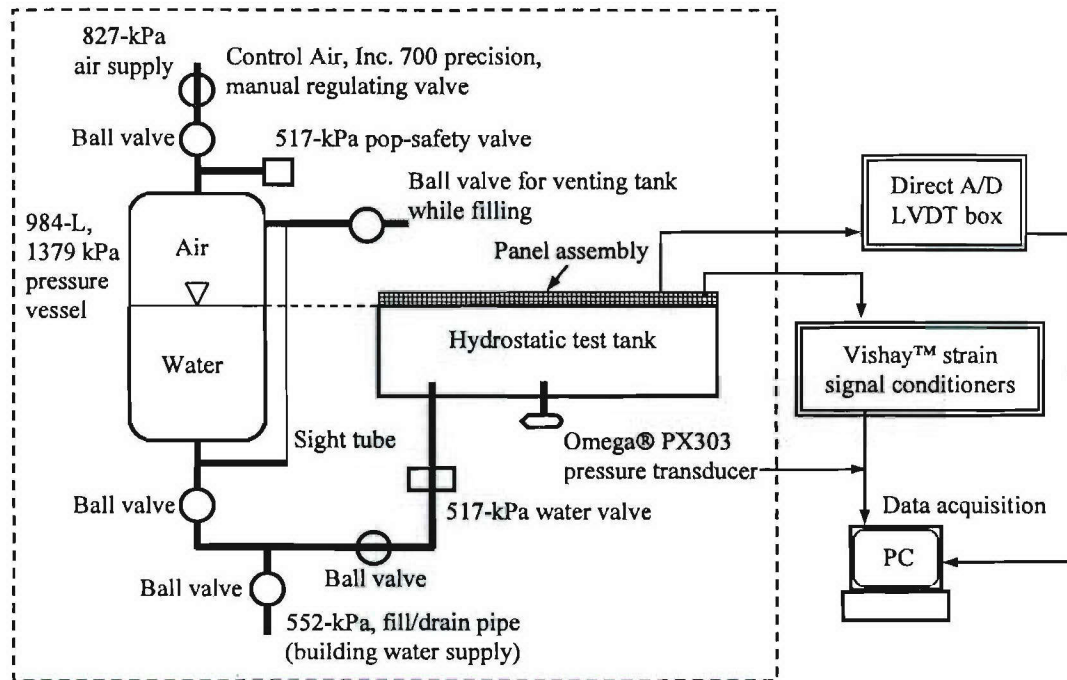


**Figure 4.24. Schematic of Hydrostatic Pressure Test Setup**

Testing of the hybrid panel assembly was conducted in a cyclic fashion. Cyclic testing was used to study the stiffness degradation of the structural system due to repetitive loading cycles, and to assess the load level at which the onset of damage occurred. The complete test was composed of a total of six cycle sets, as shown in Figure 4.25. Each cycle set was comprised of three equal load cycles. The pressure level was varied in increments of 6.90 kPa, from atmospheric pressure to a peak value of 248 kPa (three times the design pressure of 82.74 kPa). Load, displacement and strain data were recorded at each pressure step.

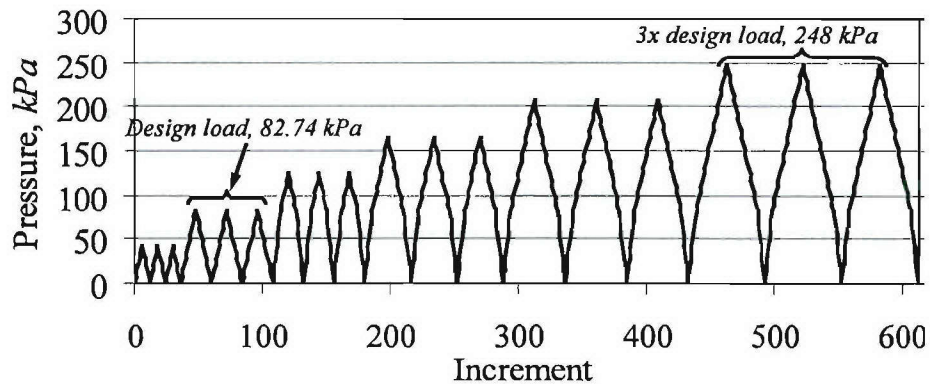


**Figure 4.25. Pressure Cycle History**

#### 4.5.3. Instrumentation

Due to the large scale of the panel assembly and the limited number of available channels for data acquisition, instrumentation of all four panels was unfeasible. Instead, only two of the four panels (P01 and P03) were heavily instrumented, using metal foil strain gages and linear variable displacement transducers (LVDTs), to measure strains and vertical displacements at discrete locations on the panels and the steel I-beam members. The applied pressure was measured using an Omega® PX303 pressure transducer, mounted on one of the side walls of the test tank. In addition, photogrammetry targets were used to monitor the displacement field.

Strain gages were procured from Micro-Measurements Group, Inc. A total of forty-eight uniaxial gages, type CEA-00-250UW-350, and four rosette gages, type CEA-00-250UR-350, were installed on the composite panel surfaces. A total of fourteen uniaxial gages, type CEA-06-250UW-350, were mounted on the steel members. A total of fifteen MacroSensors™ LVDTs were used to measure the vertical displacement of the panels and the I-beam members. Six LVDTs were placed on each panel, P01 and P03, and one LVDT was placed at the crossing point of the I-beams to monitor the global



displacement of the assembly. For P02 and P04, one LVDT was placed at the center of each panel.

Figure 4.26 shows a schematic of the hybrid panel assembly and the naming conventions used to identify its various components. The small panels are identified as P01 and P02, while the large panels are identified as P03 and P04. Doubler plate designations are shown in the figure, where the centerpiece doubler is designated as CP. A local coordinate system is used for each panel and labeled according to the panel number, i.e.  $x_1, y_1$ , for small panel 1 (P01), etc. The origin of the coordinate systems is located at the center of CP. Strain gages and LVDTs were designated according to the instrumentation naming convention presented in Table 4.1.

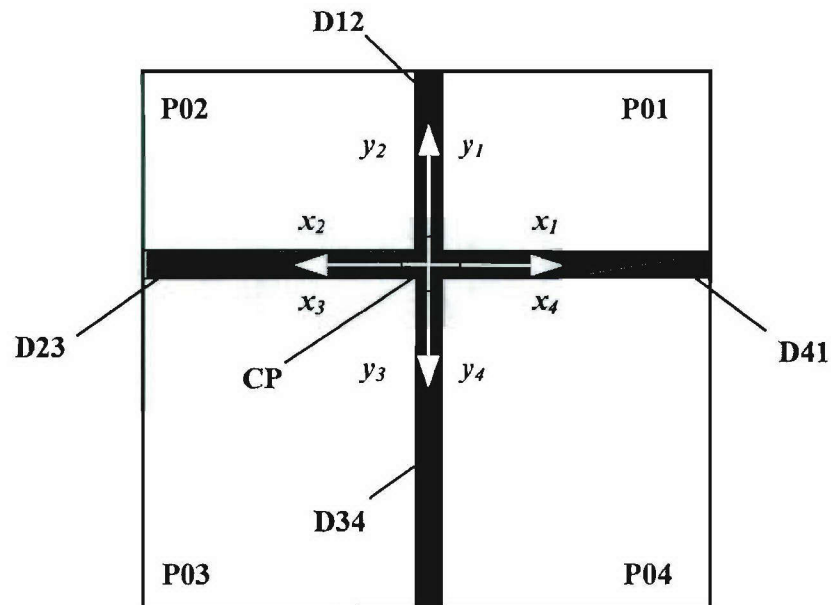


**Figure 4.26. Naming Conventions and Coordinate Systems for Hybrid Assembly Components**

**Table 4.1. Instrumentation Naming Convention**

<b>Device I.D.</b>	<b>Description</b>	<b>Location</b>
ST#-# (strain, top)	Uniaxial strain gage	Top surface of the panel (wet side)
SB#-# (strain, bottom)	Uniaxial strain gage	Bottom surface of the panel (dry side)
SD#-# (strain, doubler)	Uniaxial strain gage	Doubler plates (wet side)
SF#-# (strain, flange)	Uniaxial strain gage	Flanges of the steel I-beam (dry side)
SCB#-# (strain, I-beams)	Uniaxial strain gage	Crossing of steel I-beam members
RT#-# (rosette, top)	Rosette strain gage	Top surface of the panel (wet side)
RB#-# (rosette, bottom)	Rosette strain gage	Bottom surface of the panel (dry side)
DP#-# (disp., panel)	LVDT	Dry surface of the panel
DCB#-# (disp., I-beams)	LVDT	Crossing of steel I-beam members

In Table 4.1, the first number following the letters corresponds to the panel number on which the device was installed, and the second number corresponds to the device number. For instance, ST1-1 stands for “Strain gage on the Top surface, panel 1, gage number 1.” Similarly, DP1-1 stands for “Displacement sensor, Panel 1, LVDT number 1.”

Figure 4.27 shows a schematic of the strain gage configuration for the wet side of P01, while Figure 4.28 shows that of the dry side. The geometric locations of the strain gages on the wet and dry surfaces of the panel are presented in Tables 4.2 and 4.3, respectively. The LVDT configuration for P01 is depicted in Figures 4.29 and 4.30. The geometric locations of the LVDTs are summarized in Table 4.4.

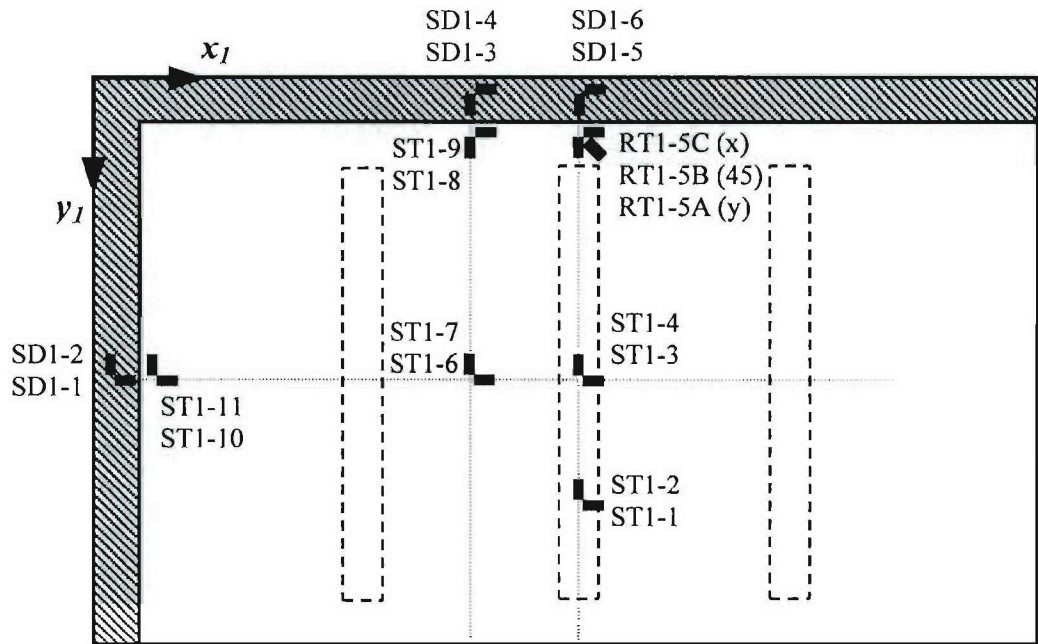


Figure 4.27. Strain Gage Configuration for P01, Wet Side

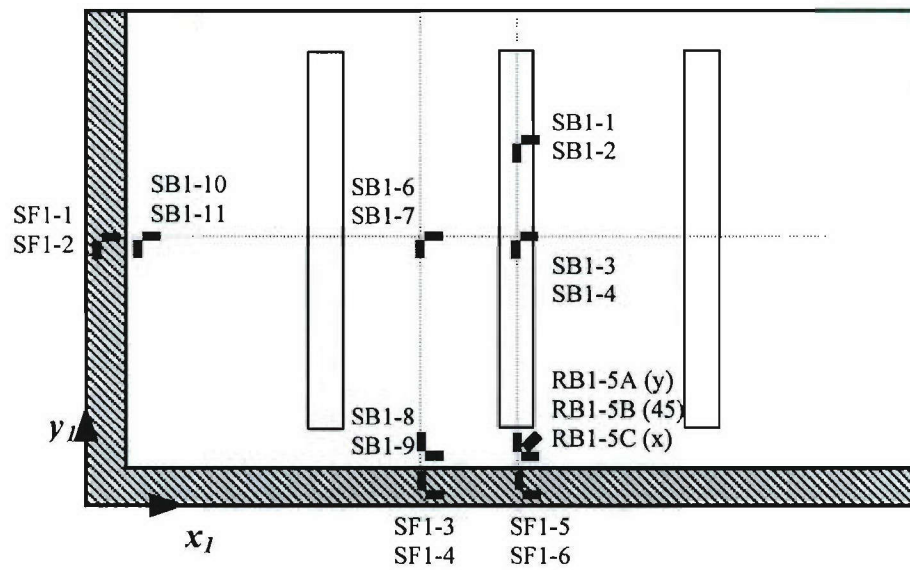


Figure 4.28. Strain Gage Configuration for P01, Dry Side



**Table 4.2. Strain Gage Locations for P01, Wet Side**

<b>Gage I.D.</b>	<b>Gage type</b>	<b><math>x_I</math> (mm)</b>	<b><math>y_I</math> (mm)</b>	<b>Location</b>	<b>Gage direction</b>
ST1-1	Uniaxial	813	719	Panel, Top	$x_I$
ST1-2	Uniaxial	813	711	Panel, Top	$y_I$
ST1-3	Uniaxial	821	522	Panel, Top	$x_I$
ST1-4	Uniaxial	813	522	Panel, Top	$y_I$
RT1-5A	Rosette	813	144	Panel, Top	$y_I$
RT1-5B	Rosette	813	144	Panel, Top	$y_I$
RT1-5C	Rosette	813	144	Panel, Top	$x_I$
ST1-6	Uniaxial	586	522	Panel, Top	$x_I$
ST1-7	Uniaxial	606	522	Panel, Top	$y_I$
ST1-8	Uniaxial	606	127	Panel, Top	$y_I$
ST1-9	Uniaxial	606	117	Panel, Top	$x_I$
ST1-10	Uniaxial	127	524	Panel, Top	$x_I$
ST1-11	Uniaxial	117	524	Panel, Top	$y_I$
SD1-1	Uniaxial	48	524	D12, Top	$x_I$
SD1-2	Uniaxial	38	524	D12, Top	$y_I$
SD1-3	Uniaxial	581	48	D41, Top	$y_I$
SD1-4	Uniaxial	581	41	D41, Top	$x_I$
SD1-5	Uniaxial	813	52	D41, Top	$y_I$
SD1-6	Uniaxial	813	41	D41, Top	$x_I$

**Table 4.3. Strain Gage Locations for P01, Dry Side**

Gage I.D.	Gage type	$x_I$ (mm)	$y_I$ (mm)	Location	Gage direction
SB1-1	Uniaxial	813	719	Panel, Bottom	$x_I$
SB1-2	Uniaxial	813	711	Panel, Bottom	$y_I$
SB1-3	Uniaxial	821	522	Panel, Bottom	$x_I$
SB1-4	Uniaxial	813	522	Panel, Bottom	$y_I$
RB1-5A	Rosette	813	144	Panel, Bottom	$y_I$
RB1-5B	Rosette	813	144	Panel, Bottom	$y_I$
RB1-5C	Rosette	813	144	Panel, Bottom	$x_I$
SB1-6	Uniaxial	586	522	Panel, Bottom	$x_I$
SB1-7	Uniaxial	606	522	Panel, Bottom	$y_I$
SB1-8	Uniaxial	606	127	Panel, Bottom	$y_I$
SB1-9	Uniaxial	606	117	Panel, Bottom	$x_I$
SB1-10	Uniaxial	127	524	Panel, Bottom	$x_I$
SB1-11	Uniaxial	117	524	Panel, Bottom	$y_I$
SF1-1	Uniaxial	48	524	FY	$x_I$
SF1-2	Uniaxial	38	524	FY	$y_I$
SF1-3	Uniaxial	581	48	FX	$y_I$
SF1-4	Uniaxial	581	41	FX	$x_I$
SF1-5	Uniaxial	813	52	FX	$y_I$
SF1-6	Uniaxial	813	41	FX	$x_I$

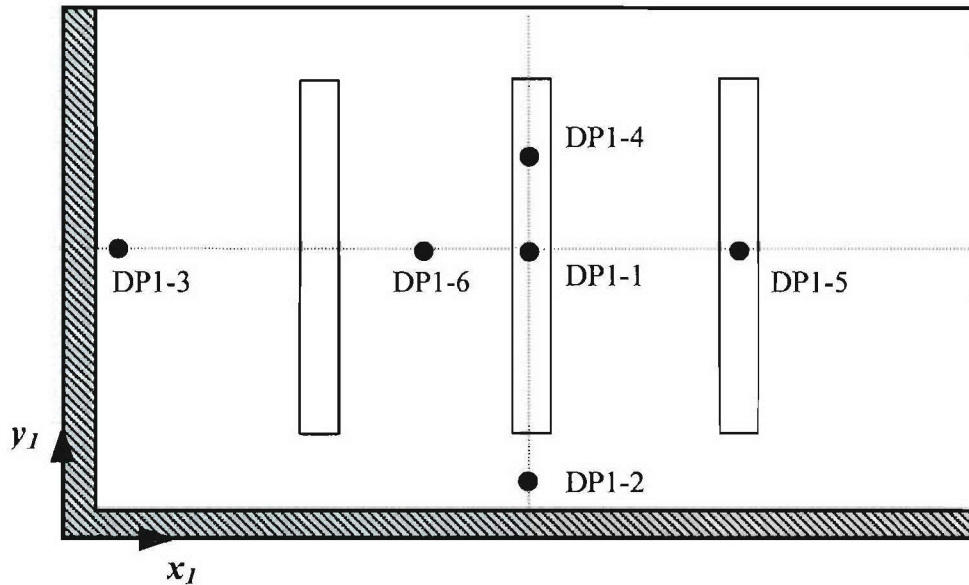


**Figure 4.29. LVDT Configuration for P01, Plan View**

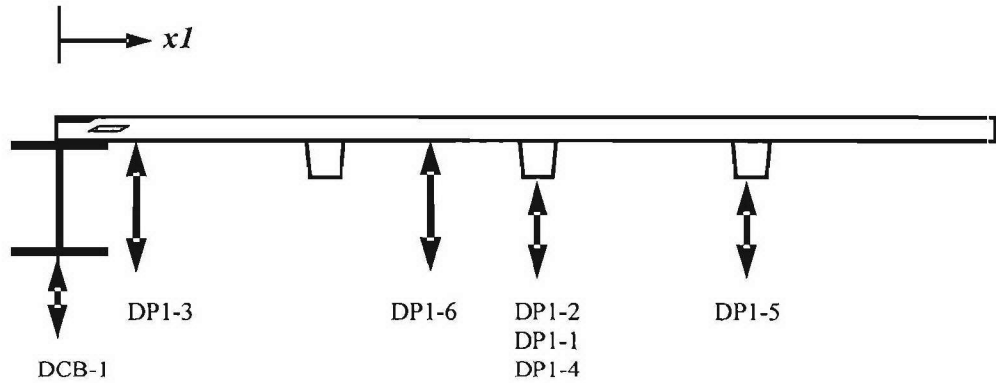


**Figure 4.30. LVDT Configuration for P01, Side View**

**Table 4.4. LVDT Locations for P01, Dry Side**

LVDT I.D.	Location	$x_l$ (mm)	$y_l$ (mm)	Sensor Range (mm)
DP1-1	Middle stiffener	800	521	+/- 76.2
DP1-2	Joint region	800	127	+/- 12.7
DP1-3	Joint region	146	521	+/- 12.7
DP1-4	Middle stiffener	800	724	+/- 50.8
DP1-5	Outer stiffener	1207	521	+/- 12.7
DP1-6	Panel surface	559	521	+/- 50.8

Schematics of the strain gage configuration for the wet and dry sides of P03 are shown in Figures 4.31 and 4.32, respectively. Strain gage locations are summarized in Tables 4.5 and 4.6. LVDT configuration schematics for P03 are presented in Figures 4.33 and 4.34 and their geometric locations are presented in Table 4.7.



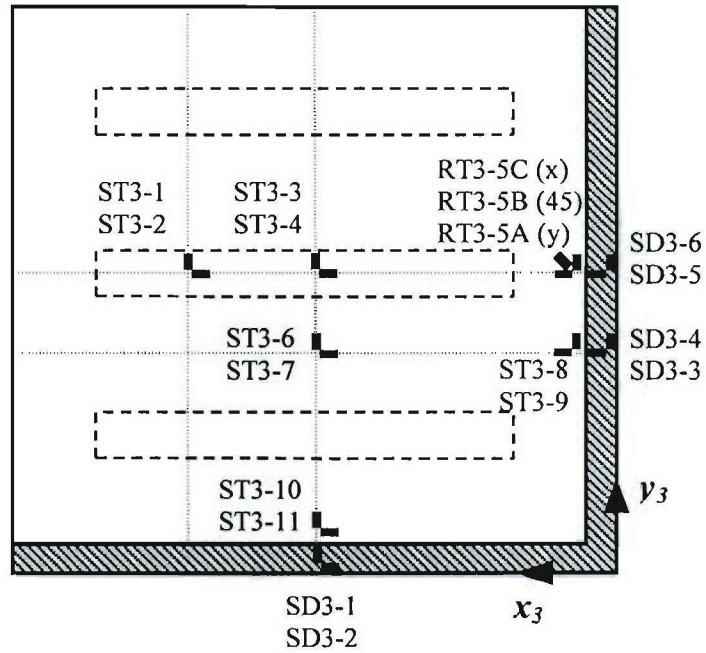


Figure 4.31. Strain Gage Configuration for P03, Wet Side

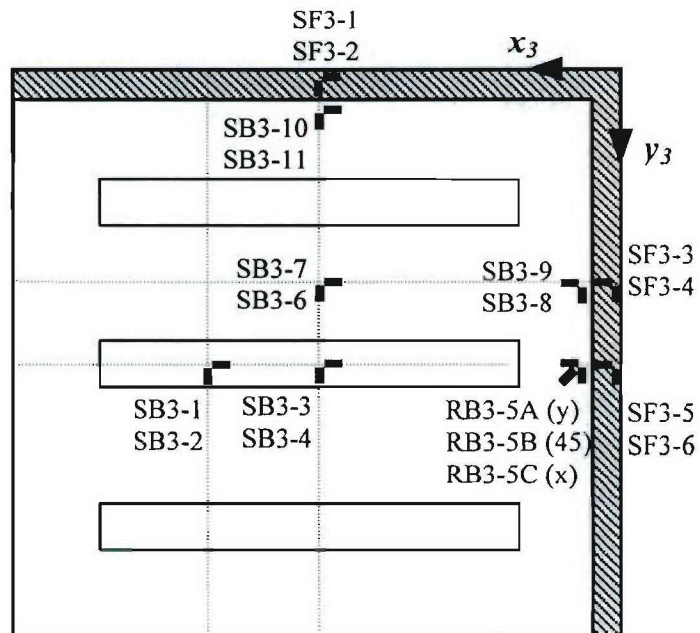


Figure 4.32. Strain Gage Configuration for P03, Dry Side

**Table 4.5. Strain Gage Locations for P03, Wet Side**

<b>Gage I.D.</b>	<b>Gage type</b>	<b><math>x_3</math> (mm)</b>	<b><math>y_3</math> (mm)</b>	<b>Location</b>	<b>Gage direction</b>
ST3-1	Uniaxial	1149	864	Panel, Top	$y_3$
ST3-2	Uniaxial	1162	864	Panel, Top	$x_3$
ST3-3	Uniaxial	813	864	Panel, Top	$y_3$
ST3-4	Uniaxial	813	864	Panel, Top	$x_3$
RT3-5A	Rosette	121	864	Panel, Top	$y_3$
RT3-5B	Rosette	121	864	Panel, Top	$x_3$
RT3-5C	Rosette	121	864	Panel, Top	$x_3$
ST3-6	Uniaxial	813	578	Panel, Top	$y_3$
ST3-7	Uniaxial	813	565	Panel, Top	$x_3$
ST3-8	Uniaxial	117	578	Panel, Top	$y_3$
ST3-9	Uniaxial	127	578	Panel, Top	$x_3$
ST3-10	Uniaxial	810	130	Panel, Top	$y_3$
ST3-11	Uniaxial	810	121	Panel, Top	$x_3$
SD3-1	Uniaxial	806	51	D23, Top	$y_3$
SD3-2	Uniaxial	806	38	D23, Top	$x_3$
SD3-3	Uniaxial	48	578	D34, Top	$x_3$
SD3-4	Uniaxial	38	578	D34, Top	$y_3$
SD3-5	Uniaxial	48	864	D34, Top	$x_3$
SD3-6	Uniaxial	38	870	D34, Top	$y_3$

**Table 4.6. Strain Gage Locations for P03, Dry Side**

<b>Gage I.D.</b>	<b>Gage type</b>	<b><math>x_3</math> (mm)</b>	<b><math>y_3</math> (mm)</b>	<b>Location</b>	<b>Gage direction</b>
SB3-1	Uniaxial	1149	864	Panel, Top	$y_3$
SB3-2	Uniaxial	1162	864	Panel, Top	$x_3$
SB3-3	Uniaxial	813	864	Panel, Top	$y_3$
SB3-4	Uniaxial	813	864	Panel, Top	$x_3$
RB3-5A	Rosette	121	864	Panel, Top	$y_3$
RB3-5B	Rosette	121	864	Panel, Top	$x_3$
RB3-5C	Rosette	121	864	Panel, Top	$x_3$
SB3-6	Uniaxial	813	578	Panel, Top	$y_3$
SB3-7	Uniaxial	813	565	Panel, Top	$x_3$
SB3-8	Uniaxial	117	578	Panel, Top	$y_3$
SB3-9	Uniaxial	127	578	Panel, Top	$x_3$
SB3-10	Uniaxial	810	130	Panel, Top	$y_3$
SB3-11	Uniaxial	810	121	Panel, Top	$x_3$
SF3-1	Uniaxial	806	51	FX	$y_3$
SF3-2	Uniaxial	806	38	FX	$x_3$
SF3-3	Uniaxial	48	578	FY	$x_3$
SF3-4	Uniaxial	38	578	FY	$y_3$
SF3-5	Uniaxial	48	864	FY	$x_3$
SF3-6	Uniaxial	38	870	FY	$y_3$



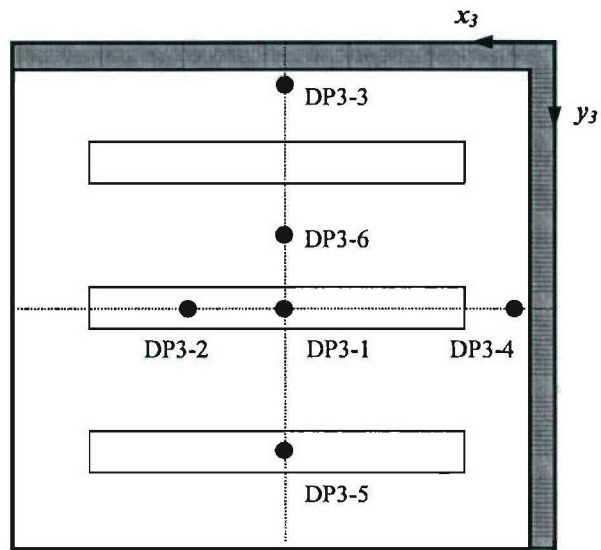


Figure 4.33. LVDT Configuration for P03, Plan View

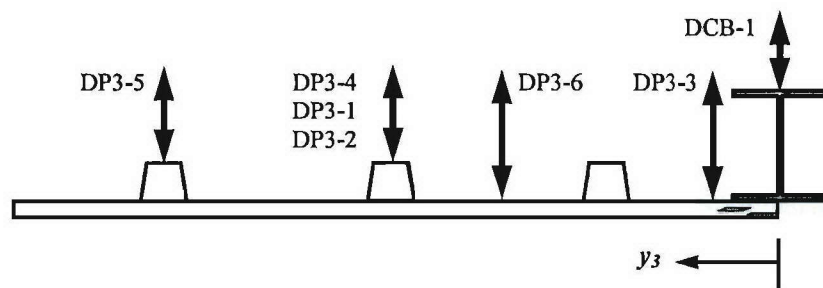


Figure 4.34. LVDT Configuration for P03, Side View

**Table 4.7. LVDT Locations for P03, Dry Side**

<b>LVDT I.D.</b>	<b>Location</b>	<b><math>x_3</math> (mm)</b>	<b><math>y_3</math> (mm)</b>	<b>Sensor Range (mm)</b>
DP3-1	Middle stiffener	813	889	+/- 76.2
DP3-2	Middle stiffener	1041	889	+/- 25.4
DP3-3	Joint region	813	165	+/- 25.4
DP3-4	Joint region	140	889	+/- 25.4
DP3-5	Outer stiffener	813	1448	+/- 25.4
DP3-6	Panel surface	813	483	+/- 25.4

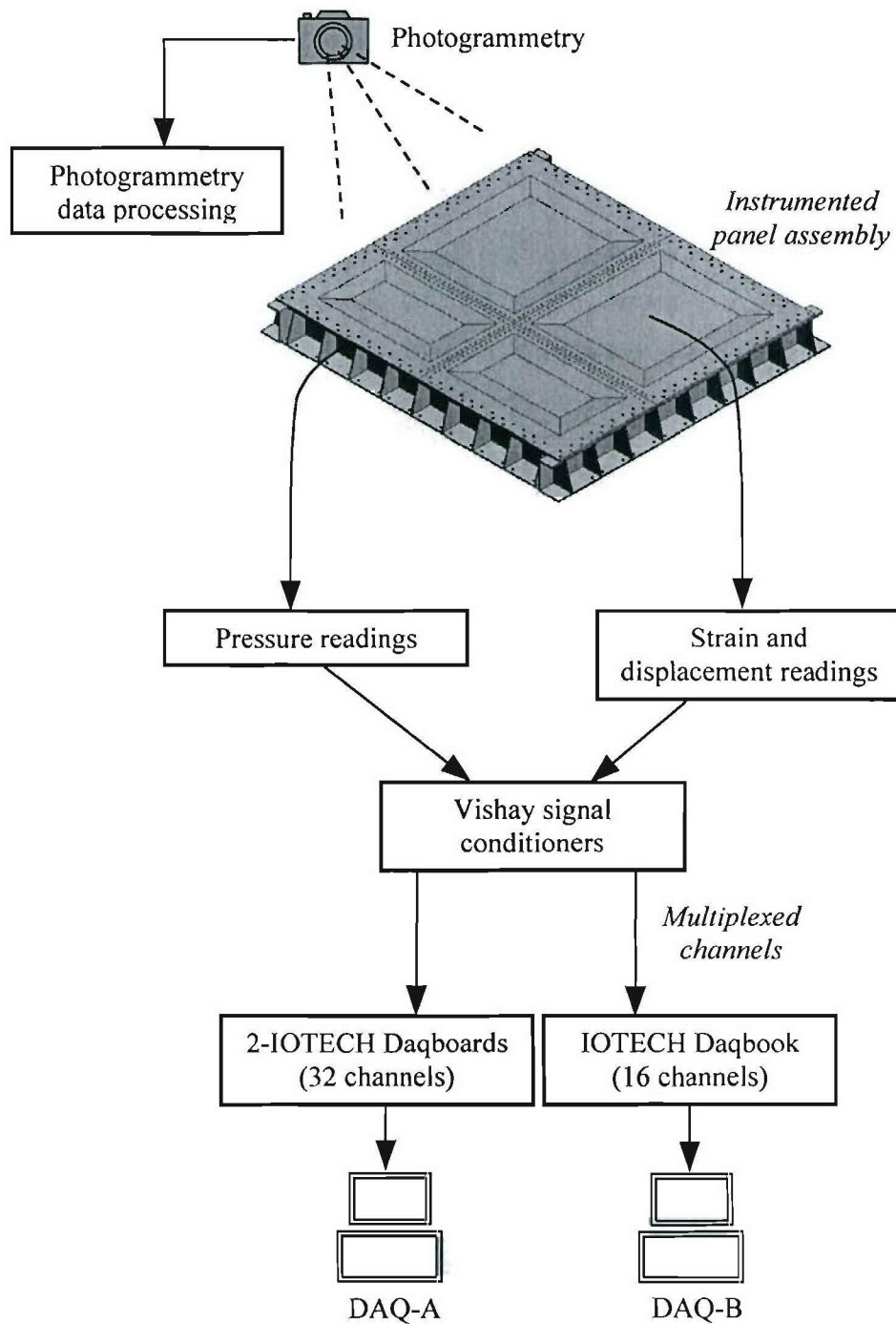
#### **4.5.4. Data-Acquisition Configuration**

Figure 4.35 shows a schematic of the data-acquisition system. Data-acquisition was carried out using two Pentium™ 4, 2.4 GHz, 512-MB RAM systems, two IOTECH™ Daqboard 2000 cards, a Daqbook 200, and nine Vishay™ 2120 multi-channel strain signal conditioners. These systems have 16 bit analog-to-digital conversion resolution and are capable of reading a total of forty-eight channels at a throughput rate of 1 kHz, which was appropriate for the rate of testing used in this study.

The data-acquisition process was controlled using the *DAQFI\_D5* software, written at the University of Maine. Load, displacement and strain values were recorded at every load step. A timed data taking routine was used to trigger the system every three minutes, which was found to be an adequate time interval to allow pressure stabilization inside of the test tank. Strain readings from seven signal conditioners were multiplexed in order to accommodate all strain gages and the available number of channels. To reduce the errors due to instrumentation noise, multiple samples were averaged during data acquisition. Photogrammetry data was taken during the initial stage, prior to loading of the assembly, and at the peak pressure values of 124 kPa and 248 kPa.

The data acquisition systems were labeled as DAQ-A and DAQ-B. DAQ-A was equipped with the two DAQboard 2000 boards, capable of reading 32 channels, while DAQ-B was configured with the Daqbook 200 to read 16 channels. The multiplexed strain values were recorded using the DAQ-B system. Pressure transducer values were

recorded with both systems. For data-acquisition purposes, the DAQ-A system acted as the master system, which triggered DAQ-B to record data every three minutes.



**Figure 4.35. Data-Acquisition System Schematic**



## **4.6. Panel Testing Results**

The panel testing results were subdivided into four distinct sections: 1) load versus displacement curves; 2) displaced panel shapes; 3) load versus strain curves; and 4) failure modes. Testing of the panels to failure allowed the verification of the panel design and the manufacturing techniques. Additionally, it allowed an assessment of the feasibility of implementing the DS-4 joint configuration into a large-scale panel assembly. Correlation of the displacements recorded with LVDTs and photogrammetry is also presented in this section.

### **4.6.1. Load versus Displacement Curves**

Load versus displacement curves at various load steps are used to provide an indication of stiffness degradation and to observe the onset of damage and ultimate structural failure. The load versus displacement curves for panels P01 and P03 are presented in Figures 4.36 and 4.37, respectively. These curves correspond to the vertical displacement values recorded at the center of the middle stiffeners (DP1-1, DP3-1). Each figure presents curves for the first three load cycle sets and the loops for the entire test.

Figures 4.36a and 4.37a show the load versus displacement curves for the initial loading cycle set, with a peak pressure value of 41.37 kPa, one half of the panel design load. For this case, the pressure was increased in steps of 3.45 kPa for the 0-21 kPa range, and 6.90 kPa for the 21-41.37 kPa range. The curves for P01 and P03 exhibit a stable, linear response, as the loading and unloading paths are nearly identical. For this load cycle set, the maximum displacement values recorded for P01 and P03 were 3.26 mm and 3.47 mm, respectively.

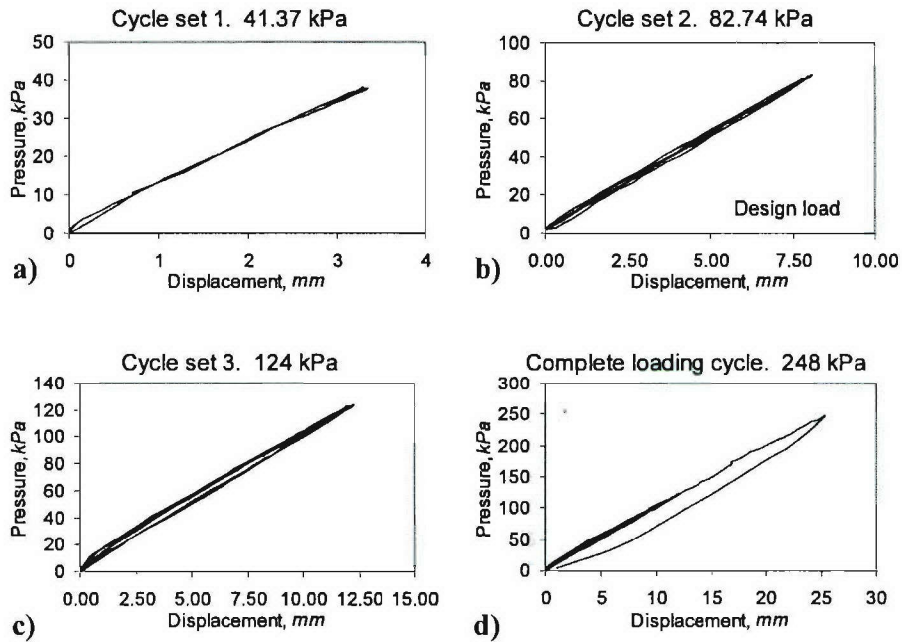


Figure 4.36. Load versus Displacement Curves for P01 (DP1-1)

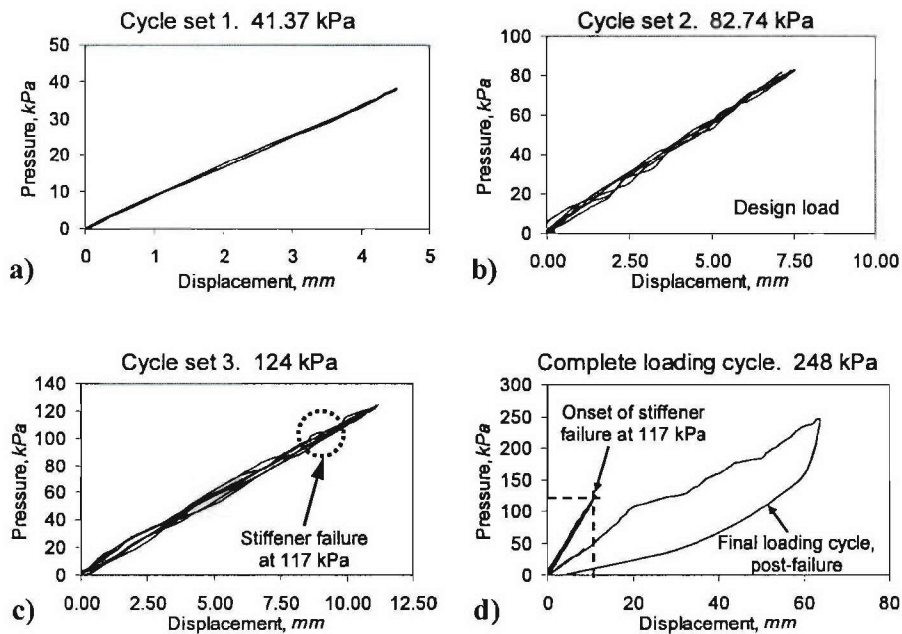


Figure 4.37. Load versus Displacement Curves for P03 (DP3-1)

Figures 4.36b and 4.37b show the load versus displacement curves of panels P01 and P03, when loaded to the design pressure of 82.74 kPa. Linear behavior of the system was observed and visual inspection of the panel assembly indicated no apparent damage. The design load was reached without damage to the joint or the composite panels. For this load cycle set, the maximum displacement values recorded for P01 and P03 were 8.70 mm (DP1-6) and 8.42 mm (DP3-6), respectively, which correspond to the displacements recorded between stiffeners.

As described by Thompson et al. [2005], the peak deflection of the panels,  $\Delta_{\max}$ , was established according to Equation (4.1), where  $L$  is the span of the panel and  $b$  is the design factor. The panels were designed with a target value of  $b_{\text{design}} = 200$ . Table 4.8 summarizes the maximum panel displacements at the design load, along with the values of  $b_{\text{exp}}$ , computed using the experimental results. For both small and large panels, this ratio is very close to the design target, with a peak difference of 9.14 percent for the large panel.

$$\Delta_{\max} = \frac{L}{b} \quad (4.1)$$

**Table 4.8. Maximum Panel Displacements at Design Load, P = 82.74 kPa**

Panel	$L$ (mm)	$\Delta_{\max}$ (mm)	$b_{\text{exp}} = L / \Delta_{\max}$	$b_{\text{design}}$	% Difference
P01	1638	8.70	193.45	200	3.28
P03	1838	8.42	218.29	200	9.14

Figures 4.36c and 4.37c show the load versus displacement curves for the third set of cycles, where the hybrid assembly was loaded to a pressure of 124 kPa. A slight opening of the curves was observed for this loading step. At 117 kPa, failure was visibly observed at the stiffener/panel interface, on the outer stiffener of P03, but was not observable from the curves in Figure 4.37c, since damage was localized at the tapered

region of the stiffener (Figure 4.38) and was not captured by the LVDT located at the center of the stiffener (DP3-1). The onset of damage produced load redistribution from the outer stiffener to the middle and inner stiffeners, until failure of all stiffeners occurred during the last loading cycle set. For this set of loading cycles, the peak displacements recorded for P01 and P03 were 13.47 mm (DP1-6) and 12.84 mm (DP3-6), respectively.

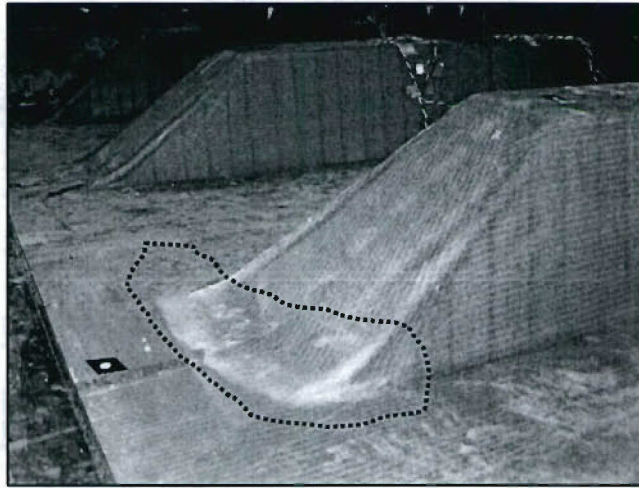


**Figure 4.38. Onset of Damage at the Stiffener/Panel Interface (P03)**

Load versus displacement curves for the entire test are shown in Figures 4.36d and 4.37d. In both cases, the unloading path was different from the loading path, which indicated permanent stiffness degradation within the composite panels. For the small panel, P01, a peak displacement of 27.67 mm (DP1-6) was recorded, with no noticeable damage occurring at either the stiffener/panel interfaces or at the joint region. For the large panel, P03, a displacement of 63.76 mm (DP3-1) was recorded at the center of the panel. Because the middle stiffener had completely separated from the composite panel at this stage, the peak displacement was taken to be 51.94 mm (DP3-6). Failure of the panels is described in Section 4.6.5. The complete set of load versus displacement plots for all LVDT locations are presented in Appendix H.

Tables 4.9 through 4.11 summarize the peak displacement readings for all four panels and I-beams, at four different pressure levels. For the first three loading cycle sets, the displacement values recorded were relatively close to each other for any given



location on the panels. The values recorded for DP3-1 and DP4-1 (center of middle stiffeners on large panels) during the last loading cycle indicated imminent failure of the middle stiffeners. The peak displacement recorded for the intersection of the I-beam members was 7.58 mm at a pressure of 248 kPa.

**Table 4.9. Summary of Displacements for P01**

Pressure (kPa)	Displacement (mm)					
	DP1-1	DP1-2	DP1-3	DP1-4	DP1-5	DP1-6
41.37	3.26	1.63	1.27	3.25	2.68	3.73
82.74	8.09	3.61	2.53	6.50	5.35	8.70
124	12.24	5.32	3.39	10.07	8.30	13.47
248	25.33	11.50	7.16	19.82	17.25	27.67

**Table 4.10. Summary of Displacements for P03**

Pressure (kPa)	Displacement (mm)					
	DP3-1	DP3-2	DP3-3	DP3-4	DP3-5	DP3-6
41.37	3.47	3.31	1.28	1.72	2.18	3.75
82.74	7.53	6.63	2.67	3.44	4.35	8.42
124	11.16	10.07	3.80	4.97	6.58	12.84
248	63.76	49.26	14.09	11.94	28.56	51.94

**Table 4.11. Summary of Displacements for P02, P04 and I-beams**

Pressure (kPa)	Displacement (mm)		
	DP2-1	DP4-1	DCB-1
41.37	3.72	3.37	1.28
82.74	7.44	6.74	2.56
124	11.15	10.69	3.39
248	23.73	74.99	7.58

#### 4.6.2. Displaced Panel Shapes

Figures 4.39 and 4.40 present the displaced shapes for panels P01 and P03 at various pressure load levels, respectively. These shapes were plotted using displacement values recorded at discrete LVDT locations, along the  $x$  and  $y$  directions for P01 and P03, versus the LVDT location. In a qualitative sense, the curves for the first three pressure level values indicate a nearly proportional increase of displacement with increasing pressure.

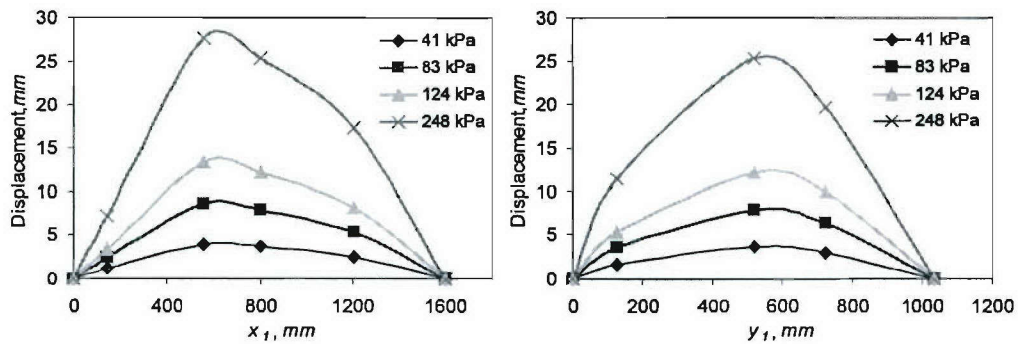


Figure 4.39. Displaced Shapes for P01

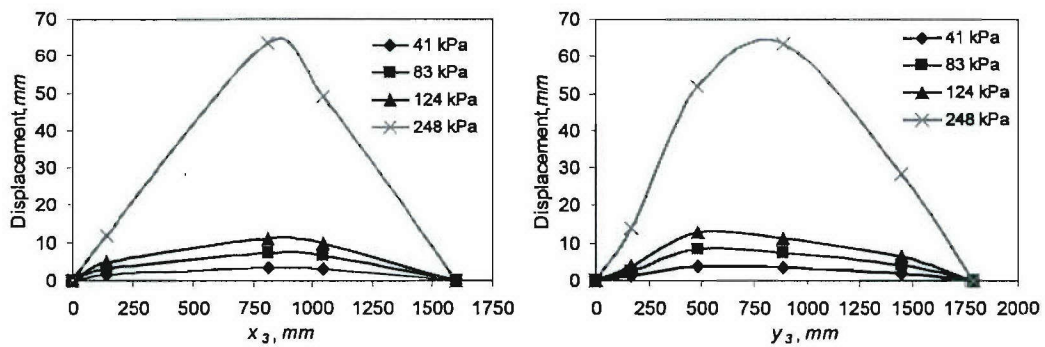


Figure 4.40. Displaced Shapes for P03

#### 4.6.3. Correlation of Displaced Panel Shapes to Photogrammetry

Figures 4.41 and 4.42 present the displaced shapes for P01 and P03, for a pressure of 124 kPa. These curves were plotted using displacement values recorded at discrete locations, from LVDTs and photogrammetry targets. As depicted in Figure 4.26, the  $x_1$  axis is aligned transversely to the stiffener direction and  $y_1$  is in the stiffener direction, for P01. For P03, the  $x_3$  axis is aligned with the direction of the stiffeners and  $y_3$  is transverse to the stiffeners. In general terms, and for a pressure load level of 124 kPa, good agreement was observed between the values recorded from the LVDTs and those from the photogrammetry targets, with a peak discrepancy of 7 percent.

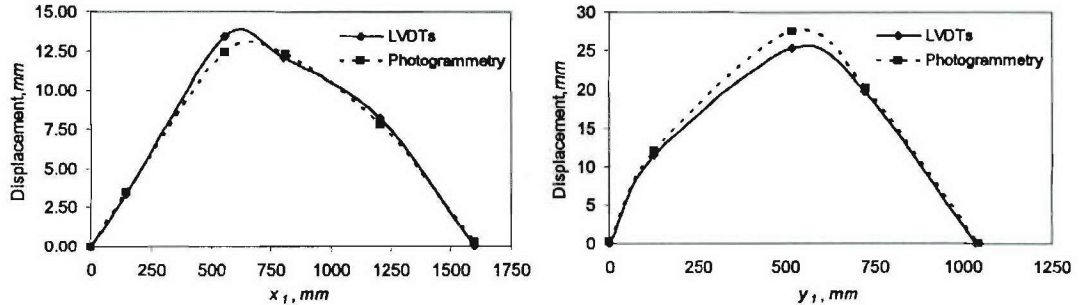


Figure 4.41. Displaced Shapes for P01 at 124 kPa

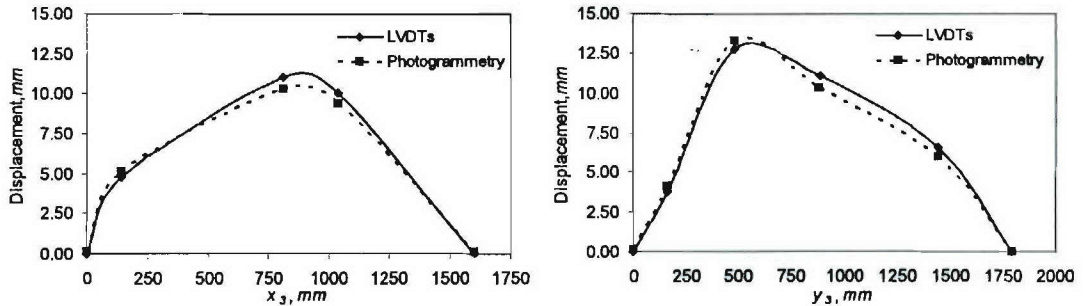


Figure 4.42. Displaced Shapes for P03 at 124 kPa

Figures 4.43 and 4.44 present the displaced shapes for P01 and P03, respectively, for a pressure load of 248 kPa, after failure of the stiffeners had occurred on the large panels. Good agreement was observed between the LVDT and photogrammetry target readings for P01. In the case of P03 along the  $x_3$  direction, the curves in Figure 4.44

show a clear discrepancy between the recorded values at the middle stiffener. This was attributed to severe bending of the LVDT rods at this load level, which in turn under predicted the deflection values on the large panels, particularly at the region where the stiffeners had completely separated from the composite panel. For the curves plotted along the  $y_3$  direction, the LVDT and photogrammetry curves showed good agreement, except for the readings at the center of the middle stiffener, which differed by 13 percent.

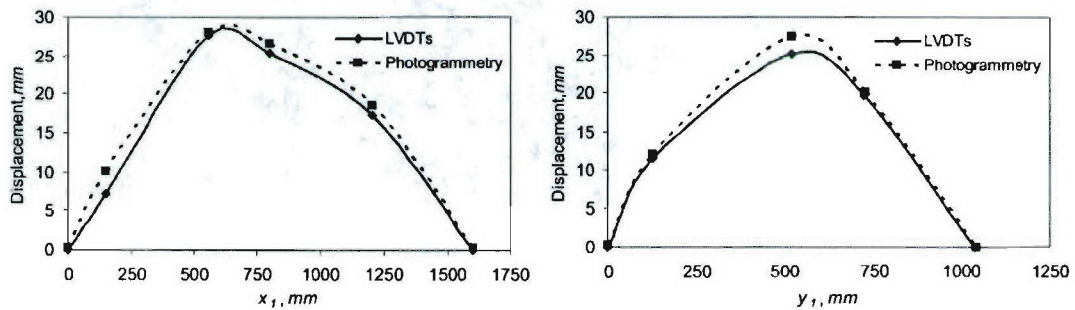


Figure 4.43. Displaced Shapes for P01 at 248 kPa

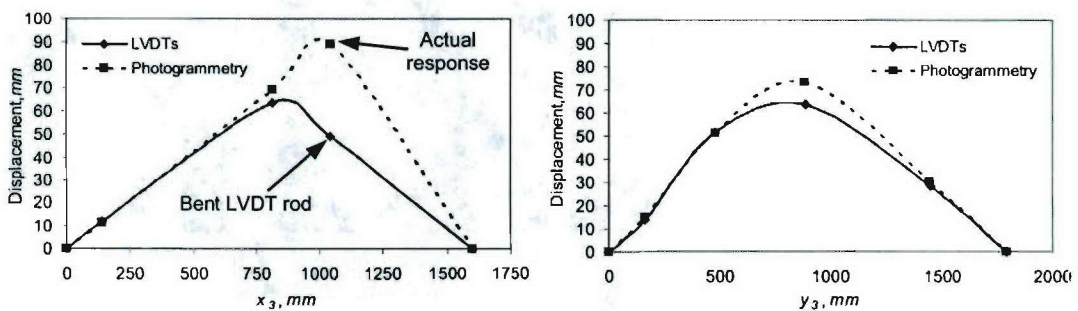
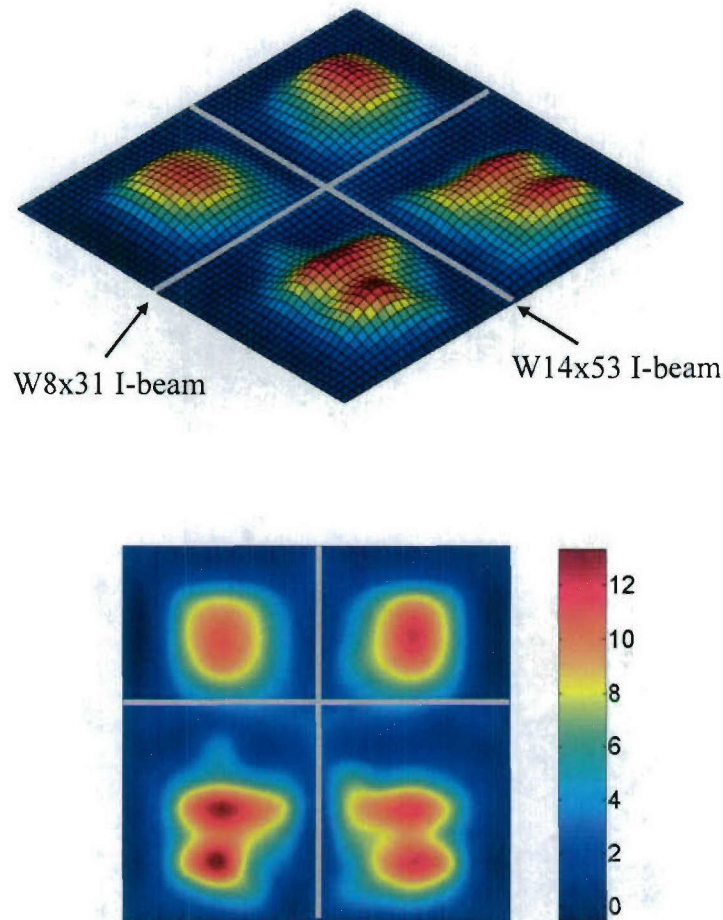


Figure 4.44. Displaced Shapes for P03 at 248kPa

Readings from the photogrammetry targets were used to create surface plots of the displaced panel assembly, as shown in Figures 4.45 and 4.46. The use of photogrammetry aided in visualizing the global behavior of the panel assembly, which would have not been attainable using the few, discrete displacement LVDT readings. Figure 4.45 shows a surface plot of the displaced panel assembly when loaded to 124



kPa. The valley-shaped regions in P03 and P04 display the effect of the stiffeners, while the surfaces in red represent the regions between stiffeners, which show the peak displacement values recorded, at 12.84 mm (DP3-6).



**Figure 4.45. Surface Plot of Displaced Panel Assembly at 124 kPa Using Photogrammetry (in mm)**

Figure 4.46 presents the surface plot of the displaced panel assembly loaded to 248 kPa, after failure of all stiffeners on the large panels had occurred. Prominent peaks are observed at the stiffener locations on P03 and P04, which depict the separation of the middle stiffeners from the composite panels. At this stage, the stiffeners were no longer effective, and peak displacements are observed on the stiffener regions closer to the fixed boundary of the test tank.

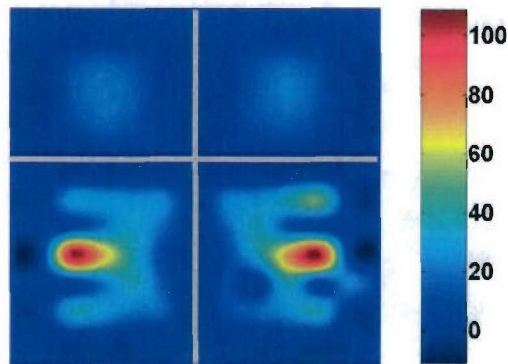
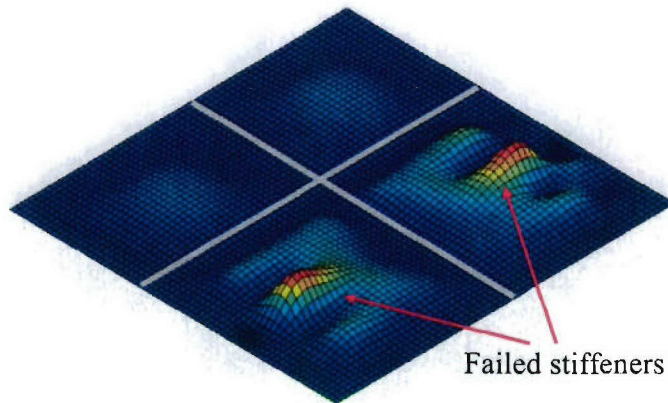


**Figure 4.46. Surface Plot of Displaced Panel Assembly at 248 kPa Using Photogrammetry (in mm)**

#### **4.6.4. Load versus Strain Curves**

Figure 4.47 shows selected load versus strain curves for P01. These values were recorded from gages mounted on the surface of the middle stiffener (center of the panels). In Figure 4.47a, the strain readings for P01 correspond to gages mounted on the middle stiffener (SB1-1, SB1-2, and SB1-3) and a gage placed between stiffeners (SB1-6). Gages SB1-1 and SB1-3, transverse to the stiffener axis, are in compression, and SB1-2 and SB1-6 are in tension. A peak strain of 1000 microstrain was recorded at SB1-2. For this initial load cycle set, the load versus strain curves exhibit linear behavior. It is noted

that a failure strain of 15000 microstrain was chosen for the composite panels, based upon material coupon tests.

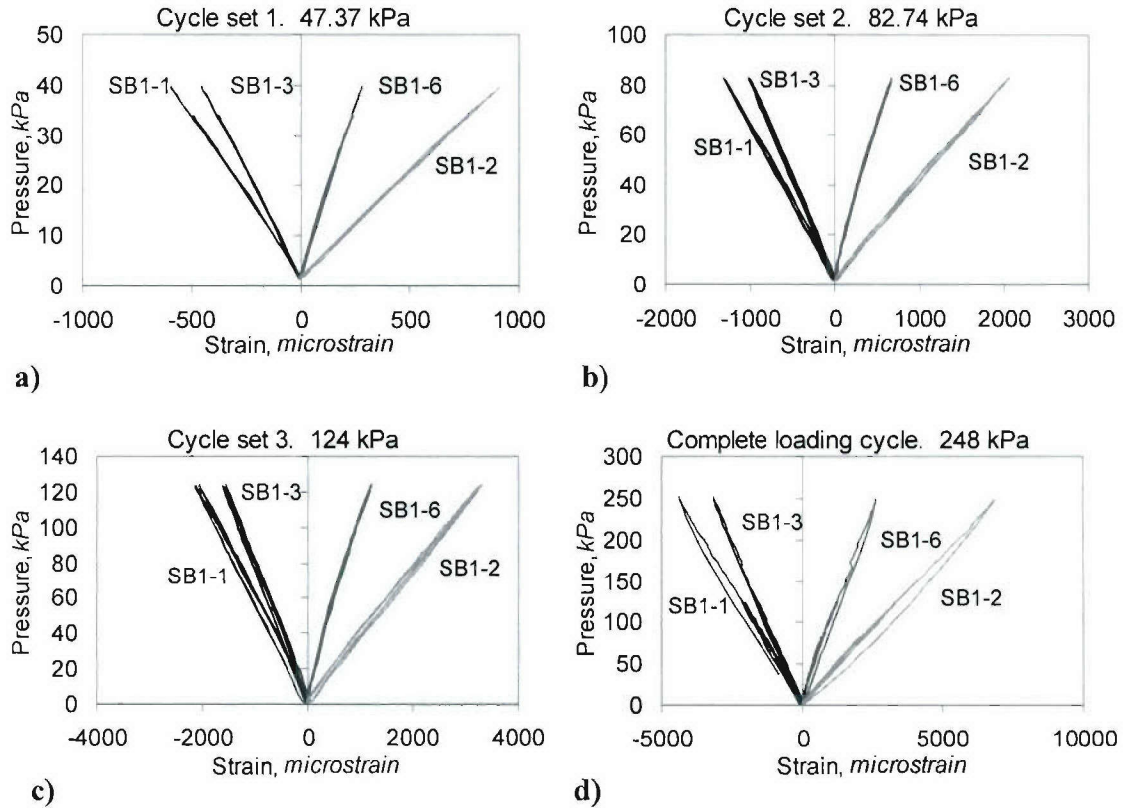


**Figure 4.47. Load versus Strain Curves for P01**

Figure 4.47b shows the load versus strain curves for P01, loaded to the design pressure of 82.74 kPa. When compared to the low level strains in Figure 4.47a, all strain values increased by roughly fifty percent, proportional with the increase in pressure. A maximum strain of 2000 microstrain was recorded at SB1-2, which is 7.5 times smaller than the failure strain. The load versus strain curves were slightly open during the third cycle set in Figure 4.47c. When compared to the strain values in Figure 4.47a, the peak strains increased by a factor of approximately 3.4.

The complete set of load versus strain curves is shown in Figure 4.47d, where a clear discrepancy in the final loading/unloading path is observed after a pressure of approximately 125 kPa. In particular, this behavior is observed in the curves for SB1-1

and SB1-2, which are gages mounted at the center of the middle stiffener. A peak strain value of 6076 microstrain was recorded at SB1-4, which is smaller than the failure strain by a factor of 2.5. At the joint region, the peak strain recorded was -3936 microstrain (SB1-11). Strain readings at the panel surface, the joint region and the I-beam flanges for P01 are presented in Tables 4.12, 4.13 and 4.14, respectively. Strains recorded at the joint region (SB1-5A, SB1-9) were about 40 times smaller than that recorded at the center of the middle stiffener (SB1-4). A peak strain of 8594 microstrain, recorded at the I-beam flange (SF1-5), was about 87 percent of the peak strain at SB1-4.

**Table 4.12. Strain Readings for P01, Dry Side (in microstrain)**

Pressure (kPa)	SB1-1	SB1-2	SB1-3	SB1-4	SB1-6	SB1-7
41.37	-610	946	-464	2288	276	-827
82.74	-1310	2053	-1015	4577	667	250
124.11	-2125	3307	-1611	6076	1211	468
248.22	-4376	6833	-3126	10264	2632	1422

**Table 4.13. Strain Readings for P01, Dry Side, Joint Region (in microstrain)**

Pressure (kPa)	SB1-5A	SB1-5B	SB1-5C	SB1-8	SB1-9	SB1-10	SB1-11
41.37	34	11	-33	-406	-63	-17	-580
82.74	111	44	-78	-821	-127	-64	-1286
124.11	305	159	-110	----	-165	-129	-2063
248.22	1272	797	-246	----	-467	-272	-3936



**Table 4.14. Strain Readings for P01, Dry Side, I-beam Flanges (in microstrain)**

<b>Pressure (kPa)</b>	<b>SF1-1</b>	<b>SF1-2</b>	<b>SF1-3</b>	<b>SF1-4</b>	<b>SF1-5</b>	<b>SF1-6</b>
41.37	-32	-62	-181	-47	-275	-26
82.74	-62	-123	-374	-87	-578	-46
124.11	-113	-160	-1098	-108	-3721	-36
248.22	-203	-388	-3024	-238	-8594	-132

The load versus strain curves for P03 are presented in Figure 4.48. The curves for the first cycle set are shown in Figure 4.48a, with a peak load of 41.37 kPa. These strain readings correspond to gages located at the top surface of the middle stiffener. Gages SB3-1 and SB3-3 were placed transverse to the stiffener axis, and SB3-2 and SB3-4 were aligned with the stiffener axis. SB3-1 and SB3-3 are in compression, and SB3-2 and SB3-4 are in tension. For this cycle set, the load versus strain loops were closed and fairly linear, with a peak strain of 610 microstrain, recorded at the center of the stiffener (SB3-4).

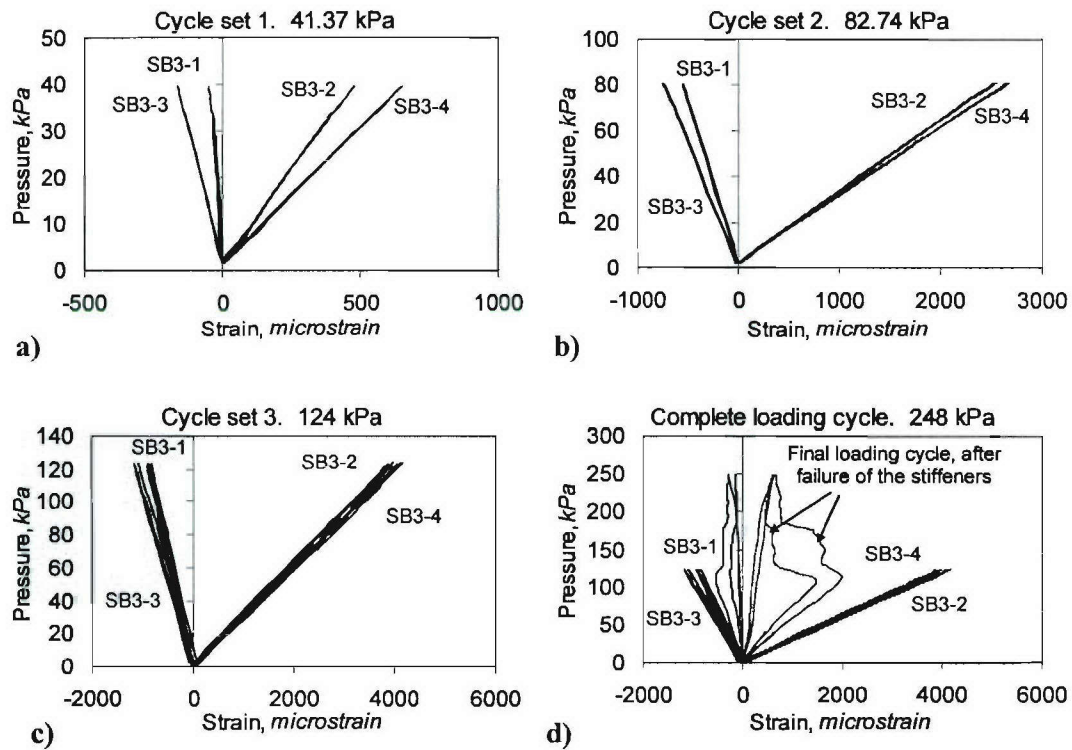


**Figure 4.48. Load versus Strain Curves for P03**

Figure 4.48b shows the load versus strain curves for P03 when the assembly was loaded to the design pressure of 82.74 kPa. When compared to the initial loading cycle strains in Figure 4.48a, the magnitudes increased by a factor of approximately 6. A maximum strain of 2700 microstrain was recorded at SB3-2, which is 5.5 times smaller than the failure strain. The panel response was observed to be linear up to its design load, with closed loops and no visible damage either on the surface of the panels or at the joint region.

As with P01, open loops were observed during the third cycle set shown in Figure 4.48c. Though difficult to differentiate in this figure, the unloading curves for SB3-1 and SB3-3 did not follow the loading path during the third cycle set. When compared to the strains during the initial loading cycle in Figure 4.48a, the peak strains recorded for this

cycle set increased by a factor of about 1.6. Due to imminent failure of the outer stiffener at this stage, it was decided to unload the panel assembly and load it up to the peak pressure of 248 kPa as a single cycle.

Figure 4.48d shows the load versus strain curves of P03 for the entire test. A dramatic shift in the strain curves indicate clear damage of the panel, which corresponds to the failure onset at the panel/stiffener interface towards the end of the third cycle set. After a pressure value of 124 kPa, the drop in strain as the pressure increased (SB3-1 and SB3-4) was due to stiffener failure. A peak strain of 4174 microstrain was recorded at SB3-2. This value is smaller than the failure strain by a factor of 3.6. A peak strain of 5682 microstrain was recorded at the joint region (SB3-9).

Strain readings at the panel surface, the joint region, the I-beam flanges, and the I-beam intersection (P03) are presented in Tables 4.15, 4.16, 4.17 and 4.18, respectively. Gages SB3-1 through SB3-4 were placed on top of the middle stiffener, SB3-6 was placed in between stiffeners, and gages SB3-9 through SB3-11 were placed at the joint region. At the crossing point of the I-beams, the peak measured strain was 1364 microstrain (SCB-2). This gage was aligned with the direction of the W14x53 I-beam. For gages SB3-1, SB3-2, SB3-3 and SB3-4, a dramatic drop in strain values was observed after a pressure of 124 kPa. These gages were placed on the middle stiffener and recorded erroneous values after separation of the stiffeners for the panel surface had occurred.

**Table 4.15. Strain Readings for P03, Dry Side (in microstrain)**

<b>Pressure (kPa)</b>	<b>SB3-1</b>	<b>SB3-2</b>	<b>SB3-3</b>	<b>SB3-4</b>	<b>SB3-6</b>	<b>SB3-7</b>
41.37	-50	481	-163	655	326	-88
82.74	-553	2686	-739	2540	780	-125
124	-921	4174	-1176	3994	1251	-155
248	-252	148	-537	1997	2737	-71

**Table 4.16. Strain Readings for P03, Dry Side, Joint Region (in microstrain)**

Pressure (kPa)	SB3-5A	SB3-5B	SB3-5C	SB3-8	SB3-9	SB3-10	SB3-11
41.37	-23	-45	----	-115	-629	-496	-64
82.74	-256	-167	----	-226	-1287	-1065	-124
124.11	-567	-522	----	-339	-1983	-1631	-130
248.22	-1460	-1290	----	-748	-5682	-3108	-512

**Table 4.17. Strain Readings for P03, Dry Side, I-beam Flanges (in microstrain)**

Pressure (kPa)	SF3-1	SF3-2	SF3-3	SF3-4	SF3-5	SF3-6
41.37	-32	-62	-181	-47	-275	-26
82.74	-370	-149	-334	-204	-648	-119
124.11	-656	-218	-551	-305	-1055	-180
248.22	-4105	-458	-2078	-714	-3960	-495

**Table 4.18. Strain Readings at the I-beam Intersection (in microstrain)**

Pressure (kPa)	SCB-1	SCB-2
41.37	-60	200
82.74	-128	416
124.11	-252	659
248.22	-490	1364

#### 4.6.5. Failure Modes

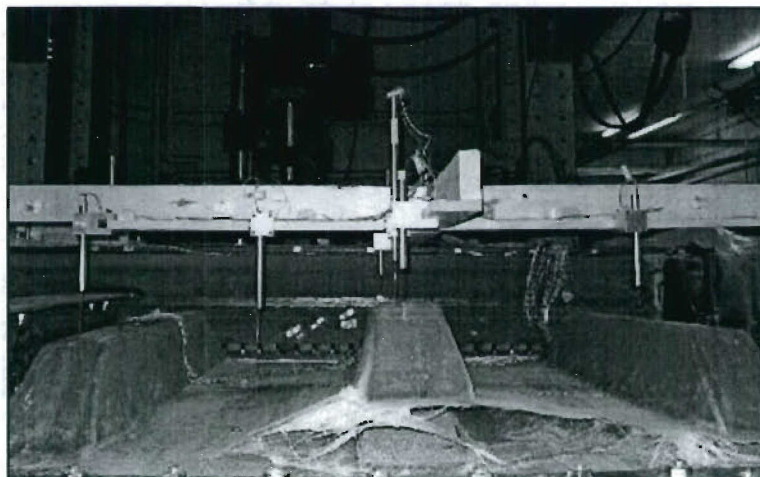
Failure of the hybrid assembly occurred as delamination of the stiffeners on the large panels, P03 and P04, while the small panels withstood the peak applied pressure without observable damage at the stiffener or joint regions. The onset of failure was observed during the last cycle of the third cycle set, at 117 kPa, at the stiffener/panel interface of the outer stiffener on P03.



Figure 4.49 shows a photograph of a failed large panel (P03) at the conclusion of the test. The numbers in the figure are used to indicate the failure sequence. Failure of the outer stiffener began near the tank boundary (1) and propagated towards the center of the stiffener. After the outer stiffener had become ineffective, load was redistributed to the other stiffeners, and subsequent damage began to occur at the middle (2) and inner stiffeners (3). Delamination of the stiffeners then began to occur near the hybrid joint region (4, 5). The outer sections of the stiffeners on P03, near the tank boundary, failed before damage was observed to initiate on P04. A close-up of the delaminated middle stiffener is shown in Figure 4.50.



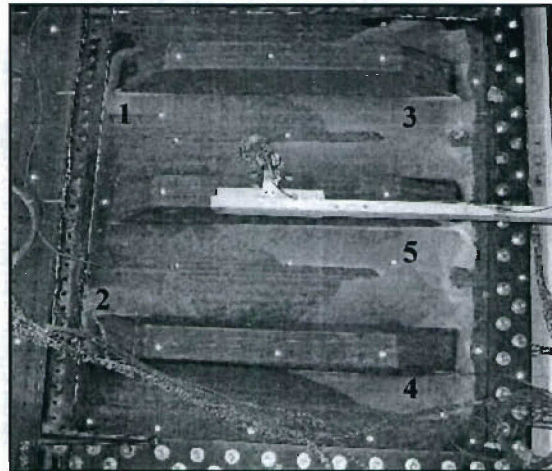
**Figure 4.49. Stiffener Failure on P03**



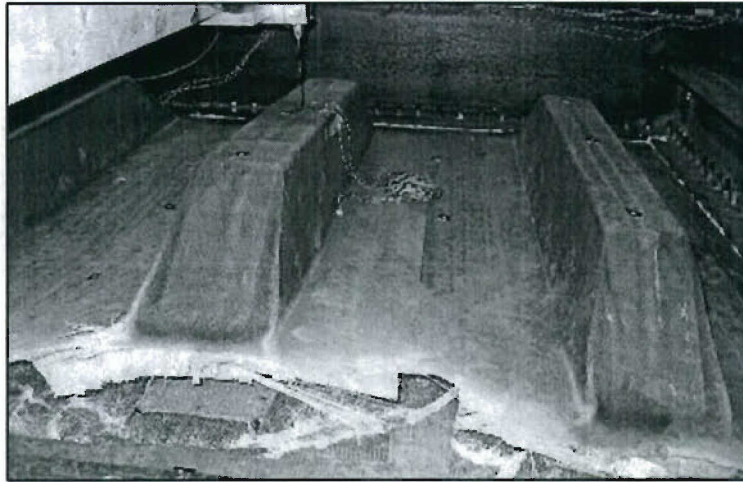
**Figure 4.50. Close-Up of Stiffener Failure on P03**

Figure 4.51 shows a photograph of P04 after failure. Damage initiated at the inner stiffener near the hybrid joint region (1), at 152 kPa, and propagated to the outer stiffener (2). The inner and outer stiffener sections near the tank boundary then began to delaminate (3, 4), until the middle stiffener section completely separated from the panel (5), as seen in Figure 4.52. At a pressure value of 234 kPa, even though all stiffeners on both large panels had failed, the panels continued to withstand the applied pressure up to 248 kPa (three times the design load). At this point, it was decided to bring the test to an end. Complete separation of the stiffeners from the composite shell was observed at this stage. No leaks were observed at the joint region, which indicated that watertight integrity of the joint was maintained.

Delamination of the stiffeners indicated that failure of the composite panels was due to the stiffener/panel interface. This type of failure resulted from a combination of stiffener geometry and techniques for bonding of the stiffeners to the flat surface of the panels. Providing more shear resistance at the interface, by interleaving fabric or by improved adhesion, would delay the initiation of this failure mode. Improvements of the manufacturing techniques should result in stronger panels.



**Figure 4.51. Stiffener Failure on P04**



**Figure 4.52. Close-Up of Stiffener Failure on P04**



## **5. FINITE ELEMENT ANALYSIS OF HYBRID BOLTED ASSEMBLY**

### **5.1. Rationale**

This chapter presents the finite element analysis (FEA) procedures used to study the local behavior of the hybrid joint and the global response of the panel assembly. The study was subdivided into two main phases: 1) finite element analysis of the sub-component joint region (local models); and 2) finite element analysis of the hybrid panel assembly (global models). All finite element models are developed using the commercial software package ANSYS, Version 10.0. The modeling techniques are verified with the available experimental data presented in Sections 3 and 4.

Analysis of mechanical joints cannot be conducted without considering the behavior of the global structure, since the mechanical response of joints is coupled to that of the structures which they connect. In other words, the geometry, materials and loading of the global structure will have a direct influence on the forces being transferred to the joint. Similarly, the stiffness of the joint will have an impact on the global response of the structure. Understanding the relationship between the response of both local and global systems is imperative in the design of structures being joined with mechanical connections.

In general, when modeling large structures, it is not be feasible to include all of the small-scale features of the joint. As described by Bonnani [2001], the usual approach for analyzing mechanical joints is to perform a global analysis of the large-scale structure using an approximate joint stiffness, in order to determine the loads being transferred to the joint. A detailed joint configuration is then developed and its stiffness can be calculated and input back into the global model to verify design criteria. This process may be repeated if further refinement of the joint is needed. For a new joint design, experimental validation is required.

For the FEA work presented in this chapter, the global structure (component) consists of a four-panel assembly of the hybrid lifting body, and the local structure (sub-component) is the hybrid joint, as shown in Figure 5.1. Based on the strength test results presented in Section 3, a short doubler joint configuration (DS-4) was selected for the hybrid connection. The experimental data for this connection scheme is used as the baseline for validation of local and global modeling techniques.



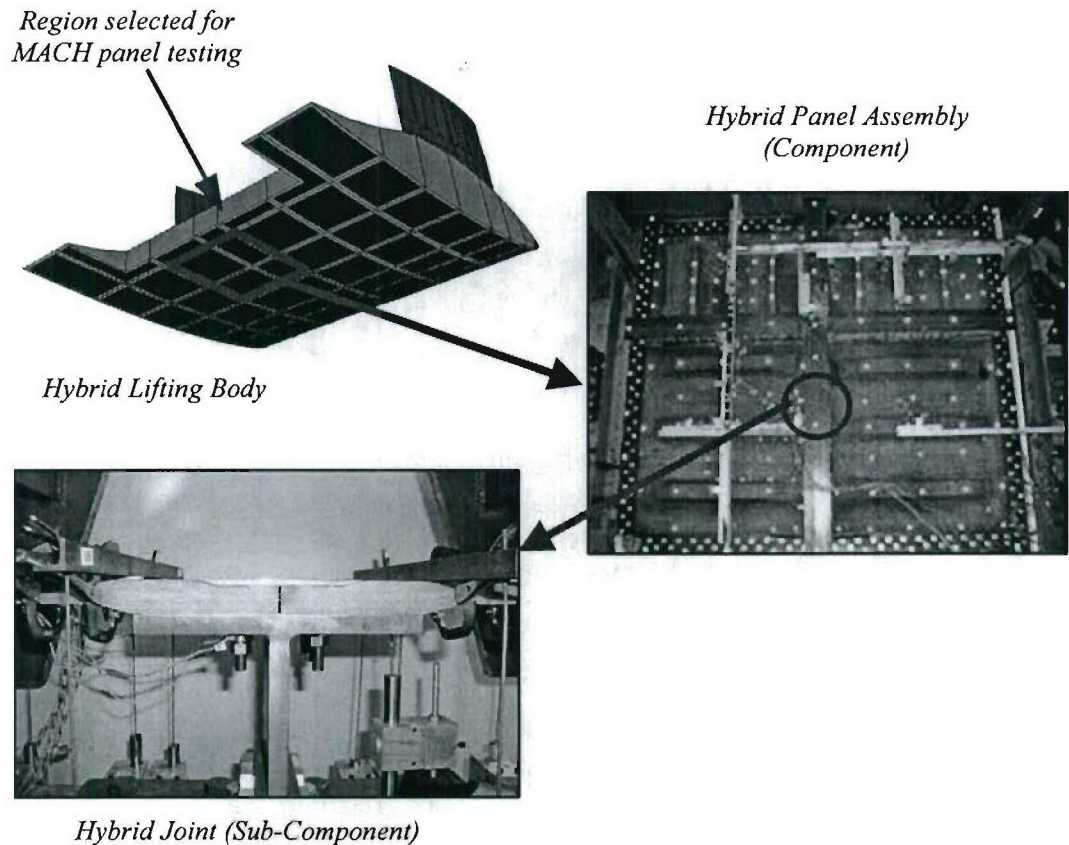


**Figure 5.1. Hybrid Lifting Body, Component and Sub-Component Structures**

## 5.2. Finite Element Analysis Objectives

The main objective of this study is to provide a simplified approach for modeling hybrid joints in large-scale structures. Figure 5.2 presents a schematic of the proposed FEA approach. First, a simplified local shell model was developed to estimate the joint stiffness, by computing the approximate rigidity of each of the hybrid joint regions. This approach was then incorporated into a global model of the hybrid panel assembly to estimate the global deflections. Lastly, a detailed 2D plane strain model was used to estimate the local stresses of the joint. Accordingly, the objectives of the FEA study are as follows:

1. To develop a simplified shell model to analyze joint structures, by modifying the shell element properties at the hybrid region;

2. To validate the finite element models using the available experimental data from both sub-component (local) and component (global) tests. These data are presented in Sections 3 and 4, respectively.
3. To perform parametric studies of the effect of joint geometry on the global response of the panel assembly (sensitivity study).
4. To develop a detailed, plane strain model of the hybrid joint, which includes the contact interactions between the joint constituents and the effect of the bolt, to provide predictions of critical stresses at the joint.

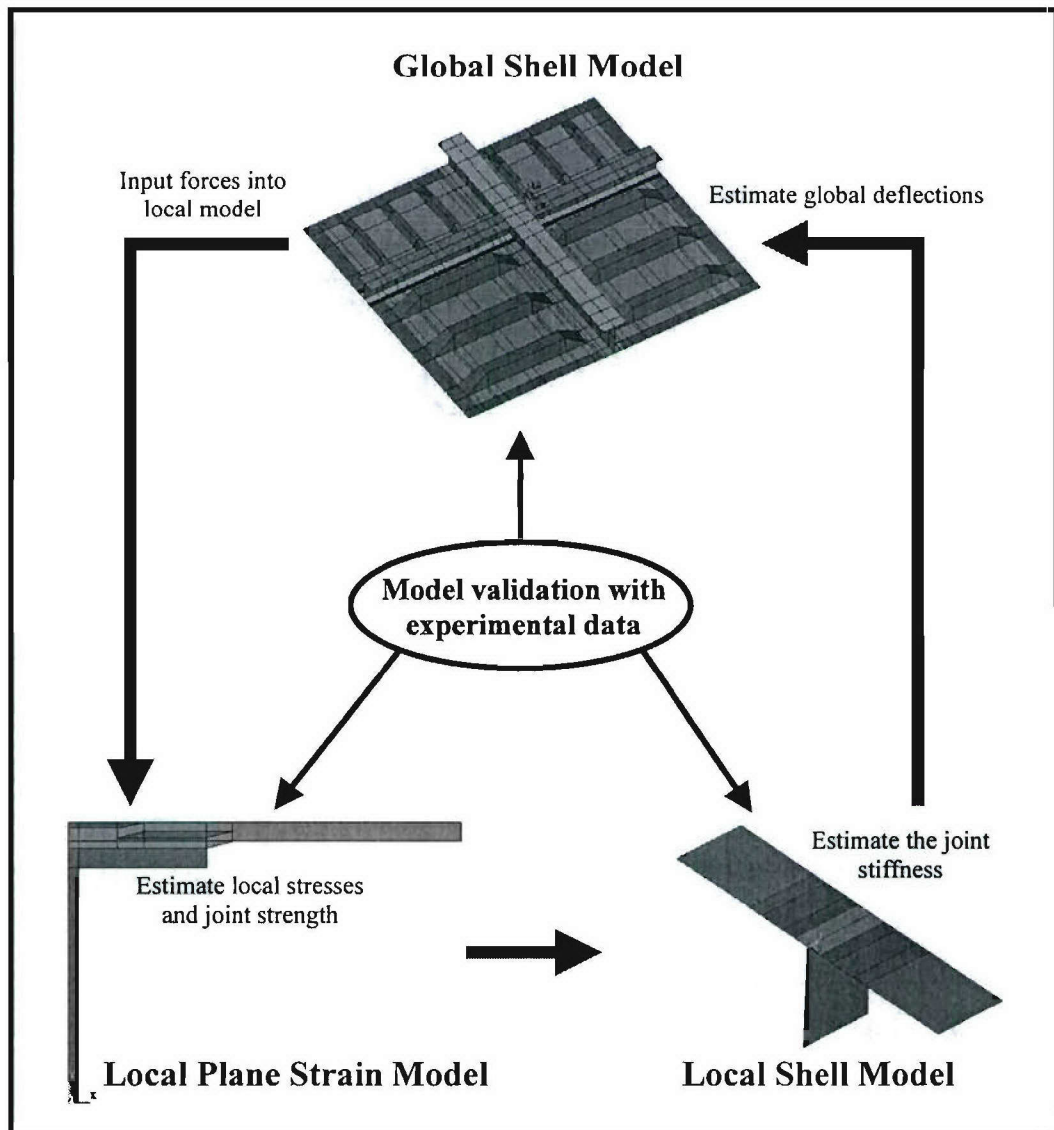


Figure 5.2. Schematic of the FEA Approach

### **5.3. Local Finite Element Model Using Shell Elements**

The purpose of the local shell model is to provide a simplified approach for estimating the joint stiffness by computing the approximate rigidities of the sections at the hybrid region. While using shells elements will limit the extent of the details that can be incorporated into the local model, the end objective is to implement this approach into a global model of the hybrid panel assembly, where extensive detailing of the joint geometry would be unfeasible. The criterion is that the shell elements capture the local stiffness of the connection.

Initially, connection elements (rotational springs) were considered to model the joint behavior, specifically, the connection of the hybrid joint region to the acreage of the composite panel. This approach may be feasible, for example, for a local model of a component or sub-component, where only three degrees of freedom (two displacements and one rotation) are considered. However, modeling the joint region of a large-scale structure such as the hybrid four-panel assembly will require a large number of connection elements, whose rotational properties need to be prescribed for all degrees of freedom involved. In a three dimensional model, such an approach would be impractical. A more feasible approach to this problem is to modify the properties of the elements at the hybrid joint region, by using effective section properties. This approach is a precursor to modeling of the joint at the global level and is the main focus of this section.

#### **5.3.1. Finite Element Model Description**

A photograph of the DS-4 sub-component joint specimen is shown in Figure 5.3. This connection scheme consists of a composite beam sandwiched between a steel flange and a steel doubler plate. A foam insert is used to align the tapered region of the composite with the edge of the steel flange. A schematic of the baseline geometry of the DS-4 joint configuration is presented in Figure 5.4. For purposes of property designation in the analysis, the joint has been sub-divided into six distinct sections: A, B, C, D, E, and F. Section A represents the region composed of the steel doubler, the composite beam and the steel flange, from the symmetry plane to the bolt-line; section B represents the steel doubler, the composite beam and the steel flange section, from the bolt-line to the edge of the doubler plate; section C represents the composite beam and steel flange in the region where a foam



insert is present; section D represents the tapered composite region; section E is the straight composite beam; and section F is the steel web.

Figure 5.5 shows the geometry of the top and side views of the shell model representation of this joint configuration. The symmetry plane is located at the center of the steel web. Computation of the properties for the hybrid regions is discussed in the section that follows. It is noted that although only half of the joint is presented in Figure 5.4, symmetry was not used for the shell model.

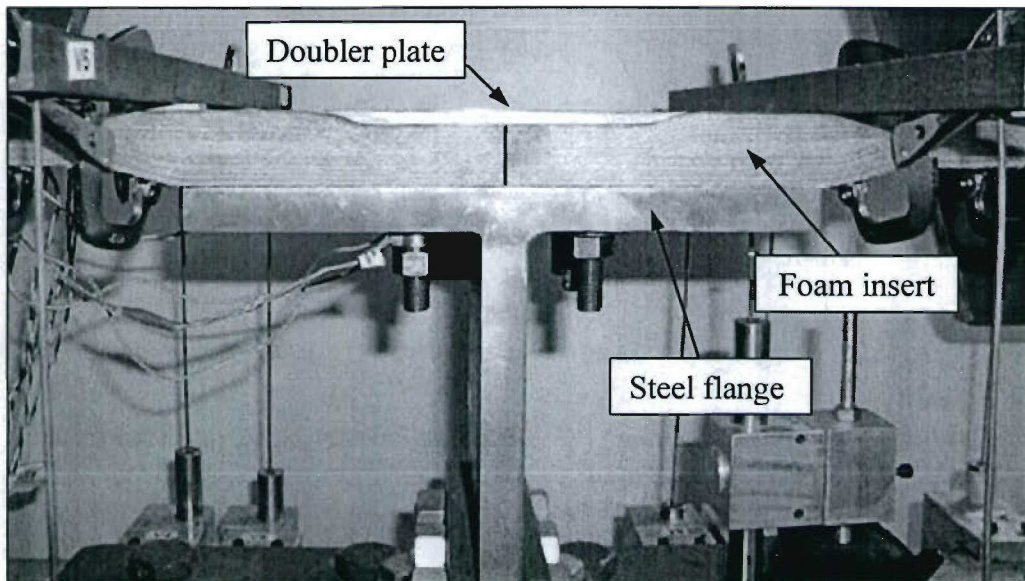


**Figure 5.3. Photograph of the DS-4 Joint Configuration**



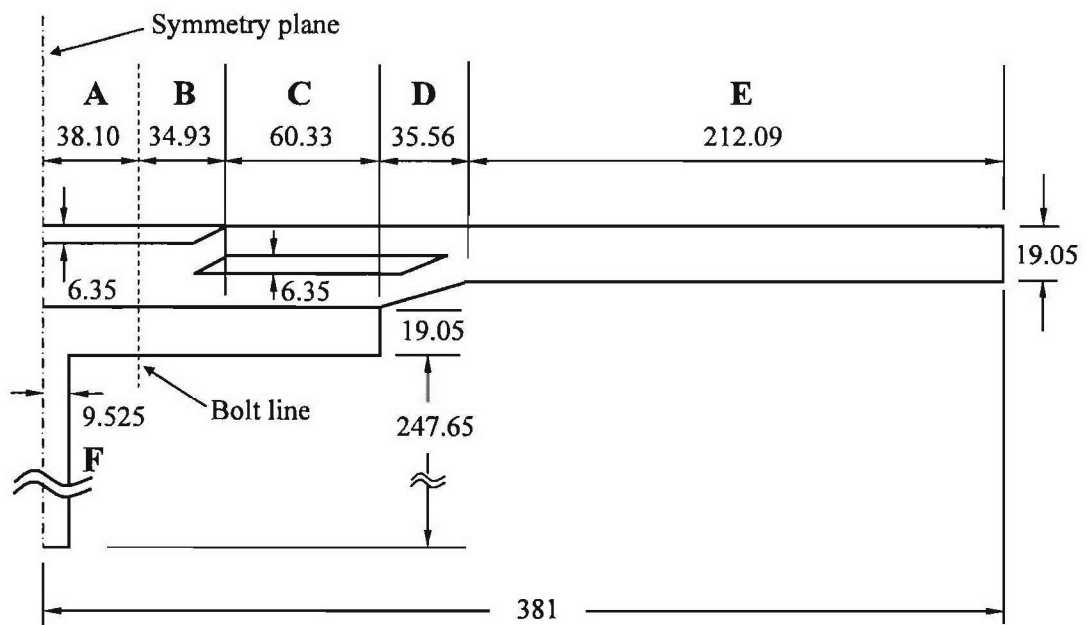


Figure 5.4. Baseline Geometry of the DS-4 Joint Configuration, in mm

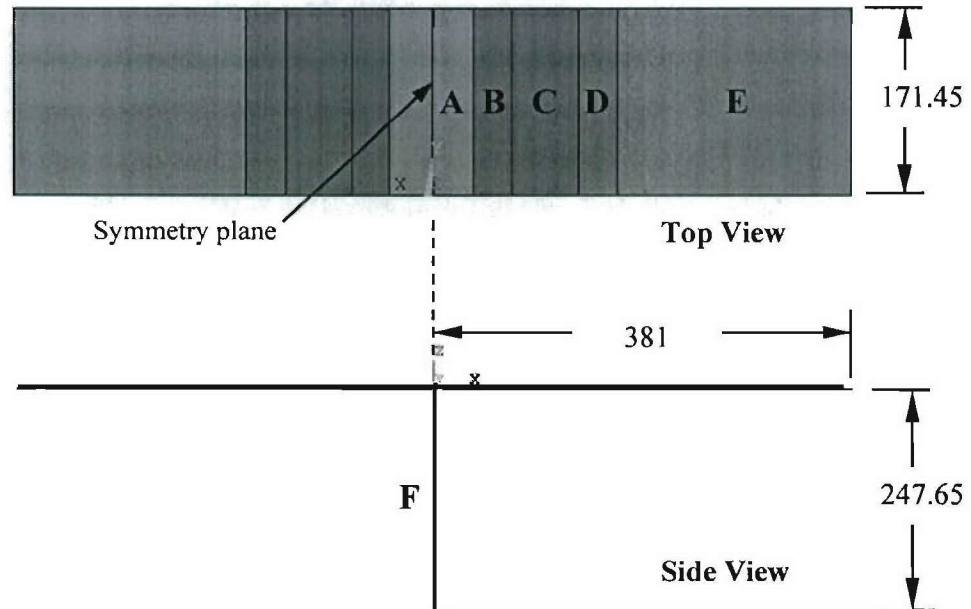
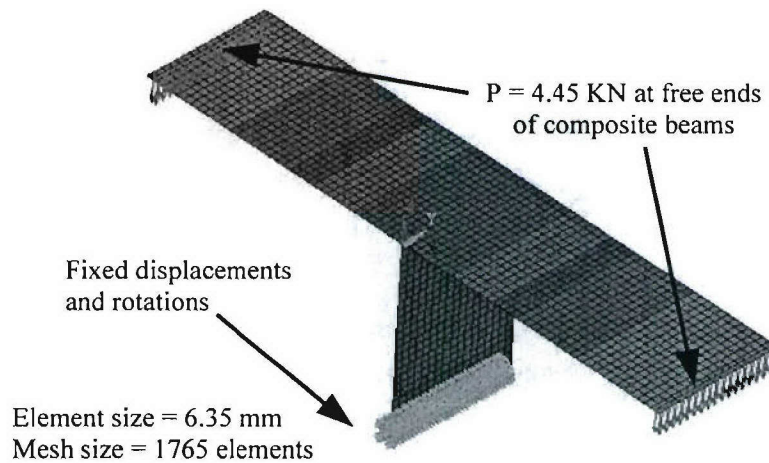


Figure 5.5. Baseline Geometry of the DS-4 Joint Shell Model, in mm

The meshed model, loading and boundary conditions are shown in Figure 5.6. Element type SHELL181, which is a 4-node element with six degrees of freedom at each node and includes the effects of shear deformation, was chosen for this study. This element is suitable for modeling thin to moderately-thick shell structures [ANSYS Online Manual, 2004]. Based on a preliminary convergence study, a mesh of 1785 elements was found appropriate. A nominal load of 4.45-KN was applied at free ends of the composite beams, which represents the force applied by the load heads. Model verification was conducted at this load magnitude, since linear response of the experimental load versus displacement and load versus strain curves was observed. To simulate a fixed base condition, all degrees of freedom at the bottom edge of section F (steel web) were constrained.



**Figure 5.6. Mesh, Loading and Boundary Conditions of DS-4 Shell Model**

### 5.3.2. Computing the Effective Properties of the Hybrid Region

A schematic of the side view of the DS-4 joint is shown in Figure 5.7a, which shows the reference plane used in the analysis. This joint configuration is used as a case study for validation of the modeling approach. Figure 5.7b presents the shell model representation of the joint. The main objective of this approach is to compute the properties of each of the hybrid joint sections for implementation into the shell finite element model. These

calculations are performed using the mid-plane of the composite beam section (E) as the reference plane. This plane was chosen as a reference for property calculations, since the objective of this approach is to extend this method to a global shell model. In a global model, it is often convenient to compute the properties with respect to the mid-plane of the panel sections, as these regions constitute the acreage of the structure. It is noted that since the properties for sections D and E are input as layered shell sections, the effective properties are computed and input for sections A, B and C.

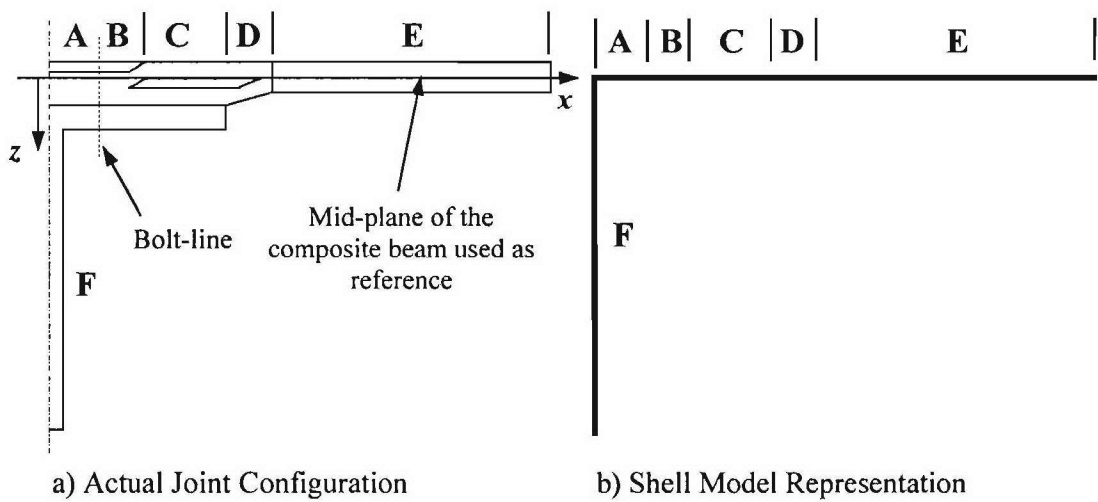


**Figure 5.7. Schematic of the DS-4 Joint Configuration**

The properties for each of the sections in Figure 5.7a need to be computed separately before implementation into an FE model. The following assumptions are made about the behavior of the sections:

1. Section A: The steel flange, the composite beam and the steel doubler (Figure 5.8) are assumed to act together (continuity) because of the clamping action of the bolt in this section. Section properties are computed about the x-axis.

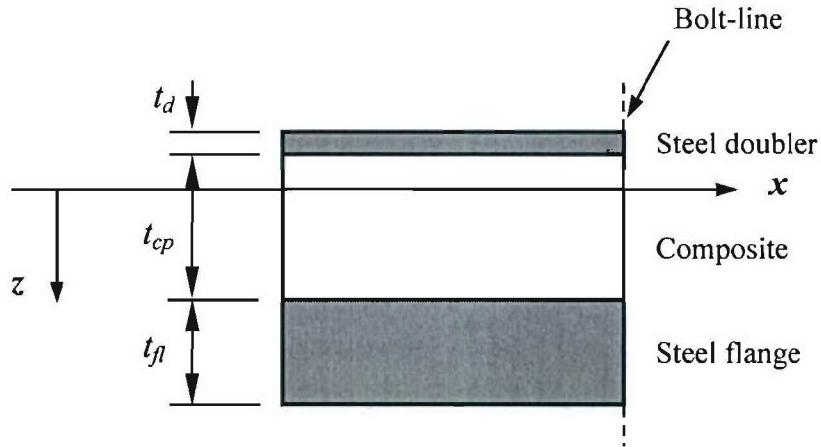


**Figure 5.8. Schematic of Hybrid Shell Section A**

2. Section B: The extensional resistance of this section (see Fig. 5.9) is assumed to be provided only by the composite region, and not the steel doubler or steel flange, given that the section begins past the bolt line. The flexural rigidity of this section is dependent upon the loading direction. When loaded upward, only the doubler plate and the composite resist the bending moment. When loaded downward, the steel flange and composite resist the bending moment. Flexural properties of each section are computed about each components own centroidal axis and the total stiffness is the sum of the individual parts.

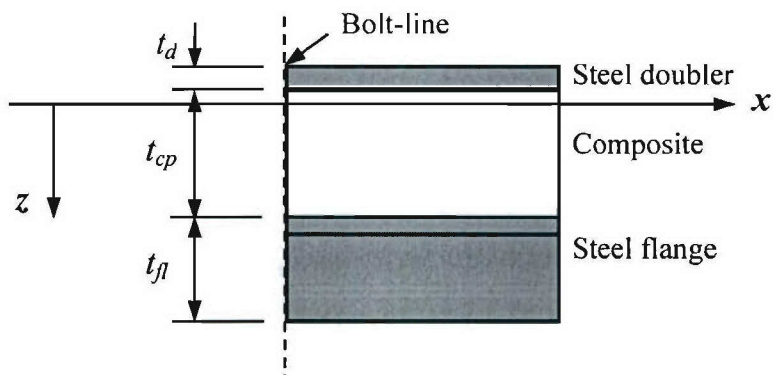


**Figure 5.9. Schematic of Hybrid Shell Section, B**



3. Section C: The extensional resistance of this section is assumed to be provided only by the composite region (see Figure 5.10). When loaded up, only the composite (with the foam insert) resists the bending moment, while the steel flange and composite resist a downward acting moment. The flexural properties of each section are computed about each components own centroidal axis as expressed in Eq. 5.1.

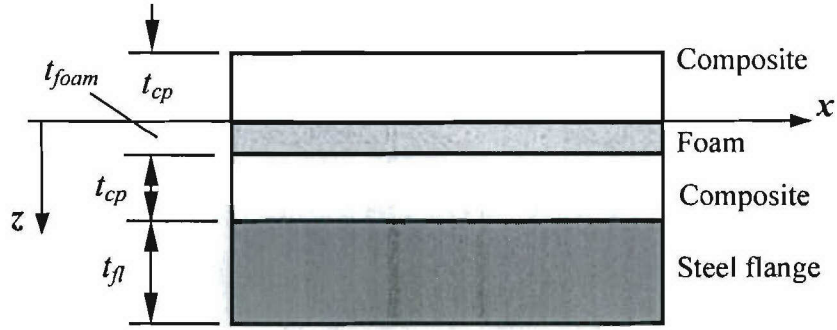


**Figure 5.10. Schematic of Hybrid Shell Section, C**

The bending rigidity of the individual sub-sections,  $(EI)_i$ , can be added in order to calculate the effective bending rigidity of the section,  $(EI)_{eff}$ , as follows:

$$(EI)_{eff} = \sum_{i=1}^n (EI)_i \quad (5.1)$$

For instance, the effective bending rigidity of section *B* when loaded downward is computed as follows:

$$(EI)_{eff} = E_{cp} I_{cp} + E_s I_{fl} \quad (5.2)$$

Where  $E_{cp}$  is the modulus of elasticity of the composite beam,  $E_s$  is the modulus of elasticity of steel, and  $I_{cp}$  and  $I_{fl}$  are the moment of inertia of the composite beam and the steel flange, respectively.

The effective section thickness,  $t_{eff}$ , can then be computed from  $(EI)_{eff}$ , as shown in Equation (5.3). This yields an effective thickness for the modified hybrid joint section.

These values of  $t_{eff}$  are then input into the finite element model as the thicknesses of the shell sections, using the SHELL SECTION LAY-UP OPTION in the ANSYS Main Menu. The properties for section E are input on a layer-by-layer basis by specifying the thickness and orientation of each lamina. The tapered section was approximated as a rectangular section of average thickness (thickness at the center of the tapered section).

$$(EI)_{eff} = \frac{1}{12} b t_{eff}^3 \quad (5.3)$$

### 5.3.3. Local Shell Model Verification

The local shell modeling approach was validated using the results obtained from the DS-4 joint specimen testing. Models with all-steel and all-composite joint sections were also created. For an all-steel joint model, all sub-sections of sections A, B and C were considered to be steel. For an all-composite case, these sections were considered to be EG/VE. These models represent the stiffest case and the most flexible case for a given joint configuration, respectively, and are used to determine the upper and lower bounds of the response of the joint.

A load of 4.45 KN was applied at the free ends of the composite beams. Displacement and strain contour plots for the model using hybrid section properties (DS-4) are shown in Figures 5.11 and 5.12, respectively. The composite beams bend in the regular shape of cantilever beams, as expected. A maximum displacement of 7.28 mm was obtained at the free end of the composite beam. A peak strain of 2881 microstrain was recorded at 203 mm from the joint centerline, which corresponds to the straight composite beam section (E).

Vertical displacement values ( $U_z$ ) were recorded along the length of the FE model and compared with the experimental values recorded at the three LVDT locations outlined in Chapter 3 (Figure 3.17): 1) the end of the steel flange (V5-V6, V7-V8); 2) 203 mm from the joint centerline (V3-V4, V9-V10); and 3) the free end of the composite beam (V1-V2, V11-V12). The strain values ( $\epsilon_x$ ) recorded at these locations correspond to gages SG5, SG3 and SG1, respectively, as shown in Figure 3.19.

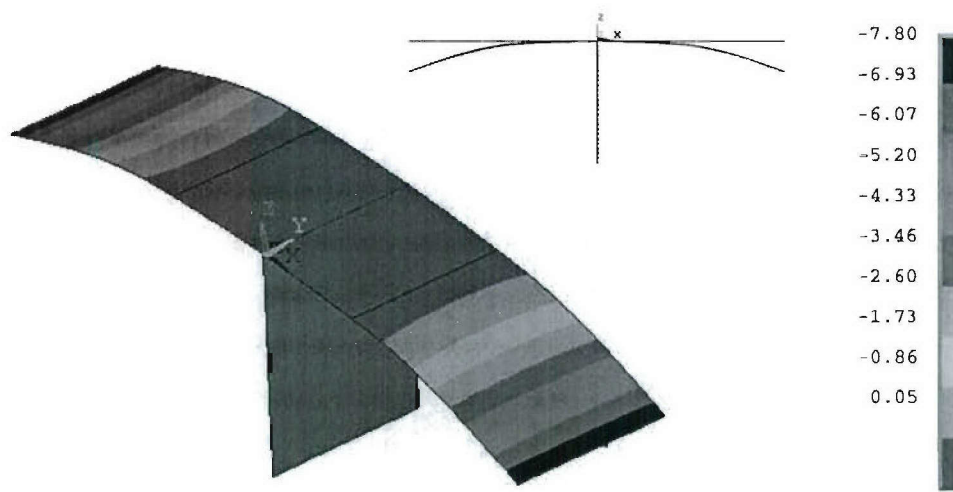


**Figure 5.11. Displacement Contour ( $U_z$ ) of DS-4 Joint (4.45 kN), in mm**

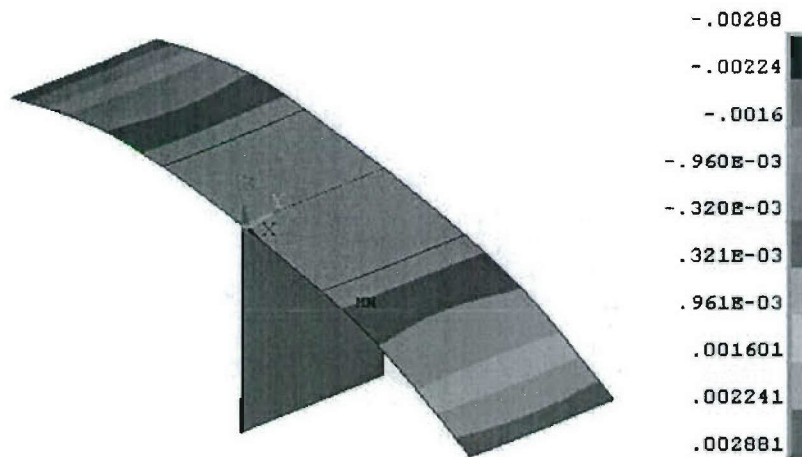


**Figure 5.12. Strain Contour ( $\epsilon_x$ ) of DS-4 Joint (4.45 kN)**

Figure 5.13 shows the deflected shape for the DS-4 joint for the three modeling cases and the experimental results and Table 5.1 summarizes the discrete vertical displacement values recorded. The deflected shapes show that using an all-steel section under predicts the

joint deflection by 22 percent at the free end of the composite beam ( $x = 381$  mm) and by 85 percent at the end of the steel flange ( $x = 133$  mm). The use of an all-composite joint overestimates the peak deflection by 21 percent and the deflection at the end of the flange ( $x = 133$  mm) by 71 percent. Using hybrid joint properties yielded fairly accurate displacement predictions, within 10 percent difference of the test results.

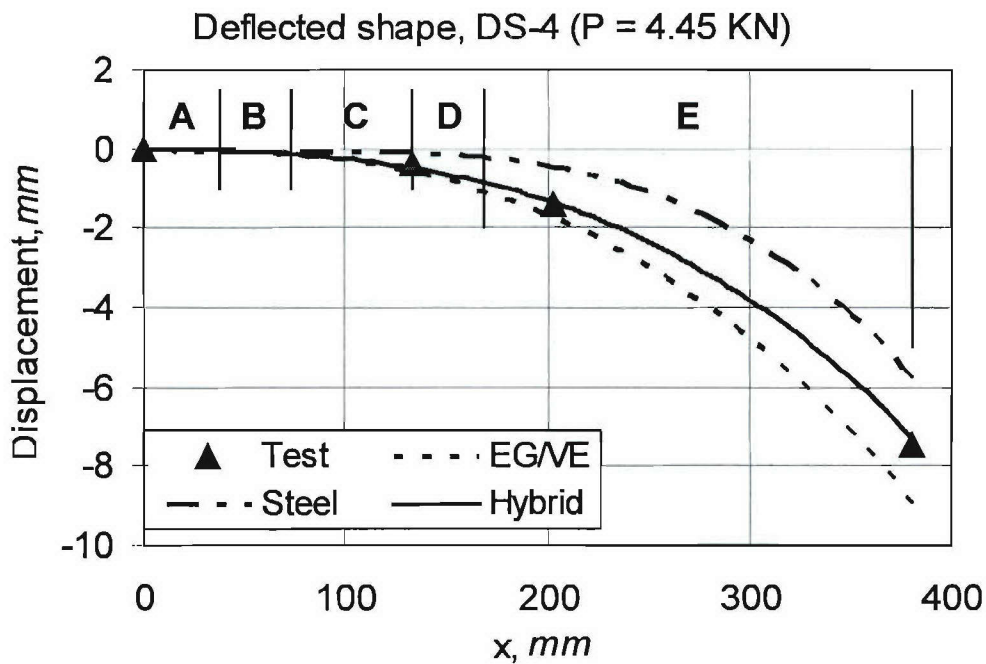


**Figure 5.13. Deflected Shape of DS-4 Joint (4.45 kN)**



**Table 5.1. Vertical Displacement of Joint Models at P = 4.45 KN.**

<b>x (mm)</b>	<b>Experiment (mm)</b>	<b>Steel Joint (mm)</b>	<b>% Diff</b>	<b>EG/VE Joint (mm)</b>	<b>% Diff</b>	<b>Hybrid Joint (mm)</b>	<b>% Diff</b>
133	0.340	0.051	-85.08	0.584	71.64	0.311	9.23
203	1.407	0.447	-68.23	1.727	22.77	1.359	3.41
381	7.437	5.801	-21.99	8.969	20.59	7.282	2.08

Figure 5.14 shows the strain profile for the DS-4 joint for the three modeling cases and the experimental results. Table 5.2 summarizes the strain values. For an all-composite joint, the strain recorded at 203 mm from the joint centerline was nearly twice as large as in the experiment, while the all-steel joint over predicted the strain by about 48 percent. Overall, the local shell model in this section was found adequate to estimate the joint stiffness, with a peak difference of 9 percent. However, the curves in Figure 5.14 show that this model is not feasible for providing estimates of the strains at the joint region. Even though the purpose of the local shell model is used to estimate the joint stiffness, a detailed 2D plane strain or 3D solid model, which include local effects such as bolt pre-load and contact interactions, is needed to predict the local stresses. Developing a local solid model will ultimately provide failure and joint survivability predictions.

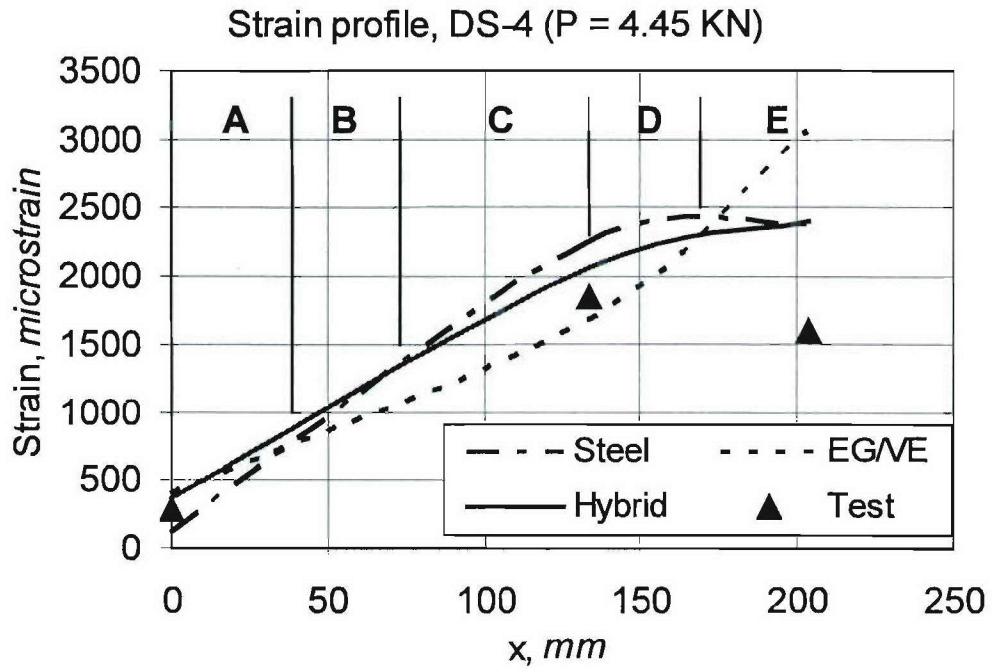


Figure 5.14. Strain Profile ( $\epsilon_x$ ) of DS-4 Joint (4.45 KN)

Table 5.2. Strain Results for Joint Models ( $\epsilon_x$ ) at P = 4.45 KN

$x$ (mm)	Experiment $\mu\epsilon$	Steel Joint $\mu\epsilon$	% Diff	EG/VE Joint $\mu\epsilon$	% Diff	Hybrid Joint $\mu\epsilon$	% Diff
133	278 (SG5)	114	59.11	398	-43.75	372	-34.44
203	1853 (SG3)	2260	-22.32	1690	9.45	2070	-12.56
381	1607 (SG1)	2384	-48.12	3060	-90.13	2412	-50.62

#### 5.4. Global Finite Element Model of Isolated Stiffened Panels

Prior to modeling the entire hybrid assembly and incorporating the modified shell approach for the hybrid region, a study was conducted to investigate the response of isolated panels with ideal boundary conditions. In other words, instead of modeling the hybrid region, the panel boundaries corresponding to the hybrid region are modeled as pinned and fixed boundaries. Hence, the contribution of the I-beam movement to the panel deflections is not accounted for in this model. This study is an attempt to investigate the bounds of the individual panel response and to compare these to the experimentally obtained displaced shapes.

Figure 5.15 depicts the various sections of a small stiffened panel (P01). Region 1 corresponds to the thickened boundaries of the panel; region 2 corresponds to the stiffened region of the panel; region 3 corresponds to the top section of the stiffeners; and region 4 corresponds to the side sections of the stiffeners. The structure is modeled as a layered shell. The material properties are input by specifying the layer thickness and orientation using the LAY-UP OPTION SHELL SECTION. Table 5.3 presents the orthotropic lamina properties for the EG/VE system used for each lamina. A detailed summary of the lamination scheme for each panel section in Figure 5.15 is presented in Table 5.4. It is noted that the same lamination scheme was used for the large panels.

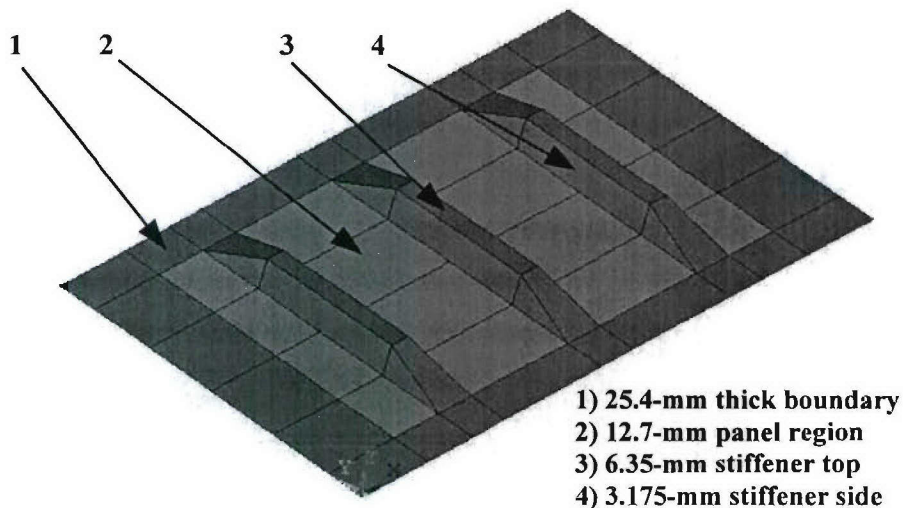


Figure 5.15. Various Sections of EG/VE Stiffened Panels

**Table 5.3. Orthotropic Lamina Properties for an EG/VE System**

$E_{11}$ (GPa)	$E_{22}$ (GPa)	$E_{33}$ (GPa)	$G_{12}$ (GPa)	$G_{13}$ (GPa)	$G_{23}$ (GPa)	$\nu_{12}$	$\nu_{13}$	$\nu_{23}$
37.93	10.56	10.56	3.192	3.192	2.258	0.29	0.29	0.439

**Table 5.4. Lamination Scheme for Stiffened Panels**

Section	Description	Thickness (mm)	Lamination Sequence
1	Thick boundary	25.4	64 layers: $[\{\pm 45/\{(0/90)_3\}_4]_s$
2	Stiffened panel	12.7	32 layers: $[\{\pm 45/(0/90)\}_4]_s$
3	Stiffener top	6.35	16 layers: $[(0/90)_3/\pm 45]_2$
4	Stiffened side	3.175	8 layers: $[(0/90)/\pm 45]_2$

**5.4.1. Verification of Isolated Panel Models**

The response of isolated composite panels was compared to the displaced shapes obtained from the experiments, as presented in Section 4.6. Model verification was conducted for the structure loaded to the design pressure of 82.74 kPa and peak displacements were recorded at the center of the panels and between the stiffeners. As shown in Figure 5.16, the I-beams are not included in these models, and the boundaries corresponding to the hybrid region are modeled as pinned and fixed. These cases represent the bounds for ideally flexible and stiff boundaries, respectively.



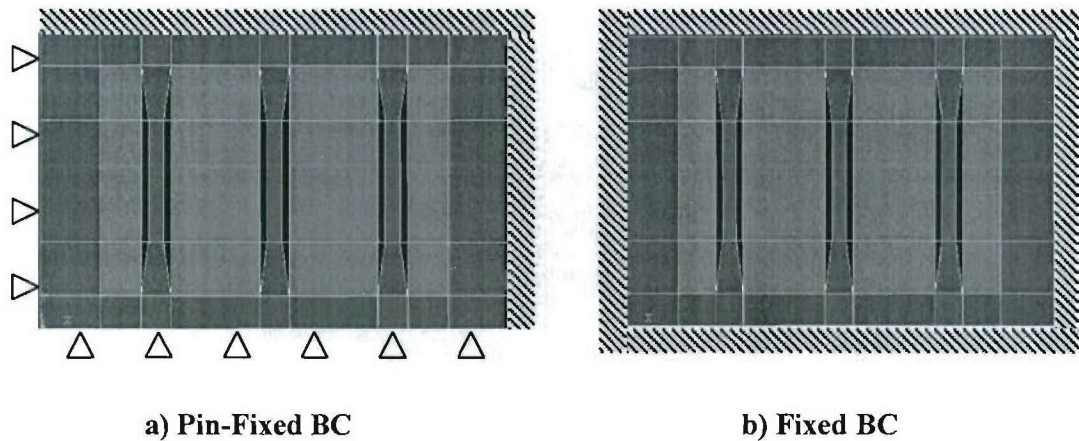
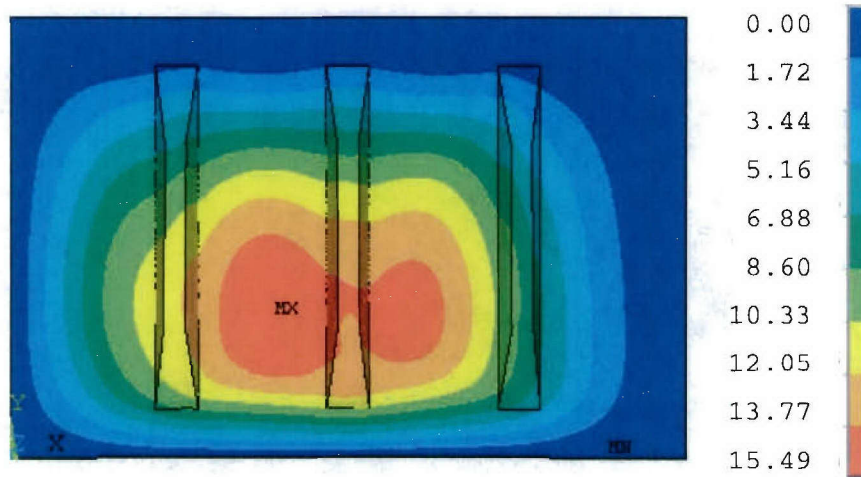


**Figure 5.16. Boundary Conditions of Isolated Panel FE Model**

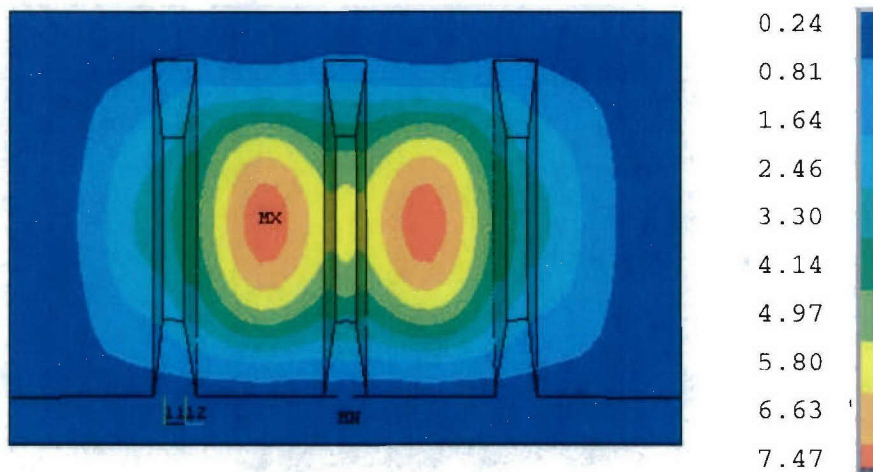
Figures 5.17 and 5.18 show the displacement contours of the isolated small panels and Figures 5.19 and 5.20 show those for the large panels for both boundary conditions, respectively. Because the entire assembly is not modeled, the panels do not act together as one structure. Hence, they are shown separately in each figure. A pinned boundary condition represents the most flexible case, as no reaction moments are created and therefore larger rotations occur. On the other hand, when using fixed boundary conditions, the panel response is over stiffened, as the reaction moments decrease the overall panel displacements and rotations. It is also noted that using either approach does not account for the displacement contribution of the I-beam members in the actual configuration.

Table 5.5 summarizes the displacement results for both boundary condition cases and the experiment. When compared to the test results, using a pinned joint over estimates the peak panel displacement by 19 percent, while a fixed joint provides a peak displacement 17 percent lower than the test results. This is also observed in the displaced shapes of the small and large panels, presented in Figures 5.21 through 5.24, respectively. For the small panel (Figures 5.21 and 5.22),  $x_1$  corresponds to the direction transverse to the stiffeners, and  $y_1$  is aligned with the stiffeners. For the large panel (Figures 5.23 and 5.24),  $x_3$  is aligned with the stiffeners and  $y_3$  is transverse to them. In a general sense, these curves show that, for the

case of isolated panels, the experimental panel response is bounded by the two ideal pinned and fixed boundary cases considered in this study.



**Figure 5.17. Displacement Contour of Isolated Small Panel, Pin-Fixed Boundary, (82.74 kPa), in mm**



**Figure 5.18. Displacement Contour of Isolated Small Panel, Fixed Boundary, (82.74 kPa), in mm**

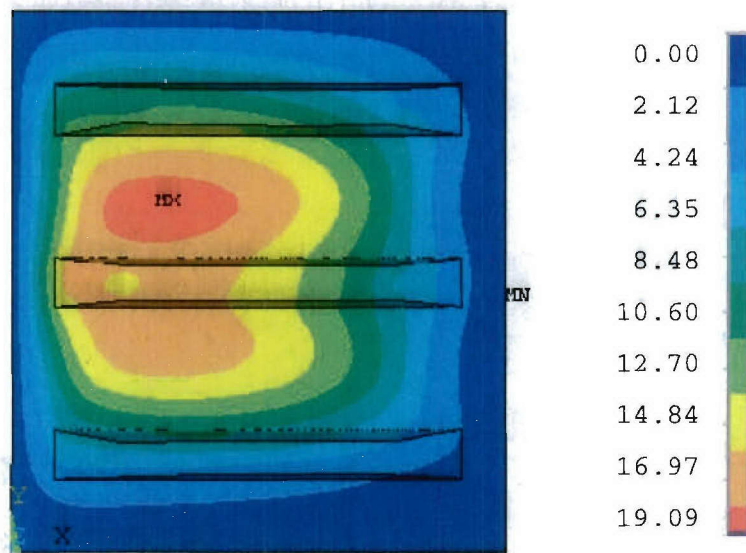


Figure 5.19. Displacement Contour of Isolated Large Panel, Pin-Fixed Boundary, (82.74 kPa), in mm

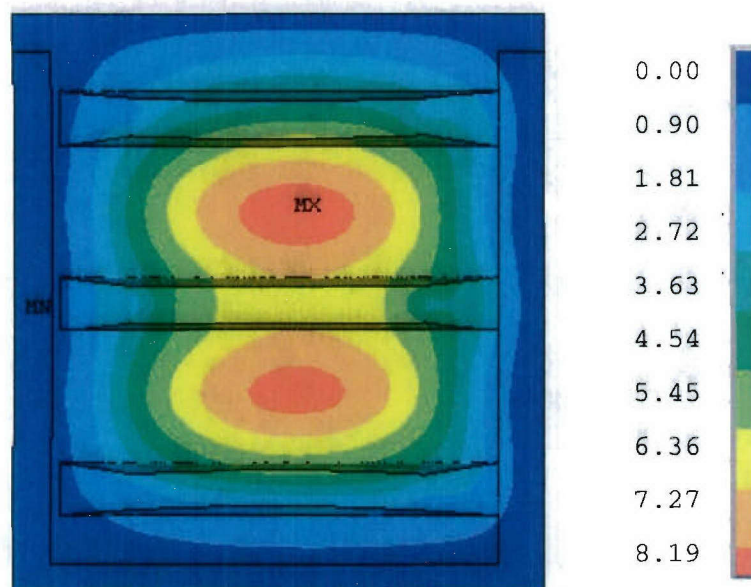


Figure 5.20. Displacement Contour of Isolated Large Panel, Fixed Boundary Condition, (82.74 kPa), in mm

Table 5.5. Vertical Panel Displacement at  $P = 82.74$  kPa

Boundary Condition	Displacement (mm)			
	Small Panel (P01, P02)		Large Panel (P03, P04)	
	Center	Between Stiffeners	Center	Between Stiffeners
Pin-Fixed	8.94	9.63	8.28	9.70
Fixed	5.12	7.41	6.58	8.18
Test	7.65	8.60	7.35	8.34

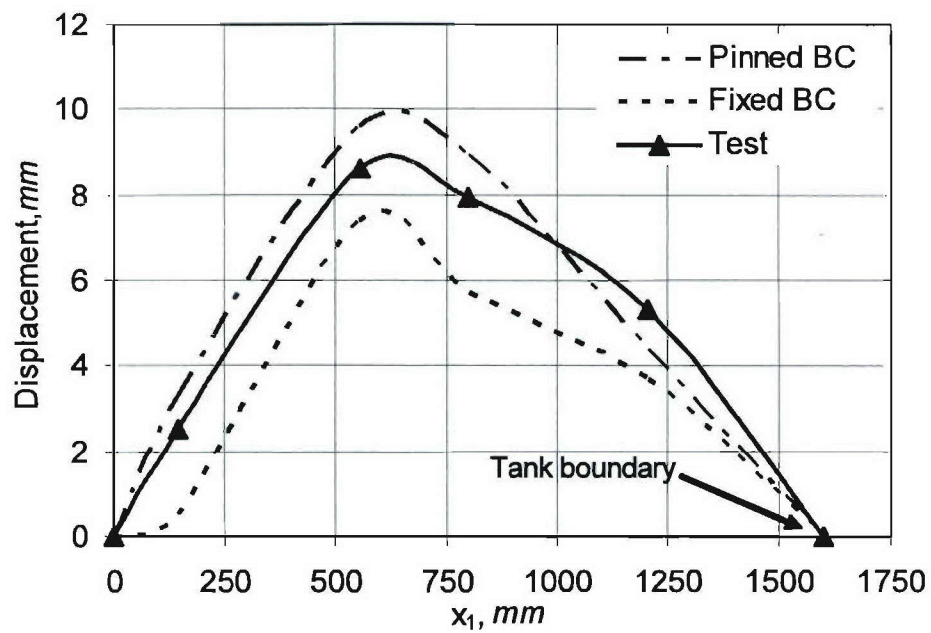


Figure 5.21. Displaced Shapes of Small Panel in the  $x_1$  direction (82.74 kPa)



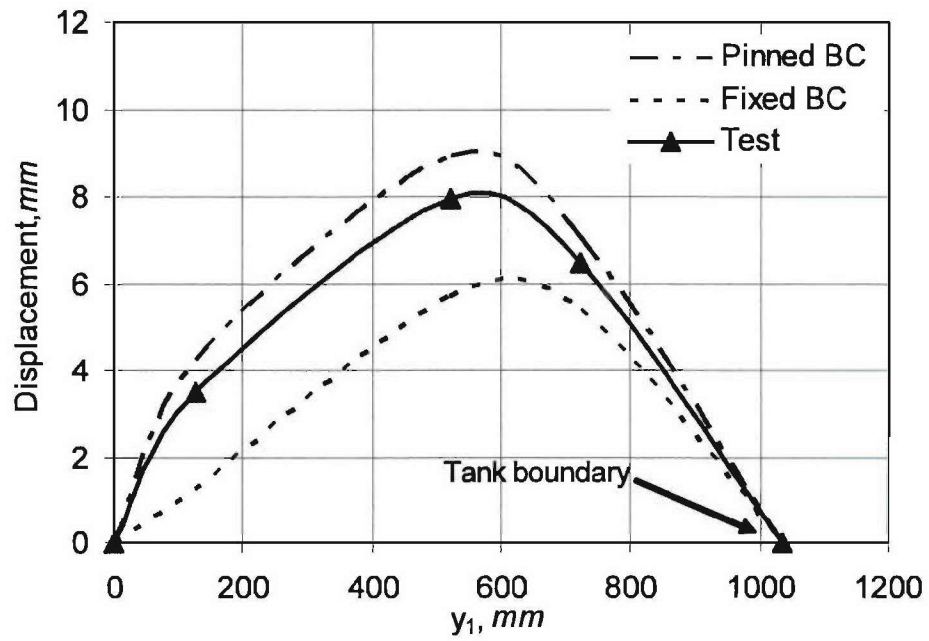


Figure 5.22. Displaced Shapes of Small Panel in the  $y_1$  direction (82.74 kPa)

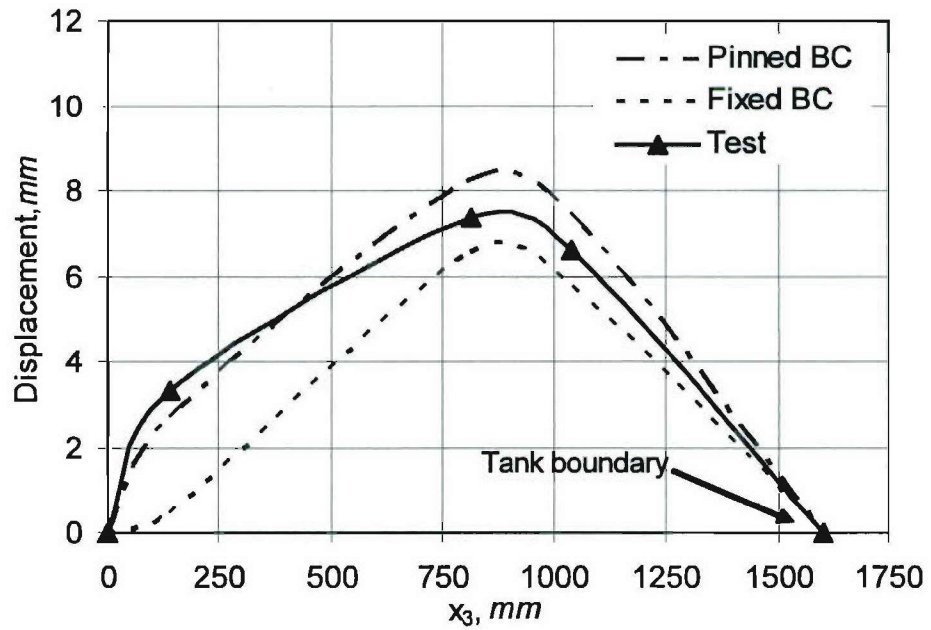


Figure 5.23. Displaced Shapes of Large Panel in the  $x_3$  direction (82.74 kPa)

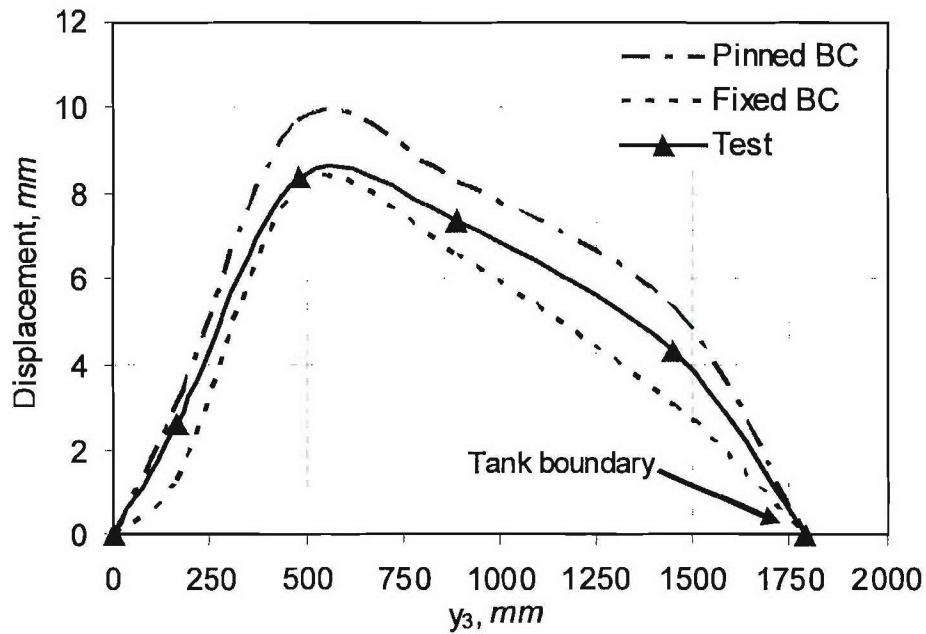


Figure 5.24. Displaced Shapes of Large Panel in the  $y_3$  direction (82.74 kPa)

### 5.5. Global Finite Element Model of Hybrid Assembly

The main objective of the global modeling approach is to extend the simplified shell approach described in Section 5.3.1 to the case of a multi-panel structure that is joined together by a hybrid joint. In this model, the four panels and the I-beams are included, in order to account for the contribution of the beams to the panel displacements. After validation of the approach, studies are conducted to investigate the sensitivity of the panel response to varying geometric parameters at the joint region. As an end objective, this study will provide a global interpretation of the variables that most strongly affect the structural response of the assembly.

When considering large-scale FE models with stiffened panels, using beam elements instead of shells is an attractive option for modeling the stiffeners. This is particularly true when the number of stiffeners and the geometric complexity of the model are significant. Initially, it was attempted to model the stiffeners using a single row of beam elements for each stiffener, but little success was achieved due to the actual breadth of the hat stiffener arrangement. For the study presented in this section, all of the panels, stiffeners and I-beam members are modeled using shell elements.

### 5.5.1. Global Finite Element Model Description

Figure 5.25 presents the hybrid assembly and panel geometry. Details of the panel and stiffener geometries are presented in Figures 4.4 through 4.9, of Chapter 4. Figure 5.26 presents a top view of the FE model of the hybrid assembly. A pressure load of 82.74 kPa (design load) was applied to the flat surfaces of the panels, as indicated by the red dots. These surfaces represent the wet side in the actual assembly configuration. All degrees of freedom at the outer edges of the panel assembly were constrained to simulate the fixed condition at the bolted boundaries of the hydrostatic test tank. Figure 5.27 shows the meshed model of the hybrid assembly, where element type SHELL181 was chosen for this study. With the exception of sections A, B and C shown in Figure 5.28, the material properties for the composite panels and stiffeners were input on a layer-by-layer basis, using the SHELL SECTION LAY-UP option in the ANSYS Main Menu and the orthotropic properties in Table 5.3, according to the lamination sequence shown in Table 5.4. Based on a convergence study, a mesh of 20540 elements was found appropriate.

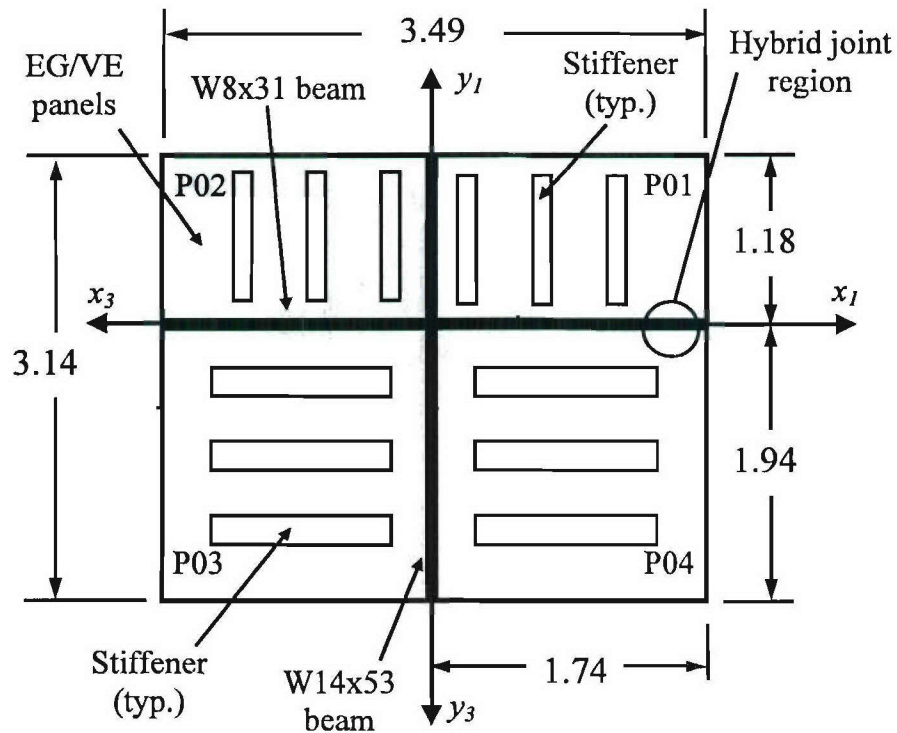
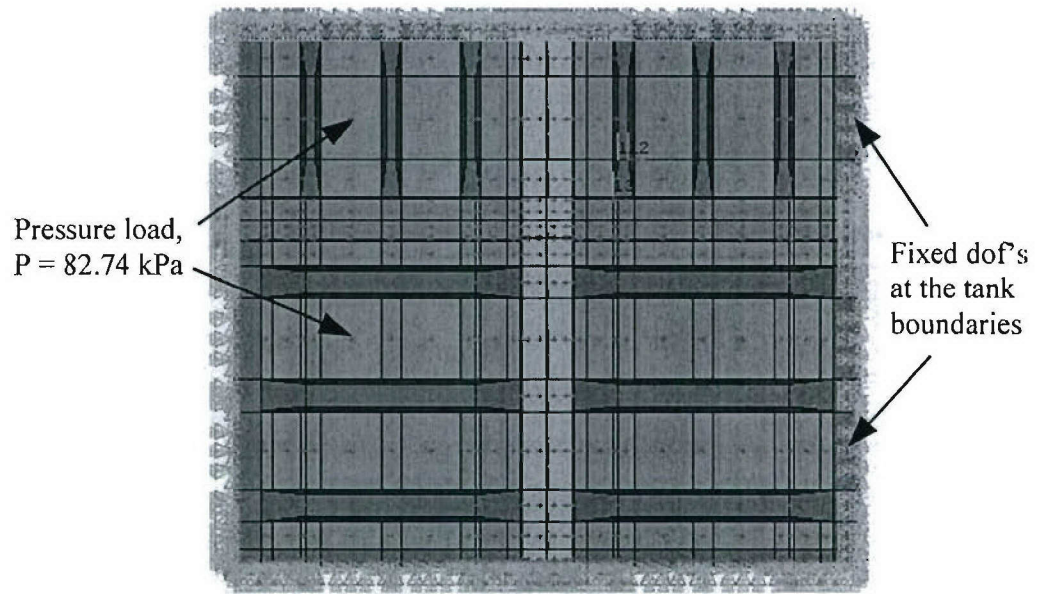


Figure 5.25. Hybrid Assembly and Panel Geometry, in meters



**Figure 5.26. Loading and Boundary Conditions of Hybrid Assembly Model**



**Figure 5.27. Meshed Model of Hybrid Assembly**



### 5.5.2. Modeling of the Hybrid Joint Region

The global model includes the full, four-panel hybrid assembly and it accounts for the contribution of the hybrid region and the contribution of the I-beam members to the panel deflections. Using a similar approach to that presented in Section 5.3.1 for the local shell model, the joint in the global assembly was modeled by computing the approximate axial, bending and coupling stiffnesses for the elements composing the hybrid region. By using this approach, the entire structure can be built using shell elements and only those sections that represent the joint region are modified and assigned effective properties.

Figure 5.28a presents a top view of the FE model of the four panel hybrid assembly. Figures 5.28b and 5.28c show detailed schematics of the hybrid joint region of the W8x31 I-beam and the W14x53 I-beam, respectively. Figure 5.28b depicts the connection of a small and large panel (P01-P04) with the W8x31 I-beam. Similarly, Figure 5.28c depicts the connection of the two large panels (P03-P04) with the W14x53 I-beam. In each figure, the hybrid joint regions (sections A, B and C), as well as the tapered and straight panel regions (sections D and E), are indicated.

A cross-sectional view of these regions and the baseline geometry for this model are shown in Figure 5.29. The approximate geometry of the I-beam member shown in the figure is summarized in Table 5.6. For this global model, the tapered region (D) extends a distance of 203.20 mm from the edge of the steel flange to the start of the stiffener region. Section E represents the flat region of the composite panel. In the local shell model, this region corresponds to the free end of the composite beam. As was done in the local shell model approach, the computation of the element properties is performed based on the mid-plane of the straight composite panel section (E).

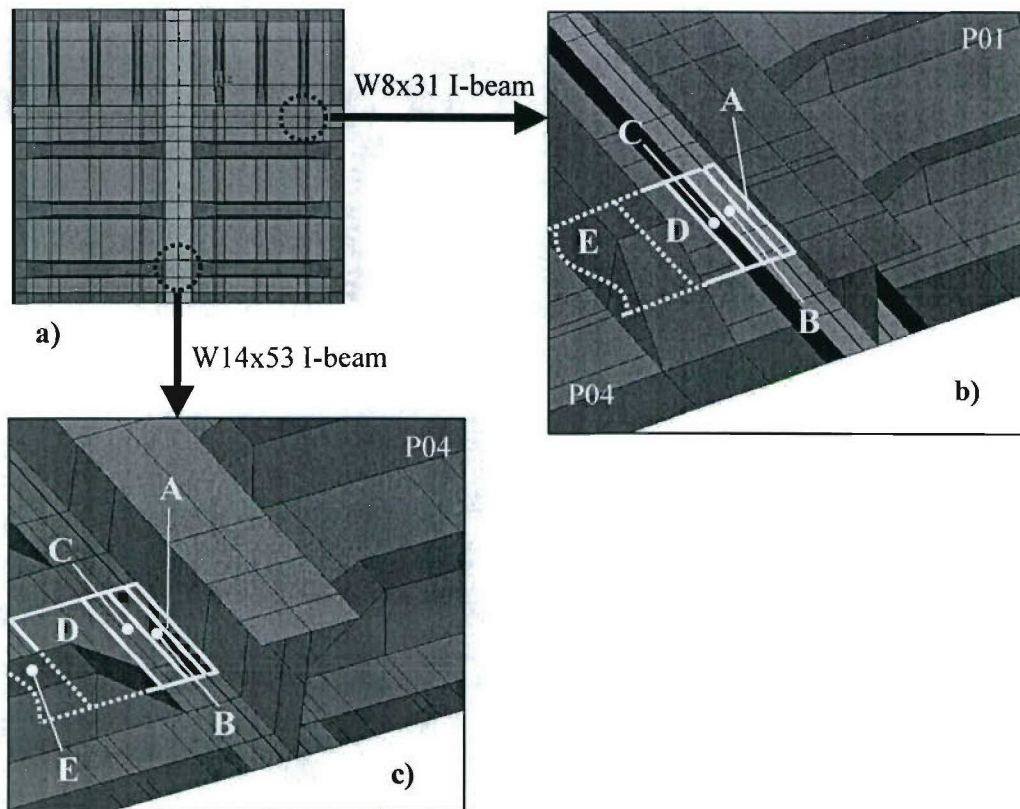


Figure 5.28. Schematic of the Hybrid Joint Regions in the Global Model

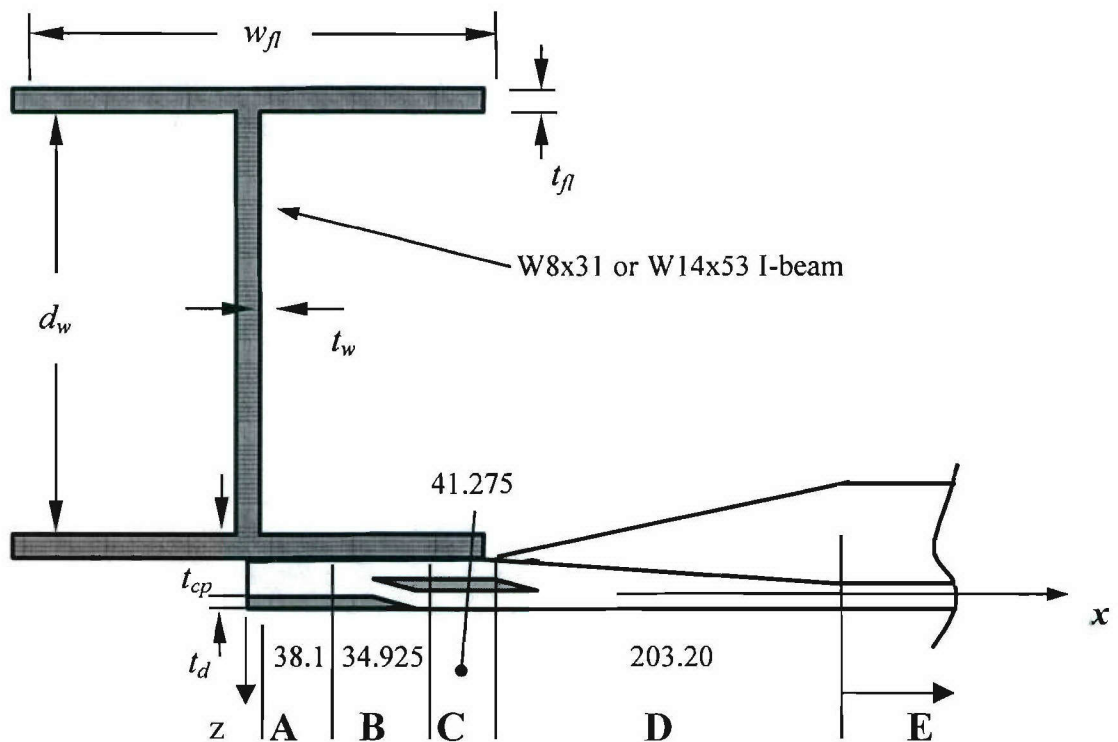


Figure 5.29. Baseline Geometry of the DS-4 Joint in the Hybrid Assembly, in mm

**Table 5.6. Approximate Geometry of the I-Beam Sections in the Hybrid Assembly**

<b>I-Beam</b>	$w_f$ <i>mm</i>	$t_f$ <i>mm</i>	$d_w$ <i>mm</i>	$t_w$ <i>mm</i>
W8x31	203.2	11.05	203.20	7.24
W14x53	203.2	16.76	353.57	9.39

### 5.5.3. Global Shell Model Verification

The loading and boundary conditions for this model are shown in Figure 5.26. Figure 5.30 shows a top view of the displacement contour of the hybrid assembly loaded to the design pressure of 82.74 kPa. Figures 5.31 and 5.32 present the individual displacement contours for the small and large panels, respectively. These plots show that the peak panel displacements occur at the regions between the stiffeners, as was observed in the experiments. As presented in Figures 5.33 through 5.36, the displaced shapes obtained from the FE models and the test results, for both small and large panels, show good agreement, with a peak difference of 10 percent. In a general sense, the displaced shapes obtained from the FE model slightly under predict the experimental displacements. This discrepancy is attributed to the differences in assumed material properties and as-built geometry, idealized joint condition in the FE model, which does not include the contact interaction between the various joint components (doubler plate, edge of the composite beam and steel flange) and the effect of the bolts in the actual structure. Also, a fixed boundary condition was assumed at the tank boundaries, which may not be a completely rigid condition in the actual test configuration.

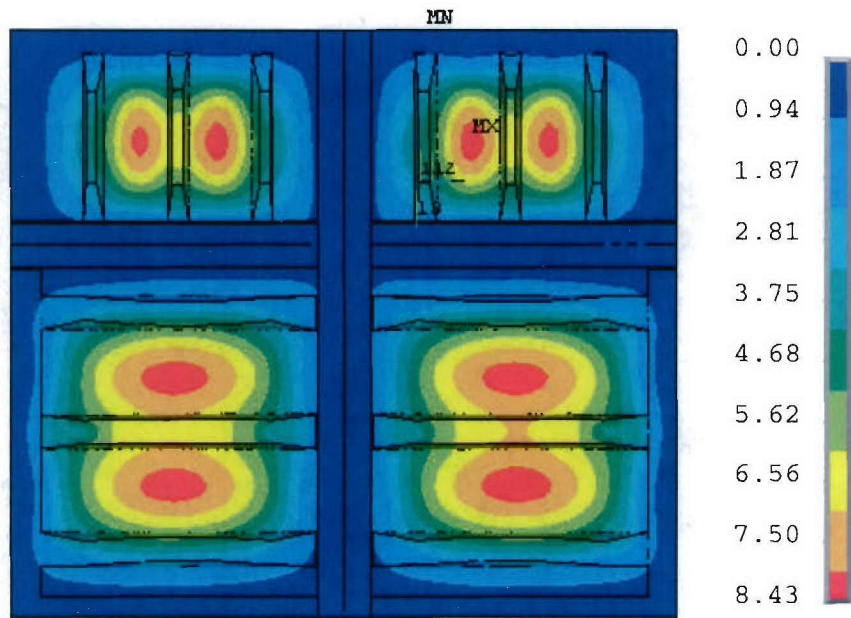


Figure 5.30. Displacement Contour of Hybrid Assembly (82.74 kPa), in mm

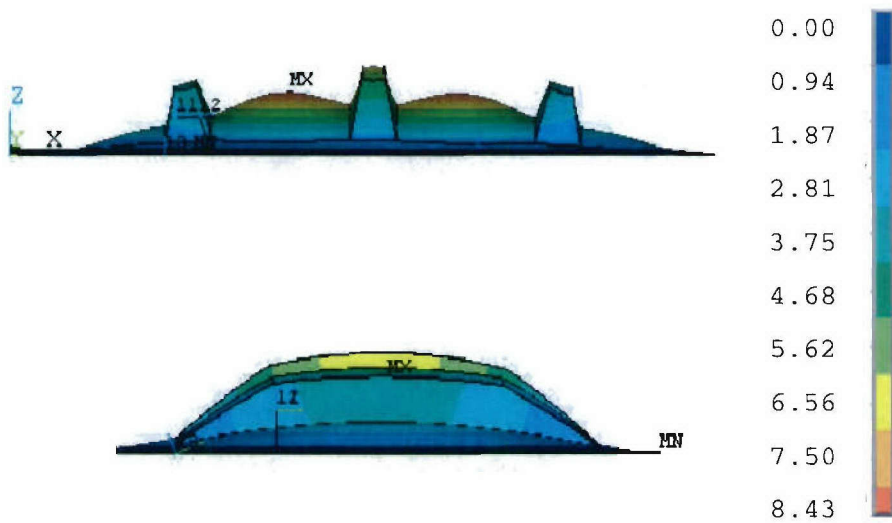


Figure 5.31. Vertical Displacement Contour of a Small Panel (82.74 kPa), in mm



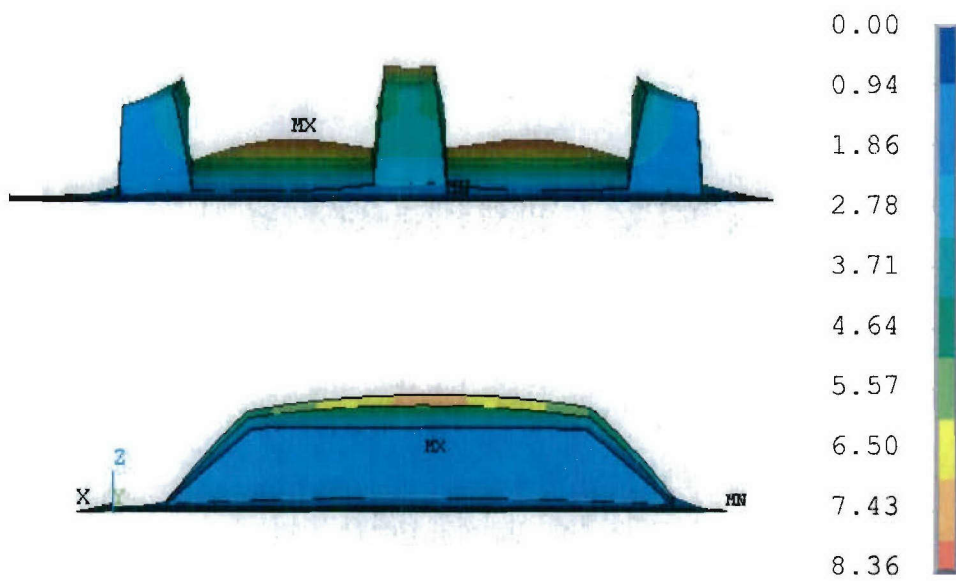


Figure 5.32. Vertical Displacement Contour of a Large Panel (82.74 kPa), in mm

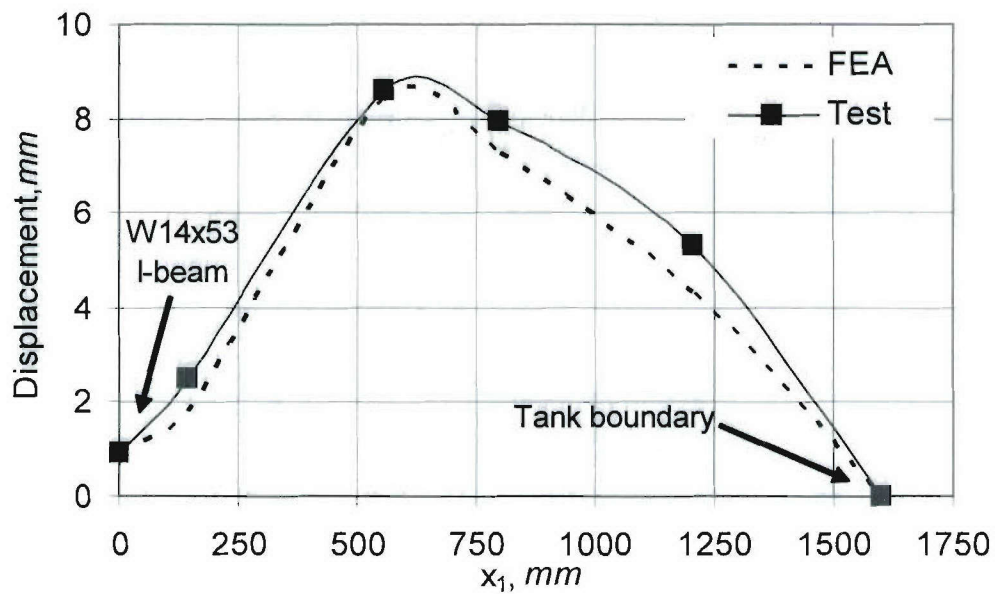


Figure 5.33. Displaced Shape of a Small Panel in the  $x_1$  direction (82.74 kPa)

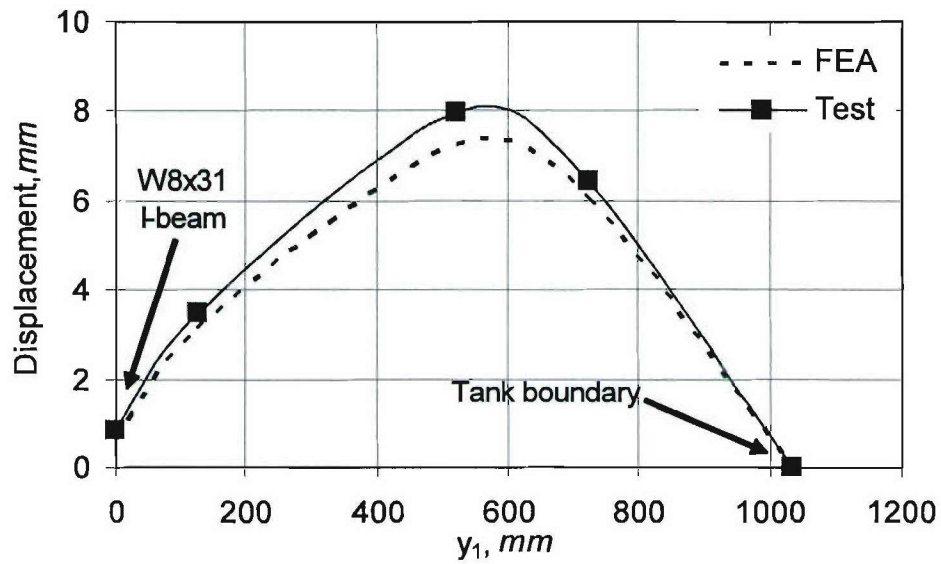


Figure 5.34. Displaced Shape of a Small Panel in the  $y_1$  direction (82.74 kPa)

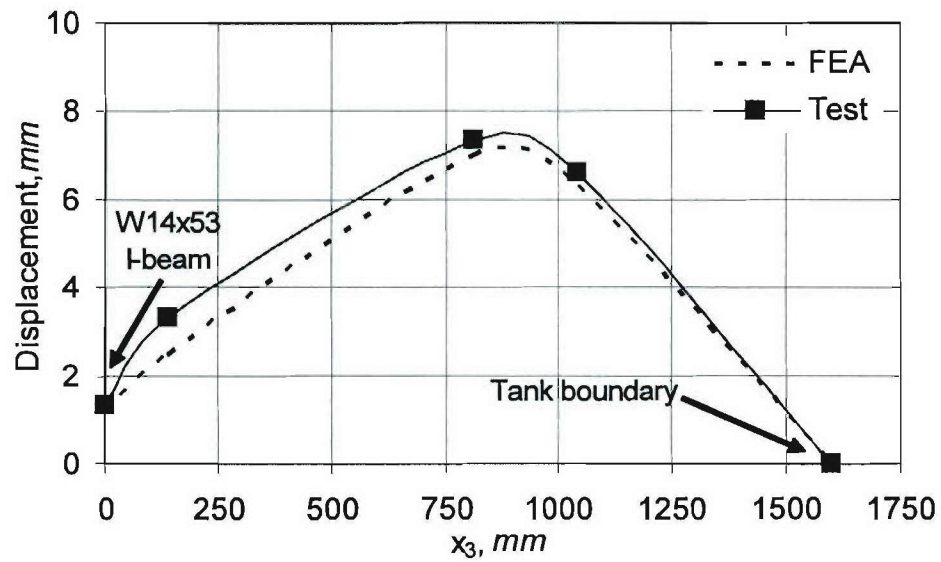
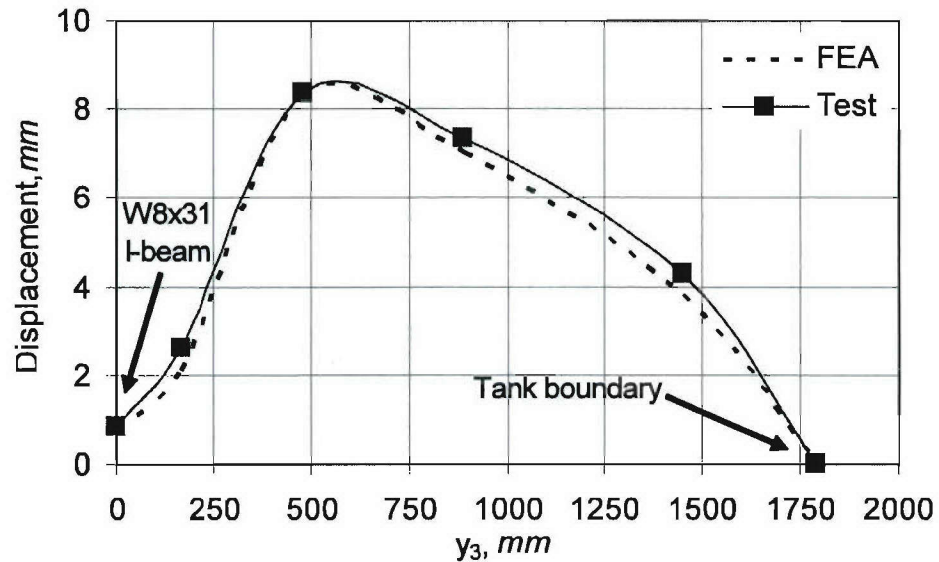


Figure 5.35. Displaced Shape of a Large Panel in the  $x_3$  direction (82.74 kPa)



**Figure 5.36. Displaced Shape of a Large Panel in the  $y_3$  direction (82.74 kPa)**

The strain contour for the small panel in the  $x_1$  direction (transverse to the stiffener direction) is presented in Figure 5.37, where the peak tensile strains are observed to occur at the regions between stiffeners, with a magnitude of 1453 microstrain. Peak compressive strains of about 2000 microstrain are observed at the tapered regions of the stiffeners. The strain profile in Figure 5.39 shows a good correlation between the experimental and the FE strains, with a peak discrepancy of about 11 percent for the strain recorded by gage SB1-6. Figure 5.38 presents the strain contour in the  $y_1$  direction (aligned with the stiffeners), where a peak value of 4833 microstrain is recorded at the center of the middle stiffener ( $y_1 = 515$  mm). For the most part, the peak tensile strains are observed to occur at the middle stiffener region, while some of the peak compressive strains are observed towards the fixed boundary and the hybrid joint region with the W8x31 I-beam. A difference of about 10 percent is observed for the FE and the experimental strains at the joint region (gage RB1-5A).

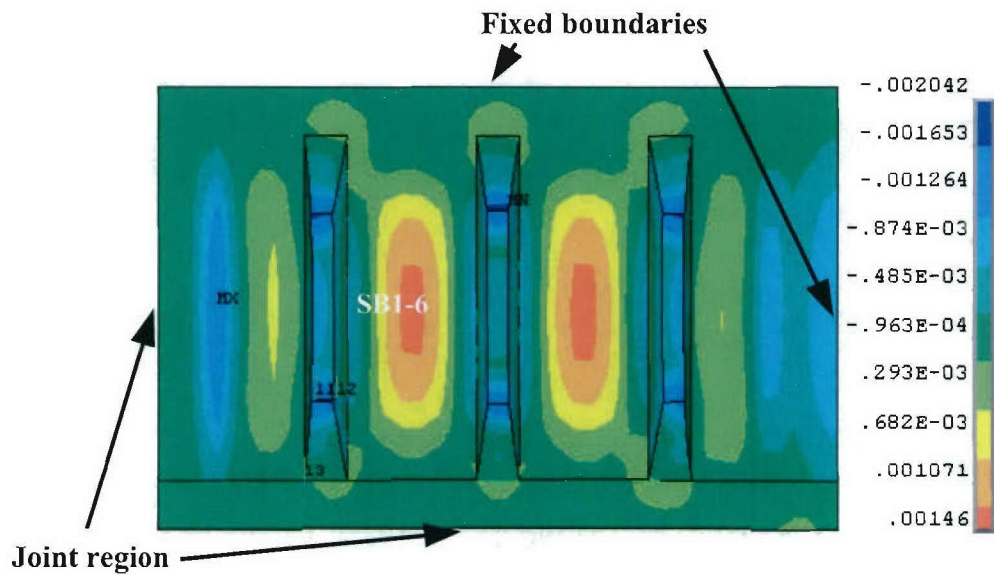


Figure 5.37. Strain Contour ( $\epsilon_x$ ) for a Small Panel (82.74 kPa)

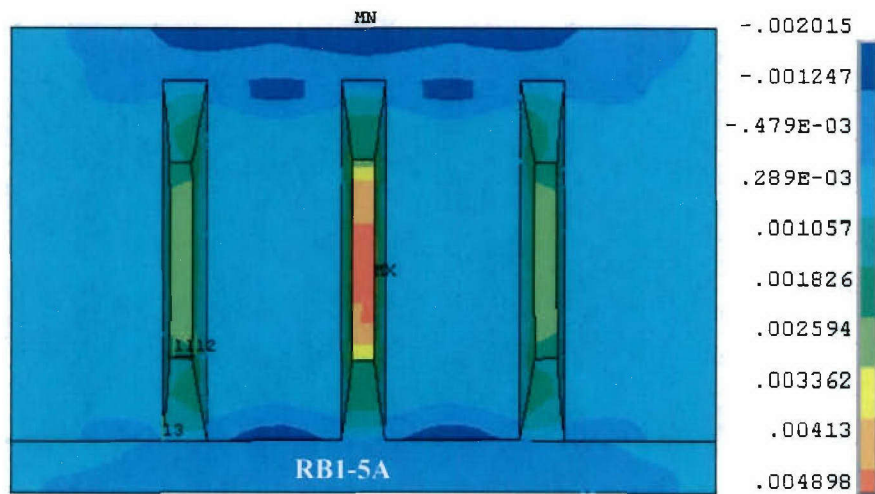


Figure 5.38. Strain Contour ( $\epsilon_y$ ) for a Small Panel (82.74 kPa)



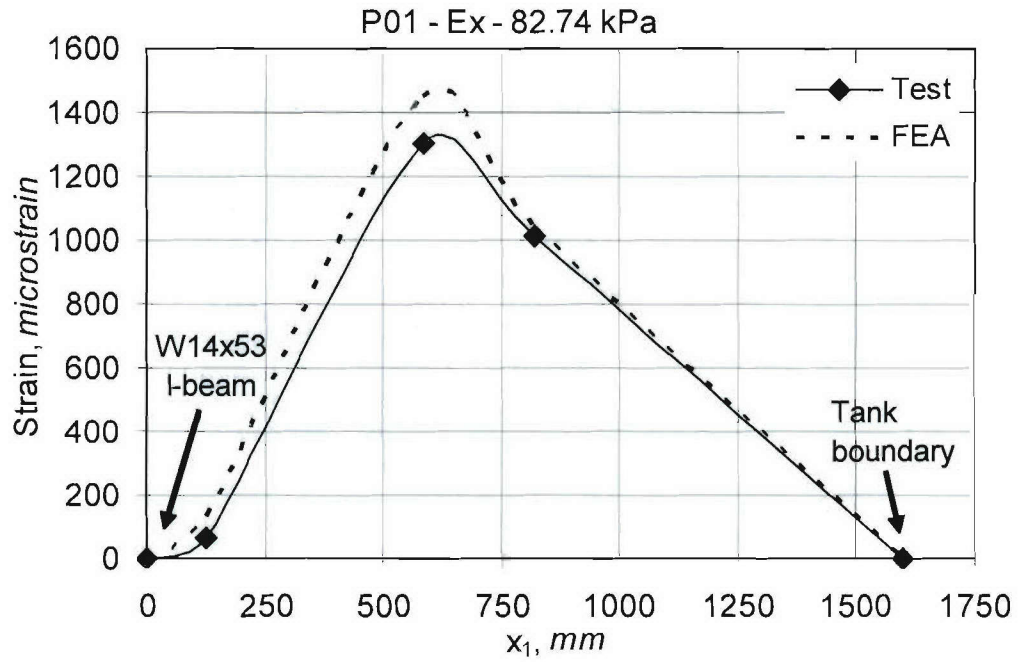


Figure 5.39. Strain Profile of a Small Panel in the  $x_1$  direction (82.74 kPa)

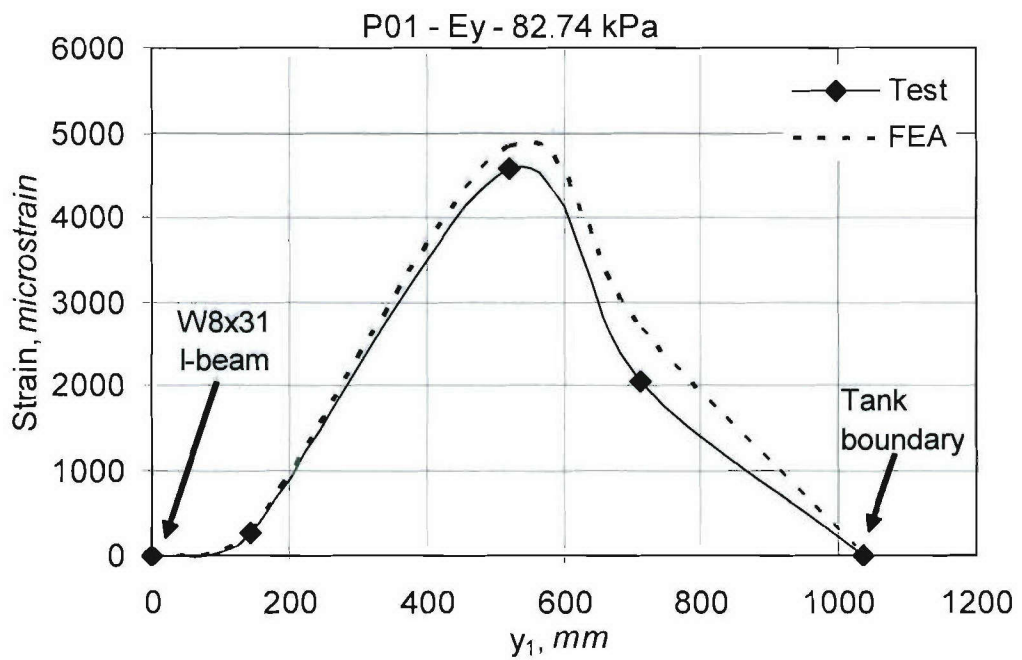


Figure 5.40. Strain Profile of a Small Panel in the  $y_1$  direction (82.74 kPa)

The strain contour for the large panel in the  $x_3$  direction (stiffener direction) is presented in Figure 5.41, where a peak tensile strain of 3080 microstrain is observed at the center of the middle stiffener. Peak compressive strains of about 2781 microstrain are observed towards the fixed tank boundary. The strain profile in Figure 5.43 shows a peak discrepancy of about 25 percent for the strain recorded at the joint region by gage RB3-5C. Figure 5.42 shows the strain contour for the large panel in the  $y_3$  direction (transverse to the stiffeners), where a peak compressive strain of 2622 microstrain is recorded at the start of the tapered region of the middle stiffener. When compared to the strain profile in Figure 5.44, the results from the FE results agree with the experimental strains, with a difference of 11 percent for the strain recorded at the region between stiffeners (gage SB3-6). Overall, the global model presented in this section is adequate for estimating the global panel deflections and the strains within the bulk of the panels. Some of the discrepancies between the numerical and the experimental strains were observed near the joint region, given that this simplified approach does not account for the three dimensional effects and contact interactions at the joint, and therefore is not expected to provide an accurate appraisal of the local stress or strain state near the joint.

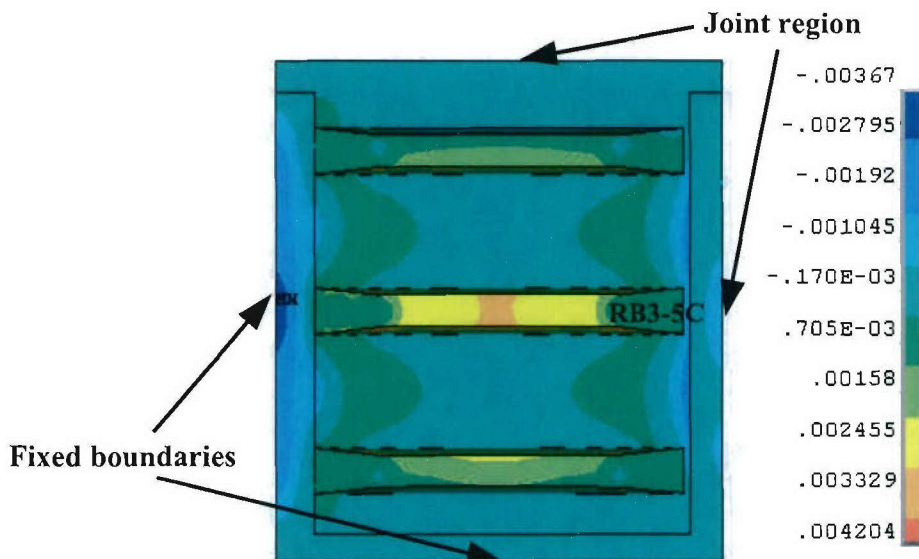


Figure 5.41. Strain Contour ( $\epsilon_x$ ) for a Large Panel (82.74 kPa)

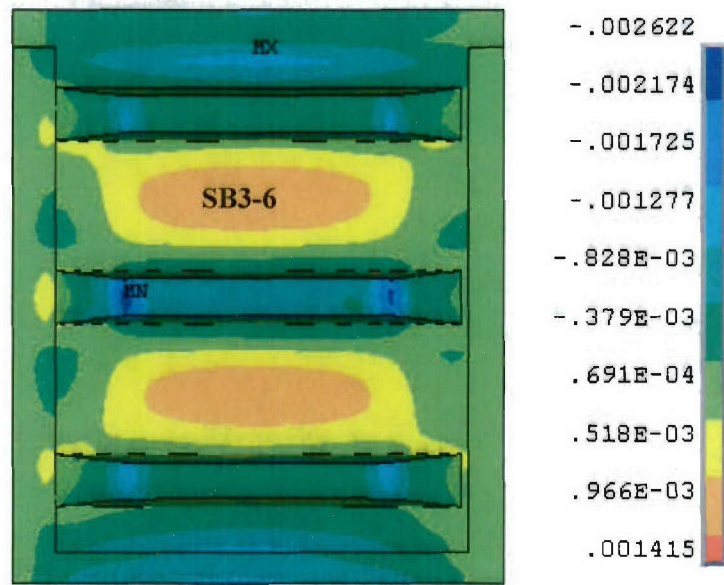


Figure 5.42. Strain Contour ( $\epsilon_y$ ) for a Large Panel (82.74 kPa)

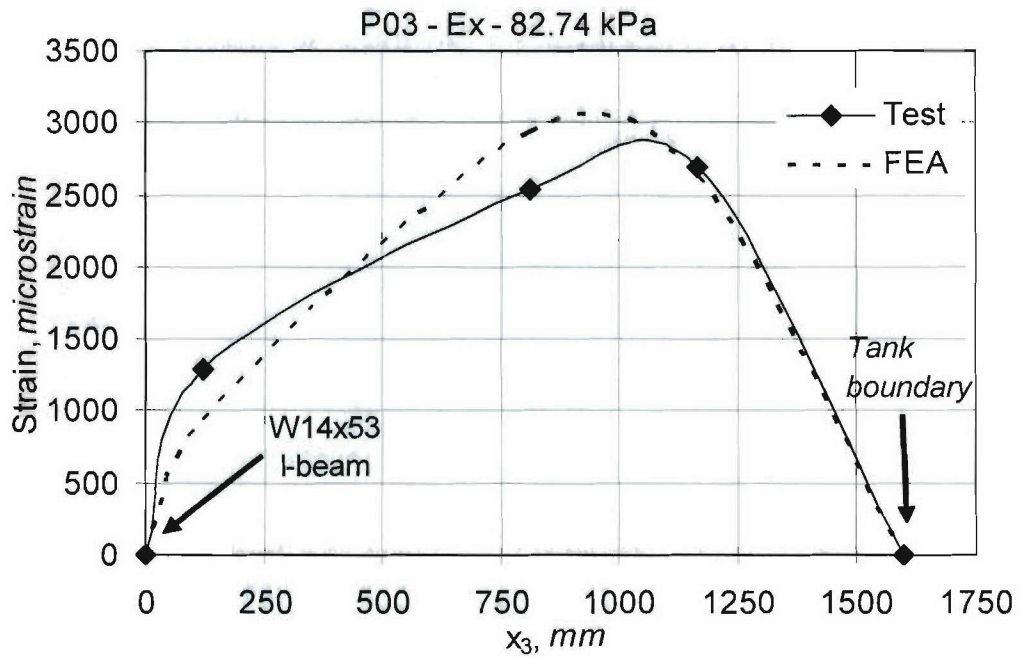


Figure 5.43. Strain Profile of a Large Panel in the  $x_3$  direction (82.74 kPa)

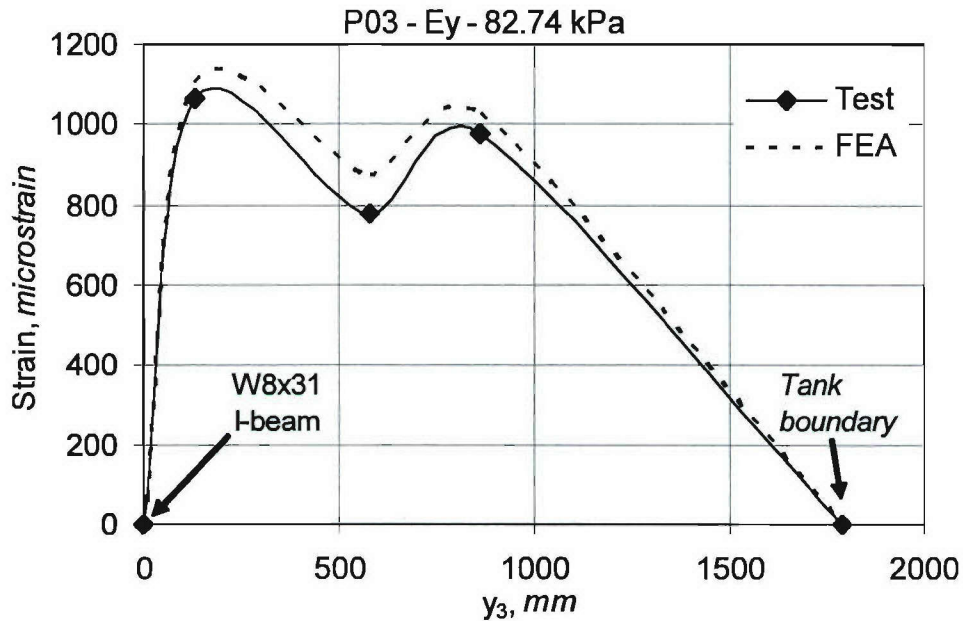


Figure 5.44. Strain Profile of a Large Panel in the  $y_3$  direction (82.74 kPa)

#### 5.5.4. Parametric Study of Global Structural Response

Using an approach similar to that described in Section 5.3.2 for a local shell model, a parametric study was conducted to observe the influence of the geometry of the joint constituents on the global response of the hybrid assembly. The main geometric variables considered for this study are: the doubler plate thickness ( $t_d$ ), the composite beam thickness ( $t_c$ ), and the thickness of the steel flange for both the W8x31 ( $t_{fl\_8x31}$ ) and the W14x53 ( $t_{fl\_14x53}$ ) I-beams.

##### 5.5.4.1. Effect of the Doubler Plate Thickness

The effect of the doubler plate thickness on the global panel response was studied for the assembly loaded to the design pressure of 82.74 kPa. According to the approach presented in Section 5.3.2, the properties of each joint section were computed for a given doubler plate thickness value,  $t_d$ , while holding the steel flange thicknesses ( $t_{fl\_8x31}$ ,  $t_{fl\_14x53}$ ) and the composite thickness ( $t_c$ ), constant (Figure 5.29). A doubler plate thickness range of  $0.5 t_d$  to  $4 t_d$  was used, with  $t_d$  being the baseline thickness of 6.35 mm.



A comparison of the displaced shapes for a small panel in the  $x_1$  and  $y_1$  direction are presented in Figures 5.45 and 5.46, respectively. In a qualitative sense, these curves show that varying the doubler plate thickness affects the small panel displacements near the hybrid joint region ( $y_1 = 120$  mm), particularly for the displaced shapes along the stiffener direction ( $y_1$  direction). The effect of the  $t_d$  decreases as  $y_1$  increases, for the region between the outer stiffener and the tank boundary, which indicates that the response of this region is mostly affected by the clamped boundary conditions at the outer edges of the panel. Transverse to the stiffeners ( $x_1$  direction), the doubler plate thickness affects the displacements at the center of the panel. These results also suggest that that W8x31 I-beam has a large influence on the response of the small panels.

Figures 5.47 and 5.48 show the displaced shapes for the large panel in the  $x_3$  and  $y_3$  directions, respectively. In the  $x_3$  direction, these curves show that the effect of the doubler thickness is significant towards the joint region ( $x_3 = 120$  mm). Transverse to the stiffeners, the effect of the doublers is observed at  $y_3 = 1425$  mm, towards the tank boundary. Increasing the doubler thickness provides additional moment resistance in bending, when compared to the baseline case of  $t_d = 6.35$  mm. For example, it is estimated that using a doubler thickness four times as large as the baseline thickness reduces the peak panel deflection by about 14 percent.

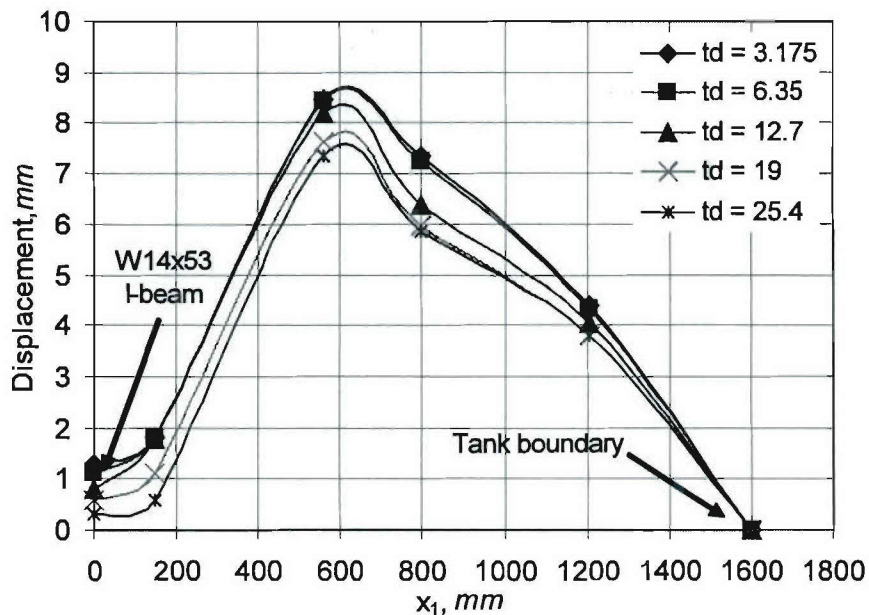


Figure 5.45. Effect of  $t_d$  on the Displaced Shapes of a Small Panel in the  $x_1$  direction (82.74 kPa)

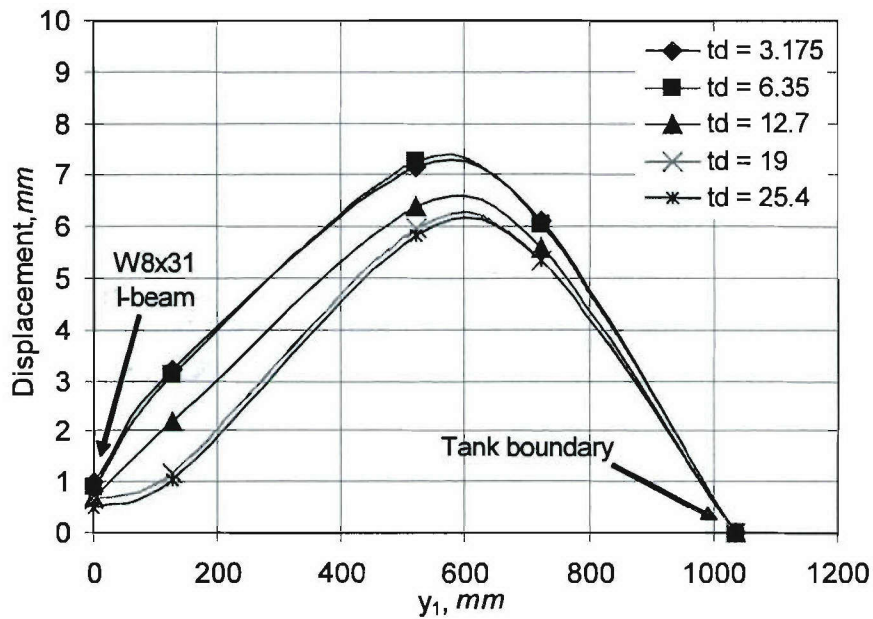


Figure 5.46. Effect of  $t_d$  on the Displaced Shapes of a Small Panel in the  $y_1$  direction (82.74 kPa)

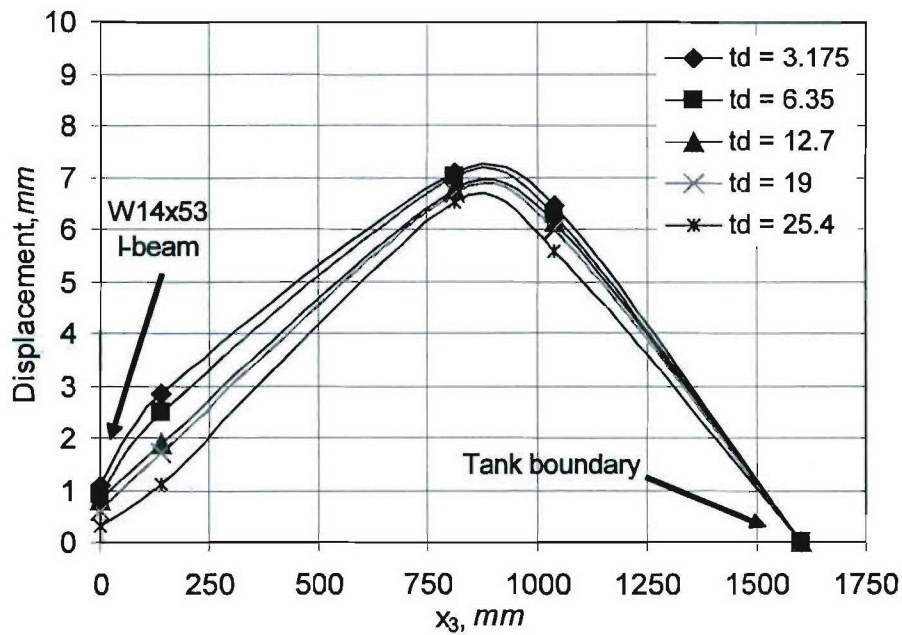


Figure 5.47. Effect of  $t_d$  on the Displaced Shapes of a Large Panel in the  $x_3$  direction (82.74 kPa)

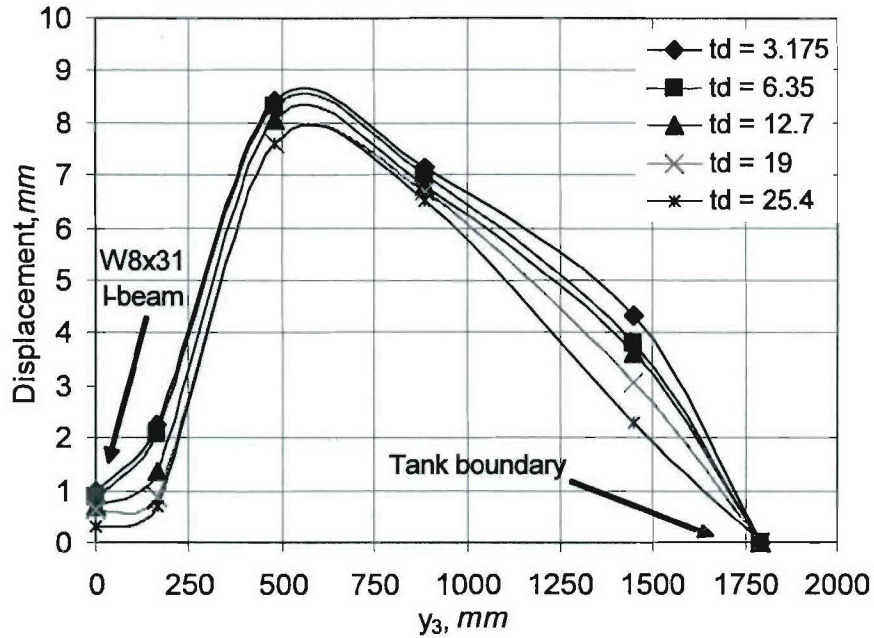


Figure 5.48. Effect of  $t_d$  on the Displaced Shapes of a Large Panel in the  $y_3$  direction (82.74 kPa)

#### 5.5.4.2. Effect of the Composite Thickness

The effect of the composite thickness on the global panel response was studied for the assembly loaded to the design pressure of 82.74 kPa. According to the approach presented in Section 5.3.2, the properties of each joint section were computed for a given composite beam thickness value,  $t_c$ , while holding the steel flange thicknesses ( $t_{f\_8x31}$ ,  $t_{f\_14x53}$ ) and the doubler plate thickness ( $t_d$ ), constant. It is noted that the composite thickness was only varied at the regions local to the joint, i.e., sections A, B and C in Figure 5.29. A composite thickness range of  $0.25 t_c$  to  $1.5 t_c$  was used, with  $t_c$  being the baseline thickness of 25.40 mm.

The displaced shapes for a small panel in the  $x_l$  and  $y_l$  directions are presented in Figures 5.49 and 5.50, respectively. These curves show that varying the composite thickness affects the local stiffness of the joint, near the hybrid region, in both directions, but it also affects the peak displacements at the center of the panels ( $x_l = 800$  mm,  $y_l = 520$  mm). In the case of the large panel, shown in Figures 5.51 and 5.52, varying the composite thickness has a local effect at the joint region which decreases towards the center of the panel in the  $x_3$  direction ( $x_3 = 770$  mm). Transverse to the stiffeners ( $y_3$  direction), variations in the

composite thickness do not significantly influence the panel response. The additional rigidity provided by increasing the composite thickness tends to reduce the deflections at the joint region and the center of the panels. For instance, for a composite thickness 1.5 times the baseline caused a 15 percent reduction in peak deflection.

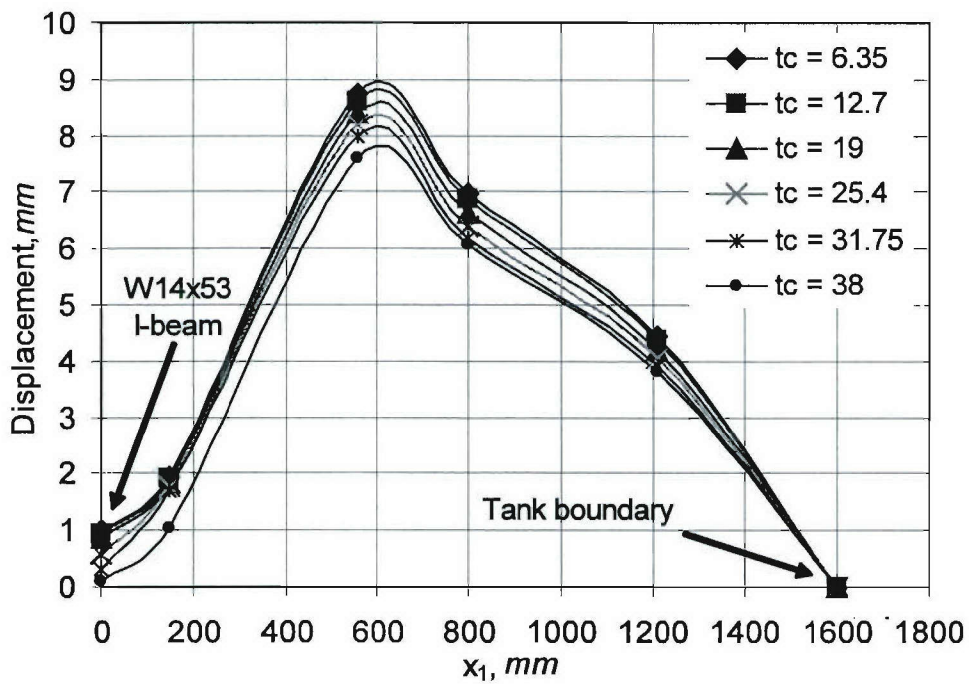


Figure 5.49. Effect of  $t_c$  on the Displaced Shapes of a Small Panel (82.74 kPa), along the  $x_1$ -direction.



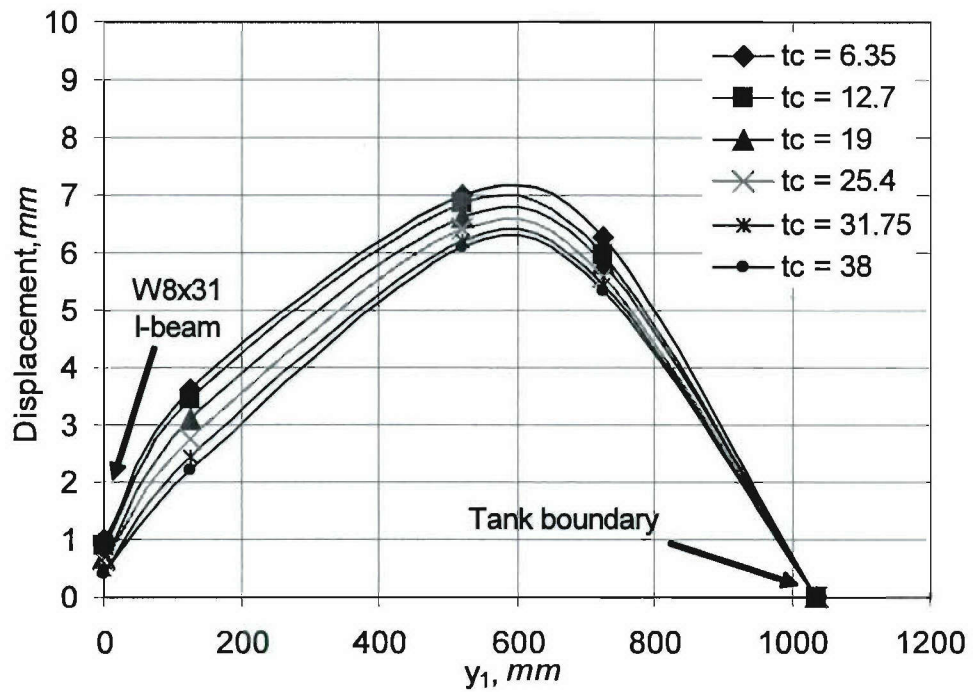


Figure 5.50. Effect of  $t_c$  on the Displaced Shapes of a Small Panel (82.74 kPa)

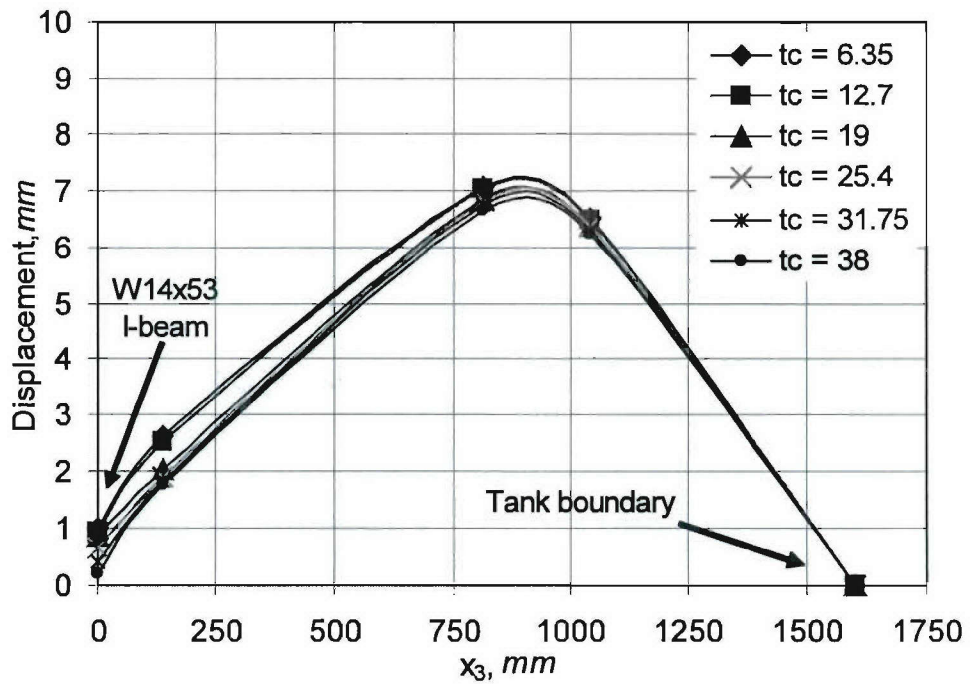


Figure 5.51. Effect of  $t_c$  on the Displaced Shapes of a Large Panel (82.74 kPa)

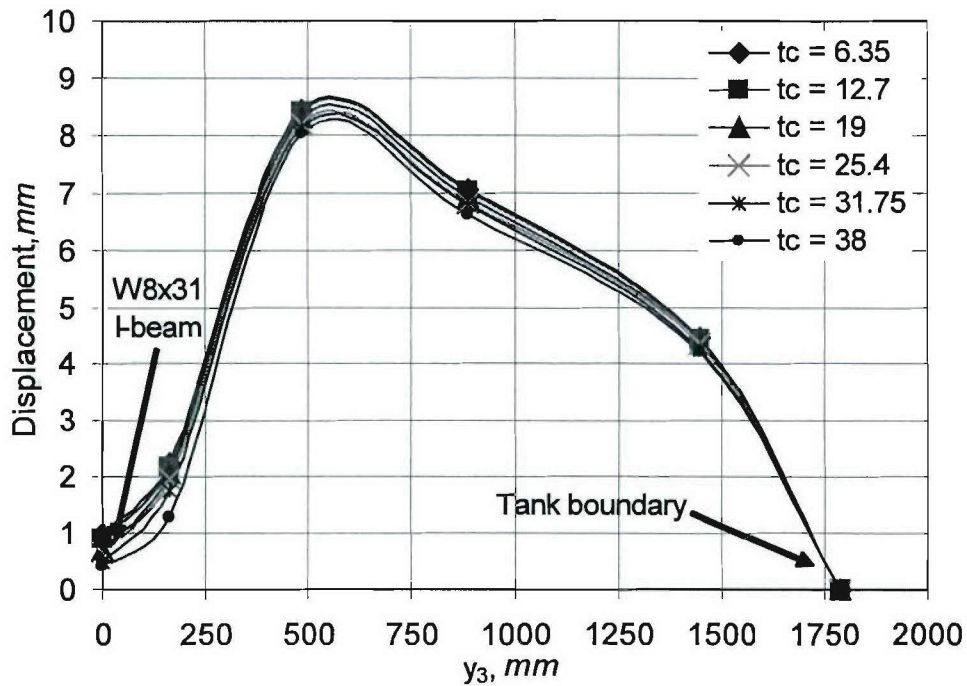


Figure 5.52. Effect of  $t_c$  on the Displaced Shapes of a Large Panel (82.74 kPa)

#### 5.5.4.3. Effect of Flange Thickness (W8x31 and W14x53 I-Beams)

The effect of the steel flange thickness on the global panel response was studied for the assembly loaded to the design pressure of 82.74 kPa, for both I-beams. According to the approach presented in Section 5.3.2, the properties of each joint section were computed for a given flange thickness value,  $t_{fl}$ , while holding the doubler plate thickness ( $t_d$ ) and the composite beam thickness ( $t_c$ ), constant. The flange thickness was modified for one I-beam at a time. For the W8x31 I-beam, a flange thickness range of  $0.50 t_{fl\_8x31}$  to  $2.5 t_{fl\_8x31}$  was used, with  $t_{fl\_8x31}$  being the baseline thickness of 11.05 mm. For the W14x53 I-beam, a flange thickness range of  $0.50 t_{fl\_14x53}$  to  $2.5 t_{fl\_14x53}$  was used, with  $t_{fl\_14x53}$  being the baseline thickness of 16.76 mm. The approximate I-beam dimensions are summarized in Table 5.6.

Figure 5.53 and 5.54 present the displaced shapes of the small panel for varying flange thickness values of the W8x31 I-beam. In the  $x_l$  direction, transverse to the stiffener direction, the flange effect is more pronounced for the middle regions of the panel ( $600 \text{ mm} < x_l < 800 \text{ mm}$ ), but not as significant at the joint region ( $x_l, y_l = 0$ ). In the  $y_l$  direction,

aligned with the stiffeners, the flange thickness has a more significant effect on the panel response, particularly towards the joint region ( $y_1 = 130$  mm). Again, this suggests that the W8x31 I-beam has a large influence on the behavior of the small panels, particularly in the stiffener direction. In the case of the large panel in Figures 5.55 and 5.56, changing the thickness of the W8x31 I-beam does not have an effect on the displacement, particularly in the direction transverse to the stiffeners.

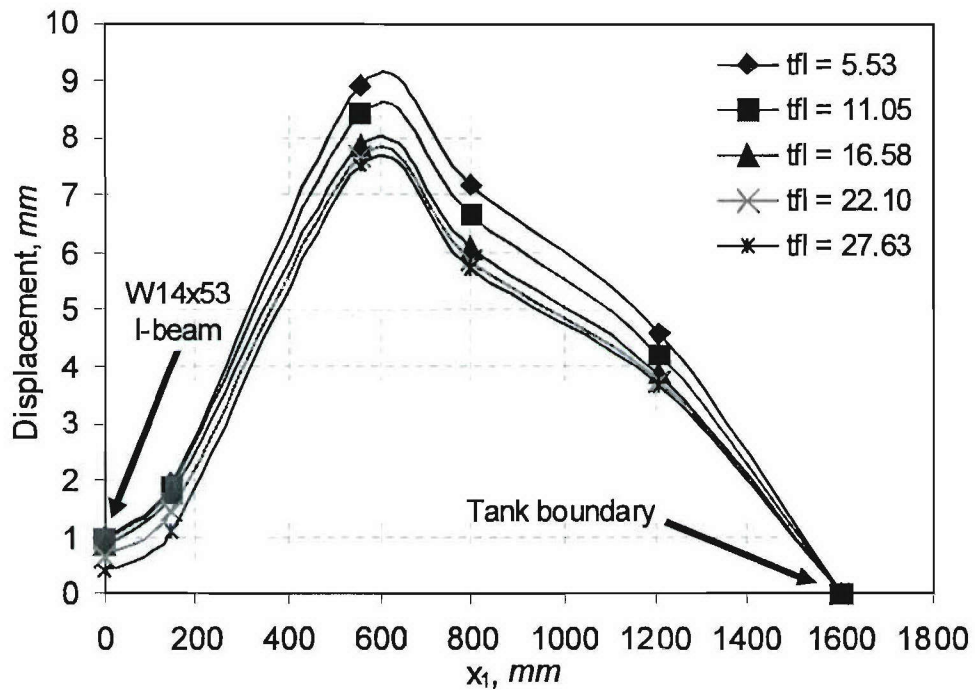


**Figure 5.53. Effect of  $t_{fl\_8x31}$  on the Displaced Shapes of a Small Panel (82.74 kPa), along the  $x_1$ -direction.**

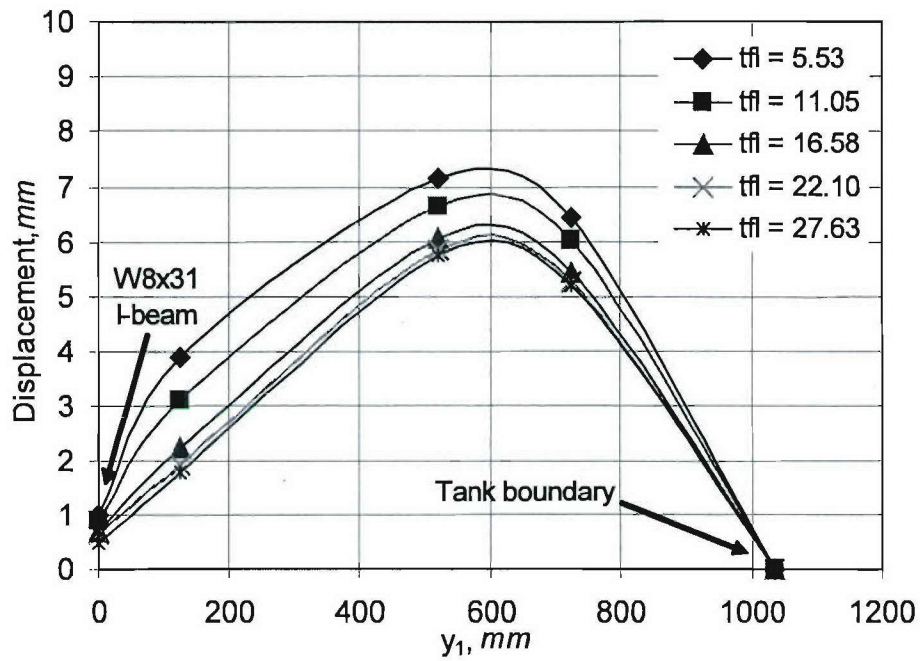


Figure 5.54. Effect of  $t_{fl\_8x31}$  on the Displaced Shapes of a Small Panel (82.74 kPa), along the  $y_1$  direction

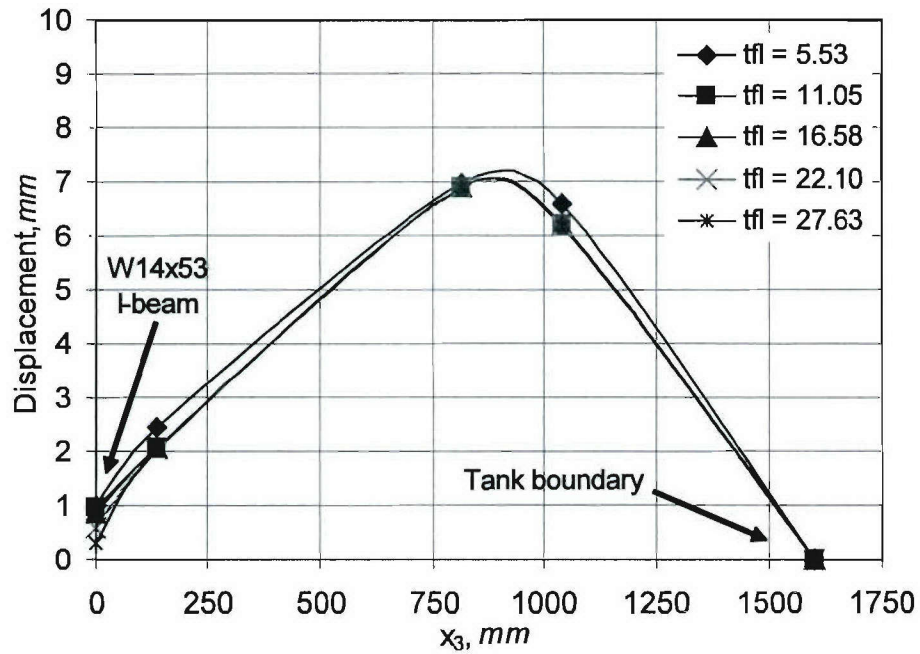
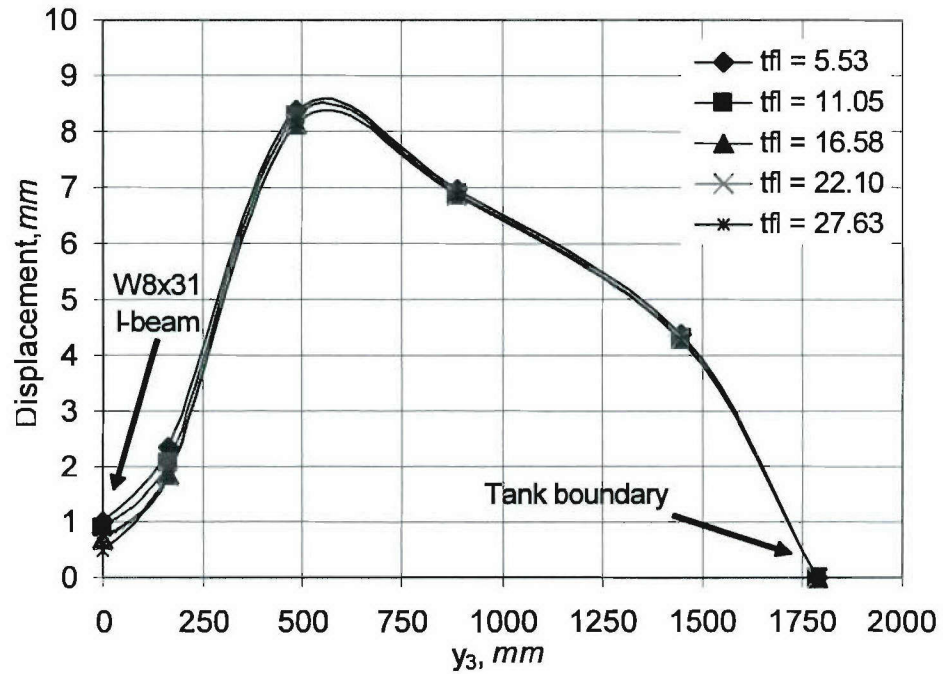


Figure 5.55. Effect of  $t_{fl\_8x31}$  on the Displaced Shapes of a Large Panel (82.74 kPa), along the  $x_3$  direction





**Figure 5.56. Effect of  $t_{fl\_8x31}$  on the Displaced Shapes of a Large Panel (82.74 kPa), along the  $y_3$  direction.**

Figures 5.57 and 5.58 present the displaced shapes of the small panel for varying flange thickness values of the W14x53 I-beam, where the flange thickness has a minor effect on the panel response, in both  $x_1$  and  $y_1$  directions. On the other hand, the curves in Figures 5.59 and 5.60 depict the strong influence of the flange thickness on the large panel response. In the stiffener direction, this influence is apparent for the displacements at the joint region ( $x_3 = 125$  mm) and at the center of the panel ( $x_3 = 770$  mm). Transverse to the stiffener direction ( $y_3$ ), the flange thickness does not affect the joint displacements, but rather the center and stiffener displacements, at  $y_3 = 500$  mm and 875 mm, respectively.

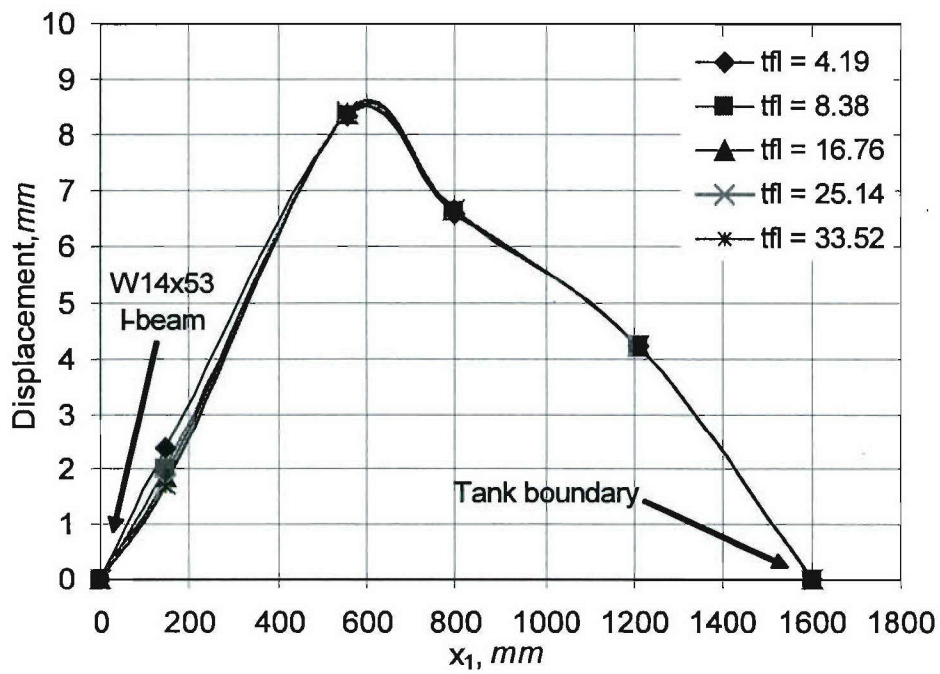


Figure 5.57. Effect of  $t_{fl\_14x53}$  on the Displaced Shapes of a Small Panel (82.74 kPa), along  $x_1$  direction.

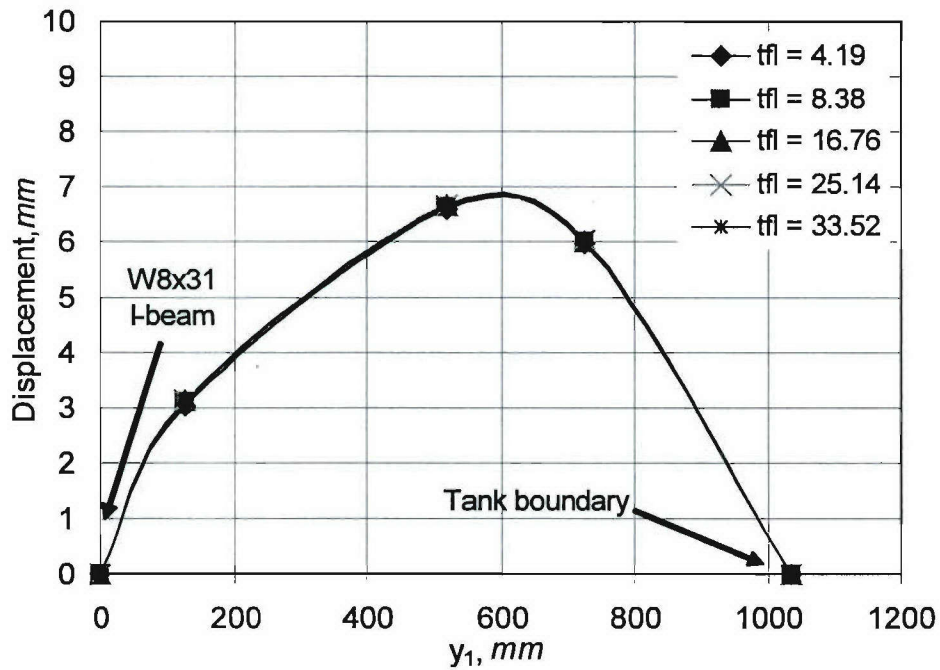


Figure 5.58. Effect of  $t_{fl\_14x53}$  on the Displaced Shapes of a Small Panel (82.74 kPa), along  $y_1$  direction.

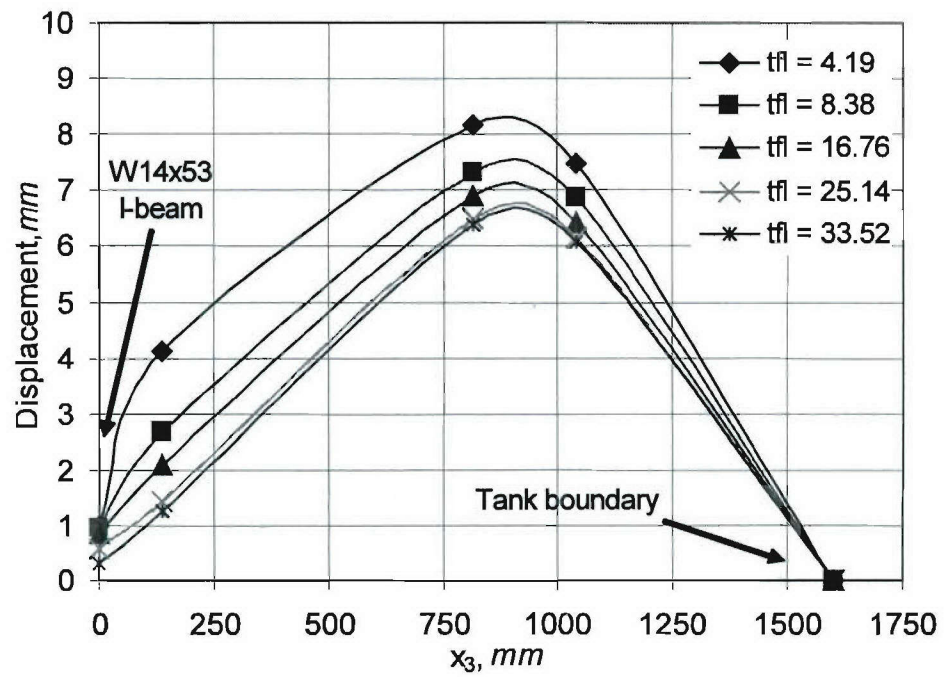


Figure 5.59. Effect of  $t_{fl\_14x53}$  on the Displaced Shapes of a Large Panel (82.74 kPa), along  $x_3$  direction.

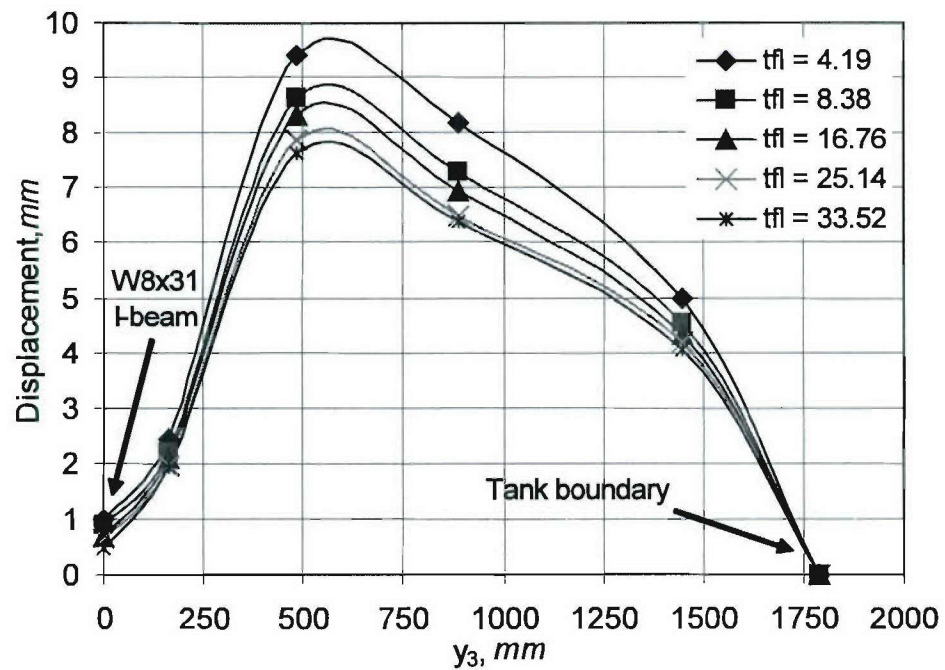


Figure 5.60. Effect of  $t_{fl\_14x53}$  on the Displaced Shapes of a Large Panel (82.74 kPa), along  $y_3$  direction.

The parametric study presented in this section shows that the global response of the hybrid assembly is most sensitive to changes in the steel component geometries, particularly the steel flange. Changes in the doubler geometry most strongly affect the local response of the small panels at the joint region, in the stiffener direction. Increasing the thickness of the composite has a modest localized effect on the joint region. As expected, the steel flange thickness has a strong effect on the moment resistance of the connection and on the global panel deflections. The study also shows that the flange stiffness of the W8x31 I-beam drives the response of the small panels, but does not significantly affect the response of the large panels. Conversely, the flange stiffness of the W14x53 I-beam drives the response of the large panels, but not that of the small panels.

### **5.6. Plane Strain Finite Element Model of the Hybrid Joint**

The shell models presented in the previous sections were found appropriate to estimate the joint stiffness. Furthermore, these models are useful for studying the global response of large-scale structures where extensive detailing of the small-scale features is not feasible. However, since details of the bolted connection are not included, shell models do not provide an accurate appraisal of the local stresses at the joint. The plane strain model presented in this section is used to estimate the local joint response in bending, by modeling the contact interactions between the joint constituents and bolt. Though a three dimensional solid model is more appropriate to compute the local stresses, the computational cost and modeling complexity would be very large and impractical for application into a large-scale structural model.

Several modeling approaches were used to envelop the response of the joints. The initial approach presented is a model of the joint as a “glued” entity, where all the components act together with continuity and contact interactions are not included. In the second approach contact modeling is prescribed by specifying the surfaces that will interact as the joint is loaded. Lastly, a contact model that incorporates the net effect of the bolt is presented. Included in this last model are the use of nodal constraints and the use of a spring element along the bolt-line. Model verification is conducted for the case of the DS-4 joint



configuration that was the connection type used for the hybrid panel assembly described in Section 4.

#### 5.6.1. Plane Strain Model Description

Figure 5.61 presents a schematic of a plane strain model of the DS-4 joint configuration and the geometry is shown in Figure 5.62. A plane strain analysis was chosen to represent this joint since this detail exists over a relatively long length when applied to the actual ship structure. The composite laminate consists of orthotropic layers that are perfectly bonded together, and a foam insert. The composite geometry was sub-divided through the thickness to include the geometry of all layers, with a layer thickness of 0.39 mm.

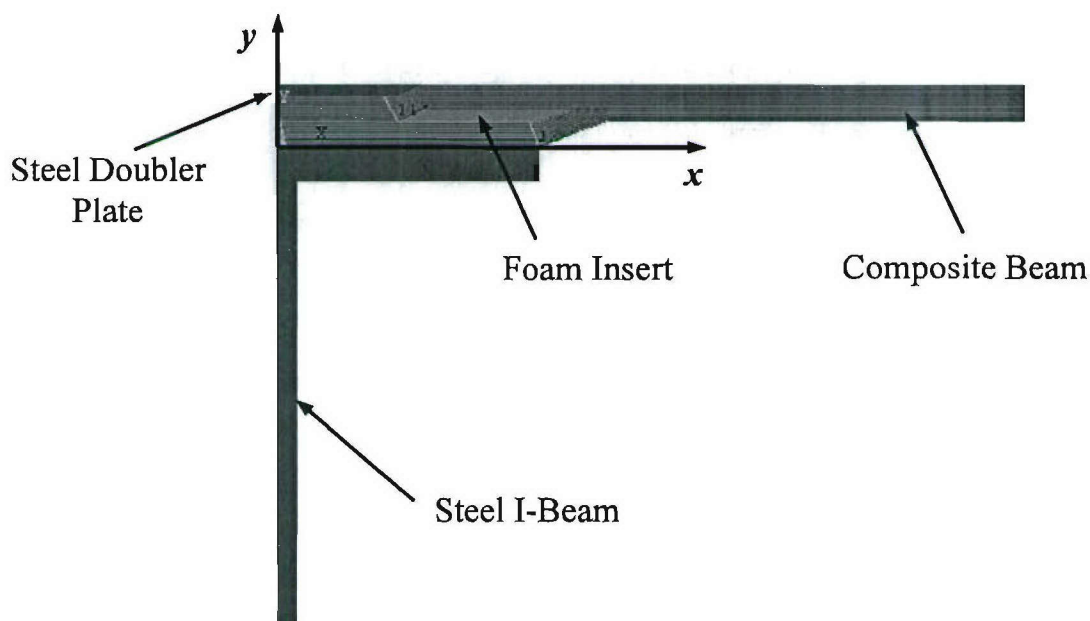


**Figure 5.61. Schematic of Plane Strain Model (DS-4)**

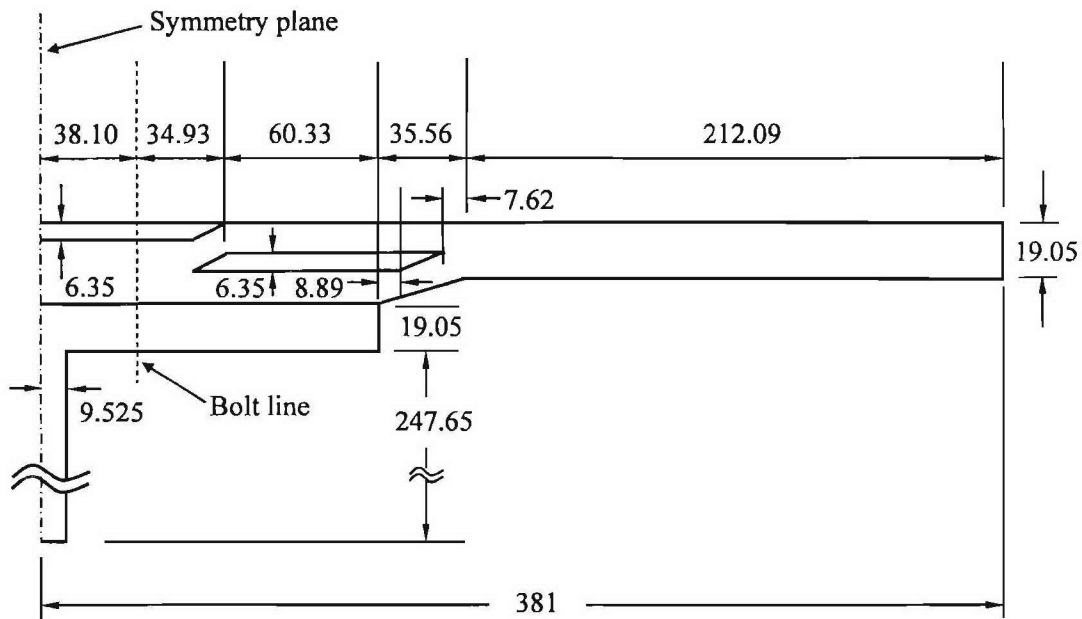


**Figure 5.62. DS-4 Joint Geometry in mm.**

Figure 5.63 shows the meshed model of the joint, where element type PLANE183 is used. PLANE183 is a higher order 2-D, 8-node element with quadratic displacement behavior. This element is defined by 8 nodes having two degrees of freedom at each node: translations in the nodal  $x$  and  $y$  directions. Higher order elements are generally well suited for bending dominated problems. To save computational time, one half of the joint is modeled. A mesh of approximately 18500 elements is used. All degrees of freedom at the bottom of the steel flange are constrained to simulate a fixed base condition. Symmetry boundary conditions are applied about the joint centerline. Nodal forces are input per unit of depth. For a total load of 4.45 kN and a specimen width of 171.45 mm, a concentrated load of 25.92 N load per unit thickness is applied to the free end of the composite beam. This represents a total load of 4.45 kN on the 171.45-mm wide joint test specimen.

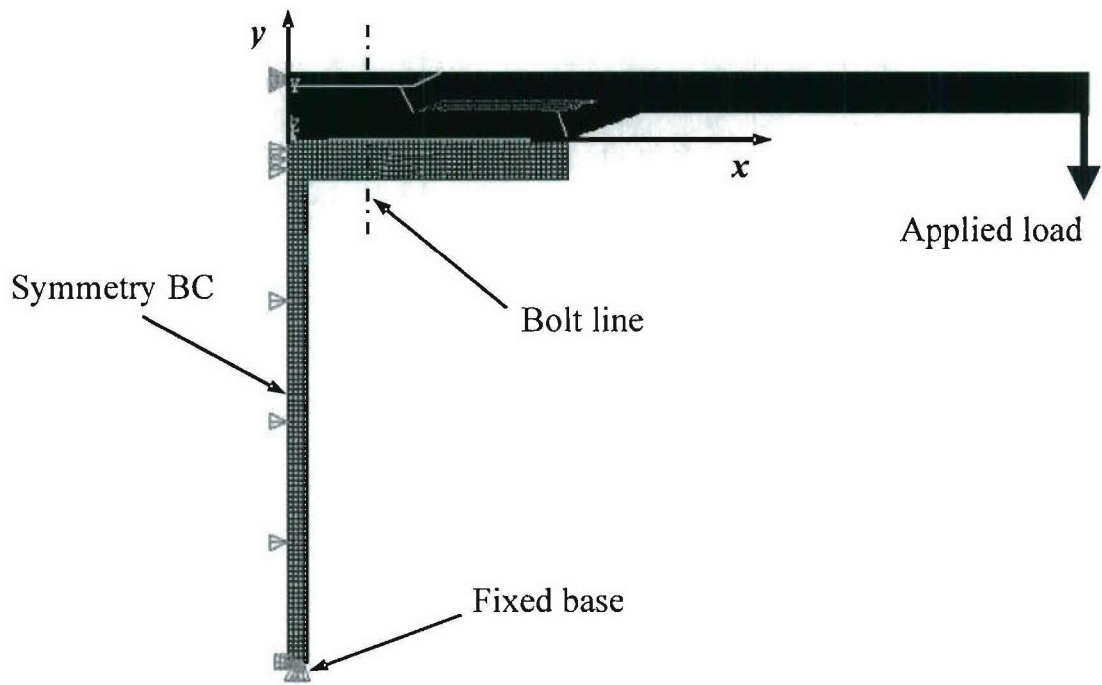


**Figure 5.63. Meshed Model of the DS-4 Joint**

The steel doubler plate and steel I-beam members are assigned an elastic modulus of 203 GPa, a Poisson's ratio of 0.30 and a yield strength of 248 MPa. The foam insert is modeled as an isotropic material, having an elastic modulus of 80 MPa and a Poisson's ratio of 0.29. The orthotropic material properties for a single EG/VE lamina (55% v.f.) in the principal material coordinates are presented in Table 5.7. For input into a plane strain model, the orthotropic material properties in terms of the elastic stiffness matrix,  $[C]$ , are used.  $[C]$  is the inverse of the compliance matrix,  $[S]$ , which is computed in terms of the engineering constants: the elastic moduli  $E_1$ ,  $E_2$ ,  $E_3$ , Poisson's ratios  $\nu_{12}$ ,  $\nu_{13}$ ,  $\nu_{23}$ , the shear moduli,  $G_{12}$ ,  $G_{23}$ ,  $G_{13}$ , and the fiber orientation,  $\theta$  [Hyer, 1998].

Table 5.8 summarizes the computed coefficients for the various ply orientations comprising the laminated beam. Terms not shown in the table are equal to zero, i.e.,  $C_{14} = 0$ ,  $C_{15} = 0$ , etc. In ANSYS, this input is done by using the ANISOTROPIC ELASTICITY MATERIAL MODEL option, in STIFFNESS FORM. The laminate architecture consists of a  $[(\pm 45, 0/90)_6]_s$  configuration at the free end of the composite and a  $[(\pm 45, 0/90)_8]_s$  at the joint region. Four different material definitions are created for the four layer orientations.

Two local coordinate systems are created for the layers in tapered regions of the composite, as shown in Figure 5.64.

**Table 5.7. Orthotropic Lamina Properties for the EG/VE System**

$E_{11}$ (GPa)	$E_{22}$ (GPa)	$E_{33}$ (GPa)	$G_{12}$ (GPa)	$G_{13}$ (GPa)	$G_{23}$ (GPa)	$\nu_{12}$	$\nu_{13}$	$\nu_{23}$
37.93	10.56	10.56	3.192	3.192	2.258	0.29	0.29	0.439
			$S_1^+$ (MPa)	$S_2^+$ (MPa)	$S_{12}^+$ (MPa)	$S_1^-$ (MPa)	$S_2^-$ (MPa)	$S_{12}^-$ (MPa)
			1117	63	41	- 662	- 311	- 41

**Table 5.8. Orthotropic Material Properties in Terms of the Elastic Stiffness Matrix,  $C$ , in GPa**

Constant	0° Ply	90° Ply	45° Ply	- 45° Ply
$C_{11}$	41.38	13.94	20	20
$C_{12}$	5.956	5.956	13.62	13.62
$C_{13}$	5.956	6.60	6.278	6.278
$C_{16}$	0	0	6.862	6.862
$C_{22}$	13.94	41.38	20	20
$C_{23}$	6.60	5.956	6.278	6.278
$C_{26}$	0	0	6.862	6.862
$C_{33}$	13.94	13.94	13.94	13.94
$C_{36}$	0	0	-0.322	-0.322
$C_{44}$	2.258	3.192	2.725	2.725
$C_{45}$	0	0	0.467	- 0.467
$C_{55}$	3.192	2.258	2.725	2.725
$C_{66}$	3.192	3.192	10.85	10.85



### 5.6.2. Contact Modeling

Non-linear structural behavior is mainly sub-divided into three types: geometric, material, and changing status non-linearity. Analyses involving contact interactions represent an important class of changing status non-linear problems. In general, contact problems are divided into two categories: rigid-to-flexible contact and flexible-to-flexible contact. In rigid-to-flexible contact problems, one or more of the contacting surfaces are treated as rigid. For flexible-to-flexible contact, the interacting bodies are treated as deformable. This section describes the use of contact surfaces in ANSYS, specific to the case of the DS-4 joint configuration.

To prescribe a contact interaction between two bodies, one of the bodies is typically established as the "target" surface, and the other one is established as the "contact" surface. In ANSYS, the contact surface moves into the target surface. The target surface is typically assigned to entities with the higher elastic modulus. These two surfaces constitute a "contact pair." Contact surfaces are created using the CONTACT MANAGER tool, PICK TARGET, PICK CONTACT. The surfaces are picked as LINES, and FLEXIBLE type. Figure 5.64 shows the two contact pairs (dashed lines) used to model the interactions between the joint constituents. It is noted that the schematic shows an exploded view of the joint components prior to assembly. In the end, these contact surfaces will overlap geometrically. The first contact pair is created between the bottom surface of the steel doubler plate (target surface) and the top surface of the composite beam (contact surface). The second pair is created between the bottom surface of the composite beam (contact surface) and the top surface of the steel flange (target surface).

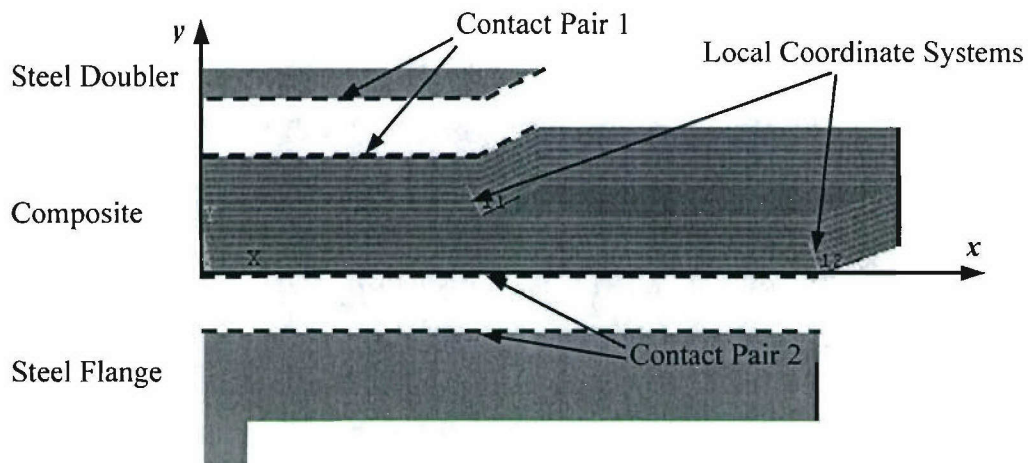


**Figure 5.64. Contact Surface Definitions for DS-4 Joint Model**

The contact elements are automatically assigned by ANSYS based on the type of element used. In this case, PLANE183 elements (2<sup>nd</sup> order) are used and contact elements are automatically created as having mid-side nodes. To define target contact surfaces, TARGET169 elements are used, which have mid-side nodes for compatibility with the element PLANE183. These elements overlay the solid elements (PLANE183) describing the boundary of the deformable body. CONTAC172 elements are used to represent contact and sliding between 2-D target surfaces and a deformable surface. This element is located on the surfaces of 2-D PLANE183 elements and also includes mid-side nodes for compatibility. It has the same geometric characteristics as the solid element face with which it is connected.

Because of the non-linear nature of contact modeling, loading of the structure is performed in steps. For most problems, at least two load steps are required. After the boundary conditions have been defined, the first load step is created in the ANSYS Main Menu, with the SOLUTION, DEFINE LOAD, LOAD STEP OPTIONS, WRITE LOAD STEP FILE command. The load step file number is assigned as "1." This initial step is a "neutral" step where the program identifies the surfaces that will come into contact. For the models presented in this section, the contacting surfaces are coincident (i.e., their edges occupy the same geometric space) and these are recognized as surfaces that will interact in subsequent steps. Once contact has been established, the second (or higher) steps are used to define structural loads. At this point, loads are applied to the structure, and a second step

(loading step) is created using the same commands, this time assigning the load step number as “2.” This may be repeated if further loading steps are necessary. To run the job, use the SOLUTION, SOLVE, FROM LS FILES and specify the starting load step as 1 and the ending load step as 2.

### 5.6.3. Modeling the Bolt

This section presents two approaches for modeling the bolt in conjunction with contact modeling. The first approach consists of coupling the nodal displacements of the different joint sections (doubler, composite and steel flange) along the bolt-line in the  $y$  direction, as shown in the schematic of Figure 5.65. This is done by using the COUPLE DOFs option and manually picking the nodes to constrain. Nodal constraints are also enforced in the  $x$  direction at the coincident nodes between the steel and composite interfaces, to prevent rigid body motion of the composite beam.

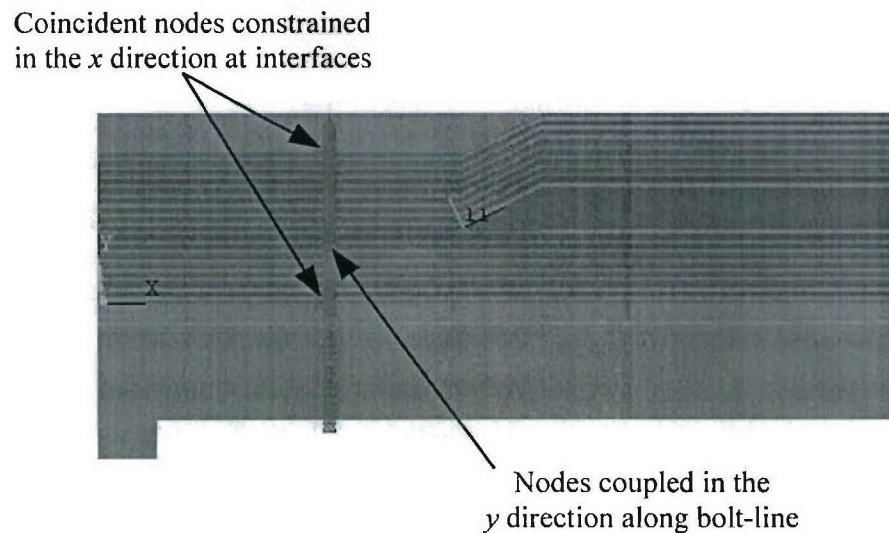


**Figure 5.65. Constrained Nodes along the Bolt-line**

The second approach consists of using a spring element to model the bolt stiffness. A schematic of this model is presented in Figure 5.66, where the spring element is depicted by a solid line attached to the upper node of the steel doubler and the lower node of the steel flange. The spring connects the top node of the steel doubler plate to the bottom node of the



steel flange. To do this, an additional line is created along the bolt-line and overlaid on top of the existing bolt-line. Element COMBI14 is used to define the spring and a real constant defines the spring stiffness,  $k$ . The spring element needs to be meshed separately, after the joint regions have been meshed and the contact surfaces defined. To create a single spring, assign the number of divisions to be 1.

For the DS-4 joint configuration, the stiffness of the linear spring can be calculated by smearing the axial stiffness of the three bolts across the width of the model. For a single bolt in axial loading, the bolt stiffness is computed as follows:

$$k_{bolt} = \frac{EA}{L_{bolt}} \quad (5.4)$$

For a grade 8, tapered-head bolt with a diameter of 12.7 mm, used in the joint specimens,  $E = 203$  GPa,  $L_{bolt} = 50.8$  mm, and  $A = 126.70$  mm<sup>2</sup>. From Eq. (5.4), the stiffness of a single bolt,  $k_{bolt}$ , is found to be 506.2 KN/mm. The smeared bolt stiffness across the width of the joint is computed using Eq. (5.5) for the joint test model, and Eq. (5.6) for the global model as follows:

$$k_{spring} = k_{bolt} \frac{n}{w} \quad (5.5)$$

$$k_{spring} = \frac{k_{bolt}}{s} \quad (5.6)$$

Where  $n = 3$ , is the number of bolts,  $w = 171.45$  mm, is the width of the joint test article and  $s$  is the bolt spacing in the global model. For the joint test model, Eq. (5.5) gives an estimate of the axial stiffness for the spring element,  $k_{spring} = 8.86$  KN/mm-mm. This value is used as input for the spring element property definition in the model. This is implemented using the real constants option in the ANSYS main menu in the spring stiffness box for the COMBI14 element.



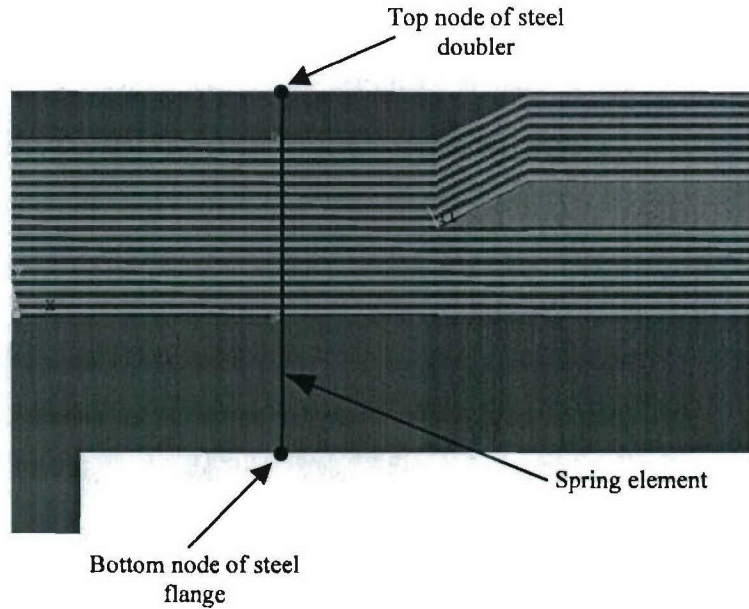


**Figure 5.66. Joint Model using a Spring Element**

#### **5.6.3.1. Effect of Spring Stiffness, $k_{spring}$**

A parametric study was conducted to study the sensitivity of the joint response to varying the spring stiffness, when loaded with a concentrated end force of 4.45 kN. Figure 5.67 presents the displacement at the free end of the composite versus the value of the smeared bolt stiffness,  $k_{spring}$ . The different stiffness between loading and unloading is depicted in the figure as the end displacements converge to different values depending upon the loading direction. For loading down, there is a sensitive response region between 0 and 2.5 kN/mm-mm; for loading up, the region extends to about 7.2 kN/mm<sup>2</sup>, after which the curves begin to plateau. The theoretical estimate for bolt stiffness of 8.86 kN/mm<sup>2</sup> lies within the flat region of the curves. This indicates that the bolt stiffness chosen for the joint lies in the region where the response is not sensitive to bolt stiffness. Figure 5.68 presents the displacement at the end of the joint region versus the bolt stiffness. For loading up, a sensitive region is observed between 0 and 3.0 kN/mm-mm; for loading down, this region extends to about 7.7 kN/mm-mm. Again, the theoretical estimate for the bolt stiffness estimate is found in the flat region of the curve. The estimate for the spring stiffness was again found to lie in the region where the response is not sensitive to this stiffness. A value of 8.86 kN/mm-mm was chosen as input to the FE model.

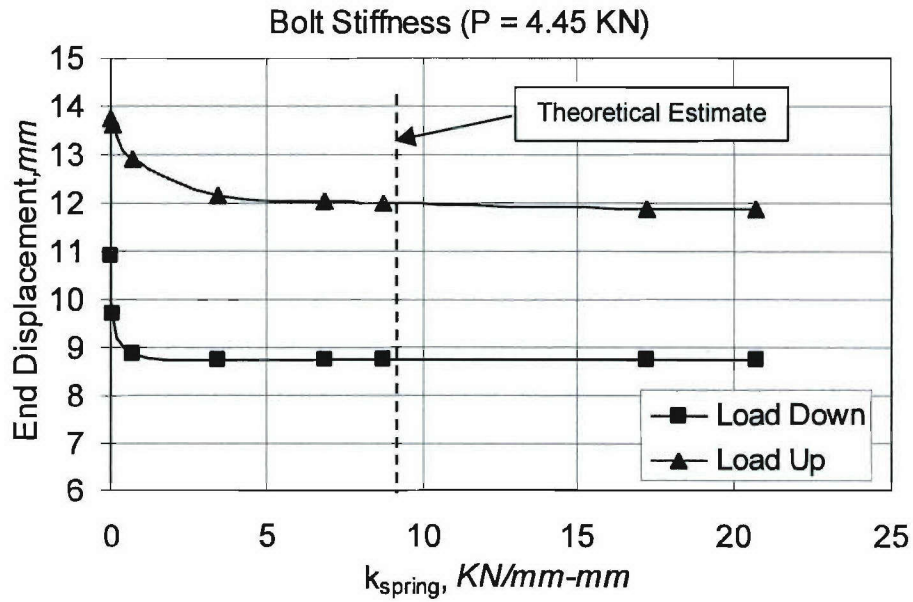


Figure 5.67. Effect of the Spring Stiffness on the End Displacement ( $x = 381 \text{ mm}$ )

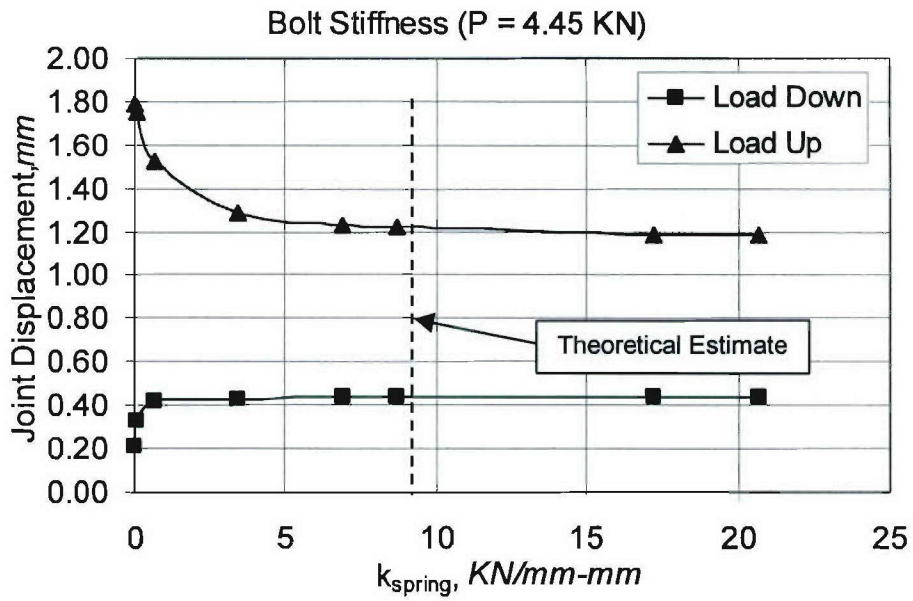


Figure 5.68. Effect of the Spring Stiffness on the Joint Displacement ( $x = 133 \text{ mm}$ )

#### 5.6.4. Model Verification

The plain strain model approach, using contact surfaces and a spring element to model the bolt, was verified for a net applied end load of 4.45 kN on a model representing the joint test specimen of 171.45 mm in width. The displacements are compared to the experimental results obtained for the DS-4 joint specimen. Figures 5.69 and 5.70 show the deflected shape of the joint loaded down and up, respectively. In a general sense, the ideal fully bonded model with no contact (designated No Contact) is the stiffest, due to the omission of the contact and the bolt, which does not allow opening of gaps at the interfaces. At  $x = 133$  mm, the three FE models are within 10 percent of the experimental displacement. The shapes begin to diverge at about  $x = 200$  mm. The model with nodal constraints along the bolt-line (designated Nodal Constraints) over predicts the displaced shape by about 20 percent at the free end of the beam. The model using a spring element (designated Spring) provides a good depiction of the deflected shape of the joint, with a difference of under 10 percent.

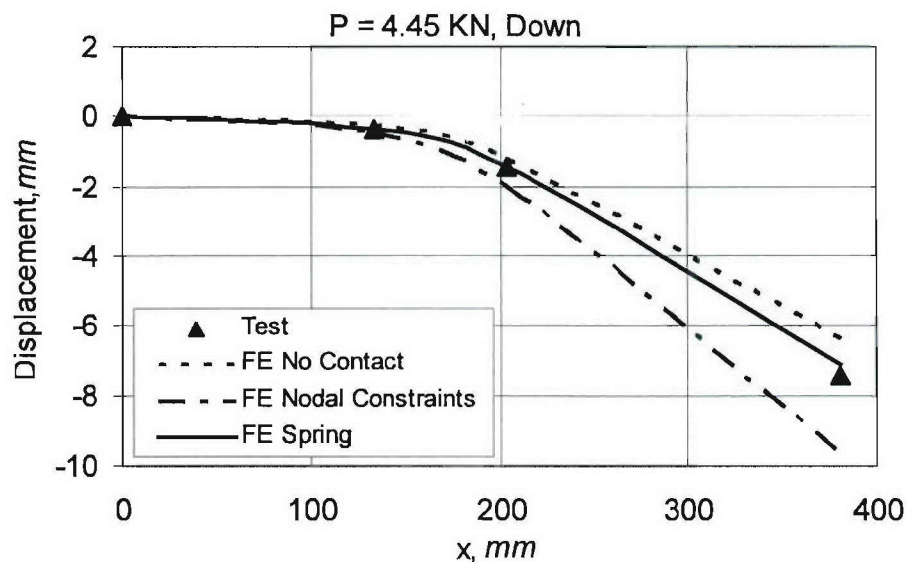
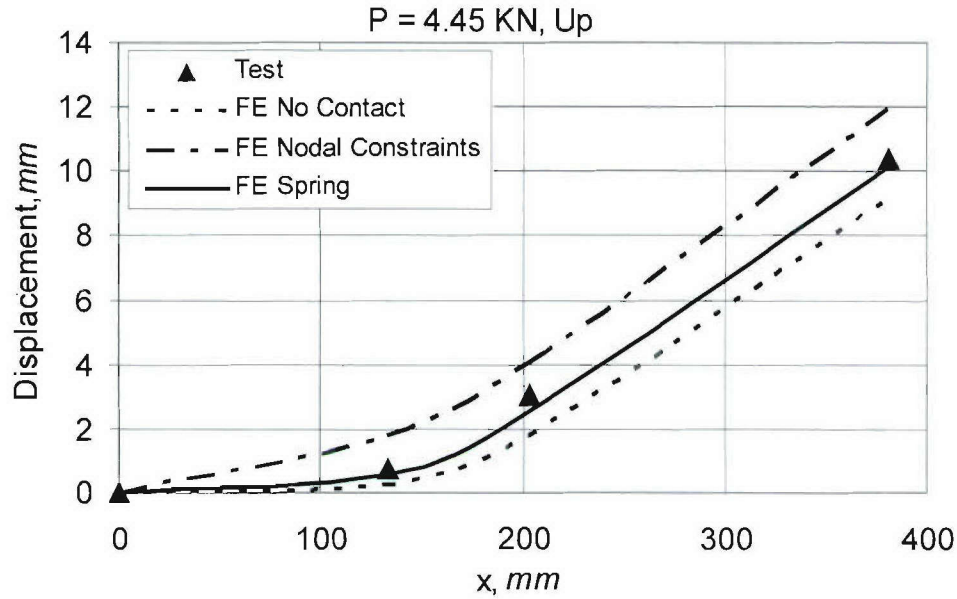


Figure 5.69. Deflected Shape of DS-4 Joint Models (4.45 kN, Down)



**Figure 5.70. Deflected Shape of DS-4 Joint Models (4.45 kN, Up)**

#### 5.6.5. Plane Strain Modeling Results Using Spring and Contact Elements

The results presented in this section correspond to the model using a spring element to account for the bolt. The structure is loaded again to 4.45 kN at the end of the beam. It is desired to study the contact pressure at the interfaces between the steel and composite components, the magnitude of the contact gap and the normal and shear stresses on the composite. The experiments showed that damage initiated at the top and bottom layers of the composite due to the bearing action of the steel doubler and flange on the composite beam. Hence, the stresses at these locations are of interest.

Figure 5.71 presents the displacement contour of the joint loaded downward. As expected, a gap opens up at the tapered interface between the steel doubler and the composite beam. Another gap is observed at the bottom left interface between the composite and the steel flange. This gap occurs due to the action of the spring and the symmetry boundary condition applied to the doubler plate, which allows movement of the composite beam in the  $y$  direction. Figure 5.72 shows the displacement contour of the joint loaded upward. In this case, the gap between the doubler and the composite at the tapered region is closed. A gap opens up at the steel flange and composite beam interface, after the bolt-line ( $x > 38$  mm). The larger displacement at the end of the beam is due to the lower bending resistance



provided by the steel doubler during upward loading, when compared to the steel flange during downward loading.

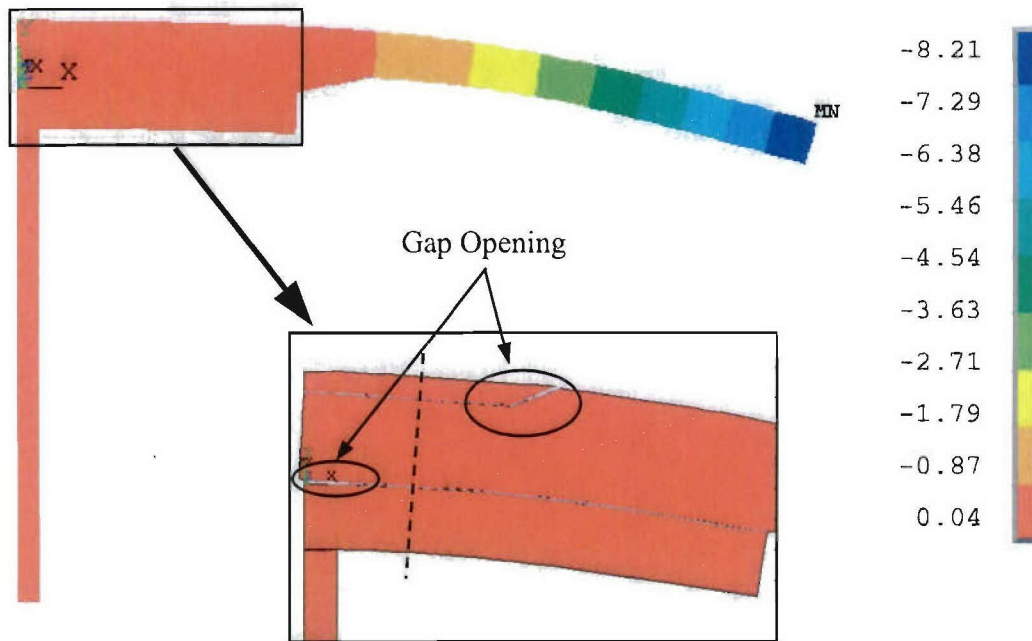


**Figure 5.71. Displacement Contour, Load Down ( $P = 4.45 \text{ kN}$ )**

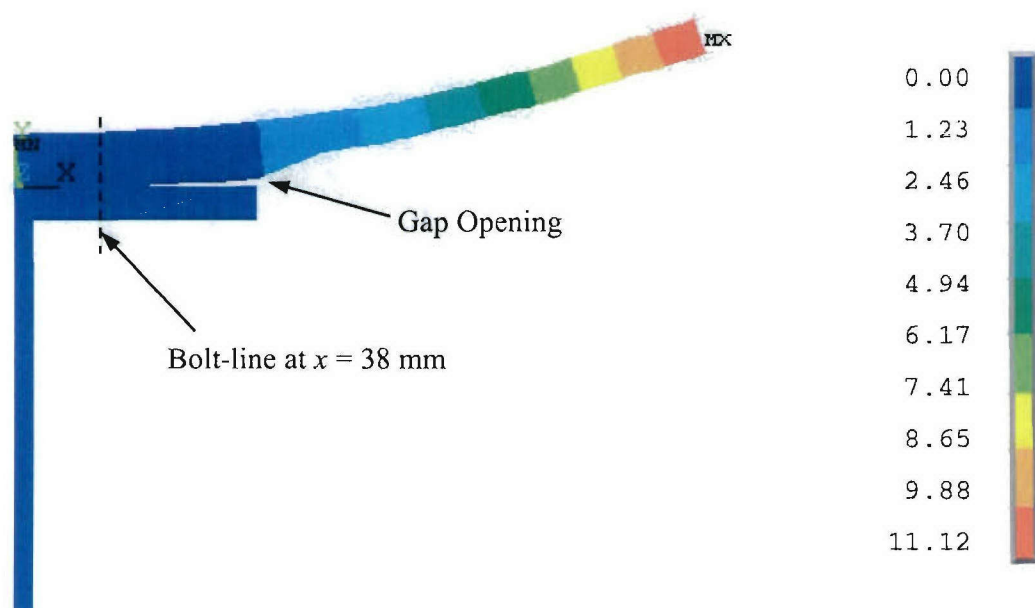


**Figure 5.72. Displacement Contour, Load Up ( $P = 4.45 \text{ kN}$ )**

Figure 5.73 shows the contact pressure distribution at the interface between the steel doubler plate and the top of the composite beam, when loaded downward. A peak pressure of about 4250 kPa occurs at  $x = 34$  mm, just before the bolt-line, and it decreases rapidly to zero, since the region of the composite located after the bolt-line does not interact with the doubler edge. For the case of loading up, shown in Figure 5.74, a contact pressure of about 7000 kPa is observed at  $x = 29$  mm, then a rapid drop to zero occurs, since the composite is bent upward. A peak pressure of 8900 kPa is observed at  $x = 61$  mm, which is a region of high stress concentrations where the edge of the steel doubler contacts the tapered region of the composite.

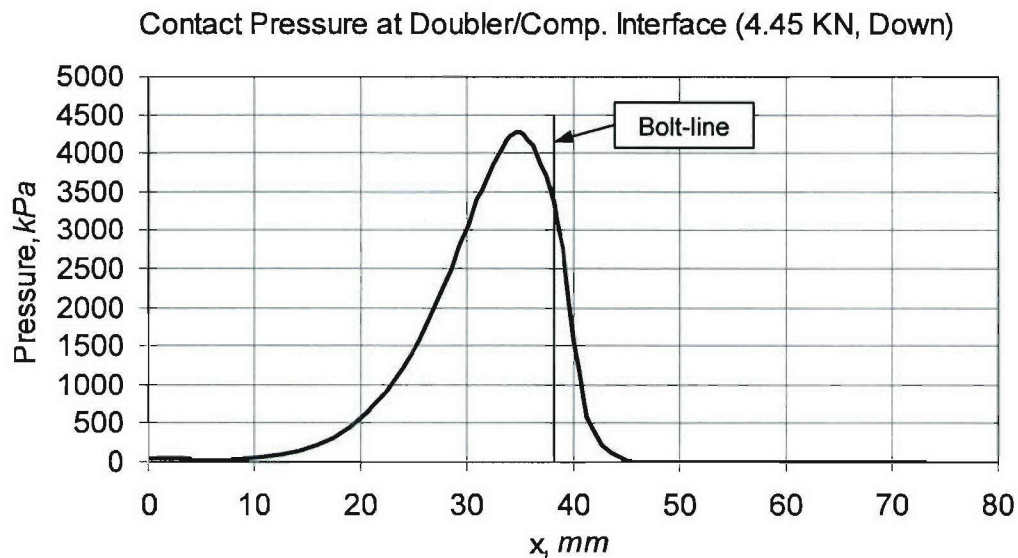


**Figure 5.73. Contact Pressure at the Doubler/Composite Interface, Load Down (4.45 kN)**

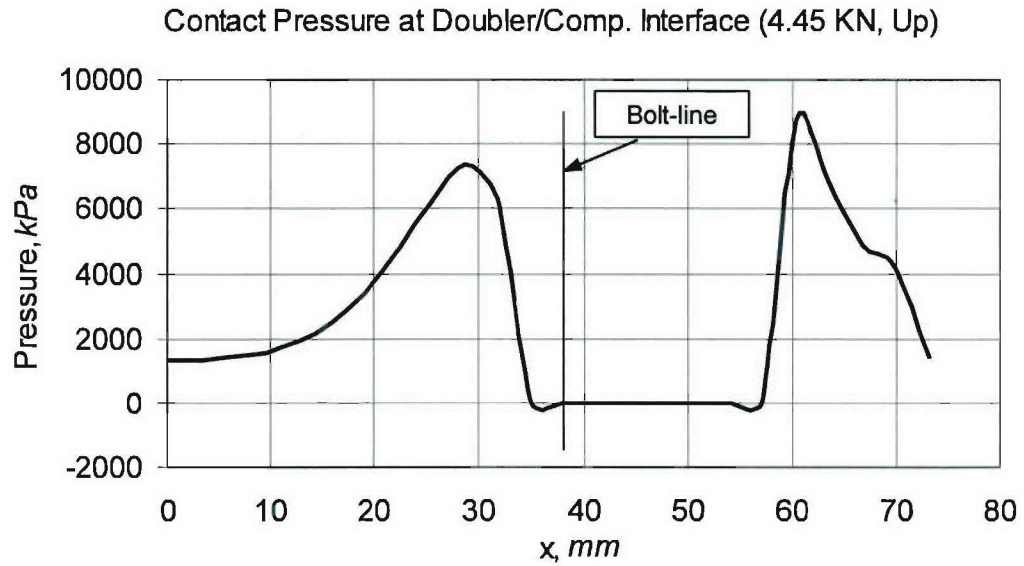


**Figure 5.74. Contact Pressure at the Doubler/Composite Interface, Load Up (4.45 kN)**

Figure 5.75 presents the contact pressure distribution at the interface between the steel flange and the bottom of the composite beam, when loaded downward. An initial pressure of about 200 kPa is observed from  $x = 0$  to 18 mm, after which the pressure dies down until it suddenly reaches a peak of 42000 kPa, which is due to the localized contact between the composite and the edge of the steel flange at 138 mm. Rounding the flange tip would help to mitigate this stress. For the case of loading up in Figure 5.76, a peak pressure of 9900 kPa occurs at  $x = 0$ , where the composite compresses against the steel flange as the joint is loaded. The pressure drops to zero just before the bolt-line ( $x = 27$  mm), due to opening of the gap at the interface.

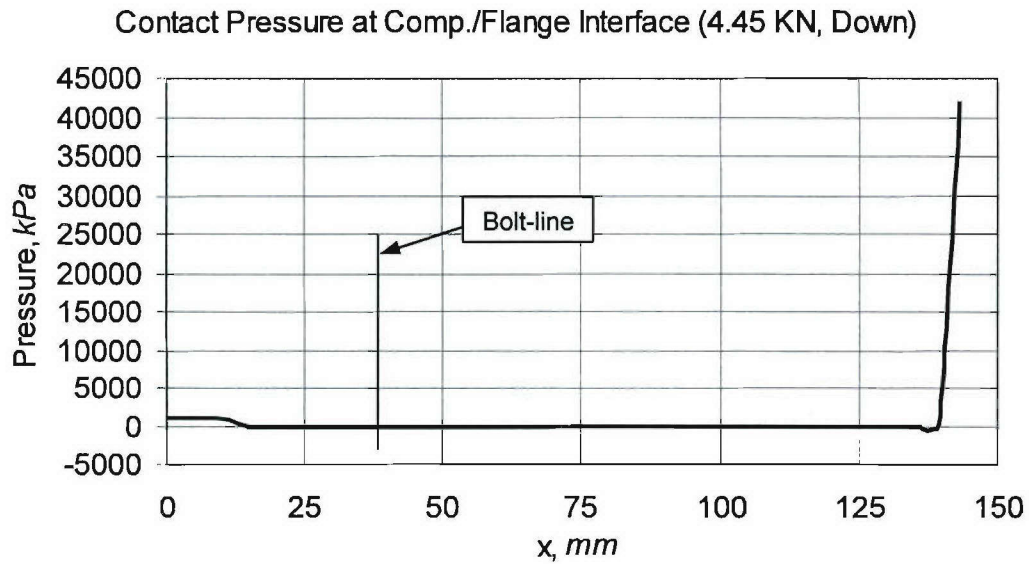


**Figure 5.75. Contact Pressure at the Composite/Flange Interface, Load Down (4.45 kN)**

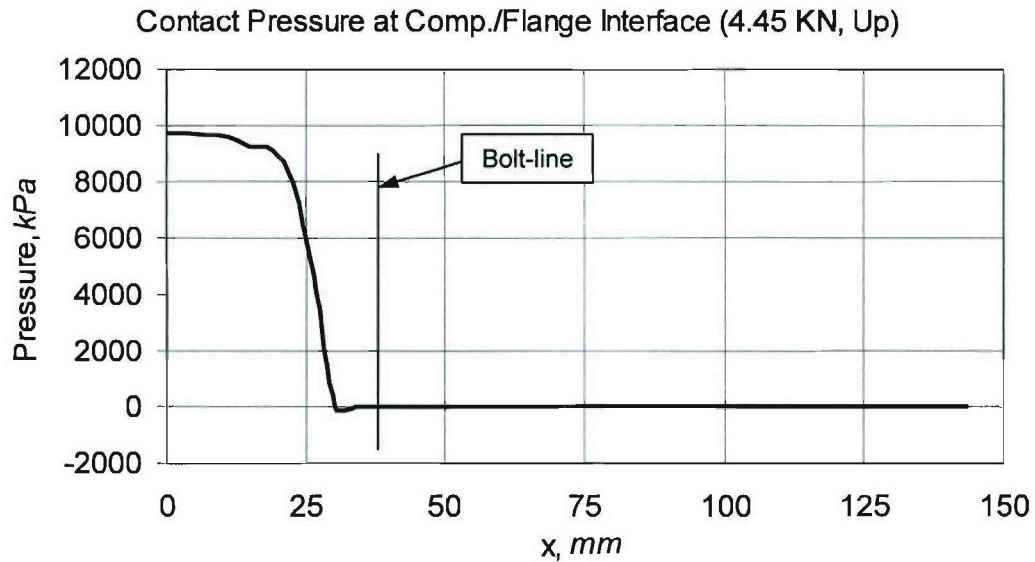


**Figure 5.76. Contact Pressure at the Composite/Flange Interface, Load Up (4.45 kN)**

Figure 5.77 shows the gap opening at the doubler and composite interface, for loading down. No gap is developed before the bolt-line. After the bolt, a gap begins to open as the



composite bends downward and it peaks at the end of the doubler ( $x = 67$  mm) to a value of 0.058 mm. When loaded upward, as shown in Figure 5.78, a gap of 0.052 mm opens up at  $x = 52$  mm. Figure 5.79 shows the gap at the composite and steel flange interface, when loaded downward. A gap begins to develop before the bolt-line to a peak of 0.040 mm at  $x = 100$  mm, due to local bending of the composite. At the edge of the steel flange ( $x = 133$  mm), the gap is closed, as expected for this loading condition. For the case of loading up in Figure 5.80, a gap begins to open up at the bolt-line ( $x = 38$  mm) and increases to a peak value of 1 mm at  $x = 133$  mm. These results show that the modeling approach is effective in modeling the contact interactions and the effect of the bolt for both loading conditions.

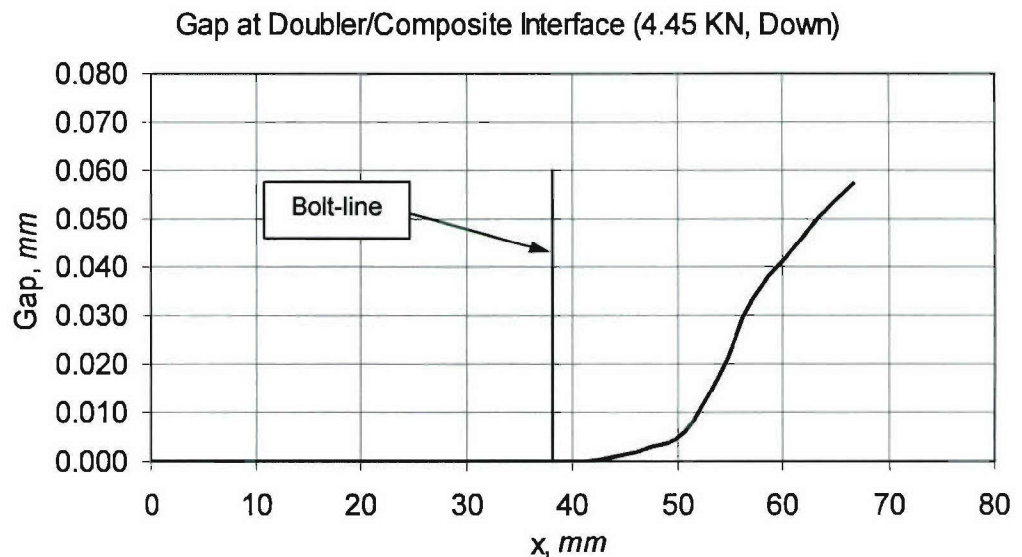


**Figure 5.77. Contact Gap at the Doubler/Composite Interface, Load Down (4.45 KN)**

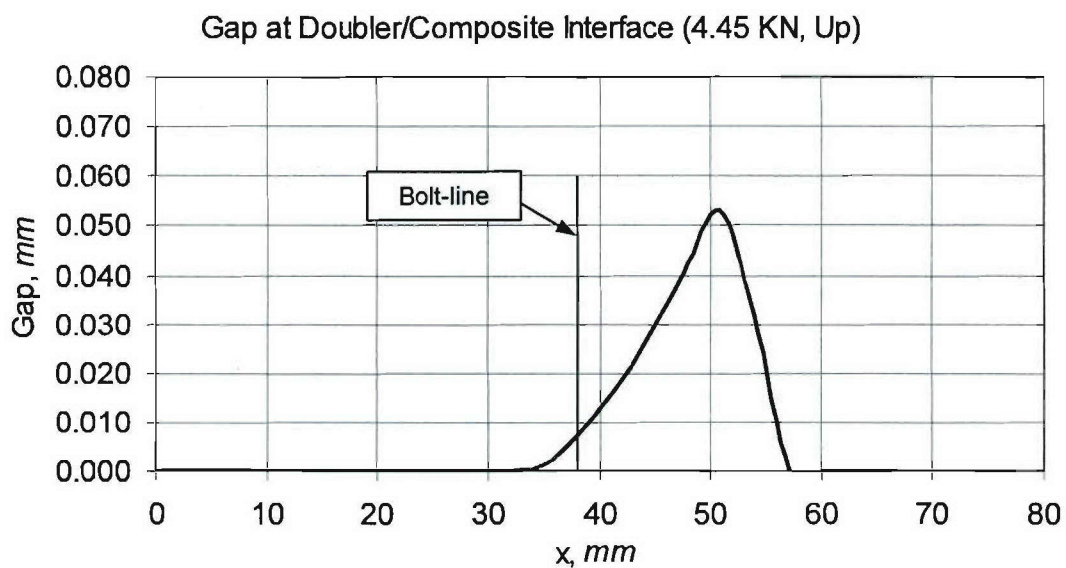


**Figure 5.78. Contact Gap at the Doubler/Composite Interface, Load Up (4.45 kN)**

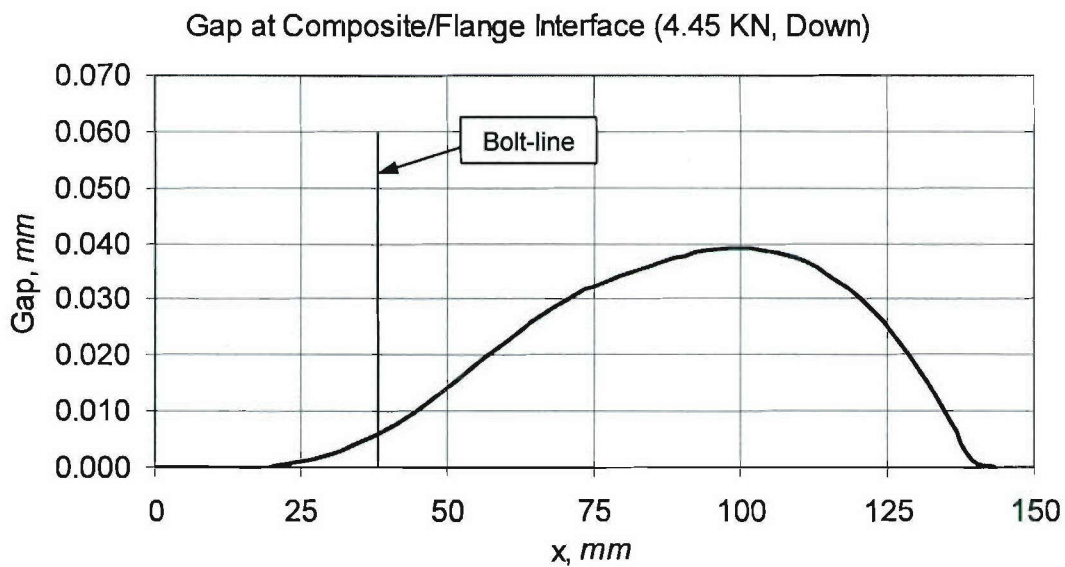


**Figure 5.79. Contact Gap at the Composite/Flange Interface, Load Down (4.45 kN)**

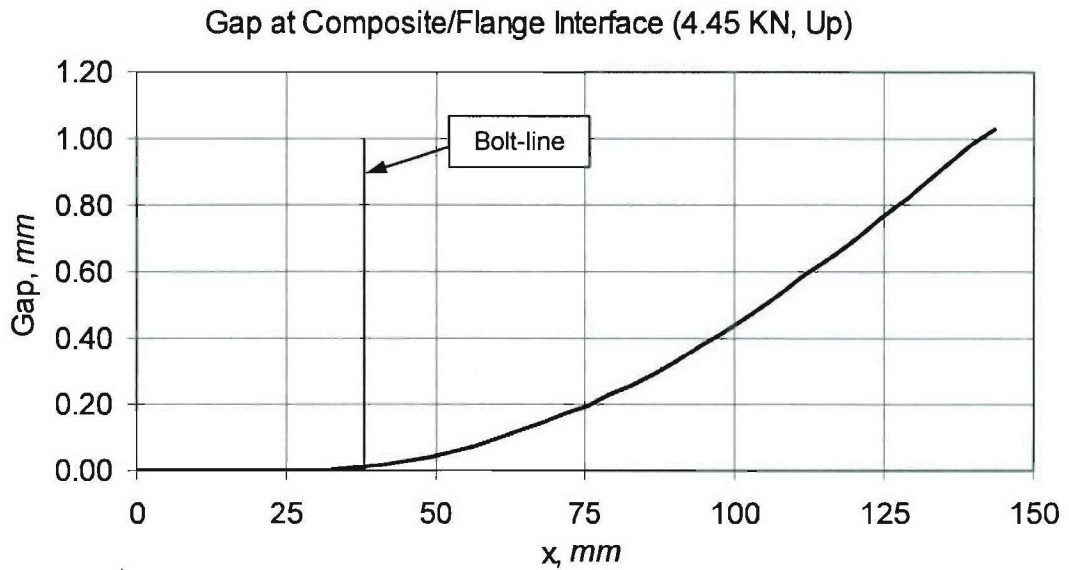


**Figure 5.80. Contact Gap at the Composite/Flange Interface, Load Up (4.45 KN)**

Figure 5.81 presents the normal stress contour for the case of downward loading. In a general sense, it is observed that the peak stresses (-134 MPa, 120 MPa) occur at the outer layers of the top and bottom surfaces of the composite, particularly at the tapered region of the composite beam. These stresses are higher than the strength, indicating that local damage will initiate at these locations prior to reaching this load level. A stress concentration is observed at the bottom left of the steel flange and at the nodes connecting the spring element to the doubler and steel flange. In the case of loading up in Figure 5.82, the peak stresses recorded (-264 MPa, 221 MPa) occur in the steel doubler plate, as a result of the compressive action of the composite beam. A peak tensile stress of 113 MPa is recorded at the end of the tapered region of the composite beam.

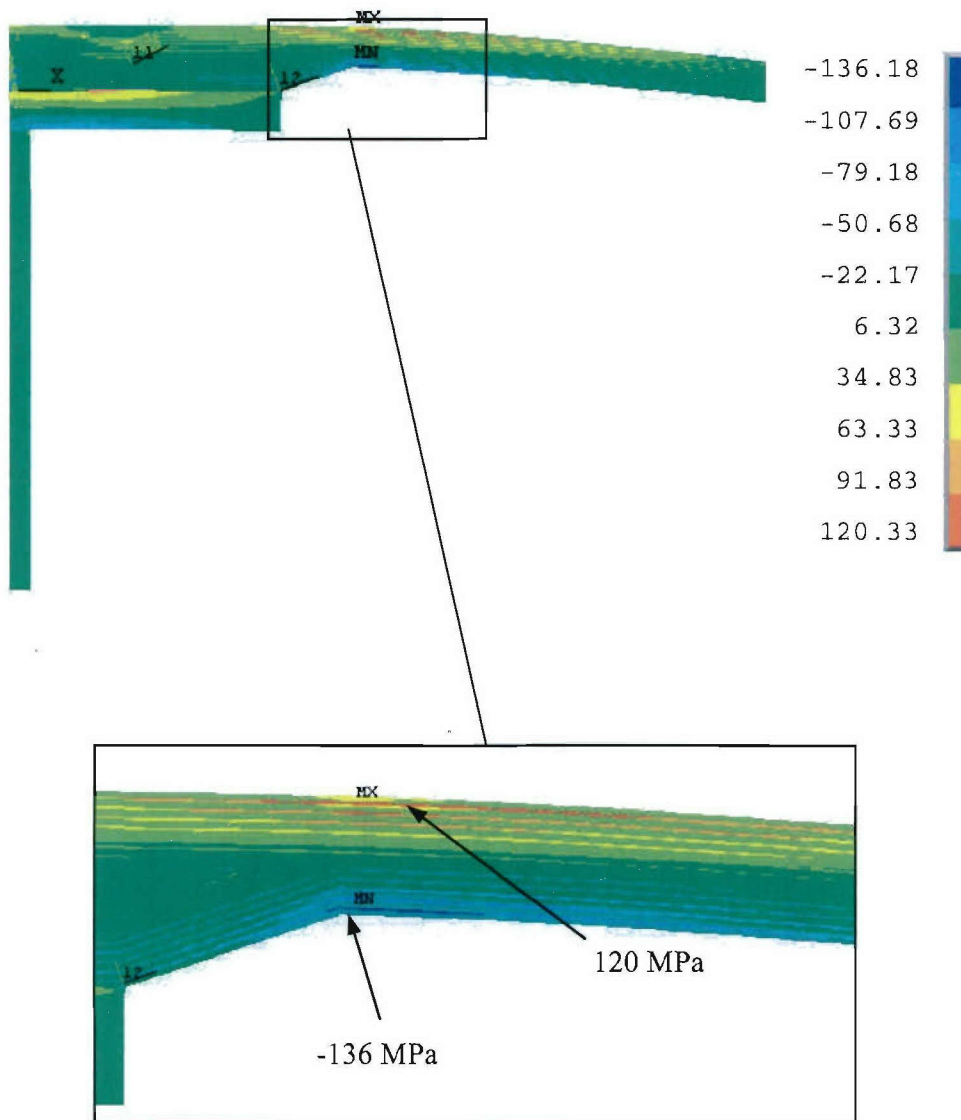


Figure 5.81. Normal Stress Contour,  $\sigma_{xx}$ , Load Down (4.45 kN)



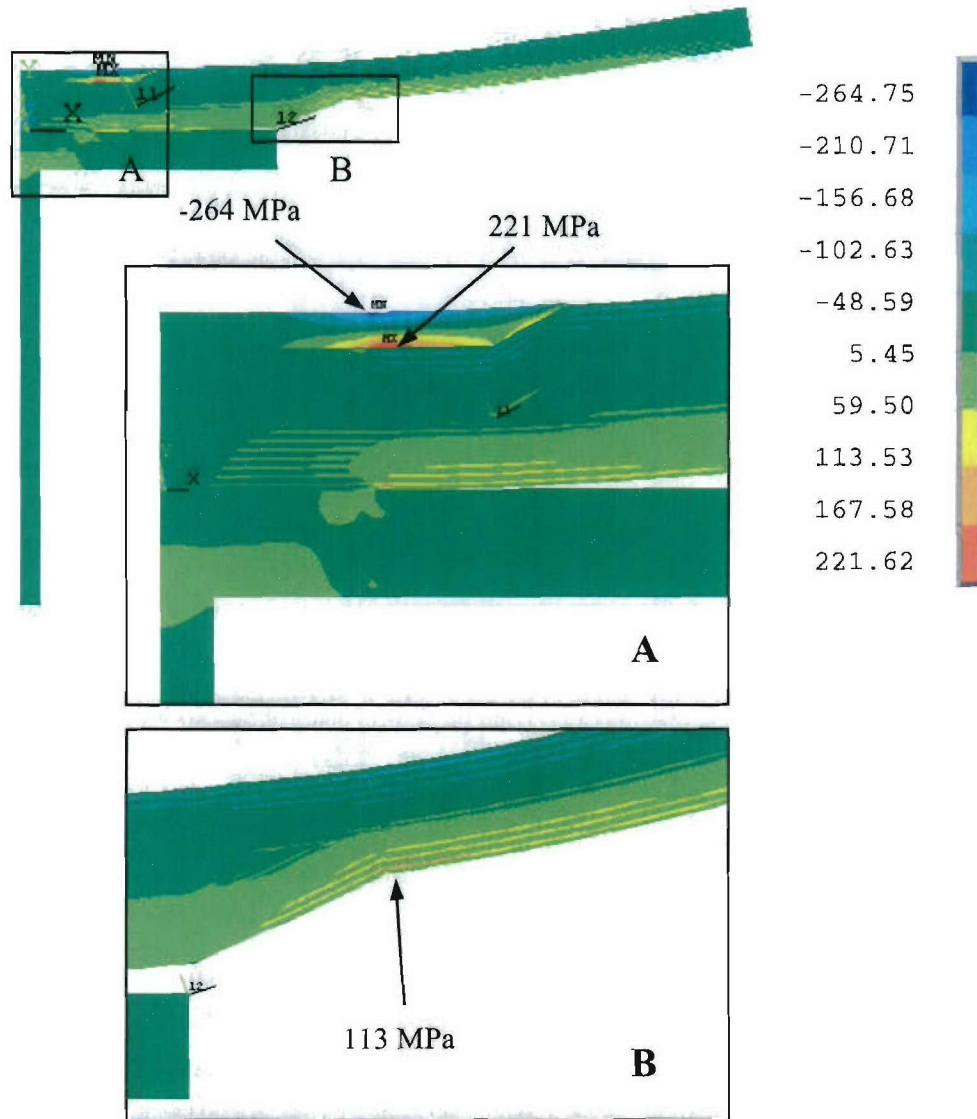


Figure 5.82. Normal Stress Contour,  $\sigma_{xx}$ , Load Up (4.45 KN)

Figure 5.83 presents the shear stress contour when the joint is loaded downward. A peak stress of 16 MPa is observed at the contact region between the lower edge of the doubler plate and the tapered section of the composite. At the bottom tapered section of the composite, a peak stress of -12 MPa is recorded. Figure 5.84 shows the shear stress contour when the joint is loaded upward. In this case, a peak stress of 54 MPa is observed at the lower edge of the steel doubler plate and a peak stress of -43 MPa is observed at the tapered composite region in contact with the doubler. At the lower tapered region of the composite, a stress of 38 MPa was calculated. The high shear stresses observed in the tapered regions of

the composite beam will lead to delamination and eventually failure along the interfaces between the composite and the foam. As observed in the experiments for joints with doubler plates and foam inserts, damage initiated at the tapered regions, due to the bearing action of the steel members, and then propagated to the foam insert and eventually caused final rupture.

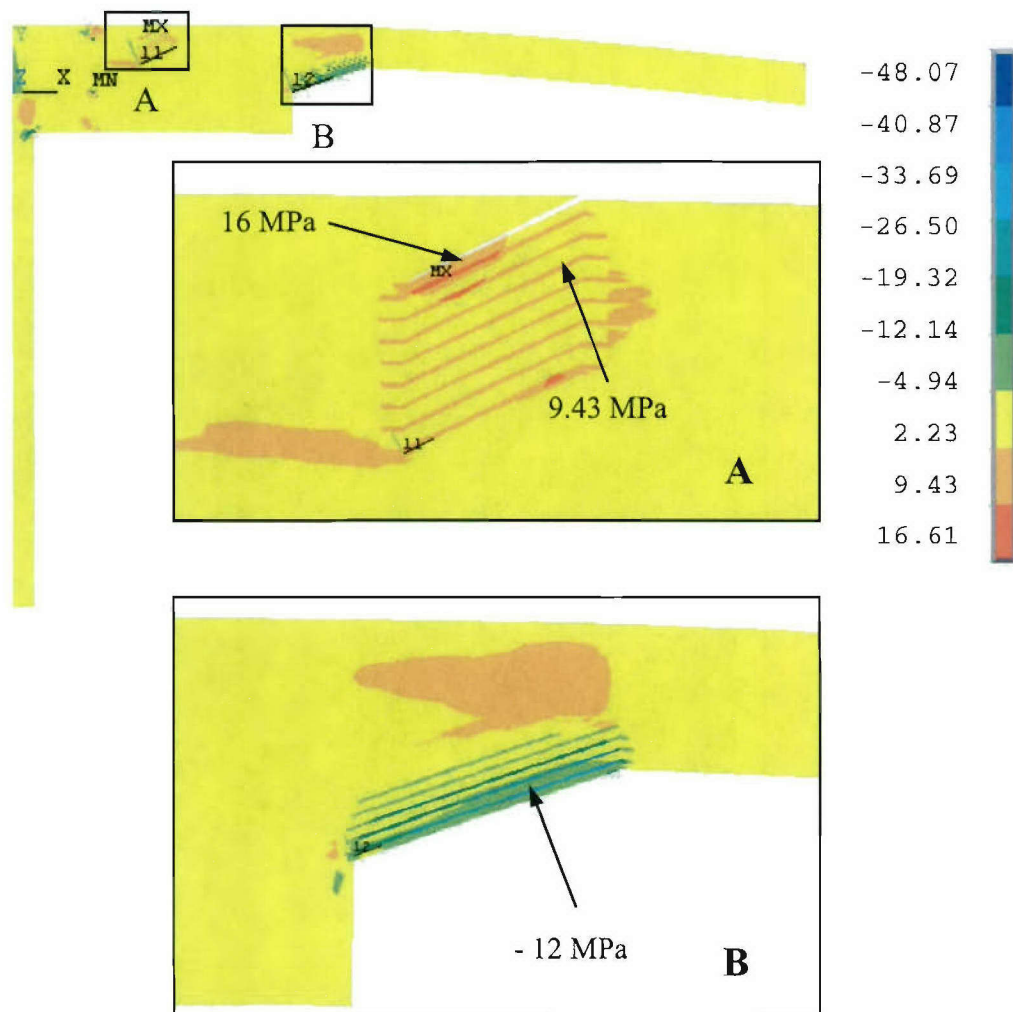


Figure 5.83. Shear Stress Contour,  $\tau_{xy}$ , Load Down (4.45 kN)

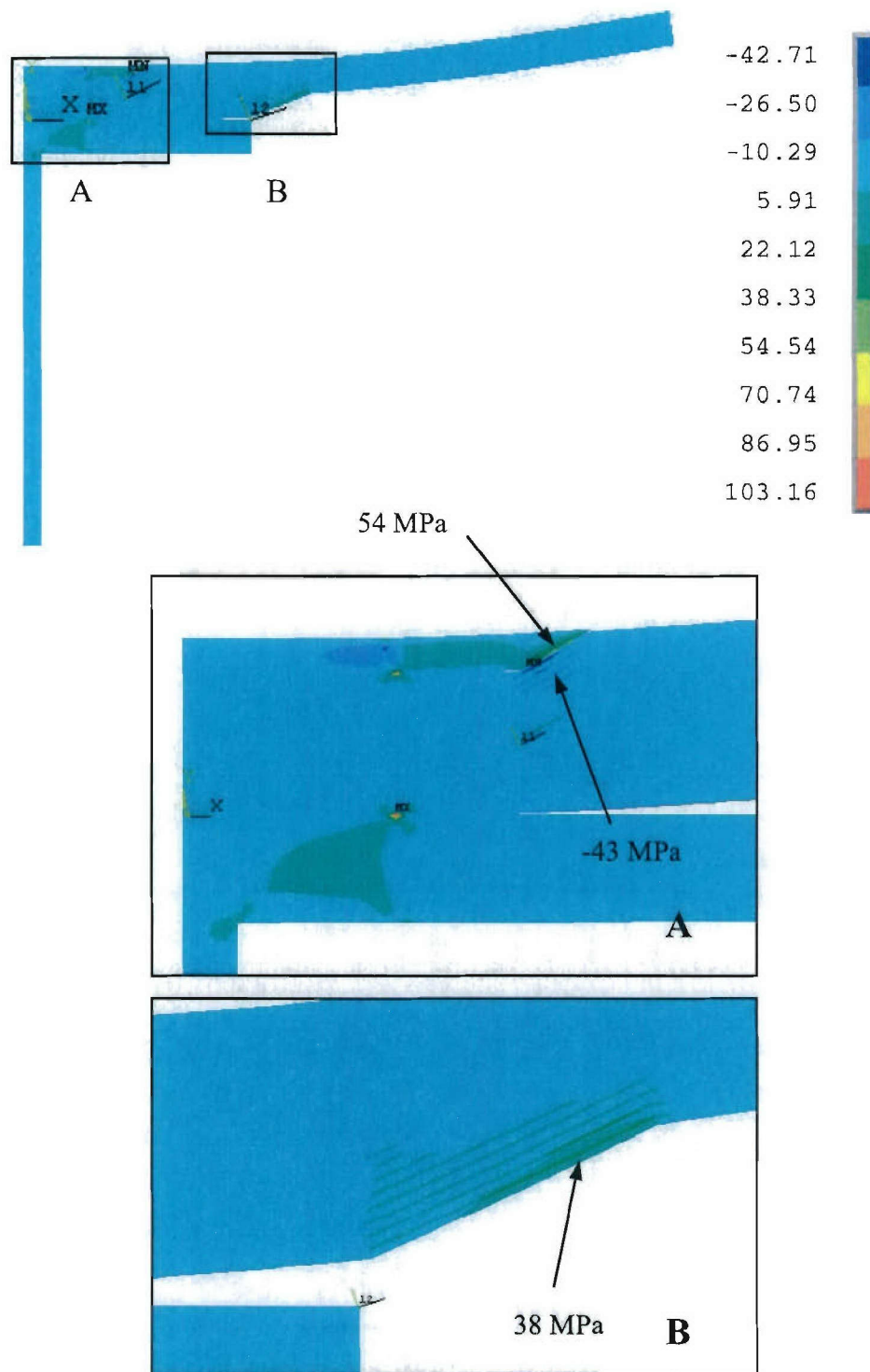


Figure 5.84. Shear Stress Contour,  $\tau_{xy}$ , Load Up (4.45 kN)

### 5.6.6. Strength Prediction

This section presents the complete load versus displacement response of the DS-4 joint and an estimate of failure initiation. The load-displacement response is shown for both loading directions. Initiation of failure is used as the strength estimate for this connection because after this load significant damage will begin to accumulate. Failure initiation is estimated by comparing the peak normal stresses obtained from the model with the strength values of each lamina as given in Table 5.7. In this analysis the joint is loaded in flexure, by applying a concentrated end load at  $x = 381$  mm, as shown in Figure 5.63. A load of 40 KN is applied in steps (increments) of 4.45 KN, for a total of 11 load steps (note that the initial step is for gap closure during initial contact, so a total of 10 steps are actually used for loading).

Figure 5.85 presents a comparison of the experimental and numerical load versus displacement envelopes for the DS-4 joint. For loading down, the response of the model closely follows the experimental results until a load of about 8 KN, after which a slight stiffness degradation is observed in the experimental data. It is theorized that this decrease is due to the cyclic loading that causes minor material damage. For loading up, the experimental and numerical results agree well up until a load value of about 8 KN. It is also noted that the response of the system is stiffer when loading down than when loading up. The discrepancies between the numerical and experimental results are attributed to the material model used for the composite layers and other differences between the model and the as-built geometry. The layers are modeled using orthotropic material property definitions, which do not account for stiffness degradation due to progressive failure that occurs in the actual joint specimen during testing.

Figure 5.86 presents a contour of the normal stresses ( $\sigma_{xx}$ ) at a downward load of 26 KN, which corresponds to load step 7. The contour shows that the peak stresses occur at the outer  $0^\circ$  layers (539 MPa - top, and -607 MPa - bottom). At this load, the stress at the lower  $0^\circ$  layer is about equal to the compressive strength of this layer in the longitudinal direction ( $S_{1+} = -607$  MPa), shown in Table 5.7, and failure of this layer is assumed to have occurred.



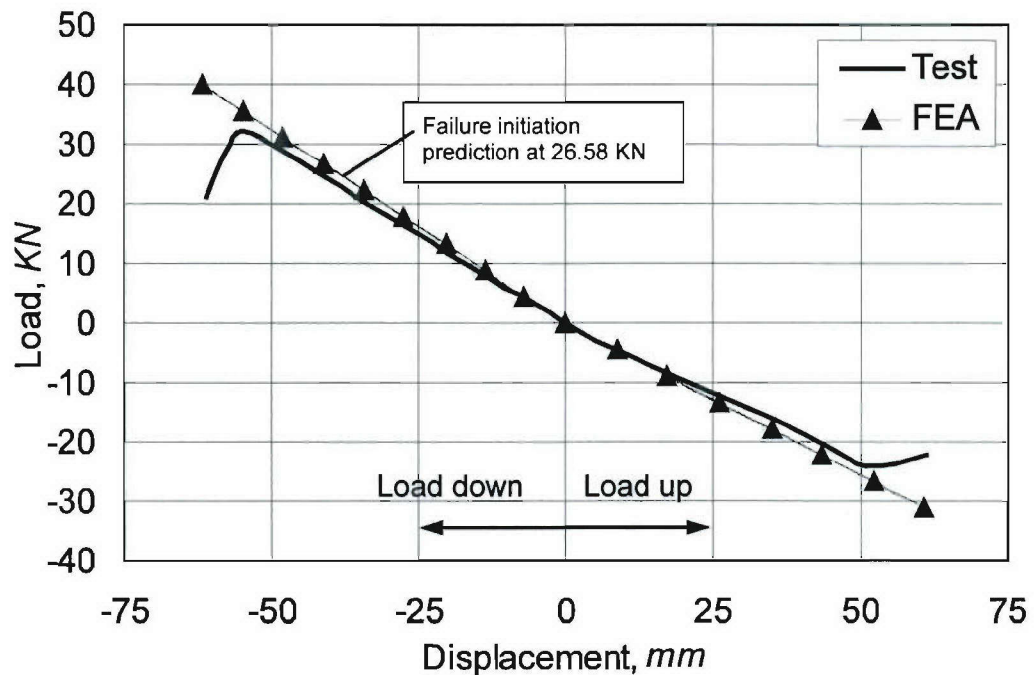


**Figure 5.85. Load versus Outer Displacement Envelope for DS-4 Joint**

The model presented in this section provides a good estimate of failure initiation, but does not account for progressive material non-linearity due to the decrease in stiffness with increasing load. In order to predict the strength of the joint, a progressive damage model is required, where the stiffness of the failed elements is reduced appropriately once the layers containing these elements reaches any of the failure criteria.

Figure 5.87 presents a contour plot of the through the thickness stress ( $S_{yy}$ ) at a load of 13 KN. The contour shows that some of the peak stresses occur at the edge of the steel flange, where it contacts with the composite beam. At this load level, a bearing stress of -77 MPa occurs, which is about equal to the strength of the matrix ( $S_m = 75.84$  MPa). It is hypothesized that these localized transverse stresses induce crushing of the matrix, which may lead to premature failure of the fibers in this region as the metal locally fails the matrix. Rounding the edge of the steel flange component may reduce this effect.

Figure 5.88 presents the load versus displacement curve of the joint during the eight set of cycles, for displacements recorded with the inner LVDTs (joint region). The first significant drop in load occurred when loading in the downward direction, where the peak load attained is about 23 KN. This drop in load may be attributed to fiber failure and is an indication of damage initiation. Loading up resulted in a similar phenomenon with a

predicted failure initiation load of 20 kN compared to the load observed in the experiment of 18.6 kN

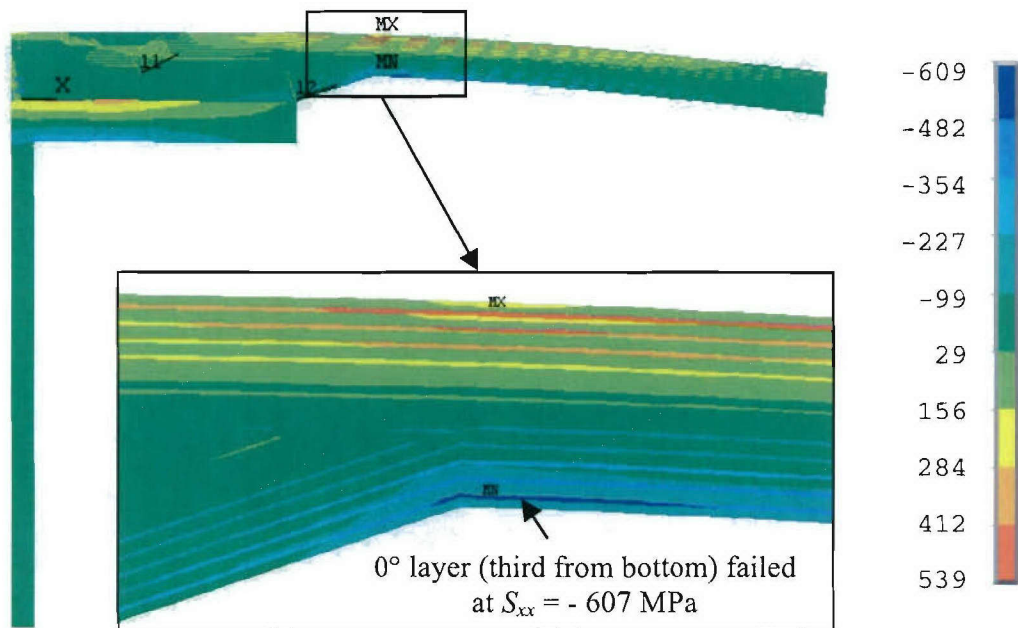


Figure 5.86. Stress Contour ( $S_{xx}$ ) at  $P = 26$  kN, Load Down, Showing First Ply Failure of a 0-deg Layer (in MPa)

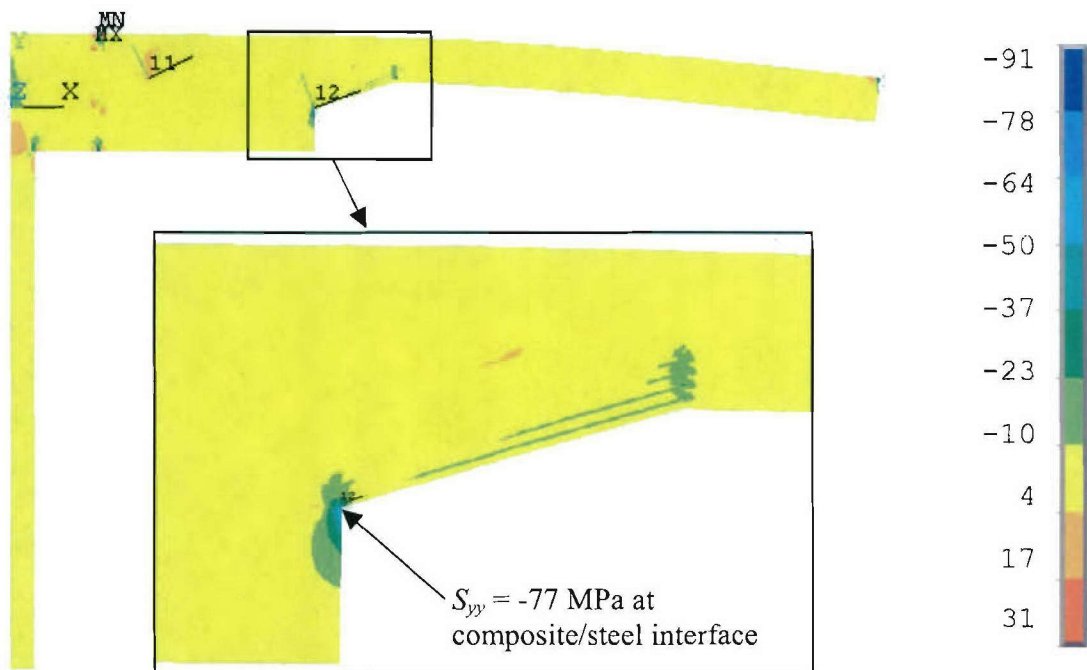
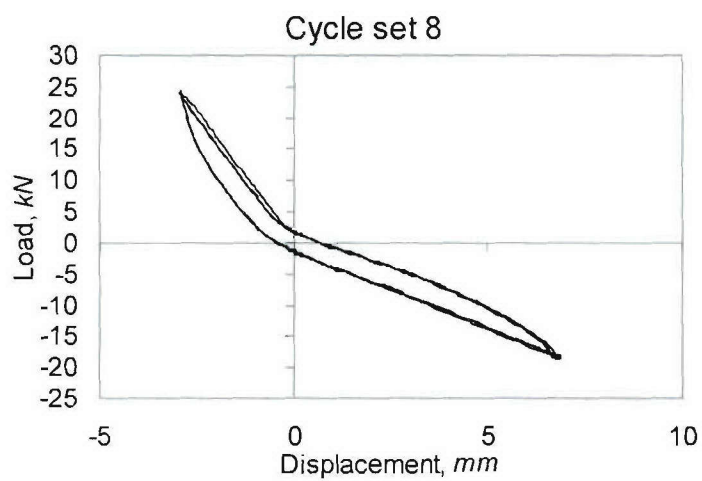
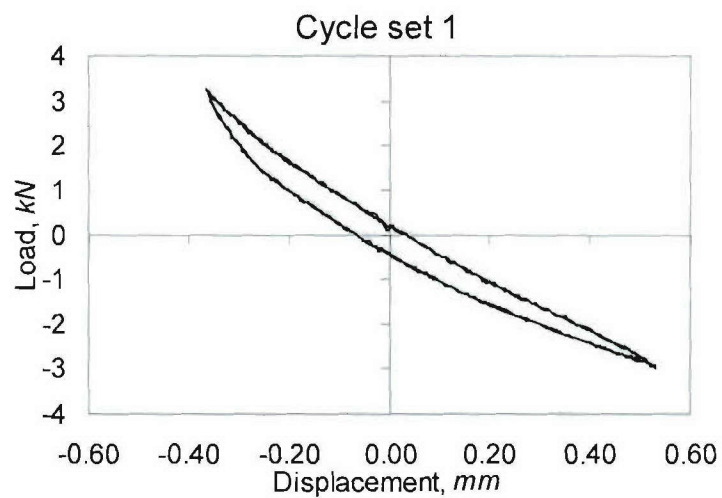


Figure 5.87. Stress Contour ( $S_{yy}$ ) at  $P = 13$  kN, Load Down, Showing Crushing of the Matrix by Steel Flange (in MPa)



**Figure 5.88. Experimental Load versus Displacement Curve of DS-4 Joint for Cycle Sets 1 and 8 (Inner LVDTs)**

## 6. CONCLUSIONS AND RECOMMENDATIONS

### 6.1. Sub-Component Joint Testing

An experimental investigation was conducted to assess the relative structural performance of hybrid composite/metal bolted connections subjected to flexural loading. Two types of hybrid connections were investigated as part of this study, namely, standard bolted joints and bolted joints with doubler plates. Overall, the goal was to develop a watertight hybrid connection to resist bending loads. This was accomplished by using tapered-head bolts in lieu of protruding-head bolts and by implementing a doubler plate, which prevents the joint from opening and decreases the bolt load loss due to creep by spreading the bolt preload over a wider area.

The response of fifteen different joint configurations was studied experimentally. Evaluation was based upon the relative performance of potential concepts with regards to joint capacity, rotational stiffness, failure mode sequence, and the ability to seal the joint for watertight integrity. This study has shown that, for resisting bending loads, joints with doubler plates can be made stronger and rotationally stiffer than standard bolted joints. For example, when compared to a bolted joint counterpart with two rows of the same diameter bolts (BT-2), a joint using a short doubler plate, a foam insert, and a single row of bolts (DS-4) was found to be at least 46 percent stronger and 29 percent stiffer when displaced downward, and 33 percent stronger and 34 percent stiffer when displaced upward. Doubler plates proved effective in mitigating opening of the joint, which will improve the ability to seal the joint and maintain watertight integrity. Hence, the additional expense and geometric complexity of using doubler plates and foam inserts may be justified for some underwater applications.

When comparing the performance of the joint configurations with doubler plates to each other, it was observed that a joint with a short doubler plate and one row of bolts (such as DS-4) can attain capacities comparable to those of joints with long doubler plates and 2 rows of bolts (such as DL-2 and DL-3). When compared to DS-4, the use of long doublers induced more catastrophic failure sequences, which ultimately led to complete separation of the composite beam from the joint region. Moreover, DS-4 requires roughly half of the material for fabrication of the doubler plates and half the number of bolts than those joints with medium and long doubler plates. This may be a



significant factor when considering installation and/or maintenance of large-scale structures that require multi-panel assemblies using bolted connections. In light of these observations, the short doubler and foam insert joint configuration (DS-4) was selected for implementation into hydrostatic testing of a hybrid, four-panel assembly.

It is recommended that future hybrid joint work focuses on: 1) repeat testing to study the variability in joint performance; 2) possible ways to fabricate joints with doubler plates and foam inserts more economically; 3) testing of joints subjected to in-plane tension and compression; 4) developing hybrid joints that may be welded as opposed to bolted; and 5) study of the fatigue resistance of the connections.

## **6.2. Panel Testing**

The main goal of testing a large-scale region of the hybrid lifting body was to assess the structural performance of the MACH concept, when applied to a modular, multi-panel assembly. A hydrostatic test system and test procedure were successfully developed and implemented for this study. The hybrid joint was assembled by attaching four E-glass/vinyl ester composite, hat-stiffened, panels to steel I-beam members, acting as bulkheads. The hat-stiffened panels were fabricated using a VARTM process. The panels were loaded to a target peak pressure of 248 kPa, which is approximately 3 times the design pressure. Loading was accomplished in a specially designed test tank, which applied water pressure to the wet side of the test article. Test results showed linear response of the system when loaded to the design pressure of 82.74 kPa. Non-linear behavior of the load-strain curves and the load-displacement curves began during the third loading set of cycles, with a peak pressure of 1.5 times the design pressure. Non-linearity of these curves indicated imminent damage, which occurred as delamination of the stiffeners on the larger panels at 1.4 times the design load. No damage was observed in the small panels. After significant failure of the stiffeners, the hybrid panel assembly withstood 3 times the design load without leakage. Hence, the response of the hybrid joint was deemed successful, as watertight integrity was achieved. Delamination of the stiffeners indicated that failure of the composite panels initiated at the stiffener/panel interface. This type of failure resulted from a combination of stiffener geometry and techniques for bonding of the stiffeners to the flat surface of the panels. Providing more shear resistance at the interface, by interleaving fabric or by improved adhesion, would

delay the initiation of this failure mode. Improvements of the manufacturing techniques should result in stronger panels.

It is recommended that future work focus on investigating the structural response of hybrid systems, which use other metal material types, such as aluminum and various joint geometries including weldable joints. It is also recommended to study the fatigue life of the hybrid assembly using various joint configurations. Finally, composite stiffener manufacturing techniques should be improved, while also conducting stiffener geometry optimization studies.

### **6.3. Finite Element Analysis of Hybrid Connections**

Global finite element analysis (FEA) was accomplished using shell element models. In so doing, a local model of the joint was used to develop a modeling methodology that was ultimately implemented on a global shell model of the 4-panel assembly. The local shell model divided the hybrid connection into five regions. Properties for each region were prescribed according to assumptions made. The predicted response was compared to experimental results for the DS-4 joint. Results show that the hybrid FEA model gives a good prediction of the connection response since the displacements were within 10% of the experimental values. Predictions of stress, strain and strength of the connection region were not accomplished with the shell model and require detailed local models. Shell finite element models of the global 4-panel assembly show good agreement with experiments with a difference in peak displacements of less than 10%. Parametric studies using the shell model show that the steel flange and doubler plate thickness have a significant impact on connection rigidity.

Detailed joint modeling was carried out using a plane strain finite element model. This model included contact between the composite and steel constituents, and a spring to represent the bolts. Different stiffness was demonstrated in pulling and pushing due to the variation in joint gap opening caused by the connection geometry. The detailed model gave a good prediction of the DS-4 joint response. Local contact pressures were shown to be high at the end of the flange, which is where failure initiated during the testing. Details to reduce this stress riser may improve the strength of the connection.

## REFERENCES

- Alm, F. (1983). GRP versus steel in ship construction. *Naval Forces*; 5; 82-86.
- ANSYS (2004). *Ansys reference manual*. Ansys Inc. Houston, PA.
- Arbur, D. R., Gerro, J. A., Dickson, J. (1995). D-box fixture for testing stiffened panels in compression and pressure. *Journal of Aircraft*; 32-6.
- ASTM Standard D6416-99. (2004). Standard test method for two-dimensional flexural properties of simply supported sandwich composite plates subjected to a distributed load. *Annual book of ASTM standards*.
- Barsoum, R.G. S. (2003). Best of both worlds: hybrid ship hulls use composites and steel. *AMPTIAC 2003*; 7-3: 52-61.
- Benchekchou, B., White, R. G. (1995a). Stresses around fasteners in composite structures in flexure and effects on fatigue damage initiation part 1: cheese-head bolts. *Composite Structures* 1995; 33; 95-108.
- Benchekchou, B., White, R. G. (1995b). Stresses around fasteners in composite structures in flexure and effects on fatigue damage initiation part 2: countersunk bolts. *Composite Structures* 1995; 33; 109-119.
- Berube, K.A. and Caccese, V. (1999). *Construction and Connection Concepts for a Modular Advanced Composite Hull-form*. Univ. of Maine Department of Mechanical Engineering, Report No. C-9914, December 1999, 33 pp.
- Black, S. (2003). Fighting ships augment combat readiness with advanced composites. *High Performance Composites* 2003; 30-33.
- Bonanni, D. L., Caiazzo, A., Flanagan, G. (2001). Design guide for joints in marine composite structures – part 1, concept development. Report No. NSWCCD-65-TR-2000/01. NSWC Carderock, January 2001.
- Boone, M.J., Caccese, V., Bragg, R., and Berube, K.A. (2003). *Mechanical Testing of Epoxy Adhesives for Naval Applications*. UM-MACH-RPT-01-03, April 2003.
- Boyd, S. W., Blake, J. I. R., Shenoi, R. A., Mawella, J. (2004a). Fatigue life and residual strength analysis of steel-composite joints. *Applied Mechanics and Materials*; 1-2; 81-86.
- Boyd, S. W., Blake, J. I. R., Shenoi, R. A., Kapadia, A. (2004b). Integrity of hybrid steel-to-composite joints for marine application. *J. Engrg for the Maritime Environment*, V218. PartM, 235-246.



- Camanho, P. P. and Matthews, F. L. (2000). Bonded metallic inserts for bolted joints in composite laminates. *Proc Instn Mech Engrs* February 2000, V214 N1, pp 33-40(8)
- Cao, J., Grenestedt, J. L. (2003). Test of a redesigned glass-fiber reinforced vinyl ester to steel joint for use between a naval GRP superstructure and a steel hull. *Composite Structures* 2003; 60-4; 439-445.
- Chalmers, D. W. (1994). The potential for the use of composite materials in marine structures. *Marine Structures* 1994; 2-5; 441-456.
- Chu, W., Wu, L., Kharbari, V. (2004). Durability evaluation of moderate temperature cured E-Glass/vinylester systems. *Composite Structures* 2004; 66; 367-376.
- Clifford, S. M., Manger, C. I. C., Clyne, T. W. (2002). Characterisation of a glass-fibre reinforced vinylester to steel joint for use between a naval GRP superstructure and a steel hull. *Composite Structures* 2002; 57; 59-66.
- Cohen, D., Hyer, M. W., Shuart, M. J., Griffin, O. H., Prasad, C., Yalamanchili, S. R. (1995). Failure criterion for thick multifastener graphite-epoxy composite joints. *American Society of Testing and Materials*.
- Collings, T. A. (1977). The strength of bolted joints in multi-directional cfrp laminates. *Composites* 1977; 43-55.
- Collings, T. A. (1982). On the bearing strength of CFRP laminates. *Composites* 1982; 13; 241-252.
- Cooper, C., Turvey, G. J. (1995). Effects of joint geometry and bolt torque on the structural performance of single bolt tension joints in pultruded GRP sheet material. *Composite Structures* 1995; 32; 217-226.
- Critchfield, M. O., Judy, T. D. (1994). Low-cost design and fabrication of composite ship structures. *Marine Structures* 1994; 2-5; 475-494.
- Dodkins, A. R., Shenoi, R. A., Hawkins, G. L. (1994). Design of joints and attachments in FRP ship structures. *Marine Structures* 1994; 7; 229-238.
- Gullberg, O., Olsson, K. A. (1990). Design and construction of GRP sandwich ship hulls. *Marine Structures* 1990; 3; 93-109.
- Grenestedt, J.L., and Suase, R. (2005). Vierendeel Steel Truss/Composite Skin Hull Test. ATLSS report No. 05-19. Lehigh University, Bethlehem, PA, August, 13 pp.
- Hart-Smith, L. (1978). Mechanically-fastened joints for advanced composites - phenomenological considerations and simple analyses. *Fourth Conference on Fibrous Composites in Structural Design* 1978; 14-17.



- Hart-Smith, L. (1991). An engineer's viewpoint on design and analysis of aircraft structural joints. International Conference on Aircraft Damage Assessment and Repair 1991;
- Herrington, P. D., Sabbaghian, M. (1993). Fatigue failure of bolted joints. Composite Materials 1993; 27; 491-512.
- Hyer, M.W., (1998). Stress analysis of fiber-reinforced composite materials. McGraw Hill, Boston, MA. 627 pp.
- Ireman, T., Ranvik, T., Eriksson, I. (2000). On damage development in mechanically fastened composite laminates. Composite Structures 2000: 49; 151-171.
- Kimpara, I. Use of advanced composite materials in marine vehicles. Marine Structures 1991; 4-2; 117-127.
- Light, K.H., and Caccese, V., (2005). Development of a Cavitation Erosion System Advanced Material System. Univ. of Maine Department of Mechanical Engineering, Report No. UM-MACH-RPT-01-05, 65 p.p. November 2005.
- Mewer, R., Vel, S.S., and Caccese, V., (2003). Detection of Bolt Stress Relaxation in Hybrid Bolted Connections for the MACH Program. University of Maine University of Maine Department of Mechanical Engineering. Report No. UM-MACH-RPT-01-07, April 2003, 78 p.p.
- Mouritz, A. P., Gellert, E., Burchill, P., Challis, K. (2001). Review of advanced composite structures for naval ships and submarines. Composite Structures 2001; 53; 21-41.
- Oh, J. H., Kim, Y. G., Lee, D. G. (1997). Optimum bolted joints for hybrid composite materials. Composite Structures 1997; 1-4; 329-331.
- Pei, J., Shenoi, R. A. (1996). An examination of key aspects defining performance characteristics of out-of-plane joints in FRP marine structures. Composites A 1996; 27; 89-103.
- Pelletier, K., Caccese, V., and Berube, K.A. (2005). Influence of Stress Relaxation in Hybrid Composite/Metal Bolted Connections. Project report for the MACH Project, University of Maine Department of Mechanical Engineering, Report No. UM-MACH-RPT-01-02, 87 p.p.
- Persson, E., Eriksson, I. (1999). Fatigue of multiple-row bolted joints in carbon/epoxy laminates: ranking of factors affecting strength and fatigue life. International Journal of Fatigue 1999; 21; 337-353.

Smith, P. A., Pascoe, J., Polak, C., Stroud, D.O. (1986). The behaviour of single-lap bolted joints in CFRP laminates. *Composite Structures* 1986; 1-3; 41-55.

Starikov, R., Schön, J. (2001). Quasi-static behaviour of composite joints with protruding-head bolts. *Composite Structures* 2001; 51; 411-425.

Starikov, R., Schön, J. (2002a). Experimental study on fatigue resistance on composite joints with protruding-head bolts. *Composite Structures* 2002; 55; 1-11.

Starikov, R., Schön, J. (2002b). Fatigue resistance on composite joints with countersunk composite and metal fasteners. *International Journal of Fatigue* 2002; 21; 39-47.

Thompson, L., Walls, J., and Caccese, V., (2005). Design and Analysis of a Hybrid Composite/Metal Structural System for Underwater Lifting Bodies. Project report for the MACH Project, University of Maine Department of Mechanical Engineering, Report No. UM-MACH-RPT-01-08, 95 p.p.

Vangrimde, B., Boukhili, R. (2003). Descriptive relationships between bearing response and macroscopic damage in GRP bolted joints. *Composite Part B: Engineering* 2003; 34; 593-605.

## Appendix A

### Material Specifications

#### A.1. DIAB Divinycell H80 Foam

Divinycell is a semi-rigid PVC foam used as a core material in conjunction with high-strength skins, to produce strong, stiff, lightweight composites structures. Divinycell H is our most commonly used core material. All Divinycell foam has a high strength-to-weight ratio, exceptional dynamic strength, excellent insulating properties, and a closed-cell structure that makes it impervious to water. Divinycell is widespread in the marine, transportation, and aerospace industries, and can be used in countless applications where strength, stiffness, and low weight are desired. This material is available in a range of densities, as standard sheets or fabricated to customer specifications.

Material Properties									
Quality		H 45	H 60*	H 80	H 100	H 130	H 160	H 200	H 250
Density	kg/m <sup>3</sup>	48	60	80	100	130	160	200	250
ASTM D 1622	lb/ft <sup>3</sup>	3.0	3.8	5.0	6.3	8.1	10.0	12.5	15.6
Compressive Strength	MPa (+22°C)	0.6	0.9	1.2	1.7	2.5	3.4	4.4	5.8
ASTM D 1621	psi (+72°F)	87	131	174	247	363	493	638	841
Compressive Modulus	MPa (+22°C)	40	70	85	125	175	230	310	400
ASTM D 1621 - B	psi (+72°F)	5800	10150	12325	18125	25375	33350	44950	58000
Tensile Strength	MPa (+22°C)	1.3	1.9	2.2	3.1	4.2	5.1	6.4	8.8
ASTM D 1623	psi (+72°F)	189	276	319	450	609	740	928	1276
Tensile Modulus	MPa (+22°C)	42	75	80	105	140	170	230	300
ASTM D 1623	psi (+72°F)	6090	10875	11600	15225	20300	24650	33350	43500
Shear Strength - ultimate	MPa (+22°C)	0.5	0.8	1.0	1.4	2.0	2.6	3.3	4.5
ASTM C 273 - 00	psi (+72°F)	73	116	145	203	290	377	479	653
Shear Strength - yield	MPa (+22°C)	0.485	0.68	0.95	1.33	1.8	2.42	**	**
ASTM C 273 - 00	psi (+72°F)	70	99	138	193	261	351	**	**
Shear Modulus	MPa (+22°C)	18	22	31	40	52	66	85	108
ASTM C 273	psi (+72°F)	2610	3190	4495	5800	7540	9570	12325	15660
Shear Strain	%	10	20	18	26	30	31	33	35

\* preliminary data for next generation Divinycell H

\*\* data not yet available

Continuous operating temperature range:	-200°C to +70°C (-325°F to 160°F)
Maximum processing temperature:	+80°C (+176°F)
Coefficient of linear expansion (ASTM D-698):	$3.5 \times 10^{-5} / ^\circ\text{C}$ ( $1.9 \times 10^{-5} / ^\circ\text{F}$ )
Poissons ratio:	0.32
Density Tolerance:	-10% / +15%

Divinycell H has a unique position in the international composite market as a core material in multifunctional sandwich constructions. The Divinycell H grade is used in a wide range of applications where there is a need for a strong, lightweight construction material with excellent mechanical characteristics. Applications include helicopter rotor blades, pleasure crafts, ship hulls and truck bodies. Divinycell H grade is available in a range of densities as standard sheets or fabricated to customer specifications.

Thermal Properties									
Quality		H 45	H 60	H 80	H 100	H 130	H 160	H 200	H 250
Density ASTM D 1622	kg/m <sup>3</sup>	48	60	80	100	130	160	200	250
	lb/ft <sup>3</sup>	3.0	3.8	5.0	6.3	8.1	10.0	12.5	15.6
Thermal Conductivity ASTM C 177 -10°C	W/m °C	0.023	0.024	0.028	0.028	0.032	0.035	0.040	0.046
	Btu in/ft <sup>2</sup> h °F	0.153	0.160	0.173	0.187	0.213	0.233	0.267	0.307
Thermal Conductivity ASTM C 177 +10°C	W/m °C	0.024	0.025	0.028	0.030	0.034	0.038	0.043	0.048
	Btu in/ft <sup>2</sup> h °F	0.160	0.167	0.187	0.200	0.227	0.253	0.287	0.320
Thermal Conductivity ASTM C 177 +37°C	W/m °C	0.026	0.027	0.030	0.032	0.036	0.040	0.046	0.052
	Btu in/ft <sup>2</sup> h °F	0.173	0.180	0.200	0.213	0.240	0.267	0.307	0.347
Water Absorption ASTM D 2842	kg/m <sup>2</sup>	0.100	0.072	0.046	0.040	0.030	0.024	0.020	0.018
	lb/ft <sup>2</sup>	0.021	0.015	0.009	0.008	0.006	0.005	0.004	0.004
Water Permeability ASTM E 96	m <sup>2</sup> /s x 10 <sup>-8</sup>	2.8	1.6	1.1	1.0	1.0	1.0	1.0	1.0
	ft <sup>2</sup> /s x 10 <sup>-8</sup>	0.26	0.15	0.10	0.09	0.09	0.09	0.09	0.09
Specific Heat ASTM E 1269	kJ/kg °C	1.90	1.80	1.75	1.70	1.65	1.60	1.55	1.50
	Btu/lb °F	0.454	0.423	0.418	0.406	0.394	0.382	0.370	0.358
R-Value Based on +10°C K factor	12.7 mm / 0.5 in	3.2	3.0	2.7	2.5	2.2	2.0	1.8	1.6
	25.4 mm / 1.0 in	6.3	6.0	5.3	5.0	4.4	4.0	3.5	3.1
	50.8 mm / 2.0 in	12.6	12.0	10.6	10.0	8.8	8.0	7.0	6.2

Continuous operating temperature range: -200°C to +70°C (-325°F to 160°F)  
Maximum processing temperature: +80°C (+176°F)  
Coefficient of linear expansion (ASTM D-698):  $3.5 \times 10^{-6}$  / °C ( $1.9 \times 10^{-6}$  / °F)  
Poissons ratio: 0.32  
Density Tolerance: -10% / +15%



## A.2. DERA KANE 8084 Vinyl Ester Resin

### High Elongation, Tough Epoxy Vinyl Ester Resin

DERAKANE® 8084 Epoxy Vinyl Ester Resin is an elastomer modified resin designed to offer increased adhesive strength, superior resistance to abrasion and severe mechanical stress, while giving greater toughness and elongation.

DERAKANE 8084 and DERA KANE 8090 Resins are the only epoxy vinyl esters available that offer this exceptional combination of properties.

### Typical Liquid Resin Properties

Property <sup>(1)</sup>	Value
Density, 25 °C / 77 °F	1.02 g/mL
Dynamic Viscosity, 25 °C / 77 °F	360 mPa·s
Kinematic Viscosity	350 cSt
Styrene Content	40%
Shelf Life <sup>(2)</sup> Dark, 25 °C / 77 °F	6 months

(1) Typical property values only, not to be construed as specifications.

(2) Unopened drum with no additives, promoters, accelerators, etc. added. Shelf life specified from date of manufacture.

### Applications and Fabrication Techniques

- DERA KANE® 8084 Resin is the resin of choice as a primer resin to prepare a substrate surface (steel or concrete) for application of a corrosion resistant lining.
- DERA KANE 8084 Resin can be use for RTM, hand-lay, spray-up, filament winding and other industrial FRP applications.
- For applications requiring even higher elasticity and impact resistance, DERA KANE 8090 Resin can be used.

### Benefits

- DERA KANE 8084 Resin has exhibited chemical resistance across a broad range of acids, bases and organic chemicals.
- Resin of choice as a primer to prepare a substrate surface for application of a corrosion resistant lining. It exhibits outstanding adhesive strength on different types of steel, aluminum and concrete.
- Superior elongation and toughness provides FRP equipment with better impact resistance and less cracking due to cyclic temperature, pressure fluctuations, and mechanical shocks providing a safety factor against damage during process upsets or during shipping and installation.
- Has exhibited superior property retention under dynamic fatigue conditions.
- Approved for use in the manufacture of ships under a DNV (Det Norske Veritas) certificate.

## Gel Time Formulations

### MEKP Gel Time Table

The following table provides typical gel times for MEKP. "Starting point" formulations for non-foaming MEKP alternatives and BPO peroxides are available in separate product bulletins. These and other information are available at [www.derakane.com](http://www.derakane.com).

### Typical Gel Times<sup>(3)</sup> Using Norox MEKP-925H<sup>(4, 5)</sup> and Cobalt Naphthenate-6%<sup>(6)</sup>

Temperature	15 +/- 5 Minutes	30 +/- 10 Minutes	60 +/- 15 Minutes
18 °C / 65 °F	3.0 phr MEKP 0.6 phr CoNap6% 0.3 phr DMA	3.0 phr MEKP 0.4 phr CoNap6% 0.2 phr DMA	2.5 phr MEKP 0.4 phr CoNap6% 0.1 phr DMA
24 °C / 75 °F	2.0 phr MEKP 0.5 phr CoNap6% 0.3 phr DMA	2.0 phr MEKP 0.4 phr CoNap6% 0.2 phr DMA	1.5 phr MEKP 0.3 phr CoNap6% 0.05 phr DMA
30 °C / 85 °F	2.0 phr MEKP 0.3 phr CoNap6% 0.2 phr DMA	1.5 phr MEKP 0.3 phr CoNap6% 0.05 phr DMA	1.5 phr MEKP 0.3 phr CoNap6% 0.025 phr DMA

(3) Thoroughly test any other materials in your application before full-scale use. Gel times may vary due to the reactive nature of these products. Always test a small quantity before formulating large quantities.

(4) phr = parts per hundred resin

(5) Materials: Norox MEKP-925H Methylthylketone peroxide (MEKP) or equivalent low hydrogen peroxide content MEKP, Cobalt Naphthenate-6% (CoNap6%), Dimethylanthine (DMA), and 2,4-Pentanedione (2,4-P). Use of other MEKP or other additives may result in different gel time results.

(6) Use of cobalt octoate, especially in combination with 2,4-P, can result in 20 to 30 % slower gel times.

## Casting Properties

### Typical Properties<sup>(1)</sup> of Postcured<sup>(7)</sup> Resin Clear Casting

Property	SI	US Standard	Test Method
Tensile Strength	76 MPa	11,000 psi	ASTM D-638; ISO 527
Tensile Modulus	2.9 GPa	4.2 x10 <sup>5</sup> psi	ASTM D-638; ISO 527
Tensile Elongation, Yield	8 to 10%	8 to 10%	ASTM D-638; ISO 527
Flexural Strength	120 MPa	19,000 psi	ASTM D-790; ISO 178
Flexural Modulus	3.3 GPa	4.8 x10 <sup>5</sup> psi	ASTM D-790; ISO 178
Density	1.14 g/cm <sup>3</sup>		ASTM D-792; ISO 1183
Volume shrinkage	8.2%	8.2%	
Heat Distortion Temperature, HDT <sup>(8)</sup>	82°C	180°F	ASTM D-648 Method A; ISO 75
Glass Transition Temperature, Tg2	115°C	239°F	ASTM D-3419; ISO 11359-2
IZOD Impact (unnotched)	480 J/m	6.9 ft.lbf/inch	ASTM D-256
Barcol Hardness	30	30	ASTM D-2583; EN 99

## Laminate Properties

### Typical Properties<sup>(1)</sup> of Postcured<sup>(9)</sup> 6 mm (¼ in) Laminate<sup>(10)</sup>

Property	SI	US Standard	Test Method
Tensile Strength	200 MPa	29,000 psi	ASTM D-3039; ISO 527
Tensile Modulus	9.8 GPa	14.0 x10 <sup>5</sup> psi	ASTM D-3039; ISO 527
Flexural Strength	190 MPa	28,000 psi	ASTM D-790; ISO 178
Flexural Modulus	7.8 GPa	11.0 x10 <sup>5</sup> psi	ASTM D-790; ISO 178
Glass Content	40 %	40 %	ASTM D-2584; ISO 1172

(1) Typical property values only, not to be construed as specifications. SI values reported to two significant figures; US standard values based on conversion.

(7) Cure schedule: 24 hours at room temperature; 2 hours at 99 °C (210 °F)

(8) Maximum stress: 1.82 MPa (264 psi)

(9) Cure schedule: 24 hours at room temperature; 8 hours at 80 °C (175 °F)

(10) 6 mm (¼ in) Construction – V/M/M/V/M/M/V/M

V = Continuous veil glass; M = Chopped strand mat, 450 g/m<sup>2</sup> (1.5 oz/ft<sup>2</sup>);

W = Woven Roving, 800 g/m<sup>2</sup> (24 oz/yd<sup>2</sup>)

### A.3. Brunswick Technologies, Inc. E-Glass Fibers

## Standard Product Specification

**CM-2408 / Version1001**

(Biaxial with binderless mat)

Current Revision: I

Supersedes: H

	Nominal Weight		Tolerance	Composition
	oz/yd <sup>2</sup>	g/m <sup>2</sup>		
0° Warp	13.00	441	+/- 5%	40.5%
90° Straight Weft	12.08	410	+/- 5%	37.7%
Mat Chopped strand	6.75	229	+/- 5%	21.0%
Stitch Yarn	0.25	8	+/- 10%	0.8%
<b>Total</b>	<b>32.08</b>	<b>1,088</b>	<b>+/- 5%</b>	<b>100.0%</b>

#### Product Specifications:

0°	Continuous E-Glass
90°	Continuous E-Glass
Mat	Binderless chopped E-Glass 2" staple
Stitch Yarn	100d Polyester

#### Material Specifications:

Stitch length	6.35 spi	Dry fabric thickness	
Stitch pattern	BTI	Material width	50" (+/-1/4")
Stitch gage	7	Roll length	70 yd
		Roll weight	125 lb

Specific material input

#### Packaging Instructions:

Core used	Use standard .10" core, 50" long
Box / Plastic	Use standard 50" box.
Pallet	Package 8 boxes per 50" pallet

## Standard Product Specification

**XM-2408 / Version 1006**

Biaxial with bindered mat

Current Revision:	E
Supersedes:	D

	Nominal Weight		Tolerance	Composition
	oz/yd <sup>2</sup>	g/m <sup>2</sup>		
<b>+45° Bias</b>	12.00	407	+/- 5%	36.8%
<b>-45° Bias</b>	12.00	407	+/- 5%	36.8%
<b>Bindered Mat Chopped strand</b>	8.10	275	+/- 10%	24.0%
<b>Stitch Yarn</b>	0.39	13	+/- 10%	1.2%
<b>Total</b>	<b>32.49</b>	<b>1,102</b>	<b>+/- 5%</b>	<b>100.0%</b>

### Product Specifications:

<b>+45°</b>	Continuous E-Glass
<b>-45°</b>	Continuous E-Glass
<b>Bindered Mat</b>	Bindered chopped strand E-Glass
<b>Stitch Yarn</b>	150d polyester

### Material Specifications:

<b>Stitches Per Inch</b>	5.00 +/- 1 stit	<b>Dry fabric thickness</b>	
<b>Stitch pattern</b>	Chain	<b>Material width</b>	50 " (+/- 1/4") Various
<b>Stitch gage</b>	3.5	<b>Roll length</b>	80 yd
		<b>Roll weight</b>	226 lb Pallet weight
<b>Specific material input</b>			2031

### Packaging Instructions:

<b>Core used</b>	Standard tube
<b>Box / Plastic</b>	Standard box
<b>Pallet</b>	Standard pallet



## Appendix B

### Instrumentation Specifications

#### B.1. Lebow 3174 Load Cells

#### **MODELS 3174, 3175 AND 3176**

Tension and compression 5,000 lbs. to 150,000 lbs.



#### **SENSOR CHARACTERISTICS: 3174, 3175 AND 3176**

MODEL NUMBER	NOMINAL LOAD LIMIT CAPACITY $F_L$		STATIC OVERLOAD CAPACITY % OF NOM. CAPACITY	FATIGUE CAPACITY % OF NOM. CAPACITY	STATIC EXTRAORDINARY LOAD LIMITS			DEFLECTION AT NOM. LOAD LIMIT INCHES	RINGING FREQUENCY $H_z$
	LBS.	NEWTONS			SHEAR $F_s$ OR $F_c$ LBS.	BENDING $M_x$ OR $M_y$ LB. INCHES	TORQUE $M_z$ LB. INCHES		
3174	5K	20K	150	100	11K	9K	12K	0.001	6,500
	10K	50K	150	100	25K	27K	24K	0.001	7,200
	20K	100K	150	100	55K	58K	35K	0.001	8,600
3175	50K	200K	150	100	32K	33K	67K	0.001	12,000
3176	100K	500K	150	100	78K	147K	196K	0.001	15,000

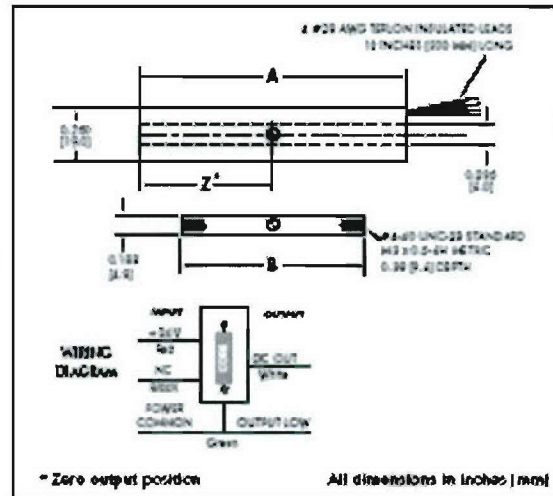
## B.2. Macrosensors Linear Variable Displacement Transducers

### General Specifications

Input Power:	24 V DC (nominal) 15-24 V DC $\pm 10\%$ , 30 mA (nominal)
Full Scale Output:	0 to 10 V DC
Output Noise & Ripple:	< 5 mV <sub>rms</sub>
Frequency Response (-3dB):	250 Hz (nominal)
Linearity Error:	$\leq \pm 0.25\%$ of FSO ( $\leq \pm 0.10\%$ of FSO optional)
Repeatability Error:	< 0.01% of FSO
Hysteresis Error:	< 0.01% of FSO
Operating Temperature:	0°F to +160°F (-20°C to +70°C)
Thermal Coefficient of Scale Factor:	-0.015%/°F (nominal) (-0.027%/°C nominal)
Vibration Tolerance:	20 g to 2 kHz
Shock Survival:	100 g, 11 ms

### Specifications

Model ▶ Parameter ▼	SE 750 -100	SE 750 -250	SE 750 -500	SE 750 -1000	SE 750 -2000	SE 750 -4000	SE 750 -6000	SE 750 -10000	SE 750 -20000
Nominal Range (inches)	0.100	0.250	0.500	1.00	2.00	4.00	6.00	10.00	20.00
Nominal Range (mm)	2.5	6.3	12.7	25.4	50.8	101.6	152.4	254	508
Scale Factor (V/inch)	100	40	20	10	5.0	2.5	1.65	1.0	0.5
Scale Factor (V/mm)	4.0	1.6	0.8	0.4	0.2	0.1	0.06	0.04	0.02
Dimension "A" (inches)	2.86	3.49	4.24	6.74	8.24	11.21	14.49	19.49	32.38
Dimension "A" (mm)	72.5	88.3	107.7	171.2	209.3	284.7	368.0	495.0	822.5
Dimension "B" (inches)	0.80	1.25	1.65	3.45	3.45	5.00	6.20	6.20	9.50
Dimension "B" (mm)	20.3	31.7	41.9	87.6	87.6	124.6	157.5	157.5	241.3
Dimension "Z" (inches)	0.58	1.00	1.10	2.07	2.33	3.07	3.45	3.95	5.42
Dimension "Z" (mm)	14.7	25.4	27.9	52.6	59.2	78.0	87.6	100.3	137.7
Weight - Body (ounces)	1.8	2.3	2.8	3.7	5.5	7.5	9.5	11.0	15.7
Weight - Body (g)	50	64	80	104	158	212	268	318	445
Weight - Core (ounces)	0.08	0.12	0.18	0.40	0.40	0.65	0.80	0.80	1.20
Weight - Core (g)	2.4	3.7	4.8	11.6	11.6	18.0	22.0	22.0	34.0



## Appendix C

### Load versus Outer Displacement Plots of Hybrid Joints

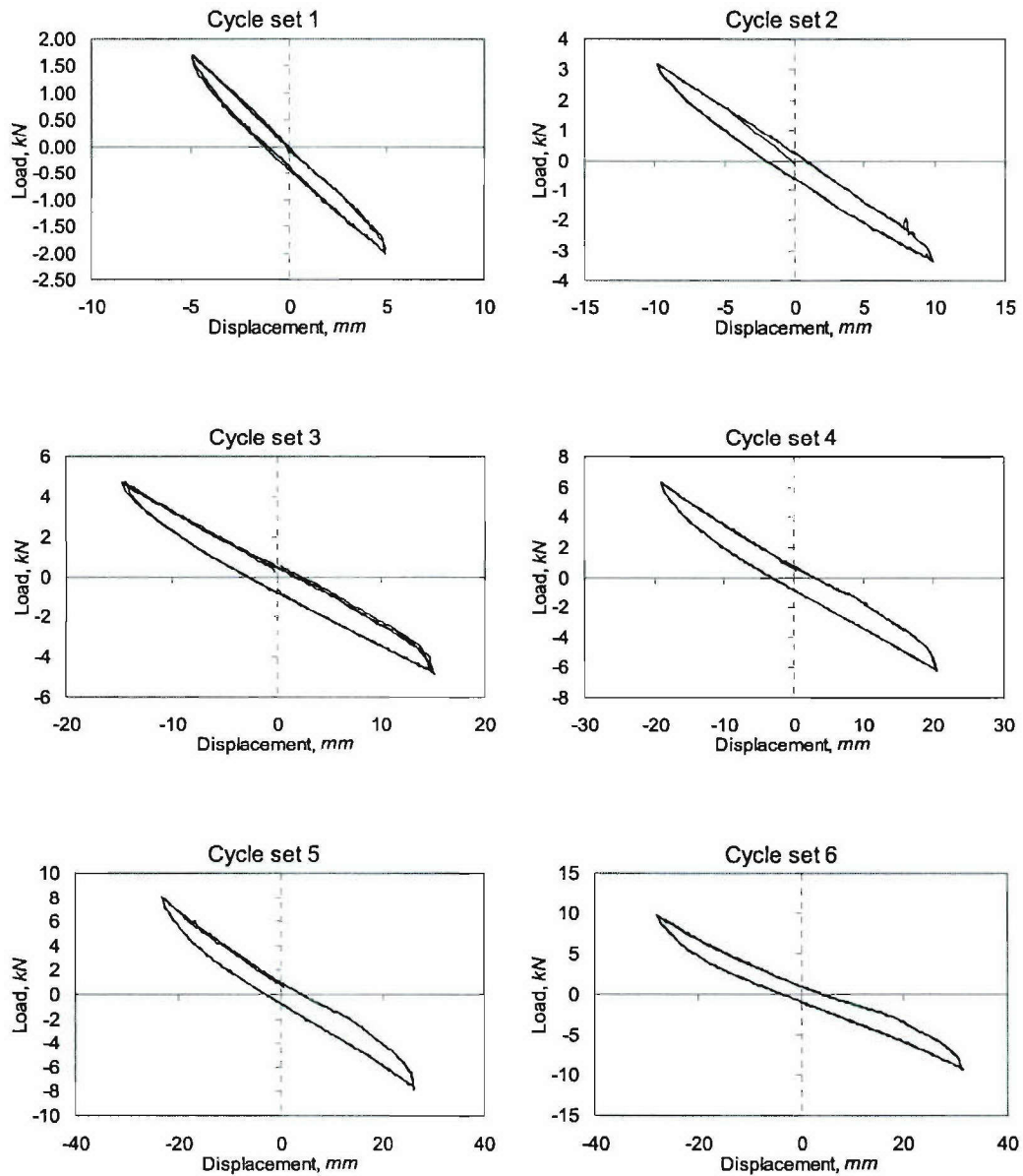
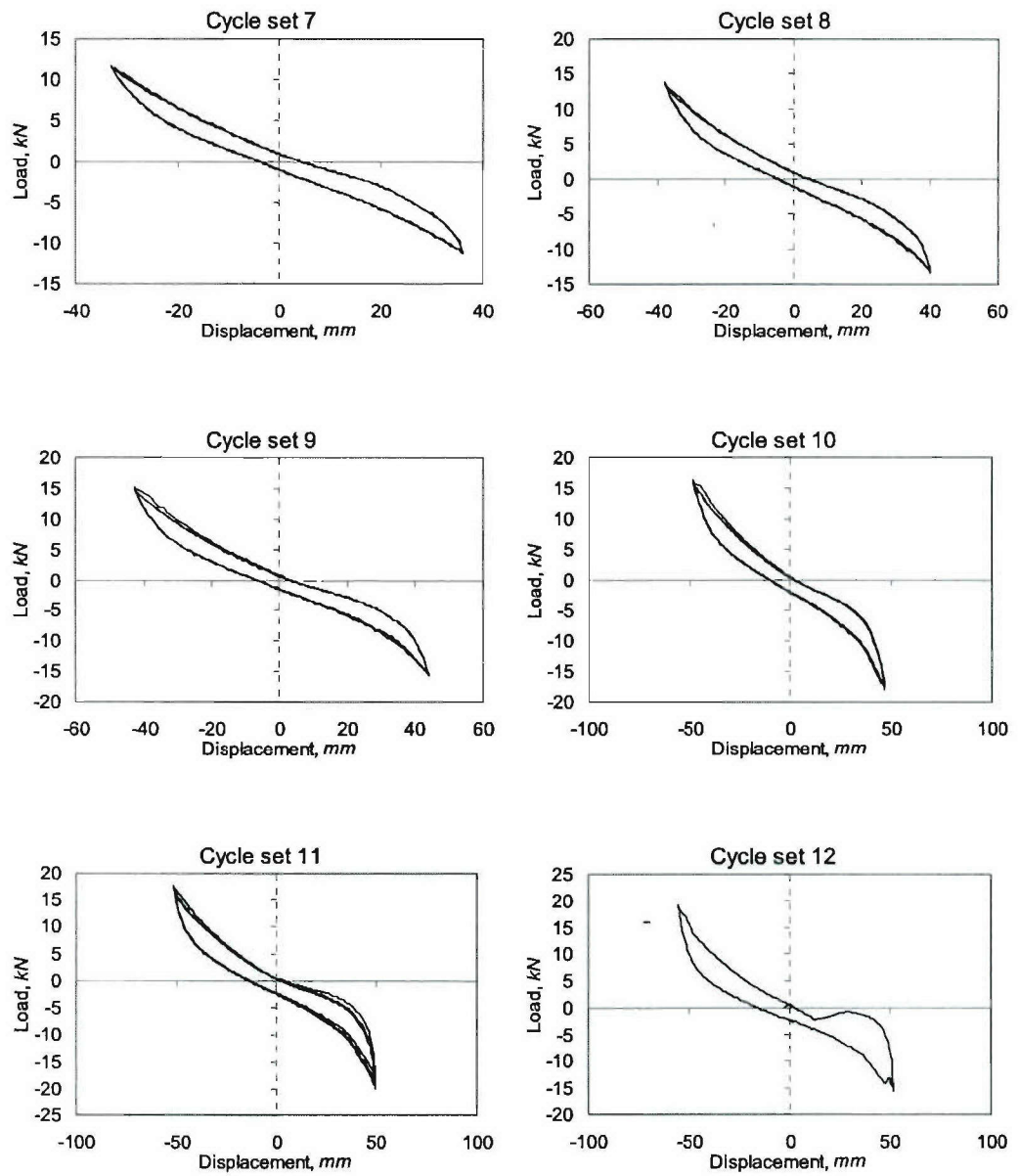
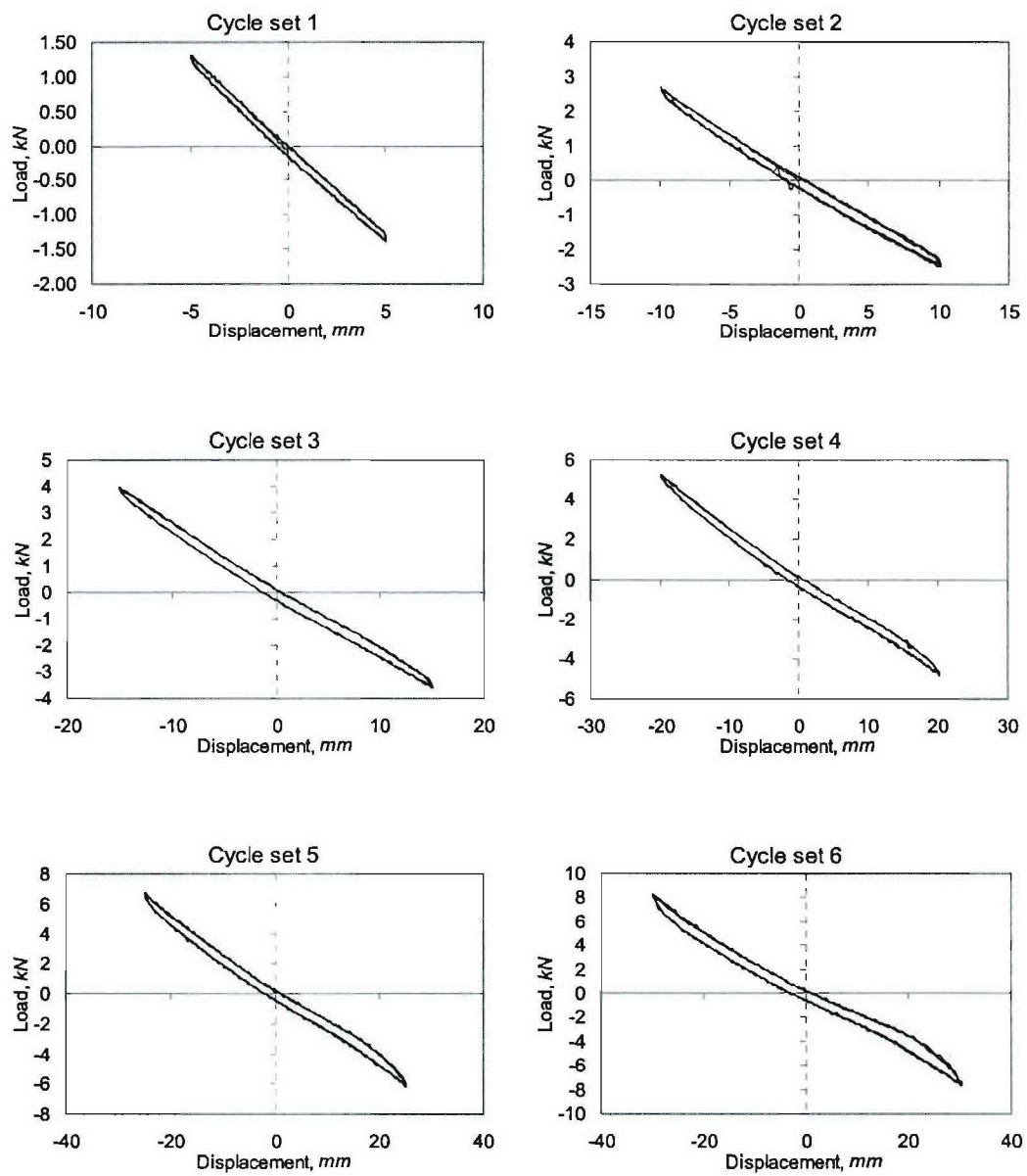


Figure C.1. Load-Displacement Curves for Specimen BP-1, Cycle Sets 1-6



**Figure C.2. Load-Displacement Curves for Specimen BP-1, Cycle Sets 7-12**





**Figure C.3. Load-Displacement Curves for Specimen BT-2, Cycle Sets 1-6**

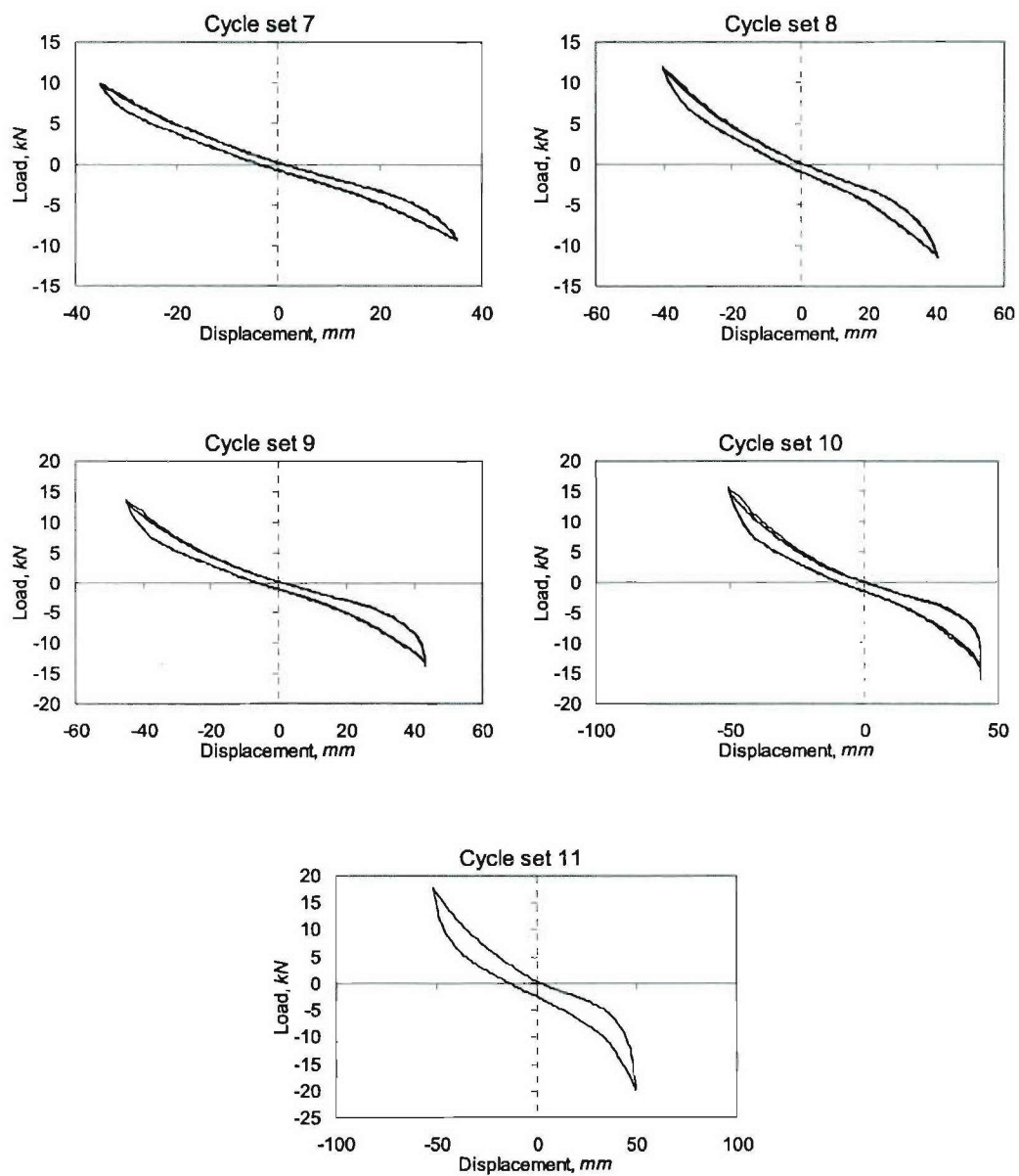


**Figure C.4. Load-Displacement Curves for Specimen BT-2, Cycle Sets 7-11**

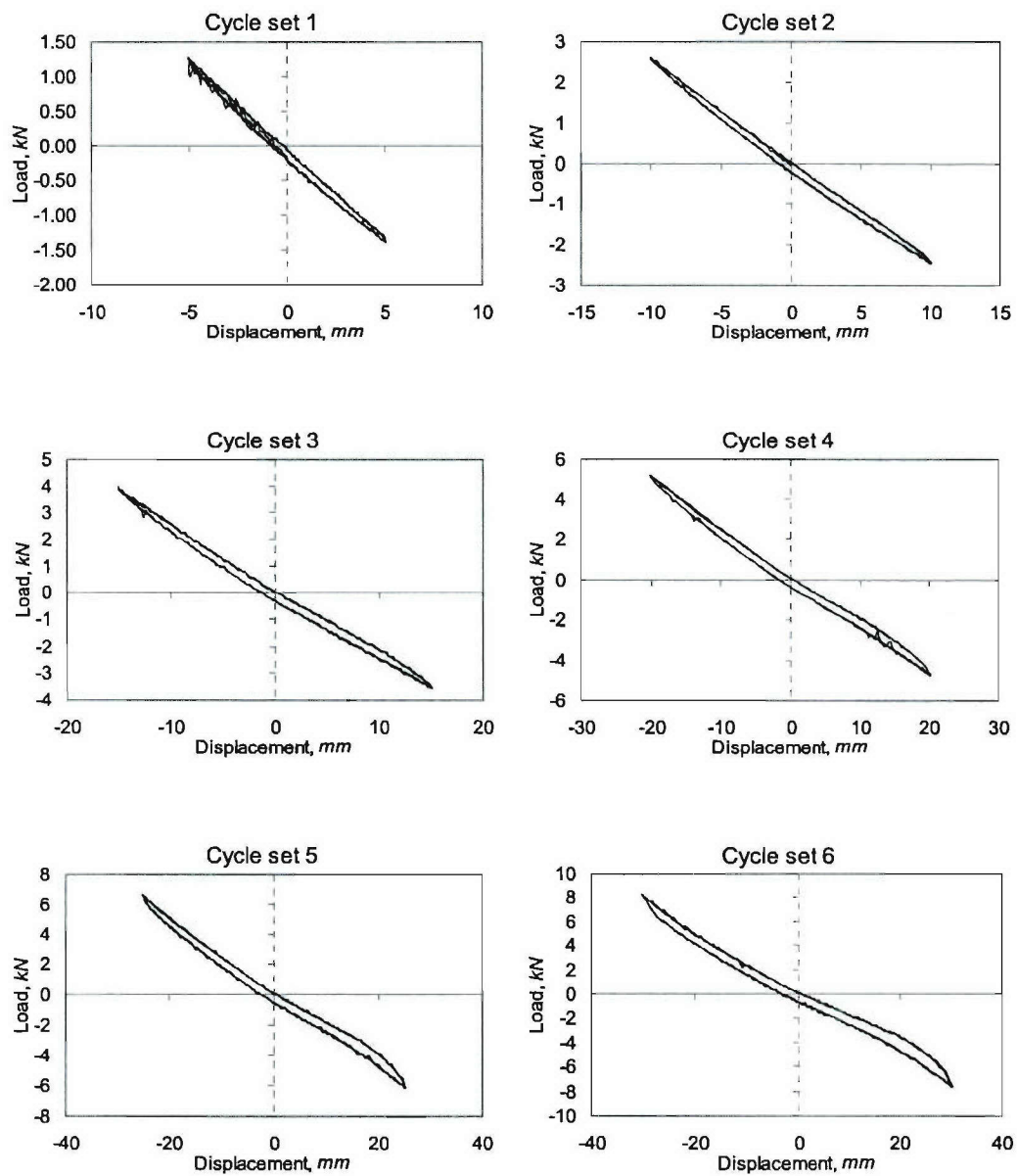


**Figure C.5. Load-Displacement Curves for Specimen BP-3, Cycle Sets 1-6**

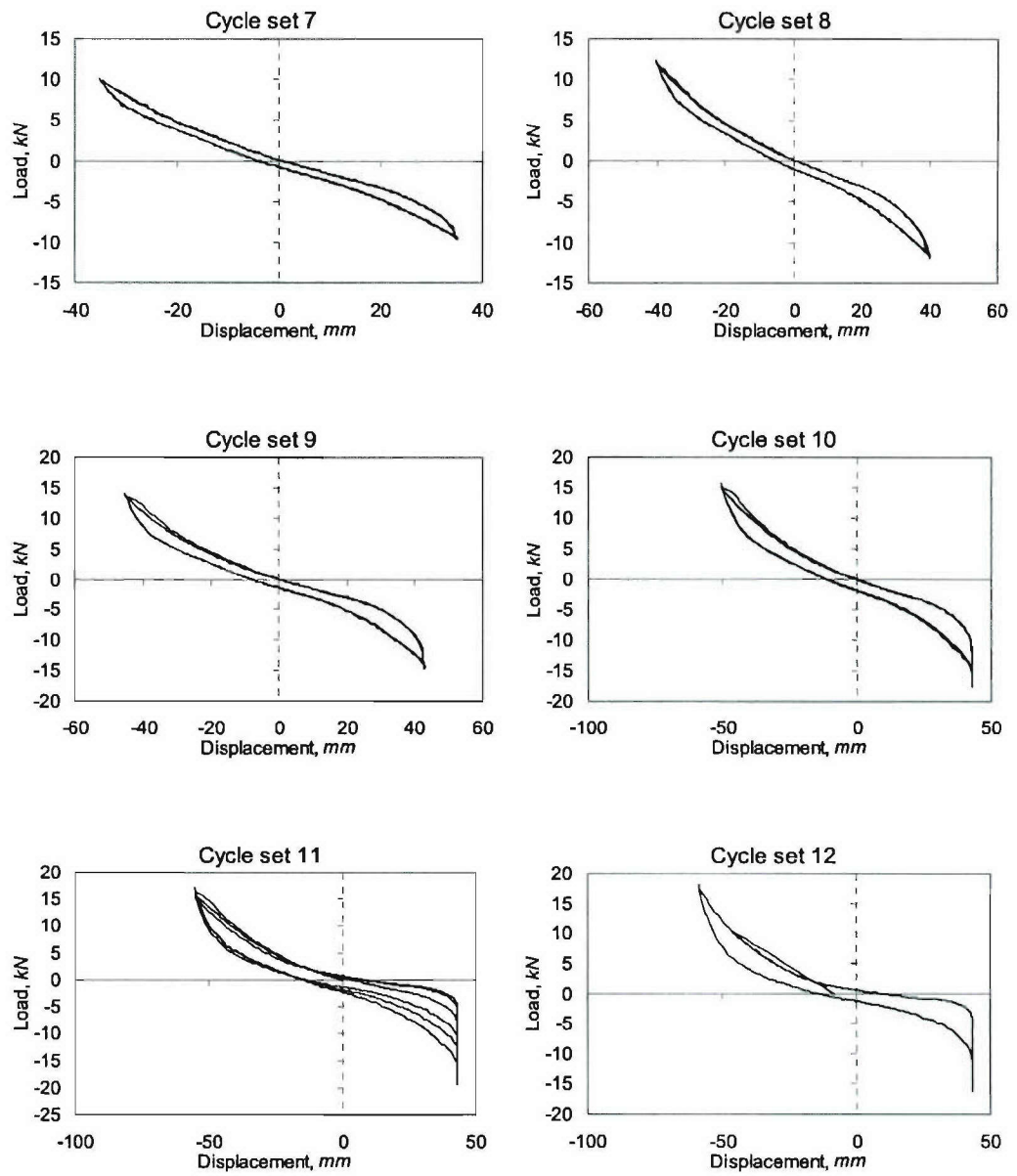


**Figure C.6. Load-Displacement Curves for Specimen BP-3, Cycle Sets 7-12**



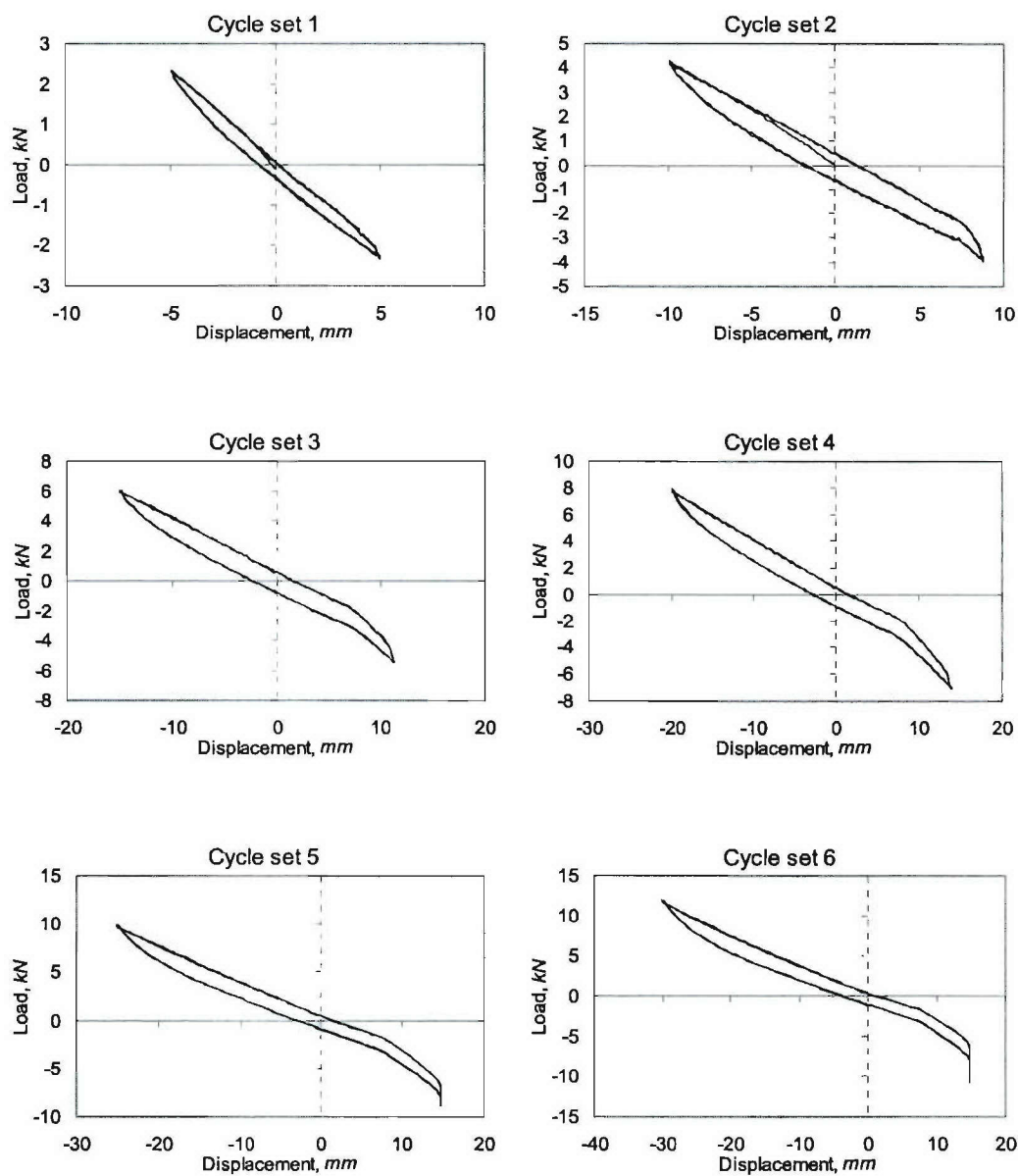


**Figure C.7. Load-Displacement Curves for Specimen BT-4, Cycle Sets 1-6**

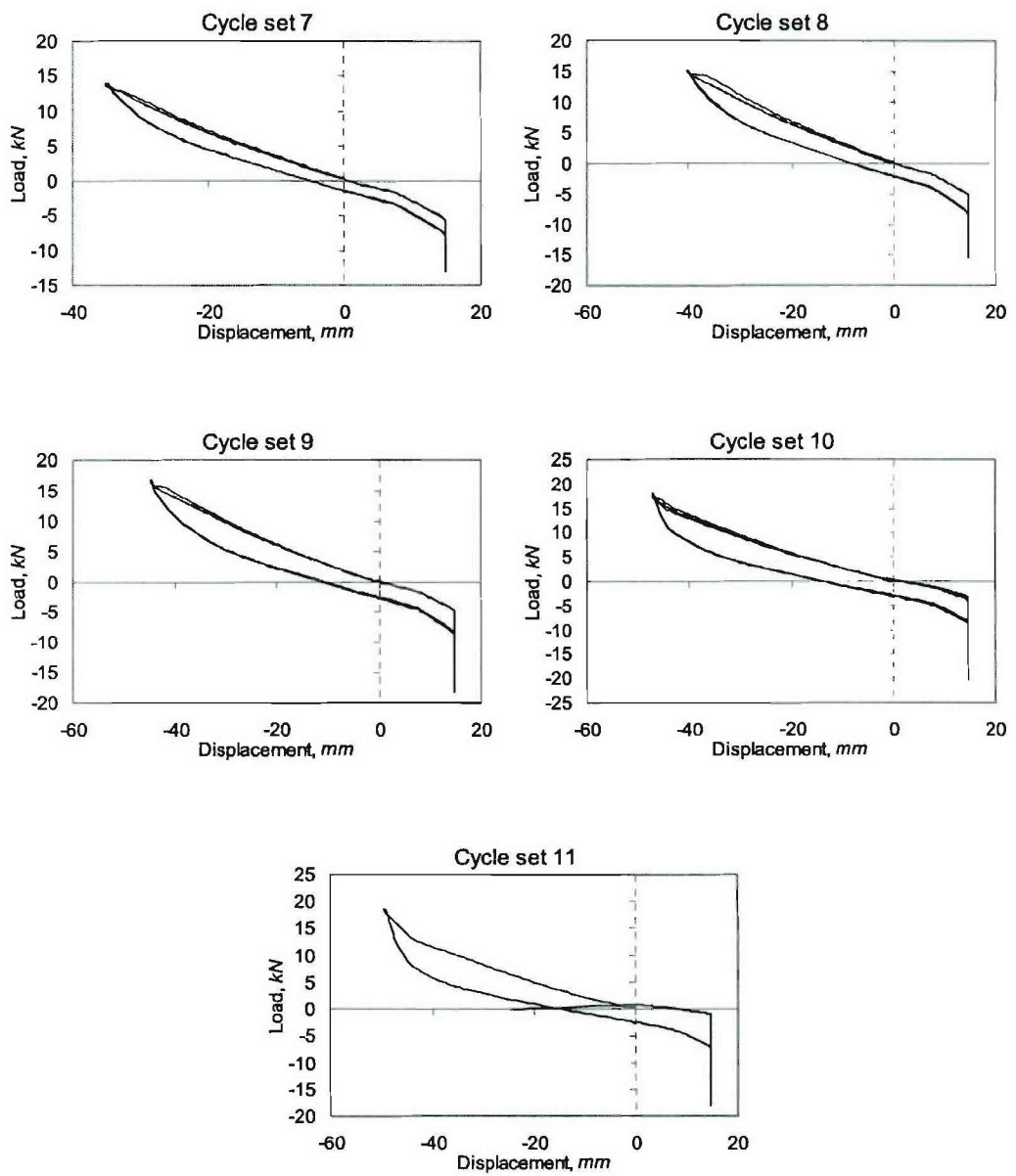


**Figure C.8. Load-Displacement Curves for Specimen BT-4, Cycle Sets 7-11**

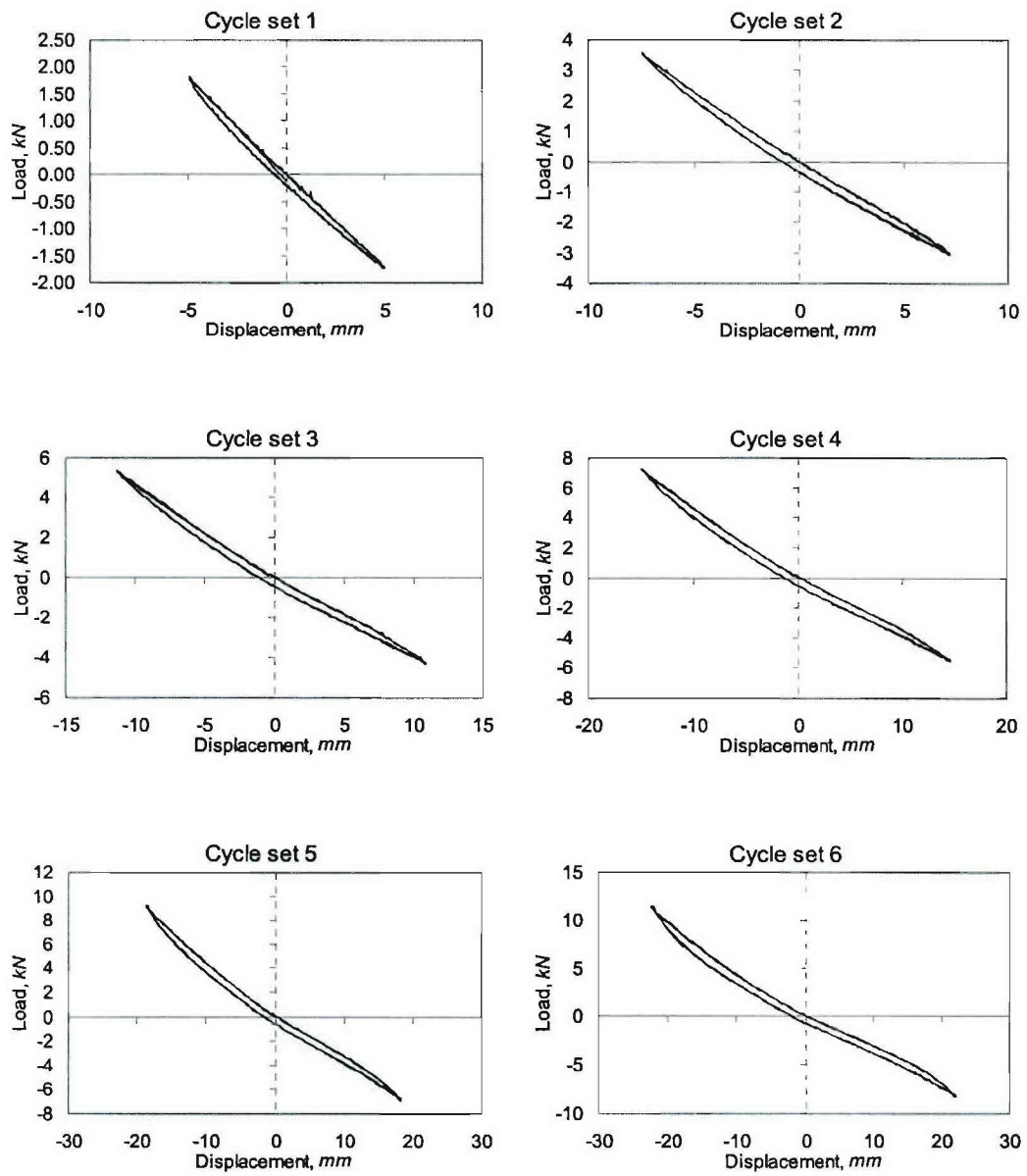


**Figure C.9. Load-Displacement Curves for Specimen BP-5, Cycle Sets 1-6**

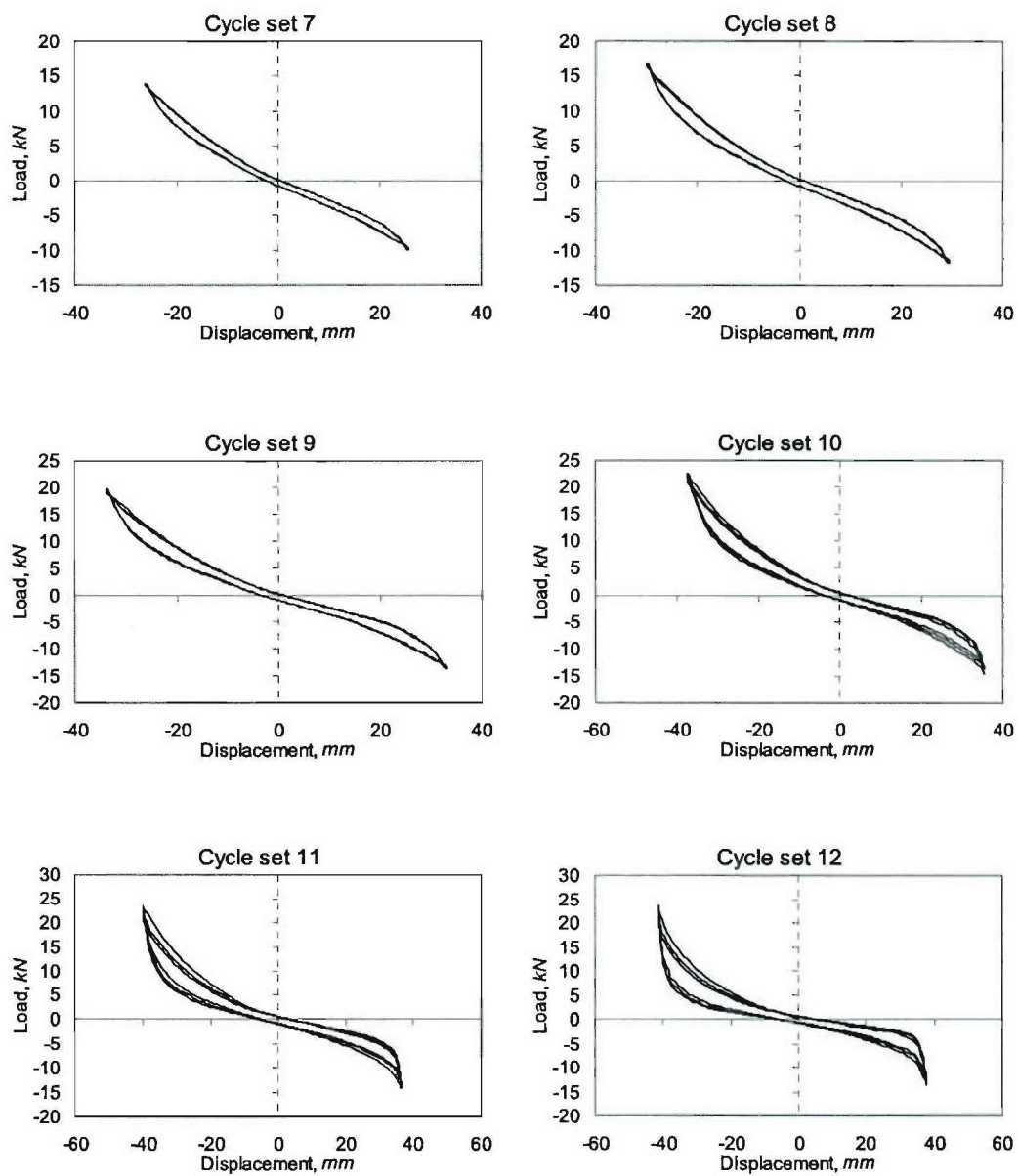


**Figure C.10. Load-Displacement Curves for Specimen BP-5, Cycle Sets 7-12**



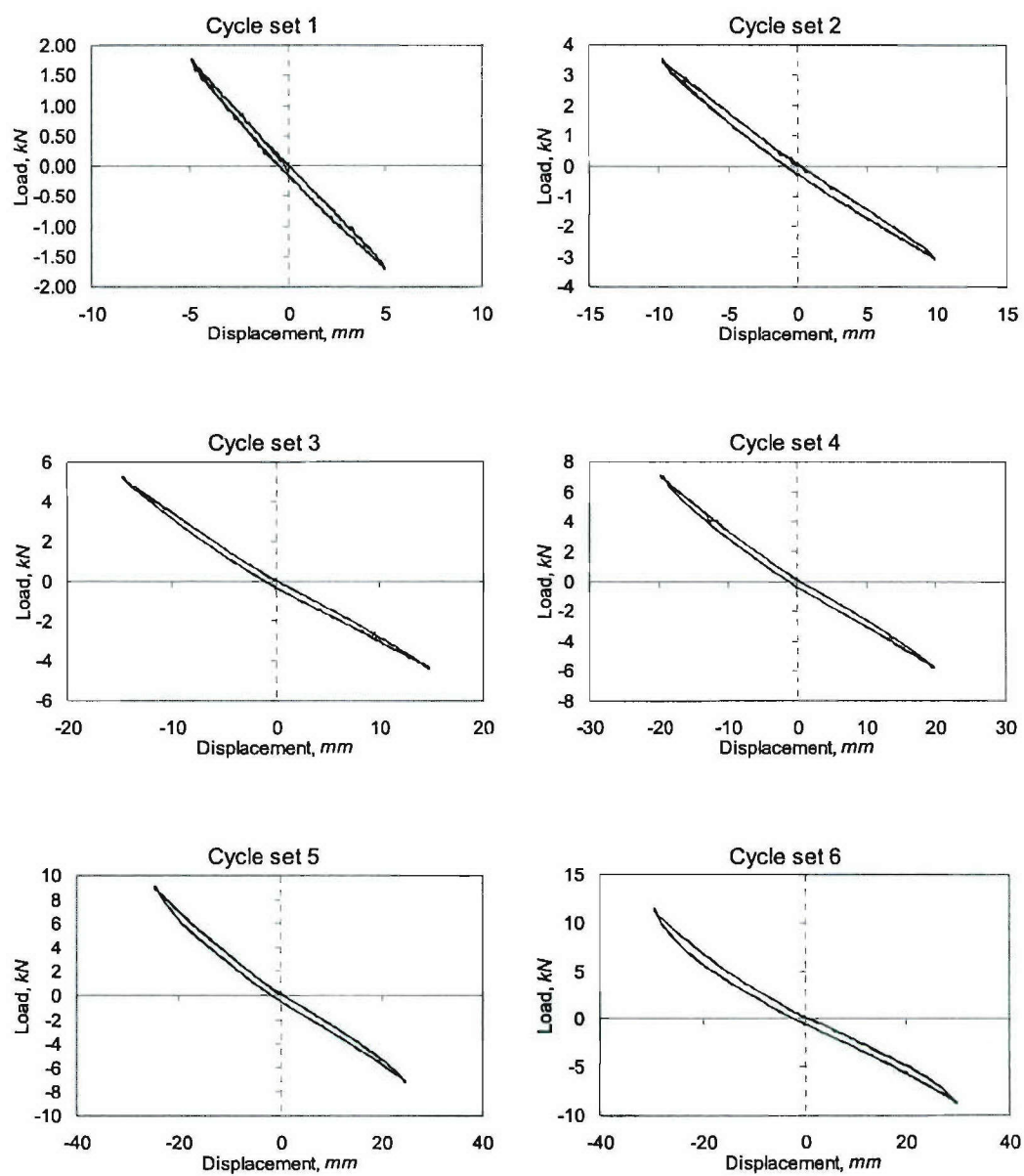


**Figure C.11. Load-Displacement Curves for Specimen BT-6, Cycle Sets 1-6**

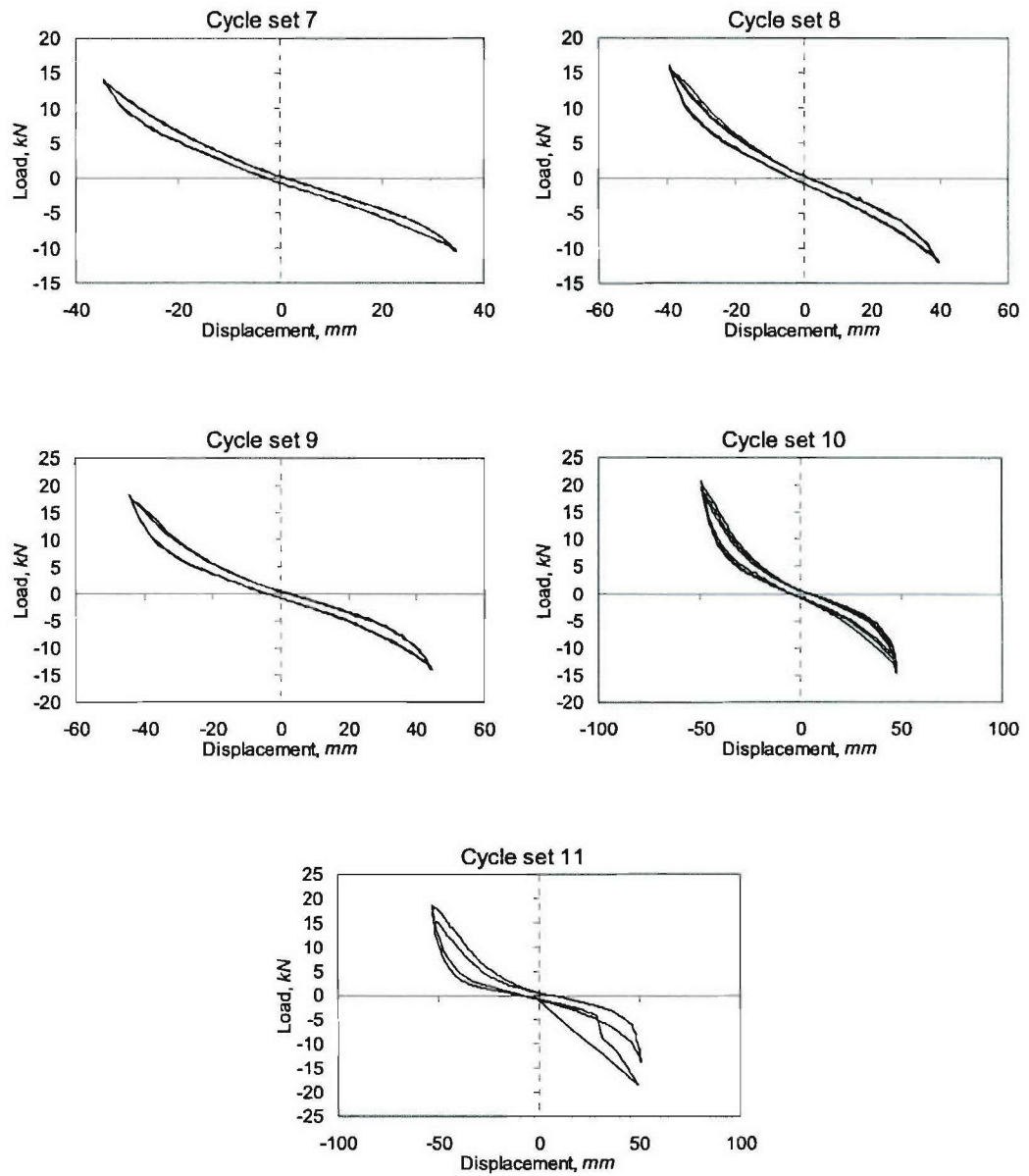
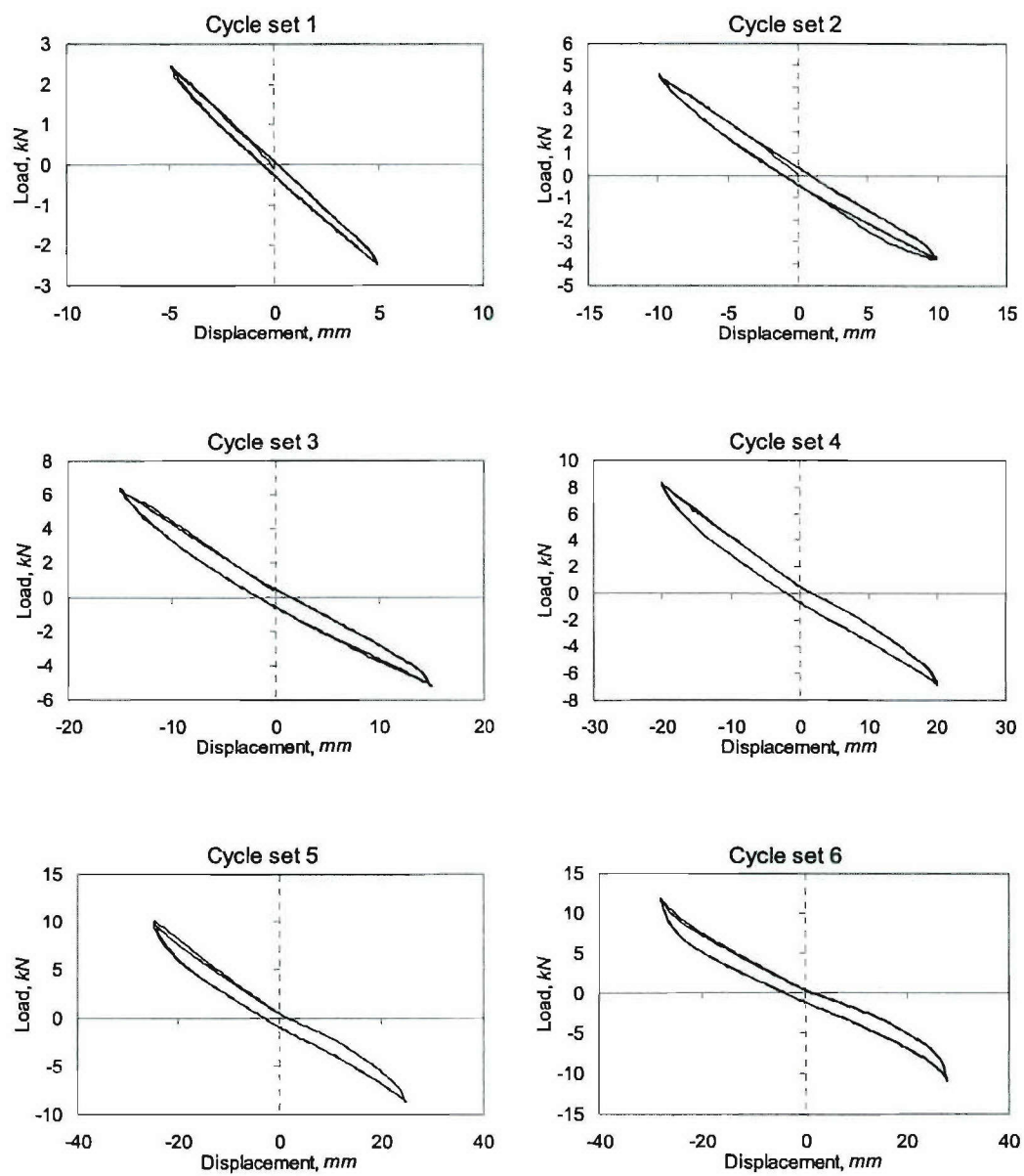
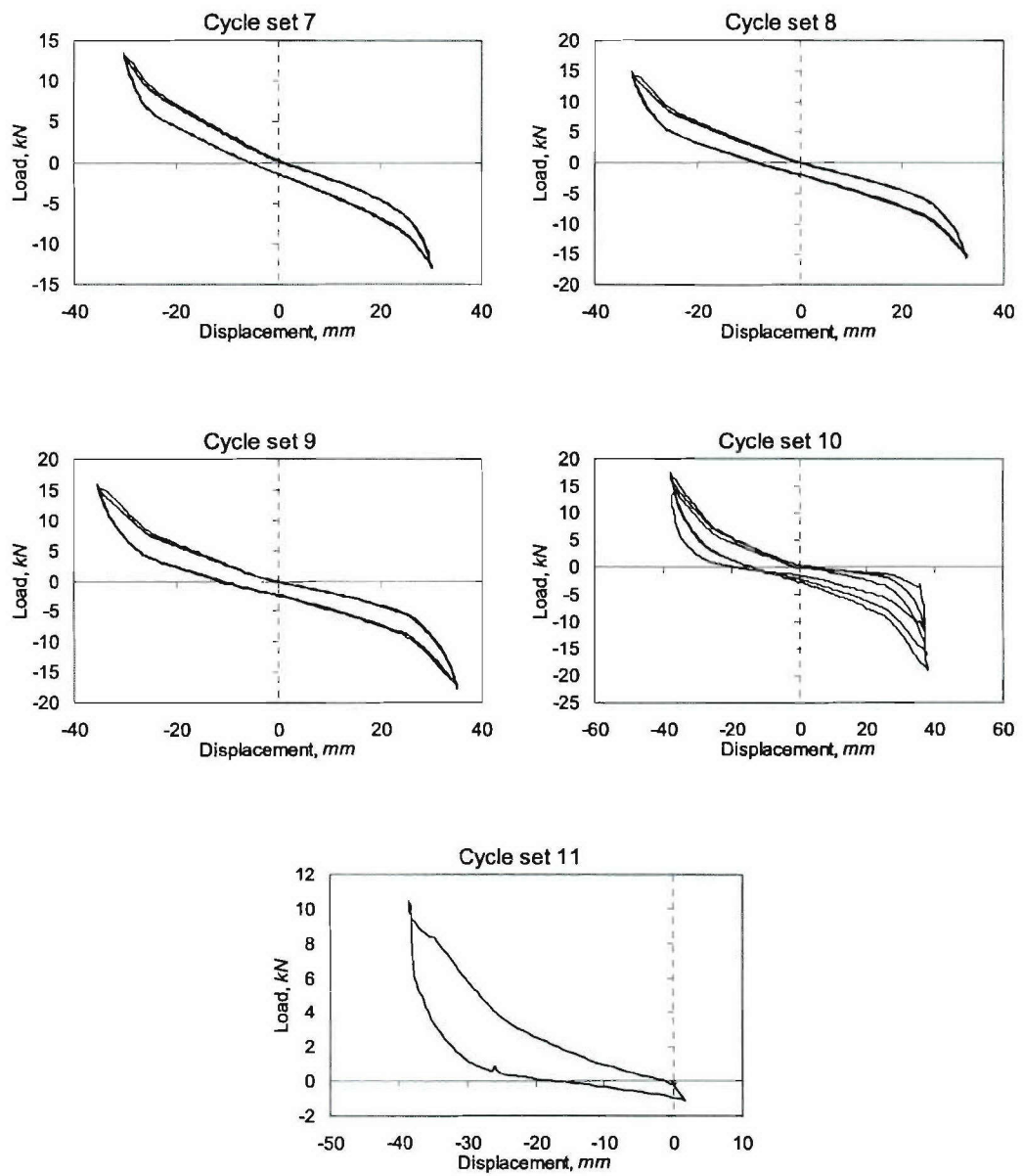


Figure C.12. Load-Displacement Curves for Specimen BT-6, Cycle Sets 7-12



**Figure C.13. Load-Displacement Curves for Specimen BT-7, Cycle Sets 1-6**



**Figure C.14. Load-Displacement Curves for Specimen BT-7, Cycle Sets 7-12**



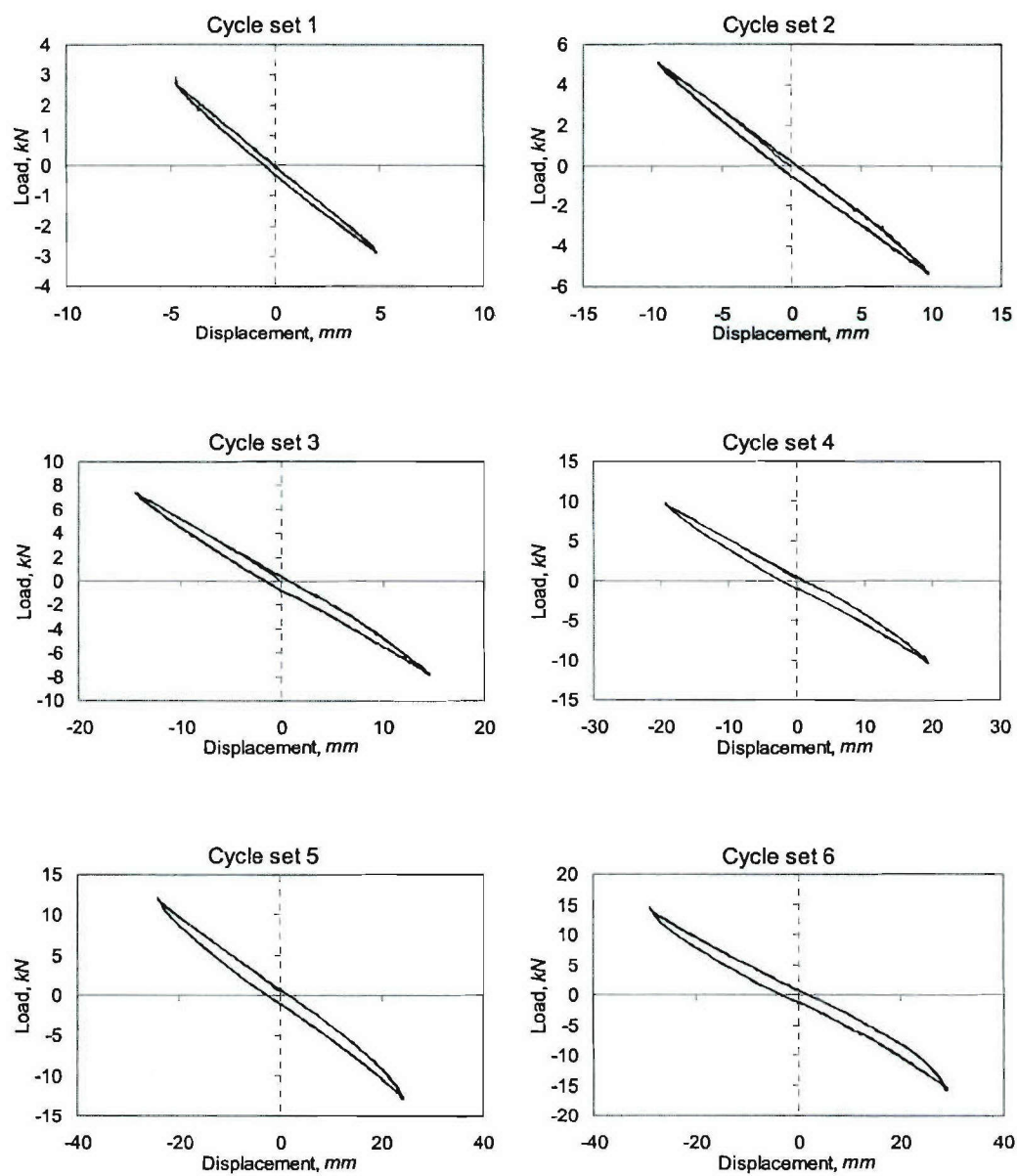


**Figure C.15. Load-Displacement Curves for Specimen DM-1, Cycle Sets 1-6**

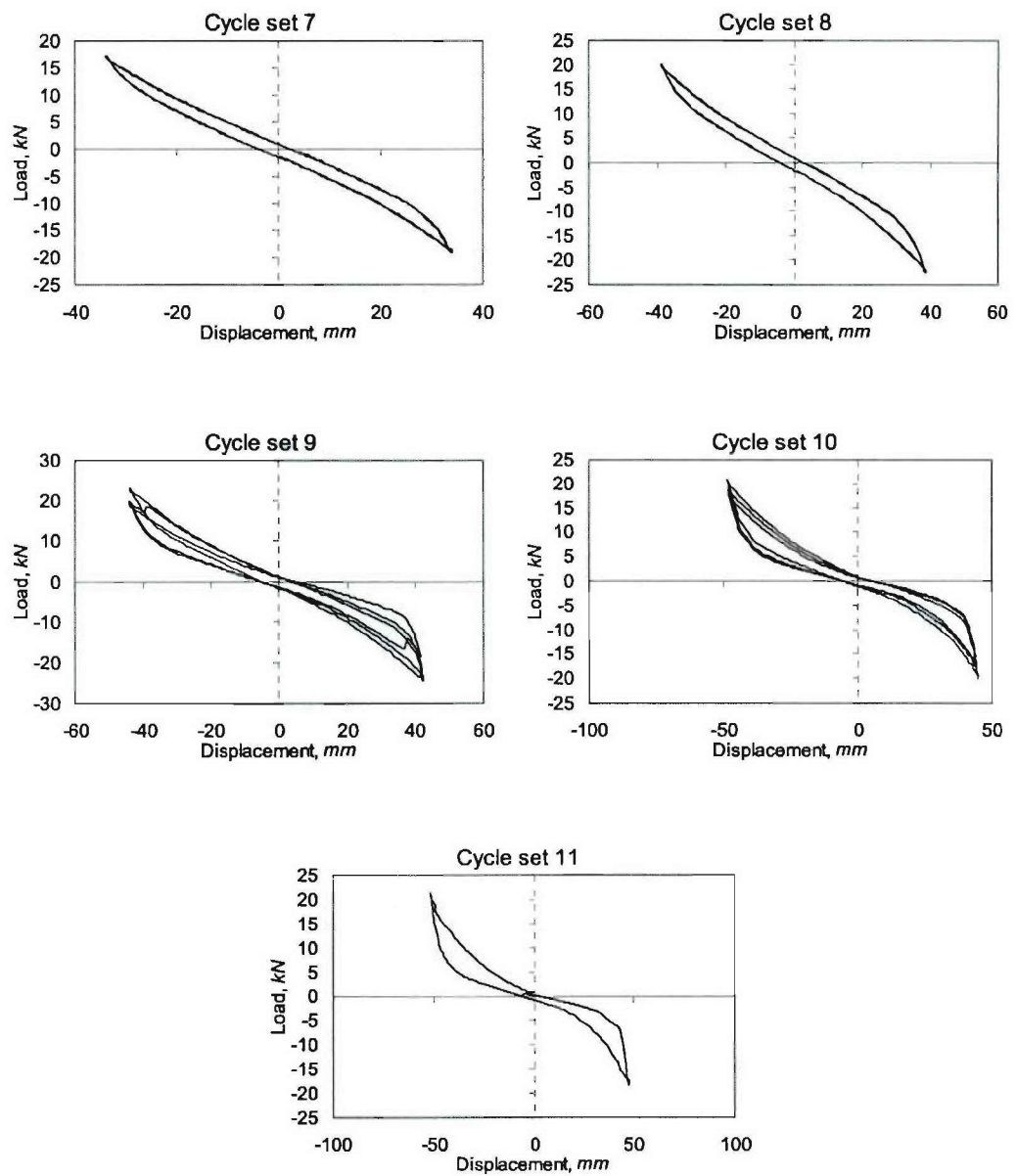


**Figure C.16. Load-Displacement Curves for Specimen DM-1, Cycle Sets 7-12**

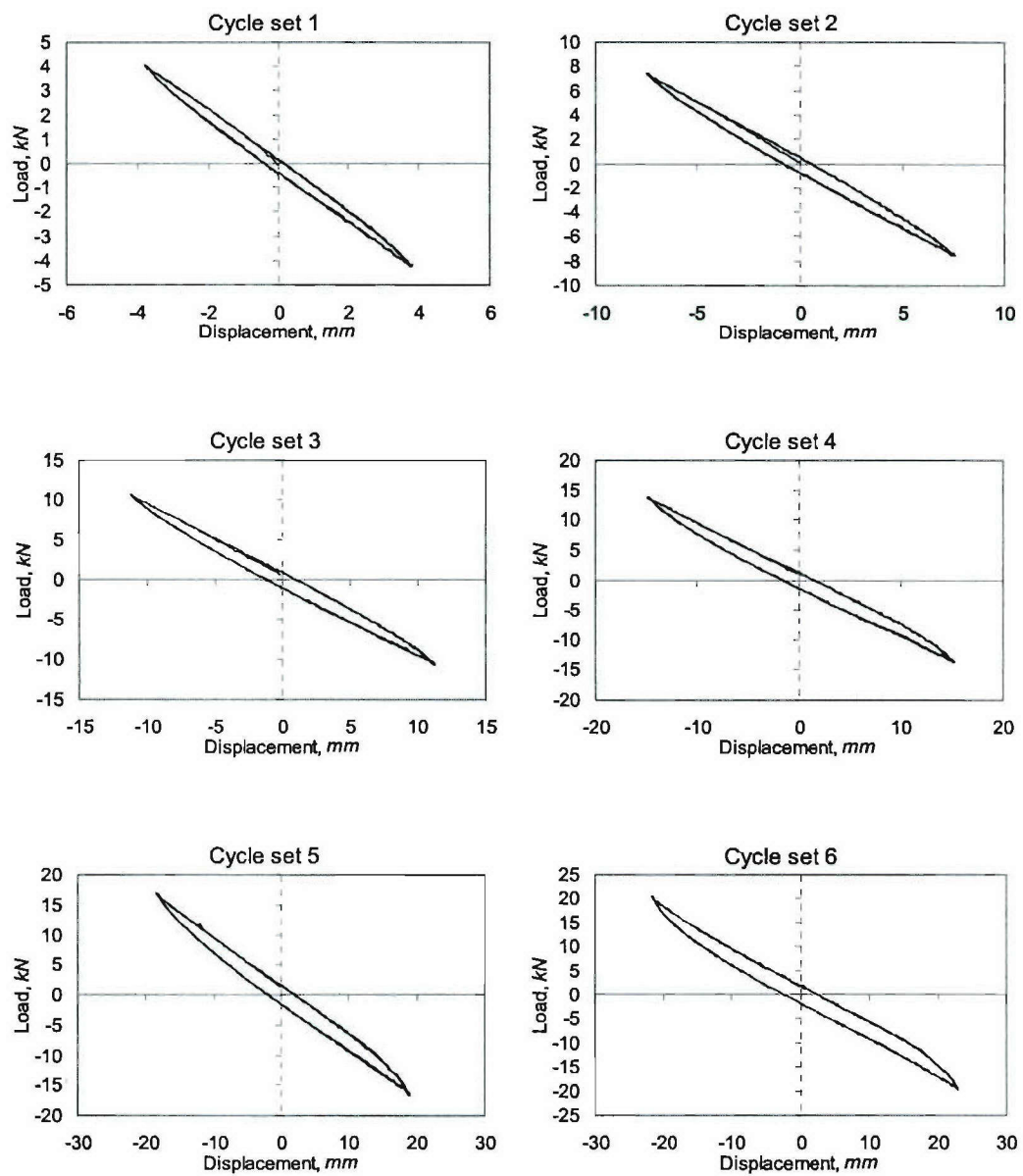


**Figure C.17. Load-Displacement Curves for Specimen DL-2, Cycle Sets 1-6**

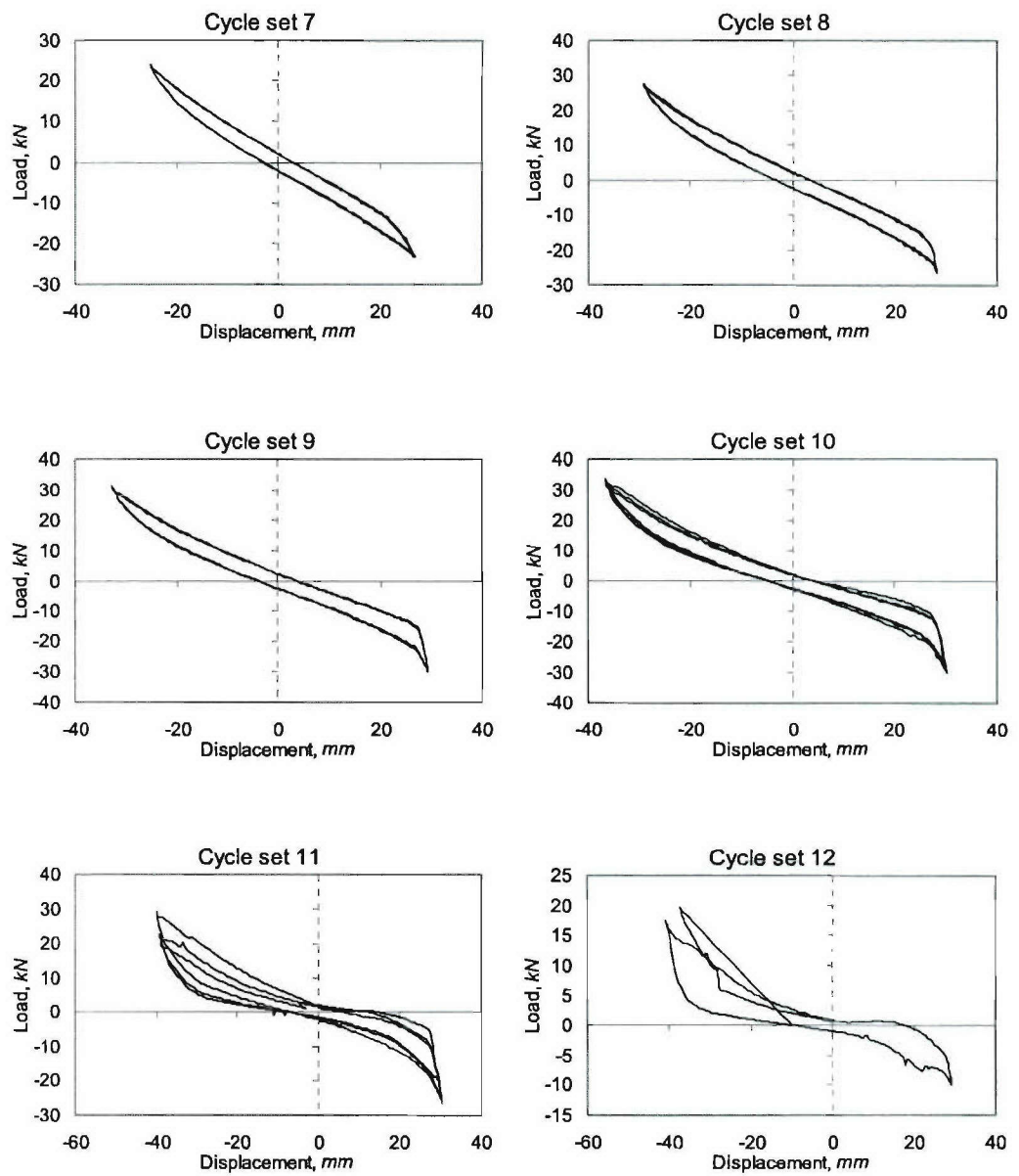


**Figure C.18. Load-Displacement Curves for Specimen DL-2, Cycle Sets 7-12**



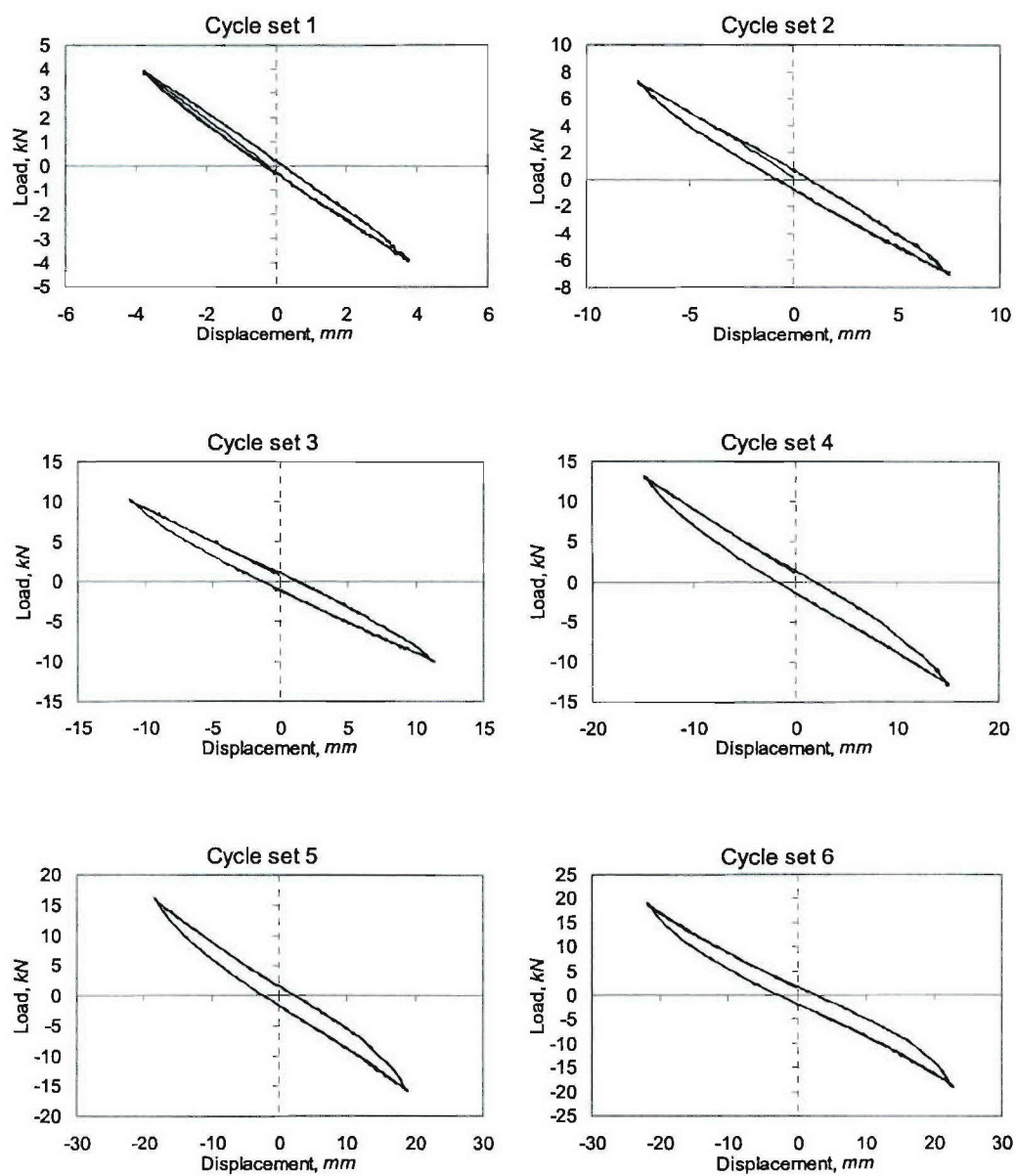


**Figure C.19. Load-Displacement Curves for Specimen DL-3, Cycle Sets 1-6**

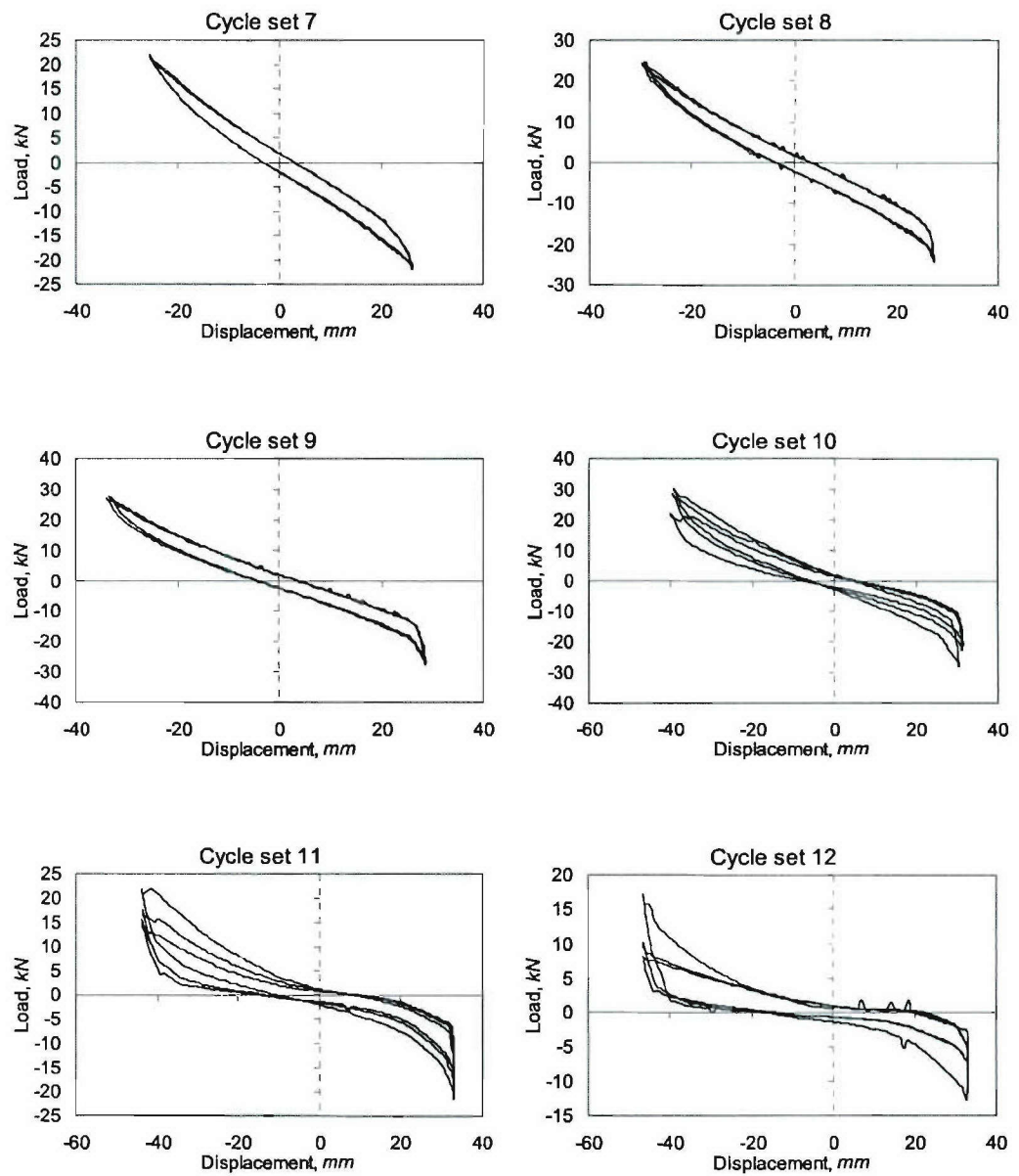


**Figure C.20. Load-Displacement Curves for Specimen DL-3, Cycle Sets 6-12**

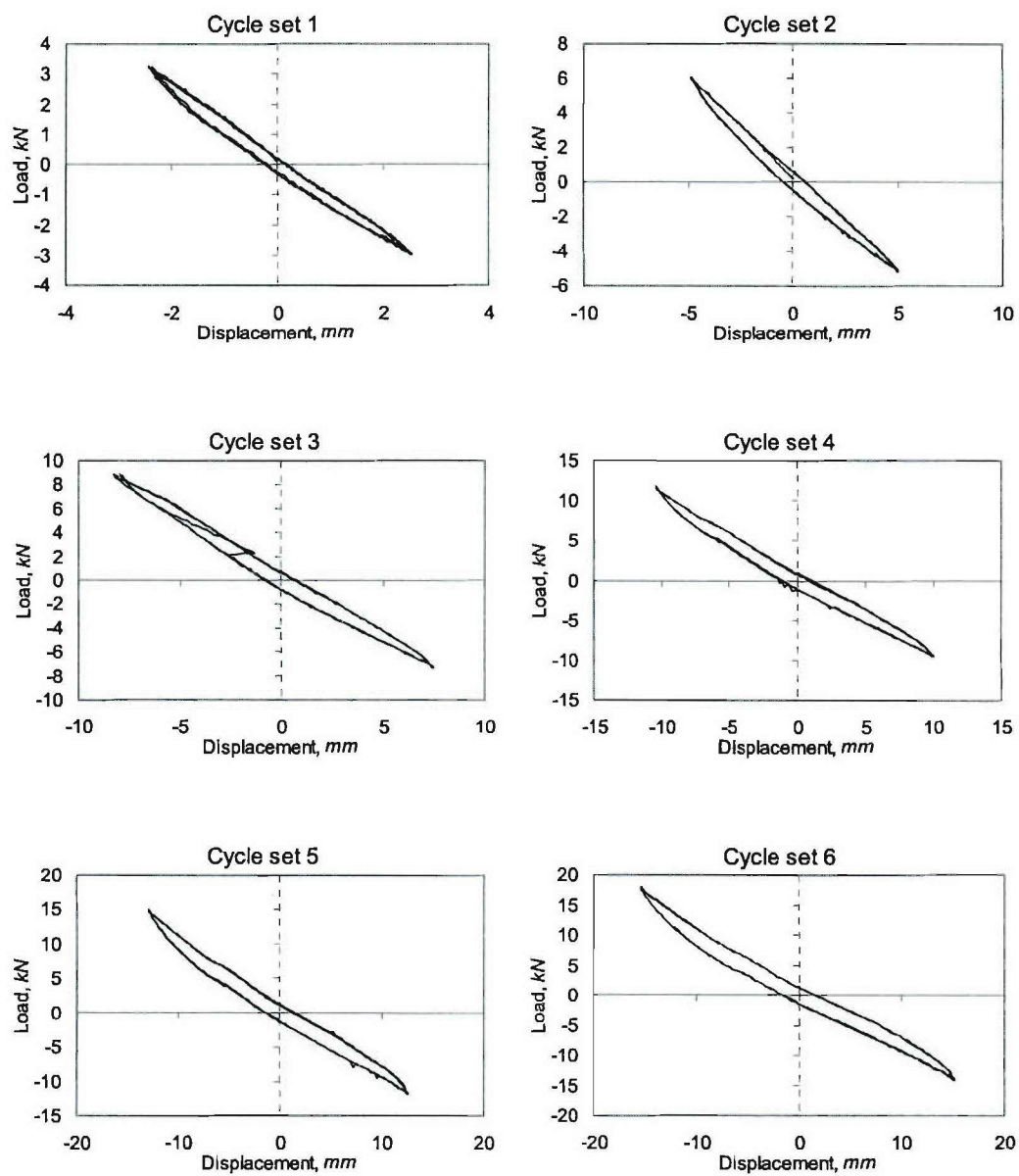
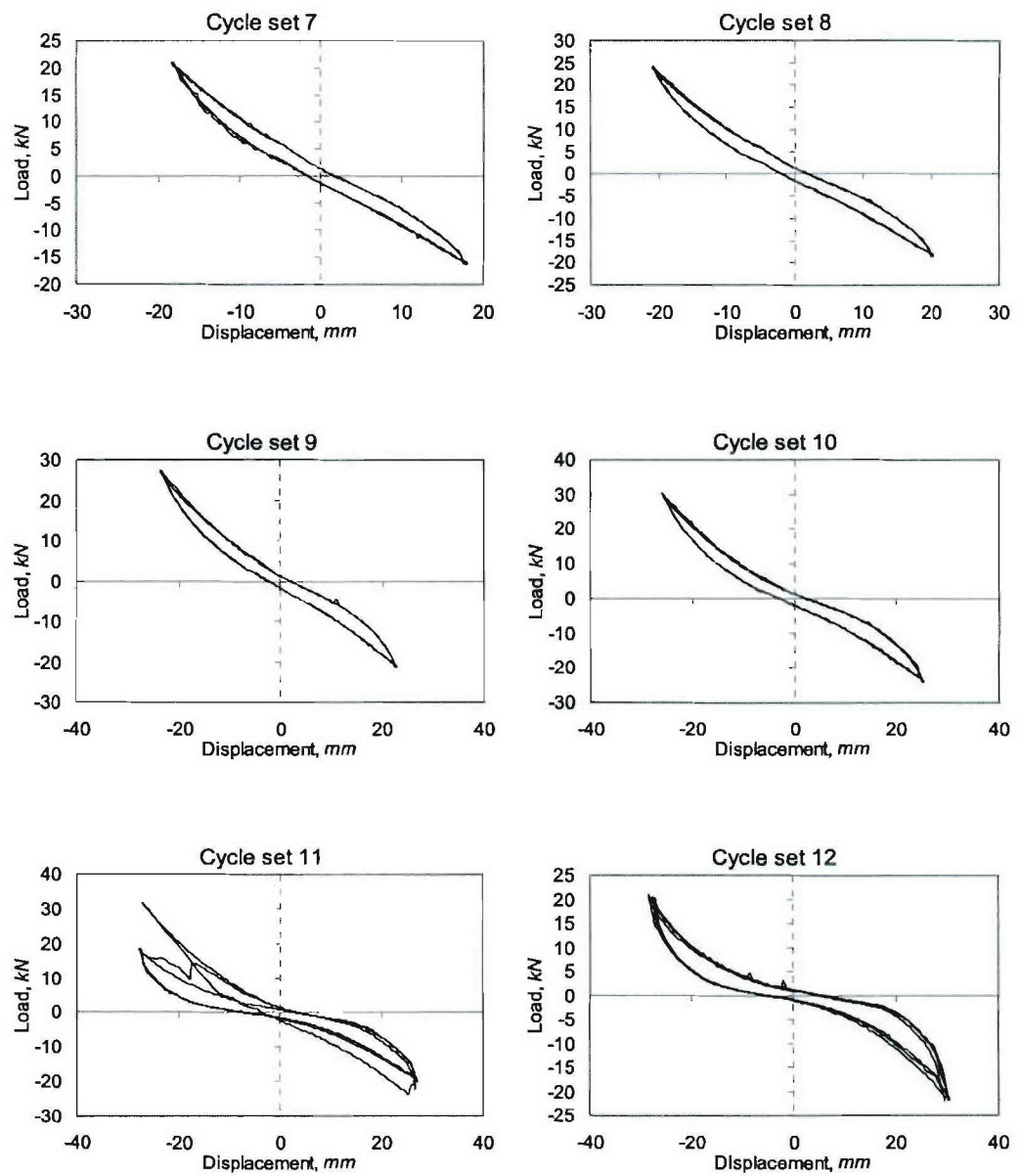
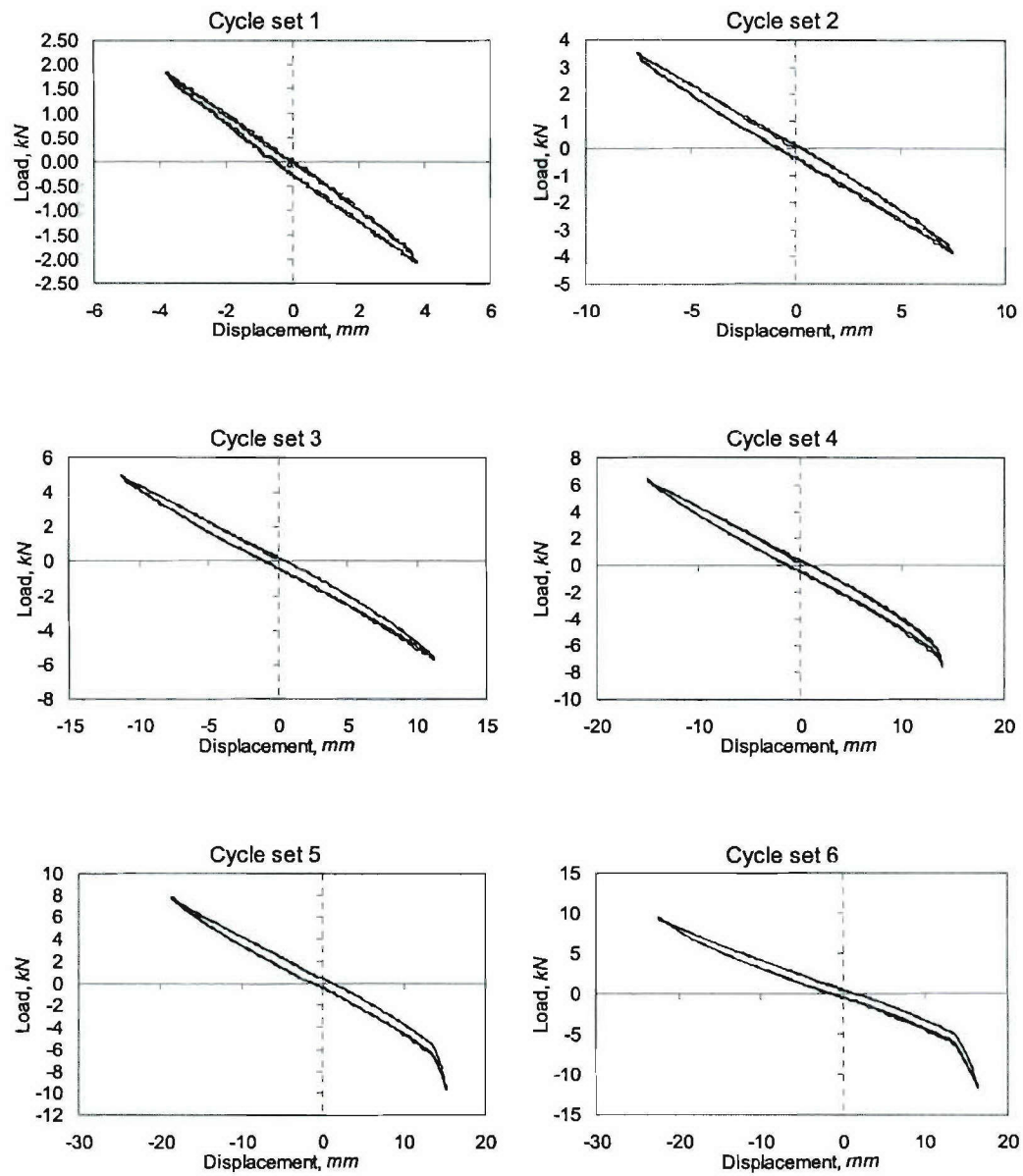


Figure C.21. Load-Displacement Curves for Specimen DS-4, Cycle Sets 1-6



**Figure C.22. Load-Displacement Curves for Specimen DS-4, Cycle Sets 7-12**





**Figure C.23. Load-Displacement Curves for Specimen DL-5, Cycle Sets 1-6**

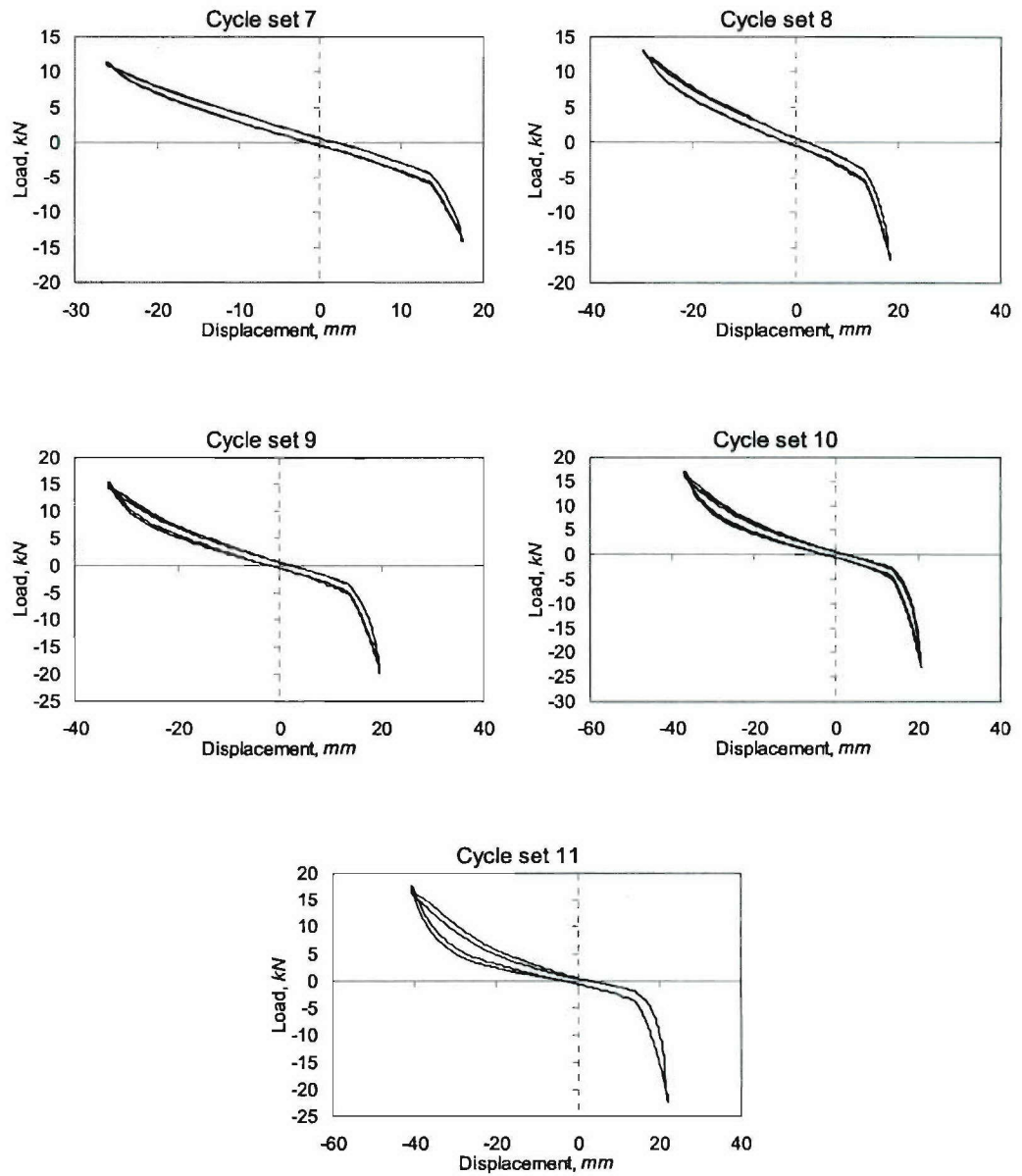


**Figure C.24. Load-Displacement Curves for Specimen DL-5, Cycle Sets 7-12**

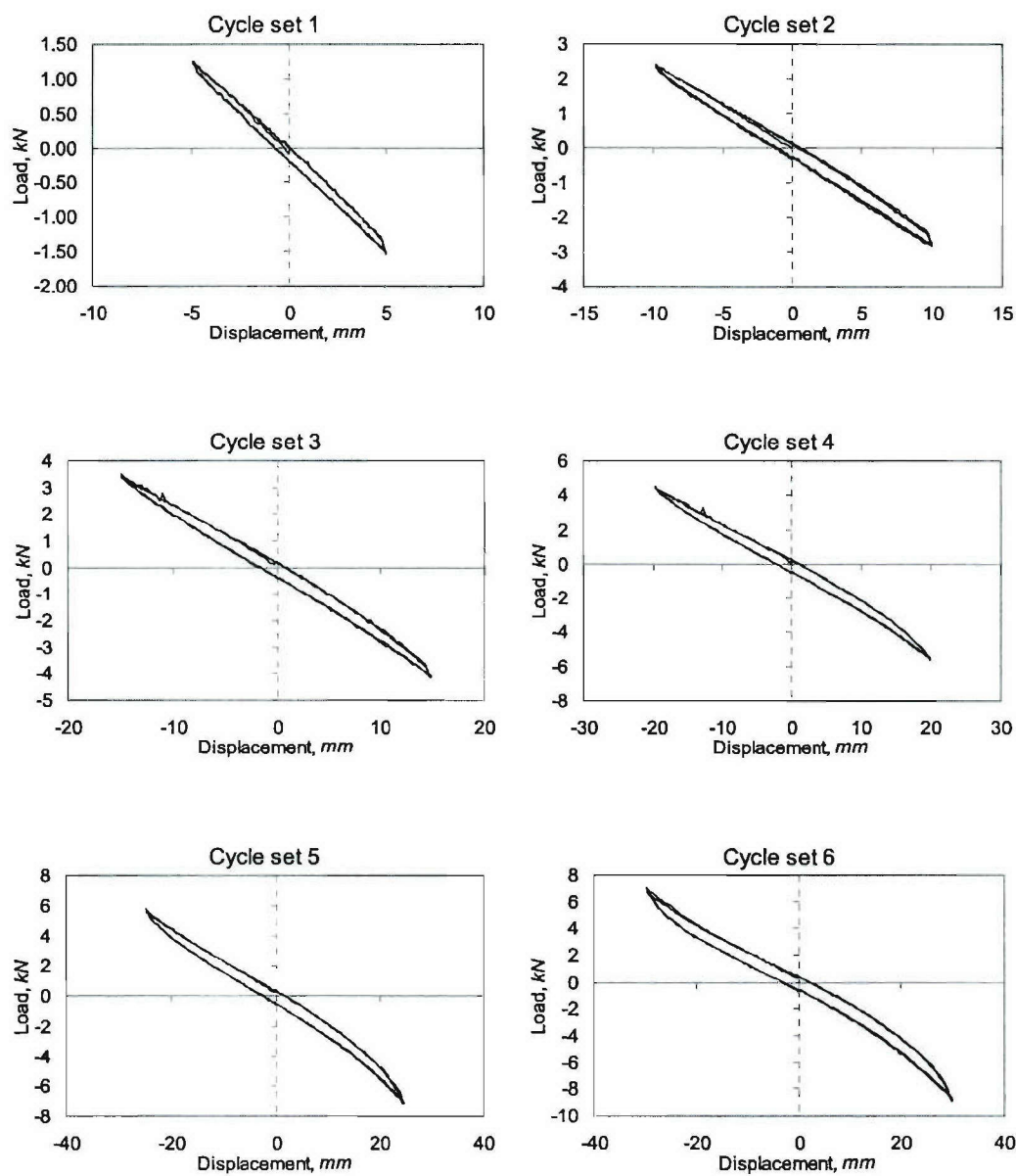


**Figure C.25. Load-Displacement Curves for Specimen DM-6, Cycle Sets 1-6**

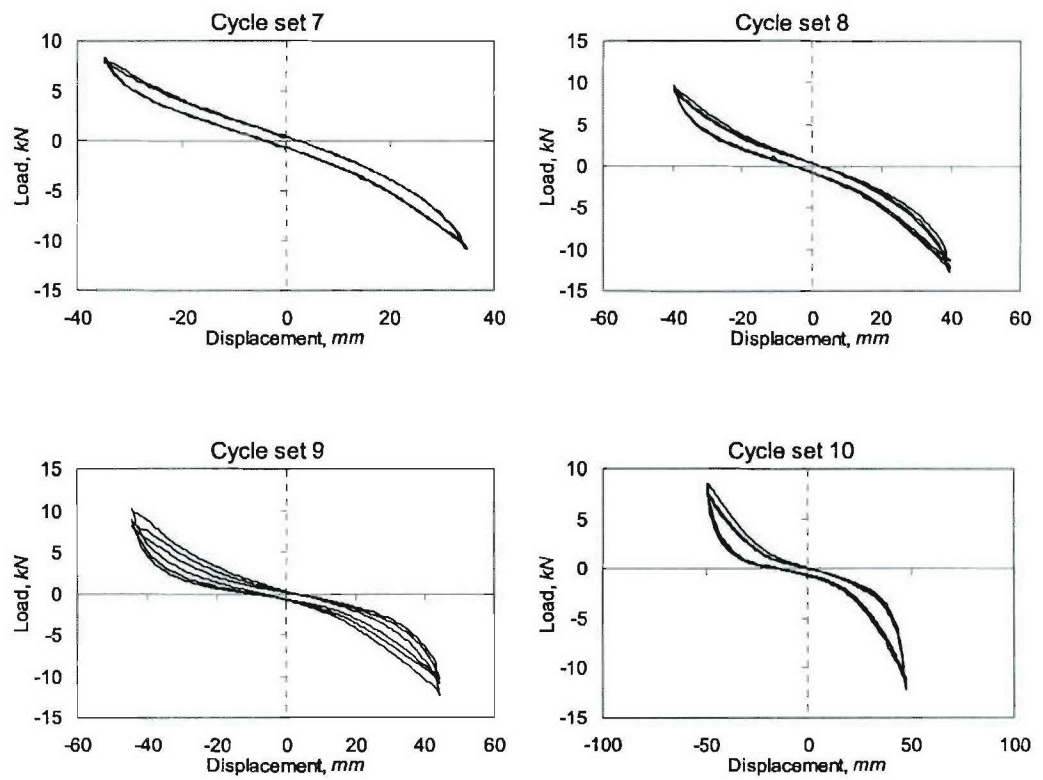


**Figure C.26. Load-Displacement Curves for Specimen DM-6, Cycle Sets 7-12**



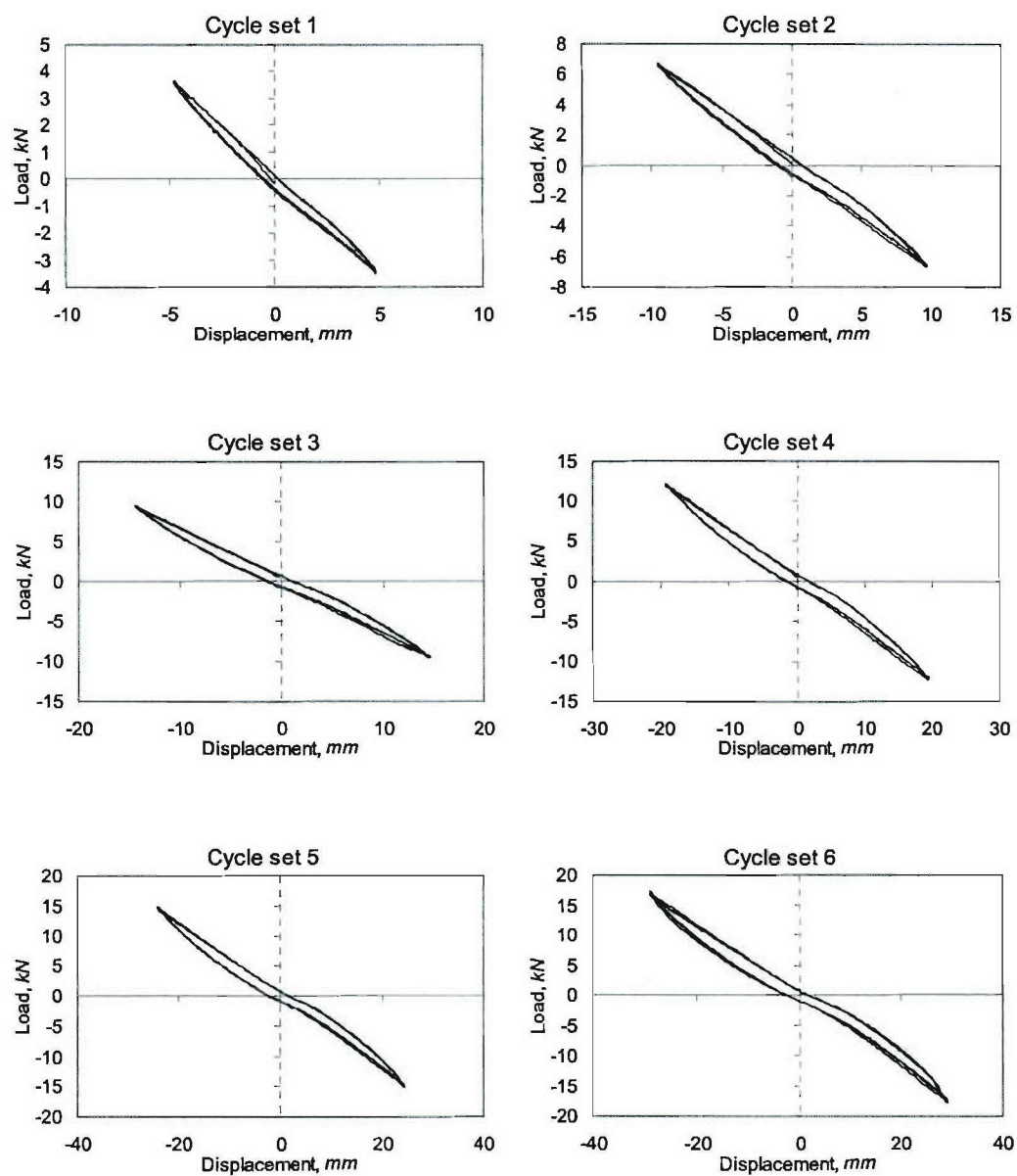


**Figure C.27. Load-Displacement Curves for Specimen DL-7, Cycle Sets 1-6**

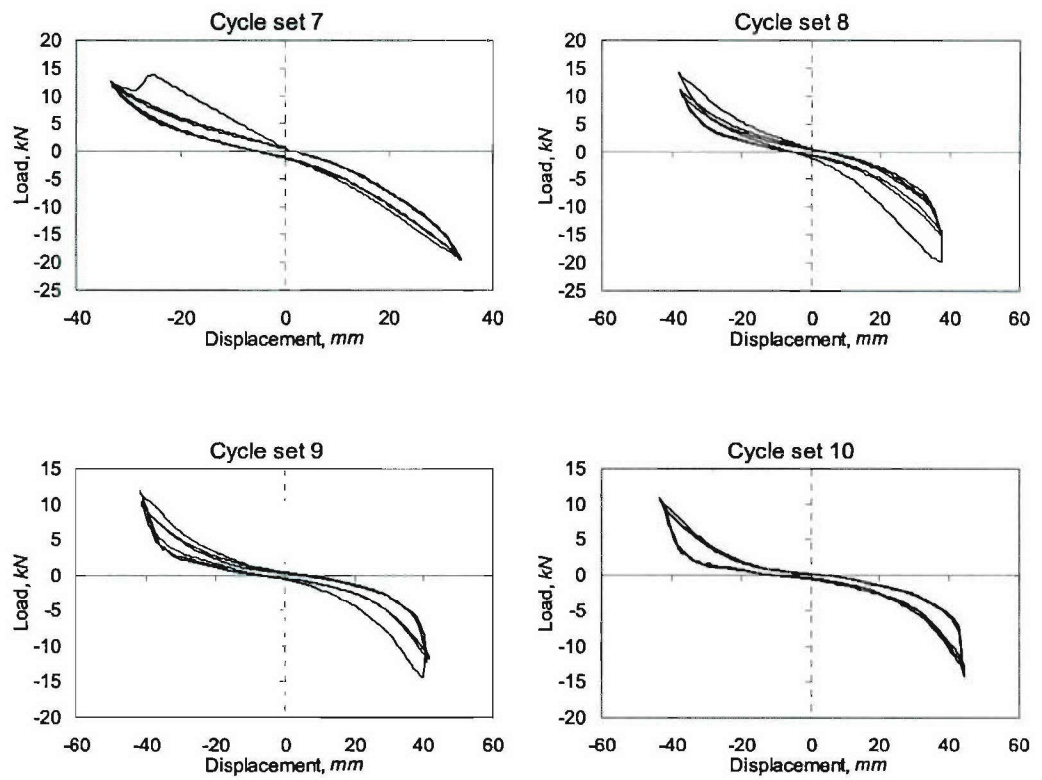


**Figure C.28. Load-Displacement Curves for Specimen DL-7, Cycle Sets 7-12**

## Appendix D

### Load versus Middle Displacement Plots of Hybrid Joints

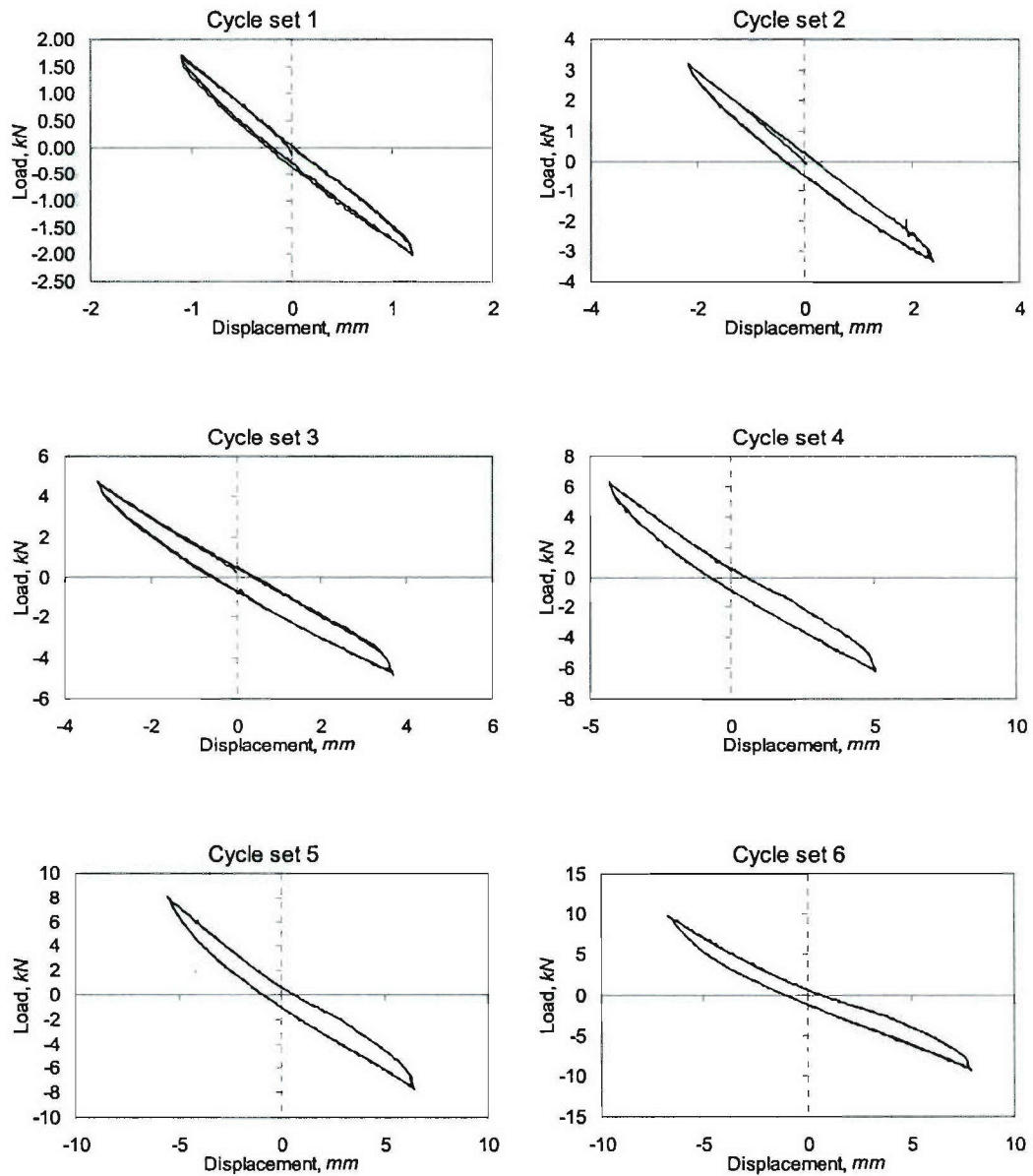
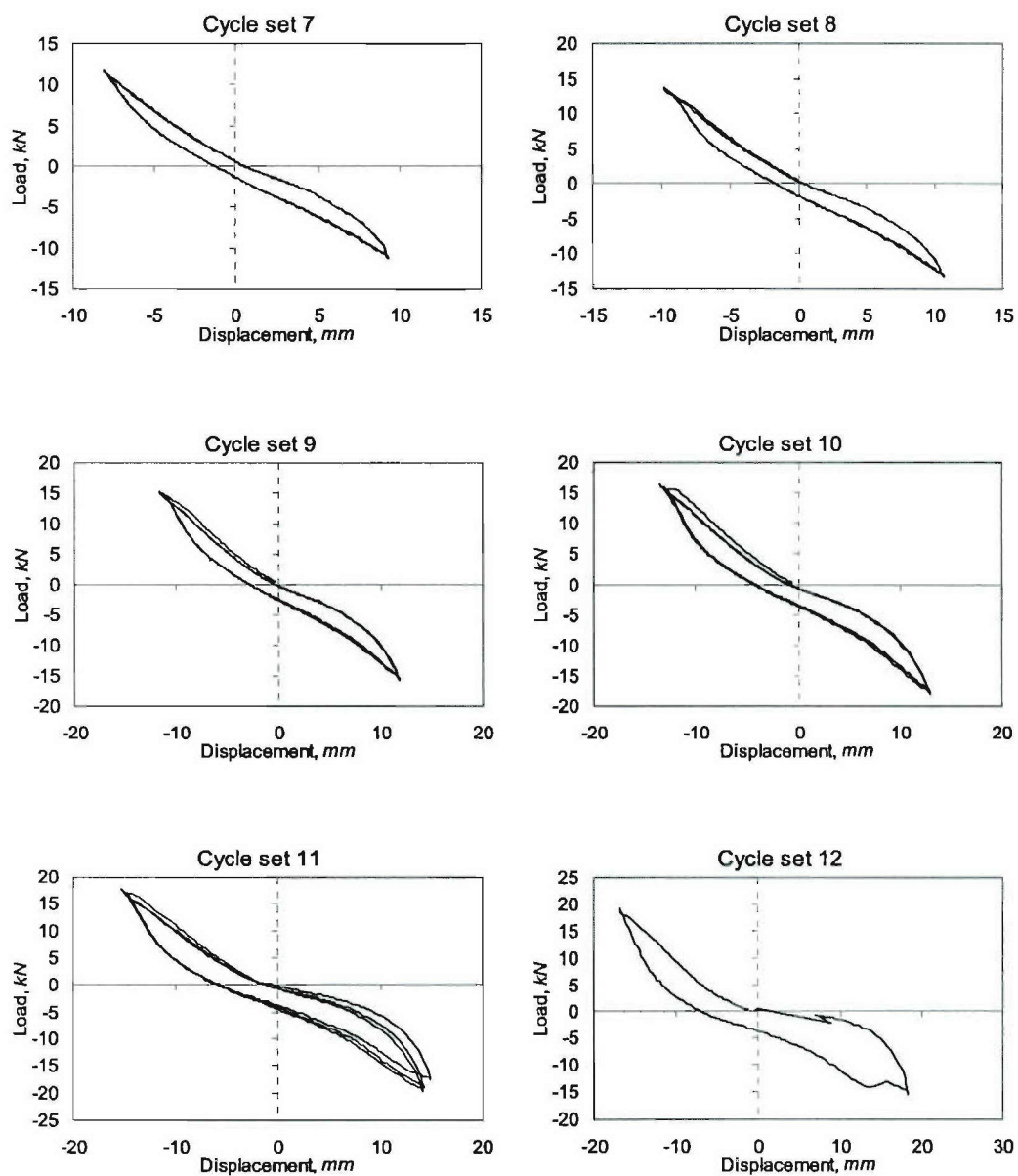
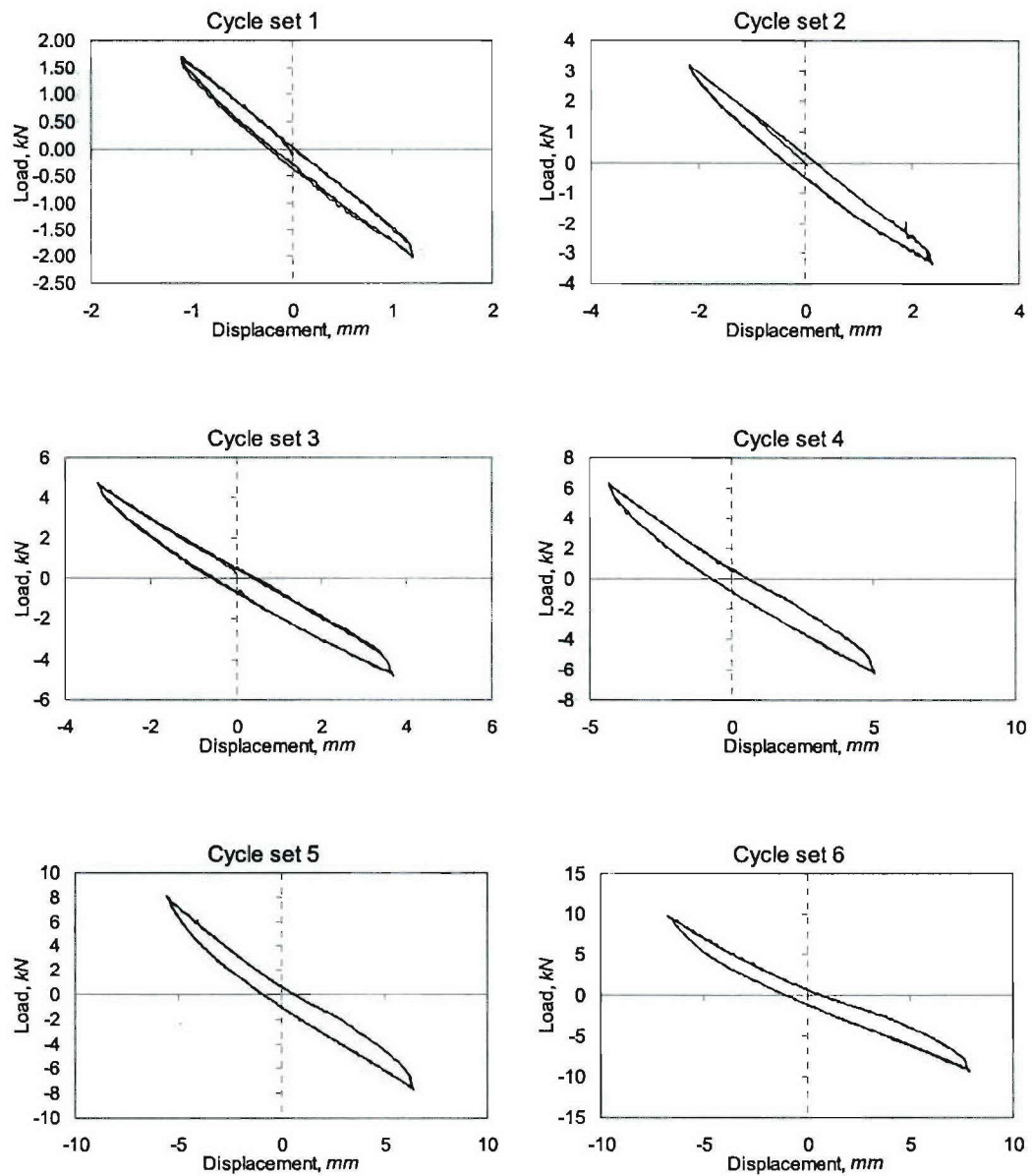


Figure D.1. Load-Displacement Curves for Specimen BP-1, Cycle Sets 1-6



**Figure D.2. Load-Displacement Curves for Specimen BP-1, Cycle Sets 7-12**





**Figure D.3. Load-Displacement Curves for Specimen BT-2, Cycle Sets 1-6**

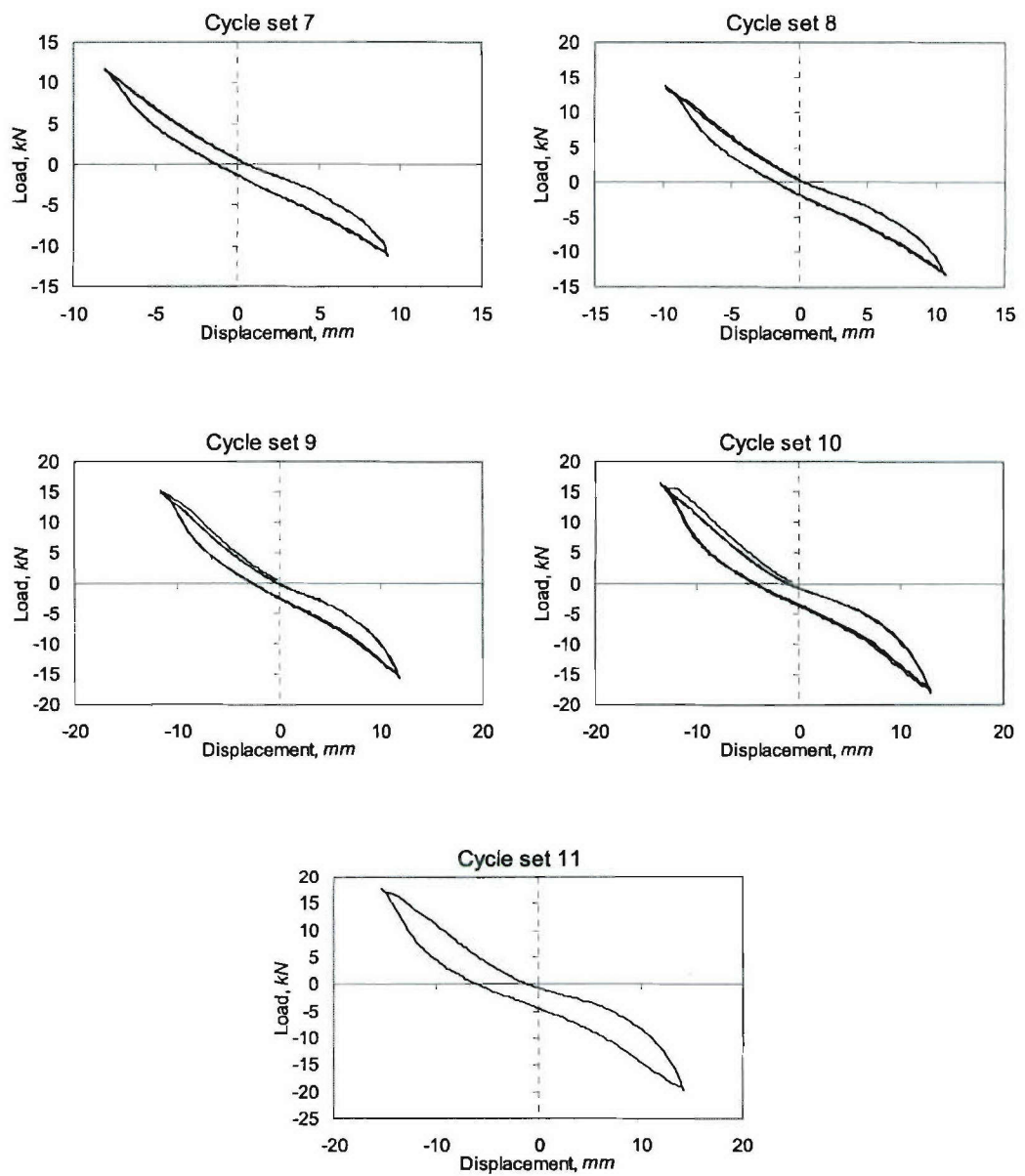


**Figure D.4. Load-Displacement Curves for Specimen BT-2, Cycle Sets 7-11**

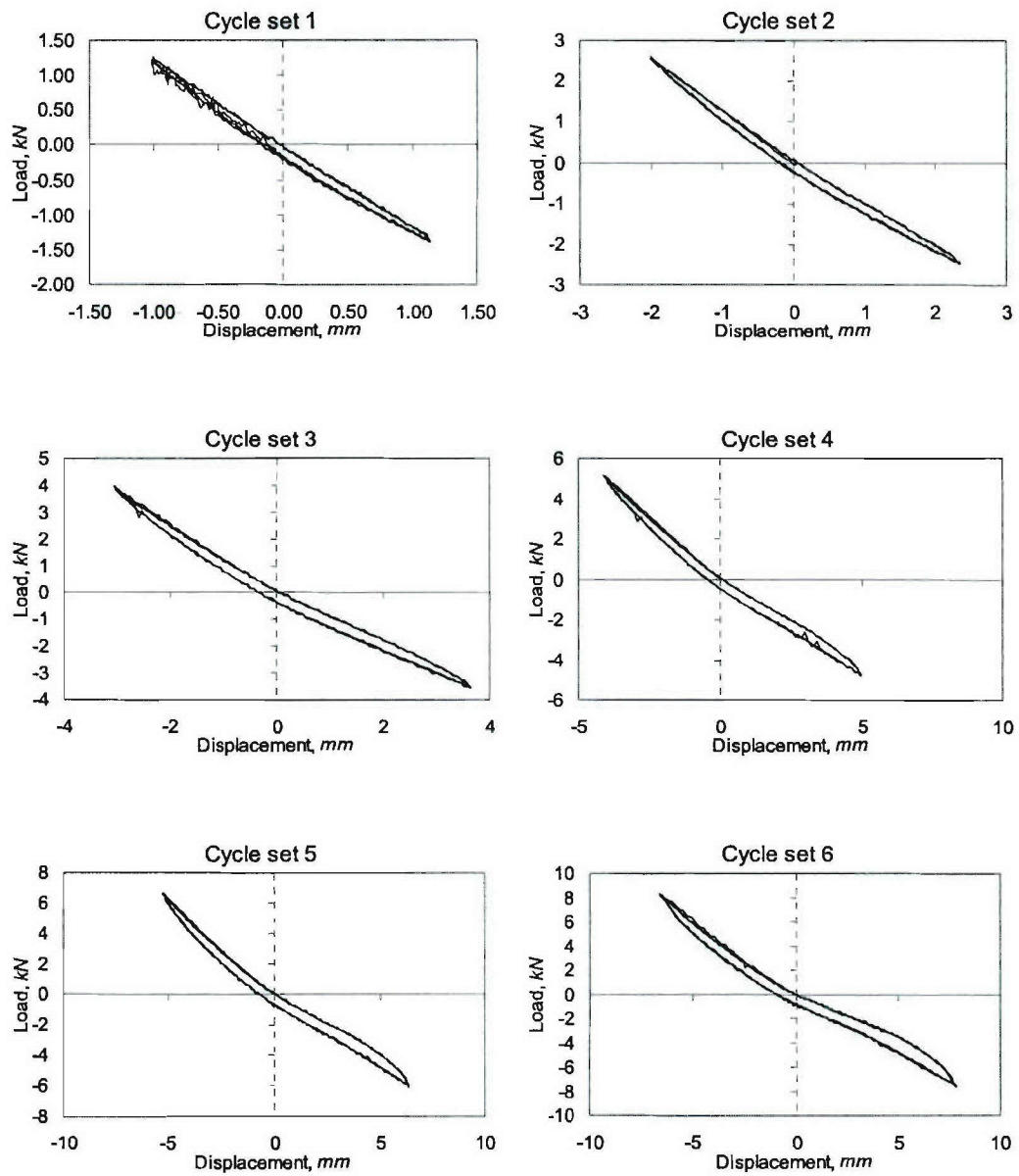


**Figure D.5. Load-Displacement Curves for Specimen BP-3, Cycle Sets 1-6**

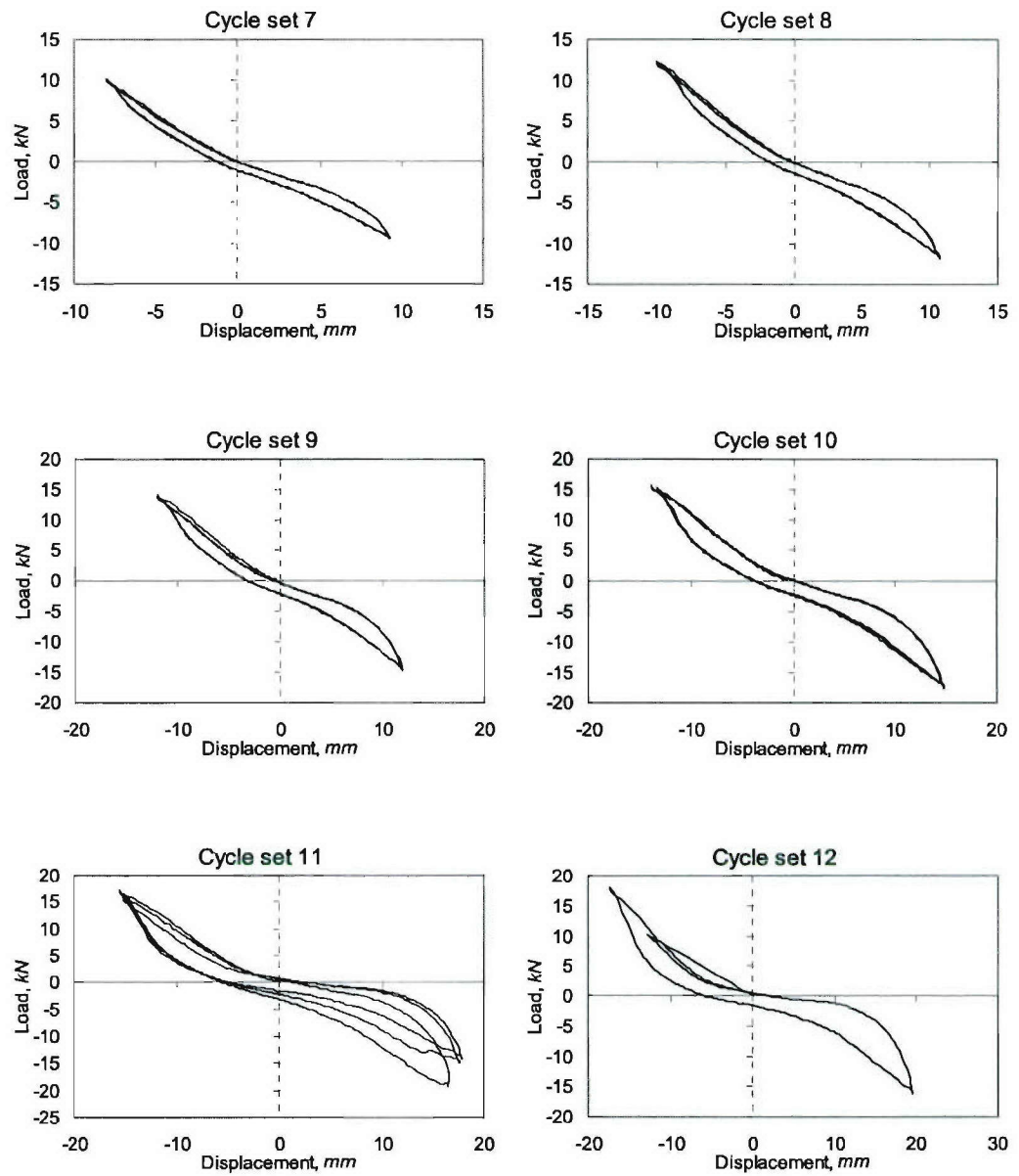


**Figure D.6. Load-Displacement Curves for Specimen BP-3, Cycle Sets 7-12**



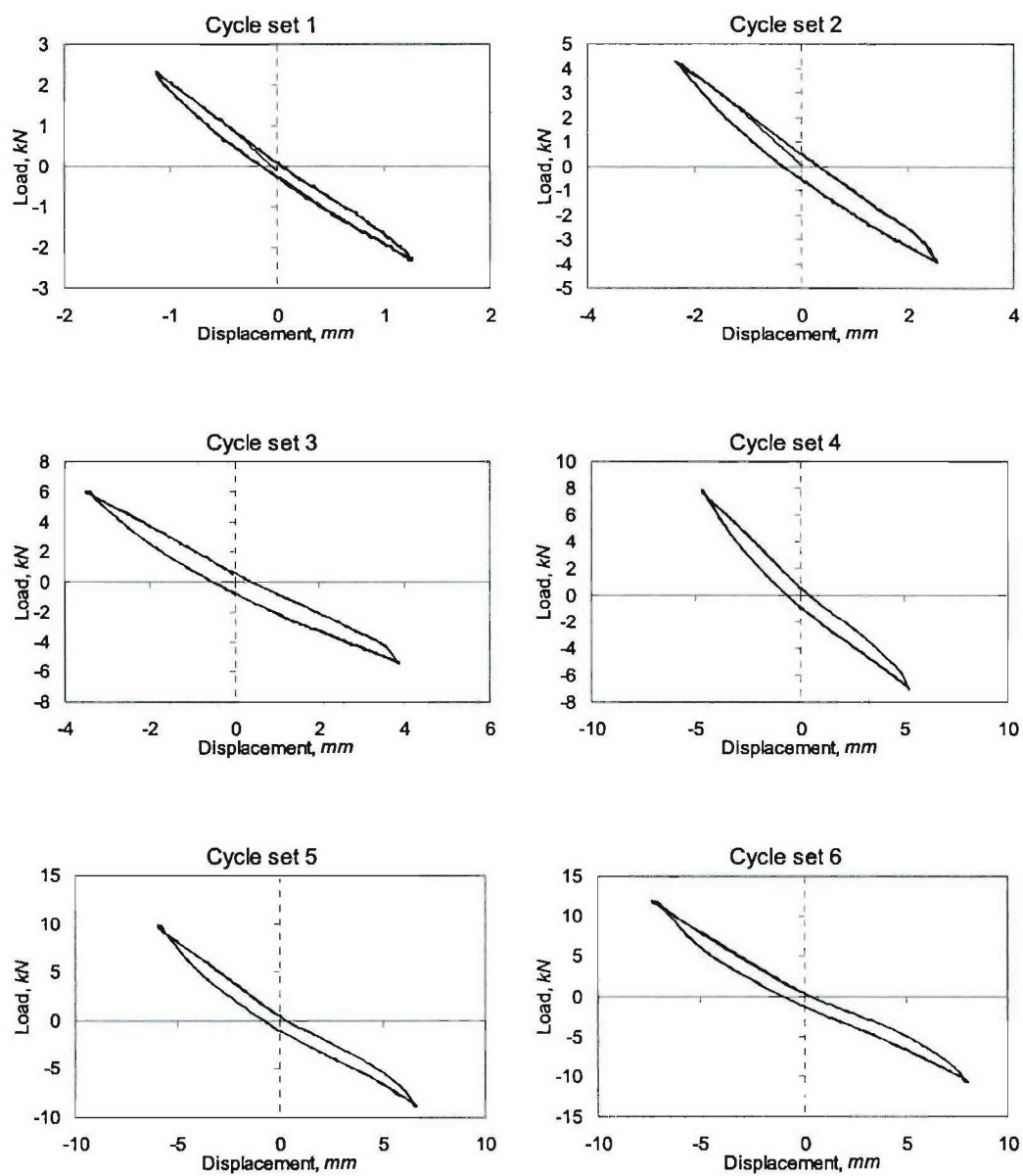


**Figure D.7. Load-Displacement Curves for Specimen BT-4, Cycle Sets 1-6**

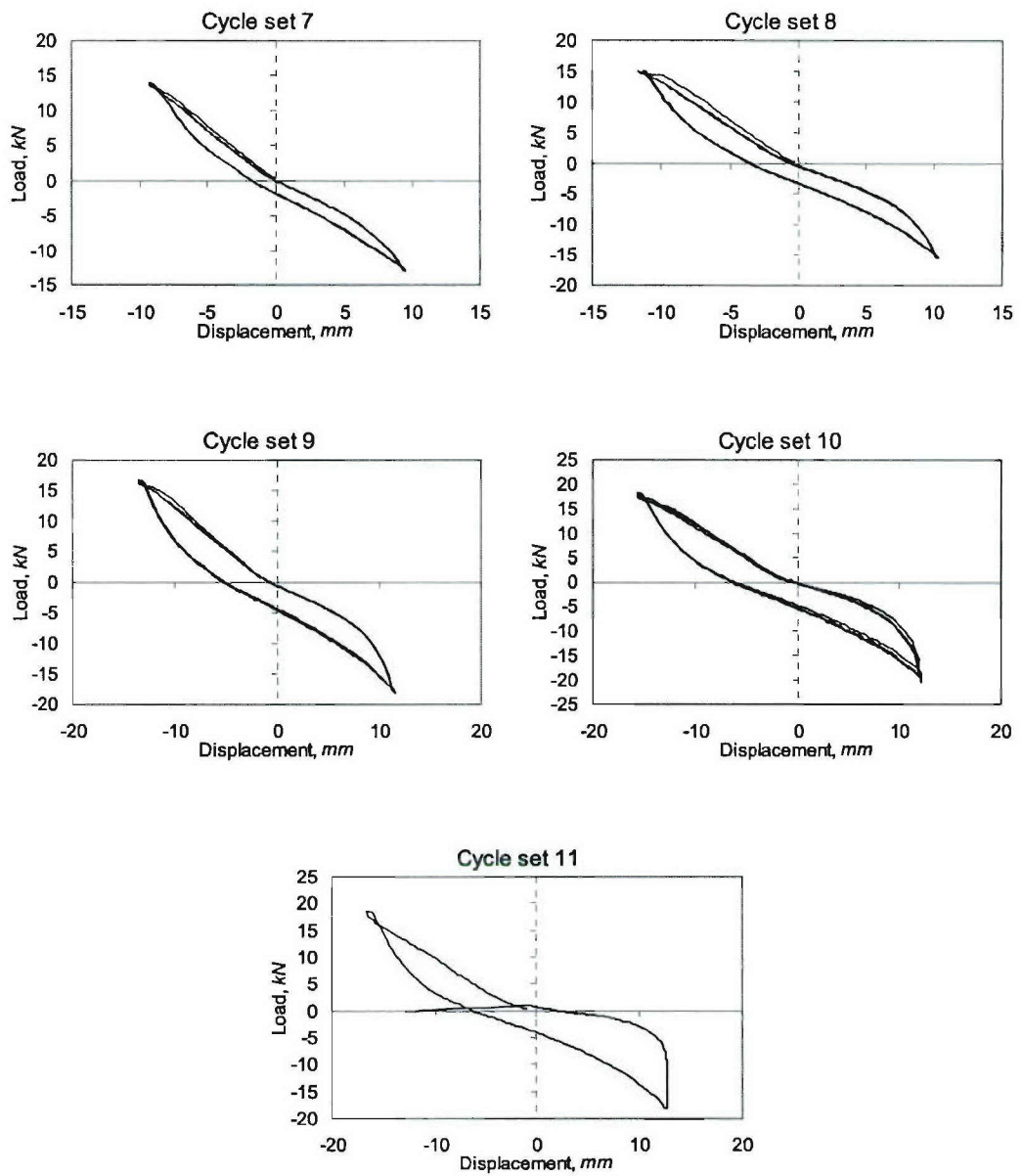


**Figure D.8. Load-Displacement Curves for Specimen BT-4, Cycle Sets 7-11**

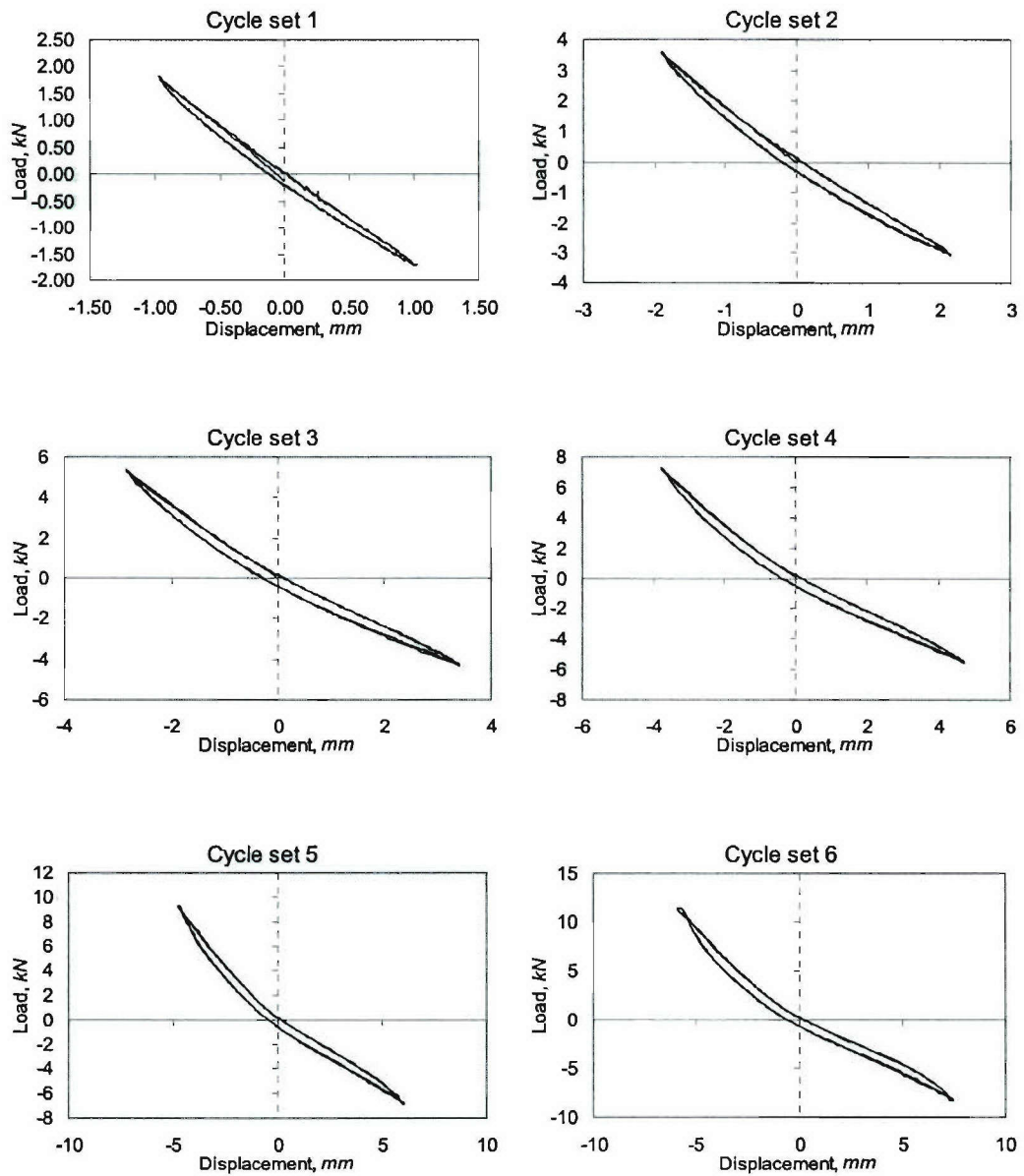
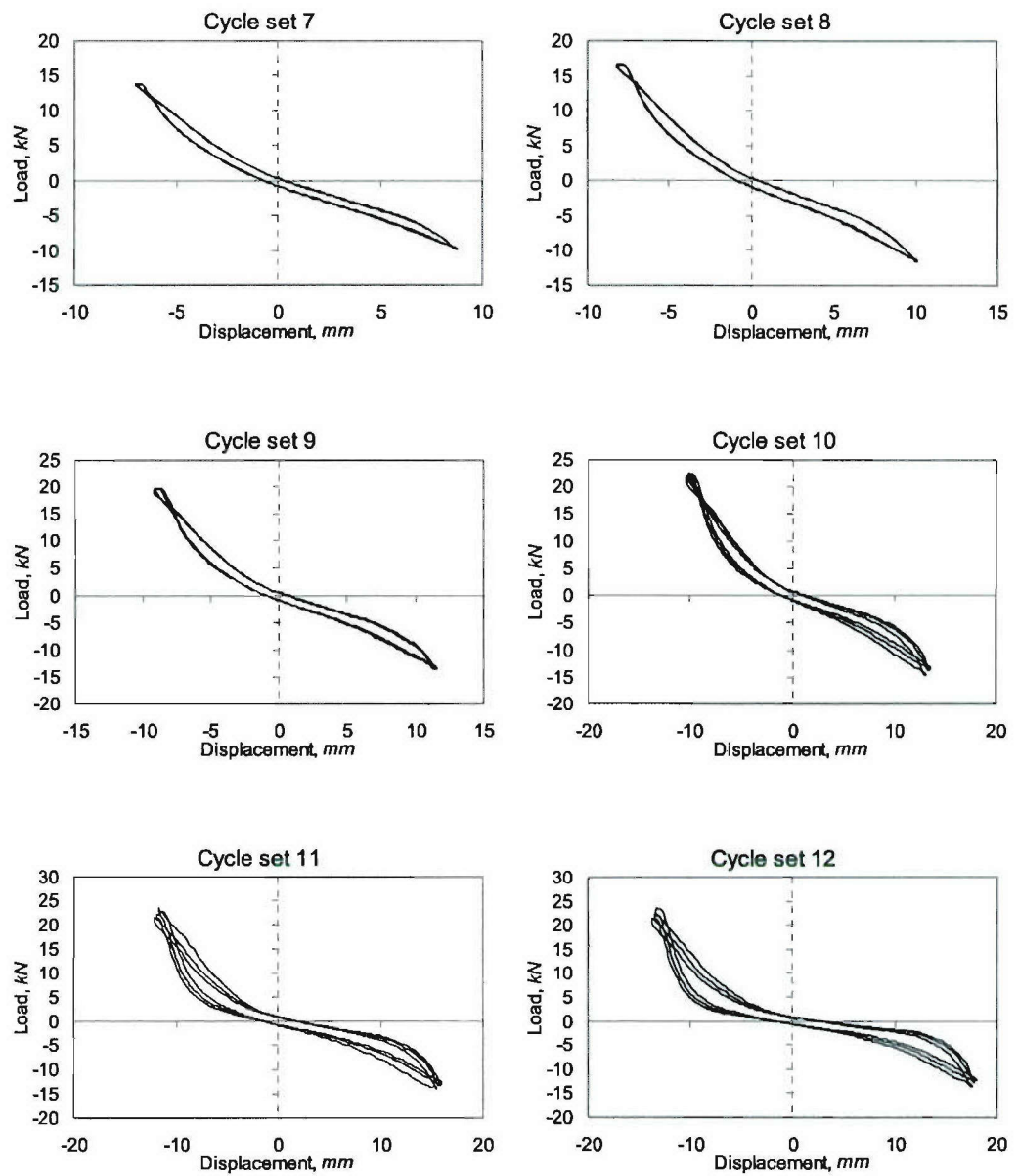
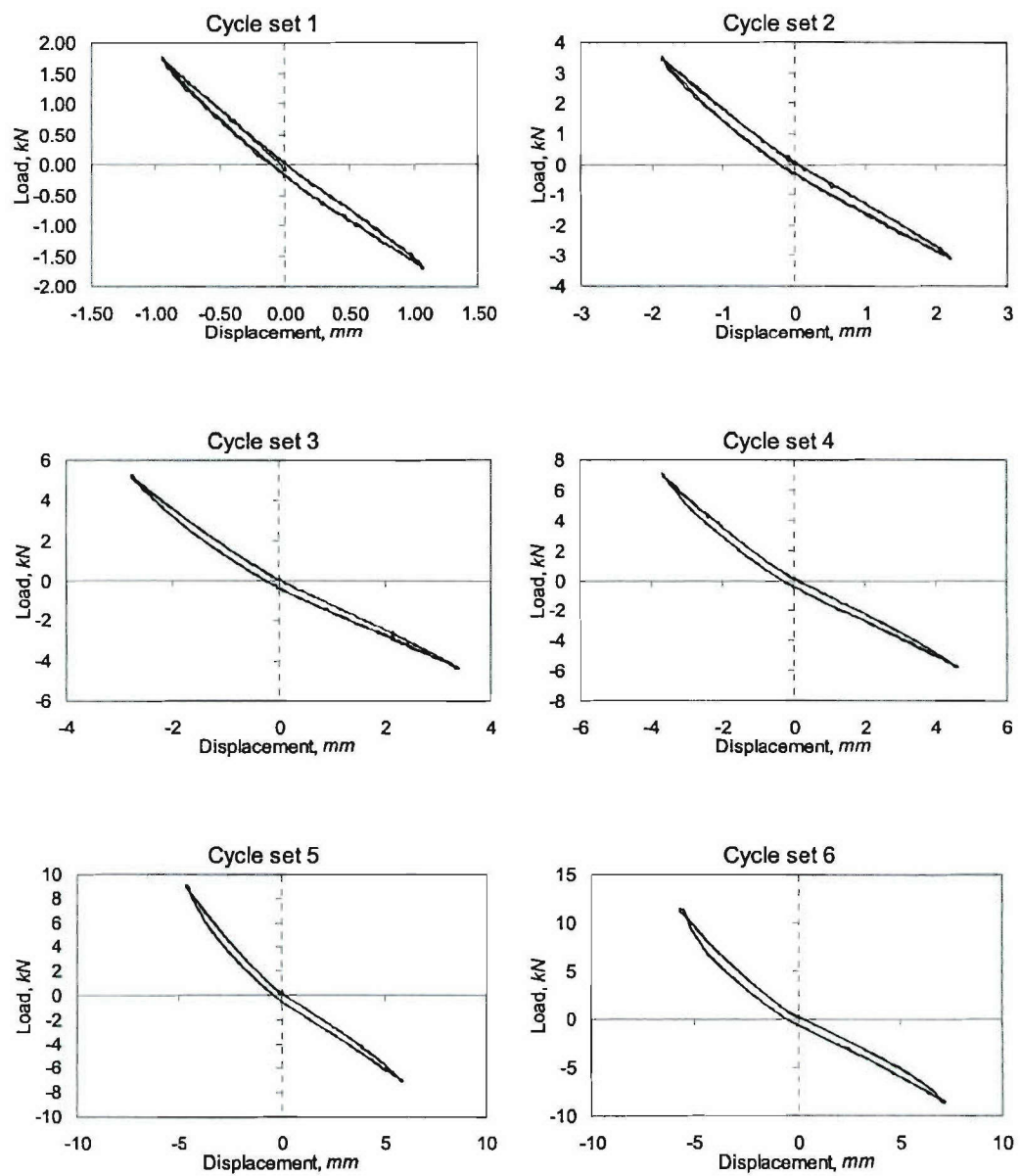


Figure D.9. Load-Displacement Curves for Specimen BP-5, Cycle Sets 1-6



**Figure D.10. Load-Displacement Curves for Specimen BP-5, Cycle Sets 7-12**





**Figure D.11. Load-Displacement Curves for Specimen BT-6, Cycle Sets 1-6**

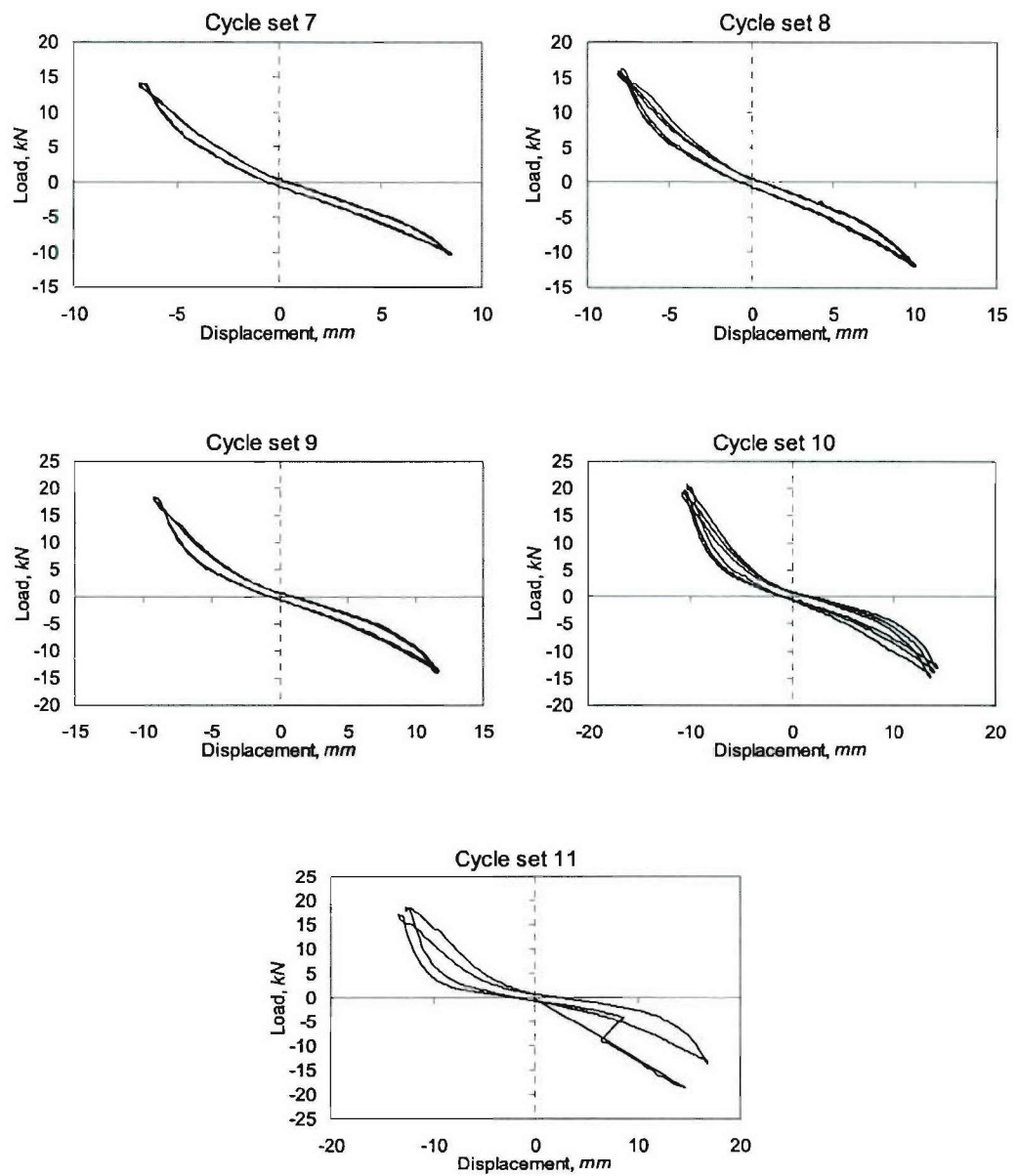


**Figure D.12. Load-Displacement Curves for Specimen BT-6, Cycle Sets 7-12**

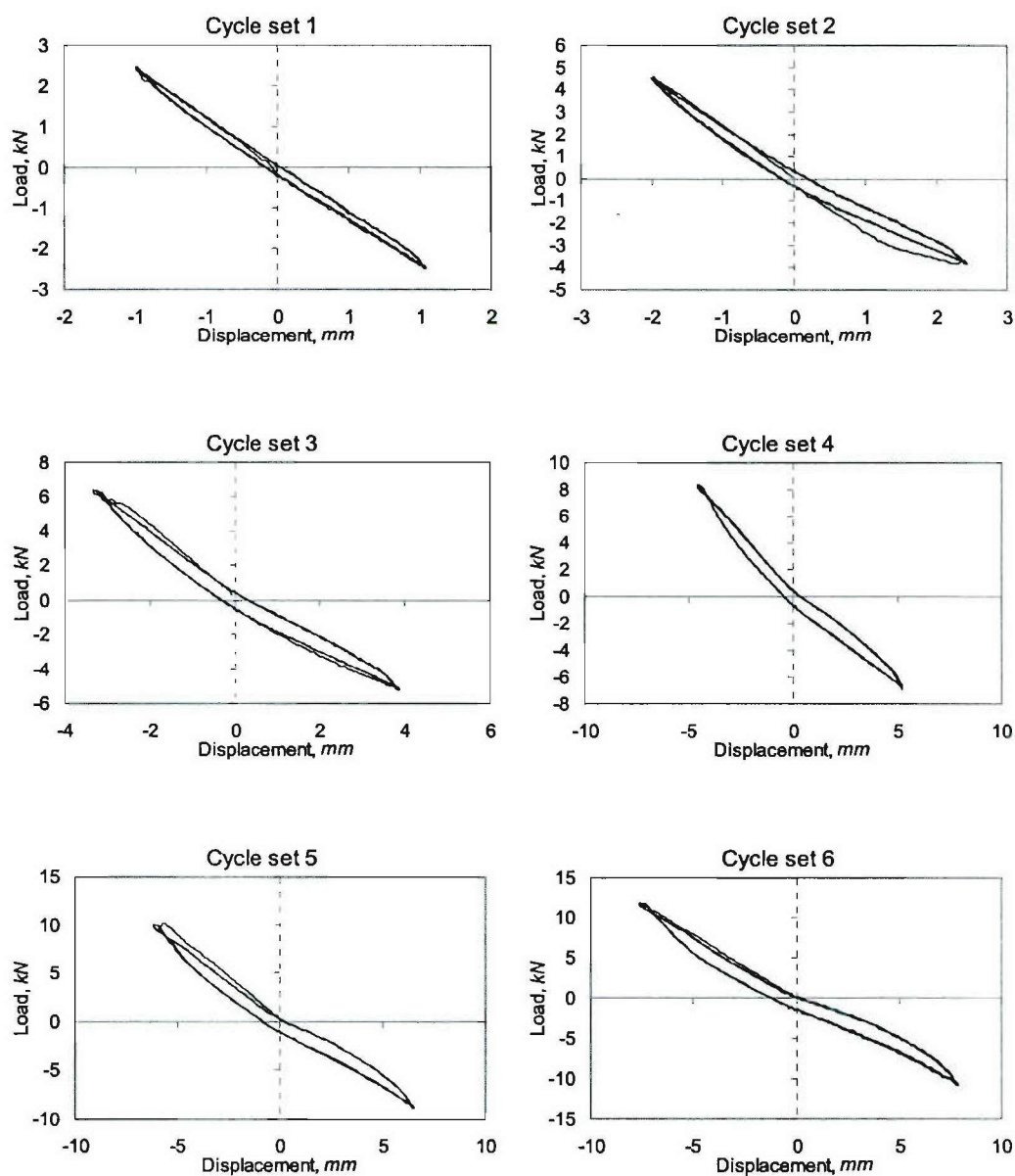


**Figure D.13. Load-Displacement Curves for Specimen BT-7, Cycle Sets 1-6**

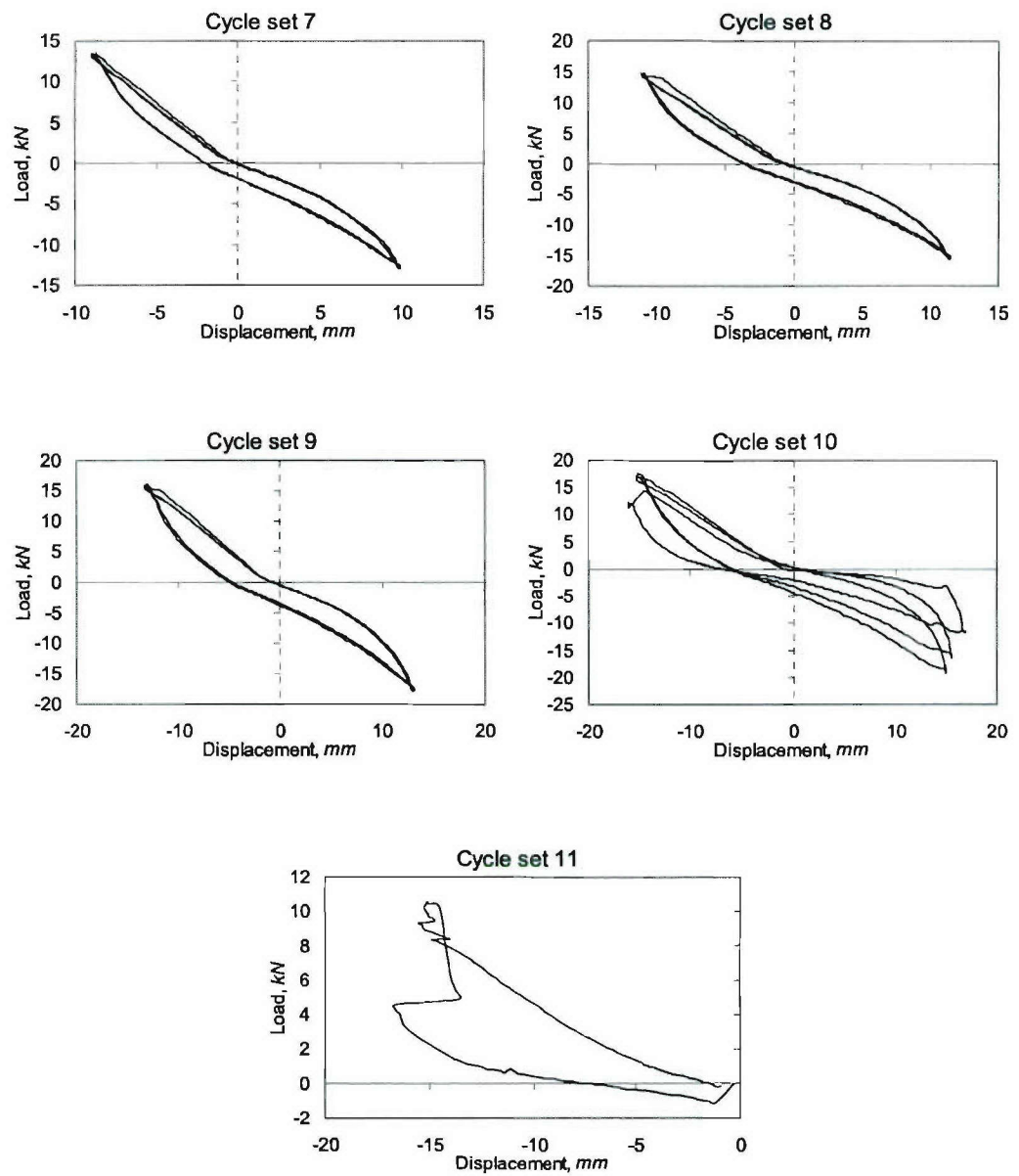


**Figure D.14. Load-Displacement Curves for Specimen BT-7, Cycle Sets 7-12**



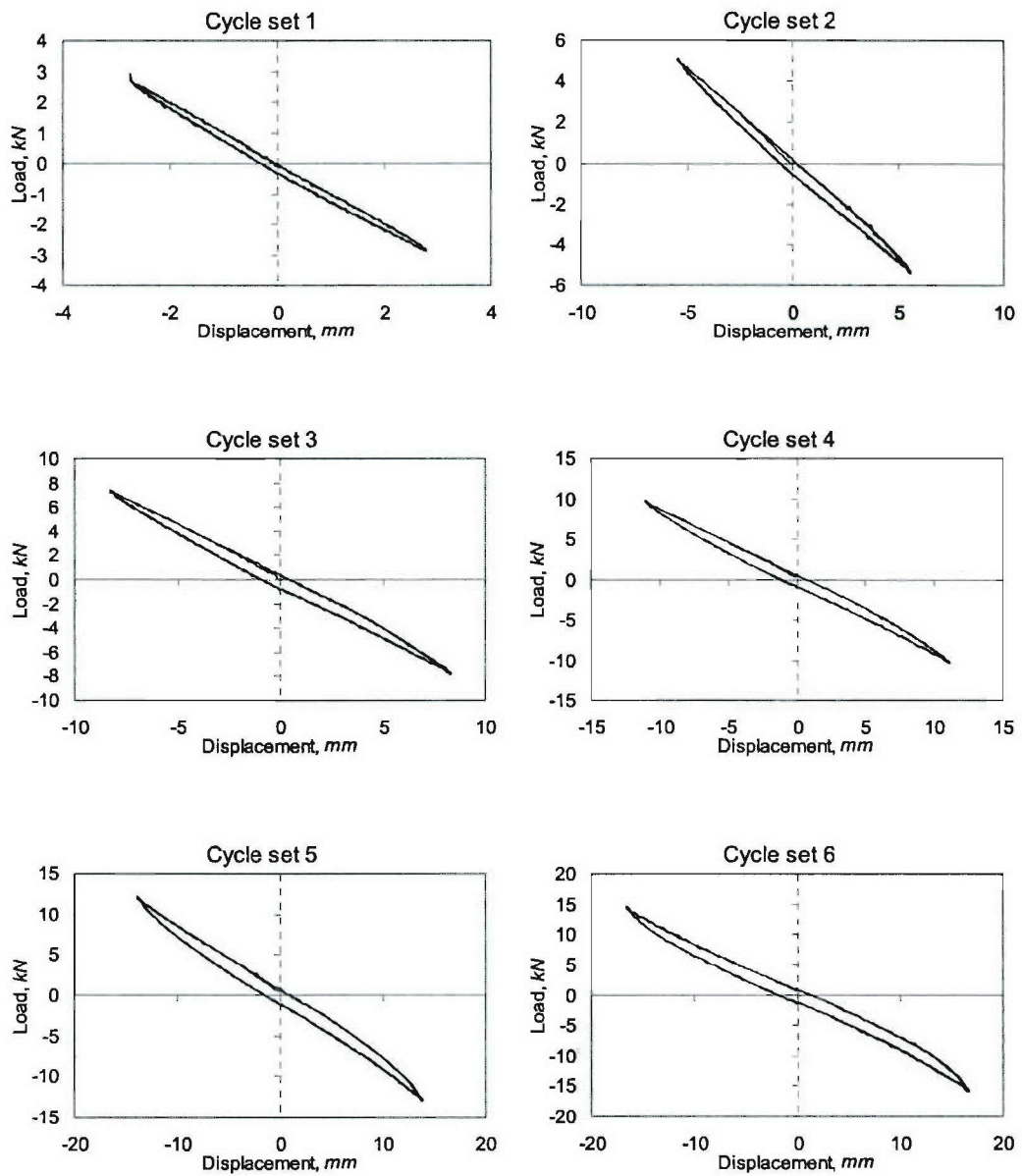


**Figure D.15. Load-Displacement Curves for Specimen DM-1, Cycle Sets 1-6**

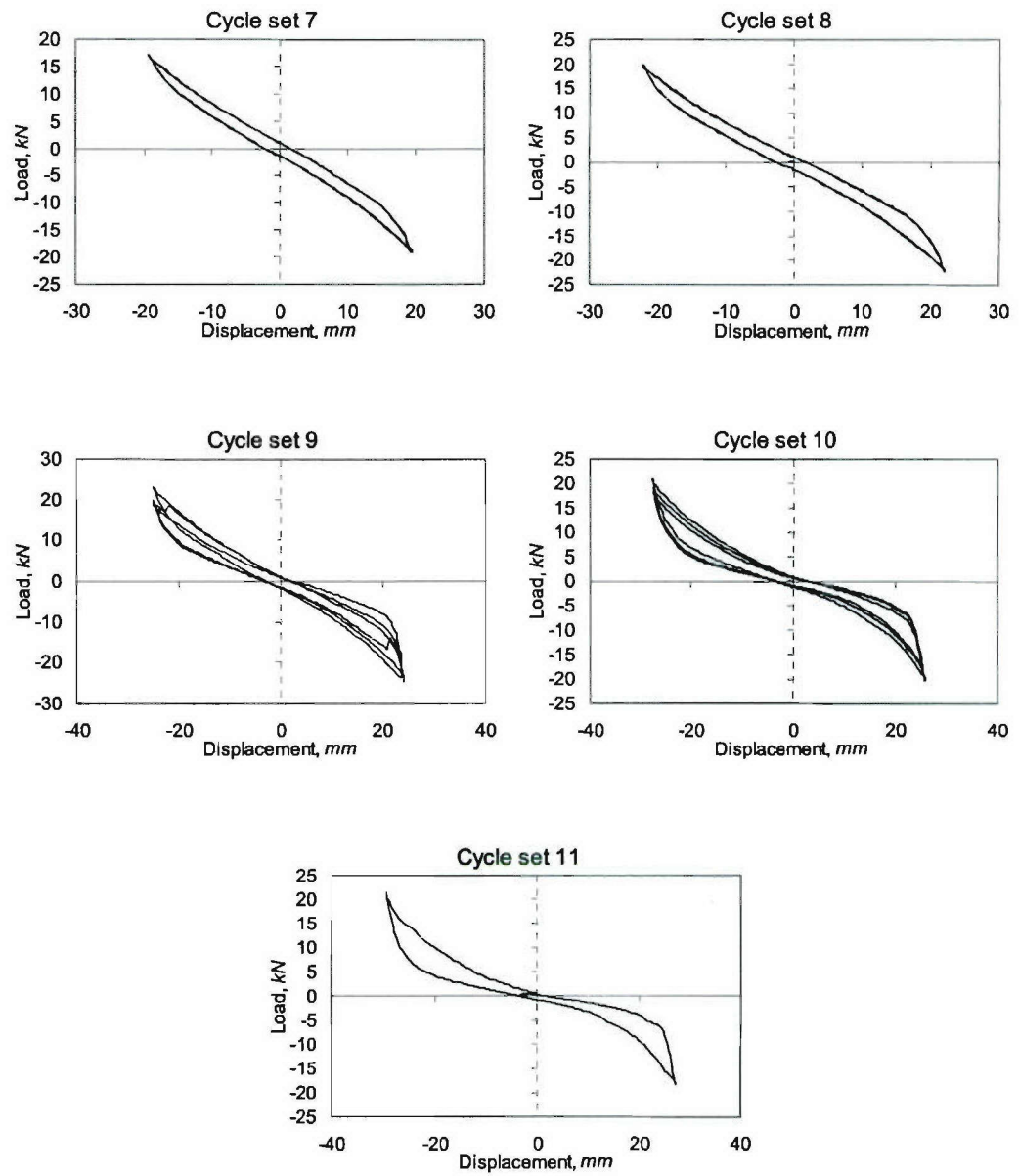


**Figure D.16. Load-Displacement Curves for Specimen DM-1, Cycle Sets 7-12**

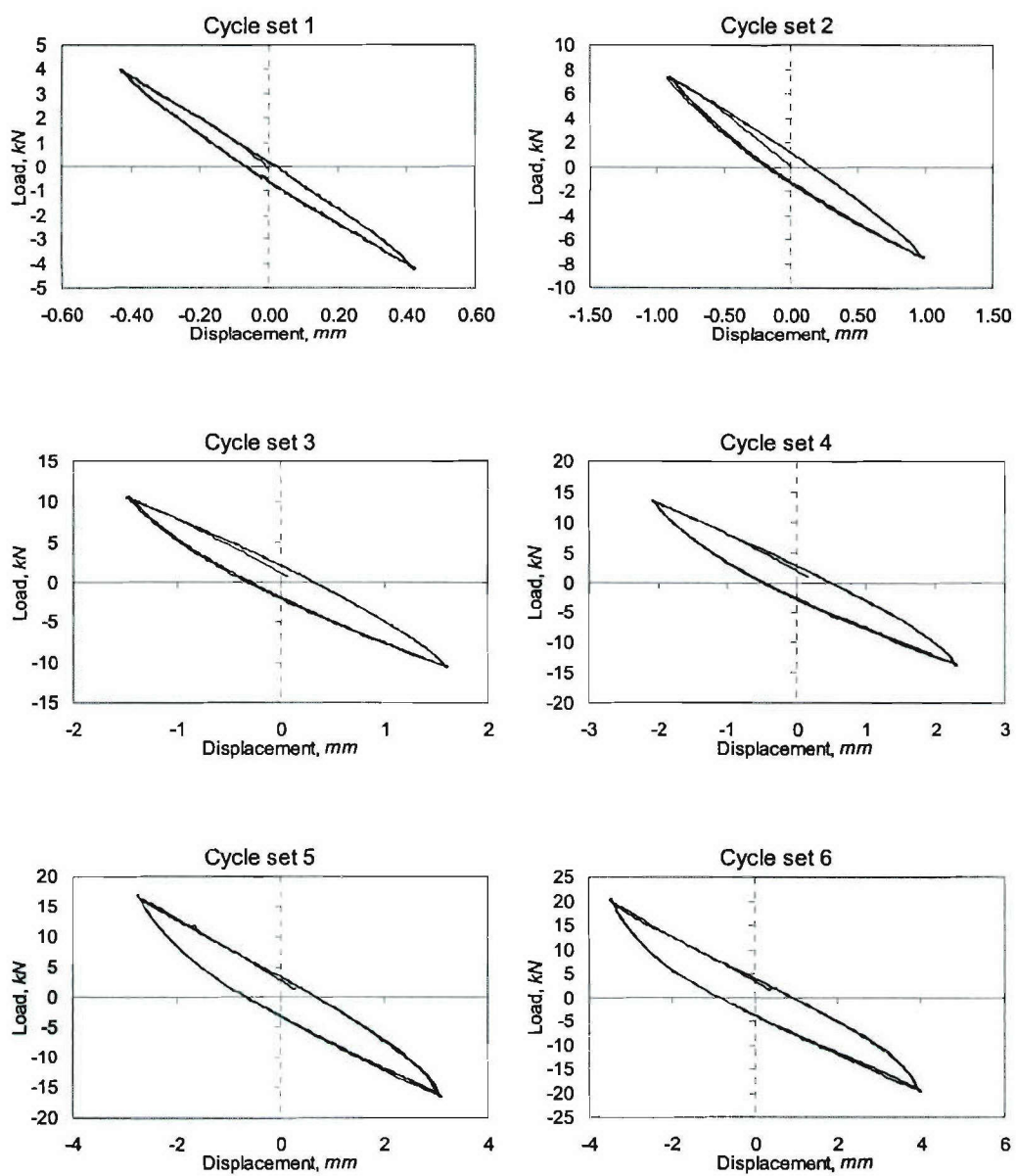


**Figure D.17. Load-Displacement Curves for Specimen DL-2, Cycle Sets 1-6**

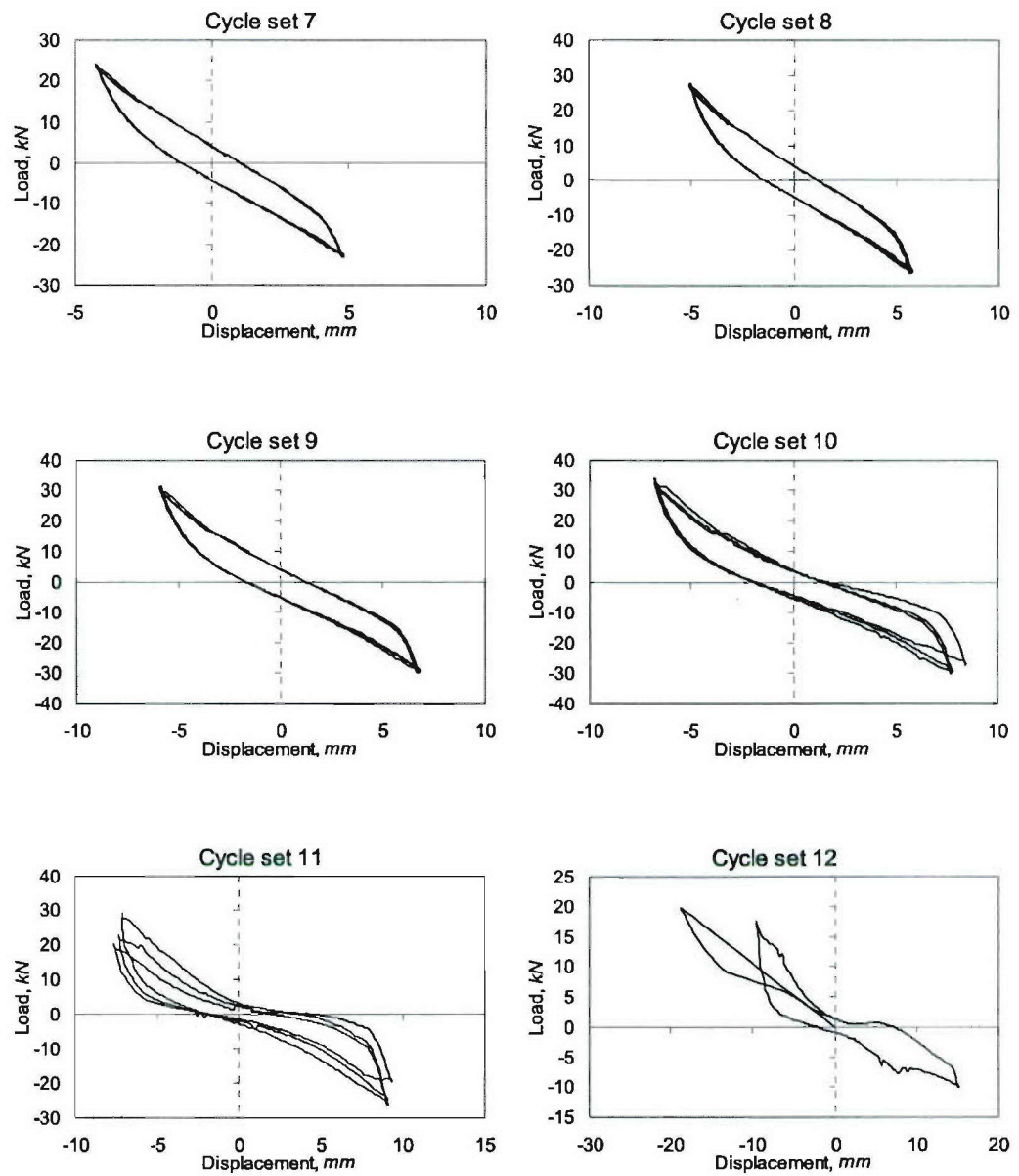


**Figure D.18. Load-Displacement Curves for Specimen DL-2, Cycle Sets 7-12**



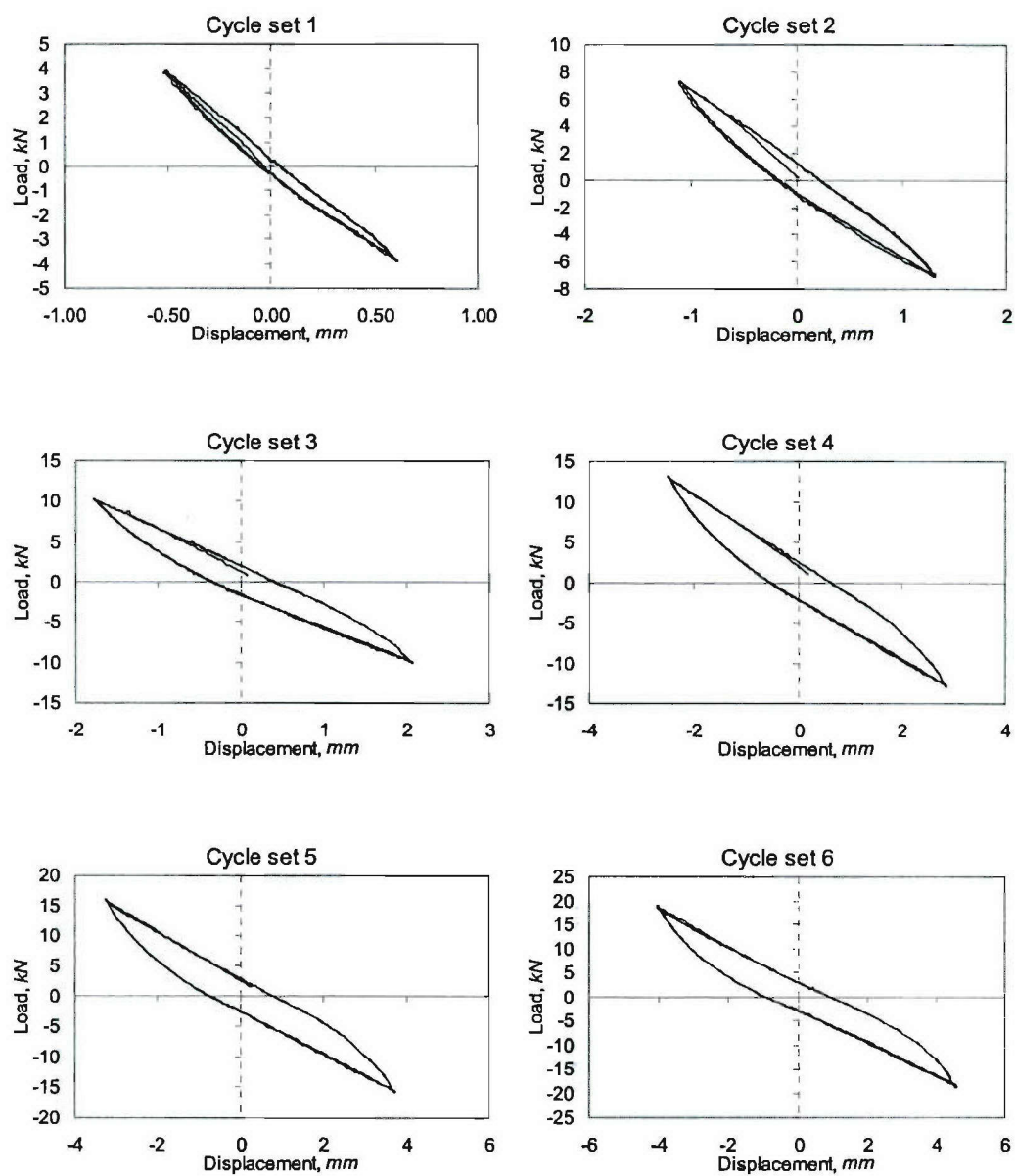


**Figure D.19. Load-Displacement Curves for Specimen DL-3, Cycle Sets 1-6**

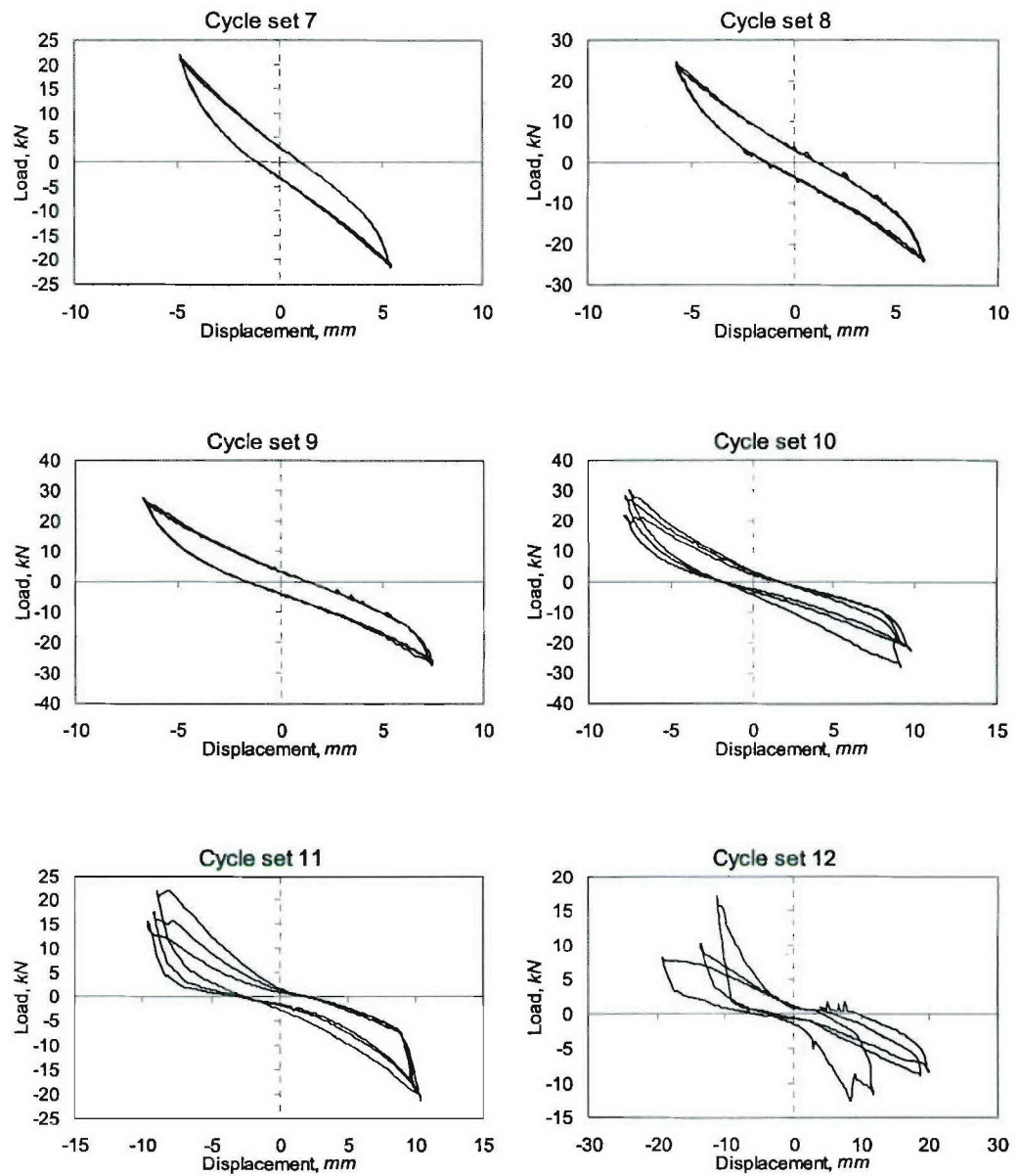


**Figure D.20. Load-Displacement Curves for Specimen DL-3, Cycle Sets 6-12**

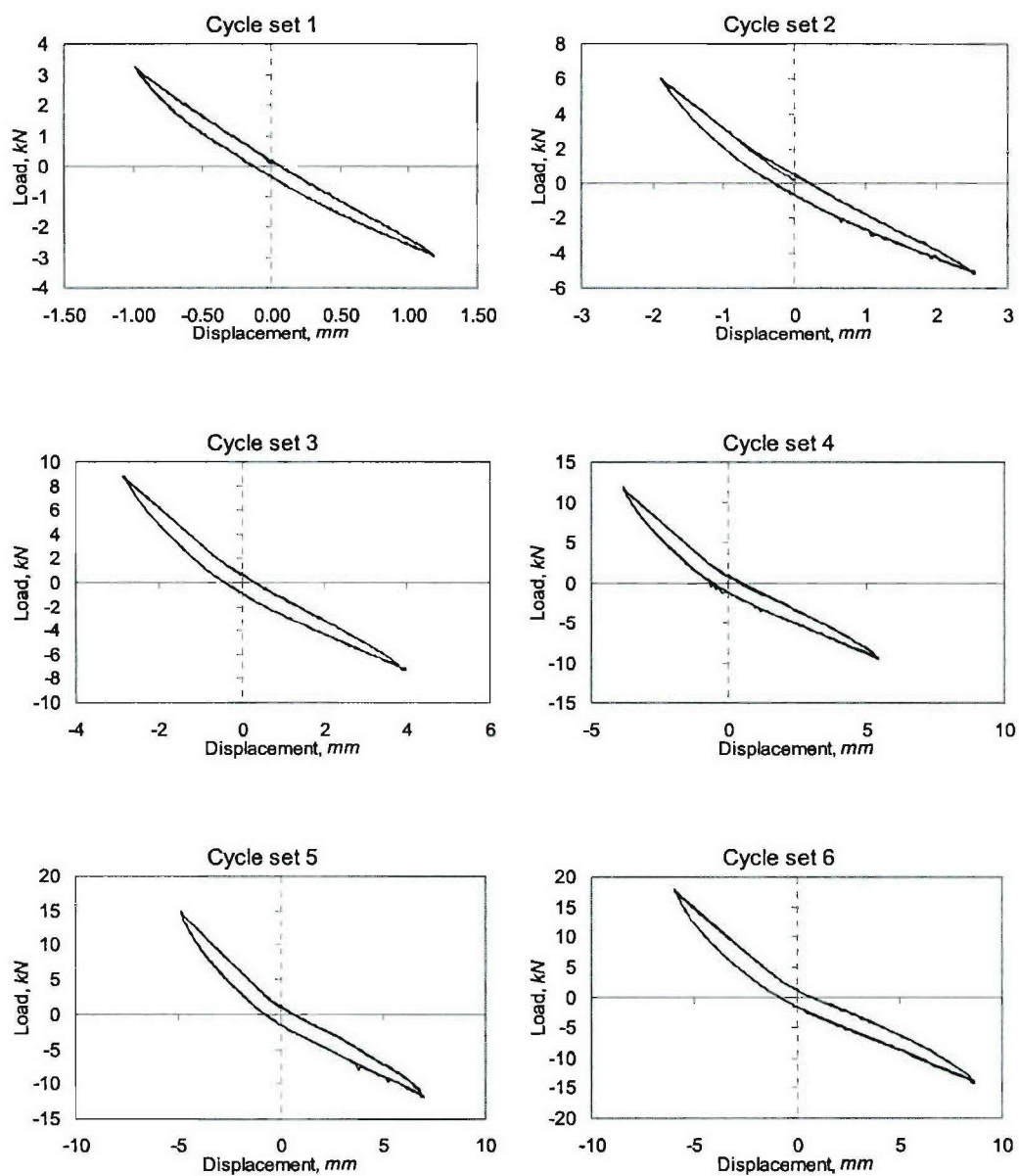


**Figure D.21. Load-Displacement Curves for Specimen DS-4, Cycle Sets 1-6**

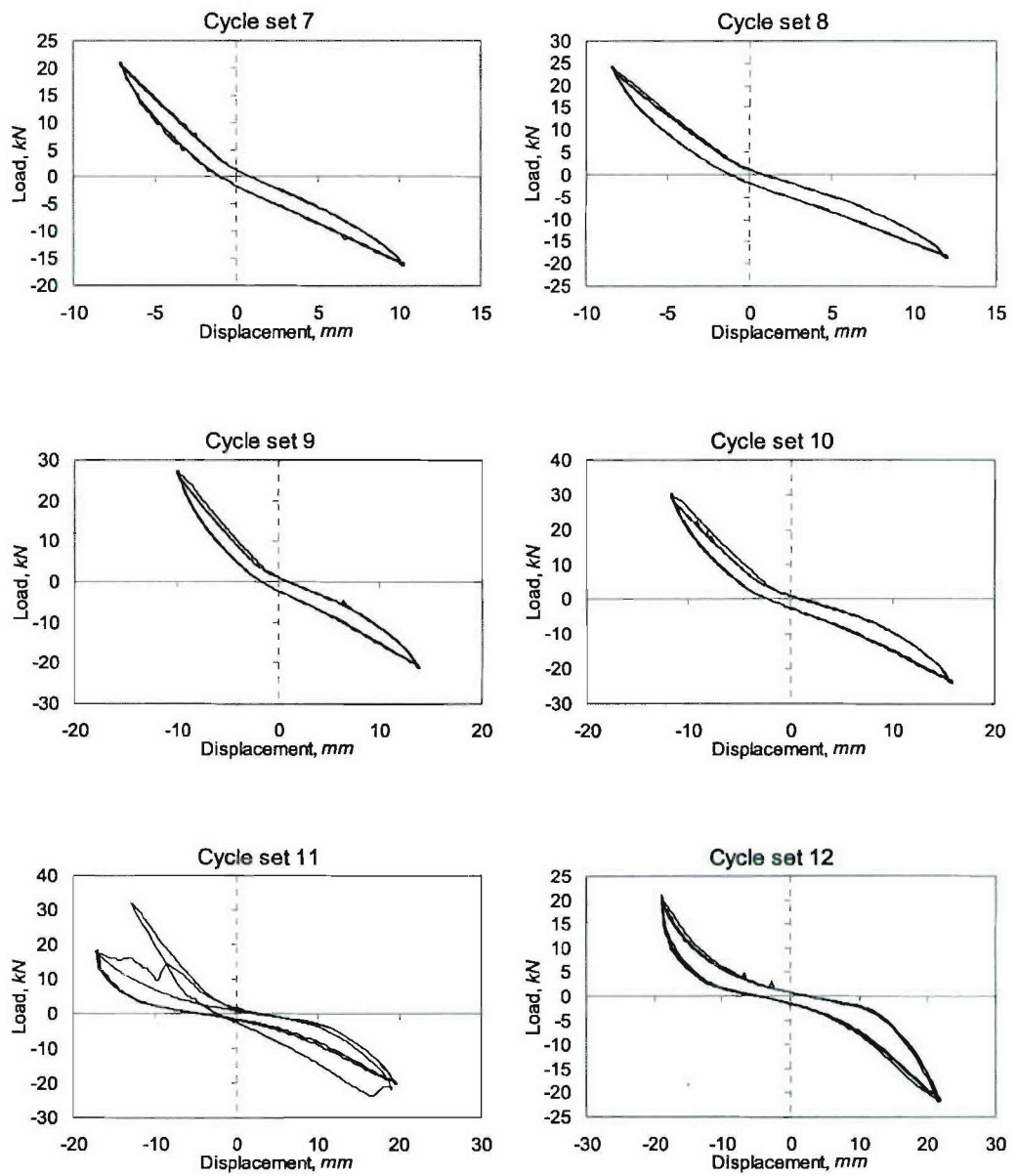


**Figure D.22. Load-Displacement Curves for Specimen DS-4, Cycle Sets 7-12**



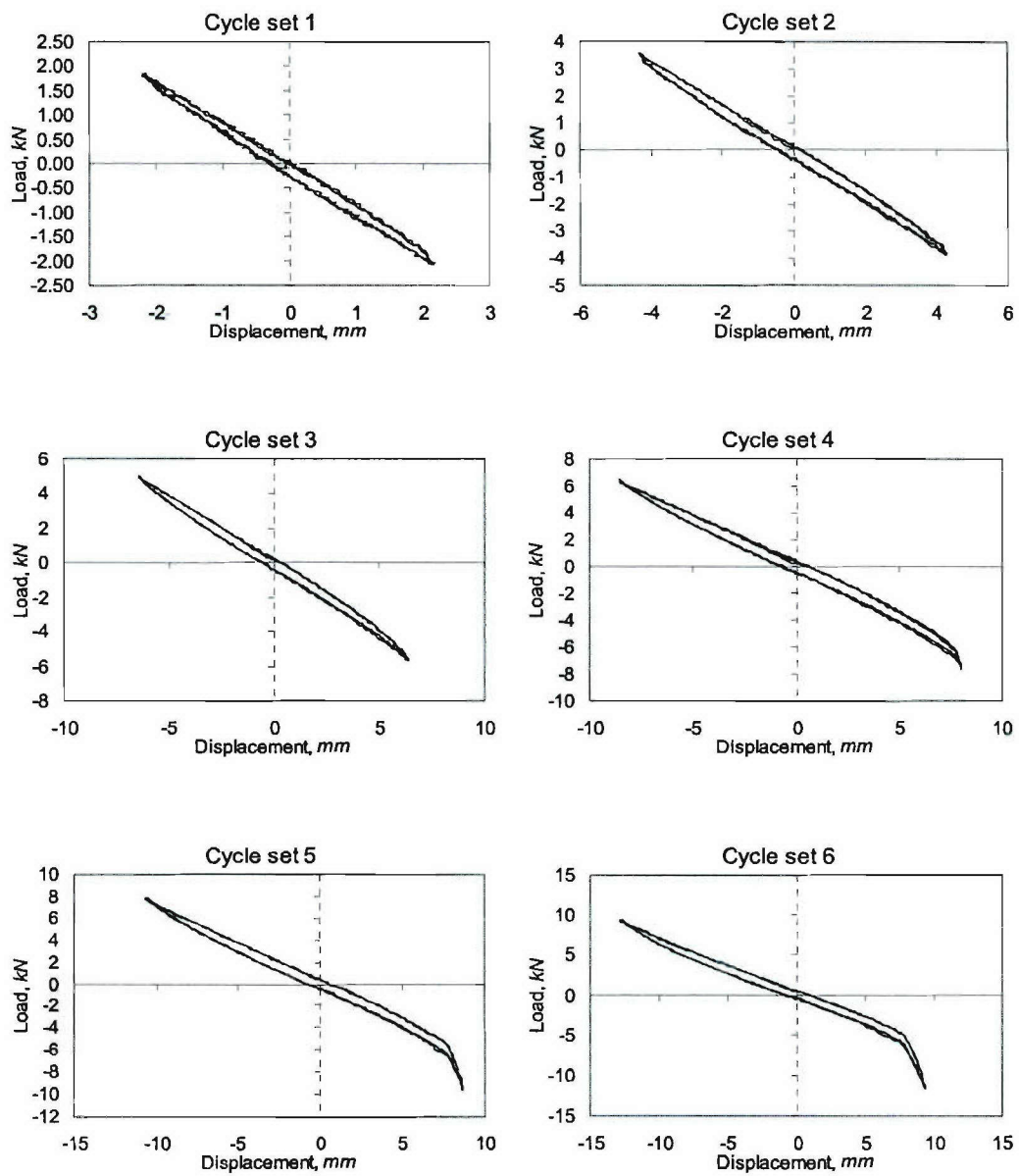


**Figure D.23. Load-Displacement Curves for Specimen DL-5, Cycle Sets 1-6**

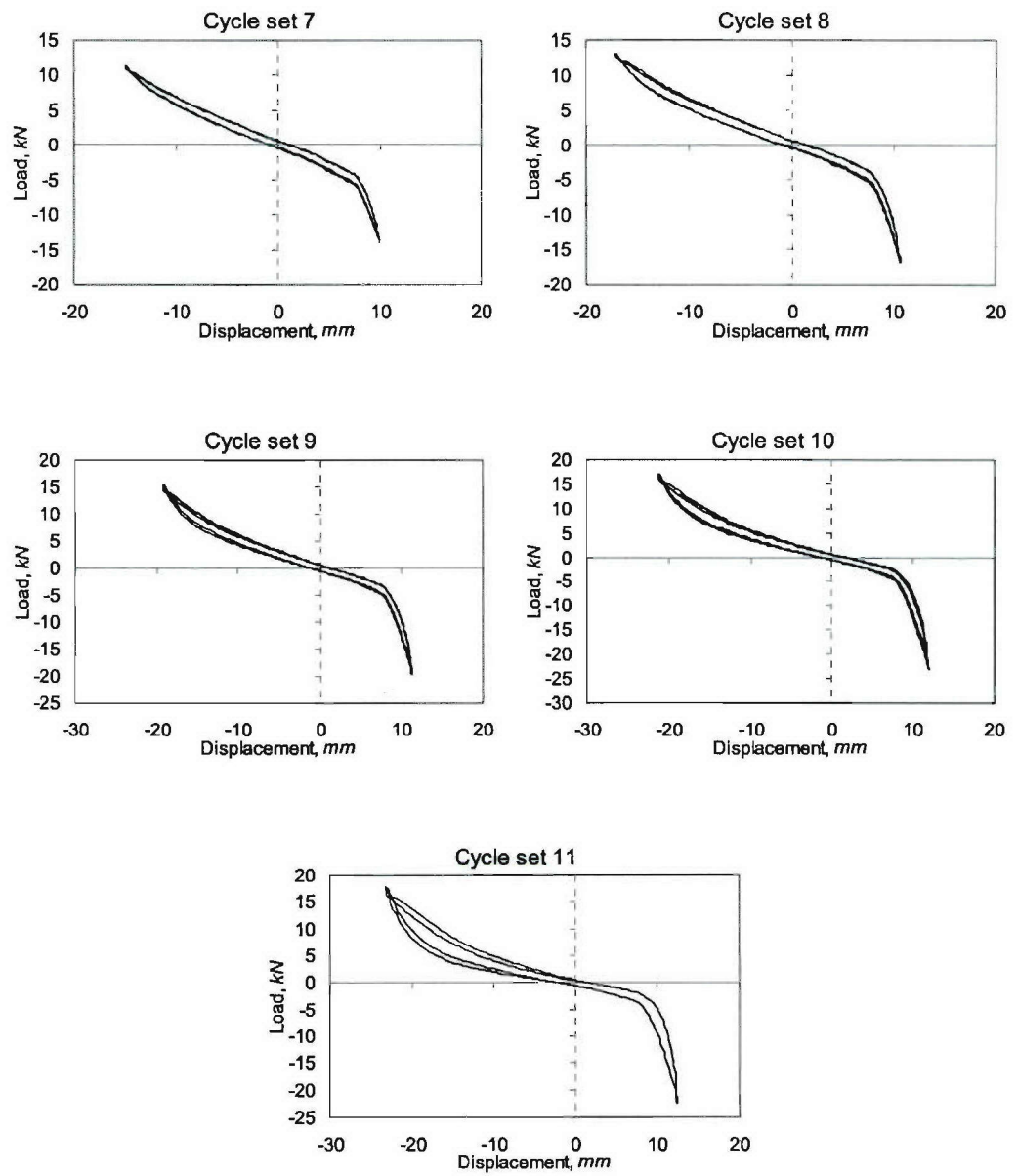


**Figure D.24. Load-Displacement Curves for Specimen DL-5, Cycle Sets 7-12**

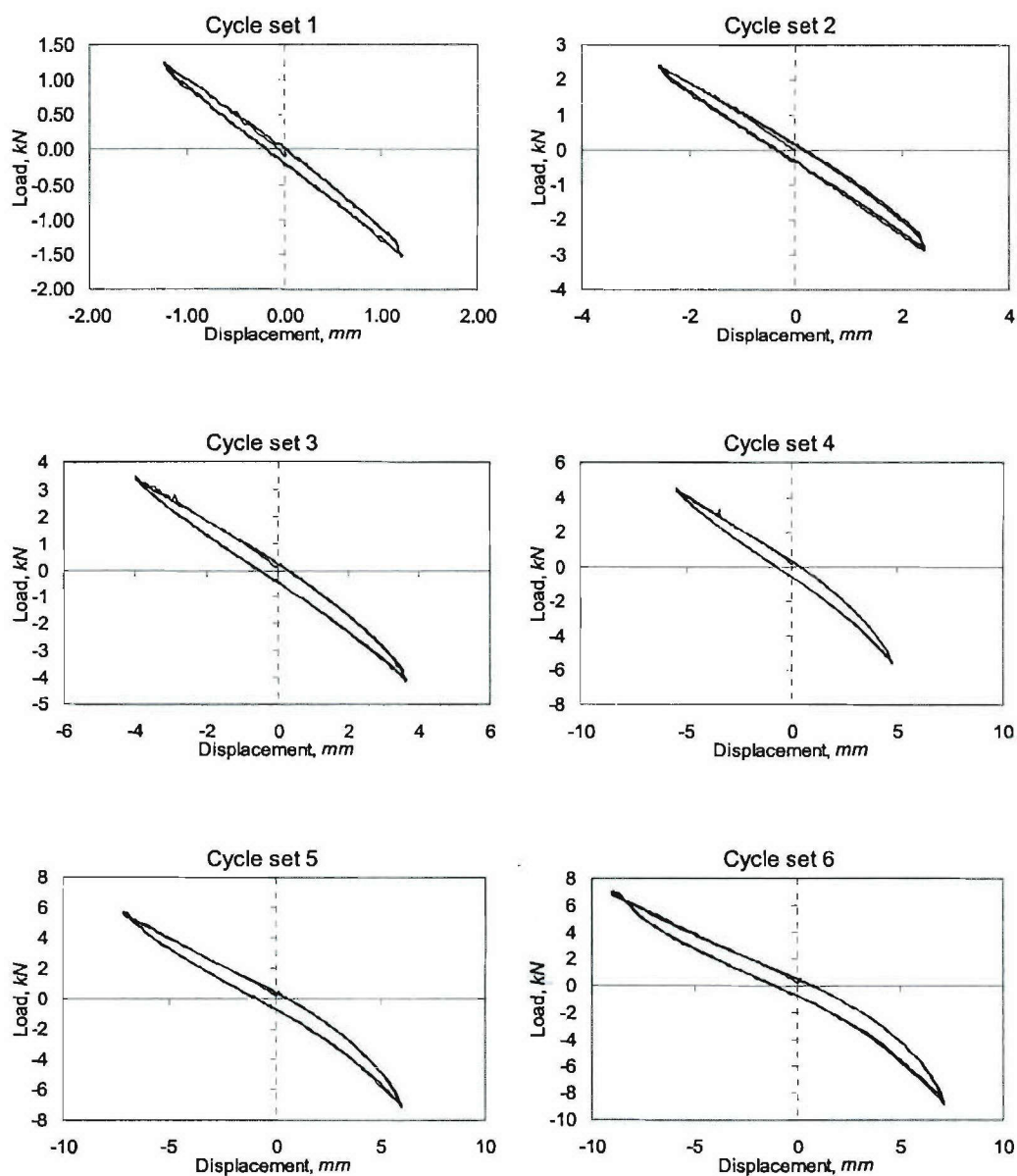


**Figure D.25. Load-Displacement Curves for Specimen DM-6, Cycle Sets 1-6**

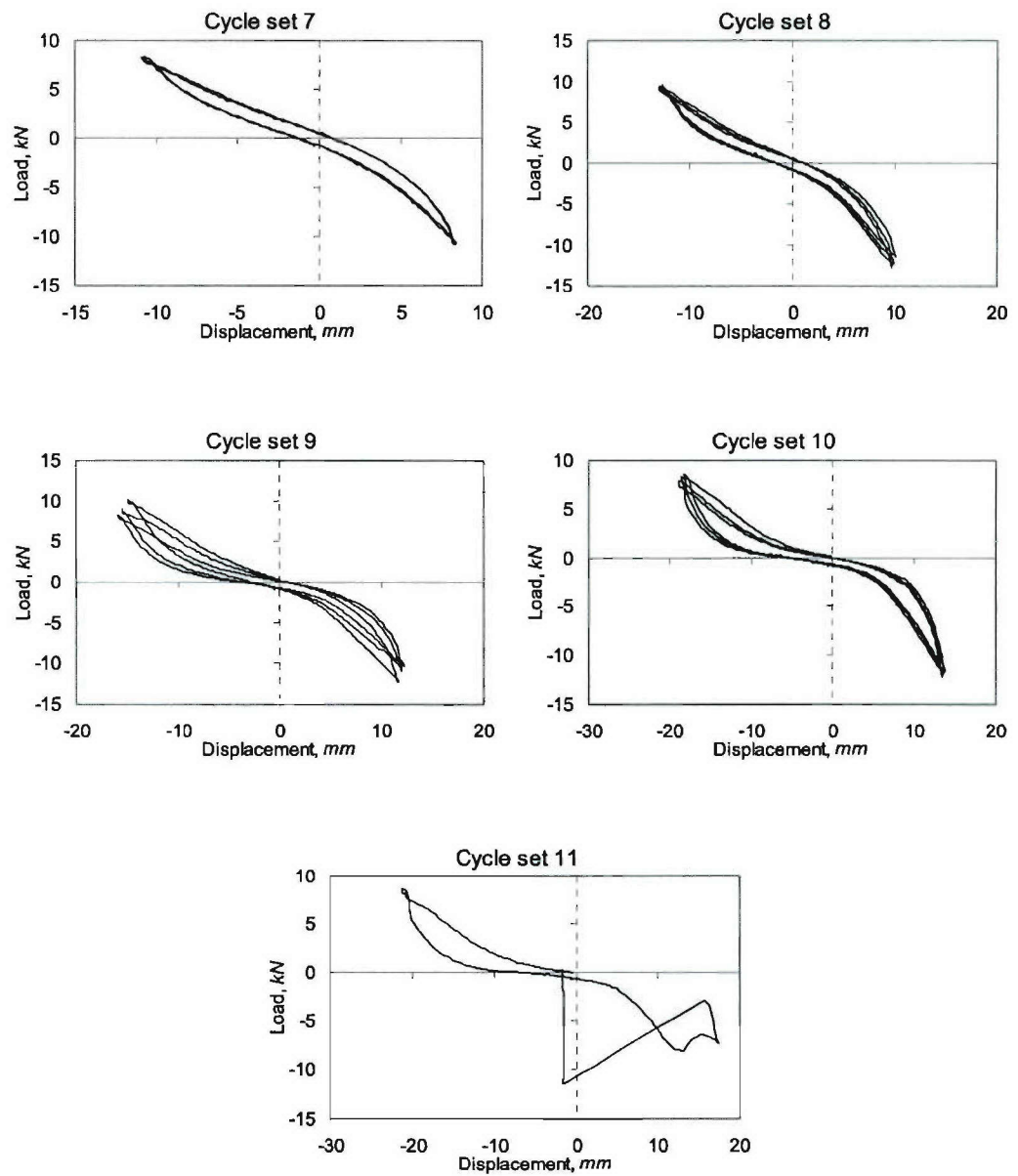
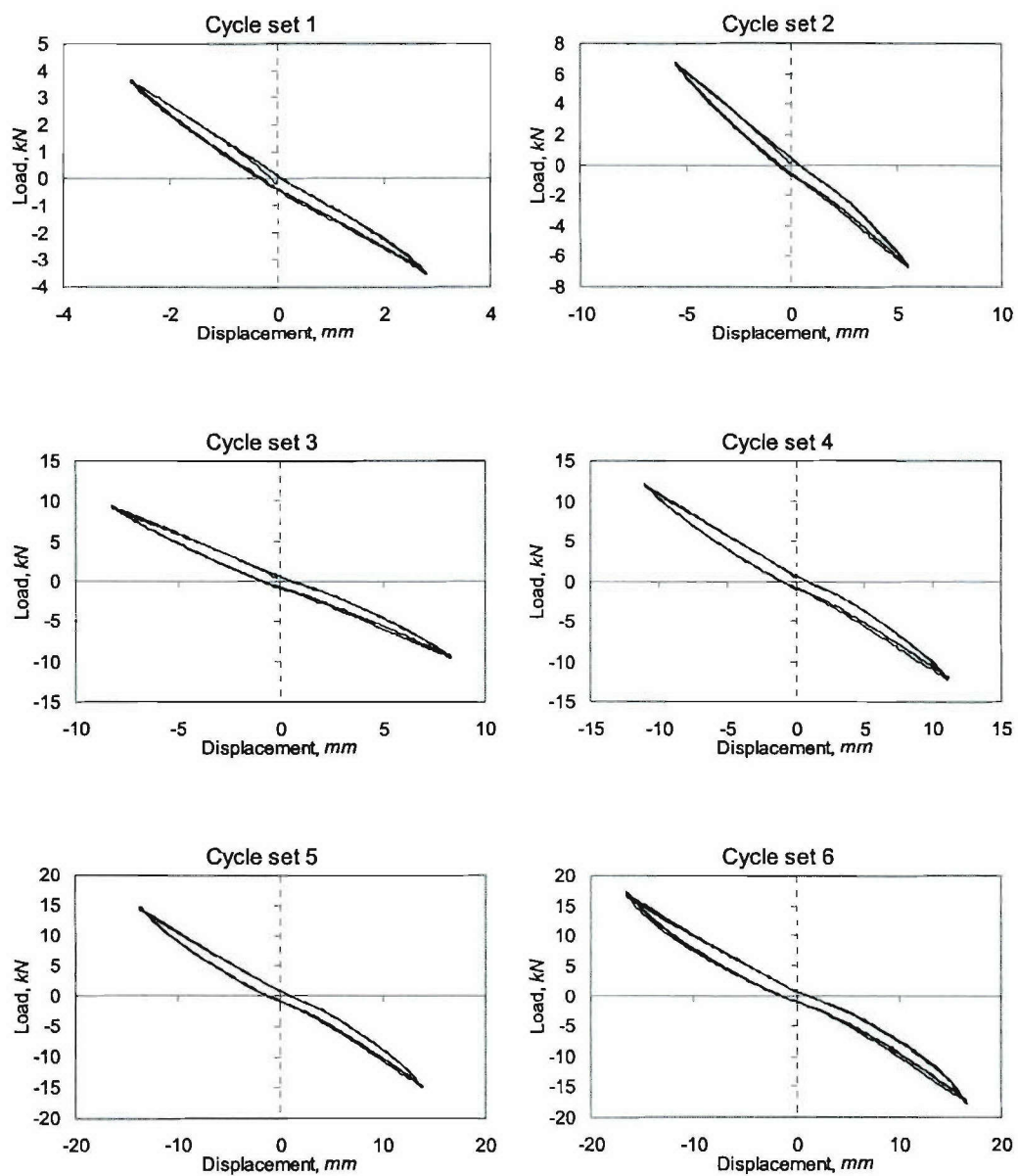
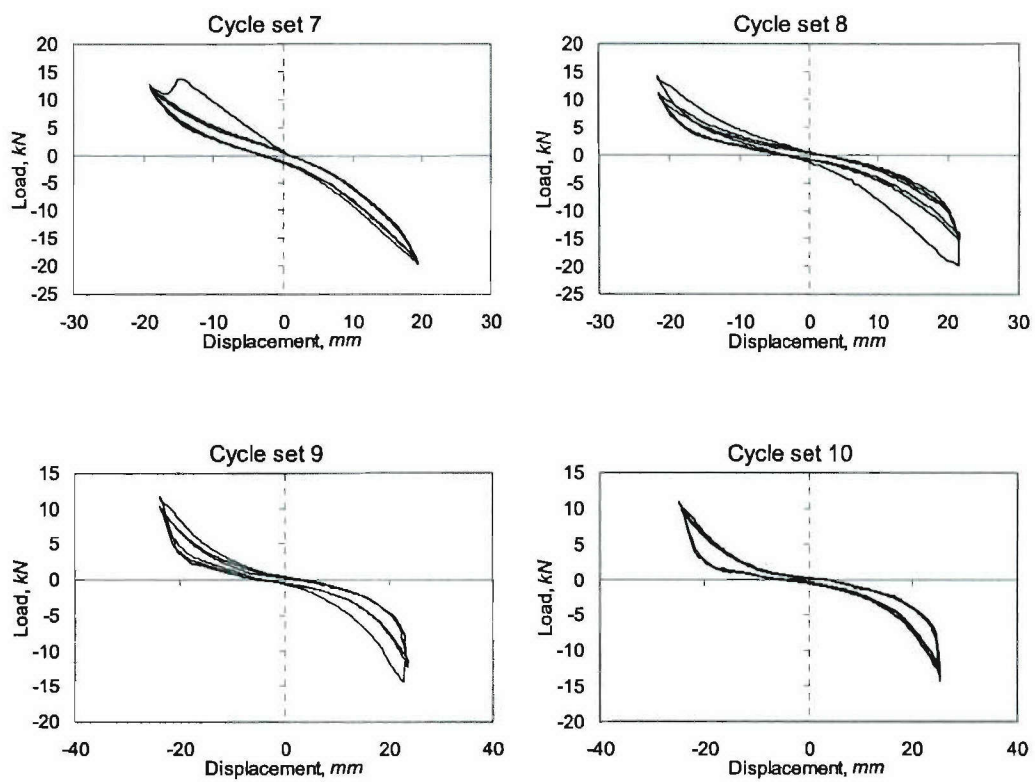


Figure D.26. Load-Displacement Curves for Specimen DM-6, Cycle Sets 7-12





**Figure D.27. Load-Displacement Curves for Specimen DL-7, Cycle Sets 1-6**



**Figure D.28. Load-Displacement Curves for Specimen DL-7, Cycle Sets 7-12**

## Appendix E

### Load versus Inner Displacement Plots of Hybrid Joints

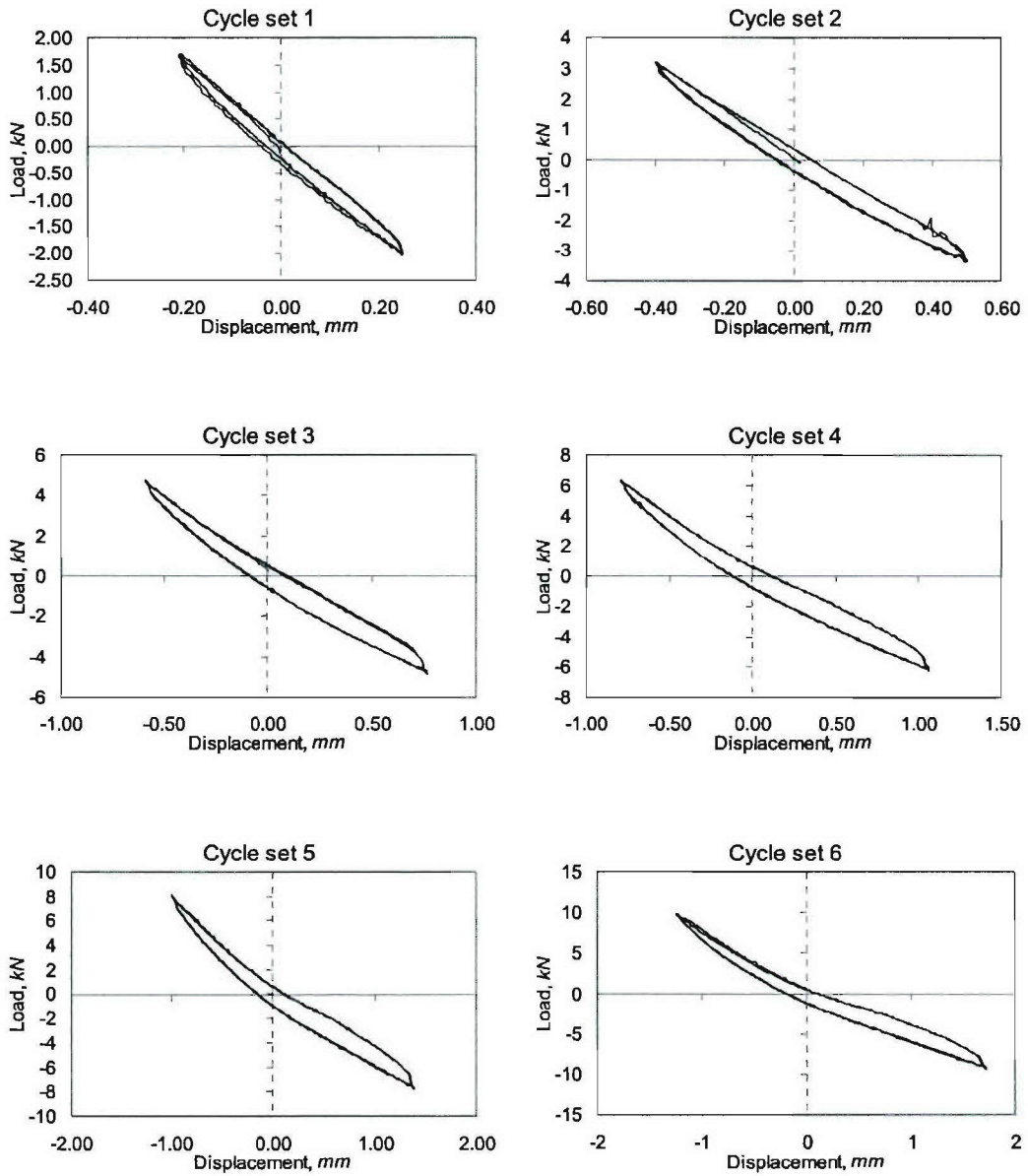
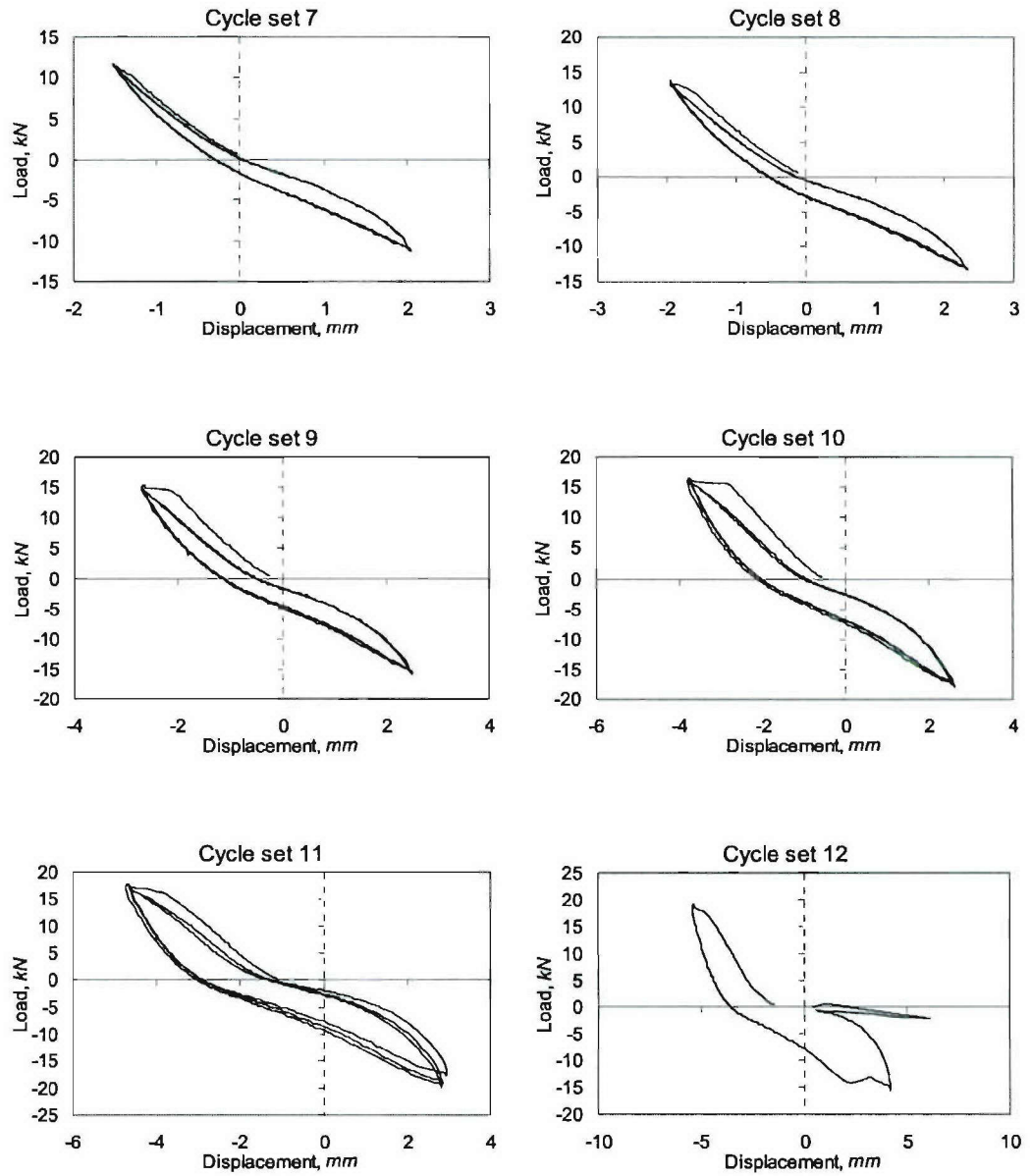
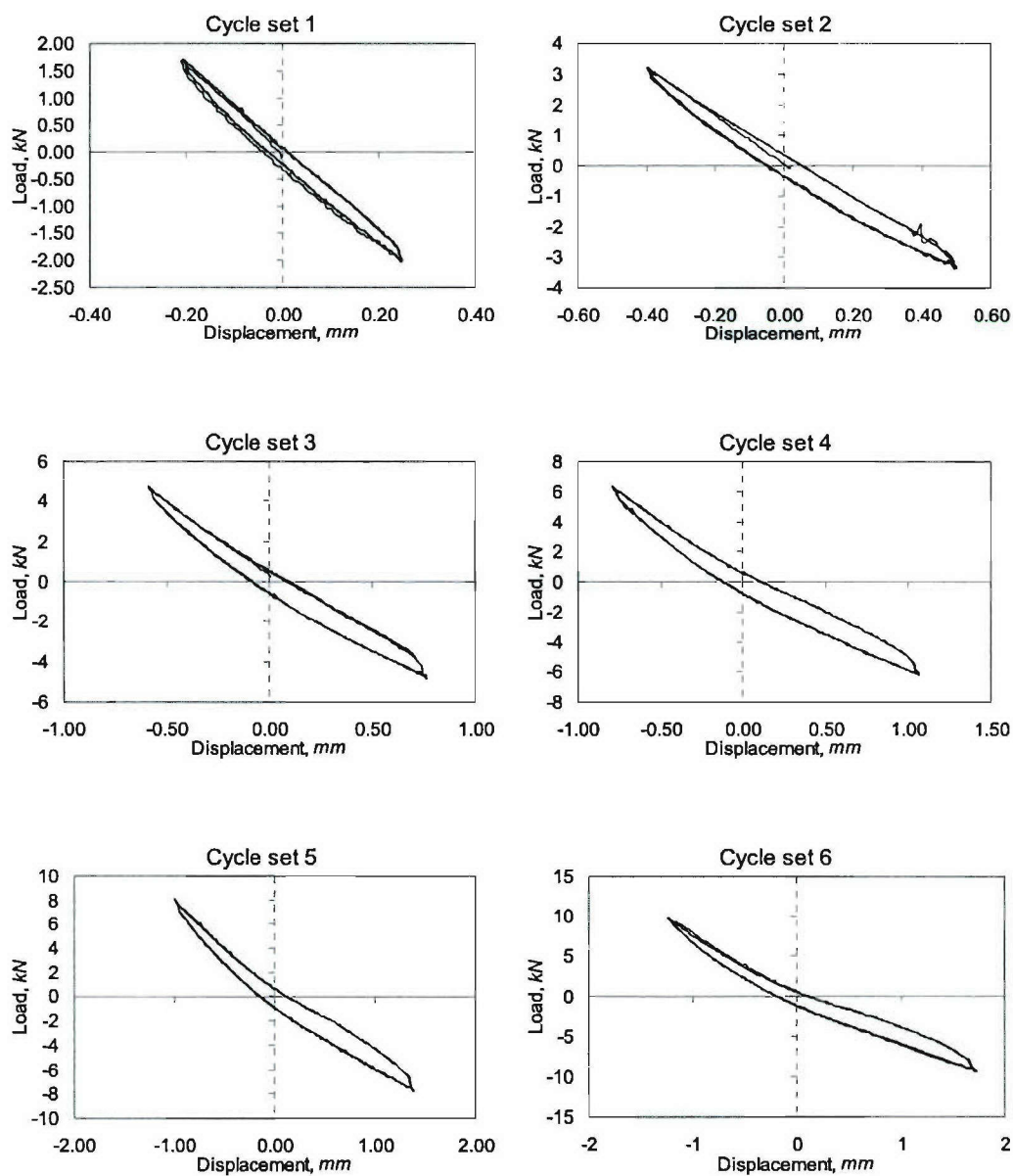


Figure E.1. Load-Displacement Curves for Specimen BP-1, Cycle Sets 1-6



**Figure E.2. Load-Displacement Curves for Specimen BP-1, Cycle Sets 7-12**





**Figure E.3. Load-Displacement Curves for Specimen BT-2, Cycle Sets 1-6**

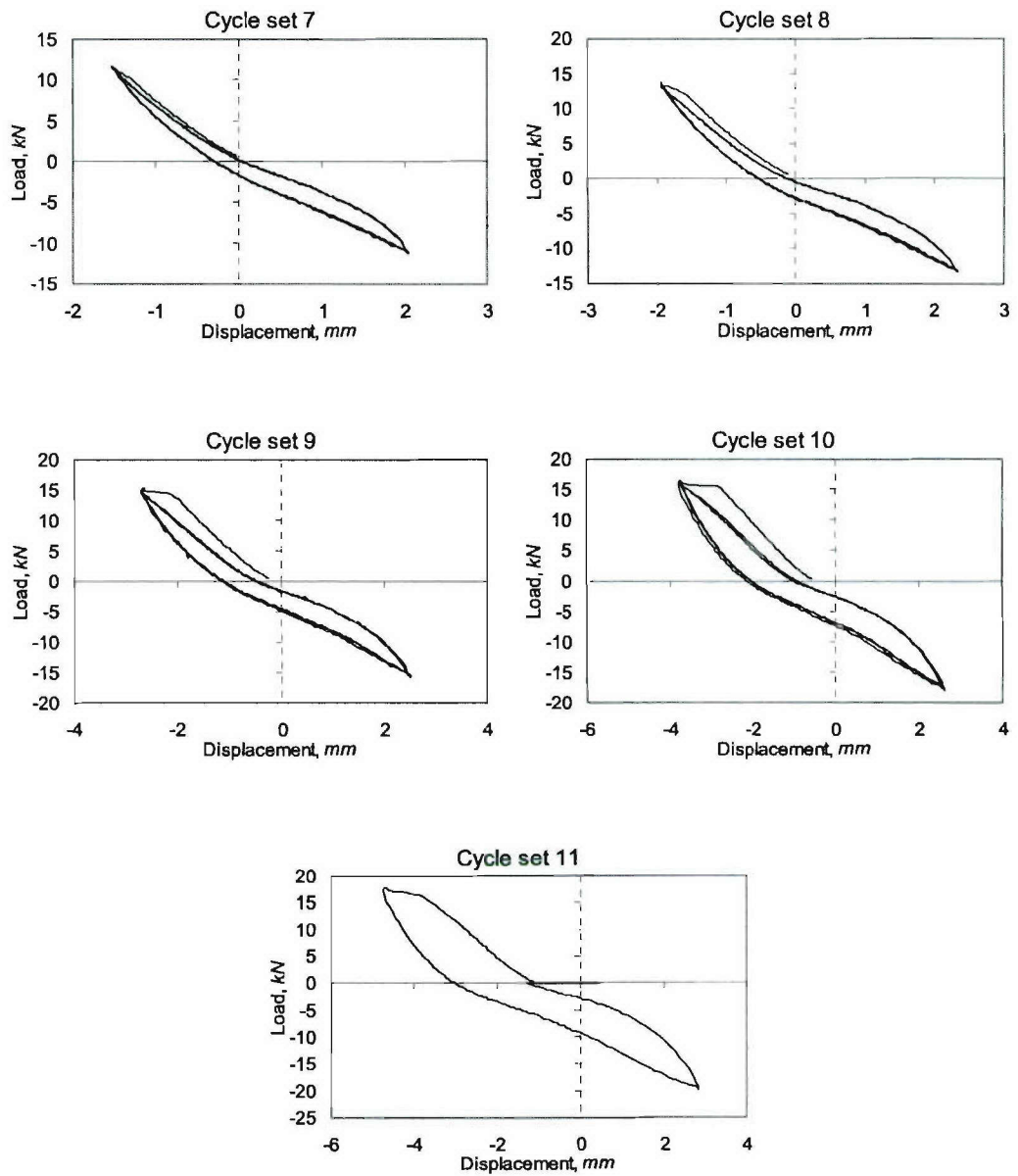
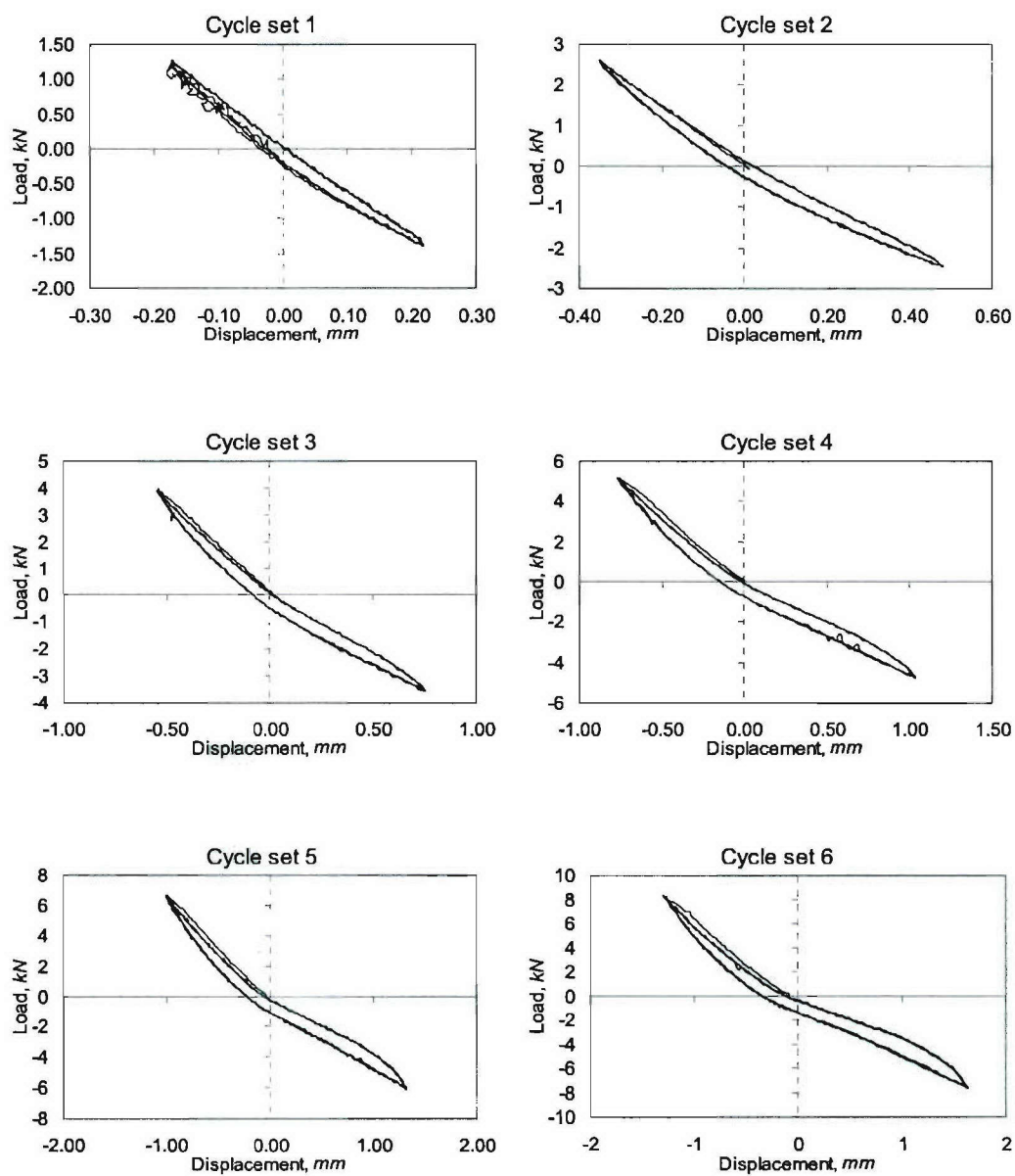
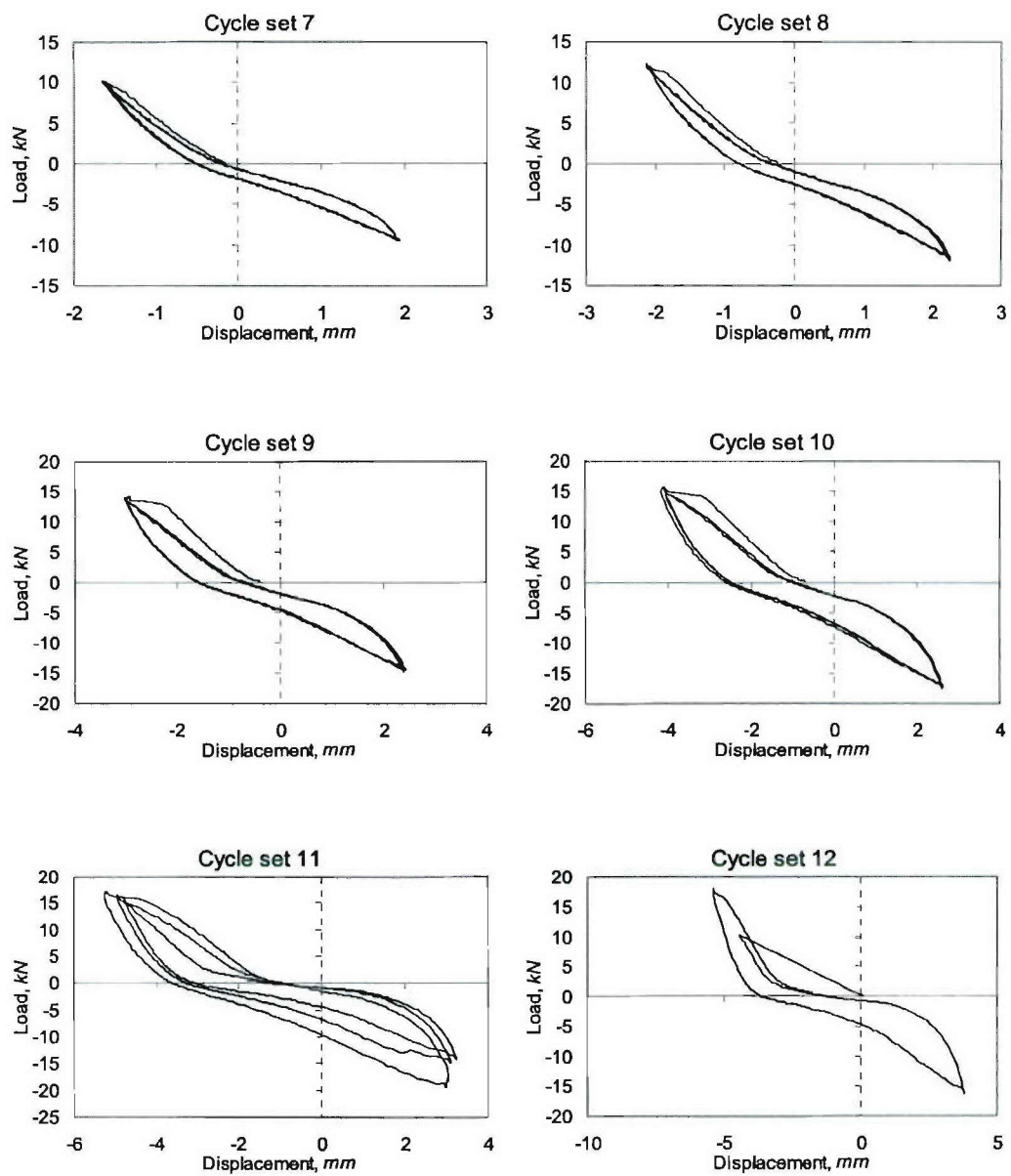


Figure E.4. Load-Displacement Curves for Specimen BT-2, Cycle Sets 7-11



**Figure E.5. Load-Displacement Curves for Specimen BP-3, Cycle Sets 1-6**



**Figure E.6. Load-Displacement Curves for Specimen BP-3, Cycle Sets 7-12**



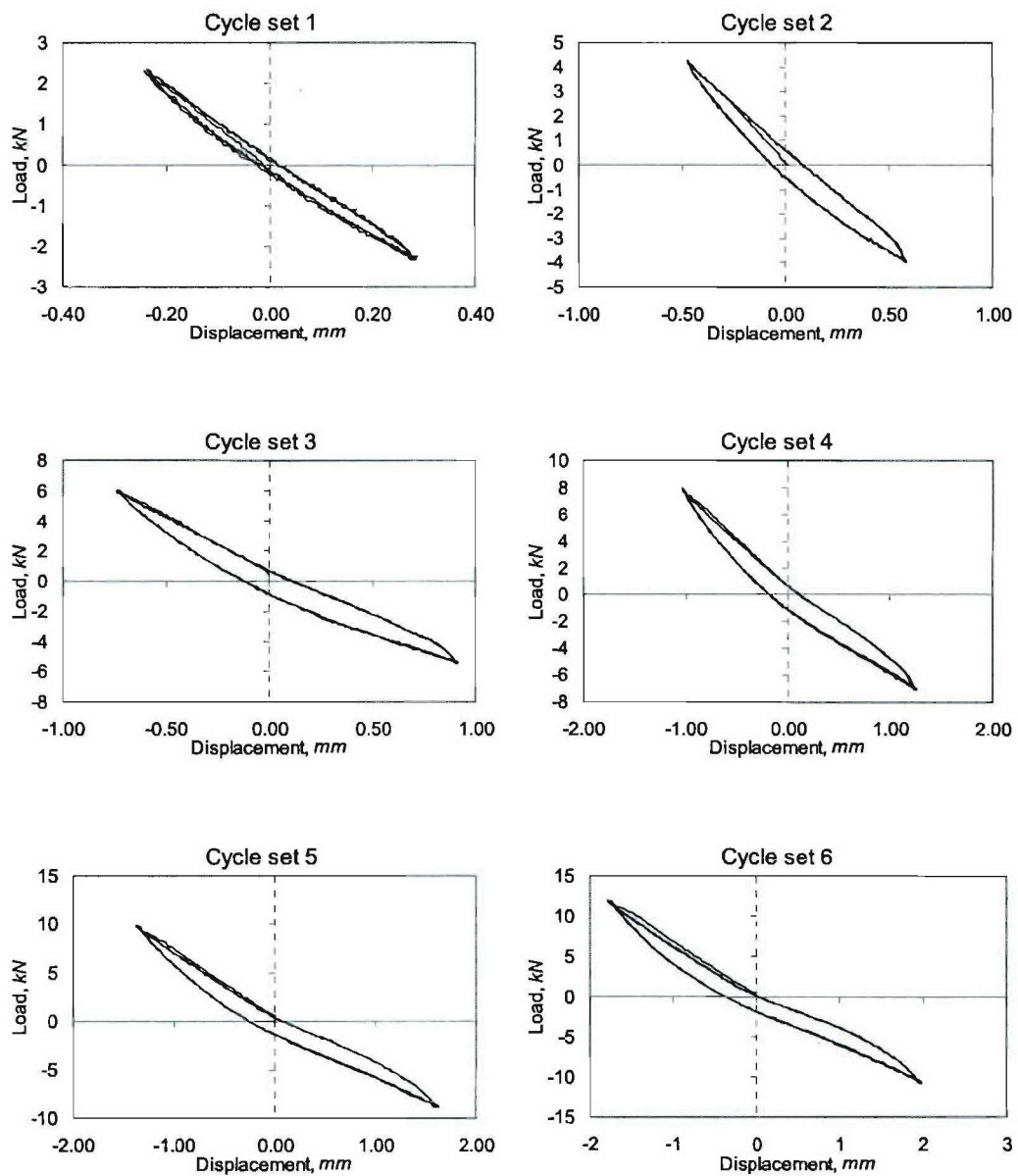


**Figure E.7. Load-Displacement Curves for Specimen BT-4, Cycle Sets 1-6**

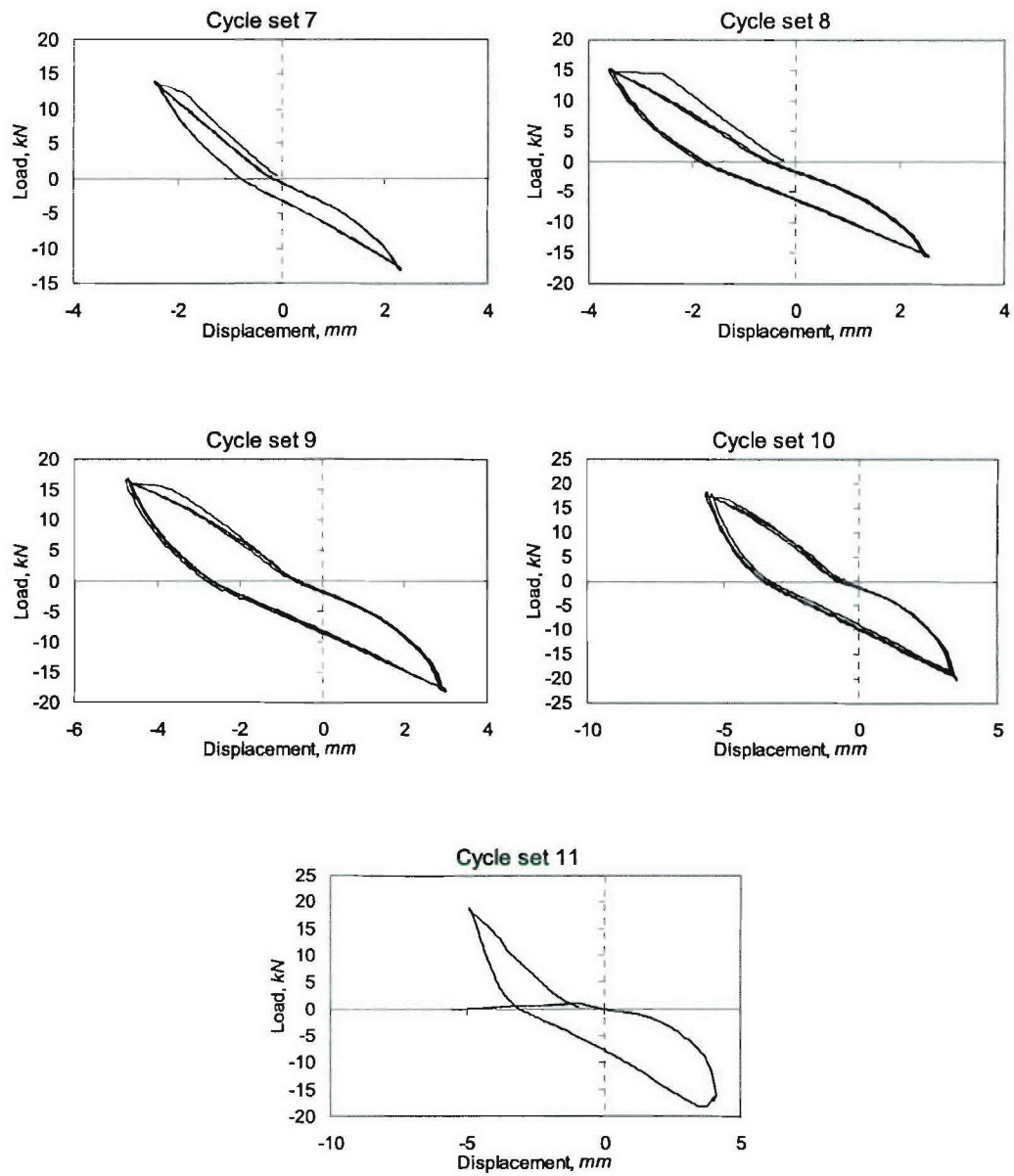


**Figure E.8. Load-Displacement Curves for Specimen BT-4, Cycle Sets 7-11**

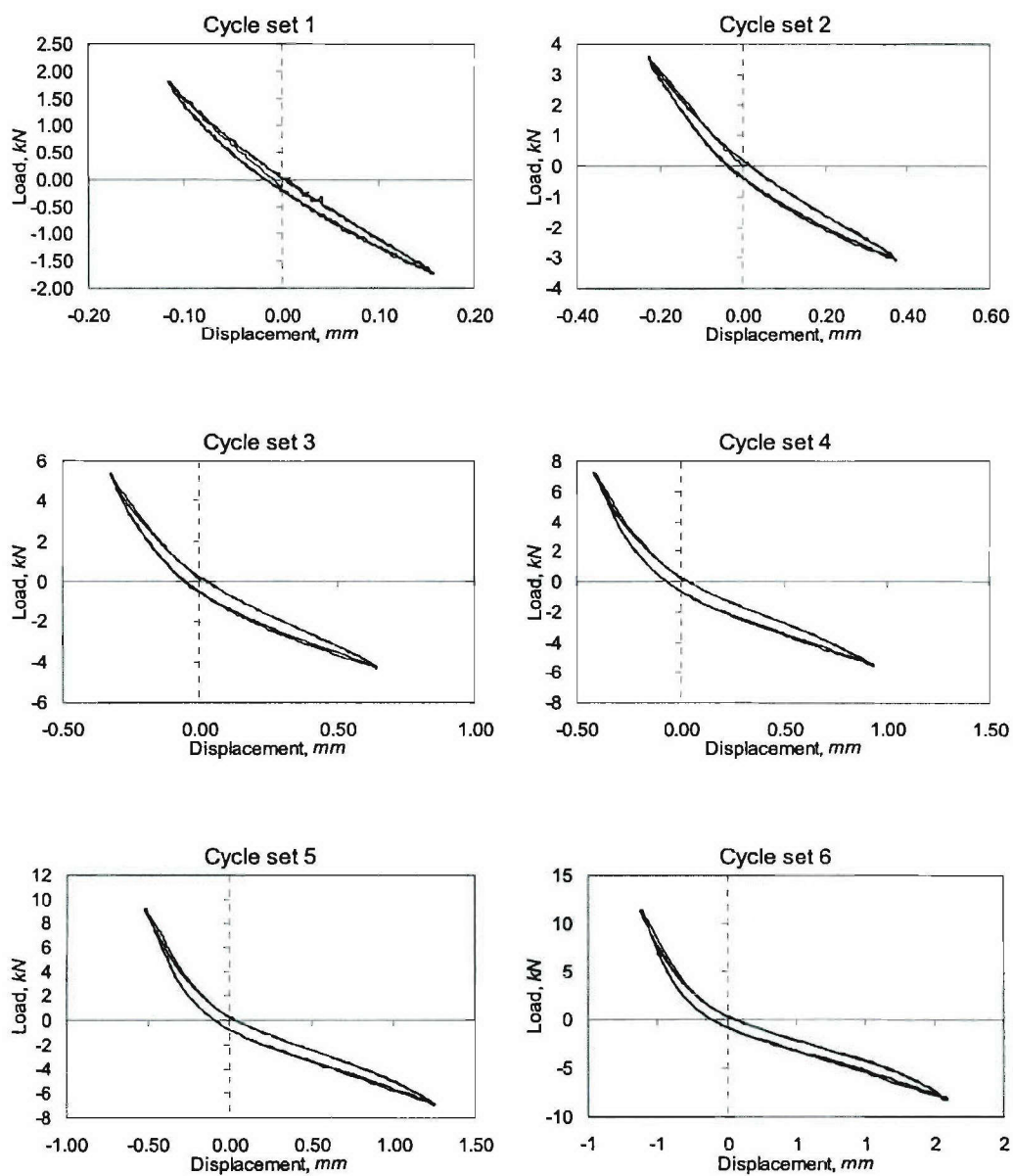


**Figure E.9. Load-Displacement Curves for Specimen BP-5, Cycle Sets 1-6**

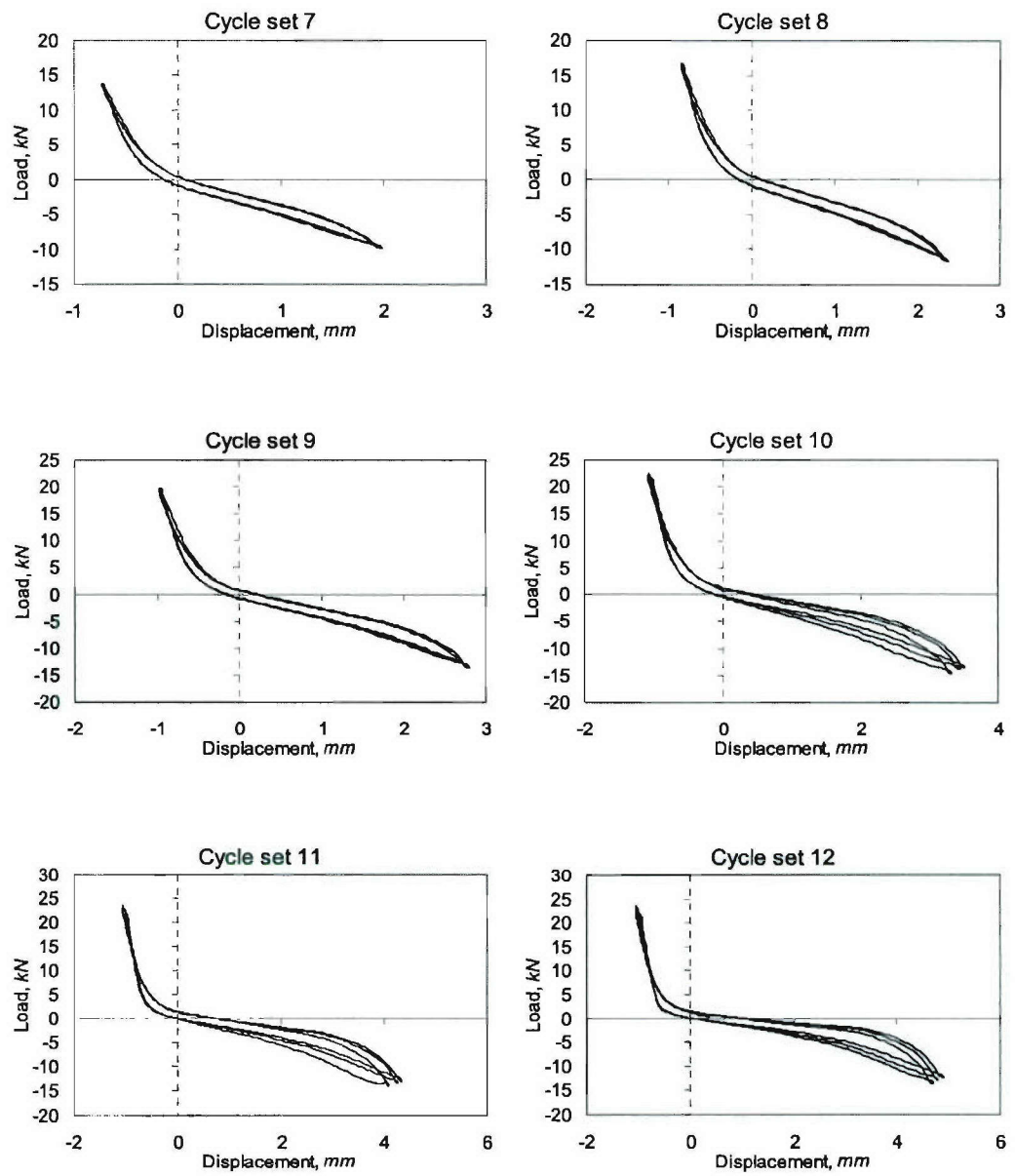


**Figure E.10. Load-Displacement Curves for Specimen BP-5, Cycle Sets 7-12**



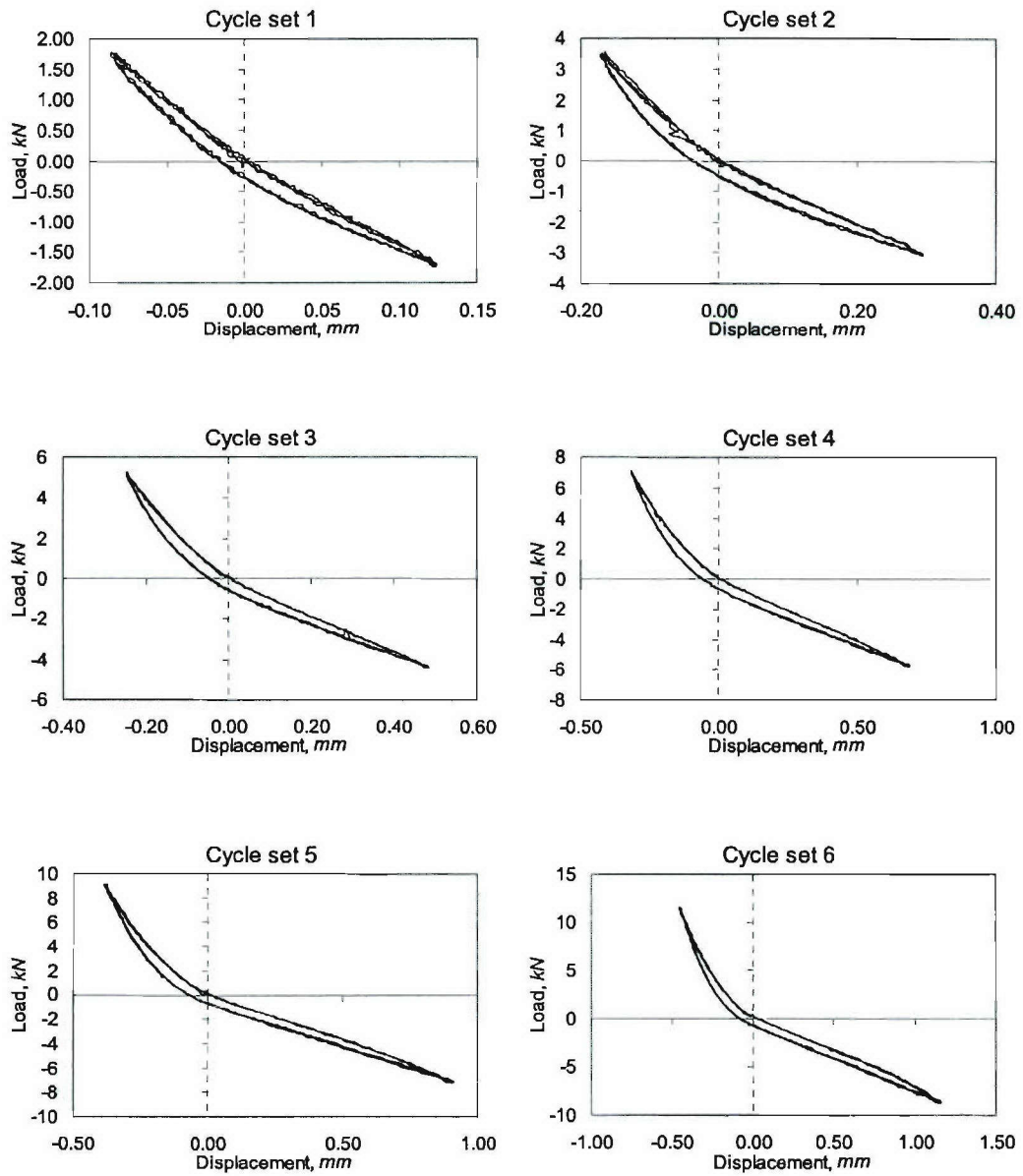


**Figure E.11. Load-Displacement Curves for Specimen BT-6, Cycle Sets 1-6**

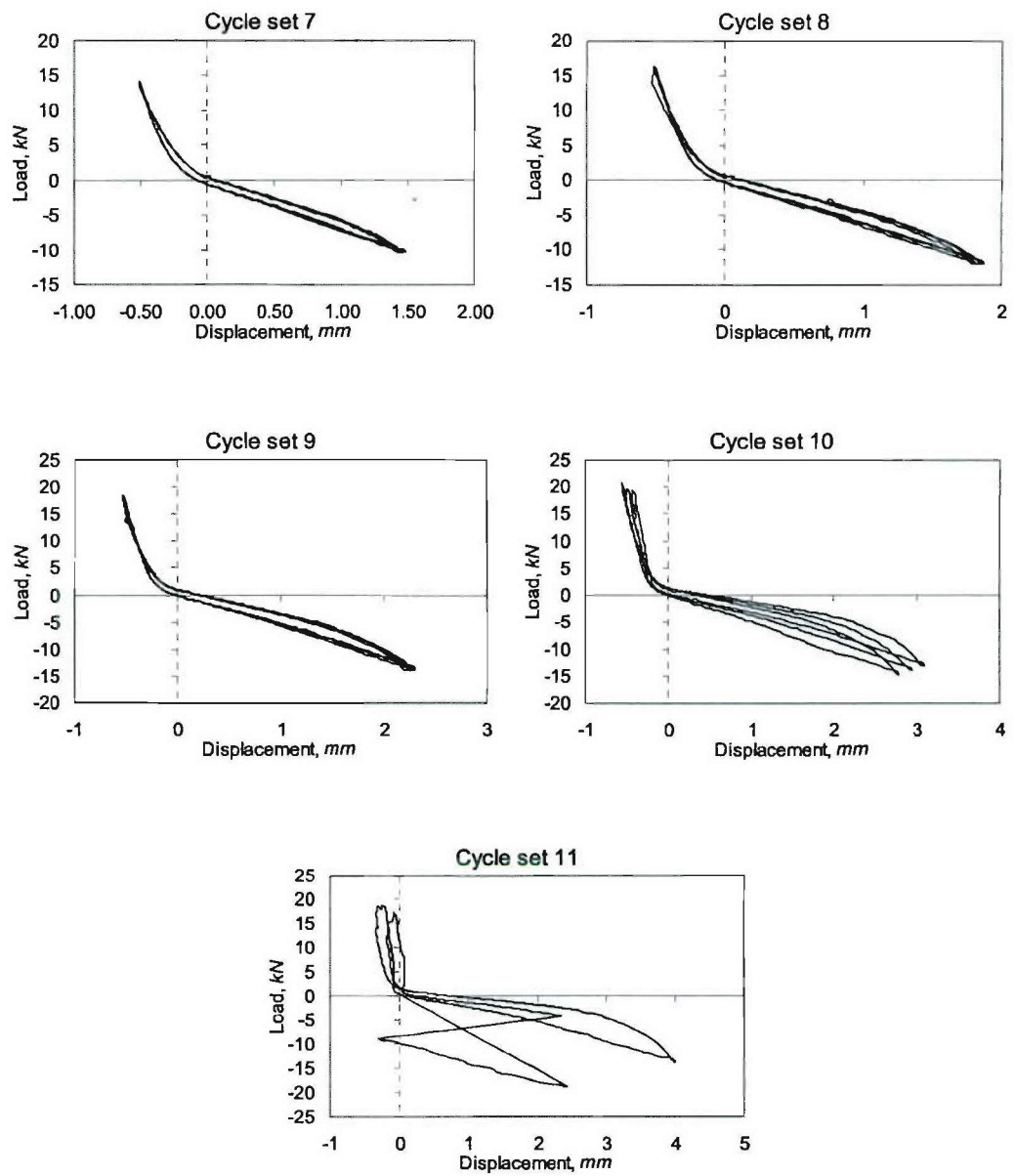


**Figure E.12. Load-Displacement Curves for Specimen BT-6, Cycle Sets 7-12**

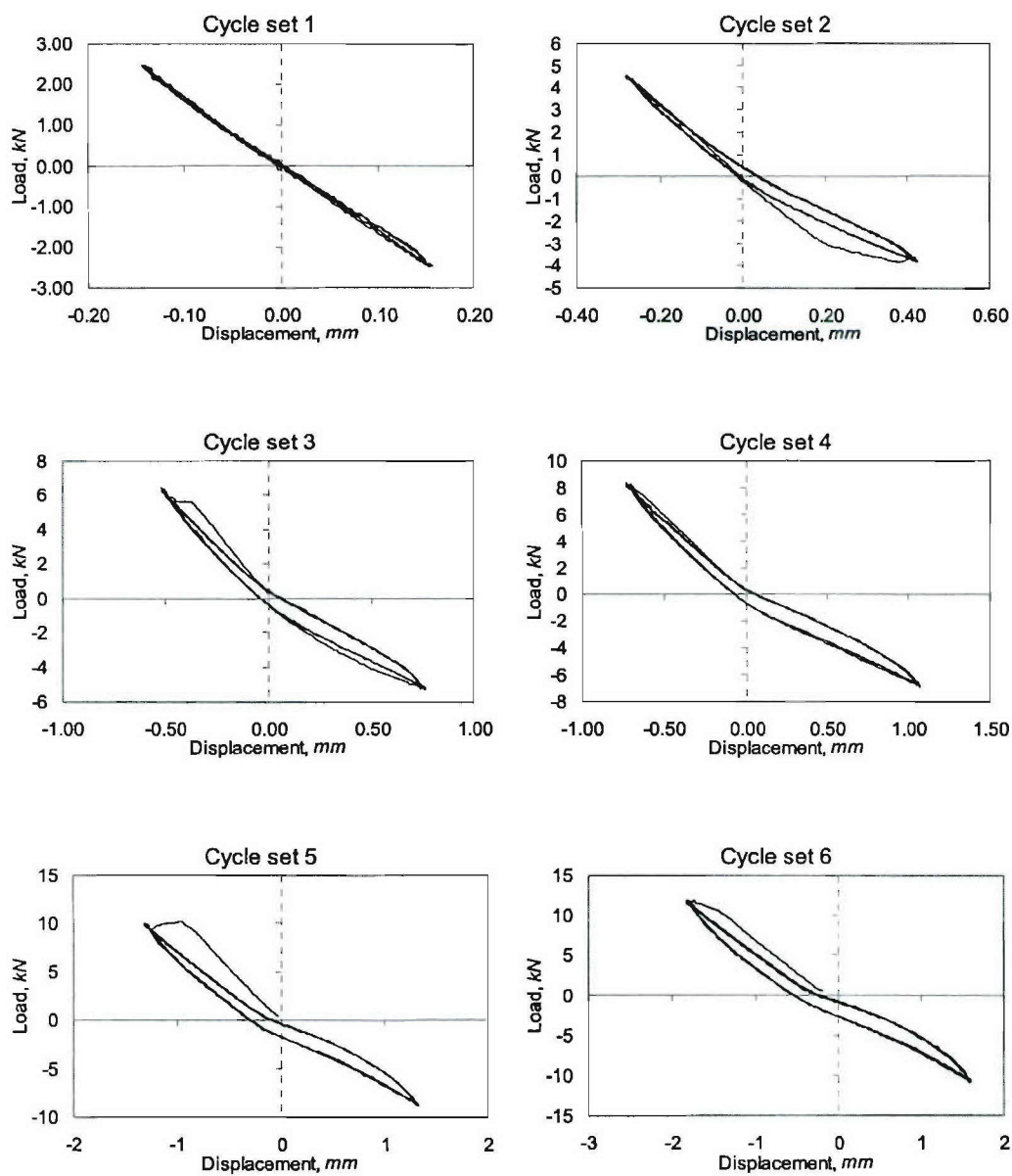


**Figure E.13. Load-Displacement Curves for Specimen BT-7, Cycle Sets 1-6**

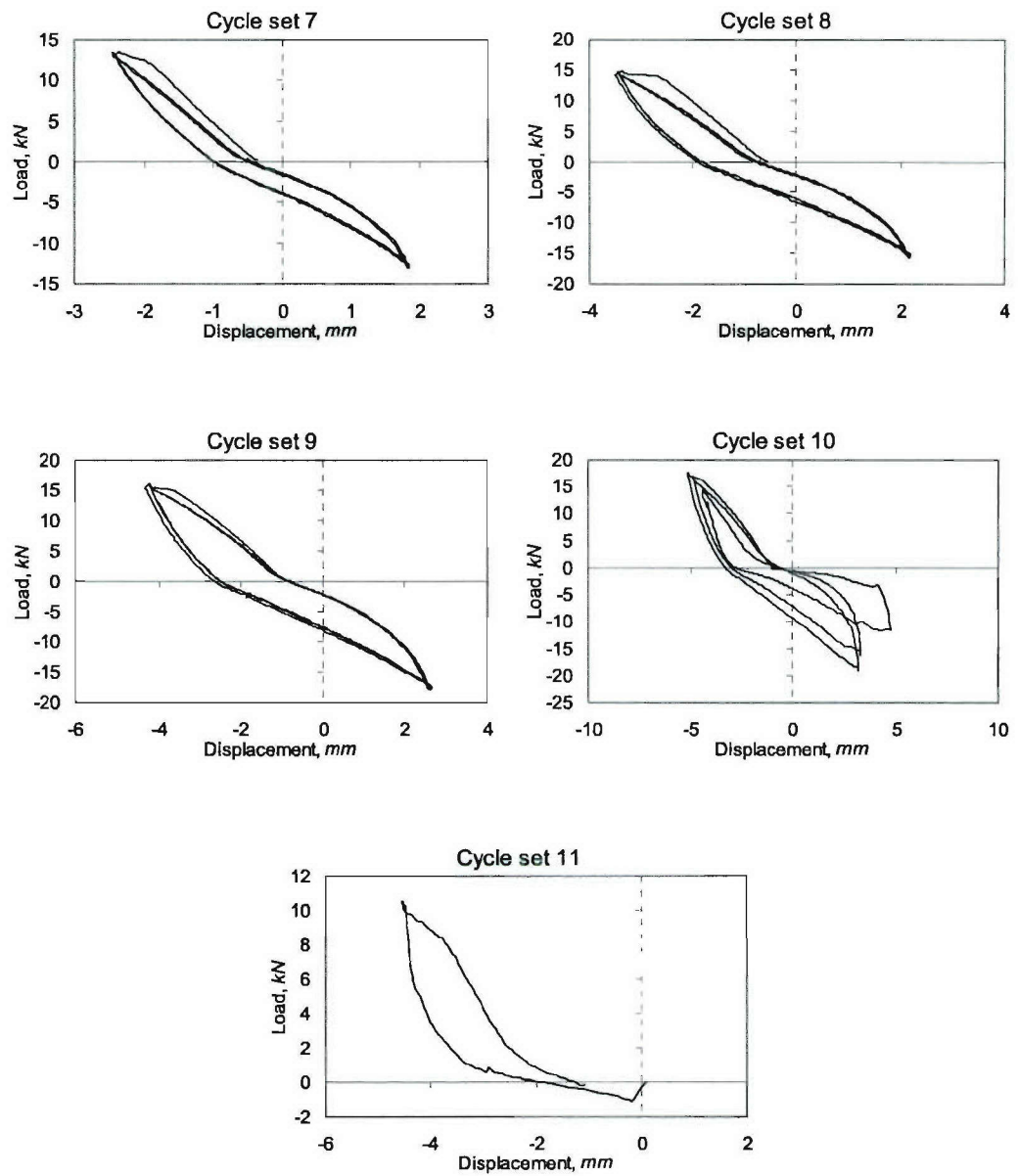


**Figure E.14. Load-Displacement Curves for Specimen BT-7, Cycle Sets 7-12**



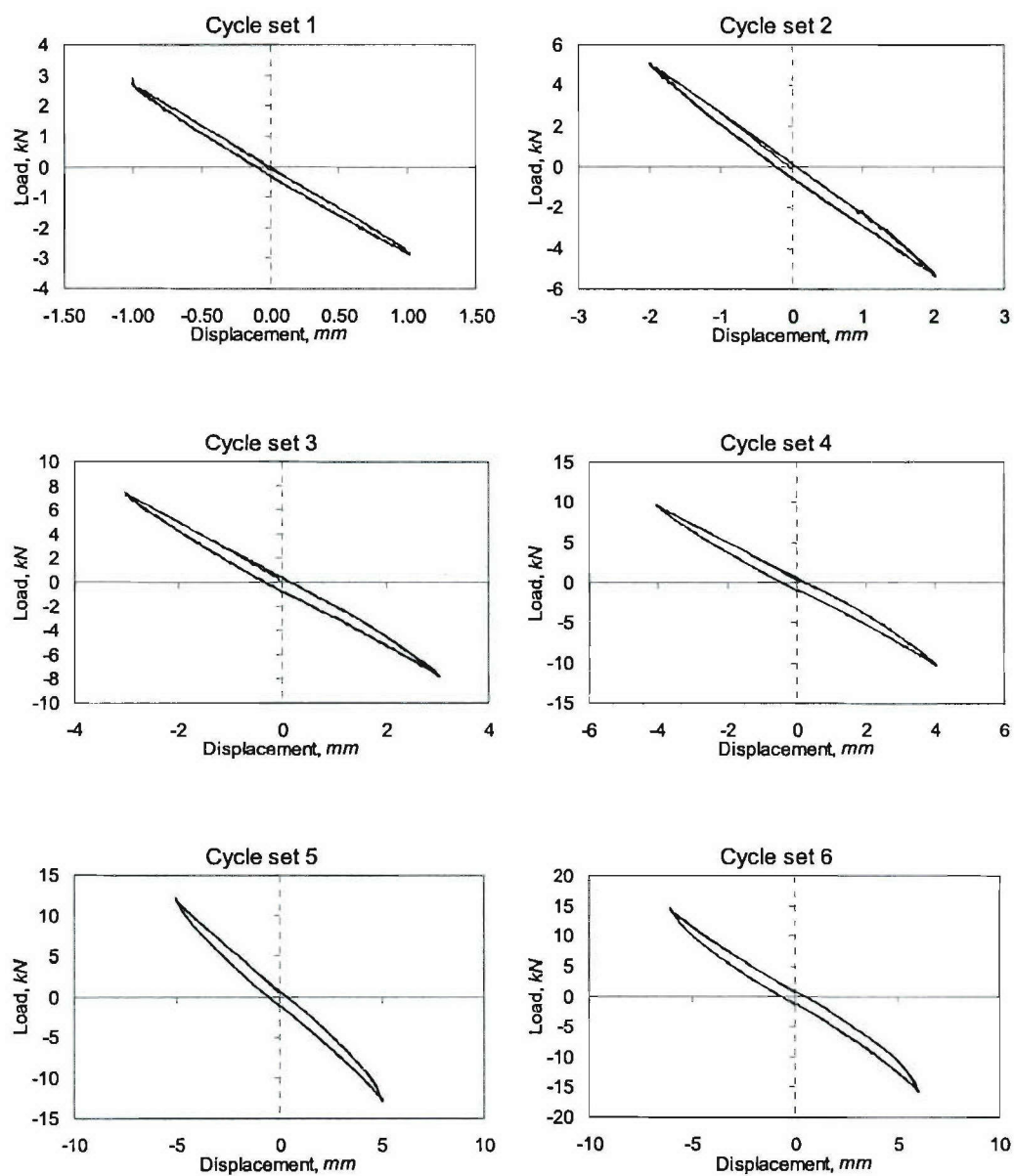
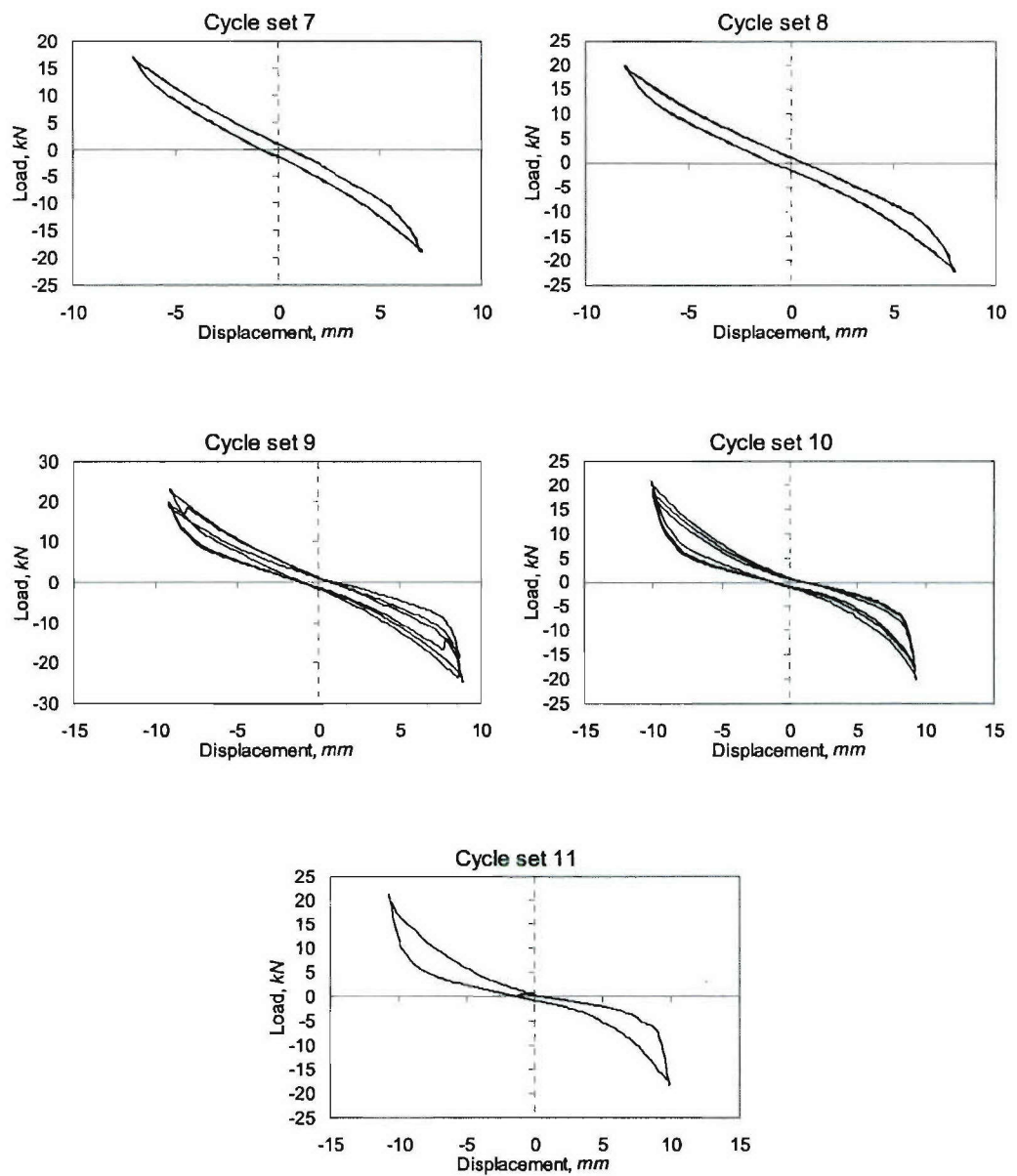
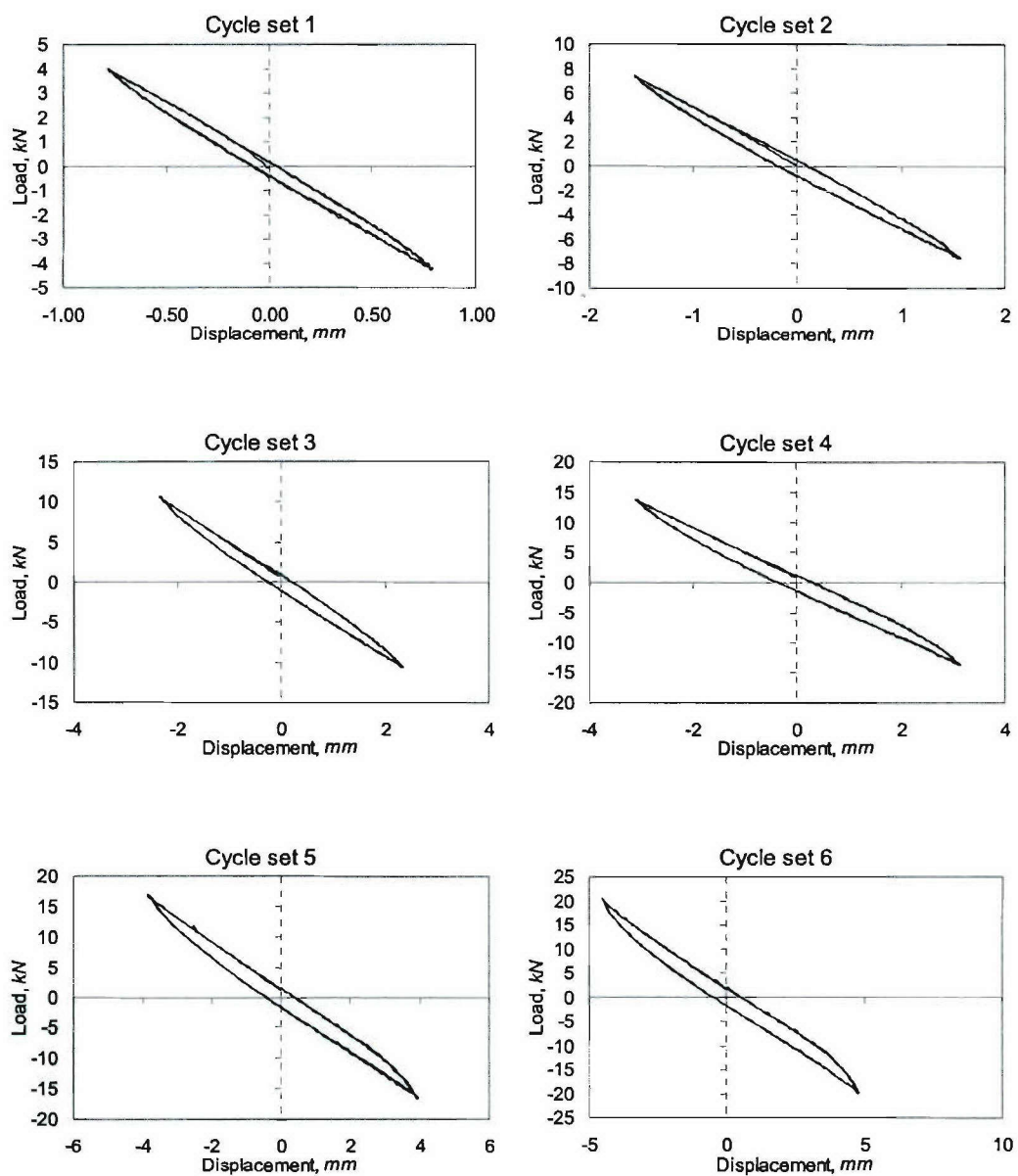


Figure E.15. Load-Displacement Curves for Specimen DM-1, Cycle Sets 1-6



**Figure E.16. Load-Displacement Curves for Specimen DM-1, Cycle Sets 7-12**



**Figure E.17. Load-Displacement Curves for Specimen DL-2, Cycle Sets 1-6**

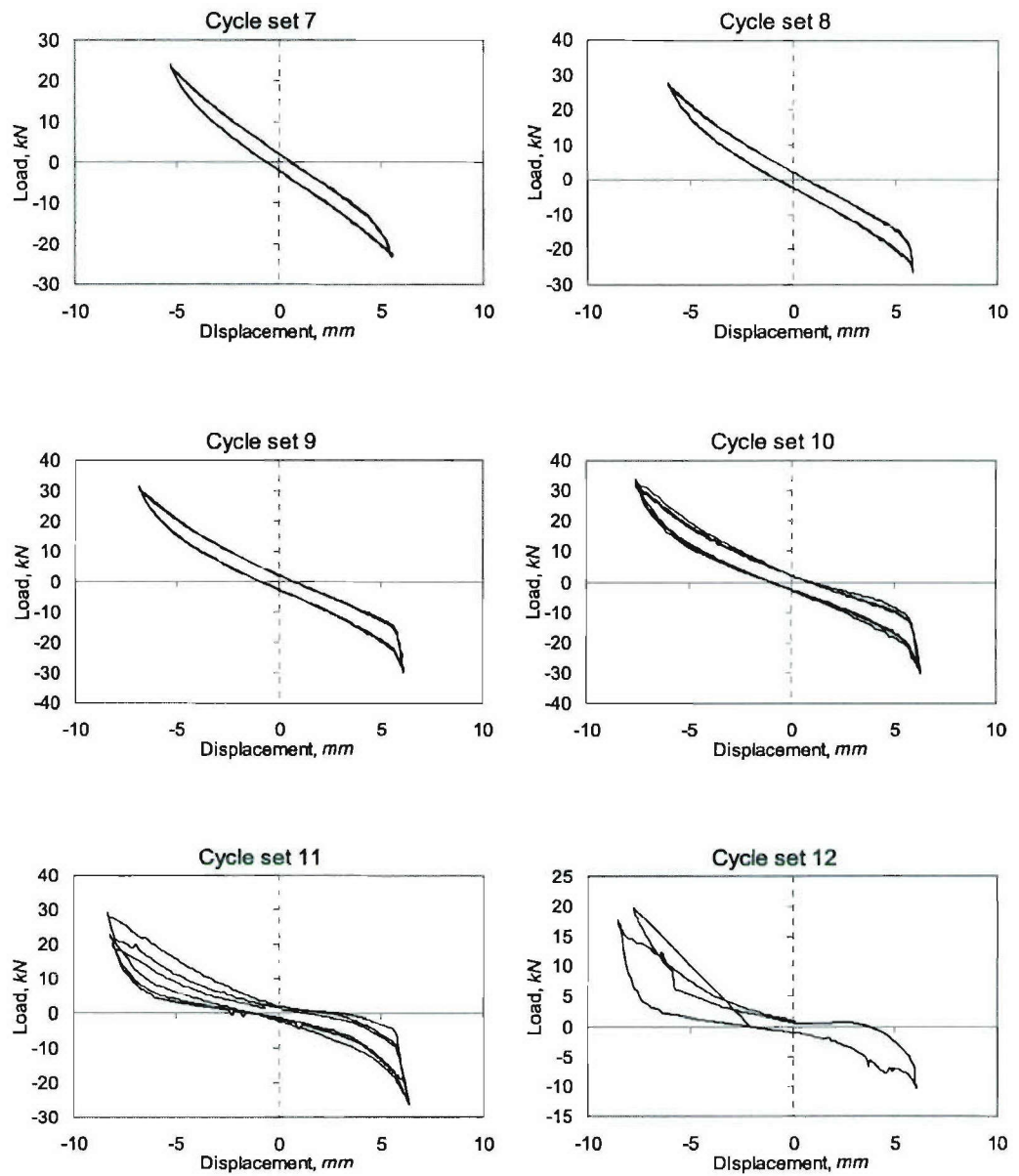


**Figure E.18. Load-Displacement Curves for Specimen DL-2, Cycle Sets 7-12**



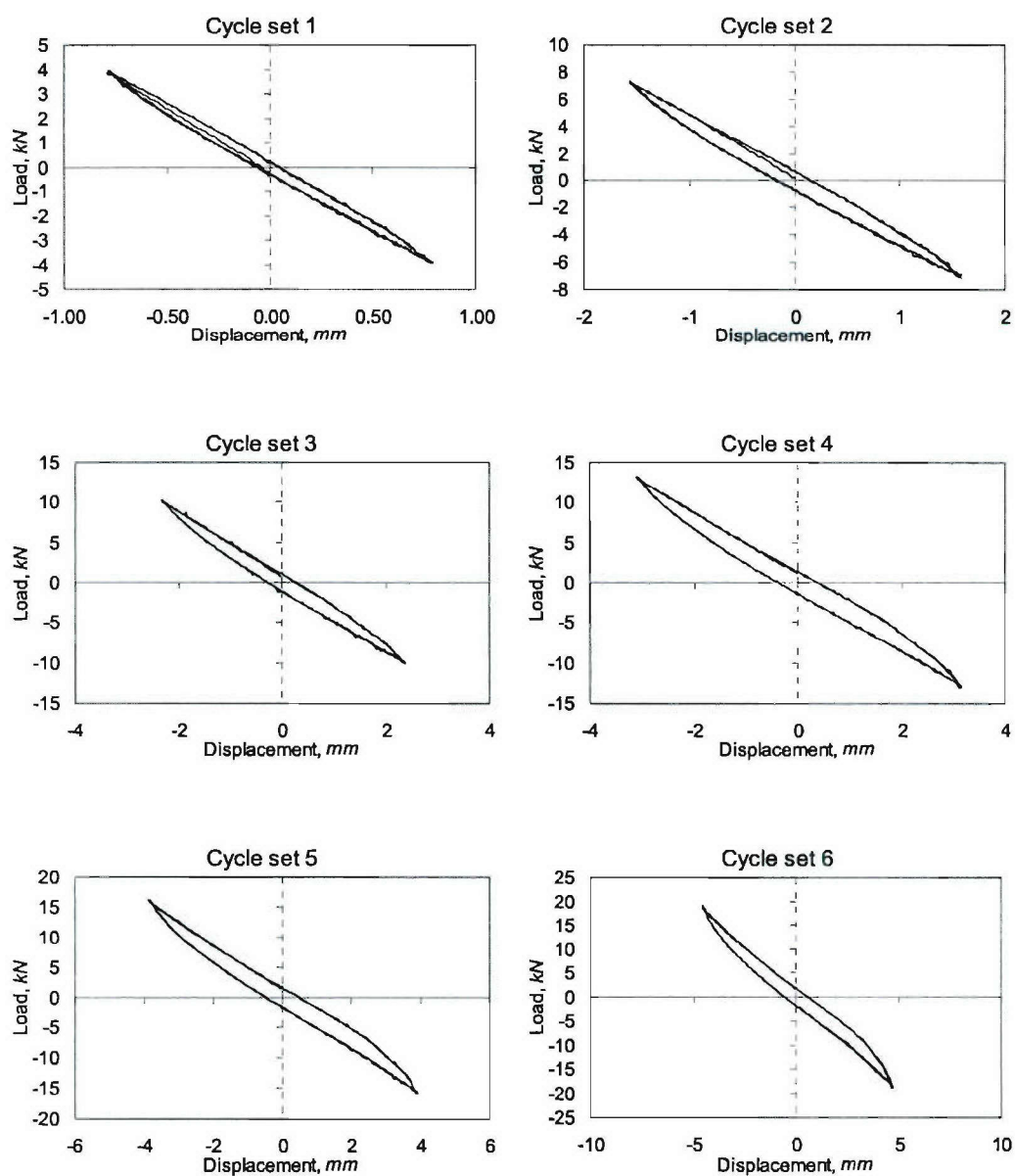


**Figure E.19. Load-Displacement Curves for Specimen DL-3, Cycle Sets 1-6**

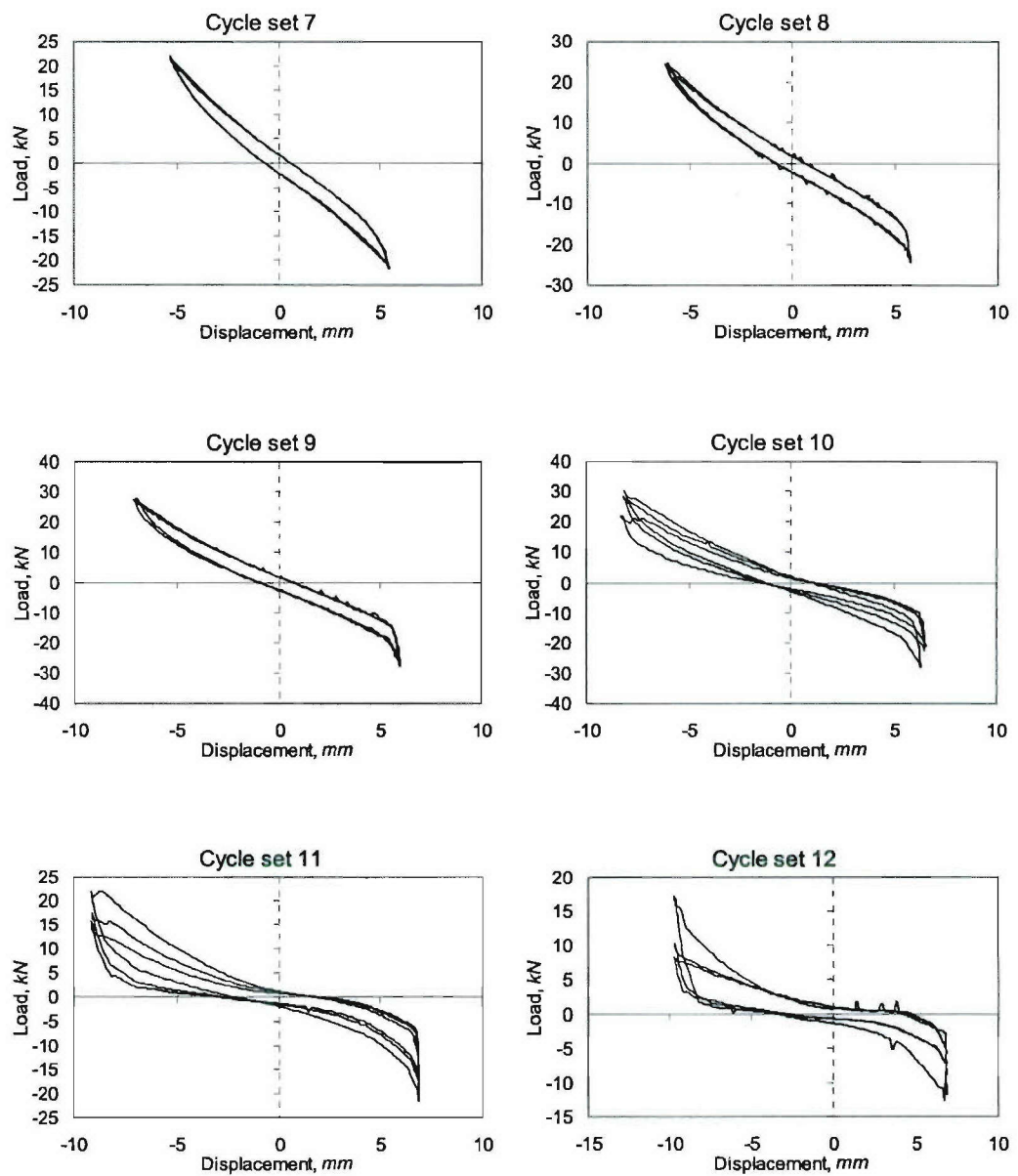


**Figure E.20. Load-Displacement Curves for Specimen DL-3, Cycle Sets 6-12**

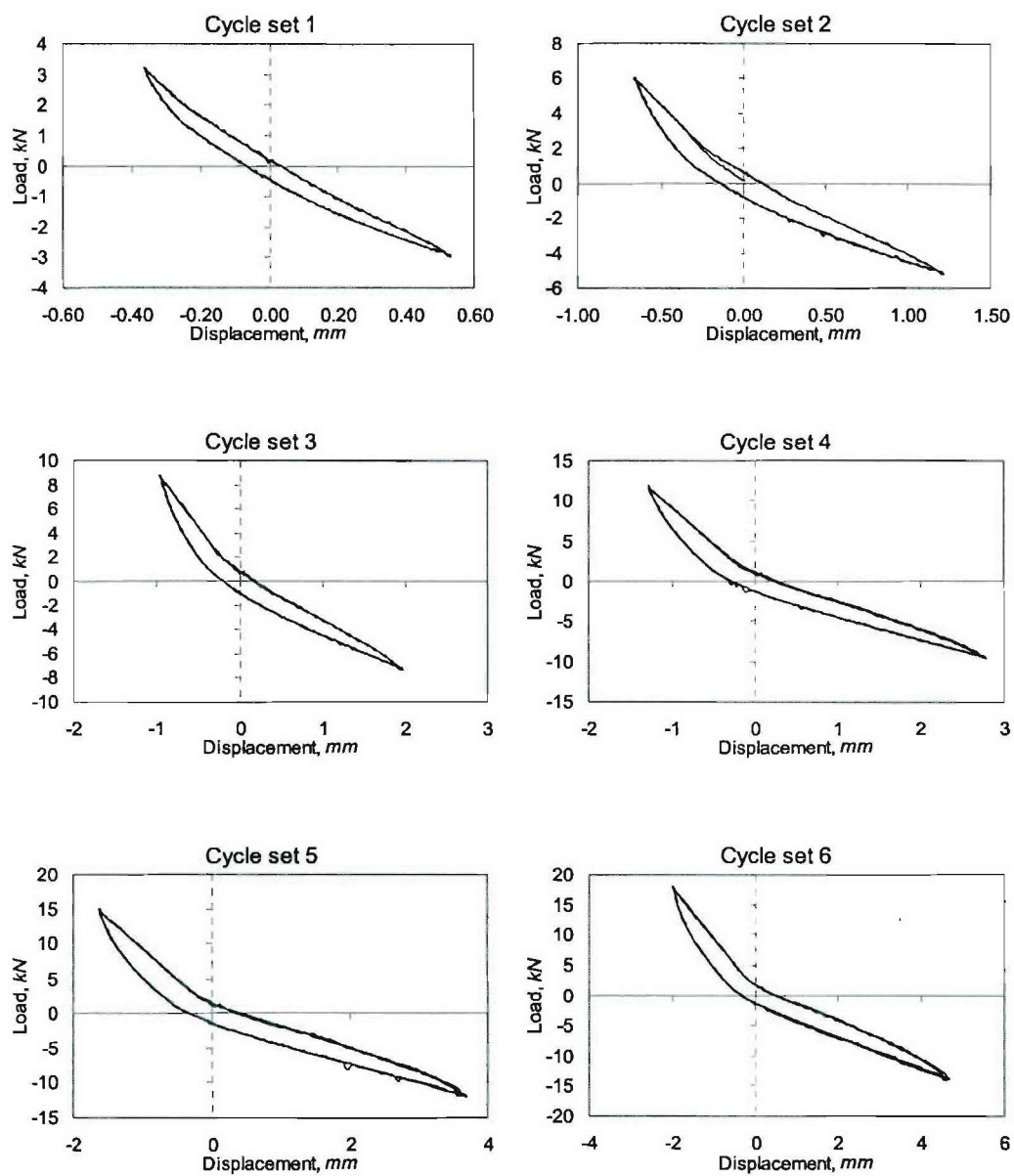


**Figure E.21. Load-Displacement Curves for Specimen DS-4, Cycle Sets 1-6**

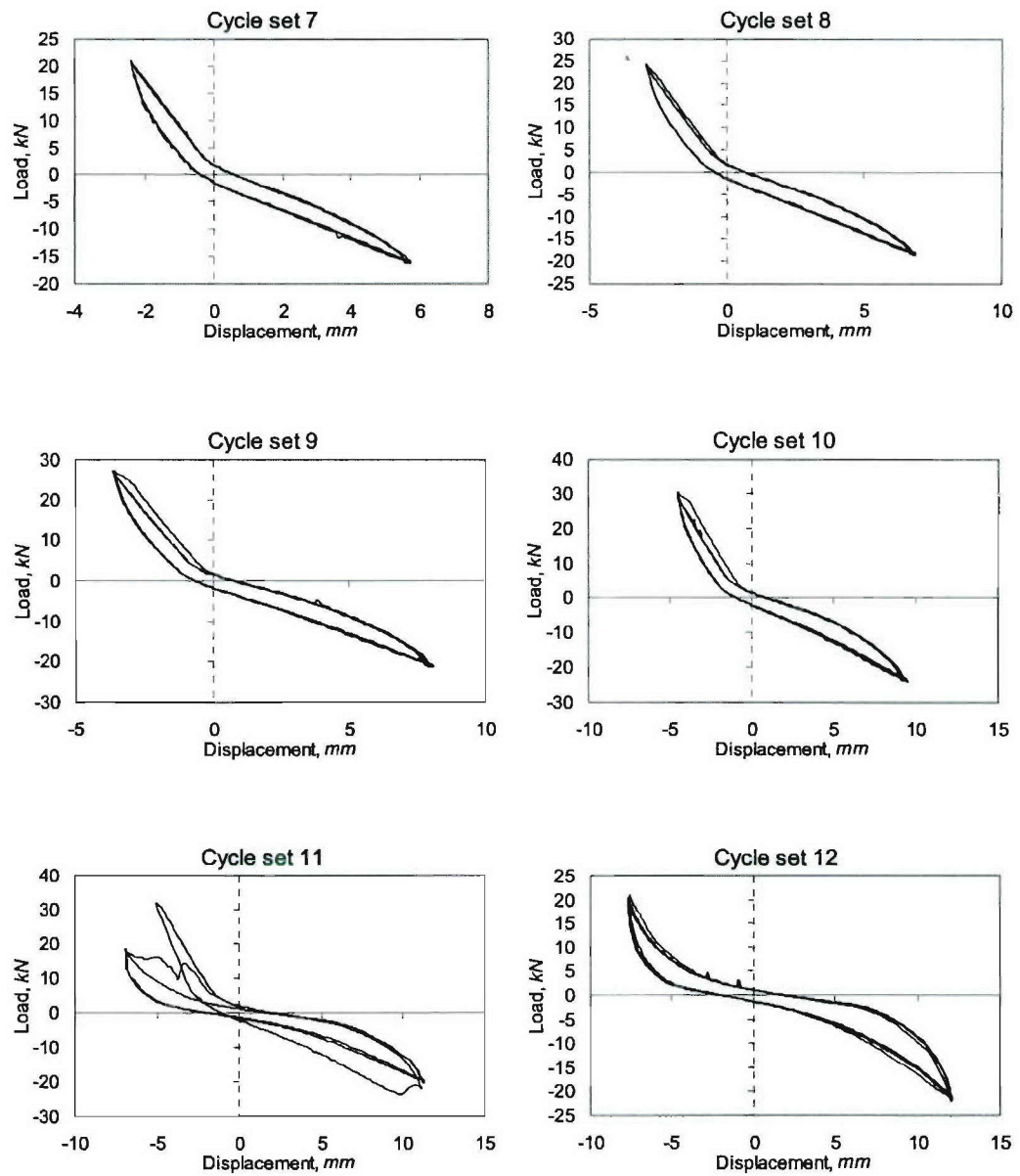


**Figure E.22. Load-Displacement Curves for Specimen DS-4, Cycle Sets 7-12**



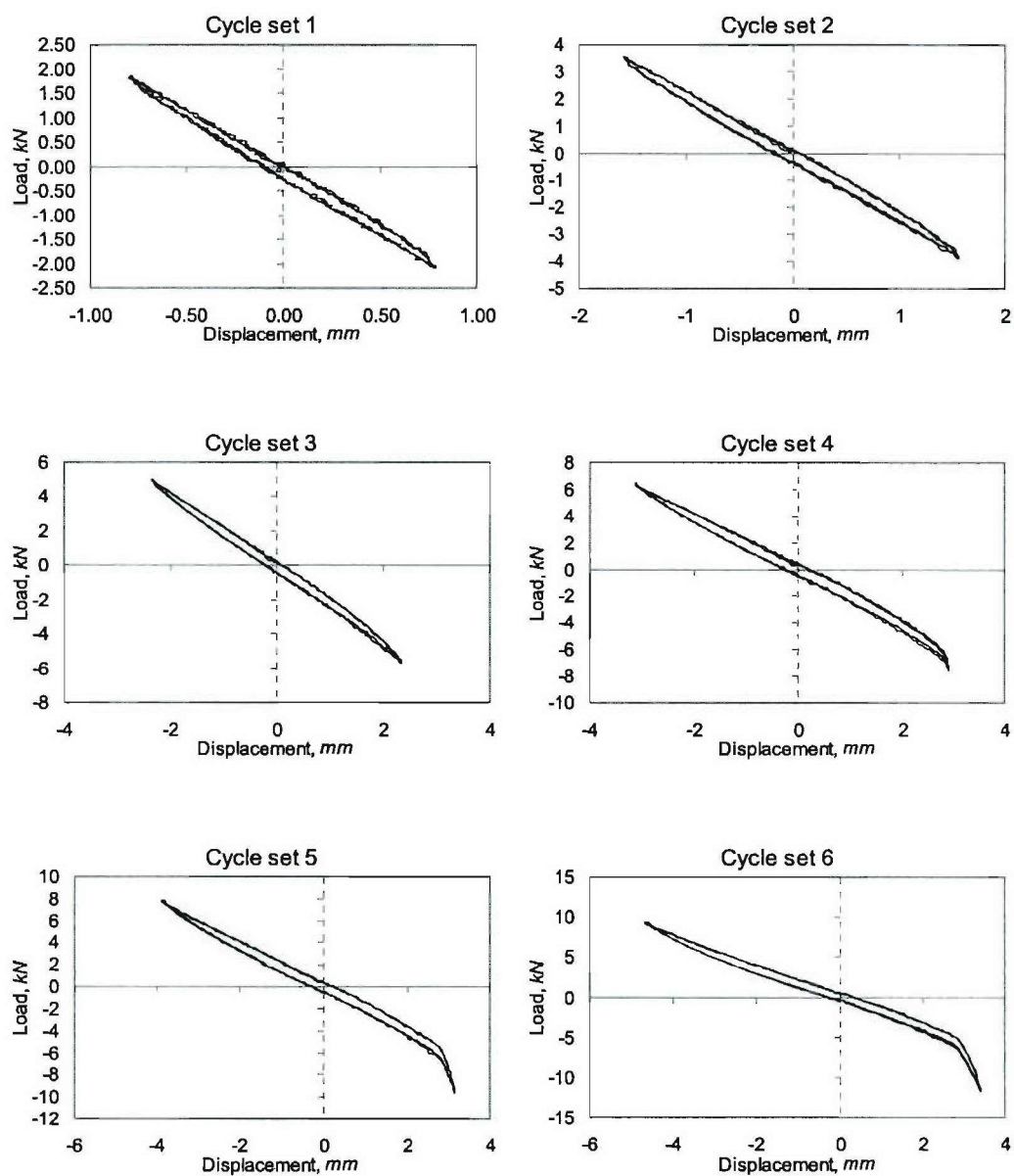


Figure E.23. Load-Displacement Curves for Specimen DL-5, Cycle Sets 1-6

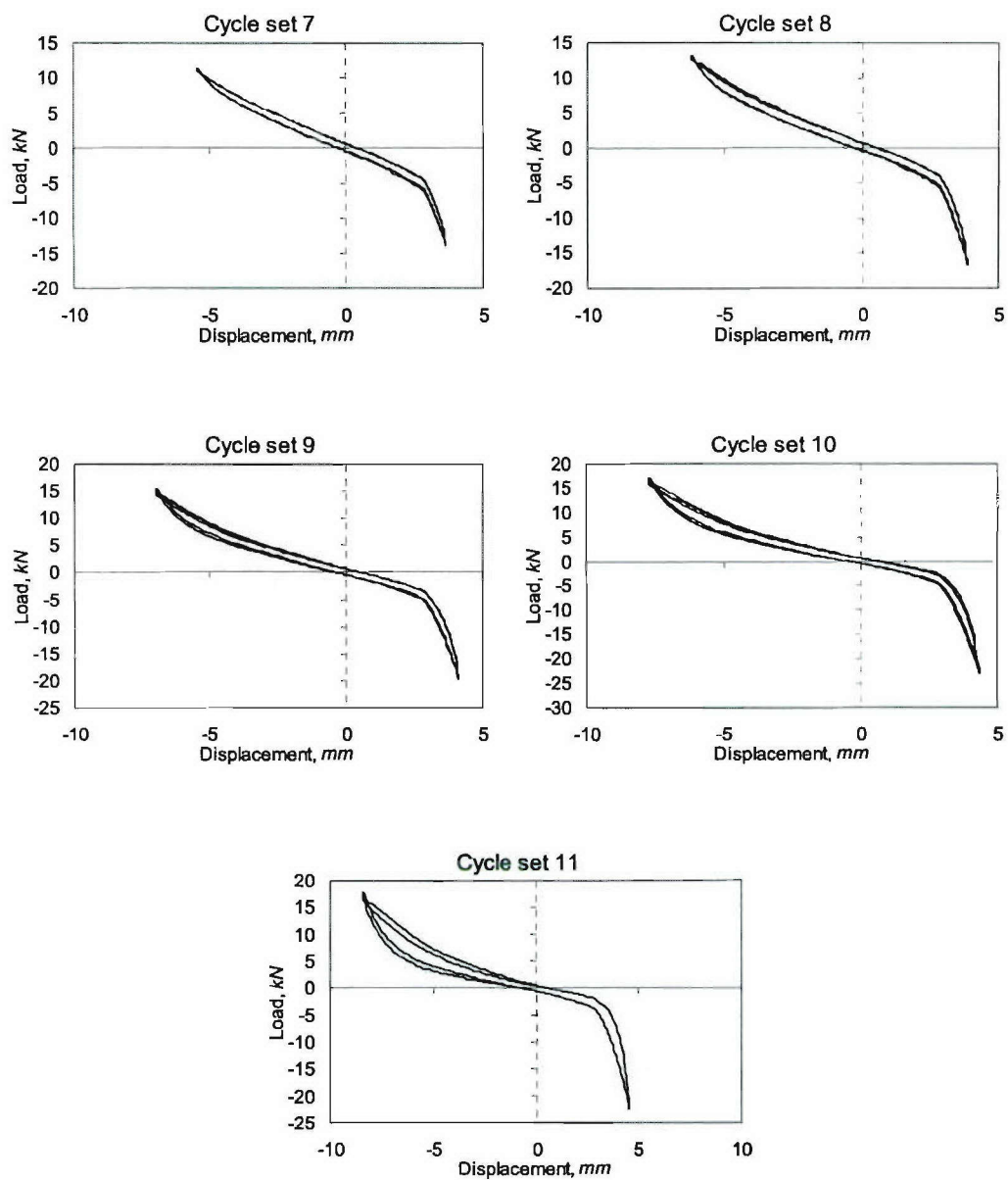
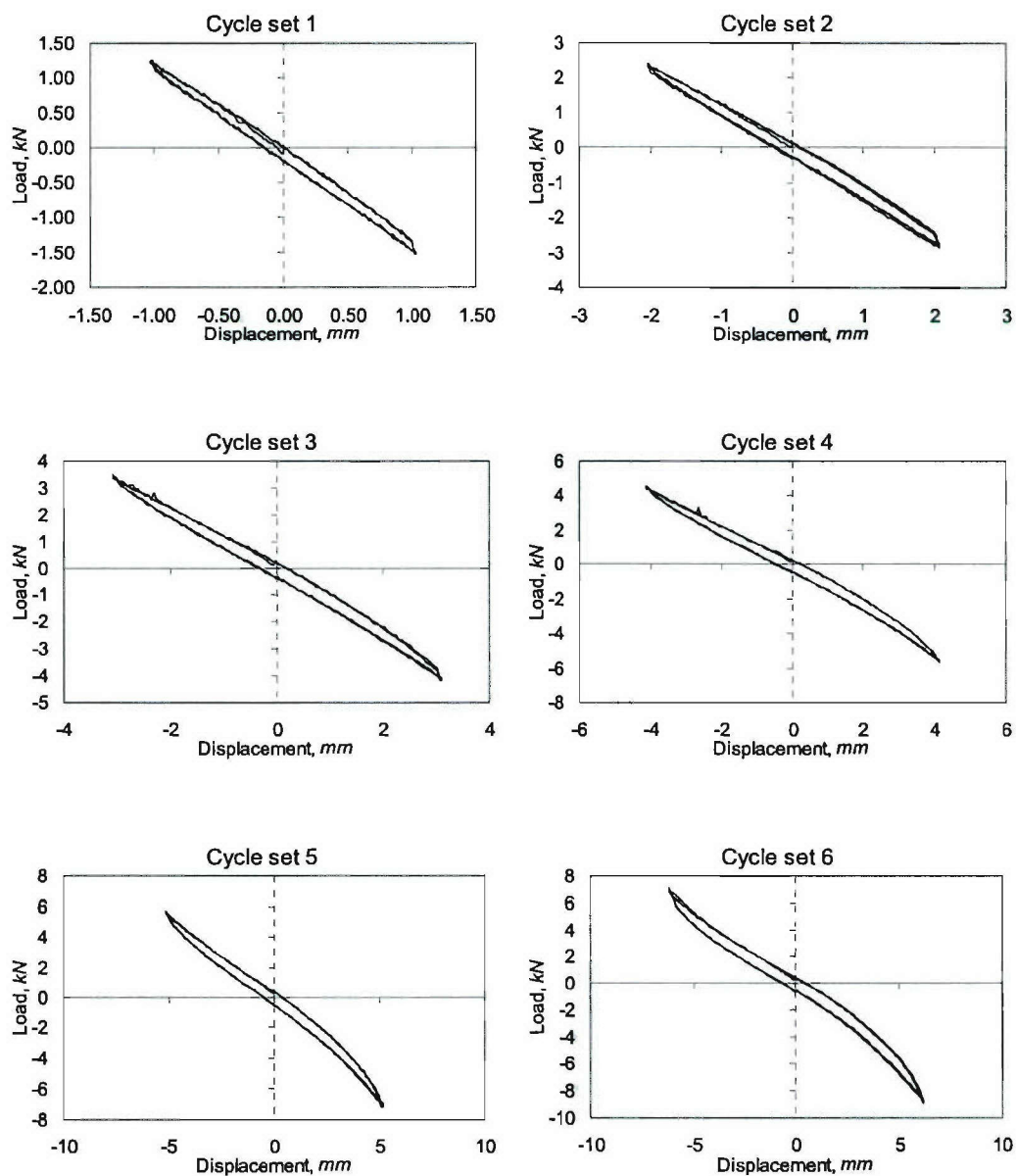
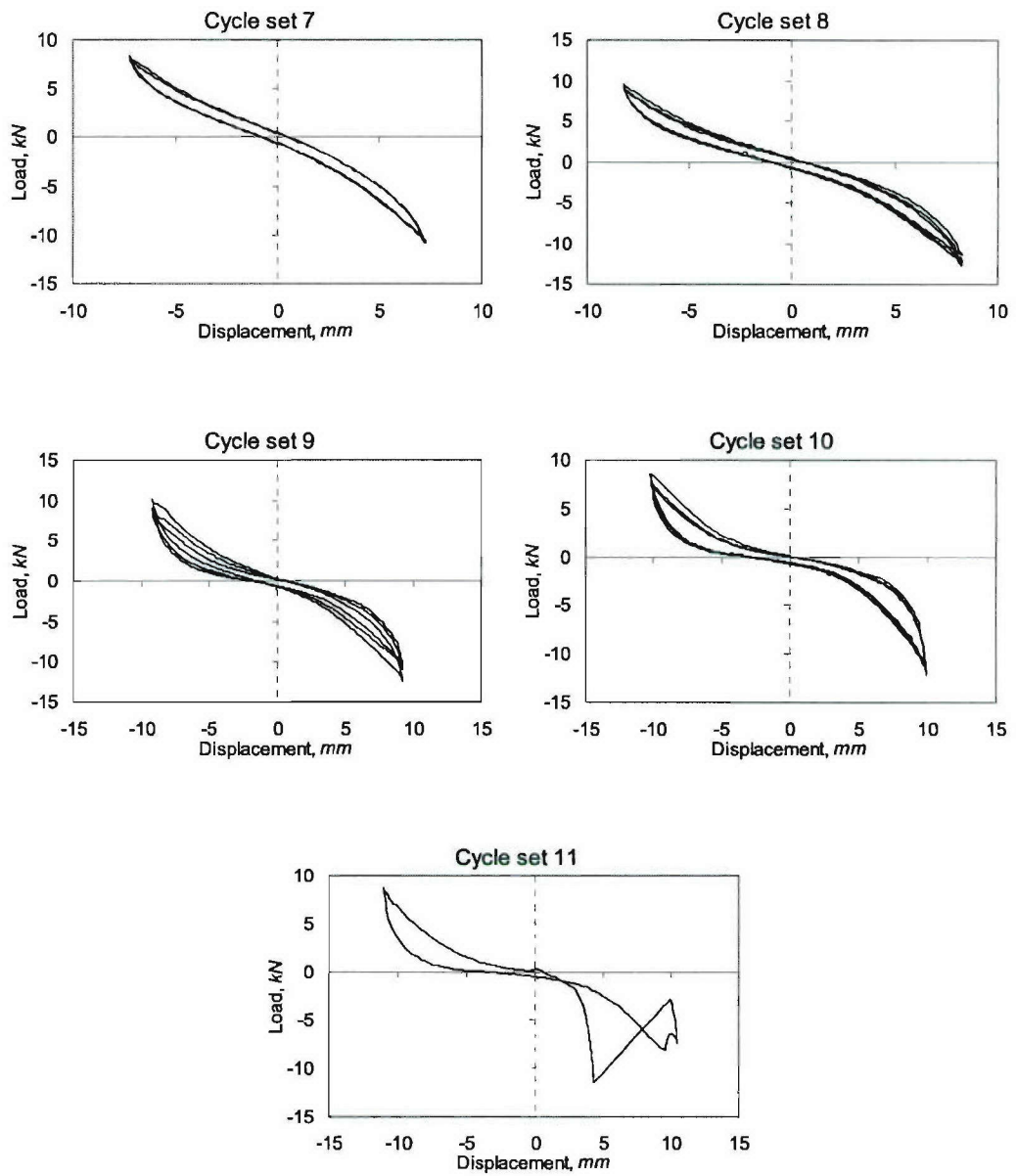


Figure E.24. Load-Displacement Curves for Specimen DL-5, Cycle Sets 7-12



**Figure E.25. Load-Displacement Curves for Specimen DM-6, Cycle Sets 1-6**



**Figure E.26. Load-Displacement Curves for Specimen DM-6, Cycle Sets 7-12**



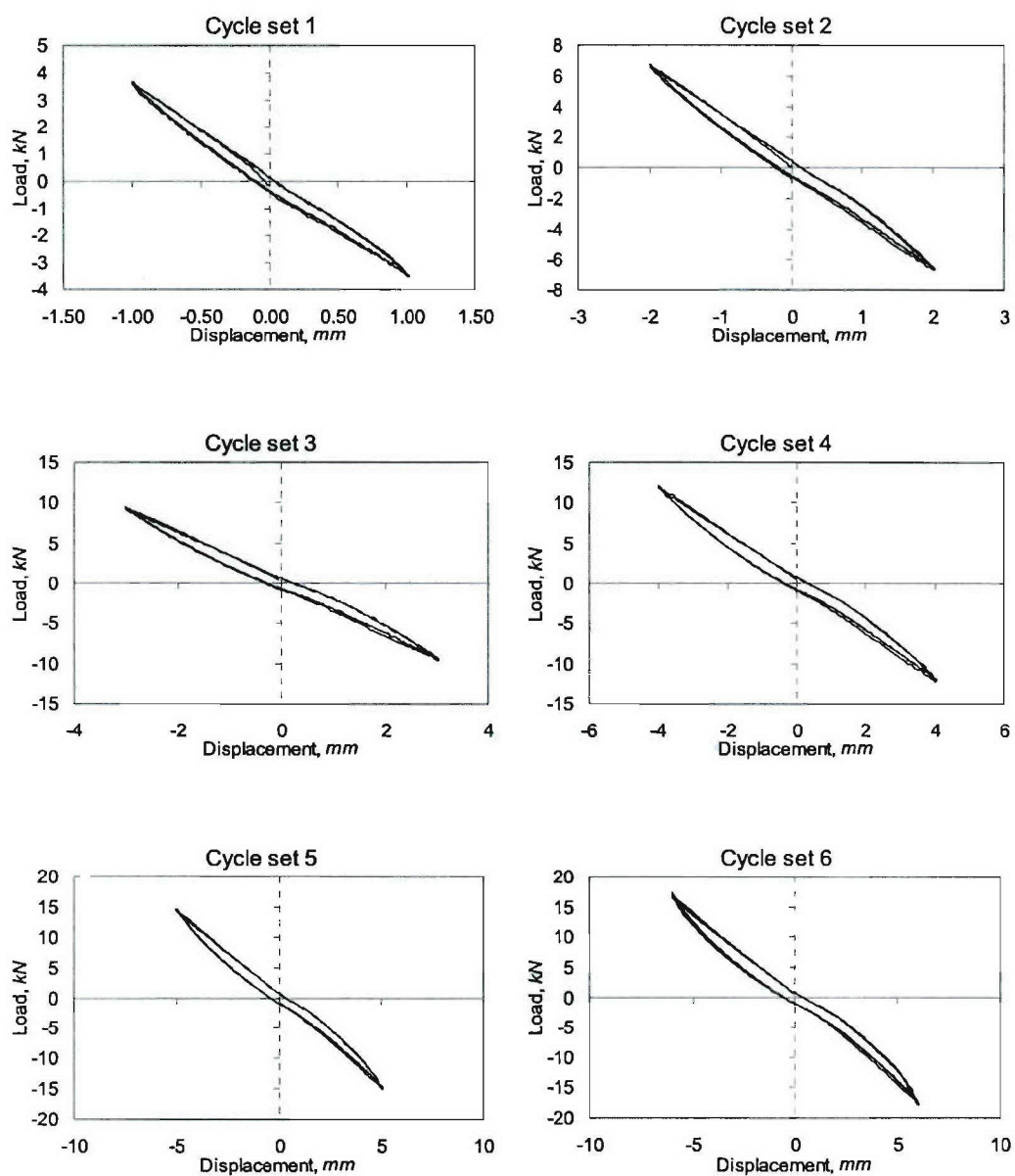


**Figure E.27. Load-Displacement Curves for Specimen DL-7, Cycle Sets 1-6**

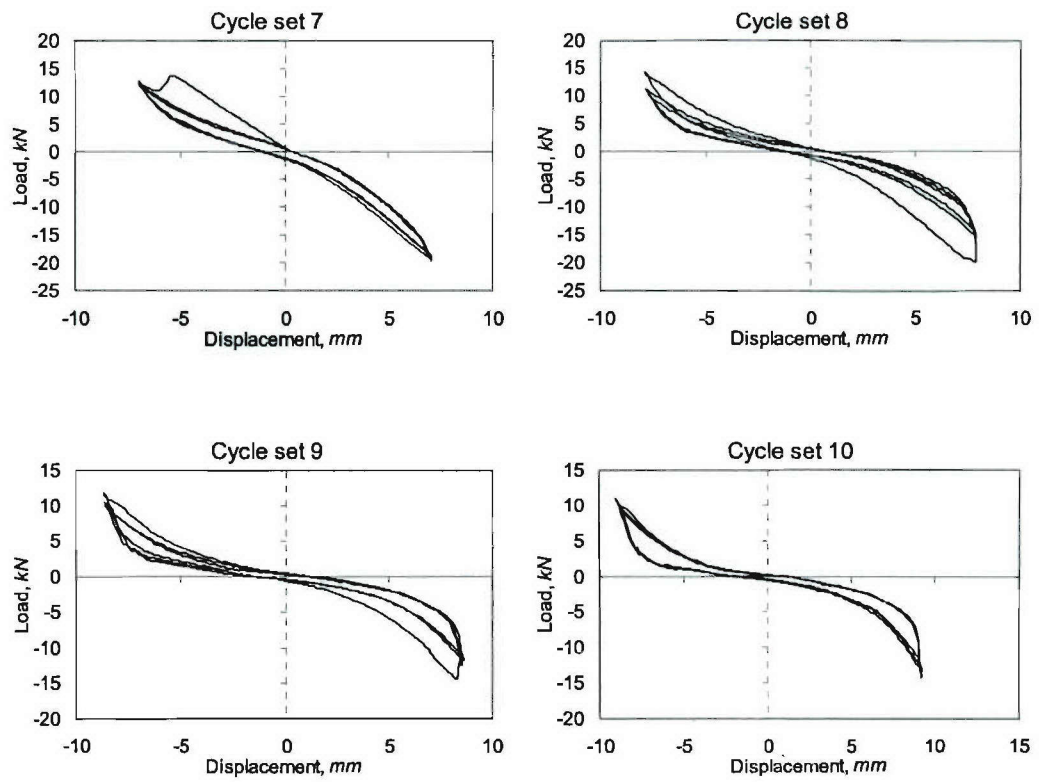


**Figure E.28. Load-Displacement Curves for Specimen DL-7, Cycle Sets 7-12**

## Appendix F

### Load versus Strain Plots of Hybrid Joints

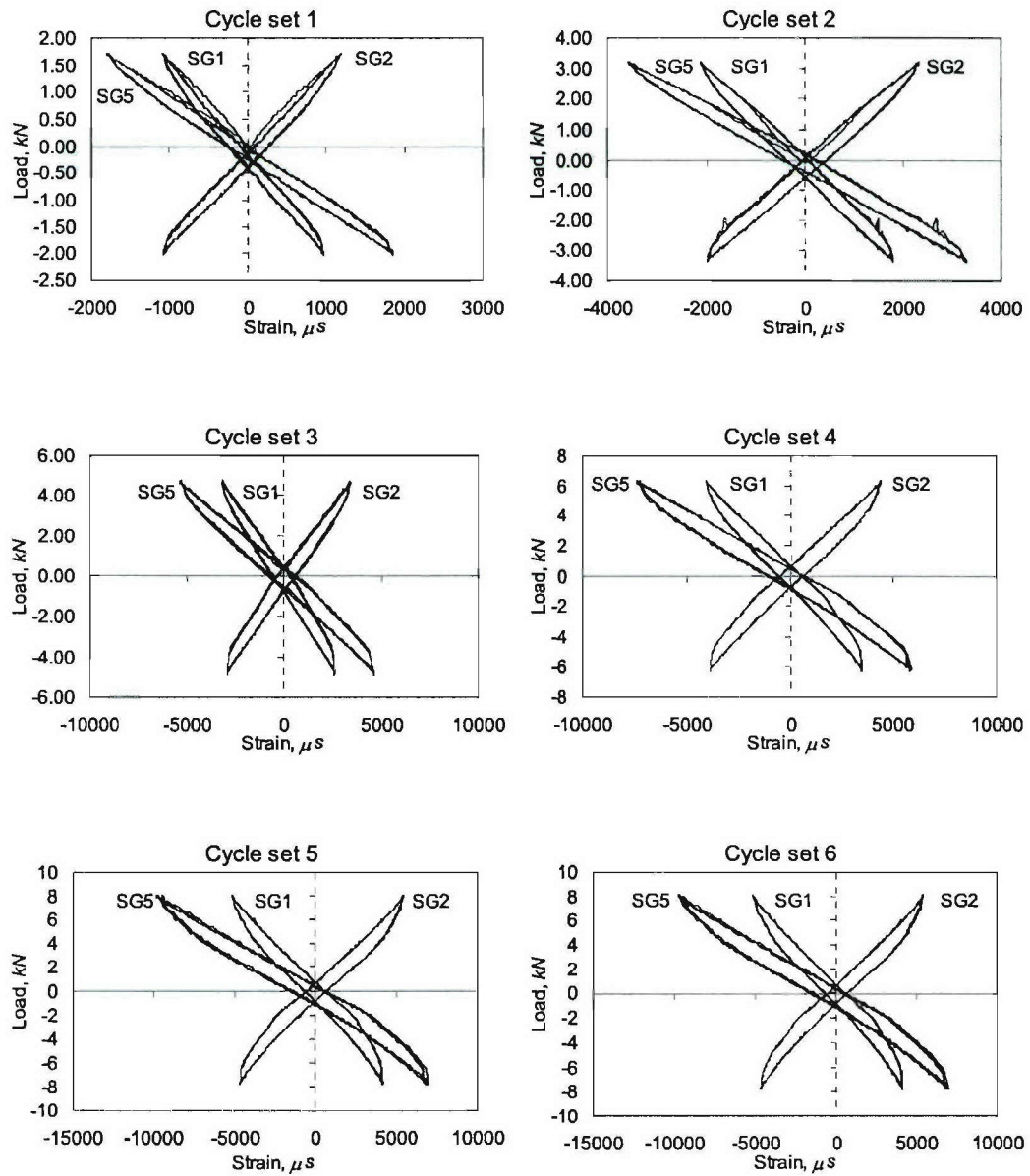
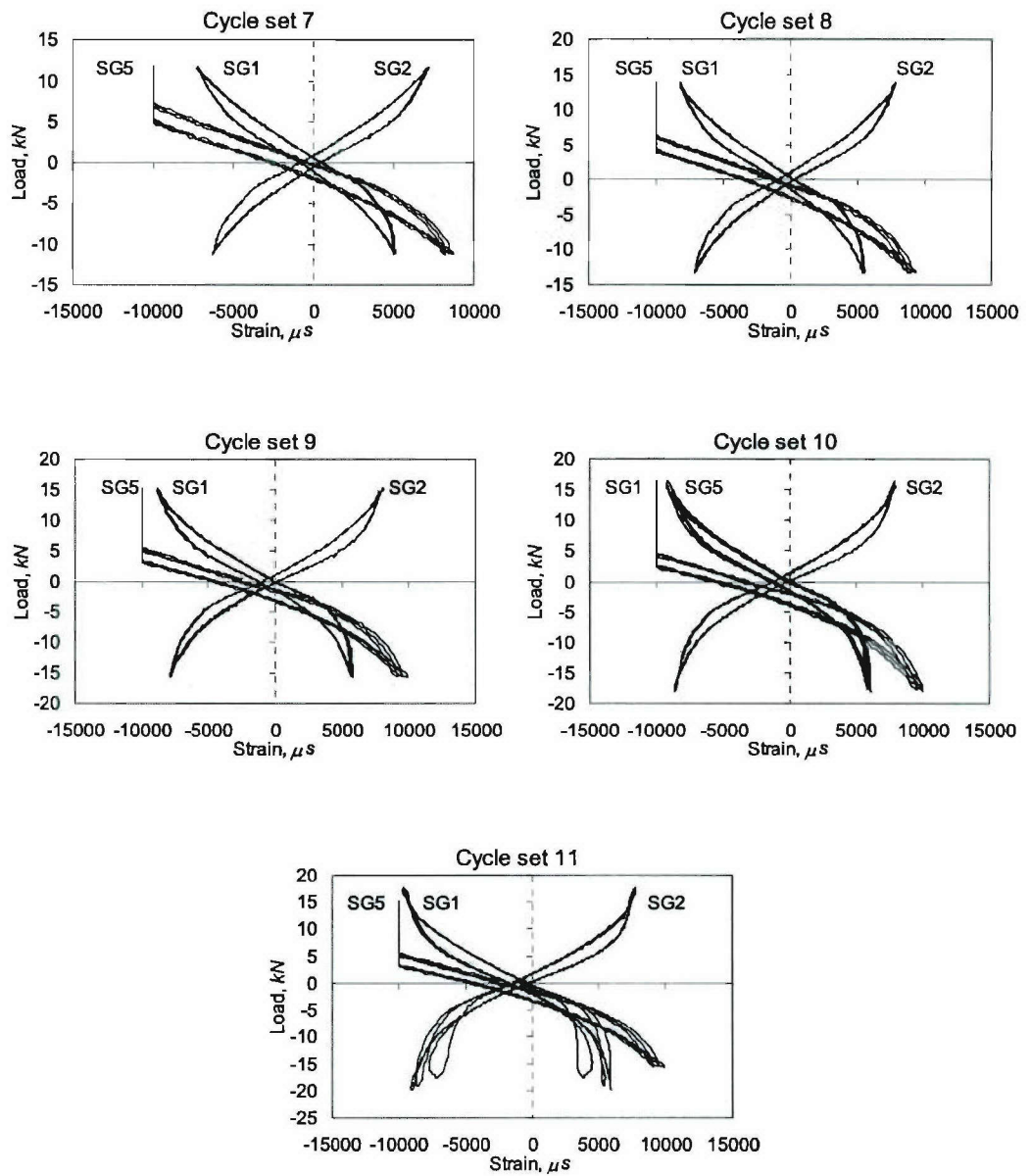
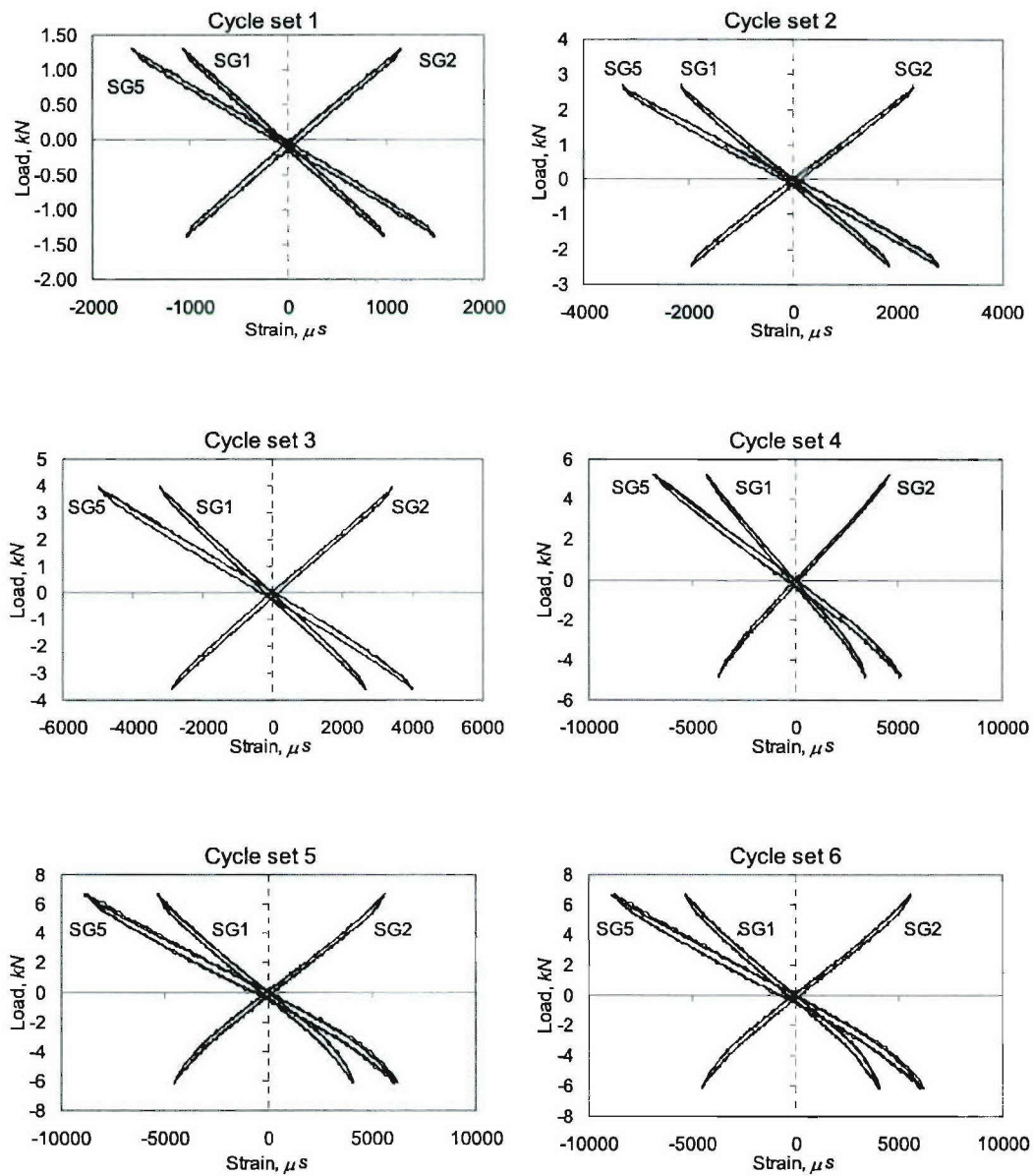


Figure F.1. Load-Strain Curves for Specimen BP-1, Cycle Sets 1-6



**Figure F.2. Load-Strain Curves for Specimen BP-1, Cycle Sets 7-12**





**Figure F.3. Load-Strain Curves for Specimen BT-2, Cycle Sets 1-6**

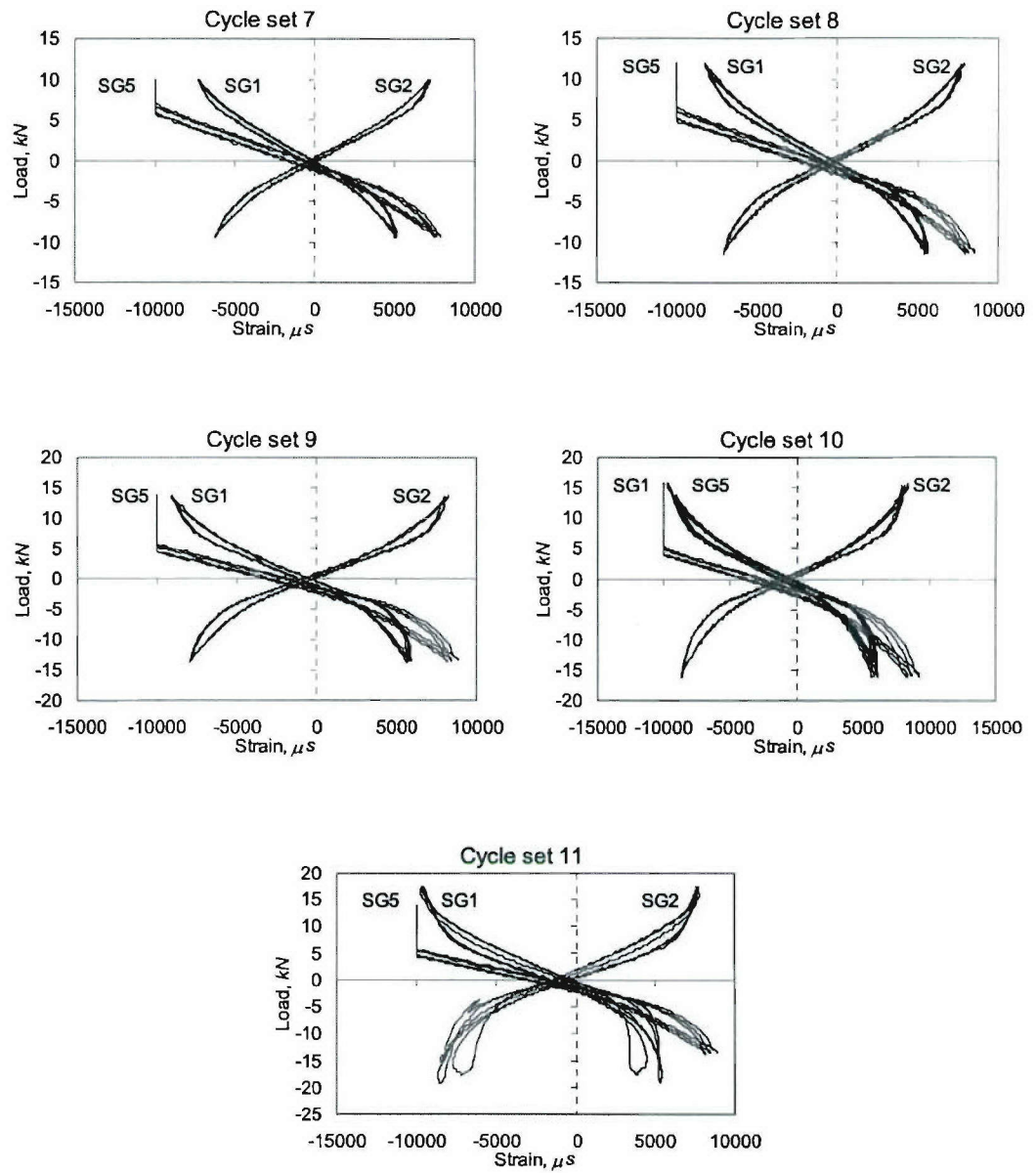


**Figure F.4. Load-Strain Curves for Specimen BT-2, Cycle Sets 7-11**

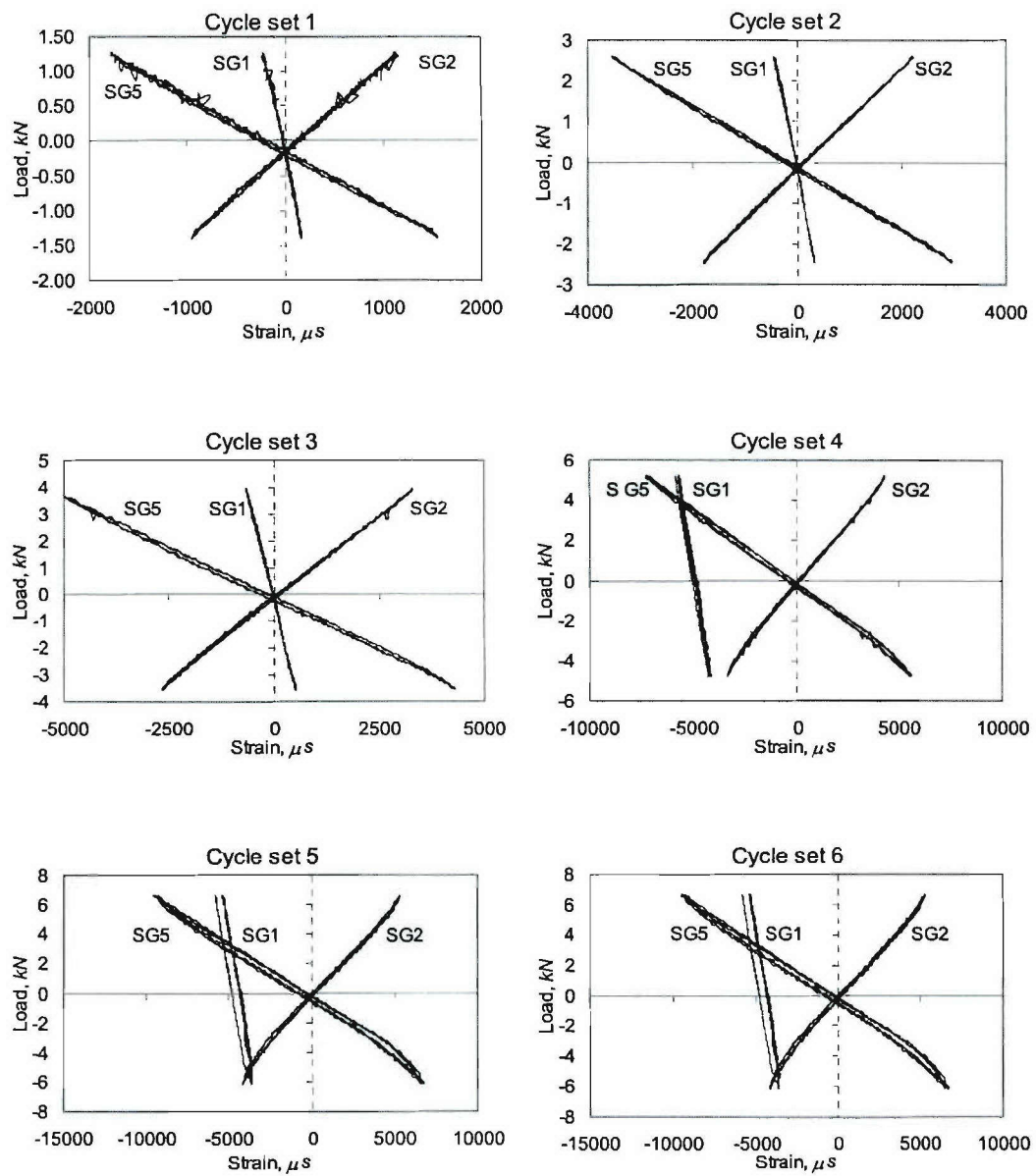


**Figure F.5. Load-Strain Curves for Specimen BP-3, Cycle Sets 1-6**

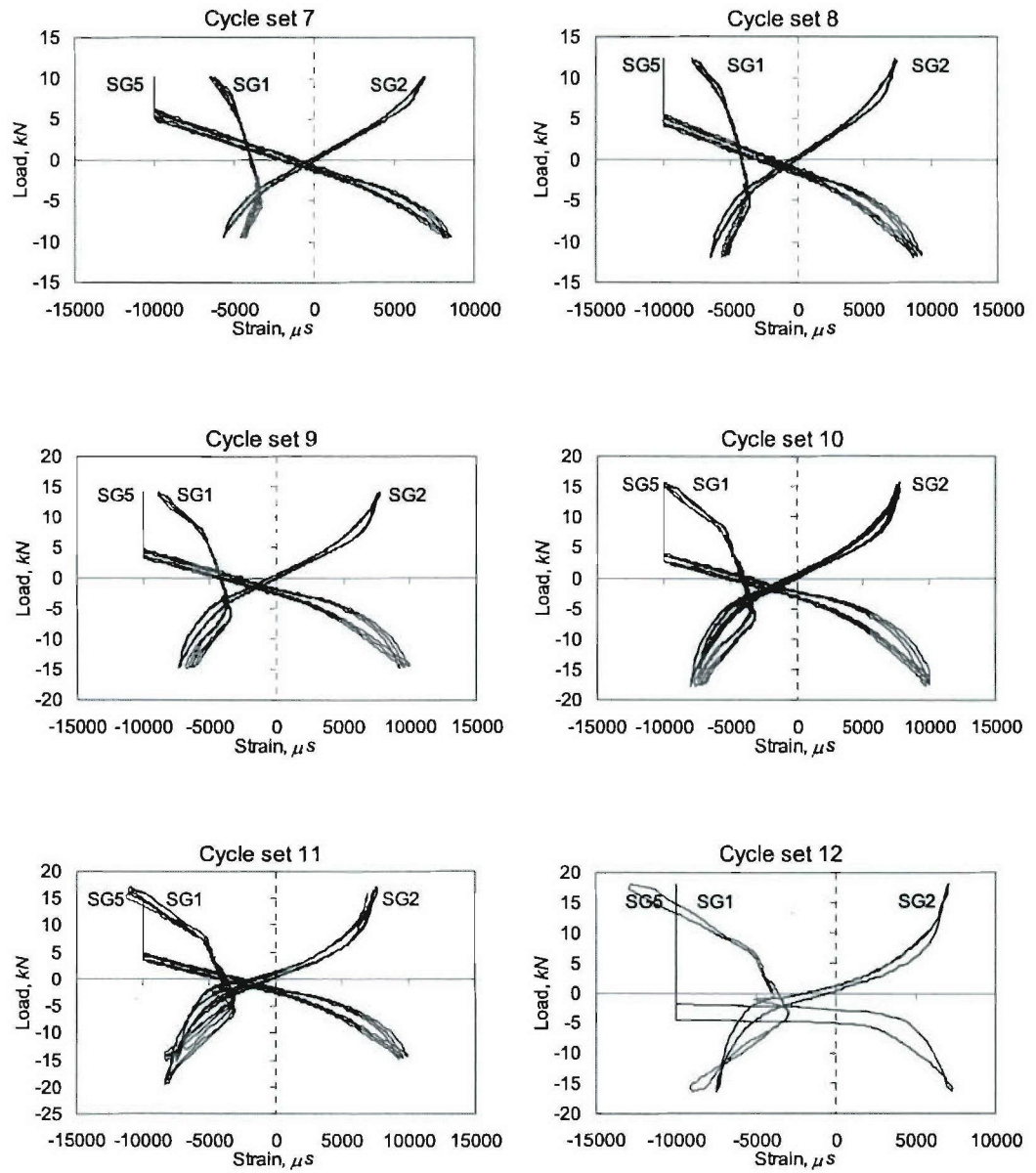


**Figure F.6. Load-Strain Curves for Specimen BP-3, Cycle Sets 7-12**



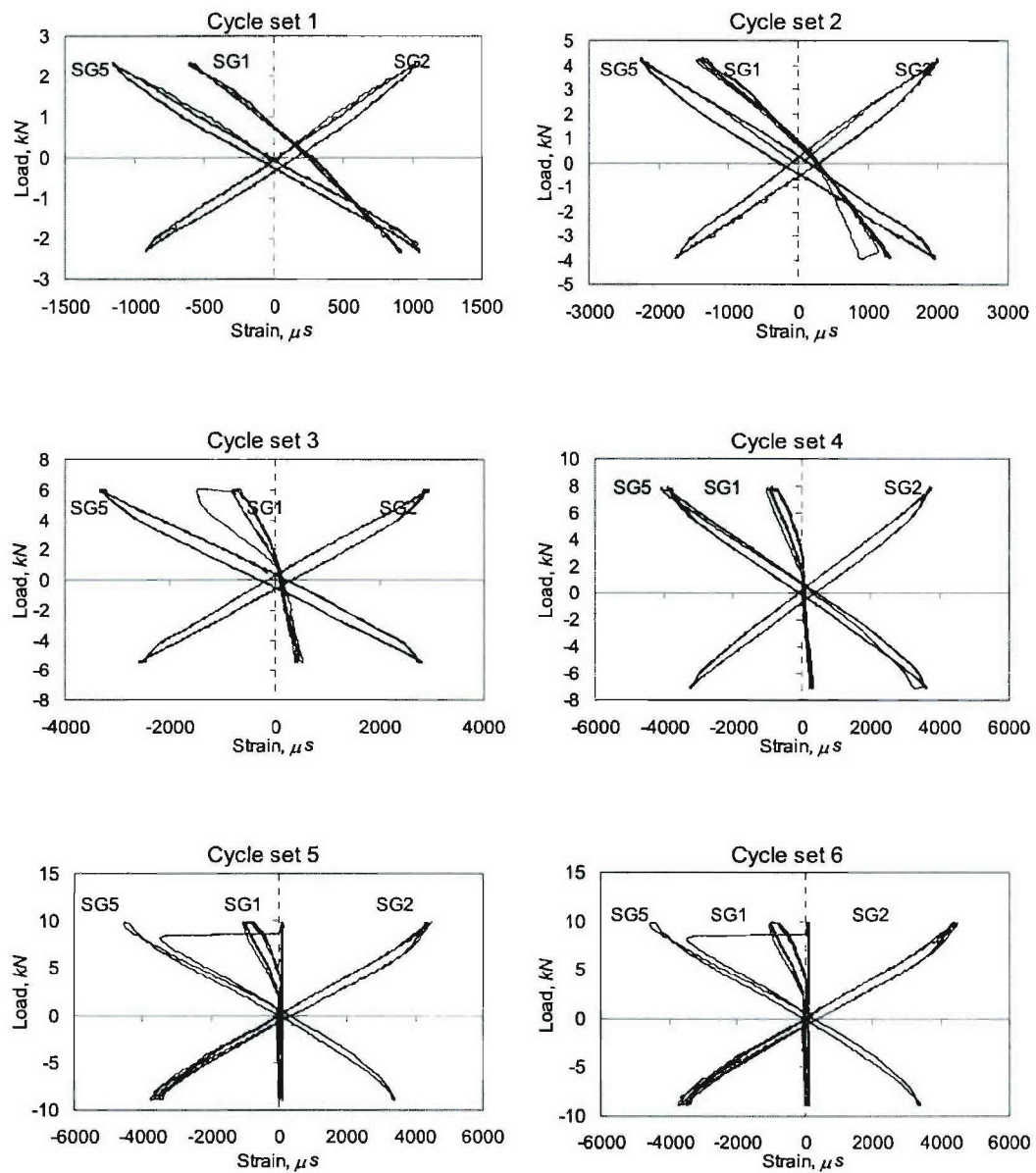


**Figure F.7. Load-Strain Curves for Specimen BT-4, Cycle Sets 1-6**

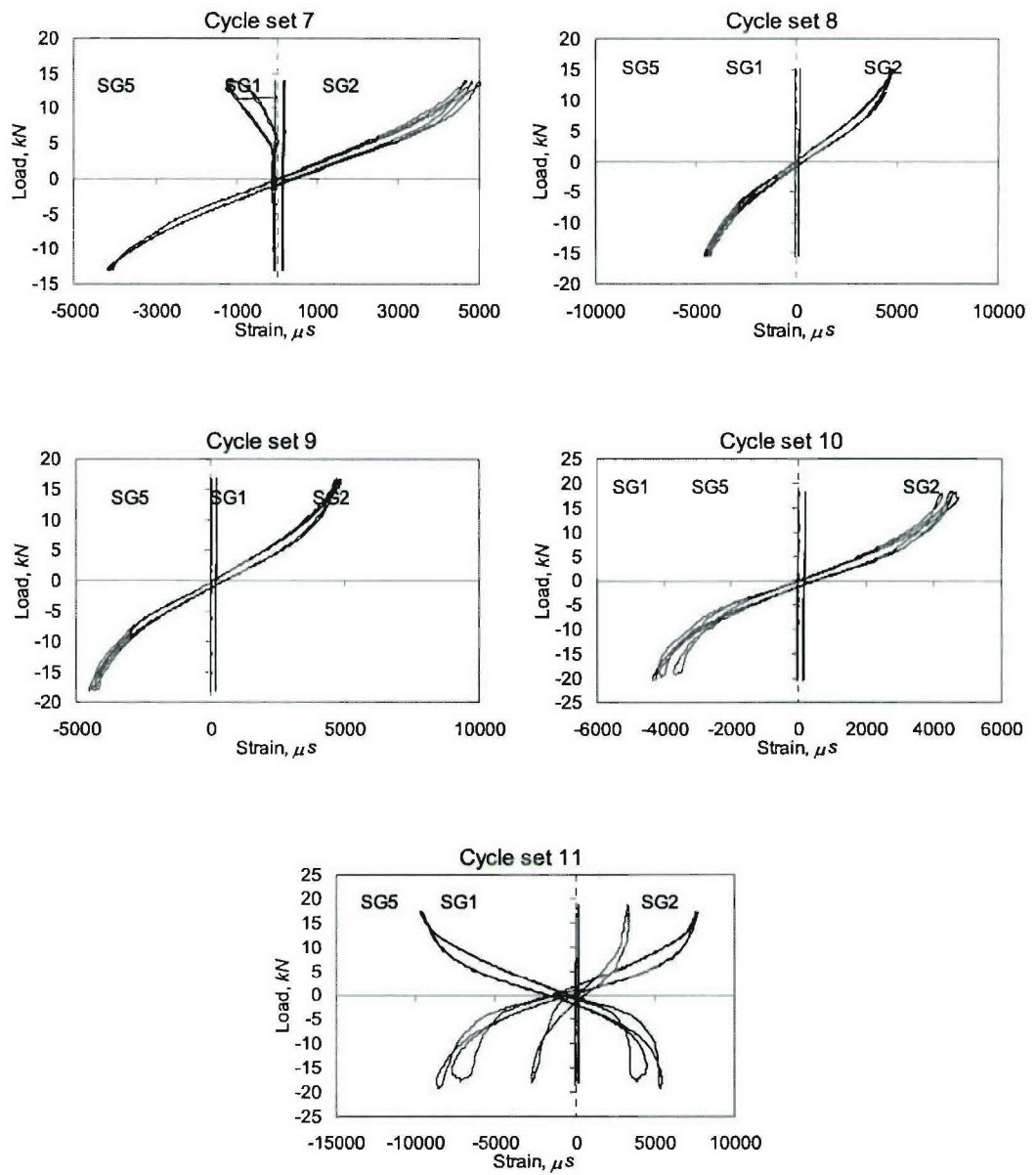


**Figure F.8. Load-Strain Curves for Specimen BT-4, Cycle Sets 7-12**

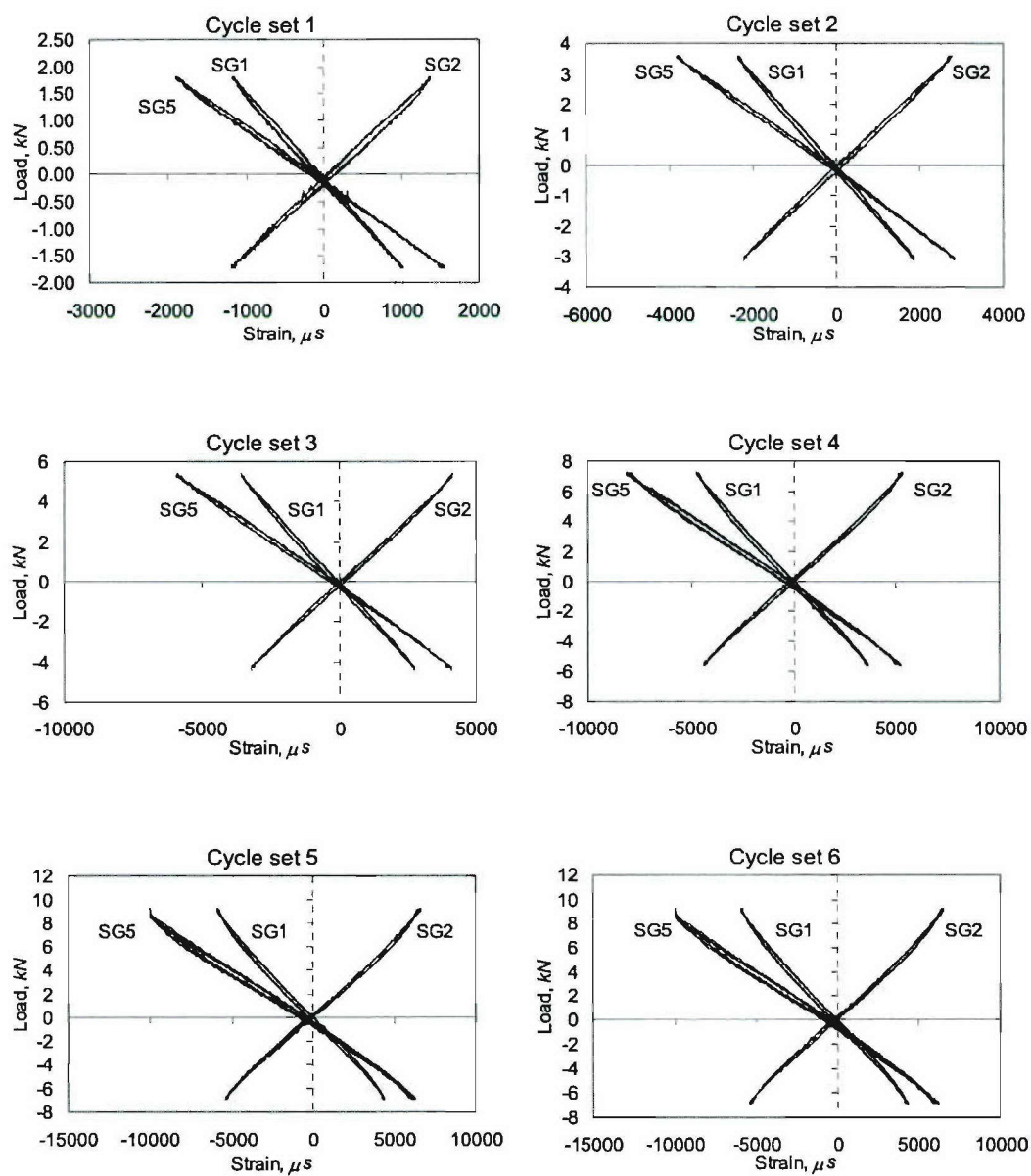


**Figure F.9. Load-Strain Curves for Specimen BP-5, Cycle Sets 1-6**

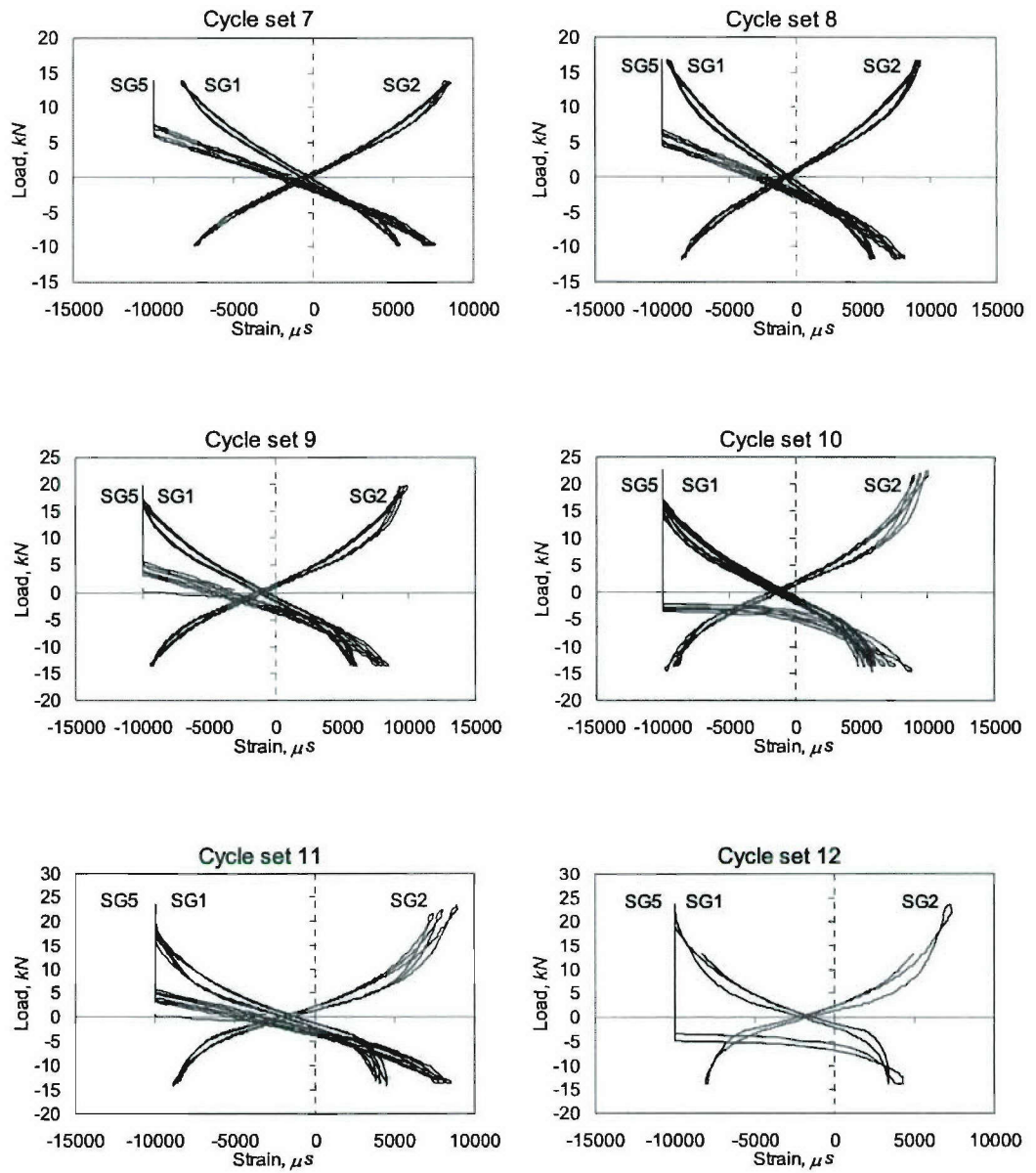


**Figure F.10. Load-Strain Curves for Specimen BP-5, Cycle Sets 7-12**



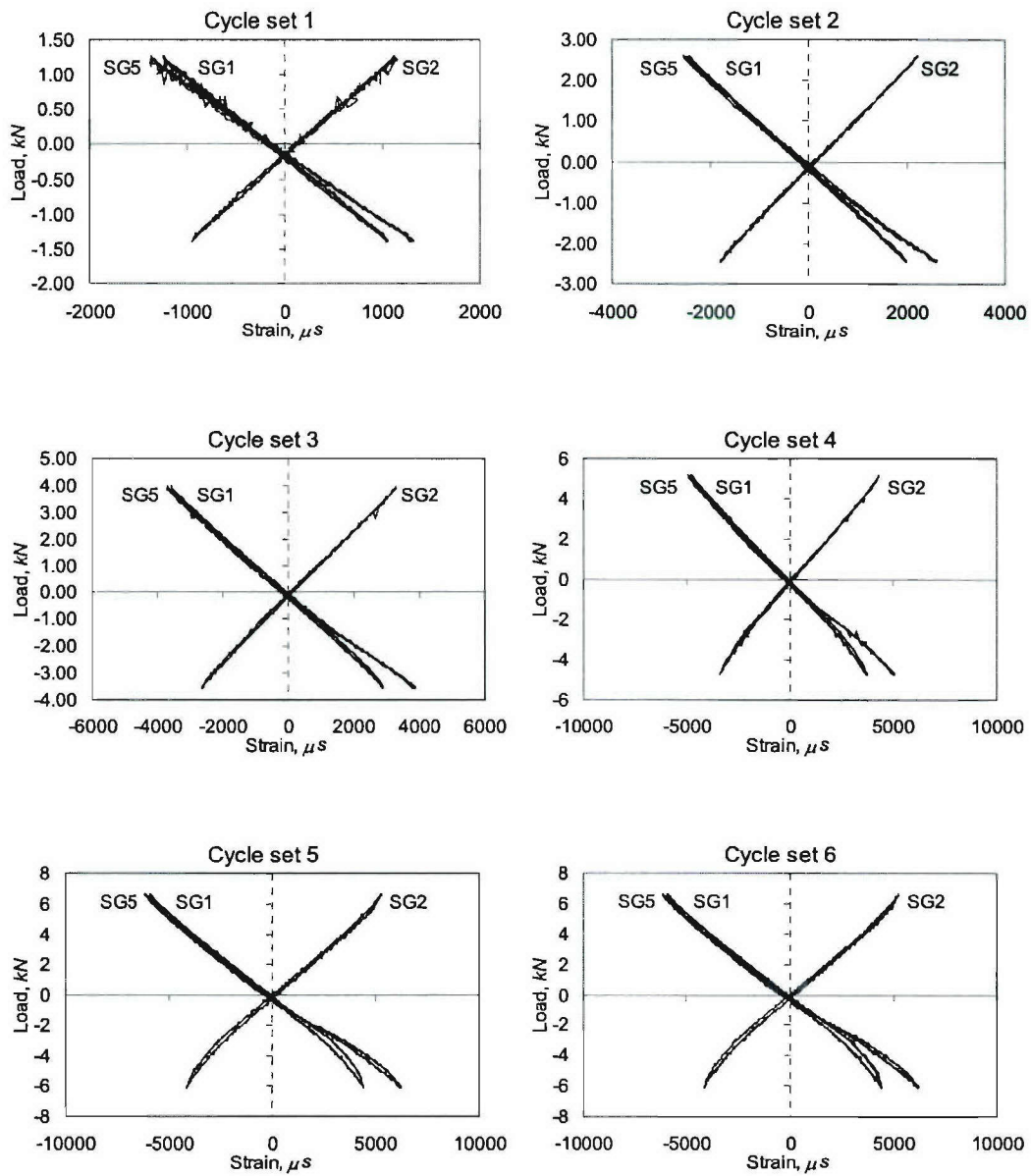


**Figure F.11. Load-Strain Curves for Specimen BT-6, Cycle Sets 1-6**

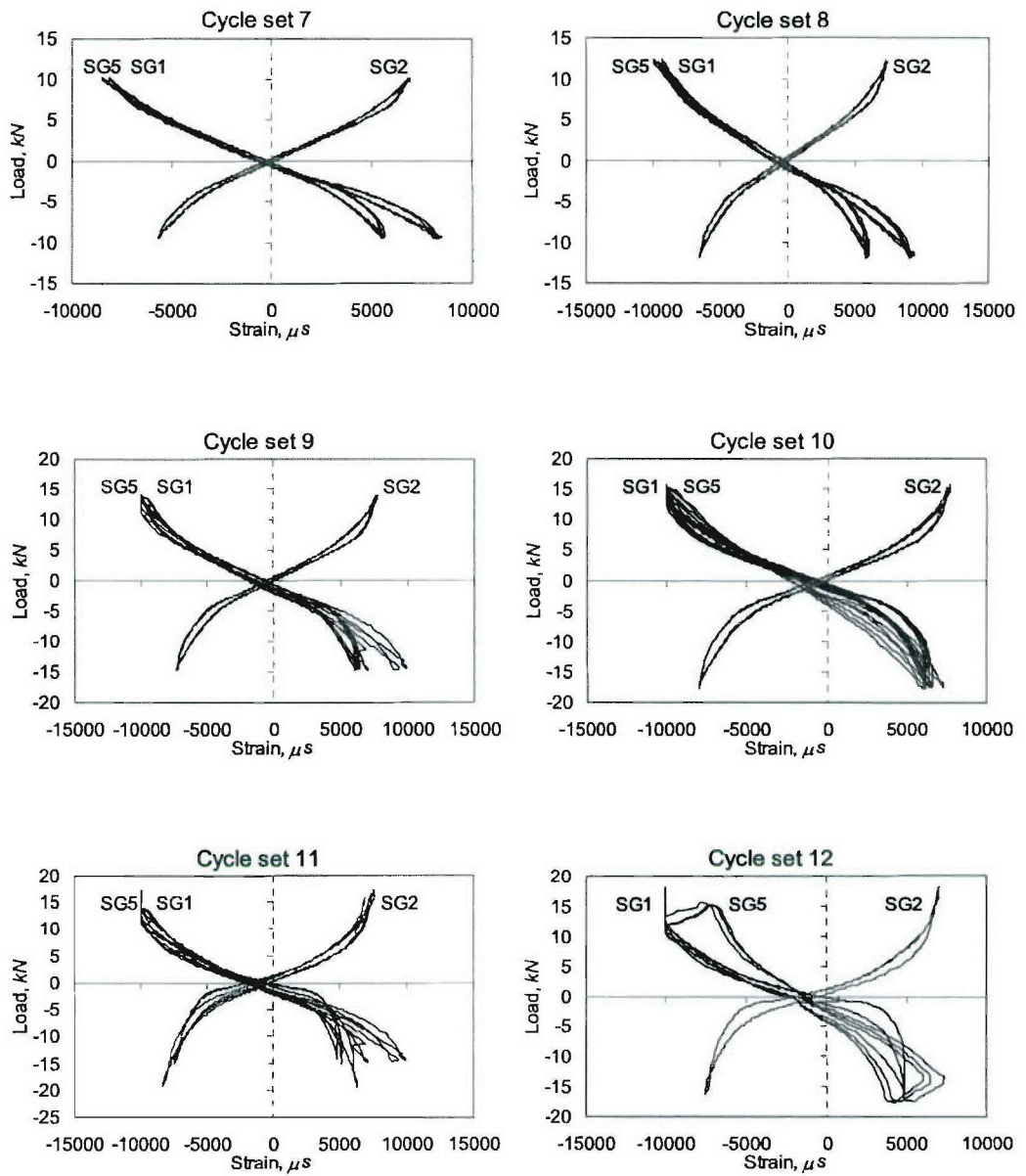


**Figure F.12. Load-Strain Curves for Specimen BT-6, Cycle Sets 7-12**

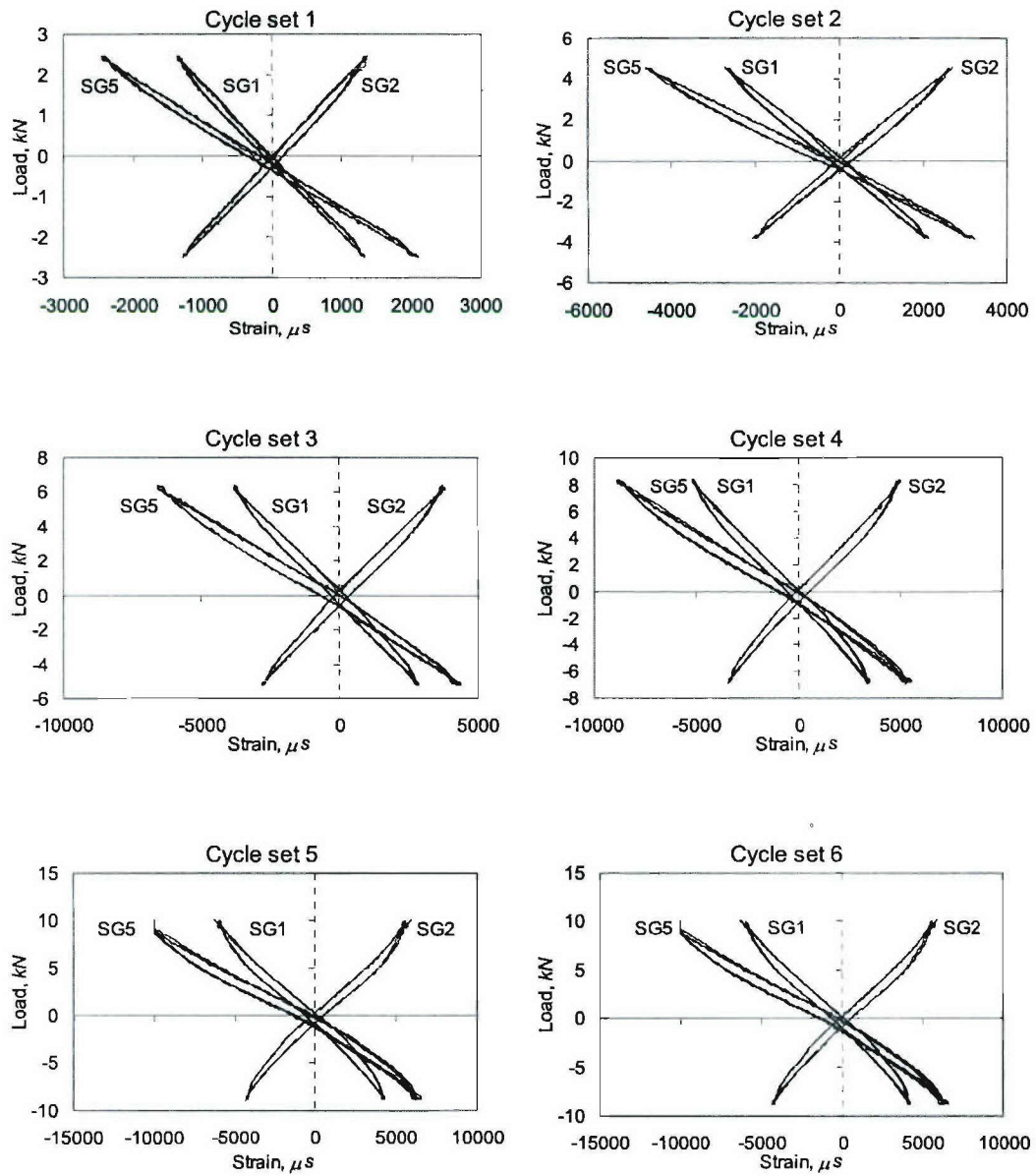


**Figure F.13. Load-Strain Curves for Specimen BT-7, Cycle Sets 1-6**

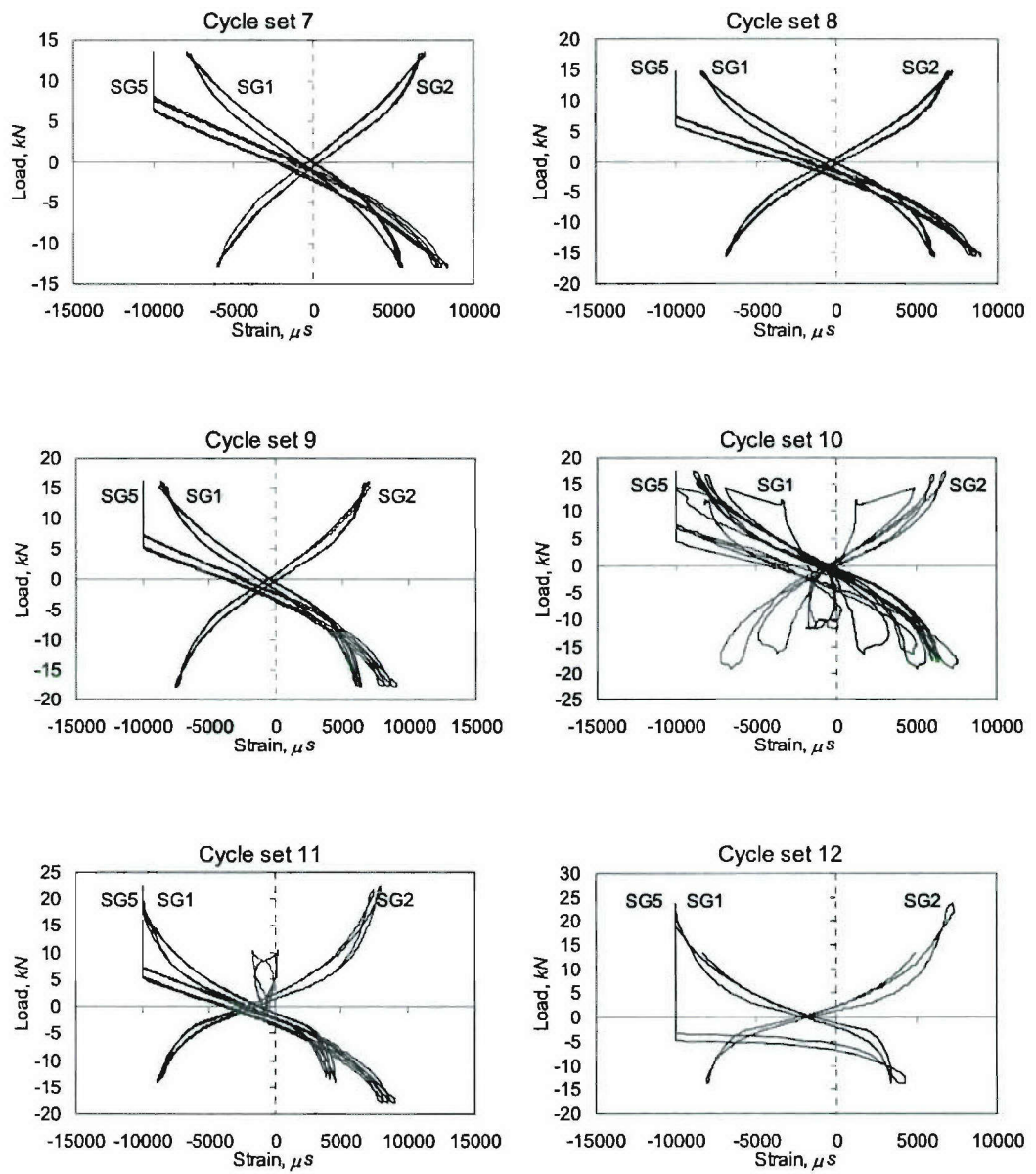


**Figure F.14. Load-Strain Curves for Specimen BT-7, Cycle Sets 7-12**



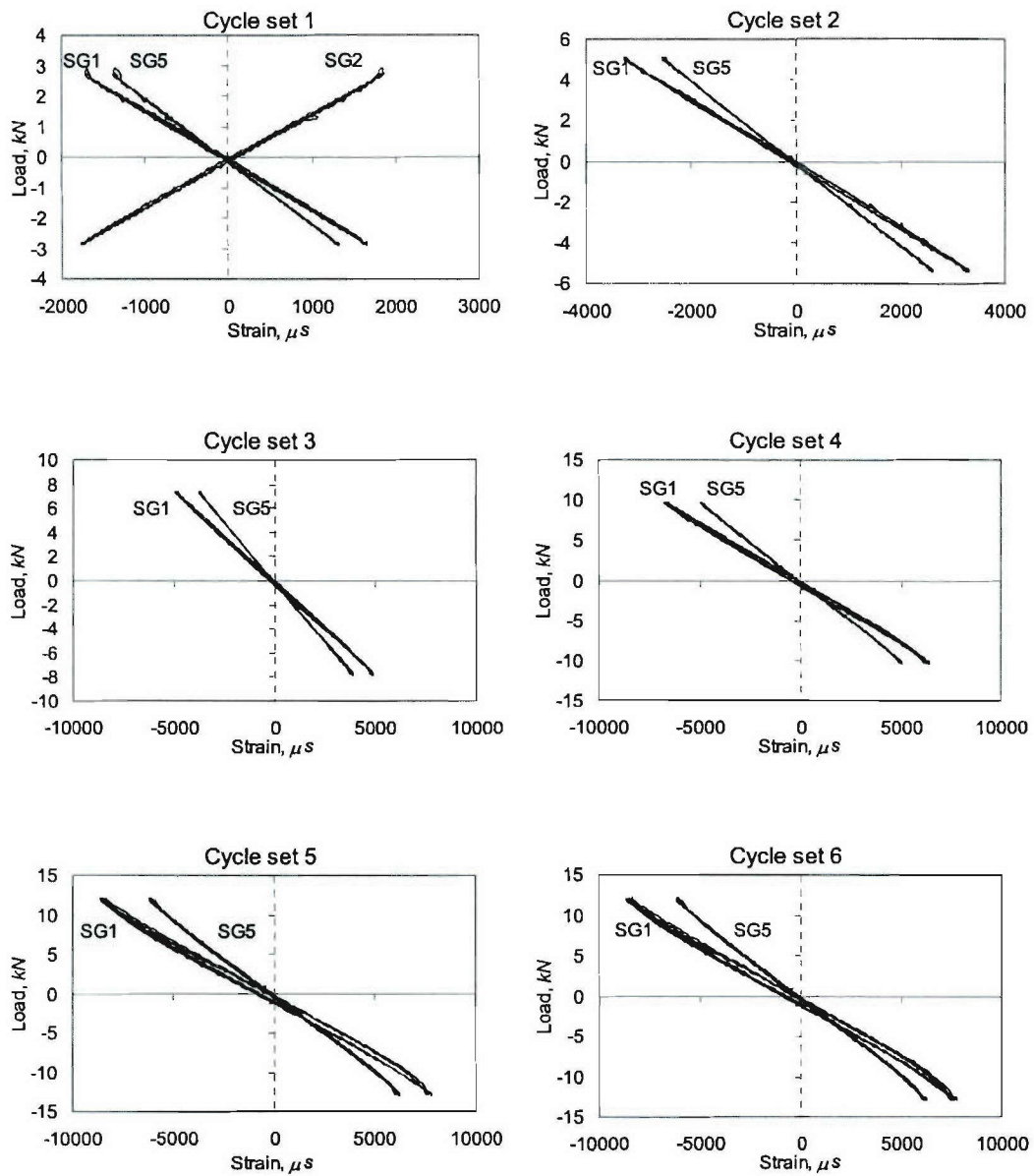


**Figure F.15. Load-Strain Curves for Specimen DM-1, Cycle Sets 1-6**

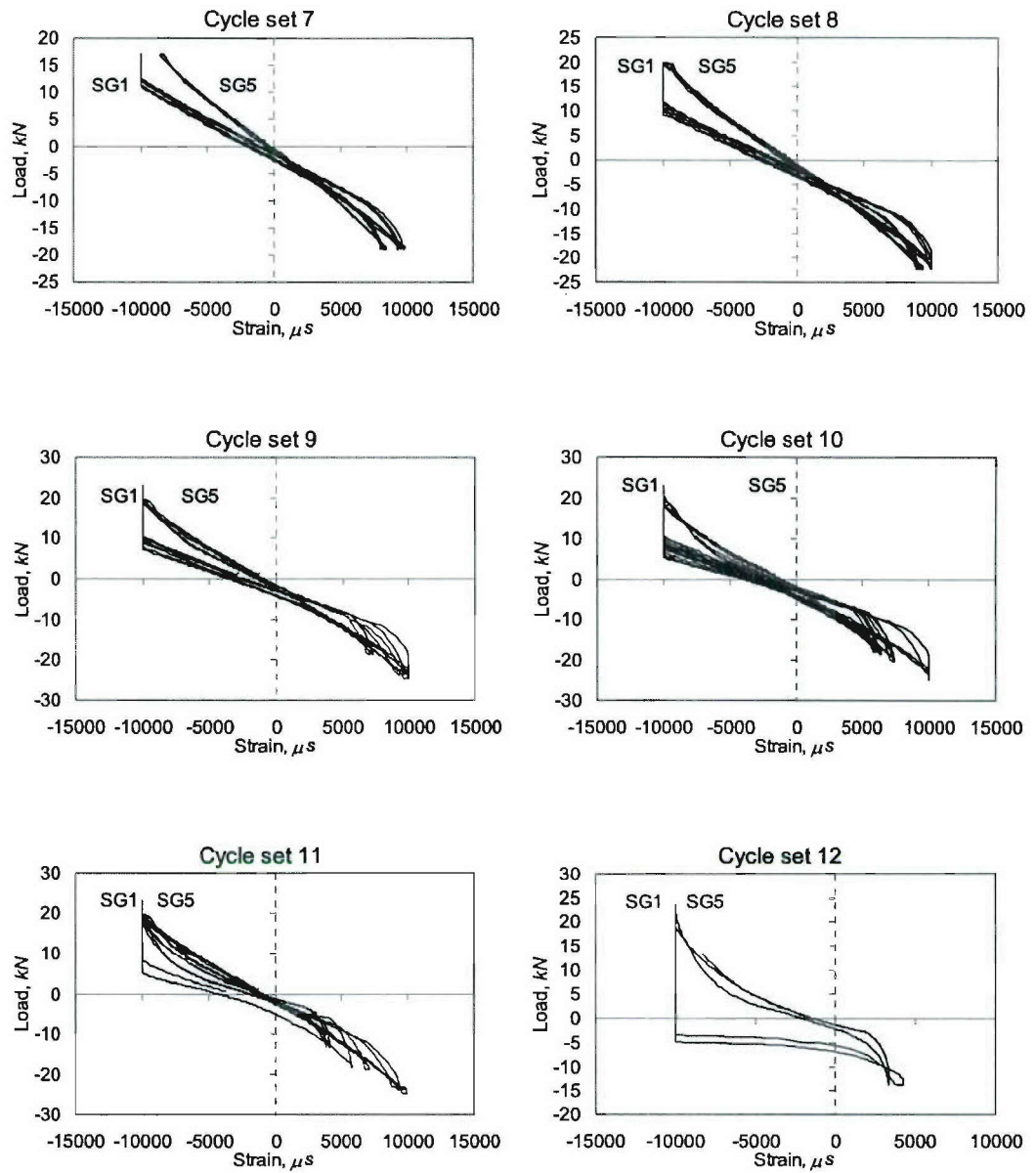


**Figure F.16. Load-Strain Curves for Specimen DM-1, Cycle Sets 7-12**

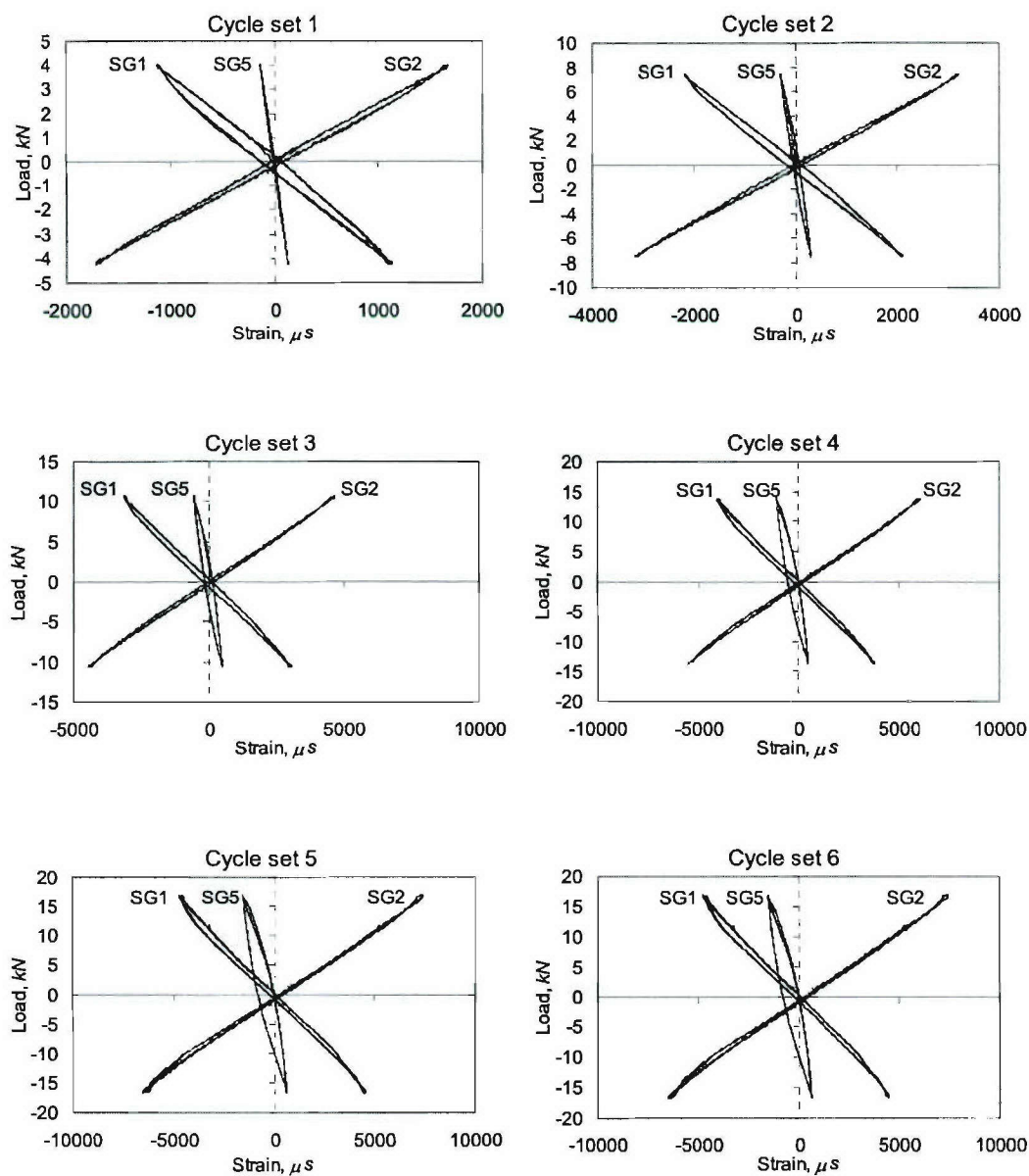


**Figure F.17. Load-Strain Curves for Specimen DL-2, Cycle Sets 1-6**

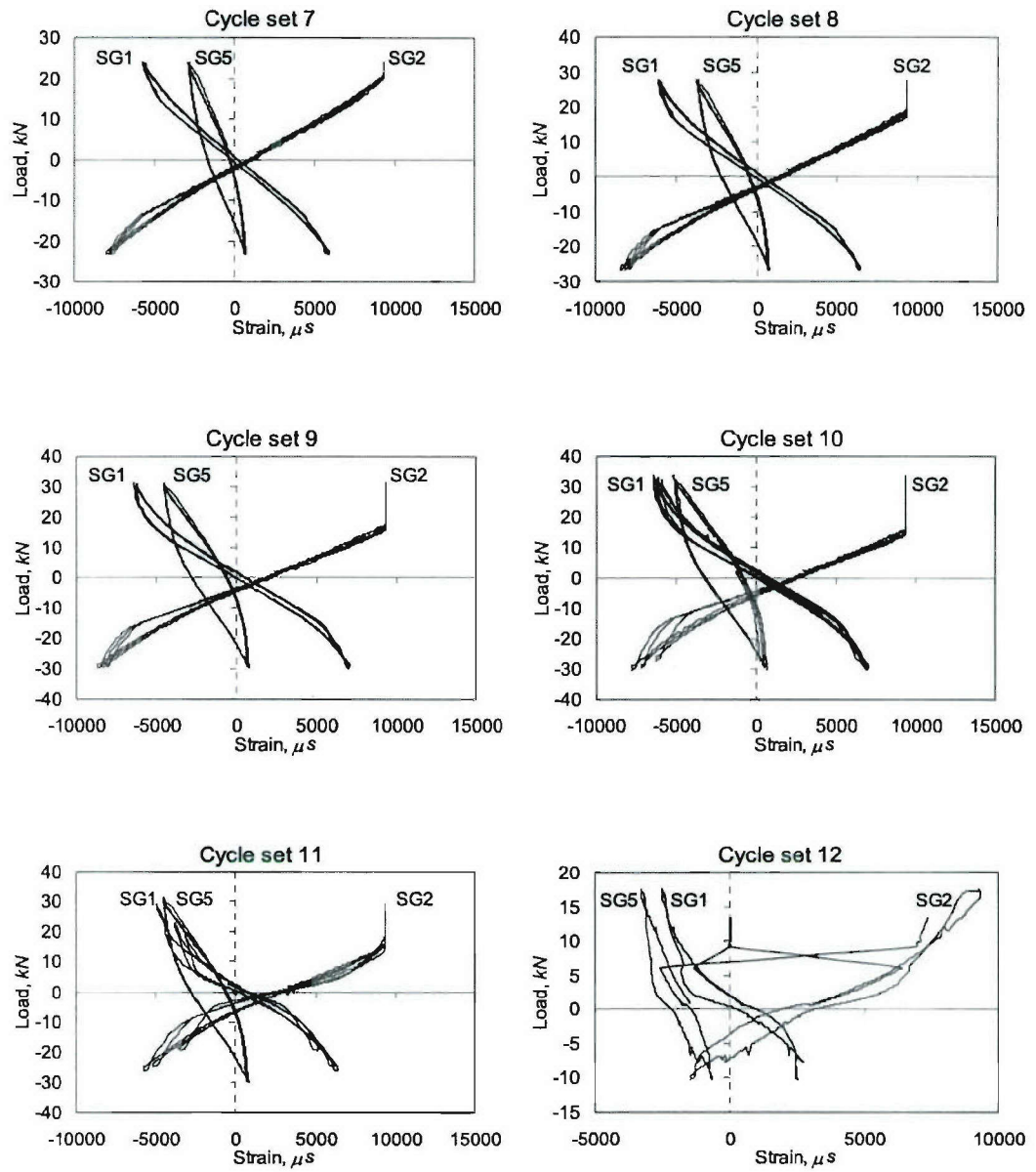


**Figure F.18. Load-Strain Curves for Specimen DL-2, Cycle Sets 7-12**



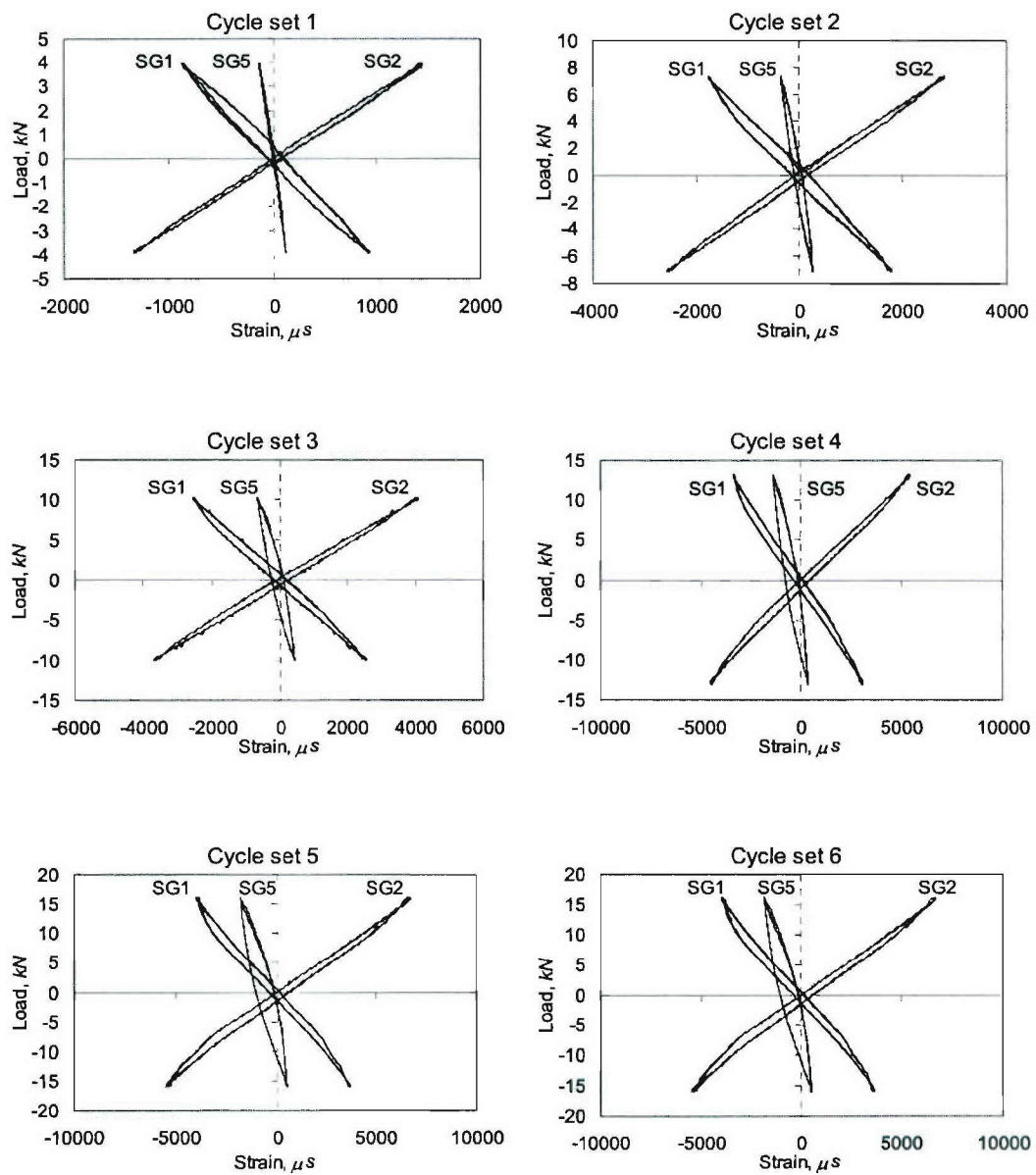


**Figure F.19. Load-Strain Curves for Specimen DL-3, Cycle Sets 1-6**

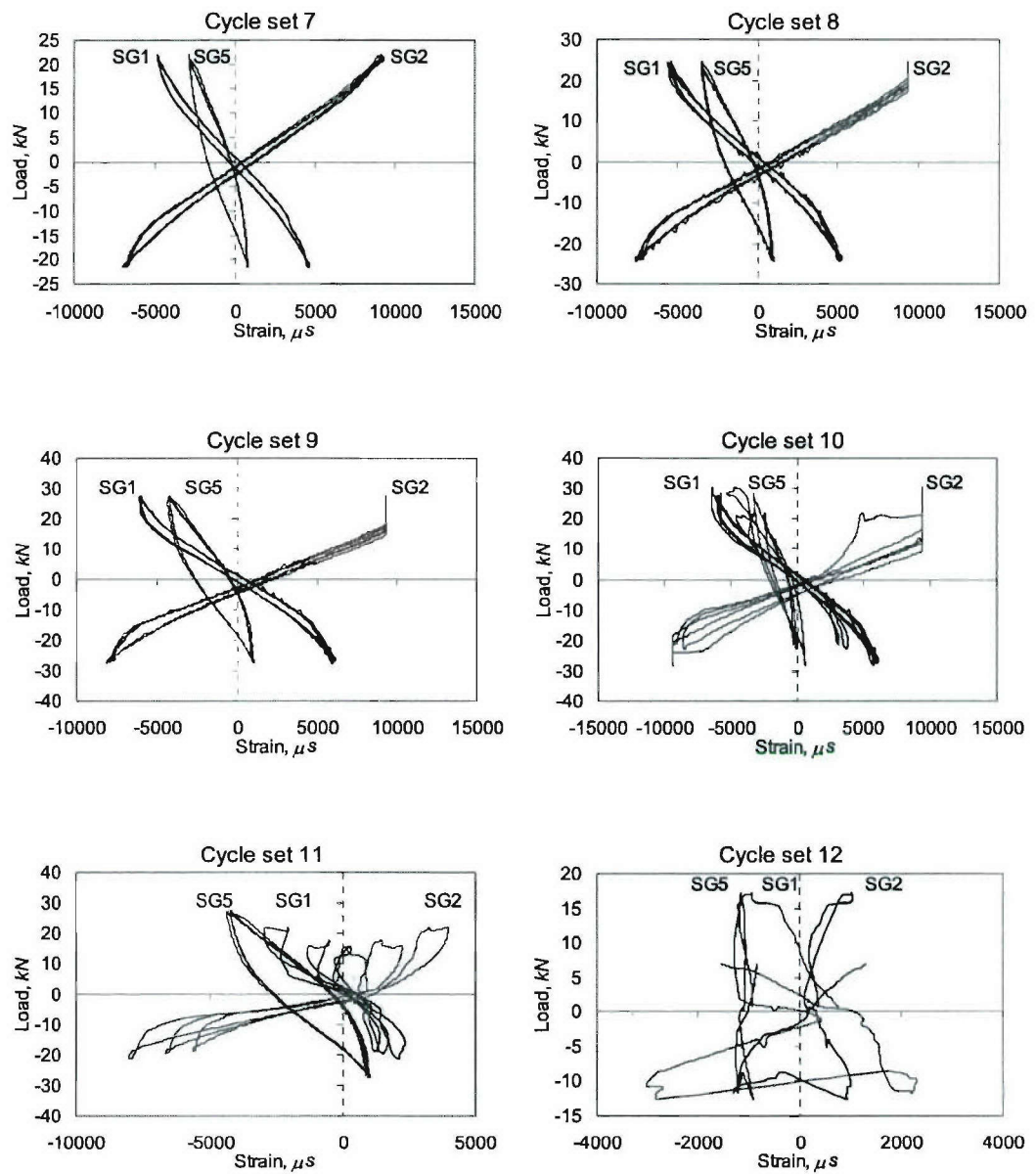


**Figure F.20. Load-Strain Curves for Specimen DL-3, Cycle Sets 6-12**

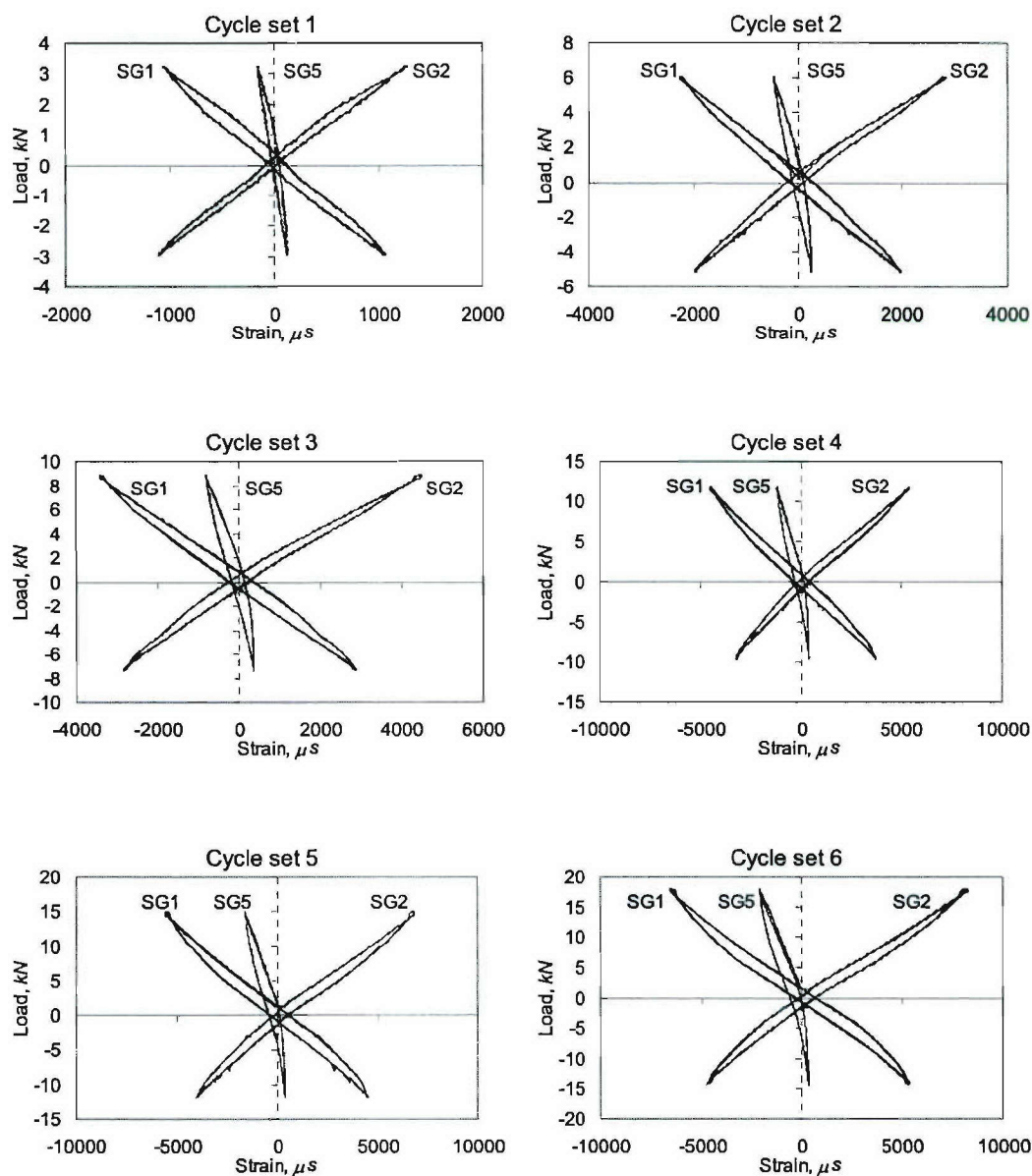


**Figure F.21. Load-Strain Curves for Specimen DS-4, Cycle Sets 1-6**

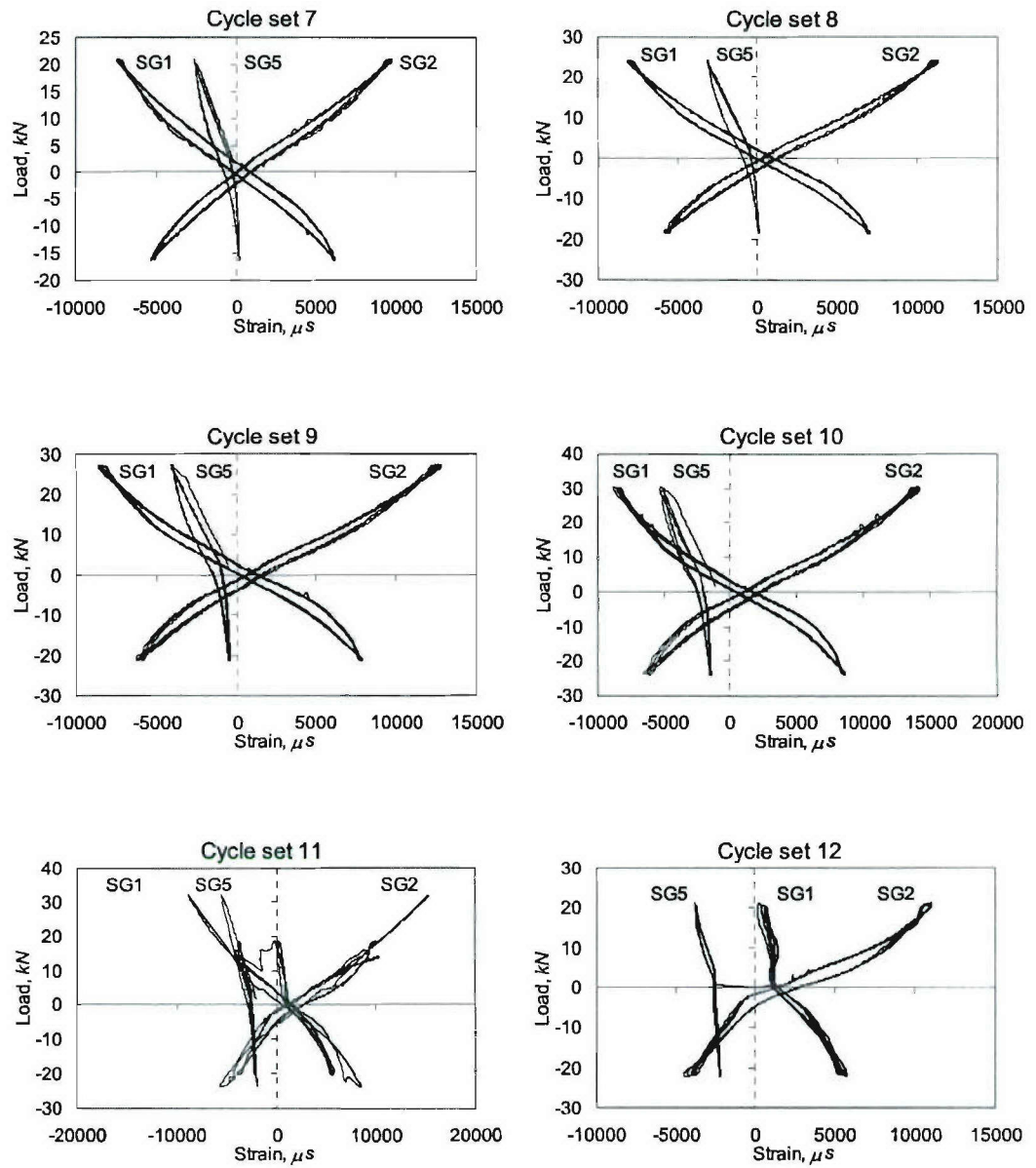


**Figure F.22. Load-Strain Curves for Specimen DS-4, Cycle Sets 7-12**



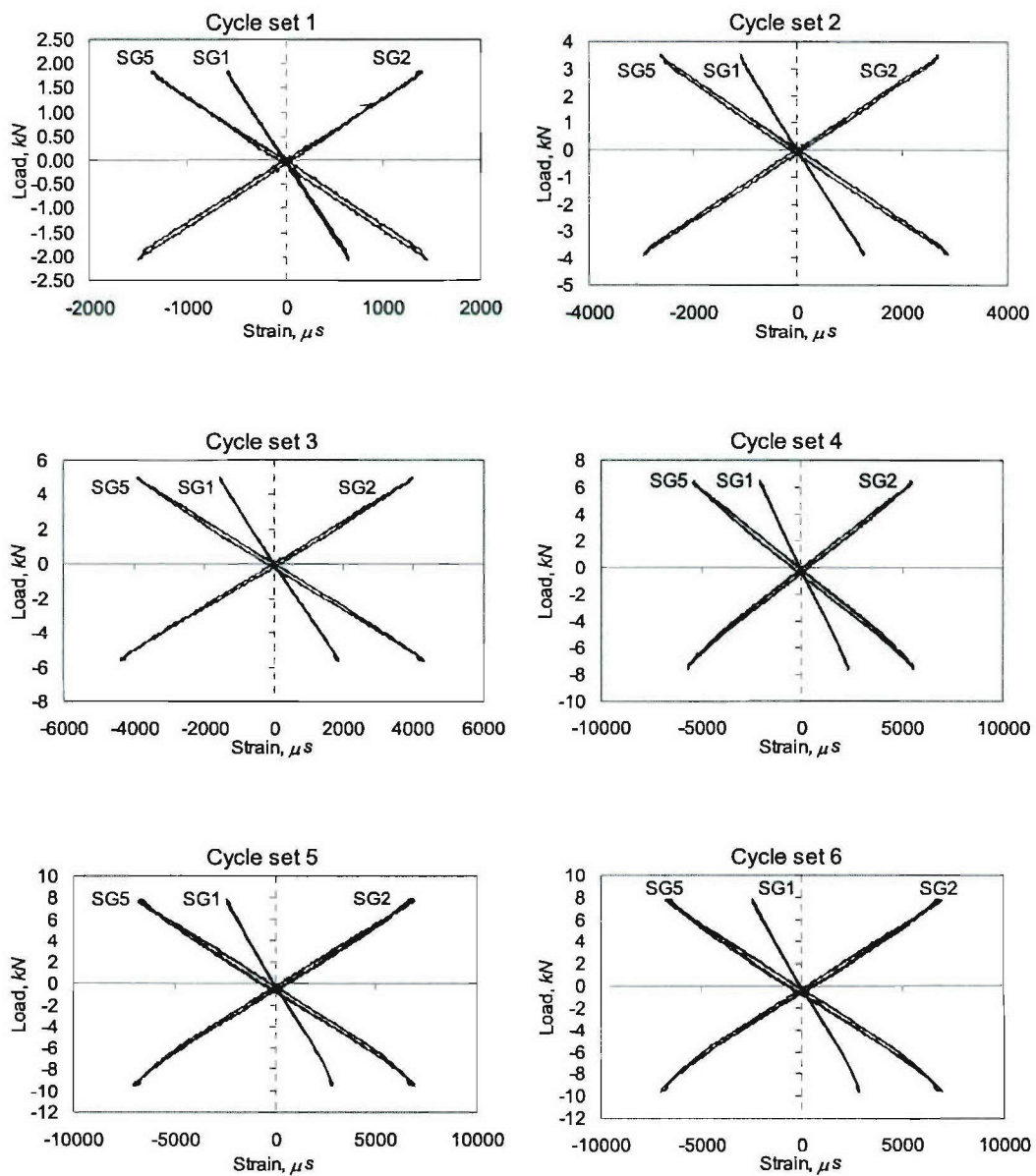


**Figure F.23. Load-Strain Curves for Specimen DL-5, Cycle Sets 1-6**

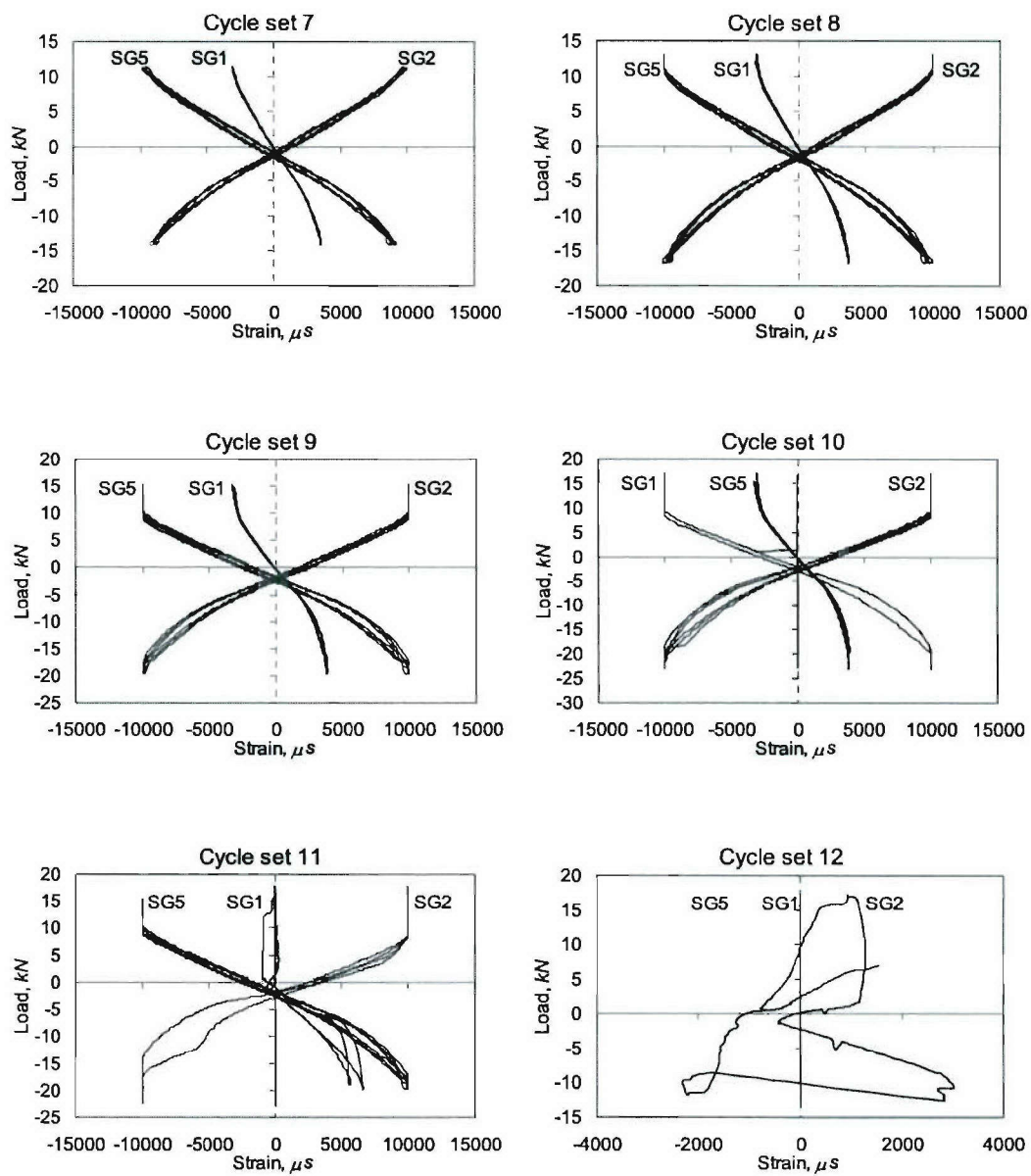


**Figure F.24. Load-Strain Curves for Specimen DL-5, Cycle Sets 7-12**

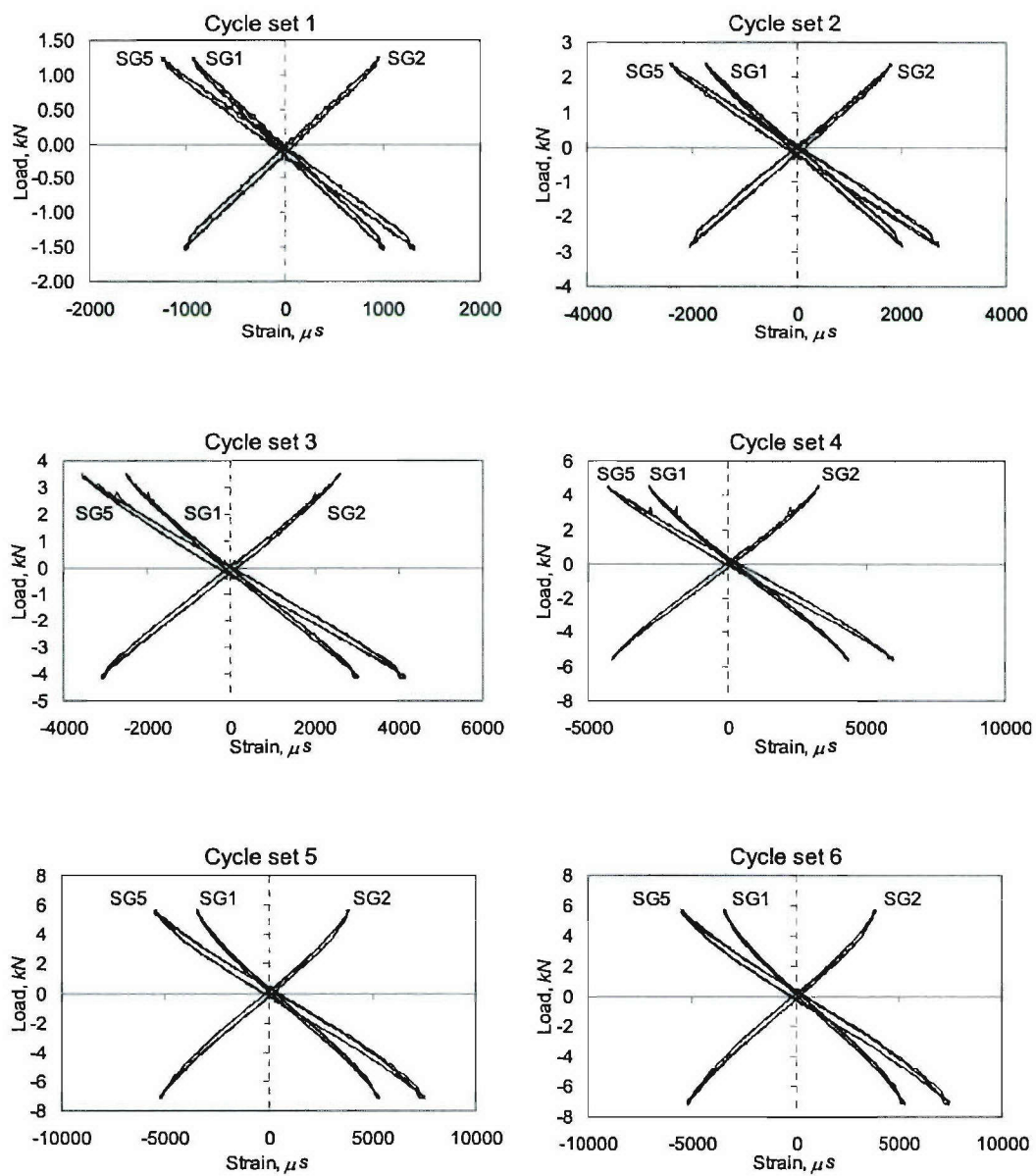


**Figure F.25. Load-Strain Curves for Specimen DM-6, Cycle Sets 1-6**

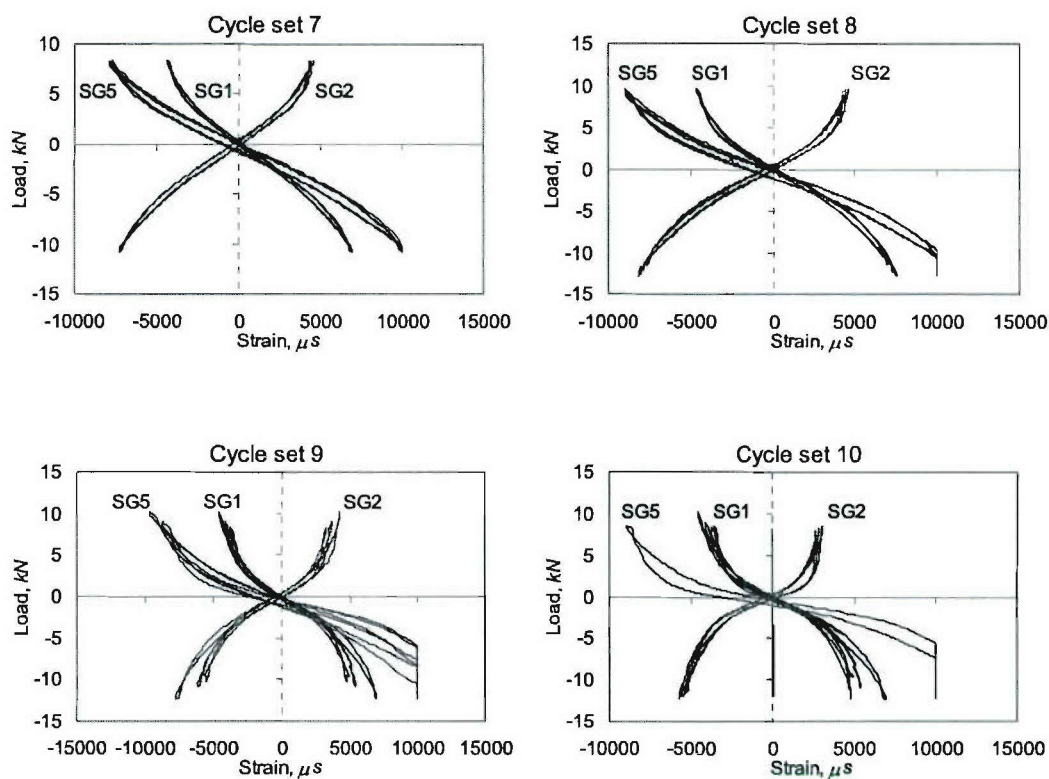


**Figure F.26. Load-Strain Curves for Specimen DM-6, Cycle Sets 7-12**



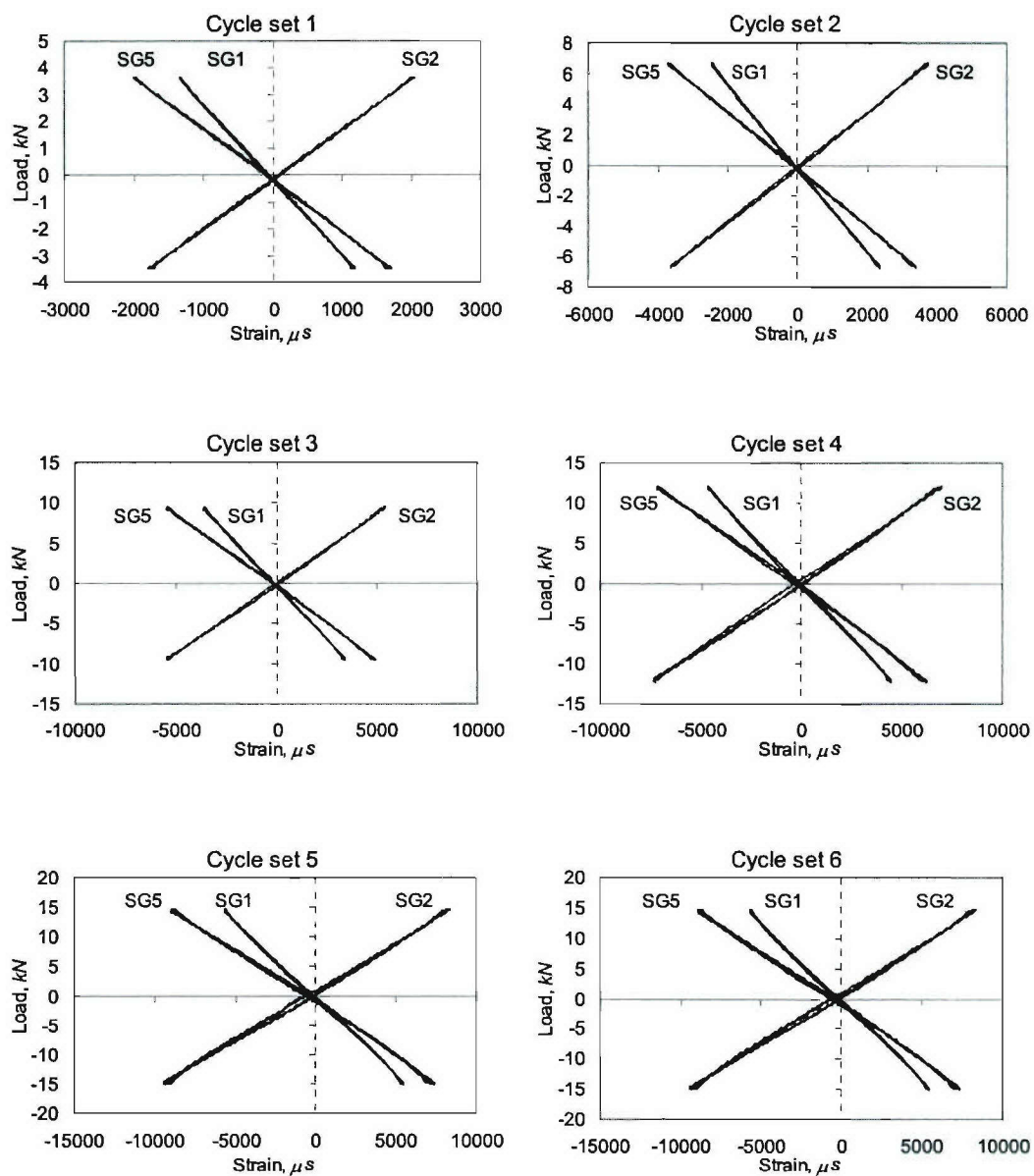


**Figure F.27. Load-Strain Curves for Specimen DL-7, Cycle Sets 1-6**

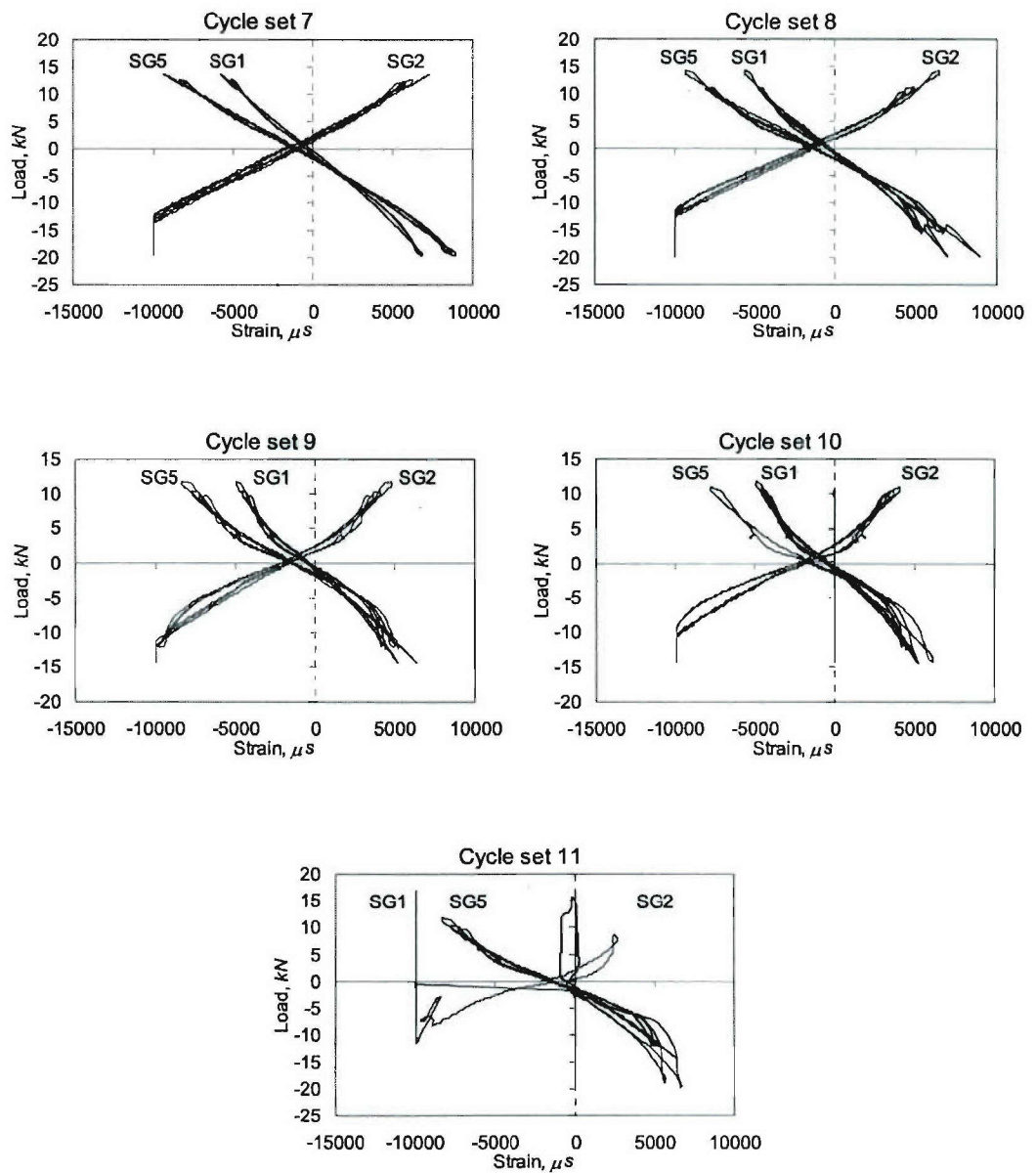


**Figure F.28. Load-Strain Curves for Specimen DL-7, Cycle Sets 7-12**

## **Appendix G**

### **Assembly of Stiffened Panels and Doubler Plates onto the Hydrostatic Test Tank**

#### **Appendix G.1. Phase 1: Sealing of the Steel Flange/Composite Panel Interfaces**

1. Using jacks, raise the desired panel off the steel I-beam, with enough clearance to clean the surfaces and apply the sealant, as shown in Figure G.1.

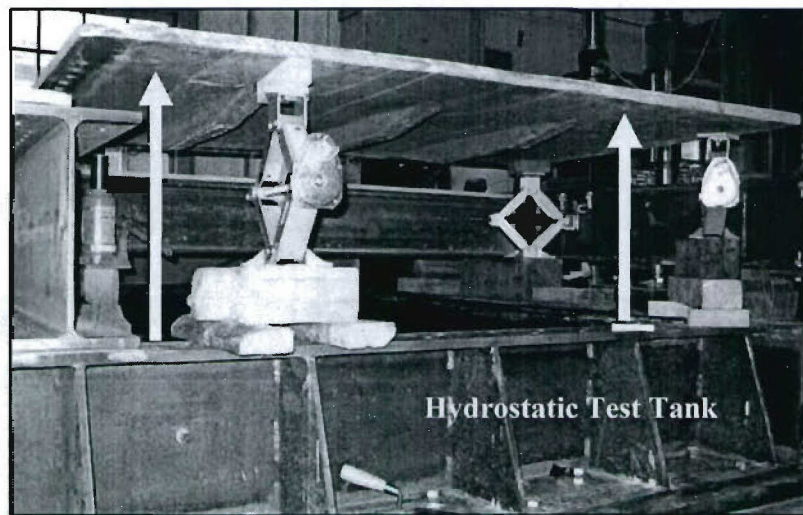


**Figure G.1. Small Panel Suspended off the Hydrostatic Test Tank**

2. Using aerosol parts cleaner, thoroughly clean the bottom surfaces of the panels, where they will interface with the steel flanges (Figure G.2).
3. Clean the top surfaces of the steel flanges, with aerosol parts cleaner (Figure G.2).

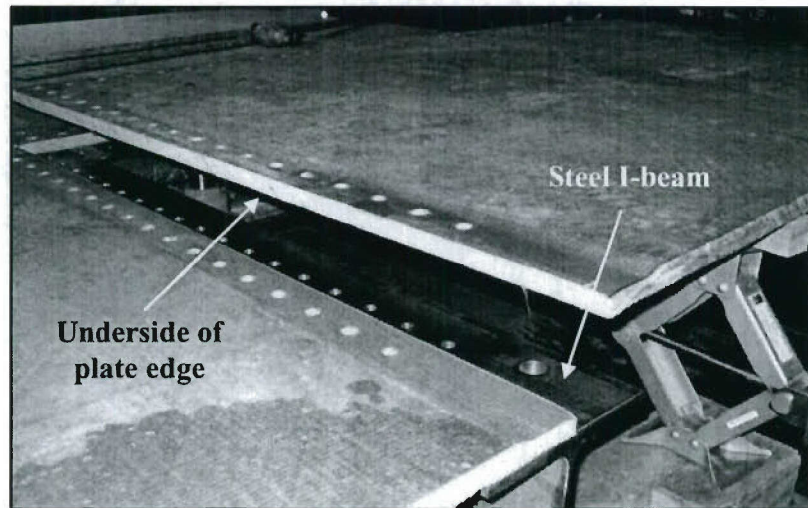


**Figure G.2. Steel I-beam and Small Panel Interfaces**

4. Apply the silicone sealant to the upper surface of the steel flanges, where it will interface with the bottom surface of the panels, as shown in Figure G.3. Two beads of sealant along the depth of the steel beam are recommended, to insure a uniform and continuous seal along the interfaces.

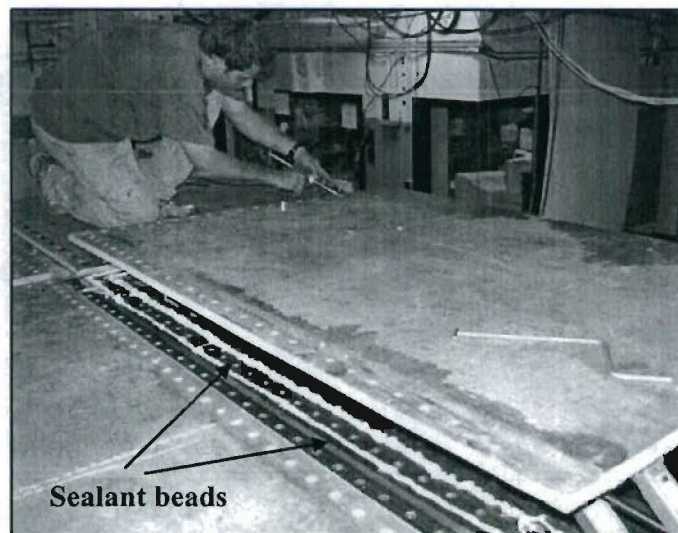


**Figure G.3. Application of Silicon Sealant at I-beam/Panel Interfaces**



5. Lower the panel into place, making sure that all holes align correctly. Installing bolts at the corners of the panel will enable proper and quicker alignment.
6. Once the panels have been aligned, install bolts at every other hole, on both rows. Figure G.4 shows the alignment and installation of the small panels onto the steel I-beam members.
7. Apply a small torque (beyond finger-tight) to the bolts, to achieve an even seal between interfaces. Begin with the corner bolt; then torque the bolts on alternating edges of the panel.

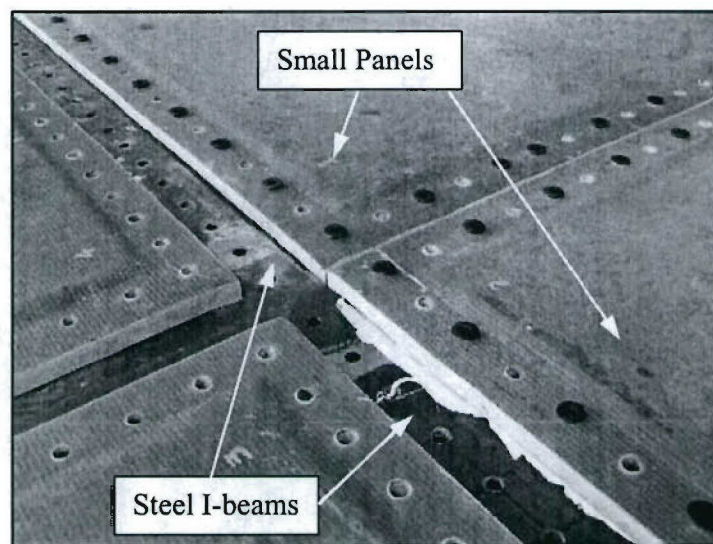


**Figure G.4. Alignment and Installation of Small Panels onto Steel I-Beams**

8. Remove any excess sealant from bolt holes, steel I-beam surfaces, and panel surfaces (the tack-free time for a typical RTV silicone sealant is approximately 30 minutes.)
9. Clamp the outer edges of the panel to the I-beam member, as shown in Figure G.5.

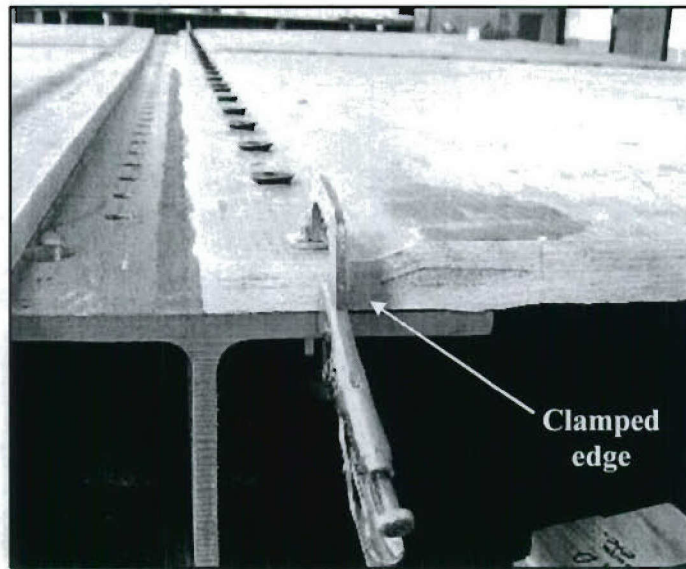


**Figure G.5. Clamped Outer Edge of the Composite Panel to the Steel I-Beam**

10. Allow sealant to cure overnight. Preliminary sealant tests showed that, for bolted joint applications, the sealant will require a longer cure time than that shown in the specifications. Figure G.6 shows the cured silicone sealant at the composite/steel interface.

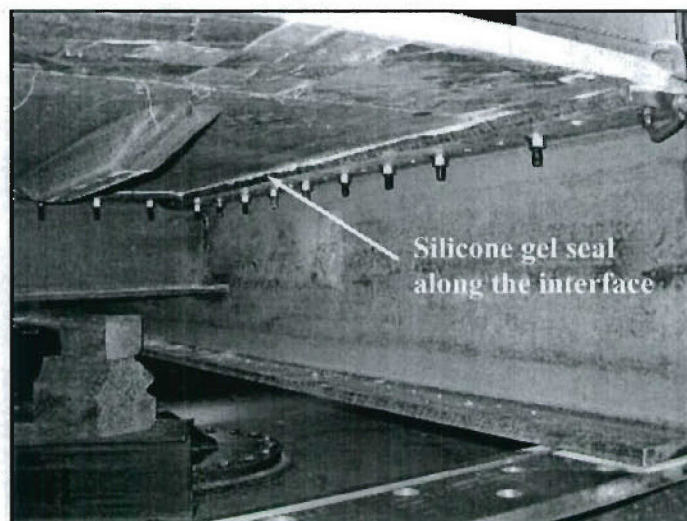


**Figure G.6. Small Panel with Cured Silicone Seal along the Composite/Steel Interface**

11. Repeat steps 1 through 10 for panels 2, 3 and 4. [Note: the interfaces between panels 1 and 2 and the steel I-beam were sealed on the same day (07-18-04) and allowed to cure for over 48 hours. The large panels (3 and 4) were sealed at a later date (07-25-04)].
12. Fill the seams between the edges of the panels with silicone sealant and smooth-flush with panels. Begin at the center of the panel, working the silicone gel outwardly, as shown in Figure G.7.

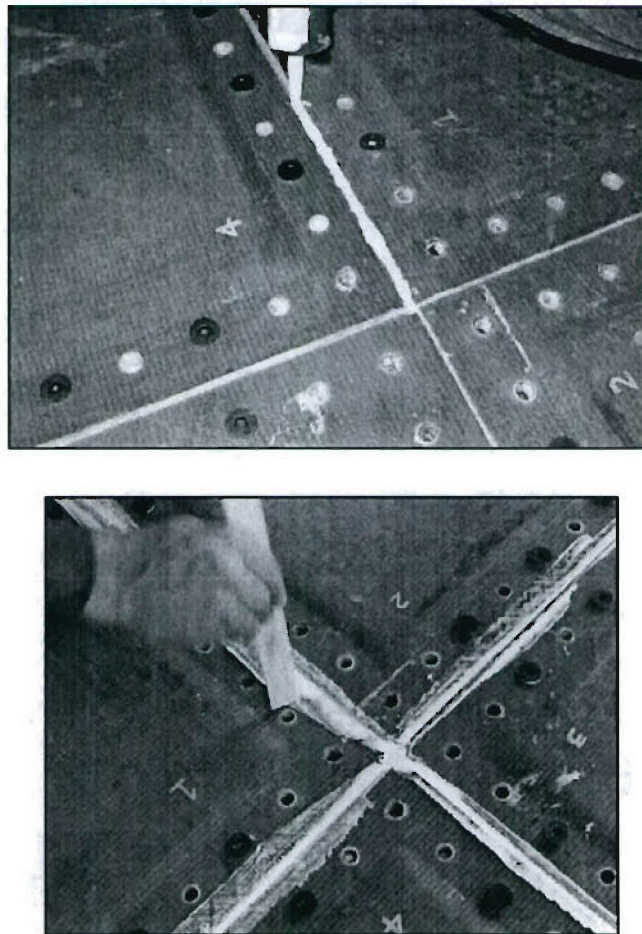


**Figure G.7. Application of the Silicone Sealant at the Panel Seams**

13. Allow the sealant to cure for a period of at least 48 hours.

## **Appendix G.2. Phase 2: Sealing of the Composite/Doubler Interfaces and Installation of the Doubler Plates**

1. Align the doubler centerpiece with the four inner corners of the composite panels and install bolts to insure a proper fit, as shown in Figure G.8.

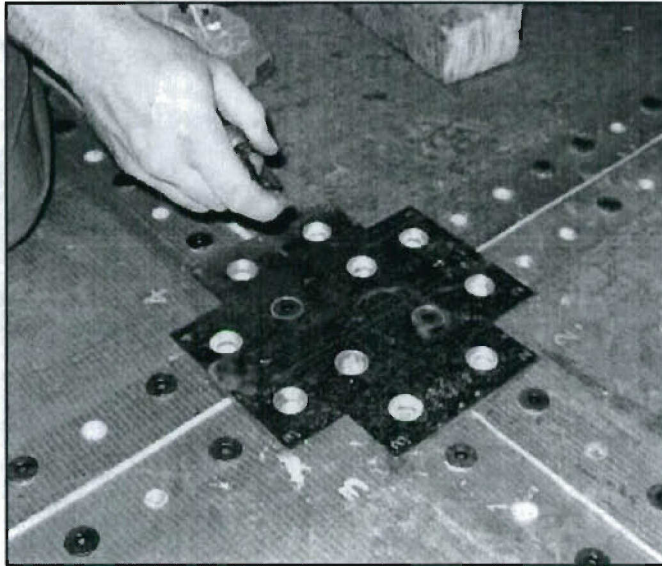


**Figure G.8. Alignment of Doubler Centerpiece and Composite Panels**

2. Remove bolts and doubler centerpiece.
3. Thoroughly clean all surfaces of the panels and surfaces of the doubler plates, with parts cleaner.
4. Apply the silicone sealant to the top surfaces of the panel assembly that will interface with the doubler centerpiece (see pattern shown in Figure G.9).



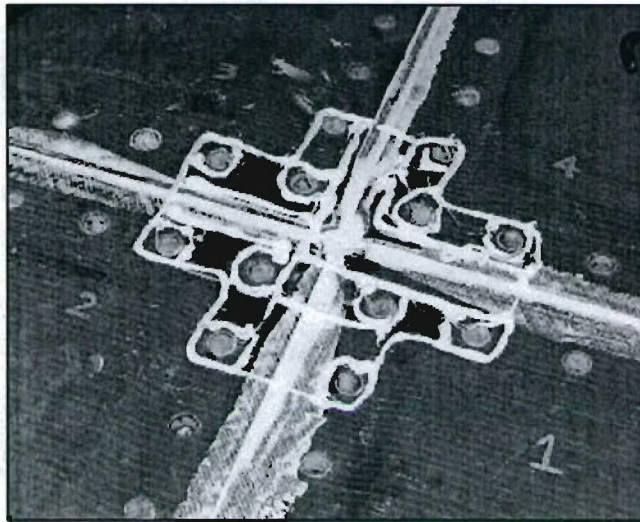


**Figure G.9. Application of the Silicone Sealant to the Top Surfaces of the Composite Panels**

5. Set doubler centerpiece on top of the composite panel corners, making sure that all holes align properly.
6. Install all bolts, without applying any torque.
7. Spray all bolts with anti-seize lubricant and install washers and nuts.
8. Apply a finger-tight torque to all bolts.
9. Apply 50 percent of the specified torque (25 ft-lb) using the torque pattern shown in Figure G.10. Begin with the bolts at the center of the doubler centerpiece and then move to the outside bolts.
10. Using the same torque pattern, apply 100 percent of the specified torque to the bolts.

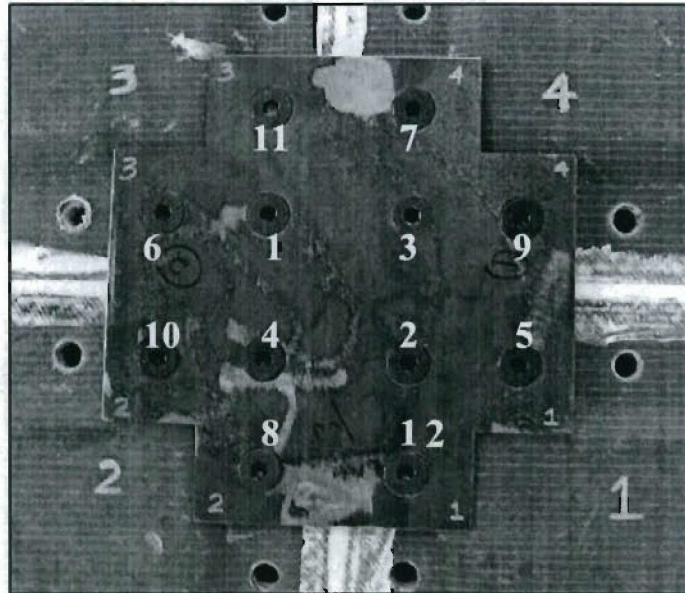


**Figure G.10. Bolt Torque Pattern Used for Installation of the Doubler Centerpiece**

11. Align the doubler plate with the edges of the composite panels and install corner bolts, to insure a proper fit.
12. Remove bolts and doubler plate.
13. Thoroughly clean all surfaces of the panels and surfaces of the doubler plates, using parts cleaner.
14. Apply the silicone sealant to the top surfaces of the panel assembly that will interface with the doubler plates, shown in Figure G.11. Using four beads of sealant is recommended for a proper sealant distribution at the interfaces.

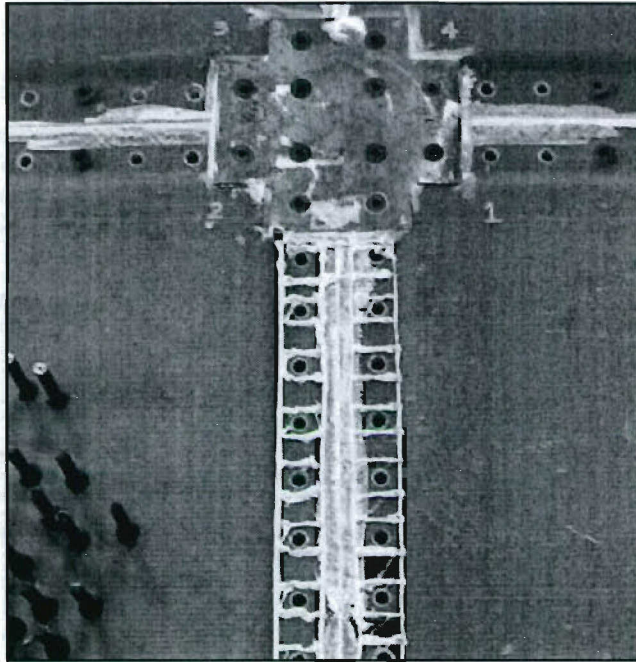


**Figure G.11. Application of Silicone Sealant at the Composite/Doubler Interfaces**

15. Set the doubler piece in place, installing two corner bolts, to insure proper alignment, as shown in Figure G.12.

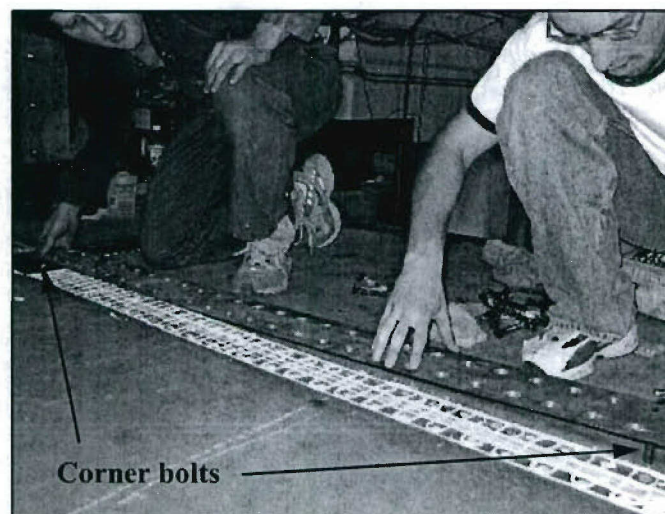


**Figure G.12. Application of Silicone Sealant at the Composite/Doubler Interfaces**

16. Install all bolts.
17. Spray all bolts with anti-seize lubricant and install washers and nuts.
18. Apply a finger-tight torque.
19. Starting with the bolts closest to the doubler centerpiece, apply 50 percent of the specified torque (25 ft-lb). Apply torque to the remaining bolts, working towards the outside edge, in the direction of the arrows shown in Figure G.13.

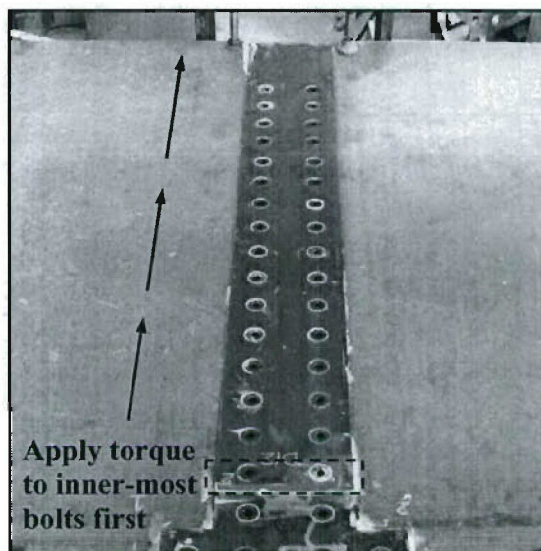


**Figure G.13. Torque Direction for Installation of Doubler Plates**

20. Using the same torque pattern in Figure G.13, apply 100 percent of the specified torque to the bolts. Clamp the outer edges of the doubler (towards the tank boundary) to achieve a uniform clamping pressure along the length of the doubler plate.
21. Repeat steps 11 through 20 for the remaining doubler plates, D23, D34, and D41. The assembled panel and doubler plate arrangement, after it sealing at the interfaces and after all bolts have been torqued to specifications, is shown in Figure G.14.



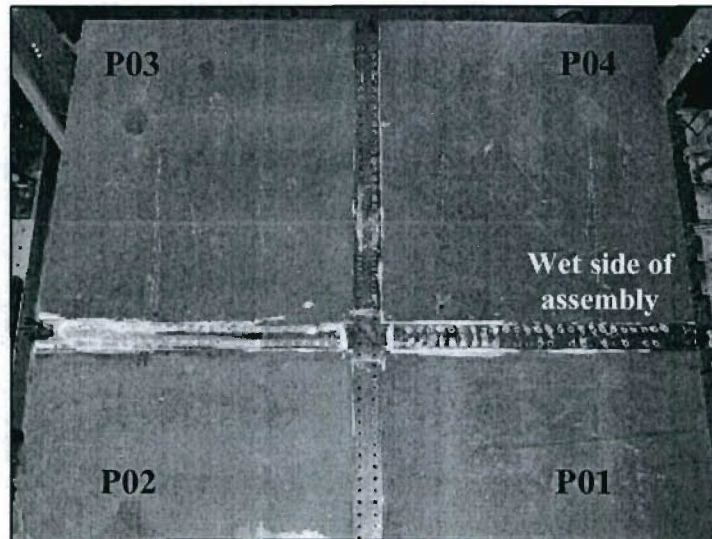


**Figure G.14. Wet Side of Hybrid Panel Assembly after Sealing and Installation of the Doubler Plates**

## Appendix H

### Load versus Displacement Plots of Stiffened Panels

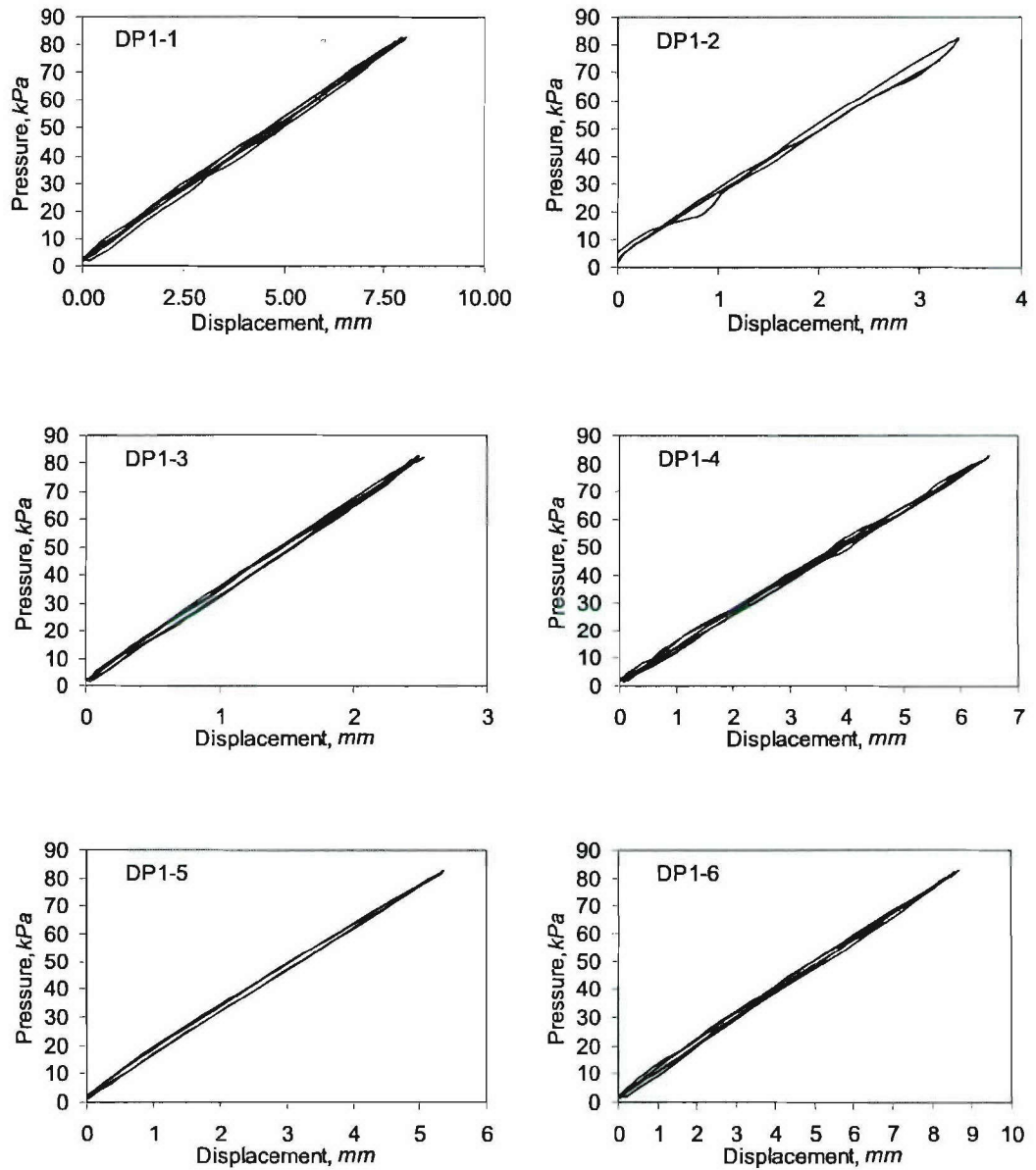
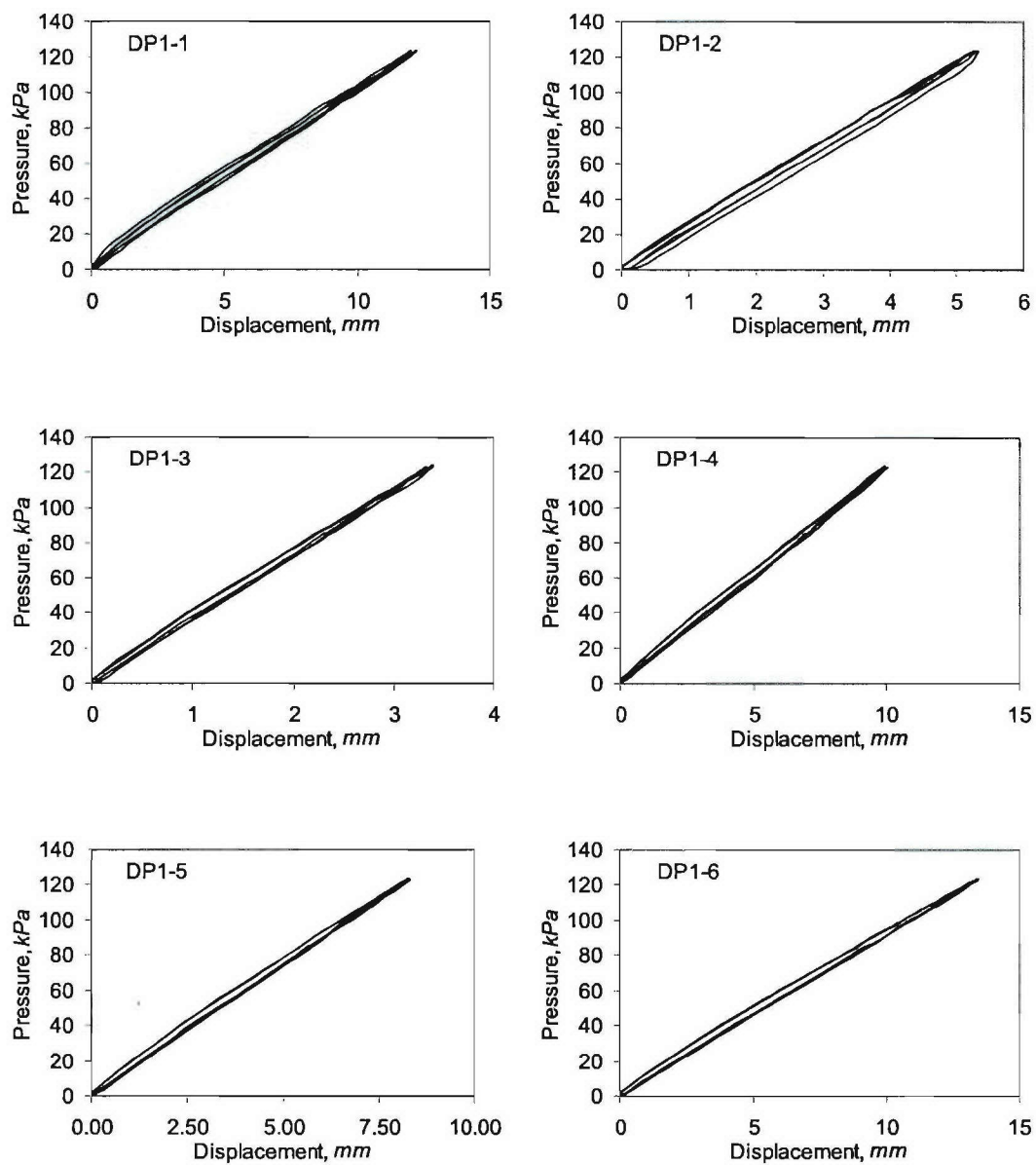
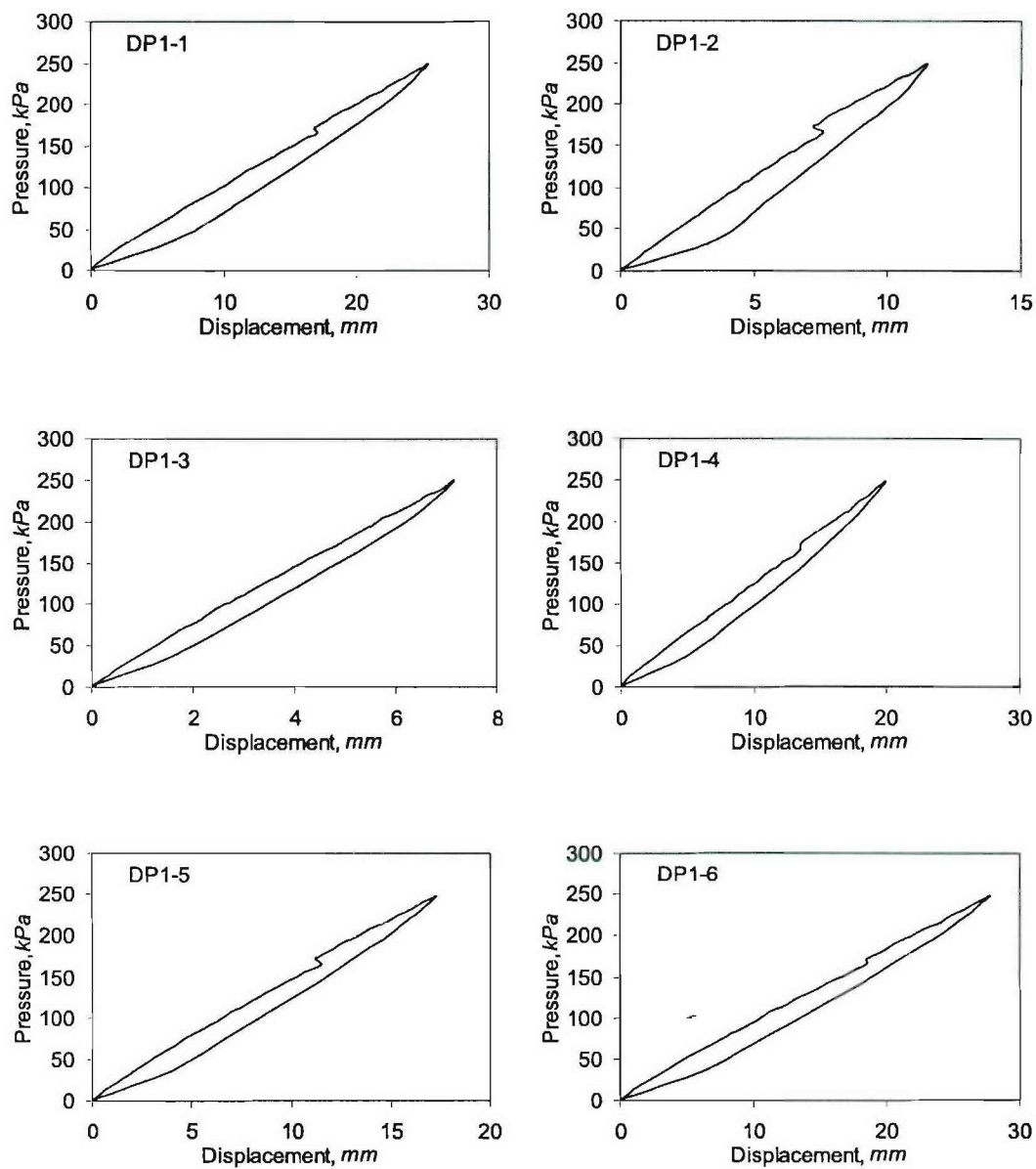


Figure H.1. Load versus Displacement Curves for P01 at 82.74 kPa



**Figure H.2. Load versus Displacement Curves for P01 at 124 kPa**



**Figure H.3. Load versus Displacement Curves for P01 at 248 kPa**



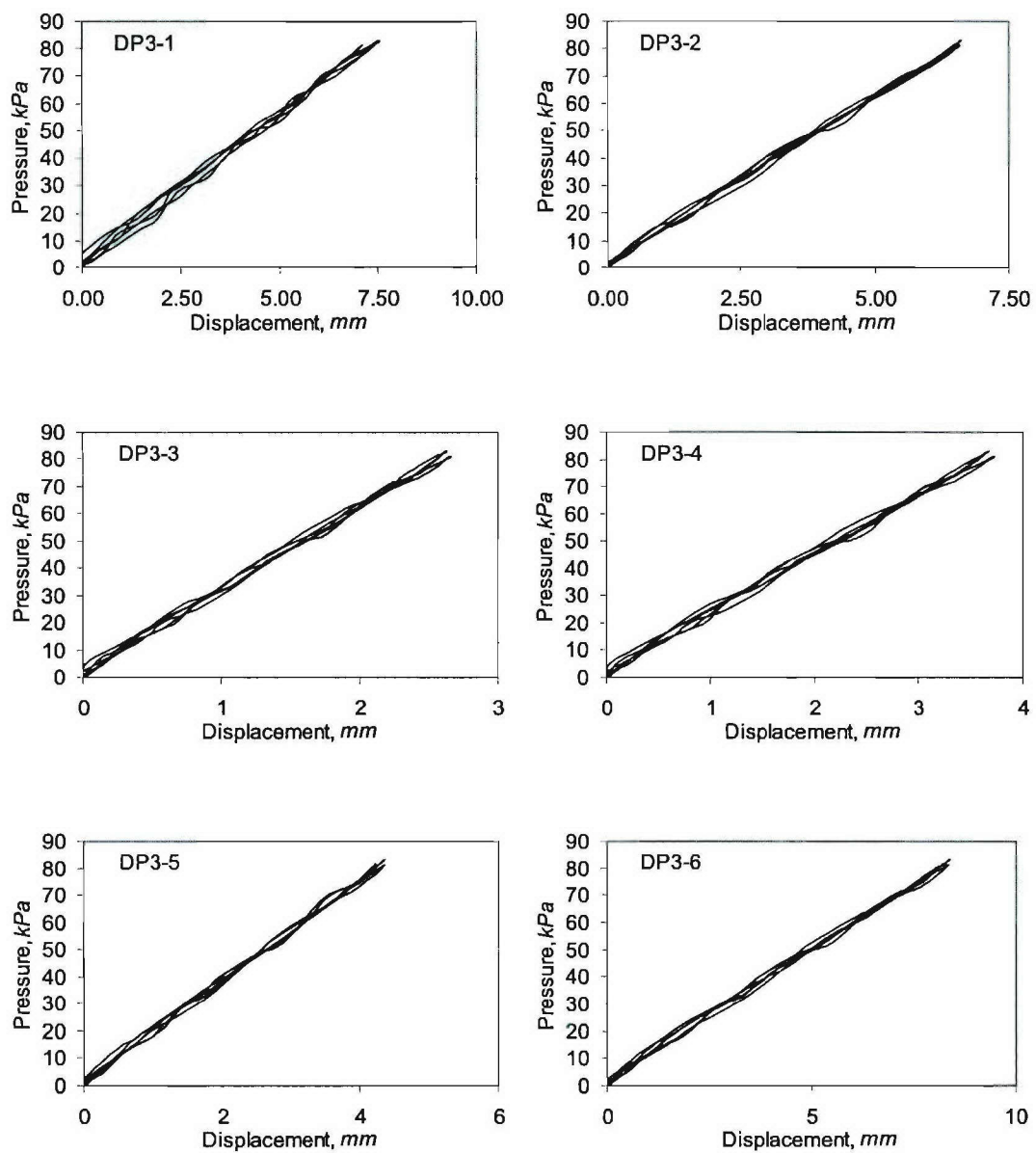


**Figure H.4. Load versus Displacement Curves for P03 at 82.74 kPa**

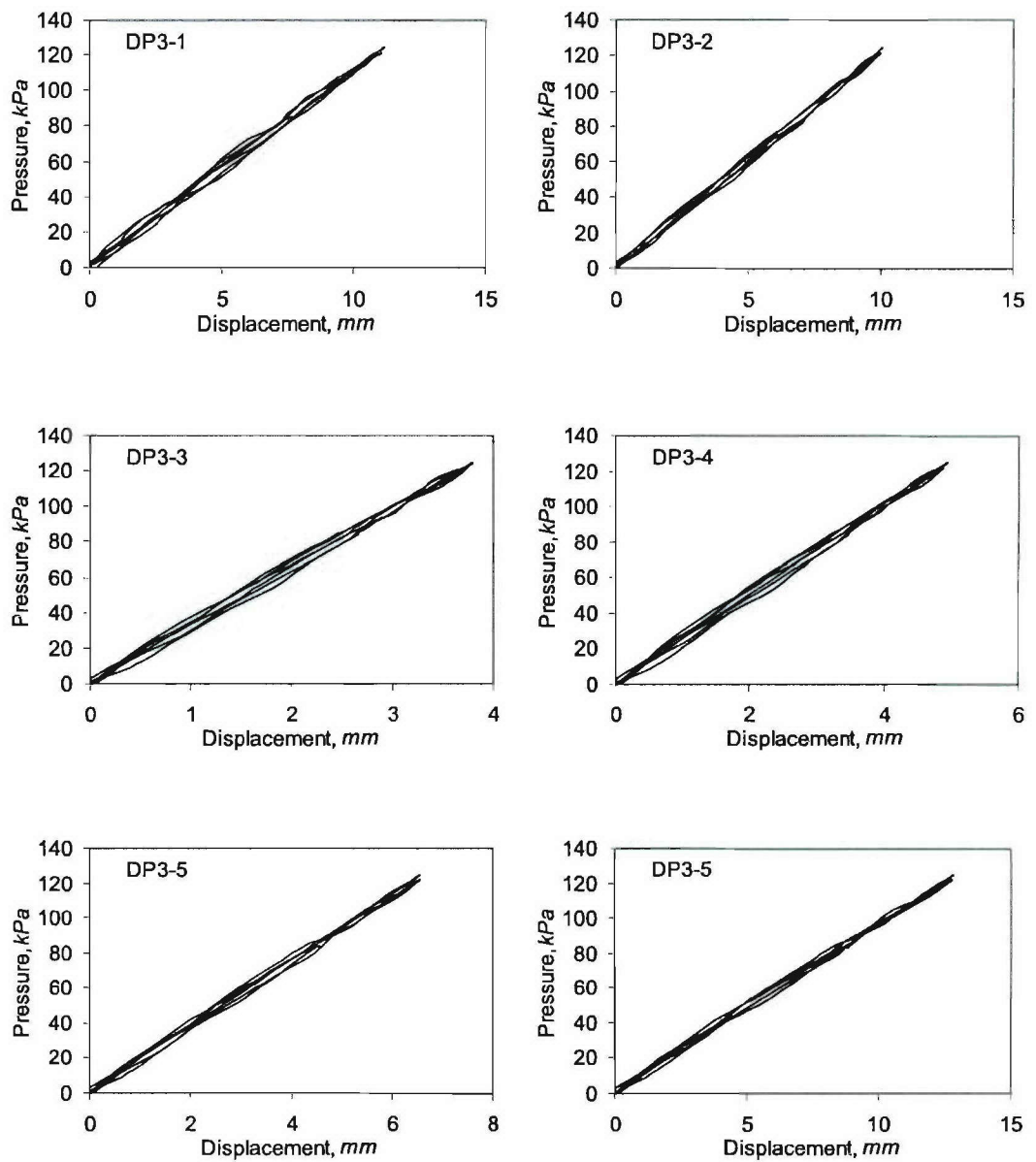


**Figure H.5. Load versus Displacement Curves for P03 at 124 kPa**

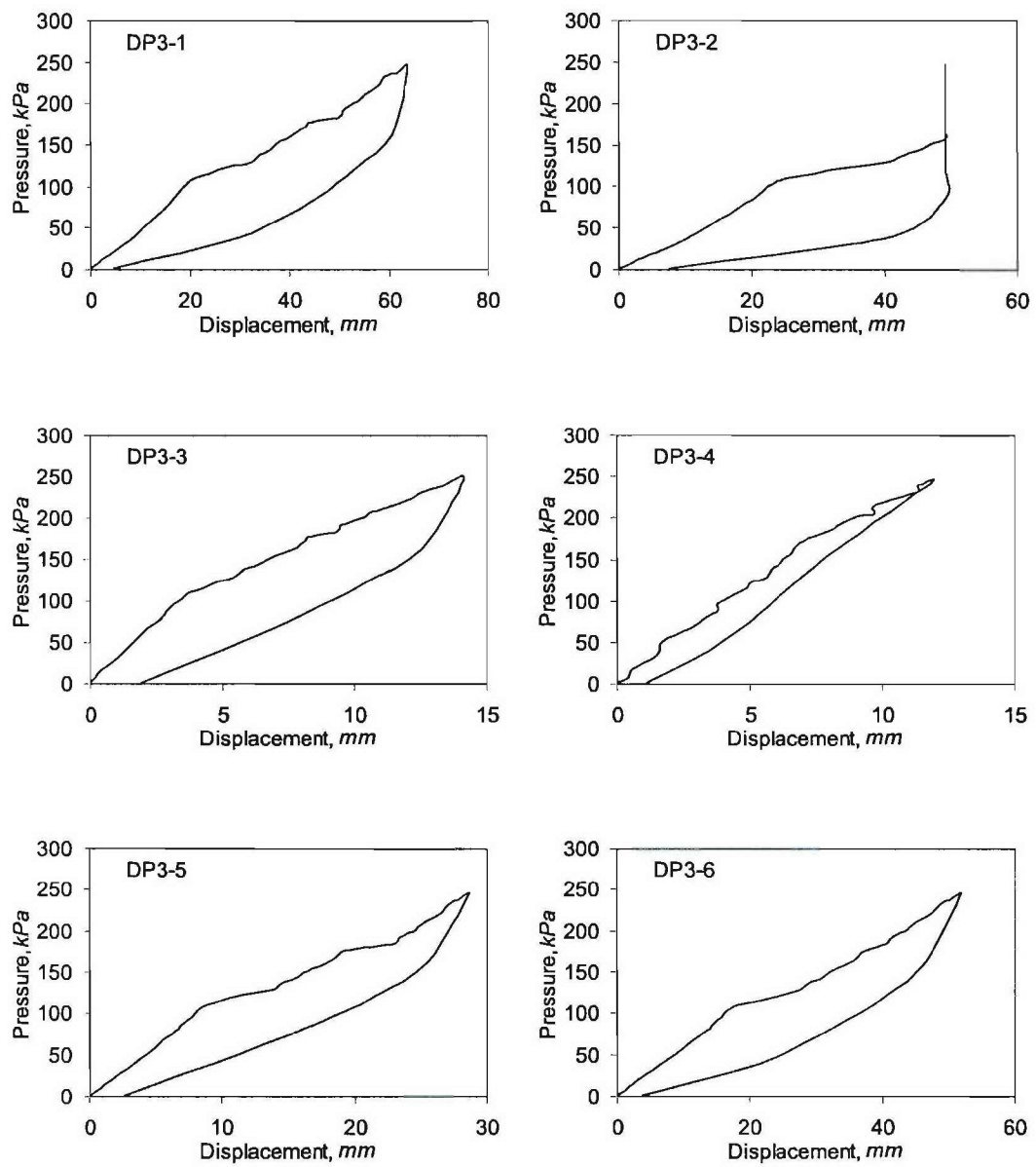


**Figure H.6. Load versus Displacement Curves for P03 at 248 kPa**

<b>REPORT DOCUMENTATION PAGE</b>				Form Approved OMB No. 0704-0188	
Public reporting burden for this collection of information is estimated to average 1 hour per response, including the time for reviewing instructions, searching data sources, gathering and maintaining the data needed, and completing and reviewing the collection of information. Send comments regarding this burden estimate or any other aspect of this collection of information, including suggestions for reducing this burden to Washington Headquarters Service, Directorate for Information Operations and Reports, 1215 Jefferson Davis Highway, Suite 1204, Arlington, VA 22202-4302, and to the Office of Management and Budget, Paperwork Reduction Project (0704-0188) Washington, DC 20503.					
<b>PLEASE DO NOT RETURN YOUR FORM TO THE ABOVE ADDRESS.</b>					
<b>1. REPORT DATE (DD-MM-YYYY)</b> 1-Mar-2006		<b>2. REPORT TYPE</b> Final Report		<b>3. DATES COVERED (From - To)</b> 1-April-2002 to 31-Dec-2005	
<b>4. TITLE AND SUBTITLE</b>  Testing and Analysis of Hybrid Composite/Metal Connections and Hull Section for the MACH Project				<b>5a. CONTRACT NUMBER</b>	
				<b>5b. GRANT NUMBER</b> N00014-01-1-0916	
				<b>5c. PROGRAM ELEMENT NUMBER</b>	
<b>6. AUTHOR(S)</b>  Kabche, Jean-Paul Caccese, Vincent Berube, K. A.				<b>5d. PROJECT NUMBER</b>	
				<b>5e. TASK NUMBER</b>	
				<b>5f. WORK UNIT NUMBER</b>	
<b>7. PERFORMING ORGANIZATION NAME(S) AND ADDRESS(ES)</b> University of Maine Office of Research and Sponsored Programs 5717 Corbett Hall Orono, ME 04469-5717				<b>8. PERFORMING ORGANIZATION REPORT NUMBER</b>  UM-MACH-RPT-01-01	
<b>9. SPONSORING/MONITORING AGENCY NAME(S) AND ADDRESS(ES)</b>  Office of Naval Research Ballston Center Tower One 800 North Quincy St. Arlington, VA 22217-5660				<b>10. SPONSOR/MONITOR'S ACRONYM(S)</b>  ONR	
				<b>11. SPONSORING/MONITORING AGENCY REPORT NUMBER</b>	
<b>12. DISTRIBUTION AVAILABILITY STATEMENT</b>  Approved for Public Release, Distribution is Unlimited					
<b>13. SUPPLEMENTARY NOTES</b>					
<b>14. ABSTRACT</b> This report summarizes the development and testing of hybrid composite metal connections and hybrid structural systems under the Modular Advanced Composite Hullform (MACH) project. Included is a description of test performed on sub-scale hybrid bolted connections where the objective was to develop watertight connections for removable panels. An experimental study was conducted to quantify the performance of numerous hybrid joints with various geometries, loaded in flexure. The test results showed that for resisting bending loads joints with doubler plates can be made stronger and stiffer than standard bolted joints, while also mitigating opening of the joint, thereby improving the ability to seal the connection for watertight integrity. The results of this study were used to select connection geometry, which was incorporated into the hydrostatic testing of a full-scale four-panel assembly. Testing of the assembly is described in this report and shows that a linear response of the system was observed up to its design pressure load of 82.74 kPa. Damage initiated as stiffener delamination at 1.4 times the design load. After failure of several stiffeners, the hybrid assembly withstood up to 3 times its design load without leakage. Hence, the response of the hybrid joint employed was deemed successful, as watertight integrity was achieved. Numerical analysis of the connections and assembly are also presented. Simplified shell finite element models were developed at both local and global levels. These models were adequate to model the joint stiffness and good correlation with the test results was observed. Strength of the system was predicted using detailed plane strain contact models to capture the 3-dimensional effects of the connection.					
<b>15. SUBJECT TERMS</b>  Hybrid Structures; Connection Design; Bolted Connections; Composites; Finite Element Analysis; Contact Analysis					
<b>16. SECURITY CLASSIFICATION OF:</b>			<b>17. LIMITATION OF ABSTRACT</b>  UU	<b>18. NUMBER OF PAGES</b>  348	<b>19a. NAME OF RESPONSIBLE PERSON</b> Vincent Caccese
a. REPORT U	b. ABSTRACT U	c. THIS PAGE U			<b>19b. TELEPHONE NUMBER (Include area code)</b> (207) 581-2131